Local Variation of Heat and Mass Transfer for Flow Over a Cavity and on a Flat Plate

A DISSERTATION
SUBMITTED TO THE FACULTY OF THE GRADUATE
SCHOOL OF THE UNIVERSITY OF MINNESOTA
BY

Matthew E. Taliaferro

IN PARTIAL FULFILLMENT OF THE REQUIREMENTS
FOR THE DEGREE OF
DOCTOR OF PHILOSOPHY

Professor Richard J. Goldstein, Adviser

September 2017

Acknowledgments

Choosing a PhD student requires a large risk on the part of the advisor, and I am grateful that Professor Goldstein took the chance and hired me. Working for him has been a great honor and pleasure. I can never thank you enough.

The OpenFOAM numerical simulations in section 2.1 were mostly set up and run by Dr. Matteo Angelino, and his continued help on otherOpenFOAM simulations are appreciated. Dr. John Gorman and Christopher Smith for their help on ANSYS CFX. What would have been three to four months of time spent on the turbulent numerical simulations was instead only a month because of their help.

Professors Terrance Simon and Alptekin Aksan always had generous open door policy. Professor Simon was always willing to patiently answer my numerous questions on experimental heat transfer, while Professor Aksan was very generous with professional advice.

The machine shop was always extremely helpful to students that might've had a theoretical understanding of engineering, but little practical experience. Many thanks to Pam Wilson, her efforts helping me during the construction on the old ME building ensured the experiments were finished. Not sure how I could have completed this thesis without her. Many thanks to John Gardner who patiently answers the same questions from multiple graduate students everyday. The questions are new to me and your guidance is invaluable.

Finally, Susan Johnson. Your proof reading of this thesis was immensely helpful. Any errors, grammatical or otherwise, are solely my responsibility.

Dedication

To my wife, this dissertation is as much yours as it is mine. We have both dreamed of finishing this thesis, and have both dreamed of what might come after:

Had I the heavens' embroidered cloths,
Enwrought with golden and silver light,
The blue and the dim and the dark cloths
Of night and light and the half light,
I would spread the cloths under your feet:
But I, being poor, have only my dreams;
I have spread my dreams under your feet;
Tread softly because you tread on my dreams.

— W. B. Yeats

In no particular order: my dad, and mom, and Nate, and Josh

Abstract

Boundary layer theory for flat plates is fundamental to our understanding of fluid flow and heat transfer. However, most of the experimental and analytical work for thermal boundary layers focus on streamwise effects. Lateral changes of heat and mass transfer near a lateral singularity in the surface boundary conditions have not been as extensively studied. Lateral heat transfer is studied using OpenFOAM to run numerical simulations for heated strips of varying width, fluids with varying thermal properties, separation lengths, and unheated starting lengths. Turbulent mass transfer is studied using the naphthalene sublimation technique for heated strips of varying depths, widths, and freestream velocities. The lateral edge effect is found to scale with the conduction thickness for both turbulent and laminar boundary layer flows. For laminar boundary layer flow the lateral edge effect extends approximately three conduction thicknesses into the flow, while for turbulent boundary layer flow it extends approximately ten conduction thicknesses into the flow. The results are useful for modeling heat transfer from discrete electronic components. In addition, the results should serve as useful benchmarks for numerical fluid models and computations where lateral transport is important.

Table of Contents

List of Tables

List of Figures

Nomenclature

Variables

English symbols

A_λ, B_λ	Eigencoefficients
c_f	Skin friction coefficient, $\frac{\tau}{\frac{1}{2}\rho U_\infty^2}$
c_p	Specific heat at constant pressure ($\mathrm{J\,kg^{-1}\,K^{-1}}$)
C	Mass concentration, $\mathrm{kg_{solute}/kg_{mixture}}$
d	Cavity depth, m
$\mathcal{D}$	Diffusion coefficient ($\mathrm{m^2\,s^{-1}}$)
$\mathcal{E}$	Voltage reading (V)
f	Stream function from Blasius solution
h	Heat transfer coefficient, $\dot{q}''/\left(T_w - T_\infty\right)$ ($\mathrm{W\,m^{-2}\,K^{-1}}$)
h_m	Mass transfer coefficient, $\dot{m}''/\left(C_w - C_\infty\right)$ ($\mathrm{kg\,s^{-1}\,m^{-2}}$)
H	Profile shape factor, $(n+2)/n$
k	Thermal conductivity ($\mathrm{W\,m^{-1}\,K^{-1}}$)
K	Acceleration parameter, $\frac{\nu}{\overline{U}_\infty^2}\frac{d\overline{U}_\infty}{dx}$
L	Length of mass transfer plate (m)
$L_{s,g}$	Latent heat of subliming ($\mathrm{J\,kg^{-1}}$)

$\dot{m}$	Mass mass transfer ($\mathrm{kg\,s^{-1}}$)
$\mathcal{M}$	Molar mass ($\mathrm{kg\,kmol^{-1}}$)
Nu_l	Nusselt number with length scale l, $\frac{hl}{k}$
p	Exponent for p-norm, where the p-norm is $(\phi_1^p + \phi_2^p)^{1/p}$
P	Pressure (Pa)
Pr	Prandtl number $\frac{c_p \mu}{k}$
$\dot{q}$	Heat transfer (W)
$\mathcal{R}$	Ideal gas constant, $8314.4598\,\mathrm{J\,kmol^{-1}\,K^{-1}}$
Re_l	Reynolds number with length scale l, $\frac{\overline{U}_\infty l}{\nu}$
Sc	Schmidt number, $\frac{\nu}{\mathcal{D}}$
Sh_l	Sherwood number with length scale l, $\frac{h_m l}{\rho \mathcal{D}}$
St	Stanton number $\frac{h}{\rho c_p \overline{U}_\infty}$
St_m	Mass Stanton number, $\frac{\bar{g}_m}{\rho \overline{U}_\infty}$
T	Temperature (K)
Tu	Turbulence intensity, $\frac{\overline{u'}}{\overline{U}}$
U_∞	Freestream velocity ($\mathrm{m\,s^{-1}}$)
$\overline{U}_\infty$	Average freestream velocity ($\mathrm{m\,s^{-1}}$)
$\vec{V}$	Velocity vector with components u, v, w ($\mathrm{m\,s^{-1}}$)
u	Velocity in the x direction ($\mathrm{m\,s^{-1}}$)
u_τ	Friction velocity at the wall, $\sqrt{\tau/\rho}$ ($\mathrm{m\,s^{-1}}$)
v	Velocity in the y direction ($\mathrm{m\,s^{-1}}$)
w	Velocity in the z direction ($\mathrm{m\,s^{-1}}$)
w_1	Half width of heated strip (m)
w_1^*	Nondimensional half width of heated strip, w_1/Δ_c
w_2	Half width of "cooled" strip (m)
w_2^*	Nondimensional half width of "cooled" strip, w_2/Δ_c

W	Width of subliming strip (m)
x	Streamwise distance from the start of mass transfer plate or the backward facing step of a cavity (m)
x'	Streamwise distance from the virtual origin of the turbulent boundary layer (m)
y	Distance normal to the mass transfer plate (m)
z	Lateral distance from edge of heated surface, positive towards the center of the heated surface (m)

Greek symbols

α	Thermal diffusivity, $k/\rho c_p$ ($\mathrm{m\,s^{-2}}$)
δ	Depth or height (m)
δ_1	Displacement thickness, $\int_0^\infty \left(1 - \frac{u}{U_\infty}\right) dy$ (m)
δ_2	Momentum thickness, $\int_0^\infty \frac{u}{U_\infty} \left(1 - \frac{u}{U_\infty}\right) dy$ (m)
δ_{99}	Velocity boundary layer location where $u = 0.99\overline{U}_\infty$ (m)
Δ_c	Conduction thickness, k/h or x/Nu_x (m)
Δ_d	Mass diffusion thickness, $\rho\mathcal{D}/h_m$ or x/Sh_x (m)
ζ	z similarity variable for laminar flow, $z\sqrt{\frac{U_\infty}{\nu x}}$
ζ^*	Non-dimensional distance from lateral edge, z/Δ_c
ζ_m^*	Non-dimensional distance from lateral edge, z/Δ_d
η	y similarity variable for laminar flow, $y\sqrt{\frac{U_\infty}{\nu x}}$
θ	Temperature relative to freestream, $T - T_\infty$ (K)
κ	von Kármán constant, 0.41
λ	Eigenvalue (m)

μ	Dynamic viscosity ($\mathrm{Pa} \cdot \mathrm{s}$)
ν	Kinematic viscosity ($\mathrm{m}^2\,\mathrm{s}^{-1}$)
ξ	Unheated/inactive starting length (m)
π	Ratio between a circle's circumference and diameter
ρ	Density ($\mathrm{kg}\,\mathrm{m}^{-3}$)
σ^2	Variance
τ	Shear stress, $\mu\frac{\partial u}{\partial y}$
τ_t	Elapsed time (s)

Math symbols

$\nabla\phi$	Gradient of ϕ
$\nabla \cdot \vec{\phi}$	Divergence of $\vec{\phi}$
$\nabla \times \vec{\phi}$	Curl of $\vec{\phi}$
$\frac{\partial\phi}{\partial x}$	Partial derivative of ϕ with respect to x
$\exp(\phi)$	Raising Euler's number to power ϕ
$\sin(\phi)$	Sine of angle ϕ
$\cos(\phi)$	Cosine of angle ϕ
$\int_a^b \phi dx$	Integral of ϕ from a to b with respect to x
$\sum_{n=1}^{\infty} \phi_i$	Sum of ϕ_i across index n from one to infinity
$\Im(\phi)$	Imaginary component of ϕ
$\log(\phi)$	Natural logarithm ϕ
$\tan^{-1}(\phi)$	Arctangent of ϕ
$\mathrm{Li}_2(\phi)$	Dilogarithm of ϕ
$\sqrt{\phi}$	Square root of ϕ

Subscripts

a	Air
c	Centerline
css	Cubic smoothing spline
g	Gas
hw	Hotwire
∞	Evaluated in the free stream
j	Component of mixture
n	Naphthalene
NC	Natural convection
sat	Saturated
tc	Thermocouple
tp	Triple point of water
v	Vortex
VD	Van Driest
w	Evaluated at the wall
$z \to \infty$	Evaluated on the wall far from the lateral edge

Superscripts

$\overline{\phi}$	Averaged quantity
$'$	Turbulent fluctuation

$''$	Per unit area
$^+$	Wall coordinates
$\hat{\phi}$	Estimate of the true value of ϕ

Chapter 1

Introduction

1.1 Outline of Present Work

Thermal management of electronic systems is a multiscaled and increasingly important problem as miniaturization of electronic devices and circuits continues (Garimella et al. 2008). Particularly, heat transfer on the scale of the individual electronic components is an important design consideration for digital systems. The present study characterizes heat and mass transfer near the lateral edge of rectangular heat sources and subliming surfaces.

For laminar flow the present study characterizes the effects of varying the Prandtl number, unheated starting length, width of the heated elements, spacing between the heated elements, and surface boundary conditions on the heat transfer from a flat plate. The temperature field is solved numerically with OpenFOAM and the Blasius solution is used for velocity boundary layer. For turbulent flow the present study characterizes the effects of the free stream velocity, width of the subliming surface, and cavity depth on the mass transfer coefficient. To accomplish this, the present study will employ a naphthalene sublimation technique in a suction type wind tunnel at the Heat Transfer Laboratory.

The extent of the region affected by the lateral edge and general correlations for a the local heat and mass flux for a flat plate are presented. As conjugate heat transfer is expensive to fully model, the results can be used as boundary conditions for conduction modeling, eliminating the need to model the momentum and energy transport in the fluid. In addition, the results can serve as a benchmark for numerical simulations where lateral transport is important.

1.2 Theoretical Background

1.2.1 General Equations

The following two equations are the fundamental transport equations for energy (eq. (1.1)) and mass components (eq. (1.2)):

$$\rho c_p \left(\frac{\partial T}{\partial t} + \vec{V} \cdot \nabla T \right) = \nabla \cdot k \nabla T, \tag{1.1}$$

$$\rho \left(\frac{\partial C_j}{\partial t} + \vec{V} \cdot \nabla C_j \right) = \nabla \cdot \rho \mathcal{D}_j \nabla C_j. \tag{1.2}$$

The mass diffusion equation assumes no species creation through chemical reactions and the Soret and Dufour effects are neglected, as the temperature and concentration differences are relatively small. The thermal energy equation assumes there is only one species present, negligible viscous dissipation, and a constant specific heat.

Equations (1.1) and (1.2) are completely analogous, with the concentration field mapping to the temperature field when ρ is equivalent to ρc_p, and $\rho \mathcal{D}_j$ is equivalent to k. If the flow has constant properties, then $\frac{k}{\rho c_p}$ is equivalent to $\mathcal{D}_j$. This analogy is referred to as the heat-mass transfer analogy, and allows solutions with equivalent boundary conditions from one domain to be mapped to the other domain. For the tur-

bulent mass transfer experiments, a constant mass concentration boundary condition is realized, which is equivalent to a constant temperature boundary condition.

1.2.2 Turbulent Boundary Layer Equations

The mass concentration boundary layer is three dimensional near the edges of the mass transfer plate, so the spanwise gradients cannot be ignored. The following assumptions can be applied to the mass diffusion equation (eq. (1.2)) near the wall to derive the constant density mass diffusion boundary layer equation,

$$
\begin{gathered}
u \gg v, w, \\
w = 0, \\
\frac{\partial C_j}{\partial y}, \frac{\partial C_j}{\partial z} \gg \frac{\partial C_j}{\partial x}, \\
\frac{\partial^2 C_j}{\partial y^2}, \frac{\partial^2 C_j}{\partial z^2} \gg \frac{\partial^2 C_j}{\partial x^2}.
\end{gathered}
$$

Applying the listed assumptions yields,

$$
\frac{\partial C_j}{\partial t} + u\frac{\partial C_j}{\partial x} + v\frac{\partial C_j}{\partial y} = \frac{\partial}{\partial y}\left(\mathcal{D}_j \frac{\partial C_j}{\partial y}\right) + \frac{\partial}{\partial z}\left(\mathcal{D}_j \frac{\partial C_j}{\partial z}\right). \tag{1.3}
$$

Using Reynolds' decomposition on eq. (1.3) and time averaging the equation, the turbulent mass diffusion boundary layer equation is

$$
\frac{\partial \overline{C}_j}{\partial t} + \bar{u}\frac{\partial \overline{C}_j}{\partial x} + \bar{v}\frac{\partial \overline{C}_j}{\partial y} = \frac{\partial}{\partial y}\left(\mathcal{D}_j \frac{\partial \overline{C}_j}{\partial y} - \overline{v' C_j'}\right) + \frac{\partial}{\partial z}\left(\mathcal{D}_j \frac{\partial \overline{C}_j}{\partial z} - \overline{w' C_j'}\right). \tag{1.4}
$$

The relative strength of the transport by lateral diffusion, represented by the $\frac{\partial}{\partial z}\left(\mathcal{D}_j \frac{\partial \overline{C}_j}{\partial z}\right)$ term, and the transport by turbulent eddies, represented by the term $-\frac{\partial}{\partial z}\left(\overline{w' C_j'}\right)$, is explored and commented on in chapter 4.

1.2.3 Convection Equations

The constitutive relations for the heat and mass fluxes are

$$\dot{q}'' = -k\nabla T \tag{1.5}$$

$$\dot{m}_j'' = -\rho\mathcal{D}_j\nabla C_j. \tag{1.6}$$

Equations (1.5) and (1.6) are applicable for diffusive processes, and are used in eqs. (1.1) and (1.2) to model the diffusive fluxes. Note that this form of eq. (1.6) assumes an ideal mixture.

It is sometimes helpful to recast eqs. (1.5) and (1.6) as follows

$$\dot{q}'' = h\left(T_w - T_\infty\right) \tag{1.7}$$

$$\dot{m}'' = h_m\left(C_w - C_\infty\right). \tag{1.8}$$

These equations are more practical than eqs. (1.5) and (1.6) for calculating the fluxes; as gradients can be difficult to measure with the required precision, or difficult to compute for complex fluid flow. In addition, for many situations the fluxes scale with temperature or mass concentration differences, and the heat and mass transfer coefficients are relatively independent of temperature and concentration in forced convection situations.

1.3 Literature Review

1.3.1 Naphthalene Sublimation Technique

A common way of conducting mass transfer experiments is to use naphthalene as the subliming substance. Naphthalene is often used because it sublimes at room temperature, and is easy to cast and machine (Souza Mendes 1991).

There are several advantages to using the naphthalene sublimation method as opposed to conducting a heat transfer experiment. Boundary conditions are easier to apply to a mass transfer experiment than to a heat transfer experiment because conduction and radiation losses are not present in a mass transfer study. Also, local measurements of the flux values can be taken nonintrusively, as depth measurements are made before and after the forced convection takes place (Goldstein and Cho 1995).

It is worth mentioning several limitations of using the naphthalene sublimation method. First, the wall normal velocity can affect the boundary layer flow if the transpiration is large enough, invalidating the heat-mass transfer analogy for a no blowing condition. Second, the temperature of the mass transfer plate has to be fairly uniform, because of naphthalene properties' sensitivity to temperature changes. Third, if the velocity is too high, viscous dissipation effects can invalidate the heat-mass transfer analogy. Fourth, external high shear flows cannot be studied, as this will cause some of the naphthalene to erode from the surface instead of subliming. Fifth, it is difficult to get transient data as all the sublimed naphthalene depth values are time averaged. Last, the naphthalene surface profile can deviate from the original surface profile by too much due to sublimation from a long experiment (Goldstein and Cho 1995). All of these concerns will be addressed in section 3.3.4.

1.3.2 Electronic Cooling

Many techniques are described in published research for increasing and managing heat transfer from heat sinks and sources, such as flow through porous metal foam (Yang and Garimella 2010; Mancin et al. 2013), pin fins (Khan et al. 2006; Siu-Ho et al. 2007), increased surface roughness (Honda and Wei 2004; Ventola et al. 2014), and microchannels (Kandlikar 2012). Despite the attention electronic cooling has received, there is little understanding of three dimensional thermal boundary layer effects on heat transfer from flush discrete heat sources.

When three dimensional effects are studied, often the local heat transfer is not presented, and rarely are lateral changes explicitly discussed. Rather, heat transfer characteristics from discrete sources are most often presented in terms of averaged Nusselt numbers. Examples of heat transfer characteristics of discrete heat sources in the open literature are Baker (1972), Incropera et al. (1986), and Tso et al. (1999). Baker (1972) noticed that for small, discrete sources, the familiar two-dimensional correlations give heat fluxes one-third smaller than experimentally found heat fluxes. Baker (1972) speculated that the increase was due to conduction and edge effects of the smaller heat sources embedded in the substrate. In addition to Incropera et al. (1986) noting that the two-dimensional turbulent correlations are inadequate for predicting the heat transfer from discrete sources; both Incropera et al. (1986) and Tso et al. (1999) reported similar results for the effect of wakes from upstream heat sources. Their experimental results showed large decreases between the first, second, and third heat sources, but almost no changes between the third and fourth heat sources. Both studies also concluded that the thermal characteristics of heat transfer are more representative of external flow; as the channel height did not appreciably affect the Nusselt number.

Finite Width Plates

In addition to looking at both single and multiple discrete heating elements with conjugate heat transfer, Ortega and Ramanathan (2003a) report the effects of finite size on local heat transfer from discrete sources. Ortega and Ramanathan (2003a) analytically describe wakes of arbitrary arrays of heated elements and local Nusselt numbers from arbitrary shaped, heated elements by using point source solutions for the energy equation, assuming bulk flow with constant surface heat flux, and then superposing the point source solution to form a general equation for the convection losses from rectangles and line sources. Using the methods developed in Ortega and Ramanathan (2003a), Ortega and Ramanathan (2003b) present numerical results for the average Nusselt number for heated elements with a variety of aspect ratios and substrate conductivities. Instead of assuming constant heat flux, as Ortega and Ramanathan (2003a) do, Yovanovich and Teertstra (2001) report the average Nu for an isothermal plate by averaging the solutions for the diffusive limit and convective limit (i.e. for low and high Re).

Hauptmann and Rotem (1967) and Robbins (1969) looked at a three dimensional thermal boundary layer embedded in two dimensional boundary layer flow. Hauptmann and Rotem (1967) propose a similarity transformation to map the three spacial dimensions of the energy equation to two dimensions based on a spanwise and wall normal similarity variables. Robbins (1969) found analytical and numerical solutions for the thermal boundary layer, and compares it to his own experimental work for laminar flow. To numerically solve for the thermal profile, he used the Blasius solution for the velocity field, and numerically solved the similarity equations from Hauptmann and Rotem (1967). To analytically solve the thermal boundary layer equations, Robbins used a Lèvêque approximation and employed operational calculus

and Fourier transforms. However, because of the Lèvêque approximation, this solution is formally valid only as the Prandtl number approaches infinity, but Robbins (1969) reported accurate results for Prandtl numbers as low as one.

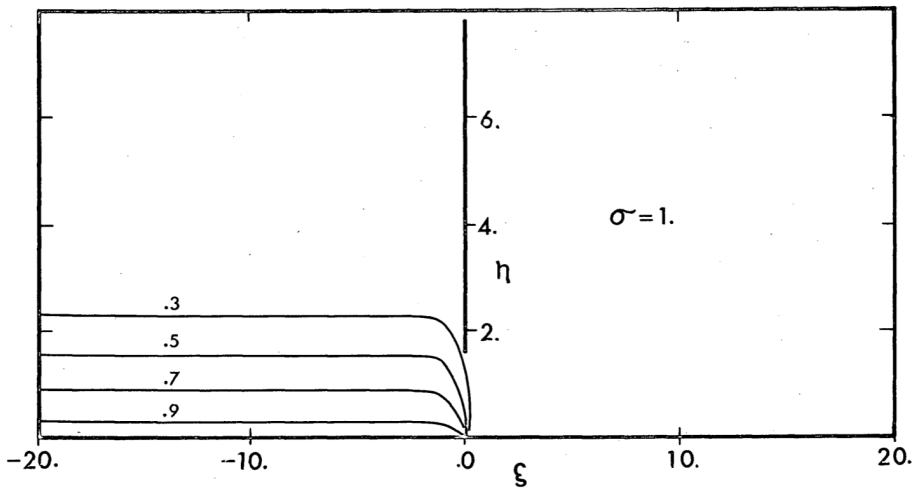

Figure 1.1: Nondimensional temperature contours for a constant temperature boundary condition, $\eta = y\sqrt{\frac{U_\infty}{\nu x}}$ and $\xi = z\sqrt{\frac{U_\infty}{\nu x}}$, $Pr = 1$,taken from Robbins (1969). Note Robbins (1969) denotes the Prandlt number using σ.

Fassio (2009) studied the lateral thermal boundary layer profile for turbulent flow. However, he only looked at the consequences of changing the flow speed in the wind tunnel, and did not look at other effects. Figure 1.2 shows the lateral profiles for the sublimed naphthalene depths at different streamwise locations at two different wind tunnel velocities. The dimensions for the subliming portion of Fassio's mass transfer plate are 121 mm × 197 mm (corresponding to the z and x directions). Overall, Fassio (2009) found that a complementary error function described both sets of data well, as shown below in fig. 1.3. In fig. 1.3, the abscissa is the distance from the edge of the plate normalized by the edge effect thickness.

Recently, Taliaferro et al. (2016) and Taliaferro et al. (2018) investigated heat transfer near a lateral edge of a flat plate in laminar and turbulent boundary layer flow. Using a conduction model, Taliaferro et al. (2016) describe the local variation

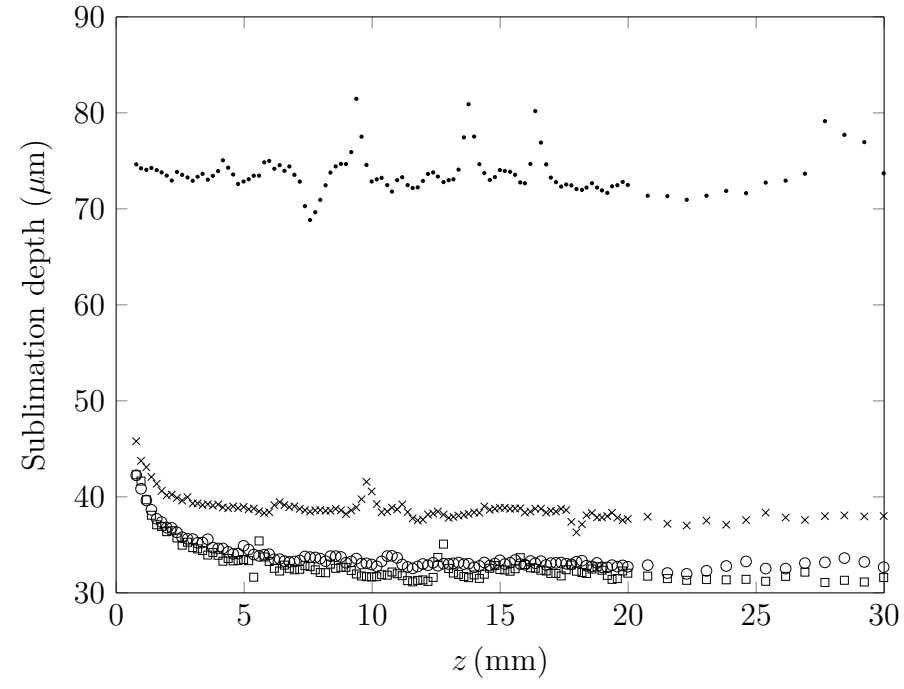

(a) $U_\infty = 3.93\,\mathrm{m\,s^{-1}}$

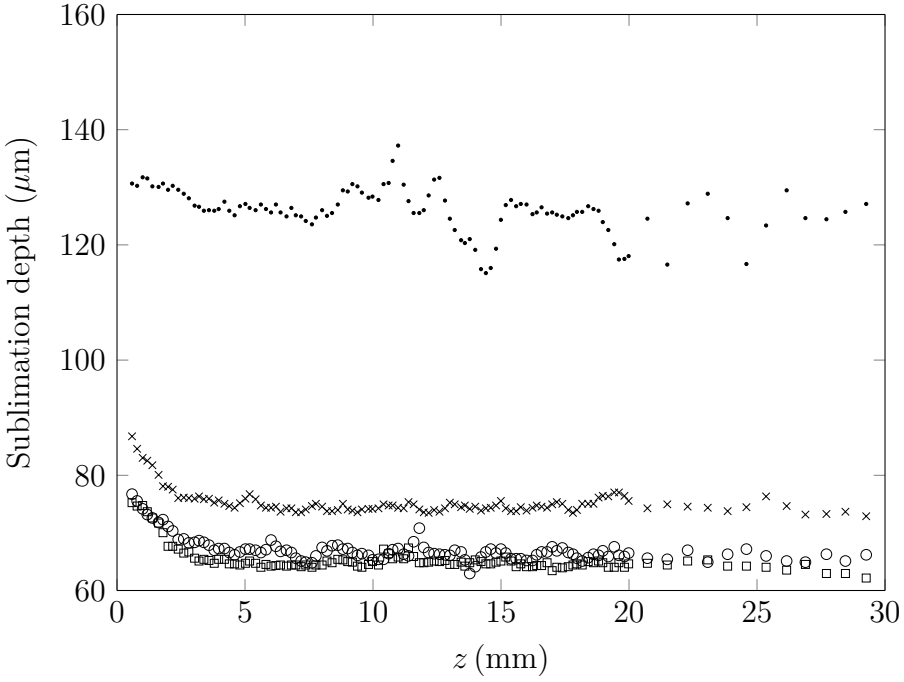

(b) $U_\infty = 13.6\,\mathrm{m\,s^{-1}}$

Figure 1.2: Change in surface height for the two free stream velocities at different stream wise locations. Symbols: • $x = 2\,\mathrm{mm}$, × $x = 31.3\,\mathrm{mm}$, ∘ $x = 89.9\,\mathrm{mm}$, □ $x = 129\,\mathrm{mm}$, taken from Fassio (2009)

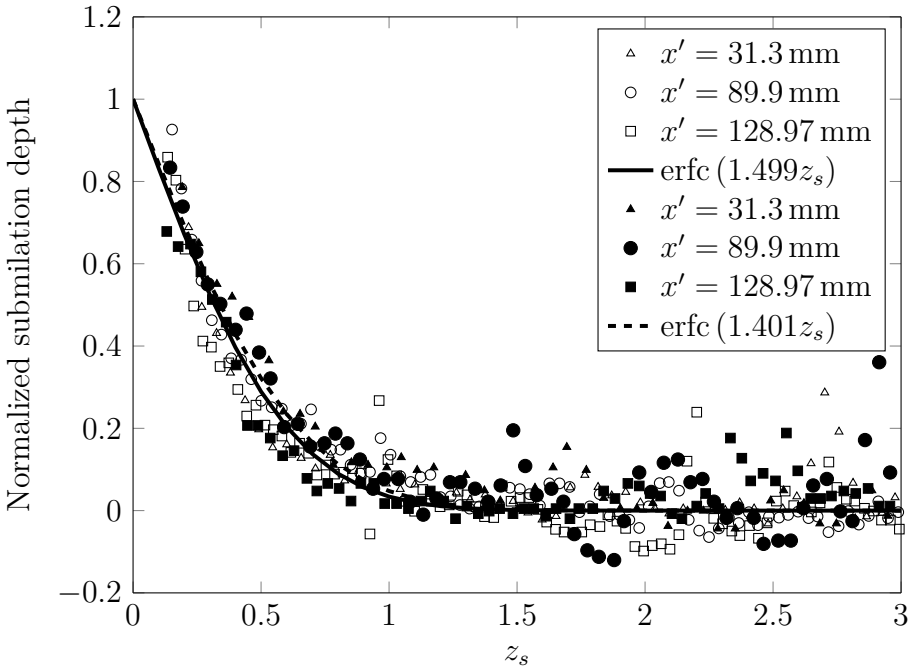

Figure 1.3: Dimensionless fit of lateral normalized sublimed naphthalene depth profile $\left(\frac{\delta_s - \delta_{c,s}}{\delta_{s,max} - \delta_{c,s}}\right)$ vs. the normalized lateral distance $\left(z_s = \frac{z}{\delta_e}\right)$, taken from Fassio (2009). The edge effect thickness is denoted as δ_e.

of heat transfer for fluids of a variety of Prandtl numbers, unheated starting lengths, and boundary conditions for laminar flow. Taliaferro et al. (2018) used the numerical and analytical results from Taliaferro et al. (2016) with experimental results from turbulent boundary layer flow to construct a correlation describing the local mass transfer near a lateral edge. The results of Taliaferro et al. (2016) are presented in section 2.1 and some of the discussion from Taliaferro et al. (2018) is presented in section 4.2.5.

1.3.3 Evaporation from Droplets

Evaporation from droplets is closely related to heat transfer from discrete sources, and useful for printing and coating processes. Deegan et al. (1997) describe how mass fluxes for a droplet with a pinned contact line causes a "coffee-ring" effect. As the

contact line is pinned, mass must flow towards the edges to maintain the droplet footprint on the surface, depositing suspended particles near the pinned contact line. Measurements by Deegan et al. (1997) and later measurements and numerical simulations by Hu and Larson (2002), describe mass transfer with a power law that tends towards infinity near the pinned edge, with exponent values of -0.5 for no contact angle and zero at a 90° contact angle. Deegan et al. (1997) used results from Jackson (1999) to estimate the local fluxes while Hu and Larson (2002) used results from finite element method simulations.

Chapter 2

Laminar Flow Over a Flat Plate

Lateral variation of the wall heat transfer in laminar boundary layer flow is investigated. For a geometry where both the heated and cooled/adiabatic surfaces are semi-infinite in lateral extent, both a similarity solution and a conduction model are compared to three dimensional numerical simulations for a variety of Prandtl numbers, boundary conditions, and unheated starting lengths. For a geometry where either (or both) heated and cooled/adiabatic surfaces are finite in lateral extent, no similarity solutions exist, so only the conduction model is compared to the three dimensional numerical simulations.

It is found that the conduction model works remarkably well at predicting the wall heat transfer and the most relevant length scale for describing the problem is the conduction thickness (see fig. 2.6). Knowing that the conduction thickness is the main length scale for describing the lateral change in heat transfer allows for the definition of a key dimensionless spanwise variable, z/Δ_c. Furthermore, the spanwise extent of the region affected by the lateral edge is of the same order of magnitude as the conduction thickness. Finally, the accuracy and computational simplicity of the conduction model allows for impressive savings in numerical modeling of conjugate heat transfer where lateral variation in heat transfer is important.

2.1 Semi-infinite Domain

The basic geometry for the semi-infinite heated plate is shown in fig. 2.1. The hot and "cold" plates are semi-infinite in lateral extent and meet at $z = 0$. The velocity is assumed to conform to the Blasius solution for laminar boundary layers.

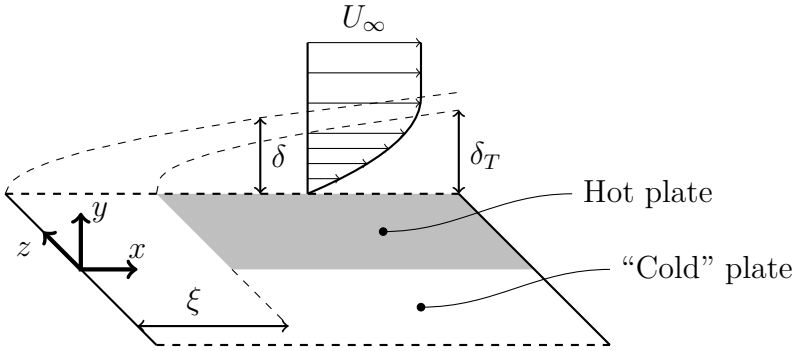

Figure 2.1: Sketch of the problem domain domain showing the unheated starting length, ξ, momentum boundary layer, δ, and thermal boundary layer, δ_T. The hot and "cold" plate are coincident at $z = 0$ and are of semi-infinite width.

The results discussed in section 2.1 appear in briefer form in Taliaferro et al. (2016).

2.1.1 Similarity Solution

Similarity Equation

If the streamwise conduction and lateral velocity are assumed negligible, then eq. (1.1) can be simplified for steady, constant property, laminar flow as shown in eq. (2.1).

$$u\frac{\partial T}{\partial x} + v\frac{\partial T}{\partial y} = \alpha\left(\frac{\partial^2 T}{\partial y^2} + \frac{\partial^2 T}{\partial z^2}\right) \tag{2.1}$$

Following the development described in Hauptmann and Rotem (1967), eq. (2.1) can be further simplified using the following similarity variable substitutions,

$$\theta = T - T_\infty, \quad \eta = y\sqrt{\frac{U_\infty}{\nu x}}, \quad \zeta = z\sqrt{\frac{U_\infty}{\nu x}}. \tag{2.2}$$

The new temperature derivatives are:

$$\begin{aligned}
\frac{\partial T}{\partial x} &= \frac{\partial \theta}{\partial \eta}\frac{\partial \eta}{\partial x} + \frac{\partial \theta}{\partial \zeta}\frac{\partial \zeta}{\partial x} \\
&= -\frac{\partial \theta}{\partial \eta}\frac{y}{2x}\sqrt{\frac{U_\infty}{\nu x}} - \frac{\partial \theta}{\partial \zeta}\frac{z}{2x}\sqrt{\frac{U_\infty}{\nu x}} \\
&= -\frac{1}{2x}\left(\eta\frac{\partial \theta}{\partial \eta} + \zeta\frac{\partial \theta}{\partial \zeta}\right) \qquad (2.3) \\
\frac{\partial T}{\partial y} &= \frac{\partial \theta}{\partial \eta}\frac{\partial \eta}{\partial y} + \frac{\partial \theta}{\partial \zeta}\frac{\partial \zeta}{\partial y} \\
&= \sqrt{\frac{U_\infty}{\nu x}}\frac{\partial \theta}{\partial \eta} \qquad (2.4)
\end{aligned}$$

$$\begin{aligned}
\frac{\partial^2 T}{\partial y^2} &= \frac{\partial}{\partial y}\left(\frac{\partial \theta}{\partial y}\right) \\
&= \frac{\partial}{\partial y}\left(\frac{\partial \theta}{\partial \eta}\frac{\partial \eta}{\partial y}\right) \\
&= \frac{\partial^2 \theta}{\partial \eta^2}\left(\frac{\partial \eta}{\partial y}\right)^2 + \frac{\partial \theta}{\partial \eta}\frac{\partial^2 \eta}{\partial y^2} \\
&= \frac{U_\infty}{\nu x}\frac{\partial^2 \theta}{\partial \eta^2} \qquad (2.5)
\end{aligned}$$

similarly,

$$\frac{\partial^2 T}{\partial z^2} = \frac{U_\infty}{\nu x}\frac{\partial^2 \theta}{\partial \zeta^2}. \tag{2.6}$$

The usual substitution for the velocities are made (Lienhard IV and Lienhard V 2012, pg. 285, eq. 6.19)

$$u = U_\infty f', \quad v = \frac{1}{2}\sqrt{\frac{\nu U_\infty}{x}}\left(\eta f' - f\right) \tag{2.7}$$

where f is the stream function for a two dimensional momentum boundary layer. Combining eq. (2.1) with eqs. (2.2) to (2.7) results in the partial differential equation shown in eq. (2.8).

$$-\frac{Pr}{2}\left(\zeta f' \frac{\partial \theta}{\partial \zeta} + f\frac{\partial \theta}{\partial \eta}\right) = \frac{\partial^2 \theta}{\partial \eta^2} + \frac{\partial^2 \theta}{\partial \zeta^2} \tag{2.8}$$

With the similarity variable choices in eq. (2.2), the three spacial dimensions in eq. (2.1) have been collapsed down to two similarity spacial dimensions in eq. (2.8). The similarity equation as presented has dimensions of temperature, but can easily be made nondimensional by dividing the whole equation by some appropriate reference temperature or temperature difference. The similarity solution for the velocity boundary layer, f, is solved for separately and supplied in tabular for to the numerical solver when integrating eq. (2.8).

Similarity Solution

Equation (2.8) is numerically solved for four different boundary conditions and two different Pr (1 and 10). Table 2.1 lists the boundary conditions used for the numerical modeling. All the laminar numerical simulations use the boundary conditions specified in table 2.1.

Table 2.1: Boundary conditions for laminar modeling

Case	Heated Surface	Cooled Surface
1	Isothermal	Isothermal
2	Isothermal	Adiabatic
3	Isoflux	Isothermal
4	Isoflux	Adiabatic

The temperature field, θ, in eq. (2.8) is solved numerically using the solver scalarTransportFoam from the open source code OpenFOAM. The size of the domain is $-20 < \eta < 20$ and $0 < \zeta < 20$. The grid has 2048×1024 cells with a minimum size at $\eta = \zeta = 0$ of about $(4 \times 10^{-4}\eta) \times (4 \times 10^{-4}\zeta)$. The boundary conditions are zero temperature at the top and left boundaries, zero gradient at the right boundary, and the conditions specified for the wall according to table 2.1. Selected contours of the numerical solution are shown for $Pr = 1$ in fig. 2.2 and $Pr = 10$ in fig. 2.3 for all the cases described in table 2.1.

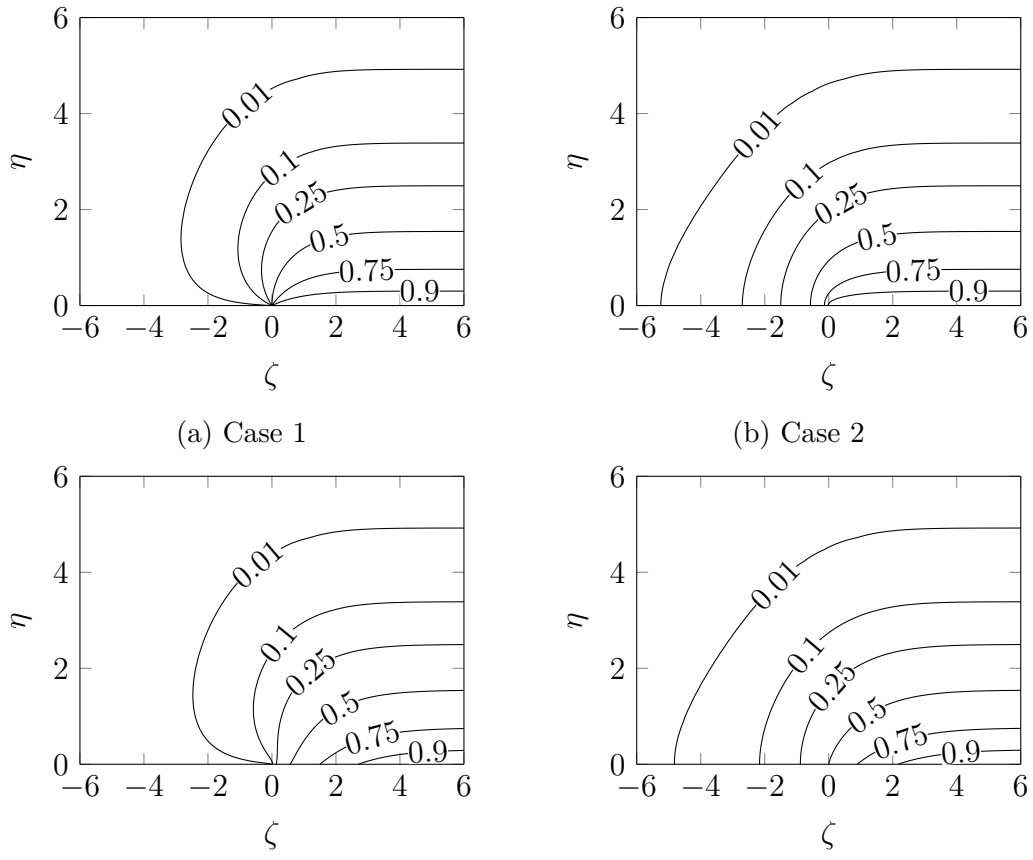

(a) Case 1

(b) Case 2

(c) Case 3

(d) Case 4

Figure 2.2: Nondimensional temperature (θ/θ_w) contours from solution of eq. (2.8) for $Pr = 1$

In figs. 2.2 and 2.3 the characteristic temperature, θ_w, for the isoflux heated plate

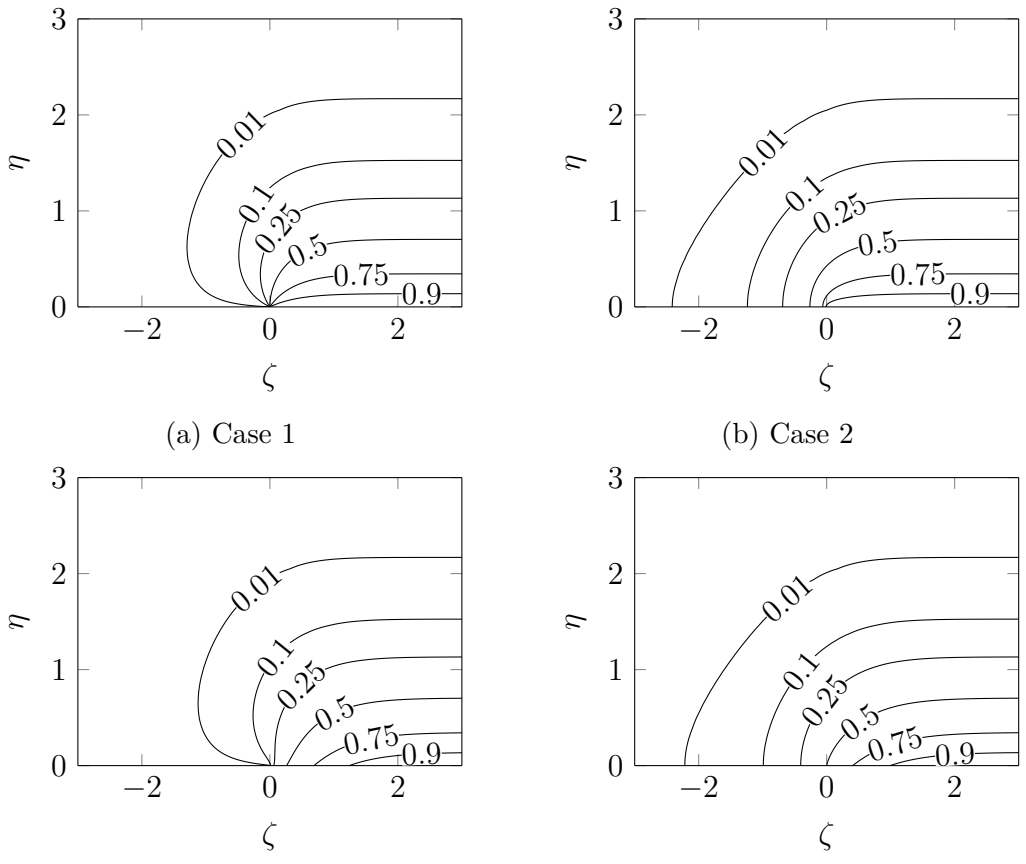

(a) Case 1

(b) Case 2

(c) Case 3

(d) Case 4

Figure 2.3: Nondimensional temperature (θ/θ_w) contours from solution of eq. (2.8) for $Pr = 10$

is defined as $\theta_w = \theta(\eta = 0, \zeta \to \infty)$, or equivalently for both cases the maximum wall temperature value at $\eta = 0$. The non-dimensional temperature fields exhibit the characteristics expected based on their respective boundary conditions. The bowing out of the temperature field over the cold plate, seen in figs. 2.2a, 2.2c, 2.3a and 2.3c, is clearly caused by holding the cooled surface at zero reference temperature, or $\theta_w = 0$ for $\zeta < 0$. For the cases with an isothermal heated surface, figs. 2.2a, 2.2b, 2.3a and 2.3b, it is clear the contour lines approach a flat temperature profile near the heated surface. Finally, for the isoflux and adiabatic plates, seen in figs. 2.2b to 2.2d and 2.3b to 2.3d, the temperature contours change on the surface in the ζ direction

because the flux is defined, not the temperature.

Figures 2.2 and 2.3 also give an indication of the scaling of the width effect for laminar flow. To take fig. 2.2d as an example, the temperature field is symmetrical about $\zeta = 0$ for $\eta = 0$. Therefore, the $\theta/\theta_w = 0.99$ contour line terminates (or begins) on the surface at $\zeta = 4.92$ ($\eta = 0$). Using the definitions from eq. (2.2), location of $\zeta = 4.92$ can be reformulated as

$$z_{99}\sqrt{\frac{U_\infty}{\nu x}} = 4.92 \tag{2.9}$$

$$\frac{z_{0.99}}{x} = \frac{4.92}{Re_x}. \tag{2.10}$$

Equation (2.9) shows the scaling for the 99 % edge effect for laminar flow when $Pr = 1$ is the same as the 99 % boundary layer thickness in both scaling and magnitude (see Lienhard IV and Lienhard V (2012, eq. 6.2, pg. 273) for 99 % velocity boundary layer scaling). Similar arguments can be made for the other boundary layer configurations. Therefore, for laminar flow over a semi-infinite heated plate without an unheated starting length, the width effect and the boundary layer thickness scale with one another,

$$\frac{z_{99}}{\delta_{99}} \sim 1. \tag{2.11}$$

This argument will be expanded to include Pr effects and unheated starting lengths in section 2.1.3.

2.1.2 Conduction Model

Domain and Equations

Several methods of approximating the temperature field in laminar flow were tried, however, modeling the heat transfer as a purely conduction problem proved to be

the best way of modeling the singularity at $z = y = 0$ and incorporating varying Pr and unheated starting lengths into the solution. For example, using an integral technique to approximately solve eq. (2.1) resulted in an answer that could not be readily extended to heat transfer characterized by different Pr, i.e. where the thermal and momentum boundary layers had different heights.

Very close to the surface, energy transport is dominated by conduction in the y-z directions and the heat transfer can be modeled by eq. (2.12).

$$0 = \frac{\partial^2 T}{\partial y^2} + \frac{\partial^2 T}{\partial z^2} \tag{2.12}$$

Indeed, if the wall normal velocity is small, the primary means of energy transport in a given plane normal to the streamwise velocity u is by conduction.

The problem domain and boundary conditions for eq. (2.12) are shown in fig. 2.4. The conduction domain is an z-y plane taken from the full three dimensional domain as shown in fig. 2.4a. Examples of the resulting conduction domain are shown in figs. 2.4b and 2.4c.

Solution

The discontinuity in the boundary conditions at $(y, z) = (0, 0)$ facilitates splitting the problem domain into two subdomains. The solution is assumed to have the form

$$\theta(y, z) = \mathbb{Y}(y)\,\mathbb{Z}(z) + \mathcal{Z}(z) \tag{2.13}$$

where $\mathbb{Y}$ and $\mathbb{Z}$ are the eigensolutions, and $\mathcal{Z}$ is the linear solution far from the surface boundary discontinuity. Two new boundary conditions are required for closure, and continuity of both lateral heat flux and temperature at the interface between the two

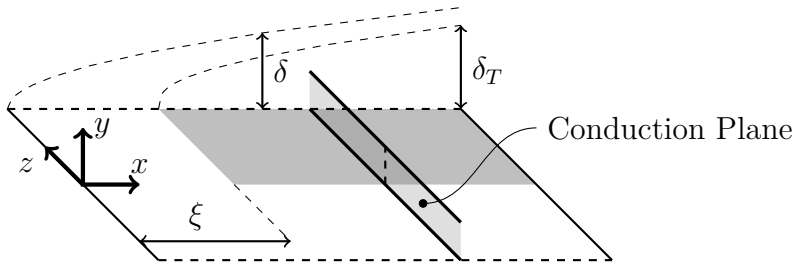

(a) Modified from fig. 2.1 showing conduction modeling domain.

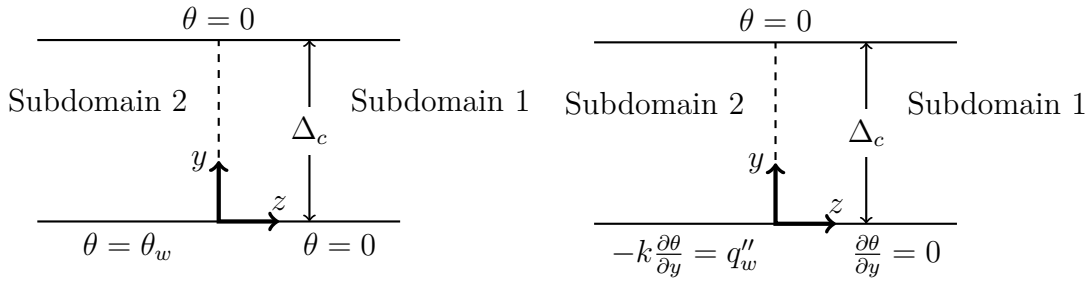

(b) Case 1 from table 2.1

(c) Case 4 from table 2.1

Figure 2.4: Problem domain for laminar conduction

subdomains at $z = 0$ are physical requirements that make the problem tractable.

$$\theta_1\left(y, z=0\right) = \theta_2\left(y, z=0\right) \tag{2.14a}$$

$$\left.\frac{\partial\theta_1}{\partial z}\right|_{z=0} = \left.\frac{\partial\theta_2}{\partial z}\right|_{z=0} \tag{2.14b}$$

The eigenfunctions for the boundary conditions for figure 2.4b, are given by Ozisik (1993) as

$$\mathbb{YZ}_{1,\lambda} = A_{1,\lambda}\exp\left(-\lambda_{n,T}z\right)\sin\left(\lambda_{n,T}y\right), \quad z > 0, \tag{2.15a}$$

$$\mathbb{YZ}_{2,\lambda} = A_{2,\lambda}\exp\left(\lambda_{n,T}z\right)\sin\left(\lambda_{n,T}y\right), \quad z < 0, \tag{2.15b}$$

where the eigenvalues, $\lambda_{n,T}$ are

$$\lambda_{n,T} = \frac{n\pi}{\Delta_c}, \quad n = 1, 2, 3, \ldots \tag{2.16}$$

The solutions far from the discontinuity for both domains are

$$\mathcal{Z}_1 = \theta_w \left(1 - \frac{y}{\Delta_c}\right), \quad z > 0 \tag{2.17a}$$

$$\mathcal{Z}_2 = 0, \quad z < 0. \tag{2.17b}$$

Combining eqs. (2.15a) and (2.17a) and applying eq. (2.14a) at the subdomain interface allows for the solution of $A_{1,\lambda}$ and $A_{2,\lambda}$.

$$A_{1,\lambda}\sin\left(\lambda_{n,T}y\right) + \theta_w \left(1 - \frac{y}{\Delta_c}\right) = A_{2,\lambda}\sin\left(\lambda_{n,T}y\right) \tag{2.18a}$$

$$-A_{1,\lambda} = A_{2,\lambda} \tag{2.18b}$$

Substituting eq. (2.18b) into eq. (2.18a) and using the integral for Fourier sine series from Arpaci (1966, pg. 187,eq. 4.26) gives the values for the coefficients of eq. (2.15a).

$$\begin{aligned} A_{2,\lambda} &= \frac{2}{\Delta_c}\int_0^{\Delta_c} \frac{\theta_w}{2}\left[1 - \frac{y}{\Delta_c}\right]\sin\left(\lambda_{n,T}y\right)dy \\ &= \frac{2\theta_w}{\Delta_c}\frac{\Delta_c\lambda_{n,T} - \sin\left(\lambda_{n,T}\Delta_c\right)}{2\lambda_{n,T}^2\Delta_c} \\ &= \theta_w\lambda_{n,T}\Delta_c = \frac{\theta_w}{n\pi} \end{aligned} \tag{2.19}$$

The full solution for case 1 (table 2.1) is

$$\frac{\theta_1}{\theta_w} = 1 - \frac{y}{\Delta_c} - \sum_{n=1}^{\infty} \frac{1}{n\pi} \exp\left(-\lambda_{n,T} z\right) \sin\left(\lambda_{n,T} y\right), \quad z > 0 \tag{2.20a}$$

$$\frac{\theta_2}{\theta_w} = \sum_{n=1}^{\infty} \frac{1}{n\pi} \exp\left(\lambda_{n,T} z\right) \sin\left(\lambda_{n,T} y\right), \quad z < 0. \tag{2.20b}$$

Following a procedure similar to Jackson (1999, pgs. 74–75), the series solution from eq. (2.20) is transformed to the explicit closed form presented in eq. (2.24). Noting that $\sin(\phi) = \mathfrak{I}\left(e^{i\phi}\right)$, eq. (2.20a) can be rewritten as

$$\frac{\theta_1}{\theta_w} = 1 - \frac{y}{\Delta_c} - \frac{1}{\pi} \mathfrak{I} \left[\sum_{n=1}^{\infty} \frac{\exp\left[n \frac{i\pi}{\Delta_c} (y + iz)\right]}{n} \right], \tag{2.21}$$

where $\mathfrak{I}$ denotes the imaginary component of the given complex value, and if $Z = \exp\left[\frac{i\pi}{\Delta_c}(y + iz)\right]$, then eq. (2.21) becomes

$$\frac{\theta_1}{\theta_w} = 1 - \frac{y}{\Delta_c} - \frac{1}{\pi} \mathfrak{I} \left[\sum_{n=1}^{\infty} \frac{Z^n}{n} \right]. \tag{2.22}$$

The series in brackets is equivalent to a natural logarithm (Olver et al. 2010, equation 4.6.1),

$$\frac{\theta_1}{\theta_w} = 1 - \frac{y}{\Delta_c} + \frac{1}{\pi} \mathfrak{I} \left[\log\left(1 - Z\right)\right]. \tag{2.23}$$

Further, the imaginary component of a logarithm is the phase of its argument (Olver et al. 2010, equation 4.2.3), so the explicit closed form of eq. (2.20a) is

$$\frac{\theta_1}{\theta_w} = 1 - \frac{y}{\Delta_c} + \frac{1}{\pi} \tan^{-1} \left[\frac{\sin\left(\pi \frac{y}{\Delta_c}\right)}{\cos\left(\pi \frac{y}{\Delta_c}\right) - \exp\left(\pi \frac{z}{\Delta_c}\right)} \right]. \tag{2.24}$$

The solution for case 4 is similar to the solution method outlined above for case 1,

and will not be shown in as much detail. The eigenfunctions that satisfy the boundary conditions shown in fig. 2.4c are given by Ozisik (1993) as

$$\mathbb{YZ}_{1,\lambda} = B_{1,\lambda}\exp\left(-\lambda_{n,F}z\right)\cos\left(\lambda_{n,F}y\right), \quad z > 0, \tag{2.25a}$$

$$\mathbb{YZ}_{2,\lambda} = B_{2,\lambda}\exp\left(\lambda_{n,F}z\right)\cos\left(\lambda_{n,F}y\right), \quad z < 0, \tag{2.25b}$$

where the eigenvalues, $\lambda_{n,F}$ are

$$\lambda_{n,F} = \frac{(2n+1)\,\pi}{2\Delta_c}, \quad n = 0, 1, 2, \ldots \tag{2.26}$$

Applying eq. (2.14a) at the interface of the two subdomains gives the solution for the coefficients for the Fourier series as shown in Arpaci (1966, pg. 189,eq. 4.32).

$$\begin{aligned} B_{2,\lambda} &= \frac{\int_0^{\Delta_c} \frac{q''_w}{2k}\left[\Delta_c - y\right]\cos\left(\lambda_{n,F}y\right)dy}{\int_0^{\Delta_c}\cos^2\left(\lambda_{n,F}y\right)dy} \\ &= \frac{q''_w}{2k}\frac{1-\cos\left(\lambda_{n,F}\Delta_c\right)}{\lambda_{n,F}^2}\frac{4\lambda_{n,F}}{2\lambda_{n,F}\Delta_c + \sin\left(2\lambda_{n,F}\Delta_c\right)} \\ &= \frac{q''_w}{k}\frac{1}{\lambda_{n.F}^2} = \frac{q''_w\Delta_c}{k}\frac{4}{(2n+1)^2\,\pi^2} \end{aligned} \tag{2.27}$$

Combining eqs. (2.25a) and (2.27) gives the temperature field for case 4.

$$\frac{\theta_1 k}{q''_w\Delta_c} = 1 - \frac{y}{\Delta_c} - \frac{4}{\pi^2}\sum_{n=0}^{\infty}\frac{1}{(2n+1)^2}\exp\left(-\lambda_{n,F}z\right)\cos\left(\lambda_{n,F}y\right), \quad z > 0 \tag{2.28a}$$

$$\frac{\theta_2 k}{q''_w\Delta_c} = \frac{4}{\pi^2}\sum_{n=0}^{\infty}\frac{1}{(2n+1)^2}\exp\left(\lambda_{n,F}z\right)\cos\left(\lambda_{n,F}y\right), \quad z < 0 \tag{2.28b}$$

The results of the integration presented in eqs. (2.19) and (2.27) are evaluated with Wolfram|Alpha.

Cases 2 and 3 proved harder to solve, because the eigenfunctions for each subdomain are different. The subdomain with an isothermal boundary condition is pro-

portional to $\sin(\lambda_T y)$ while the subdomain with an isoflux boundary condition is proportional to $\cos(\lambda_F y)$. This makes it impossible to match the two subdomain solutions near $(y, z) = (0, 0)$ because the gradients are different.

However, approximate conduction solutions can be found by fitting the eigenfunctions from eqs. (2.15a) and (2.25a) to a numerical solution of the analogous conduction problem. The solutions far from the subdomain boundaries, $\mathcal{Z}(z)$, are the same as shown in eqs. (2.17a) and (2.28). First, a conduction solution from OpenFOAM for the analogous conduction problem of eq. (2.12) and boundary conditions from table 2.1 is solved. Then, the coefficients for the eigenfunctions are estimated using linear multivariate regression. This is fairly straightforward as the solution for the temperature field is assumed to be a linear summation of the eigenfunctions.

$$\mathbb{YZ}_{T,\lambda} = \sum_{n=1}^{\infty} A_{n,\lambda} \exp(\pm\lambda_{n,T} z) \sin(\lambda_{n,T} y). \tag{2.29a}$$

$$\mathbb{YZ}_{F,\lambda} = \sum_{n=0}^{\infty} B_{n,\lambda} \exp(\pm\lambda_{n,F} z) \cos(\lambda_{n,F} y) \tag{2.29b}$$

After the coefficients in eq. (2.29) are estimated using least squares regression on the numerical data, the functional relationship between the coefficients and the eigenvalues is also estimated using linear least squares regression.

$$\log(A_n) = \log(c_A) + p_A \log(\lambda_{n,T}) \tag{2.30a}$$

$$\log(B_n) = \log(c_B) + p_B \log(\lambda_{n,F}) \tag{2.30b}$$

The linear equations in eq. (2.30a) are used to estimate the exponents, p_A and p_B, and the multiplicative constant c using least squares regression.

To ensure this procedure is reasonable, the coefficients are calculated for eqs. (2.15a) and (2.25a) and compared to the analytical solutions shown in eqs. (2.19) and (2.27).

The best fits of the coefficients in eq. (2.29) and the power law fit from eq. (2.30a) are shown in fig. 2.5 for all four cases. The power law fit agrees with the analytical coefficients to four digits for case 1 and 4, implying the procedure is accurate. The full eigenfunctions, with the fitted coefficients are shown in eq. (2.31).

$$\mathbb{YZ}_{T,\lambda} = \sum_{n=1}^{\infty} 0.854 \left(\lambda_{n,T}\Delta_c\right)^{-1.45} \exp\left(\pm\lambda_{n,T} z\right) \sin\left(\lambda_{n,T} y\right) \tag{2.31a}$$

$$\mathbb{YZ}_{F,\lambda} = \sum_{n=0}^{\infty} 1.25 \left(\lambda_{n,F}\Delta_c\right)^{-1.57} \exp\left(\pm\lambda_{n,F} z\right) \cos\left(\lambda_{n,F} y\right) \tag{2.31b}$$

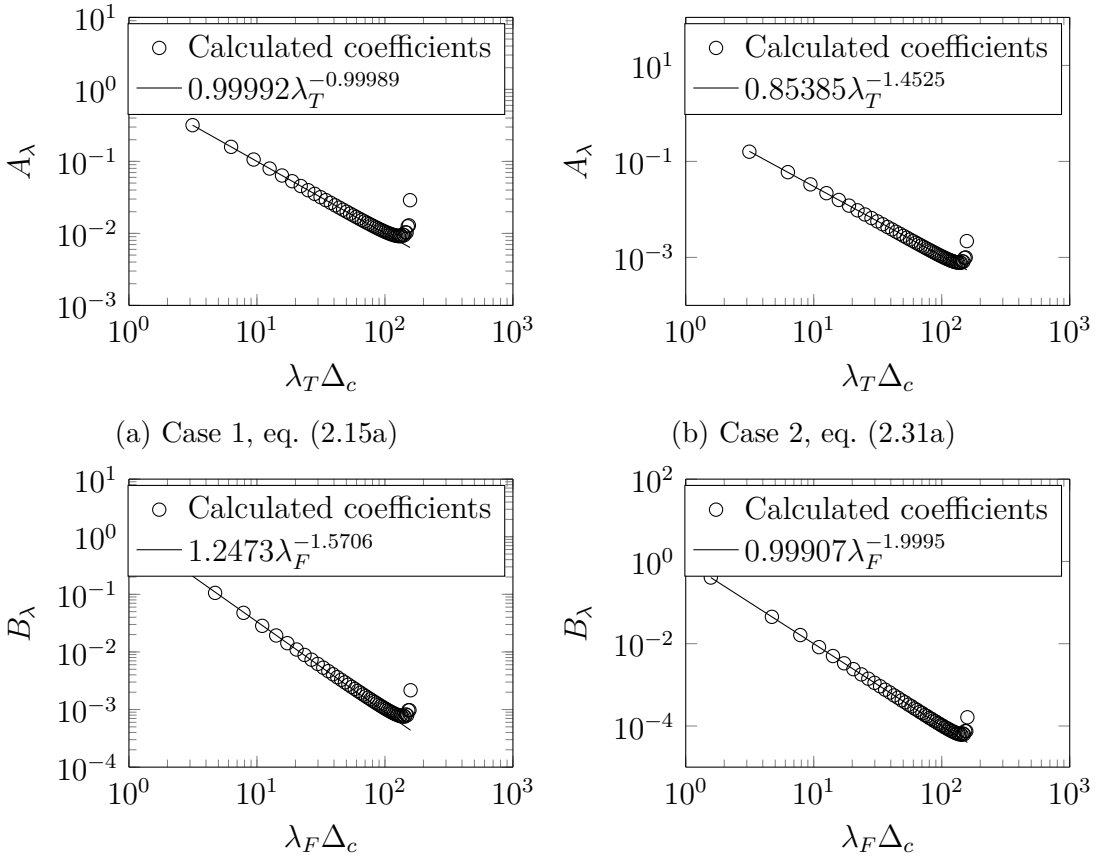

(a) Case 1, eq. (2.15a)

(b) Case 2, eq. (2.31a)

(c) Case 3, eq. (2.31b)

(d) Case 4, eq. (2.25a)

Figure 2.5: Comparison of estimated and least square fit of coefficients

In addition to comparing the numerically calculated coefficients to the expected

analytical coefficients, the overall accuracy is determined by the matching requirement between the two subdomains. The temperature matching for all the cases is fairly accurate, with cases 2 and 3 having a maximum error of 0.042 (in terms of nondimensional temperature) at $y = 0$.

Wall Normal Gradients

Of particular interest for heat transfer from a surface to a fluid is the surface normal temperature gradient evaluated at the surface. The wall normal gradients for eqs. (2.24) and (2.31a) are shown in eqs. (2.32) and (2.33), respectively.

$$\frac{\partial}{\partial y}\left(\frac{\theta}{\theta_w}\right)_{y=0} = -\frac{1}{\Delta_c}\left[1 + \frac{1}{\exp\left(\frac{\pi z}{\Delta_c}\right) - 1}\right] \tag{2.32}$$

The wall normal gradient for the mixed condition is

$$\frac{\partial}{\partial y}\left(\frac{\theta}{\theta_w}\right)_{y=0} = -\frac{1}{\Delta_c}\left[1 + 0.509\sum_{n=1}^{\infty}\frac{\exp\left(-n\frac{\pi z}{\Delta_c}\right)}{n^{0.423}}\right]. \tag{2.33}$$

For cases 3 and 4, the gradients are not needed because the temperature is normalized by the specified heat flux, which is a function of the temperature gradient. In other words, the heat flux can be found by rearranging eqs. (2.28a) and (2.31b). In addition, the form of the temperature evaluated at the surface can be transformed into known functions for case 4. With some simple manipulation, eq. (2.28a) is

$$\frac{\theta_1 k}{q''_w \Delta_c} = 1 - \frac{2}{\pi^2}\left[\mathrm{Li}_2\left(e^{-\frac{\pi z}{2\Delta_c}}\right) - \mathrm{Li}_2\left(-e^{-\frac{\pi z}{2\Delta_c}}\right)\right], \quad z > 0,\ y = 0, \tag{2.34}$$

where Li_2 denotes the dilogarithm function, defined by the series (Olver et al. 2010,

equation 25.12.1)

$$\mathrm{Li}_2(Z) = \sum_{n=1}^{\infty} \frac{Z^n}{n^2}, \quad |z| \leq 1. \tag{2.35}$$

2.1.3 Convection

Correlations

Inspecting eqs. (2.20), (2.28) and (2.31) shows the only parameter temperature is dependent on is $\lambda z/\Delta_c$. This suggests a new parameter, ζ^*, defined as

$$\zeta^* = \frac{z}{\Delta_c}. \tag{2.36}$$

Furthermore, if Δ_c is defined as the conduction thickness far from the lateral edge, the gradient evaluated at the surface by definition matches the expected gradient for a given x location as $z \to \infty$. In other words, the correlations approach the expected values for two dimensional flow far from the edge as the conduction thickness is a measure of the gradient. A sketch of the physical meaning of the conduction thickness is shown in fig. 2.6.

If $\Delta_c = x/Nu_{z\to\infty}$, then

$$\zeta^* = \frac{z}{x} Nu_{z\to\infty} \tag{2.37}$$

This new variable, ζ^*, is ζ in eq. (2.2) with Pr information. To show this, assume for laminar flow $Nu_{z\to\infty} \propto \sqrt{Re_x} Pr^n$, then

$$\begin{aligned} \zeta^* &\propto \frac{z}{x}\sqrt{Re_x} Pr^n \\ &\propto \zeta Pr^n \end{aligned} \tag{2.38}$$

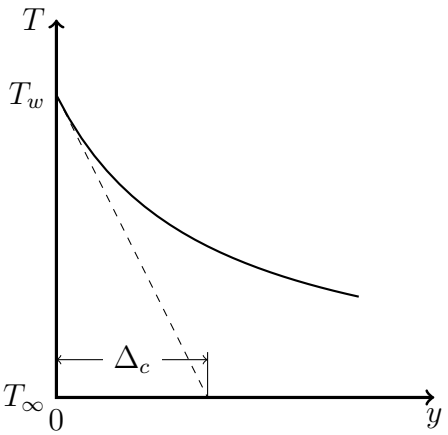

Figure 2.6: Sketch showing the physical meaning of the diffusion thickness. Adapted from Kays et al. (2005). The temperature gradient is equivalent to the temperature difference divided by the conduction thickness.

or, more precisely

$$\zeta^* = \zeta \left.\frac{\partial\theta}{\partial\eta}\right|_{\eta=0,\xi\to\infty}. \tag{2.39}$$

Using this new variable, the definition of Δ_c, and the results from section 2.1.2, convection correlations can be defined for all cases in table 2.1. For case 1,

$$\frac{Nu}{Nu_{z\to\infty}} = 1 + \frac{1}{\exp(\pi\zeta^*) - 1} \tag{2.40}$$

for case 2,

$$\frac{Nu}{Nu_{z\to\infty}} = 1 + 0.509\sum_{n=1}^{\infty}\frac{\exp(-n\pi\zeta^*)}{n^{0.423}} \tag{2.41}$$

for case 3,

$$\frac{Nu}{Nu_{z\to\infty}} = \frac{1}{1 - 0.614\exp\left(-\zeta^*\frac{\pi}{2}\right)\sum_{n=0}^{\infty}\frac{\exp(-n\pi\zeta^*)}{(2n+1)^{1.57}}} \tag{2.42}$$

for case 4,

$$\frac{Nu}{Nu_{z\to\infty}} = \frac{1}{1 - \frac{4}{\pi^2}\exp\left(-\frac{\pi}{2}\zeta^*\right)\sum_{n=0}^{\infty}\frac{\exp(-n\pi\zeta^*)}{(2n+1)^2}}. \tag{2.43}$$

Is should be clear that as ζ^* approaches infinity, the gradient matches the expected

gradient far from the lateral edge. For $Nu_{z\to\infty}$, Kays et al. (2005) recommends

$$Nu_{z\to\infty} = \frac{0.332 Re_x^{1/2} Pr^{1/3}}{\left[1 - \left(\frac{\xi}{x}\right)^{3/4}\right]^{1/3}} \tag{2.44}$$

for isothermal flat plates and

$$Nu_{z\to\infty} = \frac{1.204 Re_x^{1/2} Pr^{1/3}}{\frac{\Gamma(1/3)\Gamma(4/3)}{\Gamma(5/3)}\beta\left(1 - \left(\frac{\xi}{x}\right)^{3/4}, 1/3, 4/3\right)} \tag{2.45}$$

for isoflux flat plates, where $\beta(x, a, b)$ is the incomplete beta function and $\Gamma(x)$ is the gamma function.

For eq. (2.40), the denominator can be expanded using a Taylor series to investigate the behavior as $\zeta^* \to 0$.

$$\begin{aligned} 1 + \frac{1}{\exp(\pi\zeta^*) - 1} &= 1 + \frac{1}{1 + \pi\zeta^* + \frac{(\pi\zeta^*)^2}{2} + \ldots - 1} \\ \lim_{\zeta^*\to 0} \frac{Nu}{Nu_{z\to\infty}} &= \frac{1}{\pi\zeta^*} \end{aligned} \tag{2.46}$$

Equation (2.46) shows that Nu increases fairly quickly near the edge of a heated plate for case 1. Indeed, it increases so quickly that the average lateral Nu is infinite. Therefore, case 1, while useful for understanding lateral heat transfer is physically impossible. The only case where Nu does not approach infinity as $\zeta^* \to 0$ is the heat flux represented by eq. (2.43), as both the flux and temperature are non-zero on the heated surface. The asymptotic behavior of cases 2 and 3 will be discussed in more detail below.

Alternative Correlations for Cases 2 and 3

Equations (2.41) and (2.42) both have their drawbacks. Equation (2.41) is very slow to converge to an acceptable accuracy for small ζ^* values while eq. (2.42) converges to a finite value at $\zeta^* = 0$. For these reasons, alternative correlations are constructed that correctly model the heat transfer near the lateral edge and don't require many terms to converge to an acceptable solution.

Churchill and Usagi (1972) outline a method that accounts for asymptotic behaviors while approximately describing the regimes in between. This method is particularly useful in this case because the asymptotic values for Nu are known as $\zeta^* \to 0$ and $\zeta^* \to \infty$. By taking the p-norm of the known asymptotic relations and adjusting the constants to best fit the data, a satisfactory correlation is developed. From figs. 2.11 and 2.12 and eq. (2.41), it is clear that the general form of the p-norm correlation should be

$$\frac{Nu}{Nu_{z\to\infty}} = \left[1 + \left(\frac{c}{{\zeta^*}^{1/2}}\right)^p\right]^{1/p}. \tag{2.47}$$

Fitting eq. (2.47) to the available data, the constants for cases 2 and 3 are: c is 0.615 and 0.886 respectively and p is 3.71 and 3.86 respectively. The maximum relative error for both fits is about 2.5 %.

While it was not definitively shown that the Nu for cases 2 and 3 approach infinity as $\zeta^* \to 0$ proportional to ${\zeta^*}^{-1/2}$, there are very good reasons to assume they do. Case 2 is analogous to well known problems from electrostatics (Jackson 1999, page 78) and evaporation from a droplet (Deegan et al. 1997; Hu and Larson 2002). The solution method for these problems explicitly show $q'' \propto z^{-1/2}$. The Nu for case 3 has to approach infinity near the lateral edge as the relative temperature difference is zero by the virtue of the isothermal boundary condition. The negative one-half exponent seems to describe the data from similarity solution well (the similarity so-

lution modeled the asymptotic behavior better than the three dimensional numerical simulation), and has the added benefit of having the same value as case 3. Note in contrast to case 1, the negative one-half power means that there is a finite lateral average of the Nu for both cases 2 and 3.

Numerical Simulations

As described in section 2.1.1, the cases with an unheated starting length are modeled with eq. (2.8) and numerically solved with OpenFOAM. For cases with an unheated starting length, eq. (1.1) is solved with scalarTransportFoam from OpenFOAM with appropriate boundary conditions and constant properties at steady state.

Initially, both the velocity and temperature fields were numerically modeled. However, it was decided that fully modeling the velocity field for the unheated starting lengths specified would be prohibitively expensive both in terms of memory and time. In addition, the required domain size coupled with the small cell size required to accurately model the laminar boundary layer is also prohibitively expensive. To simplify the modeling, and also to ensure the results are easily repeatable, the velocity field is approximated with the Blasius solution (see eq. (2.7)). Two unheated starting lengths of $Re_\xi = 5 \times 10^3$ and $Re_\xi = 5 \times 10^4$ are studied. Three Pr values are used, corresponding to air, naphthalene, and water: 0.7, 2.28, and 6.

The size of the domain is $-0.02L < (x - \xi) < L$, $0 < y < 0.3L$, and $-0.1L < z < 0.1L$, where L is the length of the heated plate and ξ is the unheated starting length. The heated plate is bounded by $(x - \xi) > 0$ and $z > 0$. The domain starts before the heated plate so the numerical solver can correctly handle the sudden change in boundary conditions at the leading edge of the heated plate. For this study, the total length of the heated plate is 0.5 m.

The grid is $192 \times 64 \times 256$ cells where the smallest cell is at $(x, y, z) = (\xi, 0, 0)$

with a size of $(1 \times 10^{-4}L) \times (1 \times 10^{-4}L) \times (1.6 \times 10^{-5}L)$. The sizes are chosen to maximize the amount of cells in the z direction while still adequately modeling the thermal boundary layer far from the lateral edge for all Pr.

To check that the grid is adequate in the x and y directions, the $Nu_{z\to\infty}$ from the numerical simulations are compared to the expected values from boundary layer analysis. Figures 2.7 and 2.8 show that eqs. (2.44) and (2.45) compare well with the numerical simulations, validating the grid choices for the x and y direction. Except for the leading edge where the cells are not small enough to capture the large streamwise gradients, the relative maximum error is about 1 %–2 %.

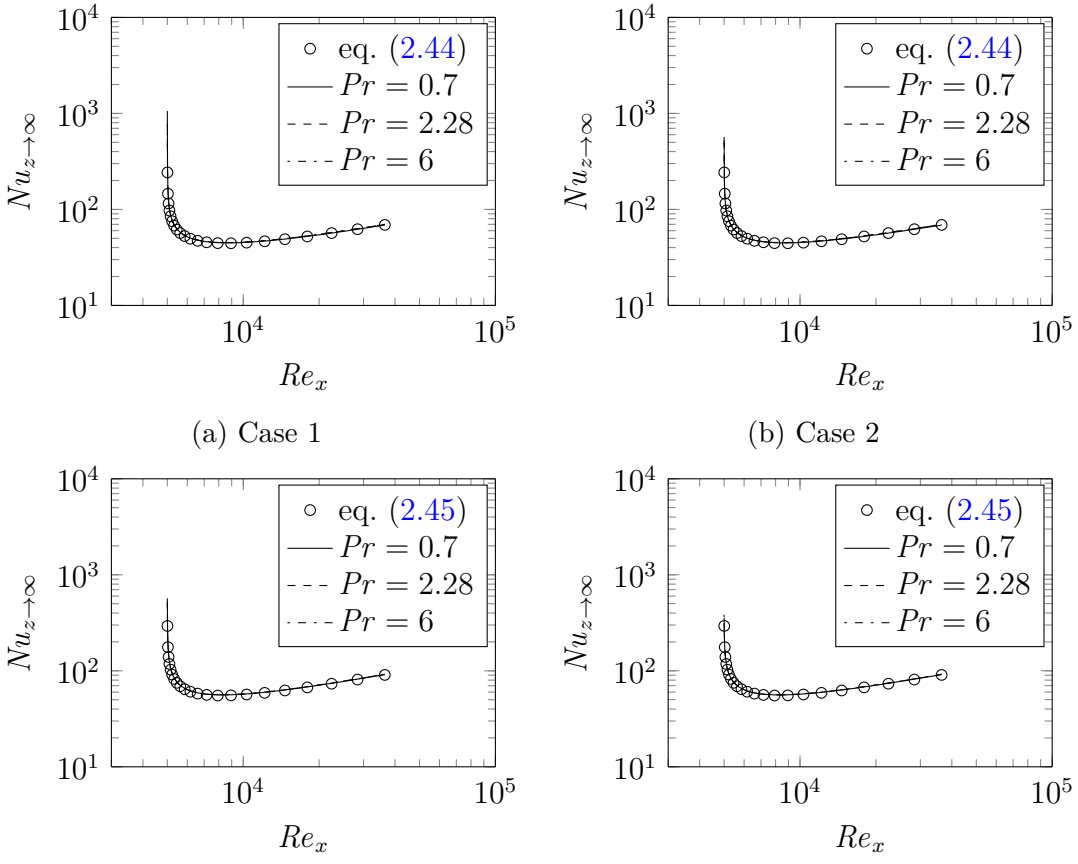

(a) Case 1

(b) Case 2

(c) Case 3

(d) Case 4

Figure 2.7: Comparison of expected $Nu_{z\to\infty}$, $Re_\xi = 5 \times 10^3$

To ensure the grid independence of the lateral edge effect on the heat transfer,

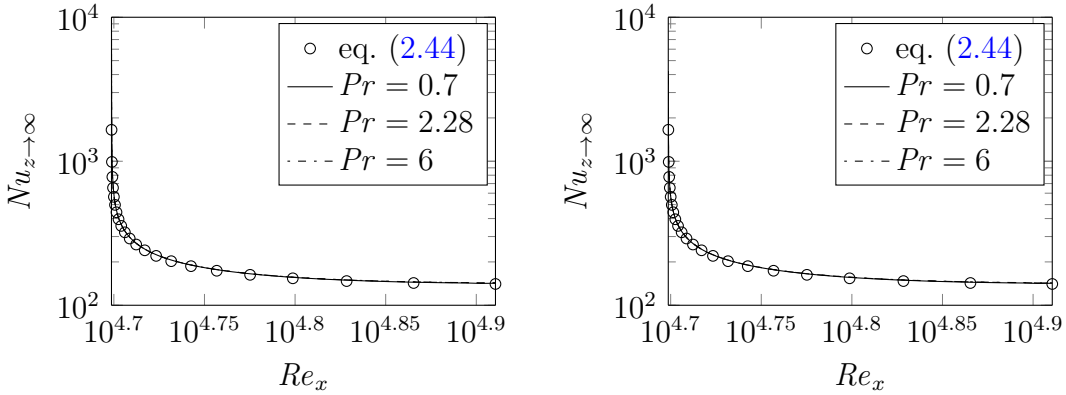

(a) Case 1

(b) Case 2

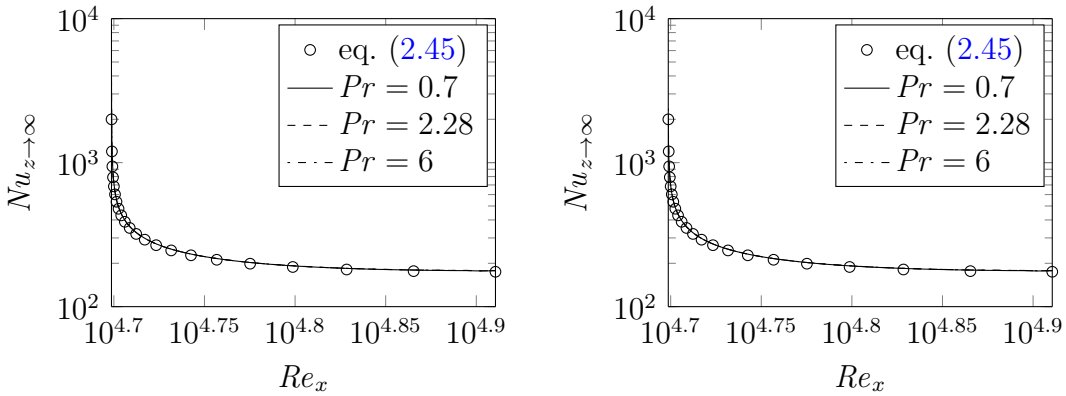

(c) Case 3

(d) Case 4

Figure 2.8: Comparison of expected $Nu_{z\to\infty}$, $Re_\xi = 5 \times 10^4$

results from the modeling of case 1 with three different mesh sizes were compared: the mesh described in the preceding paragraphs, a coarser mesh with the same number of cells but double the domain in the y and z directions, and a finer mesh with the same number of cells but half the domain in the y and z directions. These results are compared with each other, the expected result from eq. (2.40), and the results for the similarity solution described in section 2.1.1. The results are shown in fig. 2.9. Figure 2.9 shows that no grid is fine enough to completely capture the effect of the lateral edge on the heat transfer. For case 1, this is because the heat transfer at the edge approaches infinity, which no grid made of discrete cells could model. It is interesting that the data from the similarity numerical solution modeled

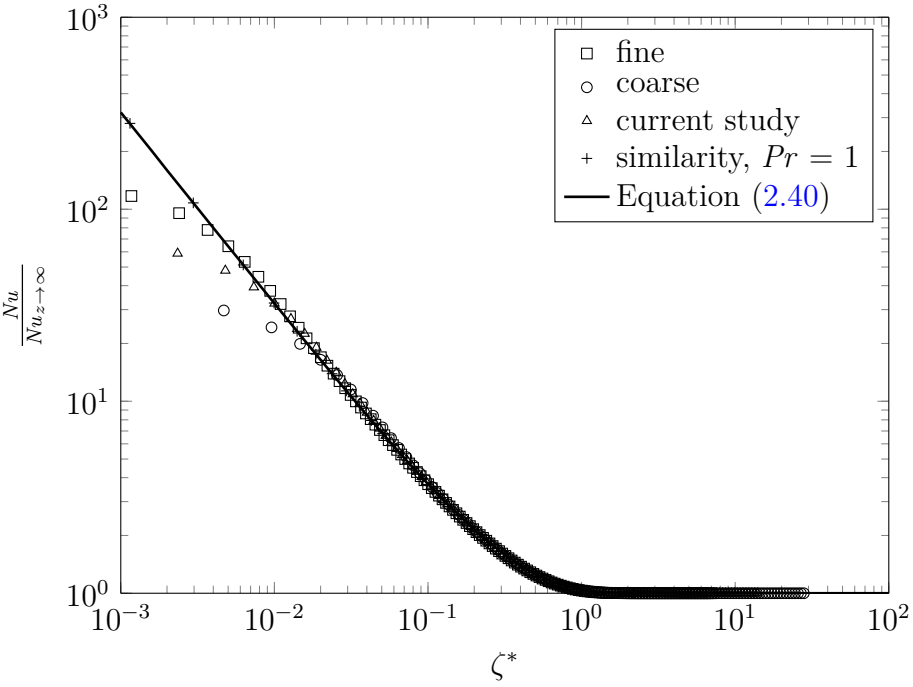

Figure 2.9: Laminar grid independence study

the heat transfer better at smaller ζ^* than the numerical modeling of the fully three dimensional energy transport.

Comparison with Numerical Results

Having validated the numerical solution method in section 2.1.3, the numerical results can now be compared to results from sections 2.1.1 and 2.1.3. Figures 2.10 to 2.13 show how well the conduction model compares with the three dimensional numerical results from OpenFOAM and the computational results of the similarity model from eq. (2.8) without any parameter fitting.

As described below, the results from this section can be used to describe spanwise extent of the region affected by the lateral edge. In particular, one would expect the spanwise extent to change in the presence of the large streamwise gradients near the leading edge, as one of the primary assumptions for the conduction model is

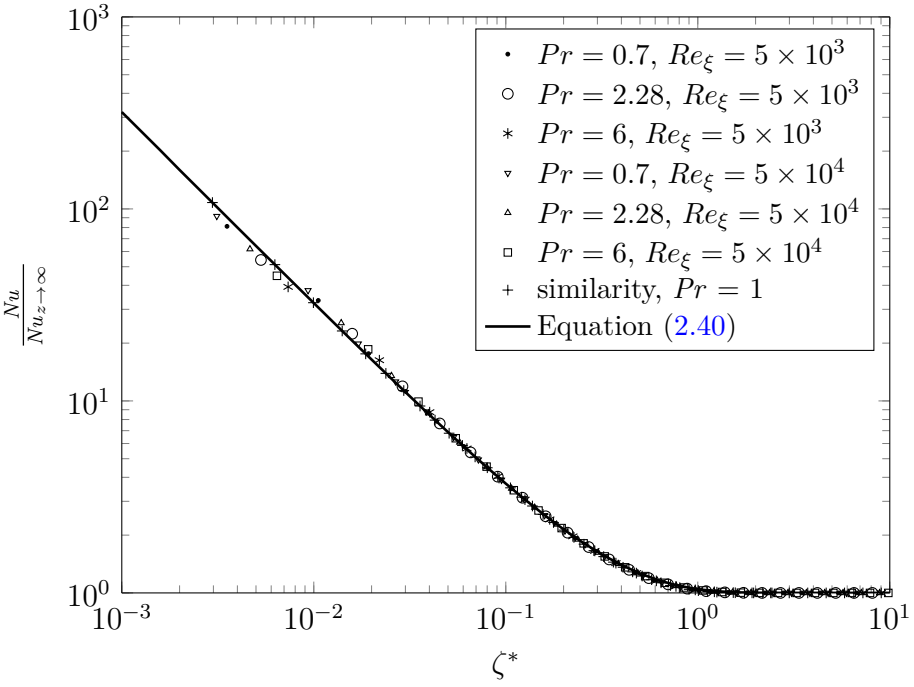

Figure 2.10: Convection results for case 1

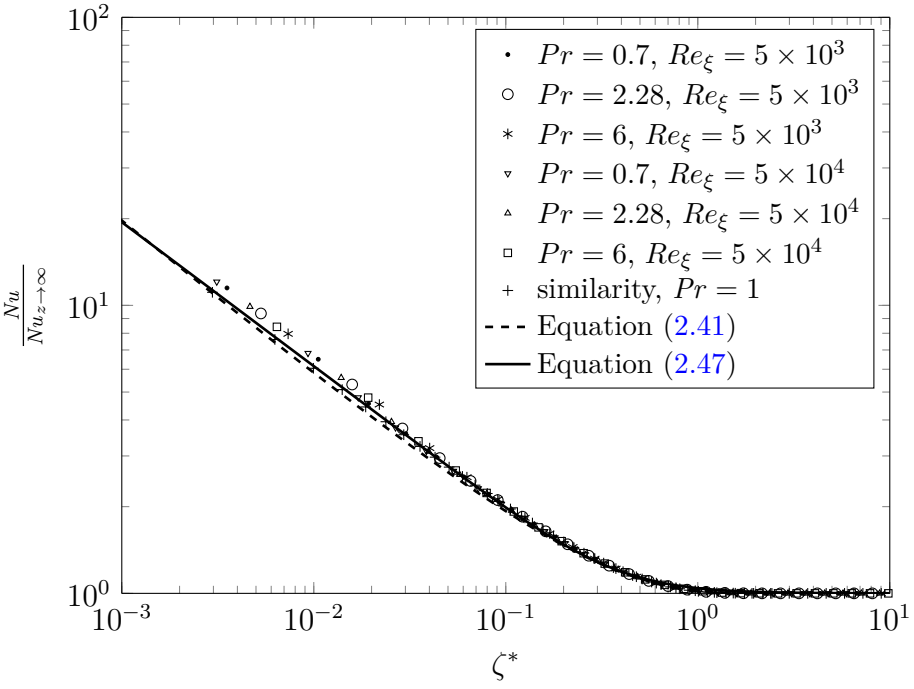

Figure 2.11: Convection results for case 2

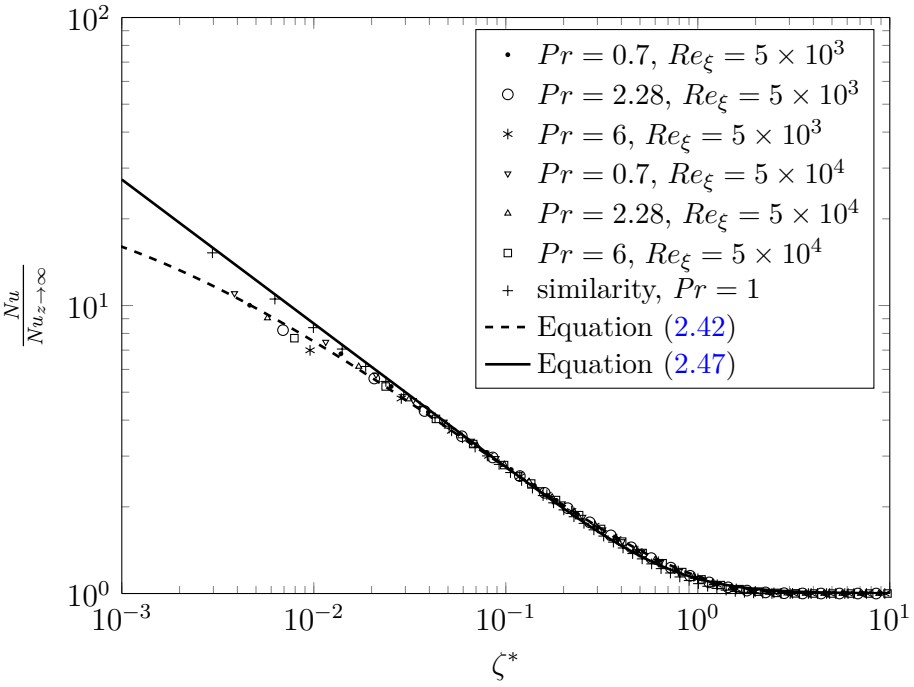

Figure 2.12: Convection results for case 3

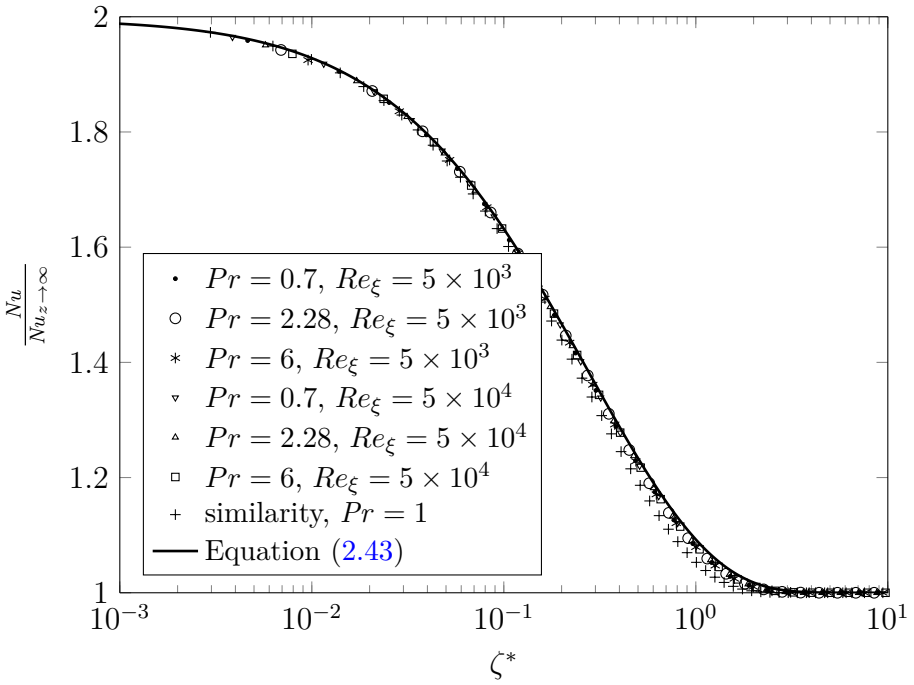

Figure 2.13: Convection results for case 4

that the principal diffusion happens exclusively in the plane perpendicular to the streamwise flow. This can be used to estimate the region where the conduction model is invalidated by proximity to the leading edge. Figure 2.14 shows how quickly the spanwise extent approaches the expected value described in table 2.2. From fig. 2.14, the conduction model is accurate for $Re_{x-\xi} \gtrsim 100$.

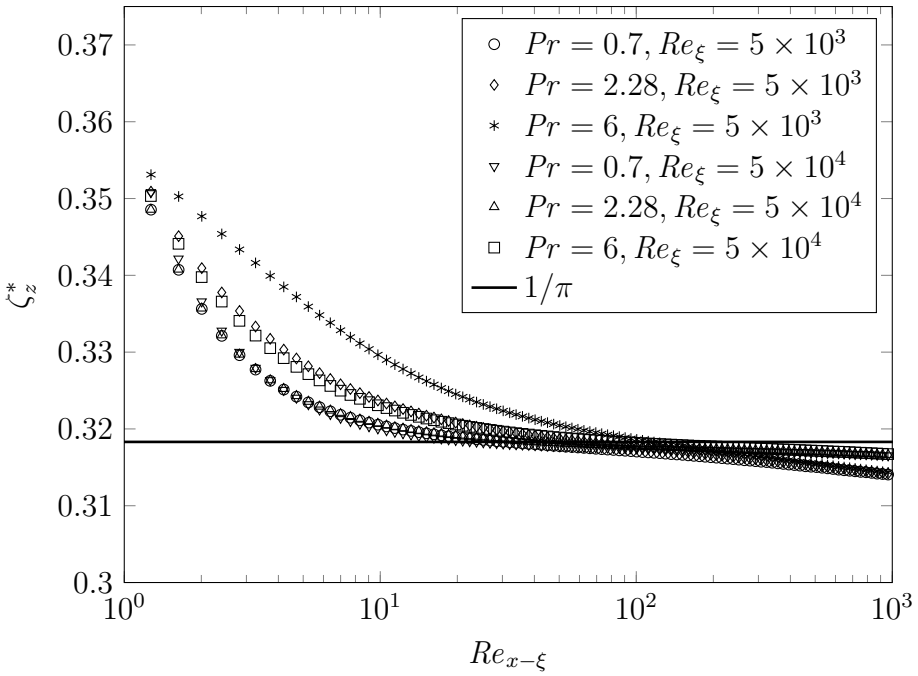

Figure 2.14: ζ_z^* for case 1

Spanwise Extent of Lateral Edge Effect

Equations (2.40), (2.43) and (2.47) can be used to estimate the spanwise extent of the lateral edge effect as a function of ζ^*. Several such measures are presented in table 2.2. The intersection measure, ζ_z^*, is the ζ^* value where the Nu line from the asymptotic regime as $\zeta^* \to 0$ intersects the Nu line from the asymptotic regime $\zeta^* \to \infty$. In other words where $1 = (c\zeta^*)^n$, where n is either negative one-half or negative one. The other measures of the spanwise extent of the lateral edge effect are

the ζ^* locations where the Nu reaches a given multiple of $Nu_{z\to\infty}$. For example, the ζ^* location where Nu comes with 10 % of $Nu_{z\to\infty}$ is the same as $Nu = 1.1Nu_{z\to\infty}$.

Table 2.2: Spanwise extent of lateral edge effect for laminar flow for semi-infinite case

	Correlations				Similarity Solution		
Case	Intersection (ζ_z^*)	1.1	1.03	1.01	1.1	1.03	1.01
1	$1/\pi$	0.763	1.13	1.47	0.706	0.988	1.24
2	0.378	0.601	1.21	2.22	0.563	0.858	1.12
3	0.785	1.19	2.35	4.21	0.936	1.37	1.74
4	—	0.955	1.68	2.36	0.759	1.22	1.60

Table 2.2 shows that for the more stringent measures of the lateral edge effect, where $Nu/Nu_{z\to\infty} = 1.01$ or 1.03, the correlation overestimates the affected area. As the slope of the Nu is quite shallow in these regions, any small error in the Nu from a given correlation results in a large change in the corresponding value of ζ^*.

2.2 Finite Domain

For electronic cooling, the heated or the cooled/adiabatic surfaces might not be semi-infinite in their lateral span. Instead, they might be narrow enough that the effects from the two lateral edges interact with one another. This section describes the effect of thin heated or the cooled/adiabatic surfaces on the centerline Nu, the lateral heat transfer profile, and average lateral heat transfer. The basic geometry is shown in fig. 2.15. The hot and "cold" plates are finite in lateral extent and meet at $z = 0$. The velocity is assumed to conform to the Blasius solution for laminar boundary layers.

2.2.1 Conduction

The introduction of a finite lateral length scale prohibits a valid similarity solution. Therefore, only the conduction and three dimensional numerical solutions are pre-

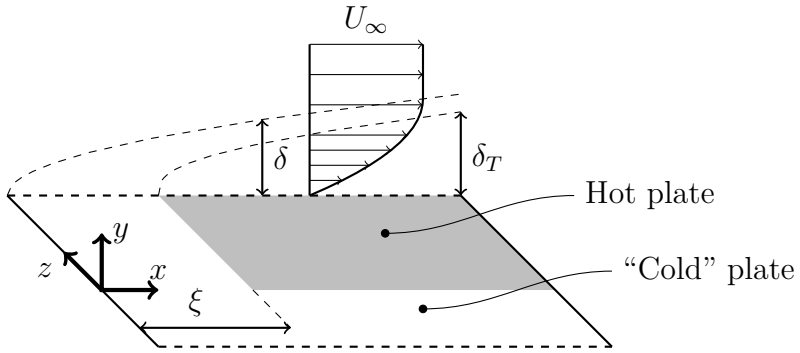

Figure 2.15: Sketch of the problem domain domain showing the unheated starting length, ξ, momentum boundary layer, δ, and thermal boundary layer, δ_T. The hot and "cold" plate are coincident at $z = 0$ and the sketch is mirrored over the dashed lines so the basic geometry repeats in an infinite spanwise array.

sented. The domain is similar to fig. 2.4, only with a finite lateral span shown in fig. 2.17.

Solution

The form of the solution is identical to eq. (2.13), where $\mathcal{Z}$ is the linear solution far from the discontinuity at the origin. In addition to the boundary conditions shown in fig. 2.17 and listed in eq. (2.14a), two additional boundary conditions are needed. The lateral heat flux out the sides of the conduction domain should be zero due to symmetry, as shown in eq. (2.48).

$$\left.\frac{\partial \theta_1}{\partial z}\right|_{z=w_1} = 0 \tag{2.48a}$$

$$\left.\frac{\partial \theta_2}{\partial z}\right|_{z=-w_2} = 0 \tag{2.48b}$$

These boundary conditions describe an array of heated rectangles, $2w_1$, wide separated by a lateral distance of $2w_2$.

The lateral boundary conditions shown in eq. (2.48) modify the eigenfunctions in

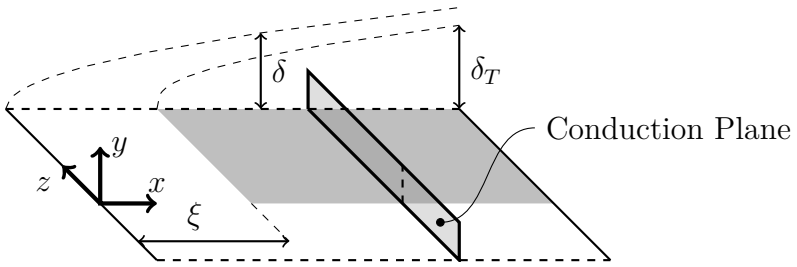

Figure 2.16: Modified from fig. 2.15 showing conduction modeling domain.

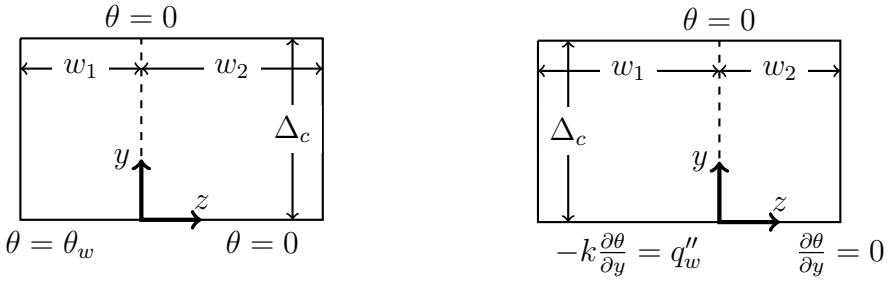

(a) Case 1 from table 2.1

(b) Case 4 from table 2.1

Figure 2.17: Problem domain for laminar conduction in a finite lateral domain

eqs. (2.15a) and (2.25a) slightly. The new eigenfunctions for case 1 are

$$\mathbb{YZ}_{1,\lambda} = A_{1,\lambda}\left[\exp\left(\lambda_{n,T}z\right) + \exp\left(\lambda_{n,T}\left(2w_1 - z\right)\right)\right]\sin\left(\lambda_{n,T}y\right), \quad z > 0, \tag{2.49a}$$

$$\mathbb{YZ}_{2,\lambda} = A_{2,\lambda}\left[\exp\left(\lambda_{n,T}z\right) + \exp\left(-\lambda_{n,T}\left(2w_2 + z\right)\right)\right]\sin\left(\lambda_{n,T}y\right), \quad z < 0, \tag{2.49b}$$

and the new eigenfunctions for case 4 are

$$\mathbb{YZ}_{1,\lambda} = B_{1,\lambda}\left[\exp\left(\lambda_{n,F}z\right) + \exp\left(\lambda_{n,F}\left(2w_1 - z\right)\right)\right]\cos\left(\lambda_{n,F}y\right), \quad z > 0, \tag{2.50a}$$

$$\mathbb{YZ}_{2,\lambda} = B_{2,\lambda}\left[\exp\left(\lambda_{n,F}z\right) + \exp\left(-\lambda_{n,F}\left(2w_2 + z\right)\right)\right]\cos\left(\lambda_{n,F}y\right), \quad z < 0. \tag{2.50b}$$

The new terms, $\exp\left(\lambda_n\left(2w_1 - z\right)\right)$ and $\exp\left(-\lambda_n\left(2w_2 + z\right)\right)$, ensure the solution is symmetric about w_1 and w_2, respectively. The eigenvalues, λ_n, are the same as given in eq. (2.16) and eq. (2.26).

Applying the same solution procedure as described in section 2.1.2, the coefficients

for the Fourier series are found by enforcing continuity of temperature and lateral flux at $z = 0$. The final solution for case 1 is

$$\begin{aligned}\frac{\theta_1}{\theta_w} &= 1 - \frac{y}{\Delta_c} + \sum_{n=1}^{\infty} \frac{1}{n\pi} \frac{\exp\left(-2\lambda_{n,T} w_2\right) - 1}{1 - \exp\left(-2\lambda_{n,T}\left(w_1 + w_2\right)\right)} \\ &\quad \times \left[\exp\left(\lambda_{n,T}\left(z - 2w_1\right)\right) + \exp\left(-\lambda_{n,T} z\right)\right] \sin\left(\lambda_{n,T} y\right), \quad z > 0,\end{aligned} \tag{2.51a}$$

$$\begin{aligned}\frac{\theta_2}{\theta_w} &= \sum_{n=1}^{\infty} \frac{1}{n\pi} \frac{\exp\left(2\lambda_{n,T} w_1\right) - 1}{\exp\left(2\lambda_{n,T} w_1\right) - \exp\left(-2\lambda_{n,T} w_2\right)} \\ &\quad \times \left[\exp\left(\lambda_{n,T} z\right) + \exp\left(-\lambda_{n,T}\left(2w_2 + z\right)\right)\right] \sin\left(\lambda_{n,T} y\right), \quad z < 0,\end{aligned} \tag{2.51b}$$

and the solution for case 4 is

$$\begin{aligned}\frac{\theta_1 k}{q''_w \Delta_c} &= 1 - \frac{y}{\Delta_c} + \frac{4}{\pi^2} \sum_{n=0}^{\infty} \frac{1}{\left(2n+1\right)^2} \frac{\exp\left(-2\lambda_{n,F} w_2\right) - 1}{1 - \exp\left(-2\lambda_{n,T}\left(w_1 + w_2\right)\right)} \\ &\quad \times \left[\exp\left(\lambda_{n,F}\left(z - 2w_1\right)\right) + \exp\left(-\lambda_{n,F} z\right)\right] \cos\left(\lambda_{n,F} y\right), \quad z > 0,\end{aligned} \tag{2.52a}$$

$$\begin{aligned}\frac{\theta_1 k}{q''_w \Delta_c} &= \frac{4}{\pi^2} \sum_{n=0}^{\infty} \frac{1}{\left(2n+1\right)^2} \frac{\exp\left(2\lambda_{n,F} w_1\right) - 1}{\exp\left(2\lambda_{n,F} w_1\right) - \exp\left(-2\lambda_{n,F} w_2\right)} \\ &\quad \times \left[\exp\left(\lambda_{n,F} z\right) + \exp\left(-\lambda_{n,F}\left(2w_2 + z\right)\right)\right] \cos\left(\lambda_{n,F} y\right), \quad z > 0.\end{aligned} \tag{2.52b}$$

Equations (2.51) and (2.52) are written in a way that makes sense in the context of the derivation of the solution, i.e. in terms of eigenvalues as opposed to nondimensional parameters. However, it should be clear that there are two nondimensional parameters imposed on the problem, w_1/Δ_c and w_2/Δ_c, by the geometry of the problem domain.

The solutions for case 2 and 3 from table 2.1 are difficult to calculate for the general case using eigenfunctions, and simple fits as shown in eq. (2.31) did not work well. Other approximate solution methods, similar to eqs. (2.41) and (2.42) are used to

estimate the Nu at the wall. Note that Philip (1972, eq. 8.7) provides a solution to the analogous momentum problem for mixed no-slip and no-shear boundary conditions using a clever conformal mapping technique; a technique and solution that would map directly to the present thermal problem. However, the method of calculating the shear stress is not given (and would be rather laborious to find), so will not be discussed here.

Wall Normal Gradient

As in section 2.1.2, the wall normal gradients are used to find an expression for Nu. Finding the wall normal gradient of eq. (2.52) is trivial. It is simply a matter of finding the multiplicative inverse of the expression. The wall normal gradient of eq. (2.51) for $z > 0$ is

$$\frac{\partial}{\partial y}\left(\frac{\theta}{\theta_w}\right)_{y=0} = -\frac{1}{\Delta_c} + \frac{1}{\Delta_c}\sum_{n=1}^{\infty}\frac{\exp\left(-2\lambda_{n,T}w_2\right)-1}{1-\exp\left(-2\lambda_{n,T}\left(w_1+w_2\right)\right)} \times\left[\exp\left(\lambda_{n,T}\left(z-2w_1\right)\right)+\exp\left(-\lambda_{n,T}z\right)\right] \tag{2.53}$$

2.2.2 Convection

Convection Numerical Simulations

The three dimensional simulations carried out for the finite width rectangular strips are very similar to the ones described in section 2.1.3. The same Pr, unheated starting lengths (0.0795 m and 0.795 m), and boundary conditions are used. However, for the finite width simulations, the height of the domain is changed depending on the Pr, as shown in table 2.3. This allowed for an increase in resolution in all axes, with the ratios of the sides of the smallest cell held constant at the same ratio described in

Table 2.3: Grid information for finite laminar simulations

Pr (-)	domain height (-)	smallest cell y direction (-)
6	$0.04L$	$1.32 \times 10^{-5}L$
2.28	$0.055L$	$1.82 \times 10^{-5}L$
0.7	$0.082L$	$2.71 \times 10^{-5}L$

section 2.1.3. The percentage increase from cell to cell was held constant for each Pr.

For all six combinations of the various Pr and unheated starting lengths, the geometry described in table 2.4 is used. In all, 198 three dimensional numerical simulations are completed for the finite width case.

Table 2.4: Permutations of widths for numerical modeling

w_1 (mm)	w_2 (mm)
0.25	50
1	50
4	50
0.25	4
4	4
1	1
0.25	0.25
4	0.25

Correlations

In addition to the nondimensional parameter defined by eqs. (2.36) and (2.37), two new nondimensional parameters are defined

$$w_1^* = \frac{w_1}{\Delta_c}, \tag{2.54}$$

$$w_2^* = \frac{w_2}{\Delta_c}. \tag{2.55}$$

Using these definitions, similar correlations to eqs. (2.40) and (2.43) can be con-

structed.

$$\frac{Nu}{Nu_{z\to\infty}} = 1 - \sum_{n=1}^{\infty} \frac{\exp\left(-2\lambda_{n,T} w_2\right) - 1}{1 - \exp\left(-2\lambda_{n,T}\left(w_1 + w_2\right)\right)} \left[\exp\left(\lambda_{n,T}\left(z - 2w_1\right)\right) + \exp\left(-\lambda_{n,T} z\right)\right] \tag{2.56}$$

$$\frac{Nu}{Nu_{z\to\infty}} = \frac{1}{1 + \frac{4}{\pi^2}\sum_{n=0}^{\infty} \frac{1}{(2n+1)^2} \frac{\exp\left(-2\lambda_{n,F} w_2\right) - 1}{1 - \exp\left(-2\lambda_{n,F}(w_1 + w_2)\right)} \left[\exp\left(\lambda_{n,F}\left(z - 2w_1\right)\right) + \exp\left(-\lambda_{n,F} z\right)\right]} \tag{2.57}$$

Conduction Numerical Simulations

As closed form solutions for cases 2 and 3 for the finite width problem are difficult to formulate, two dimensional conduction simulations are carried out for these two cases for a wide array of heated and cooled/adiabatic widths. Just over 1000 simulations are run for each case and the coefficients in eq. (2.58) estimated from the conduction modeling. This allows a rough estimation of Nu for any set of widths within the simulated range. Note that the time to run the roughly 1000 conduction simulations is on the order of the time required to run only one of the three dimensional simulations with the velocity field specified. The data in the following sections for cases 2 and 3 are either directly from the numerical conduction data or from eq. (2.58).

For all the simulation runs, the height of the domain (the conduction thickness) is held constant, while w_1 and w_2 are allowed to vary. As was done in sections 2.1.3 and 2.2.2, the normalized Nu is calculated by normalizing the temperature gradient at the surface by a representative temperature difference and domain height, Δ_c. The

lateral Nu profiles are then estimated using the following equation:

$$\frac{Nu}{Nu_{z\to\infty}} = \left[\left(\frac{a}{\sqrt{\zeta^*}}\right)^p + \left(\frac{a}{\sqrt{2w_1^* - \zeta^*}}\right)^p + b^p\right]^{1/p}. \tag{2.58}$$

The parameters are estimated by minimizing the residual sum of squares normalized by the local Nu between eq. (2.58) for each conduction simulation using the `fminsearch()` function in MATLAB (The MathWorks, Inc. 2014). The resulting surfaces for each parameter are shown in figs. 2.18 to 2.23.

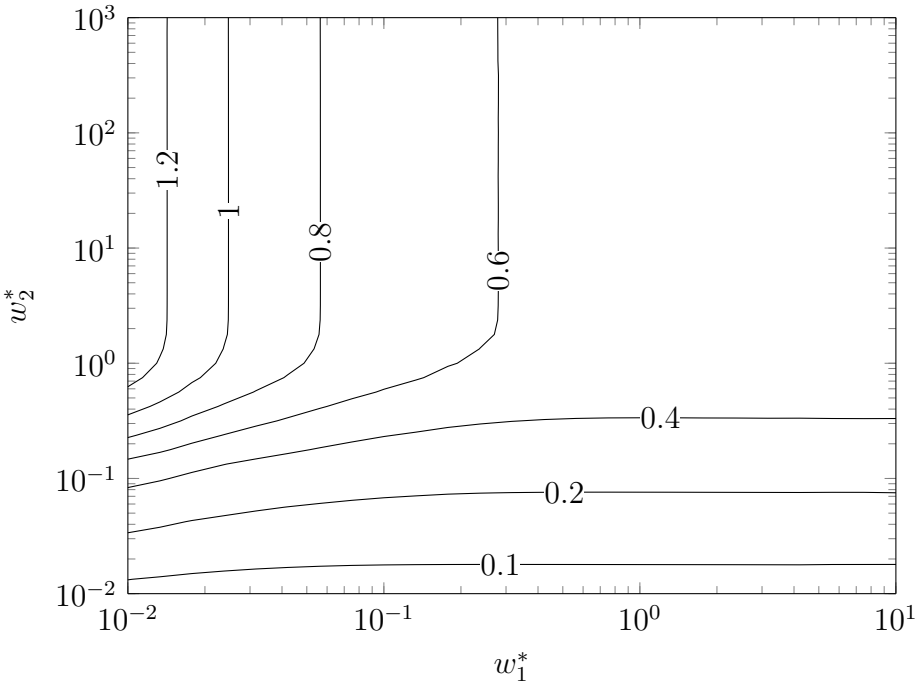

Figure 2.18: Estimate of parameter a from eq. (2.58) for case 2

The method employed in this section, with the numerical conduction modeling predicting convection from a surface, is a possible practical technique if the surface boundary conditions do not adhere to one of the four presented cases. The conduction model is clearly a fast and accurate method for modeling the lateral edge effect, and numerically solving a conduction problem is almost trivial with modern computational

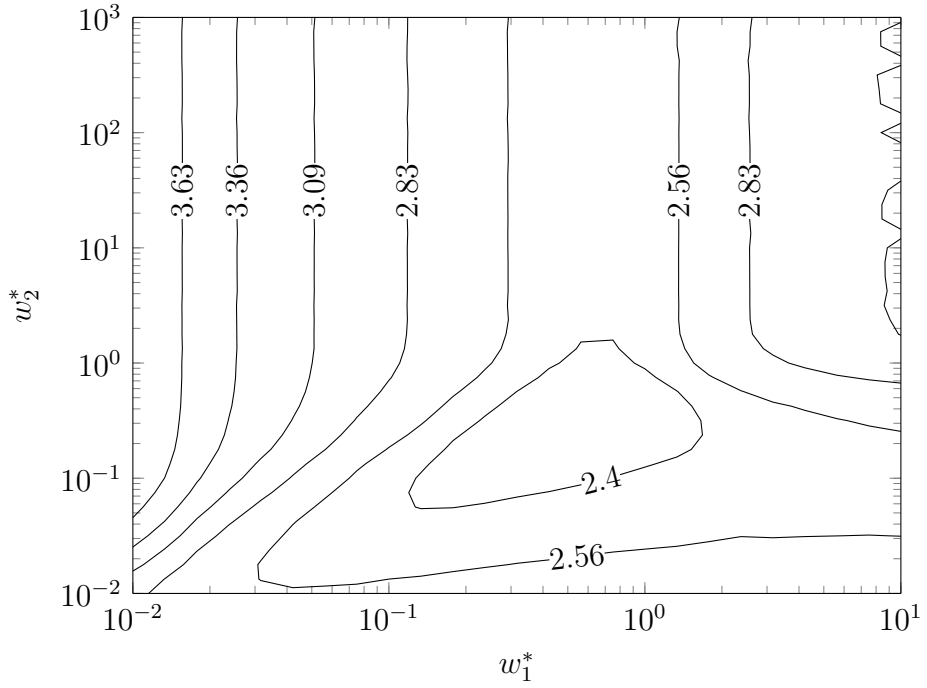

Figure 2.19: Estimate of parameter p from eq. (2.58) for case 2

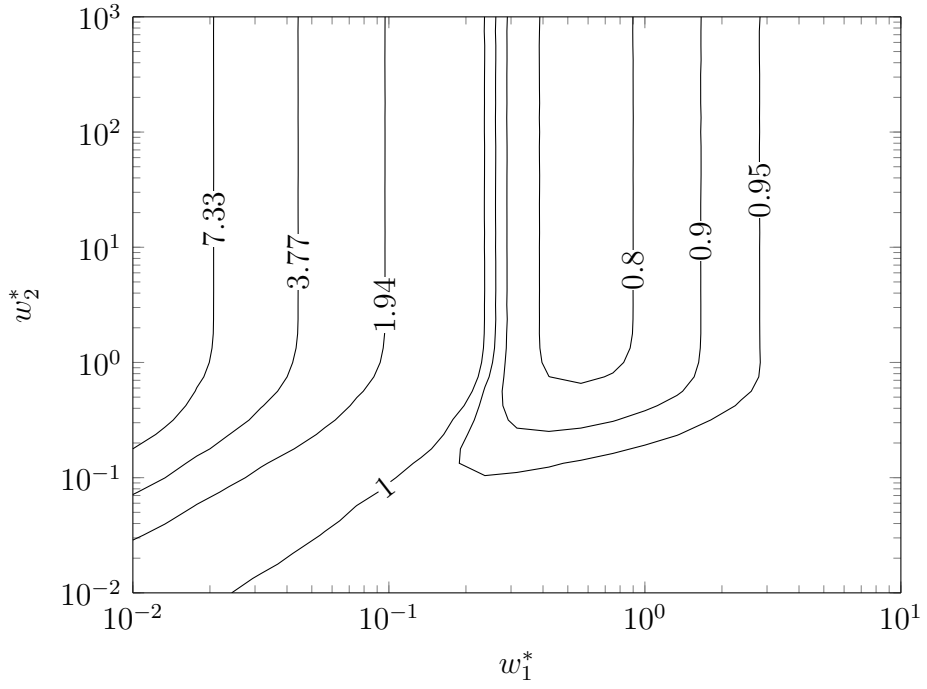

Figure 2.20: Estimate of parameter b from eq. (2.58) for case 2

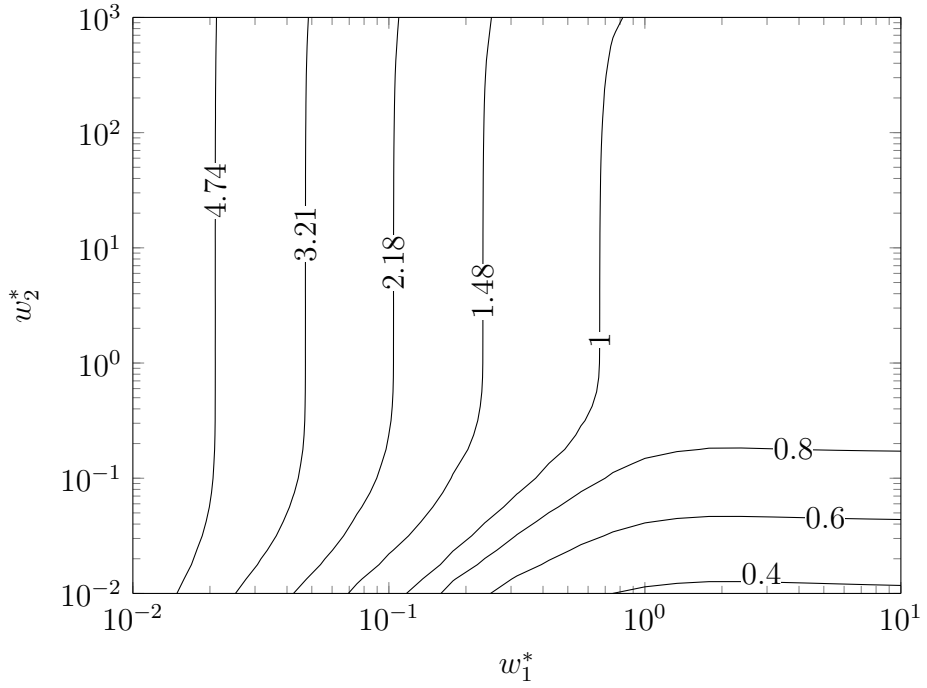

Figure 2.21: Estimate of parameter a from eq. (2.58) for case 3

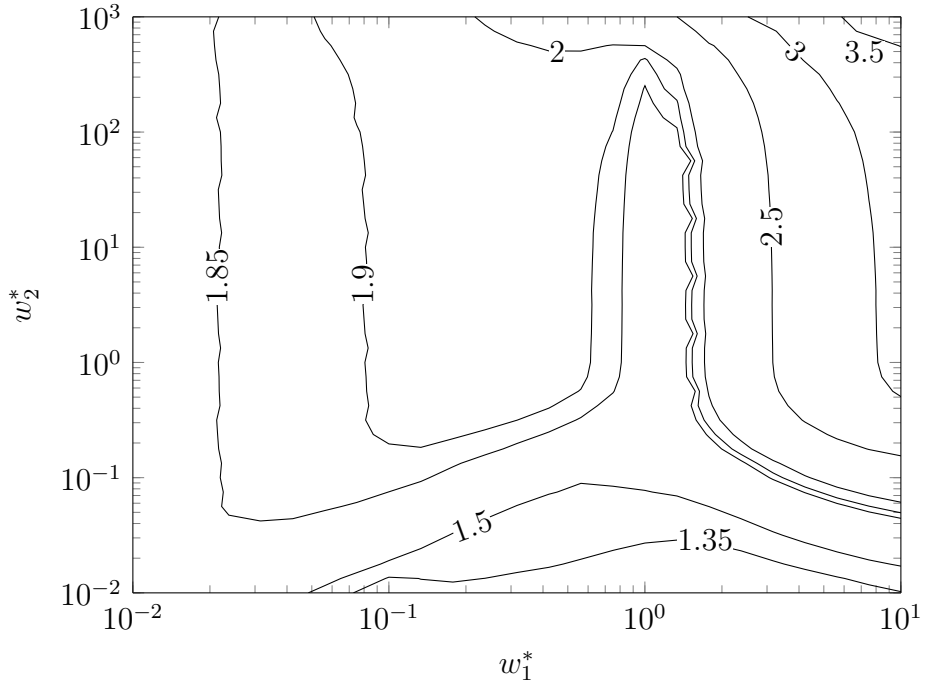

Figure 2.22: Estimate of parameter p from eq. (2.58) for case 3

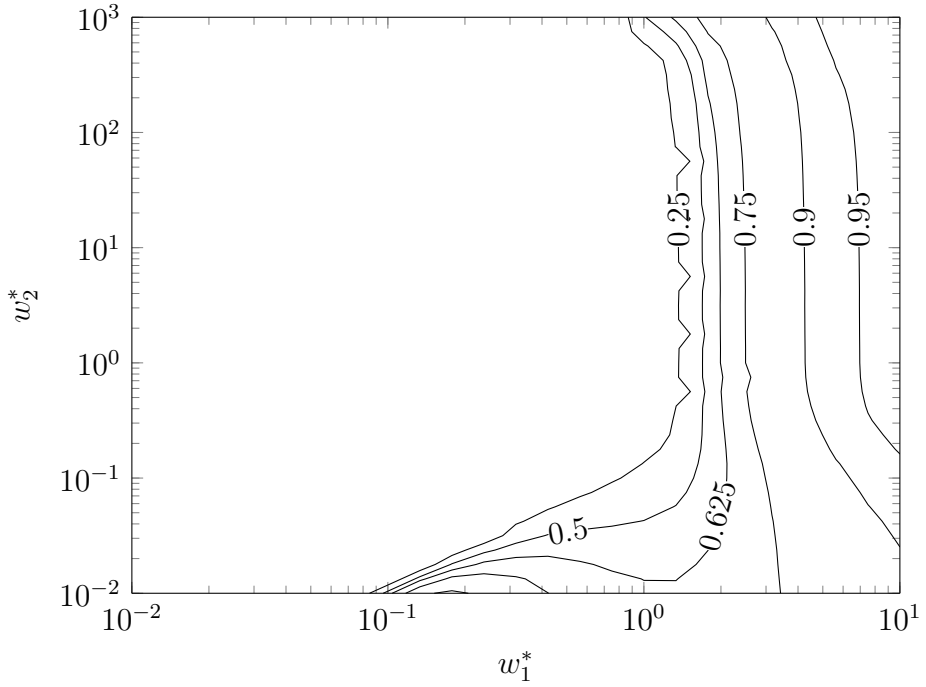

Figure 2.23: Estimate of parameter b from eq. (2.58) for case 3. The value of b in the large basin is zero.

tools.

Heat Flux at Center of Strip

A useful measure of the finite width effects is a comparison of Nu at the center, where $z = w_1$, and $Nu_{z\to\infty}$ for varying values of w_1 and w_2. Figures 2.24 to 2.27 show the Nu at the center of the streamwise rectangular strips, Nu_{w_1}, is close to the value for a semi-infinite domain, $Nu_{z\to\infty}$, when the half width, w_1, is about the same size as the conduction thickness, Δ_c. In other words, if w_1/Δ_c, then the contours shown in Figures 2.24 to 2.27 are approximately equal to one. Figures 2.24 to 2.27 also show that the centerline Nu increases very quickly as w_1 approaches zero. Figures 2.24 and 2.26 show that for the cases where the cooled surface is isothermal, the centerline Nu is primarily a function of w_1/Δ_c; while Figures 2.25 and 2.27 show that for the

surface where the "cooled" surface is adiabatic, both w_1/Δ_c and w_2/Δ_c affect the centerline Nu.

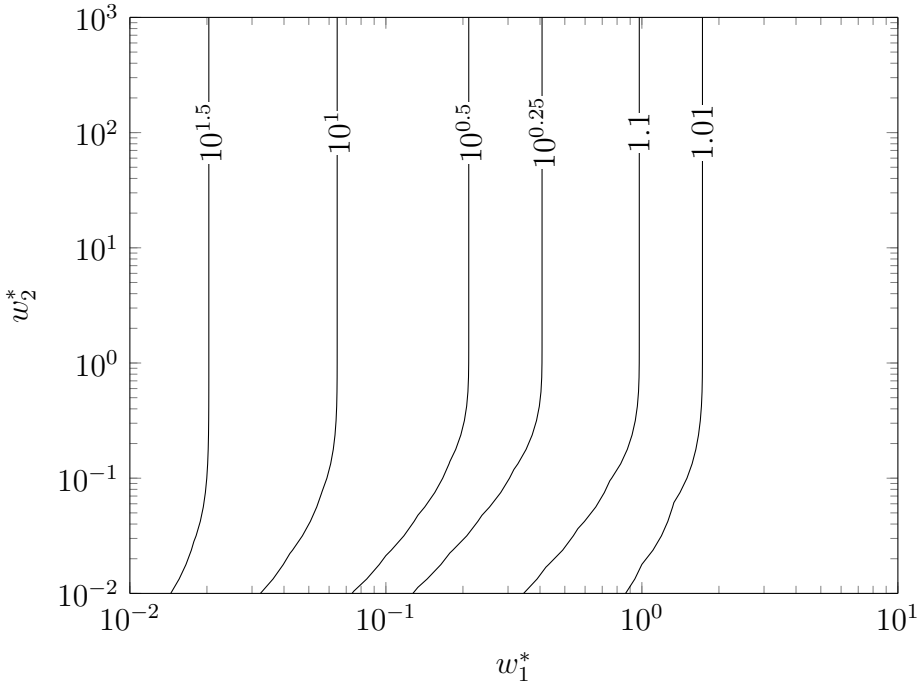

Figure 2.24: Effect of finite widths on centerline normalized Nu, $Nu_{w_1}/Nu_{z\to\infty}$, for case 1

The increase in the Nu due to the decrease in the width of the plate can be derived from eq. (2.56). At the center of the rectangular strip $z = w_1$, and for $w_2 \to \infty$ eq. (2.56), eq. (2.56) becomes

$$\begin{aligned}\frac{Nu_{w1}}{Nu_{z\to\infty}} &= 1 + \sum_{n=1}^{\infty} 2\exp\left(-n\pi w_1^*\right) \\ &= \frac{\exp\left(-\pi w_1^*\right) + 1}{\exp\left(-\pi w_1^*\right) - 1}\end{aligned} \tag{2.59}$$

By inspection, the Nu approaches infinity as w_1^* approaches zero. This is discussed in more detail in section 2.2.2 and eq. (2.65).

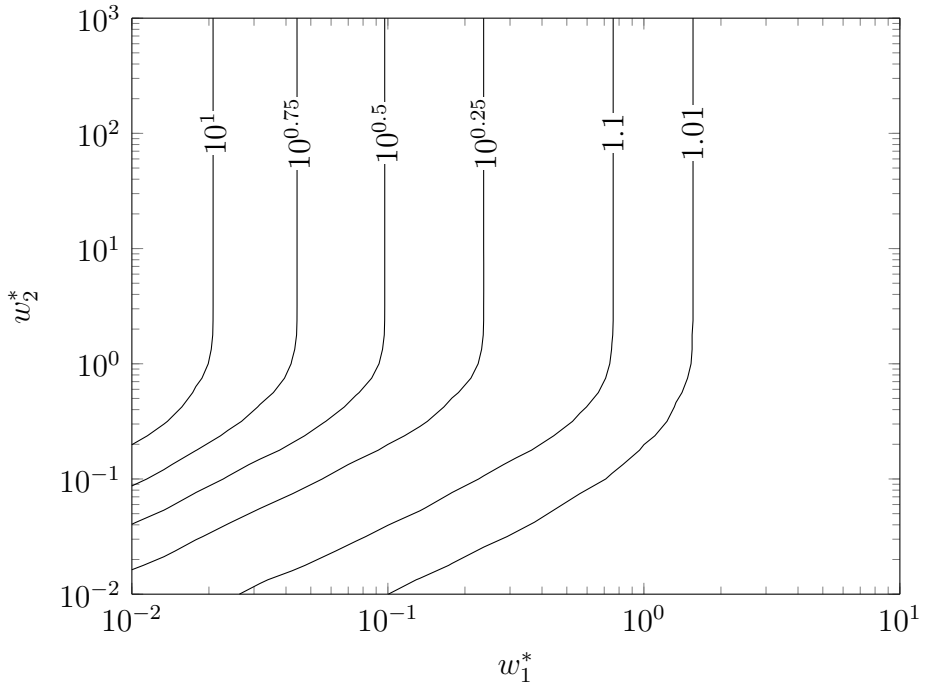

Figure 2.25: Effect of finite widths on centerline normalized Nu, $Nu_{w_1}/Nu_{z\to\infty}$, for case 2

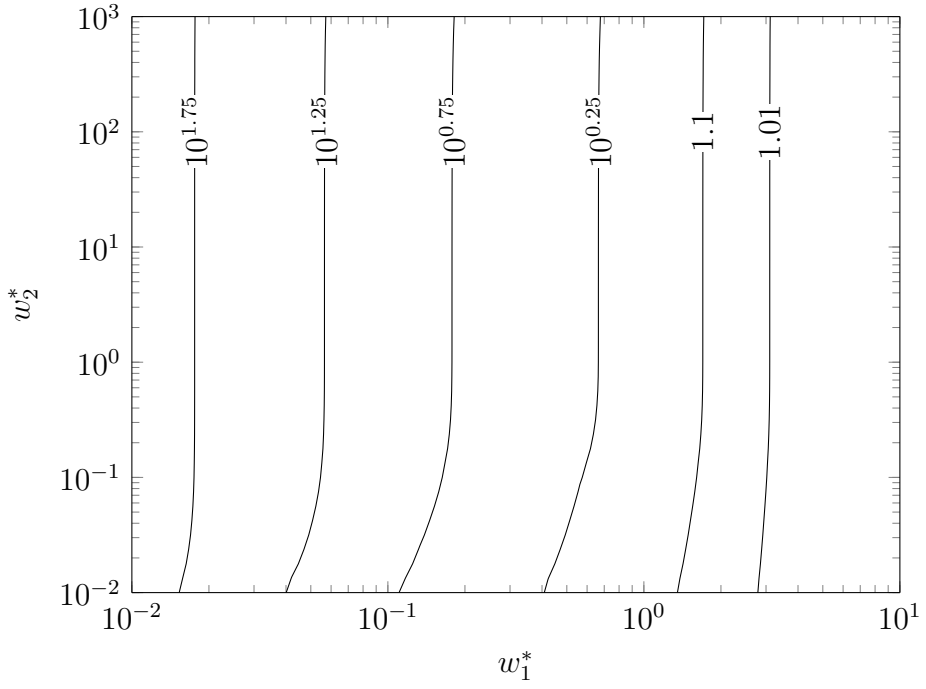

Figure 2.26: Effect of finite widths on centerline normalized Nu, $Nu_{w_1}/Nu_{z\to\infty}$, for case 3

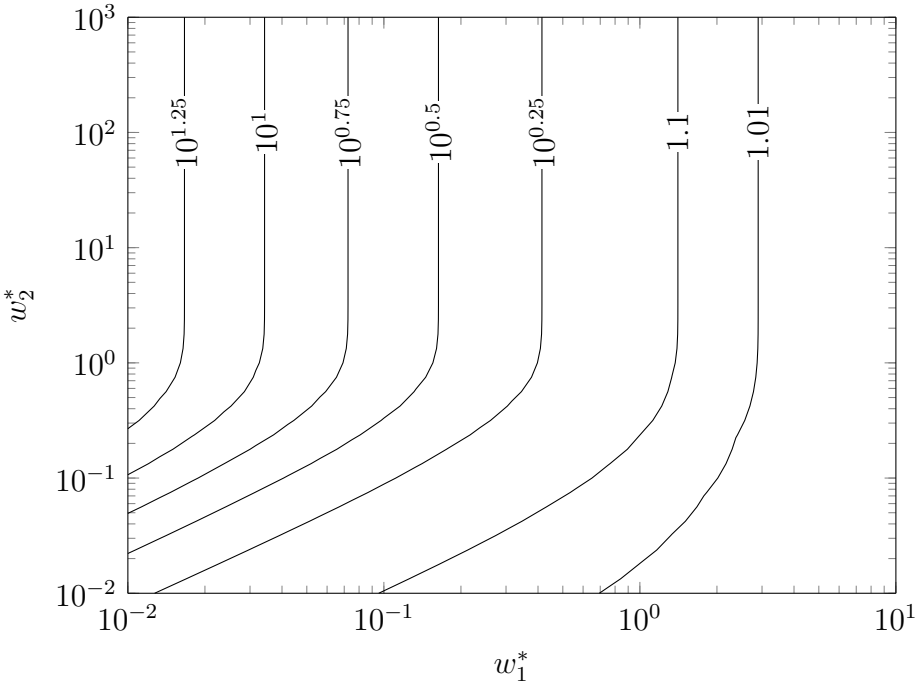

Figure 2.27: Effect of finite widths on centerline normalized Nu, $Nu_{w_1}/Nu_{z\to\infty}$, for case 4

For case 4, the value of the Nu at the center becomes

$$\begin{aligned}\frac{Nu_{w1}}{Nu_{z\to\infty}} &= \frac{1}{1-\frac{8}{\pi^2}\sum_{n=0}^{\infty}\frac{\exp(-\lambda_{n,F}w_1)}{(2n+1)^2}} \\ &= \frac{1}{1-\frac{4}{\pi^2}\left[\mathrm{Li}_2\left(e^{-\frac{\pi w_1}{2\Delta_c}}\right)-\mathrm{Li}_2\left(-e^{-\frac{\pi w_1}{2\Delta_c}}\right)\right]}\end{aligned} \tag{2.60}$$

Two identities given by Maximon (2003) for the dilogarithm function show that eq. (2.60) does indeed tend towards infinity as w_1 tends towards zero. This is discussed further in section 2.2.2 and eq. (2.67).

Figures 2.28 to 2.35 and E.1 to E.24 show how well the conduction model compares to the numerical simulations for all the boundary conditions when predicting the Nu at the center of a finite strip. It is difficult to tell whether the small inaccuracies past the region affected by the leading edge are due to the use of eqs. (2.44) and (2.45) to

calculate both $Nu_{z\to\infty}$ and ζ^*, the simplifying assumptions of the conduction model, or the inaccuracies inherent in numerical modeling. In several of the figures, namely figs. 2.28, E.1 and E.4, it is clear the the numerical data does not match eq. (2.44) near the leading edge. When analyzing the lateral trends, the data are analyzed sufficiently far from the leading edge so eq. (2.44) and the data from the numerical simulation are within a few percent of each other.

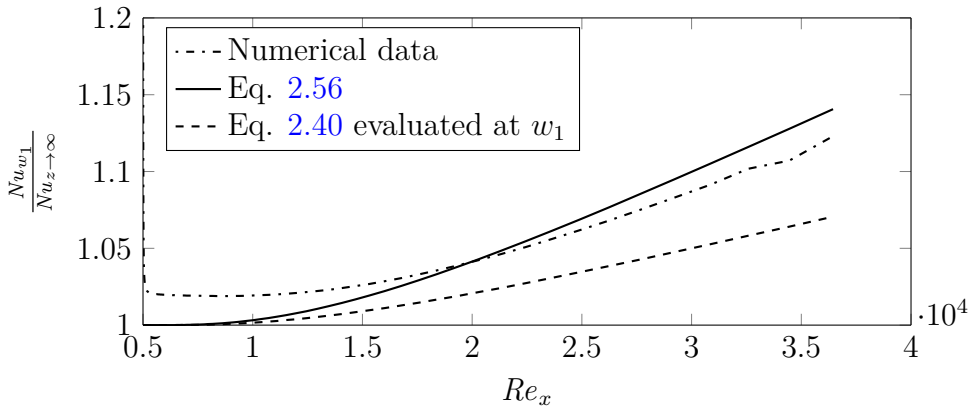

Figure 2.28: Case 1 center Nu for $Pr = 6$, $\xi = 0.0795\,\text{m}$, $w_1 = 4\,\text{mm}$, $w_2 = 4\,\text{mm}$

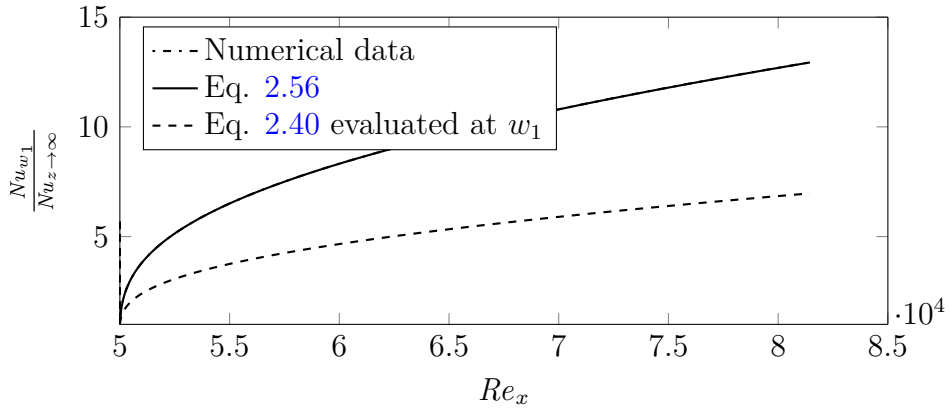

Figure 2.29: Case 1 center Nu for $Pr = 6$, $\xi = 0.795\,\text{m}$, $w_1 = 0.25\,\text{mm}$, $w_2 = 4\,\text{mm}$

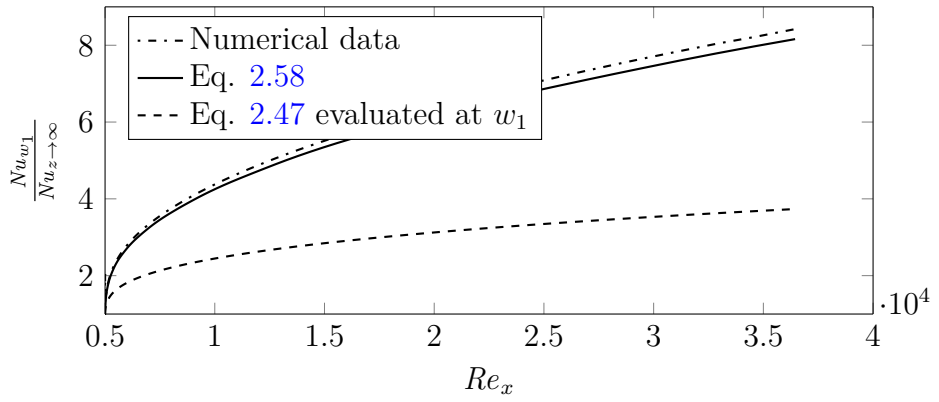

Figure 2.30: Case 2 center Nu for $Pr = 0.7$, $\xi = 0.0795\,\text{m}$, $w_1 = 0.25\,\text{mm}$, $w_2 = 50\,\text{mm}$

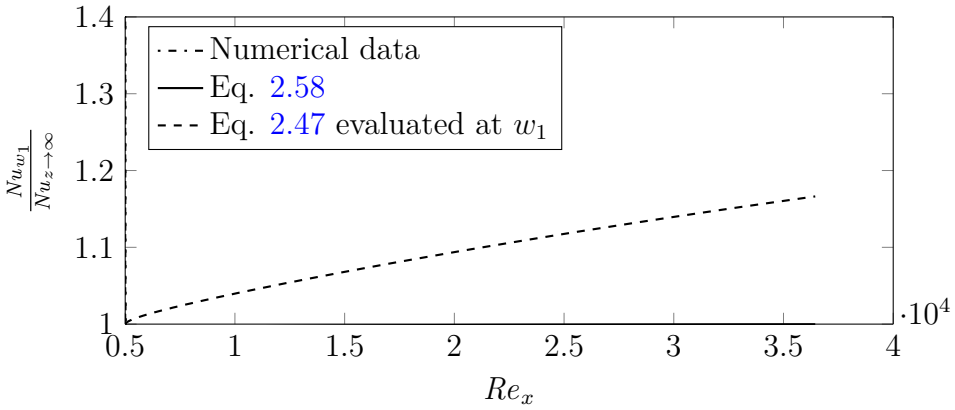

Figure 2.31: Case 2 center Nu for $Pr = 0.7$, $\xi = 0.0795\,\text{m}$, $w_1 = 4\,\text{mm}$, $w_2 = 0.25\,\text{mm}$

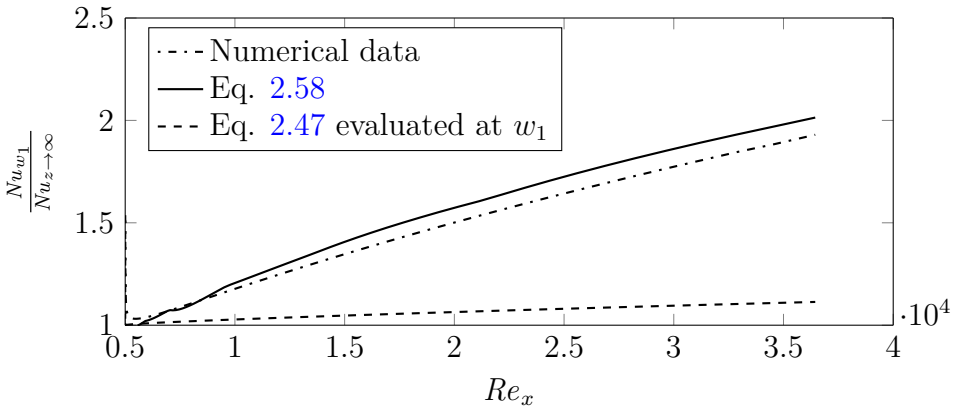

Figure 2.32: Case 3 center Nu for $Pr = 0.7$, $\xi = 0.0795\,\text{m}$, $w_1 = 4\,\text{mm}$, $w_2 = 4\,\text{mm}$

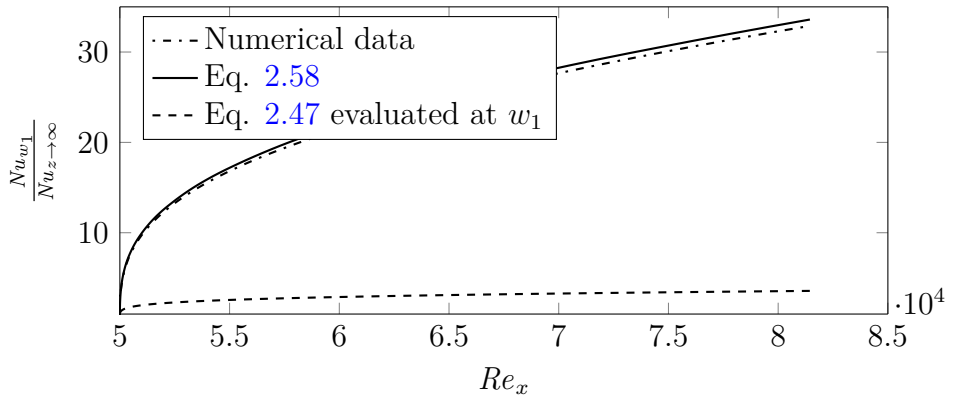

Figure 2.33: Case 3 center Nu for $Pr = 0.7$, $\xi = 0.795\,\mathrm{m}$, $w_1 = 0.25\,\mathrm{mm}$, $w_2 = 4\,\mathrm{mm}$

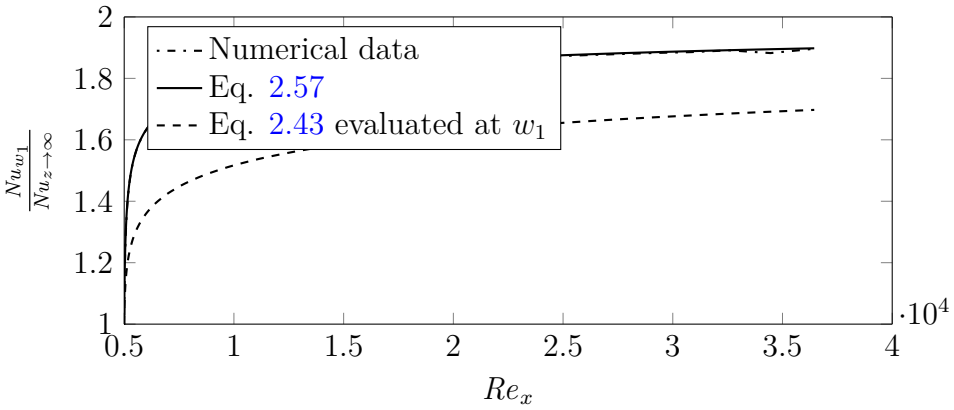

Figure 2.34: Case 4 center Nu for $Pr = 6$, $\xi = 0.0795\,\mathrm{m}$, $w_1 = 0.25\,\mathrm{mm}$, $w_2 = 0.25\,\mathrm{mm}$

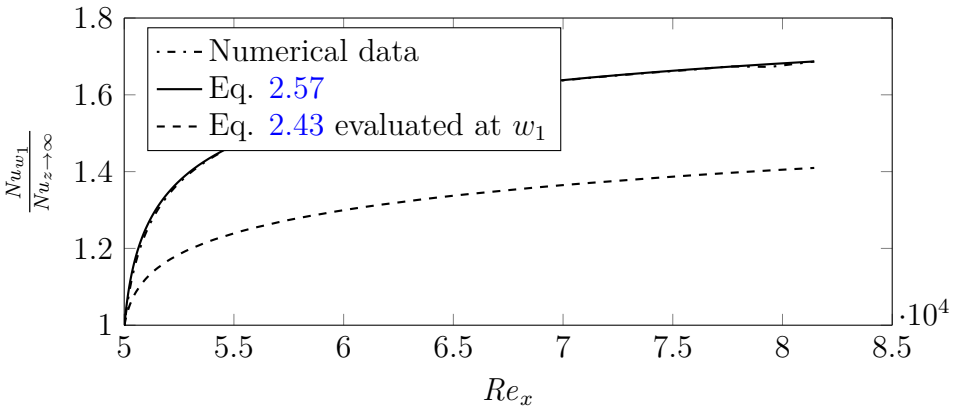

Figure 2.35: Case 4 center Nu for $Pr = 6$, $\xi = 0.795\,\mathrm{m}$, $w_1 = 1\,\mathrm{mm}$, $w_2 = 1\,\mathrm{mm}$

Lateral Variation for the Nu

Figures 2.36 to 2.41, 2.43, 2.44 and E.25 to E.48 compare the three dimensional numerical data for all the boundary conditions to the prediction from eqs. (2.56) to (2.58) for various Pr, unheated starting lengths, and lateral widths. The numerical simulation data matches eqs. (2.56) and (2.57) well without any parameter fitting, and the numerical conduction model estimate from eq. (2.58) fairly well. Several trends are worth discussing.

For case 1, most of the data closely follows to the correlation predicted by eq. (2.40) except near the center of the heated strip. This is expected, as ζ^* approaches zero, the $\exp(-\lambda_{n,T} z)$ term in eq. (2.56) becomes larger than the other terms for larger values of n. However, near the center of the finite width strip, symmetry is enforced, so the lateral profiles of the normalized Nu have to "peel off" the profile predicted by eq. (2.40).

Case 4 exhibits several features similar to case 1. There is the obvious symmetry across $z = w_1$ and the increase in the Nu for most parameters except where $w_1 > w_2$. However, as the Nu tends towards a finite value as $\zeta^* \to 0$, several new features are evident. For smaller values of w_1^* the lateral profiles of the Nu are flatter. This can be seen in figs. 2.38, 2.39 and E.43 to E.48 where the Nu profiles farthest from the leading edge change the least relative to the $Nu_{z\to\infty}$. If the width of the heated portion of the plate is small relative to the conduction thickness, the temperature profile on the heated surface is more uniform because the temperature on the adiabatic surface is higher near $z = 0$ farther down the flow. In other words, the energy lost by the heated surface has increased the temperature of the adiabatic surface near $z = 0$ the further downstream one measures.

For cases 1 and 4, it is evident from figs. 2.37 and 2.39 where the width of the

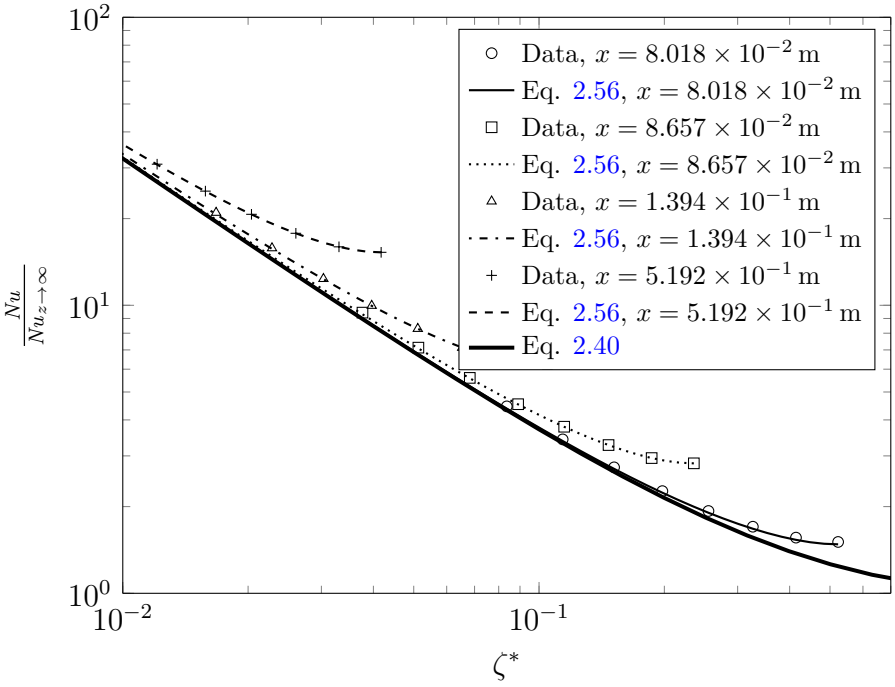

Figure 2.36: Case 1 lateral Nu for $Pr = 2.28$, $\xi = 0.0795\,\text{m}$, $w_1 = 0.25\,\text{mm}$, $w_2 = 50\,\text{mm}$

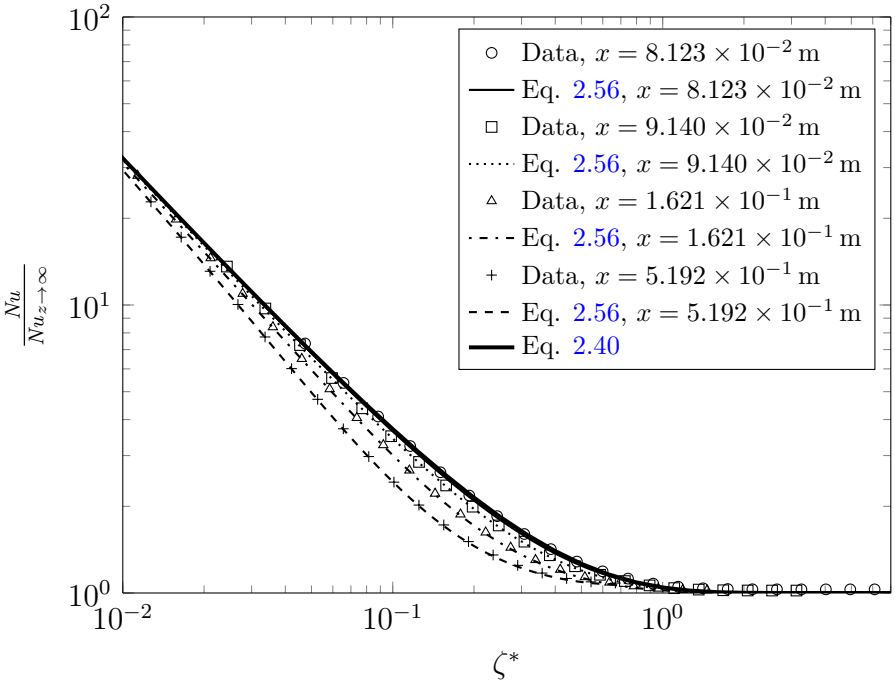

Figure 2.37: Case 1 lateral Nu for $Pr = 2.28$, $\xi = 0.0795\,\text{m}$, $w_1 = 4\,\text{mm}$, $w_2 = 0.25\,\text{mm}$

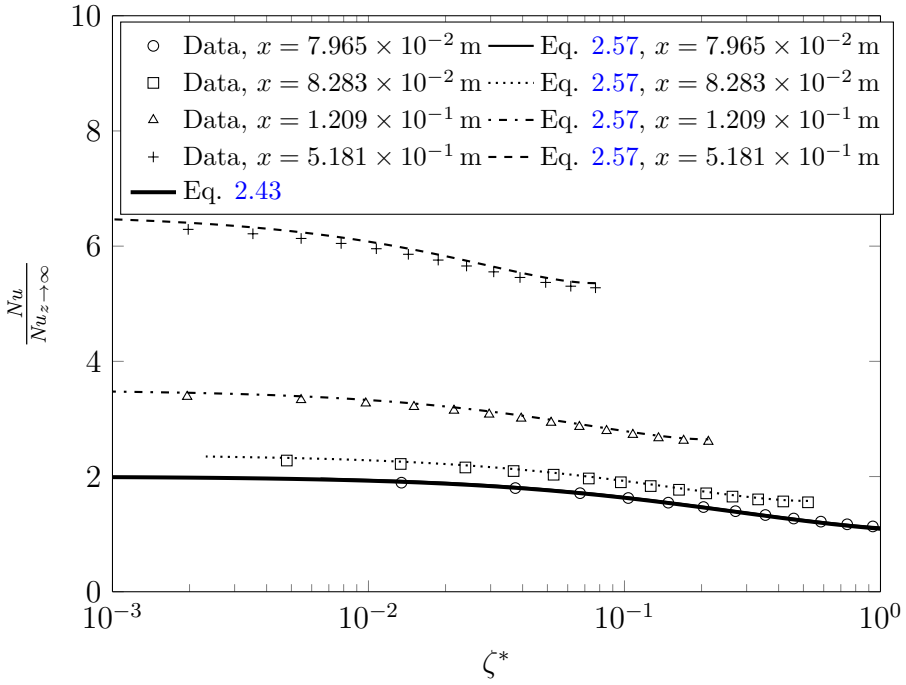

Figure 2.38: Case 4 lateral Nu for $Pr = 6$, $\xi = 0.0795\,\text{m}$, $w_1 = 0.25\,\text{mm}$, $w_2 = 50\,\text{mm}$

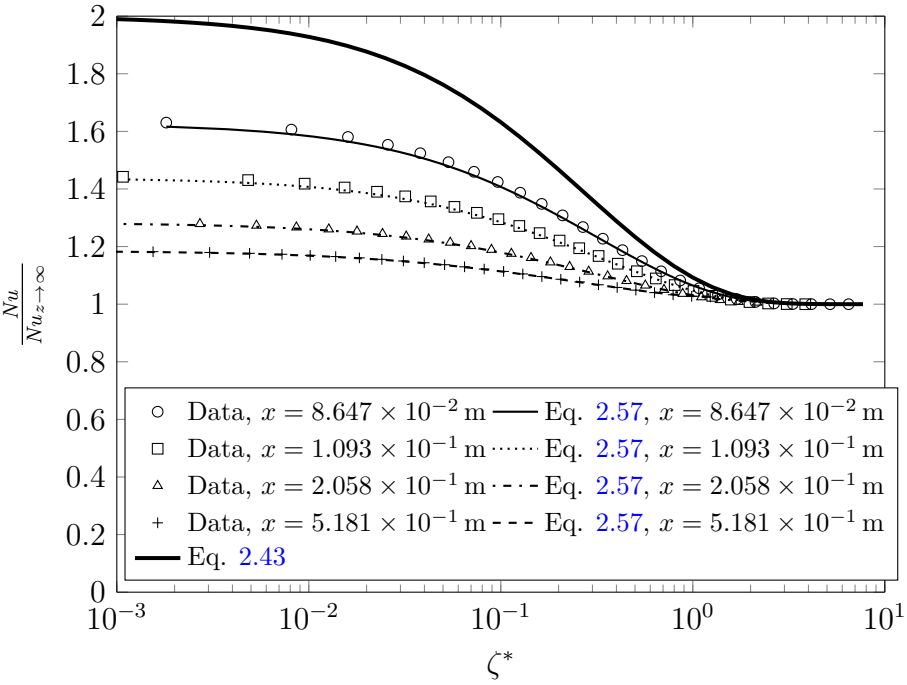

Figure 2.39: Case 4 lateral Nu for $Pr = 6$, $\xi = 0.0795\,\text{m}$, $w_1 = 4\,\text{mm}$, $w_2 = 0.25\,\text{mm}$

heated plate is significantly larger than the width of the cooled portion, the Nu is lower than the Nu from a heated surface of semi-infinite width. This can be shown analytically by taking the ratio of the argument in the summation shown in eqs. (2.56) and (2.57) and the argument in the summation shown in eqs. (2.32) and (2.43), $\exp(-\lambda_n z)$. If each element in the summation for the finite width geometry is smaller than the corresponding element for the semi-infinite geometry, the assertion is proved. Also, recall both geometries are normalized by the same Nu_∞.

$$\exp(\lambda_n z)\frac{\exp(-2\lambda_n w_2)-1}{1-\exp(-2\lambda_n(w_1+w_2))}\left[\exp(\lambda_n(z-2w_1))+\exp(-\lambda_n z)\right]= \frac{\exp(-2\lambda_n w_2)-1}{1-\exp(-2\lambda_n(w_1+w_2))}\left[\exp(2\lambda_n(z-w_1))+1\right] \quad (2.61)$$

For the Nu to be less than the semi-infinite Nu, the above ratio should be less than one,

$$2>\exp(2\lambda_n(z-w_1-w_2))+\exp(-2\lambda_n w_2)+\exp(-2\lambda_n(w_1+w_2))-\exp(2\lambda_n(z-w_1)), \quad (2.62)$$

applying $w_1 \gg w_2$,

$$2>\exp(-2\lambda_n w_2)+\exp(-2\lambda_n w_1), \quad (2.63)$$

which is true for all values of λ_n, $w1$, and $w2$. Therefore, for case 1 when $w_1 \gg w_2$, Nu is smaller relative to the semi-infinite case.

For case 4, note that eq. (2.63) is proof that each element in the summation for the finite width geometry is smaller than the corresponding element for the semi-infinite geometry. Since the summation for case 4 is in the denominator and subtracted from 1, a larger denominator relative to the semi-infinite geometry results. Therefore the

Nu of the finite width geometry is smaller than the Nu for the semi-infinite case for case 4 when $w_1 > w_2$.

This can be interpreted physically as the solution approaching the infinite lateral span condition. The wider the heated section compared to the cooled section, the closer the overall solution approximates eqs. (2.44) and (2.45). This is clearer from case 4, particularly in fig. 2.39, where the Nu profiles farther from the leading edge get progressively closer to $Nu = Nu_{z\to\infty}$ over the whole lateral span.

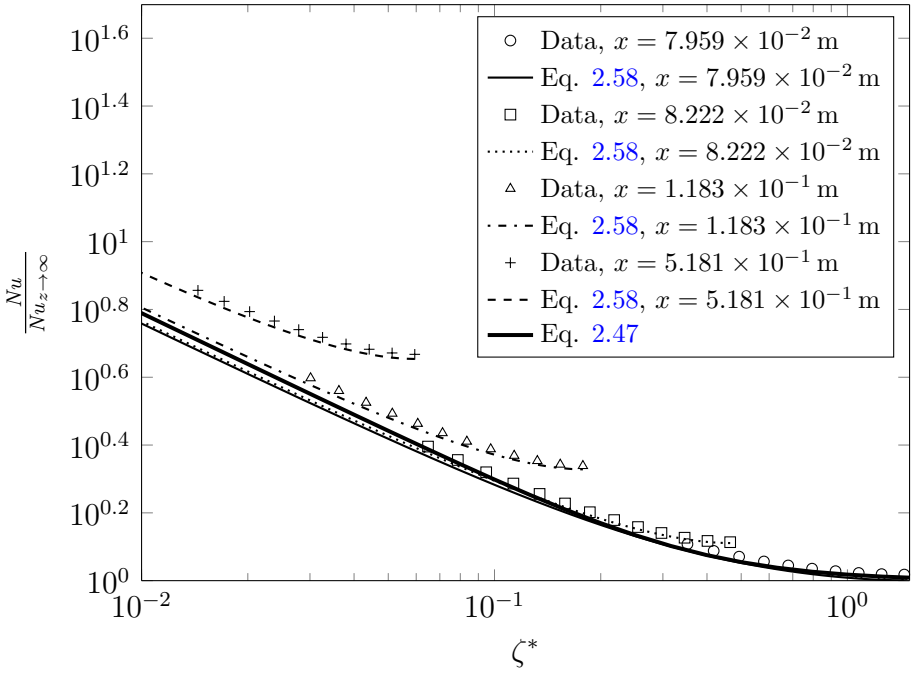

Figure 2.40: Case 2 lateral Nu for $Pr = 6$, $\xi = 0.0795\,\text{m}$, $w_1 = 0.25\,\text{mm}$, $w_2 = 50\,\text{mm}$

Figures 2.40, 2.41 and E.31 to E.36 show the behavior for case 2 is slightly different than for cases 1 and 4. In addition to the Nu being less than the semi-infinite case, for geometries where $w_2 < w_1$; Nu are also less than the semi-infinite for any geometry where $w_2^* < 1$. Using the same reasoning as above, for small w_2^* the temperature of the flow field more resembles the two dimensional temperature field for $w_1^* \to \infty$ and $w_2^* \to 0$. Case 2 differs from case 1 and 4 because the temperature of the

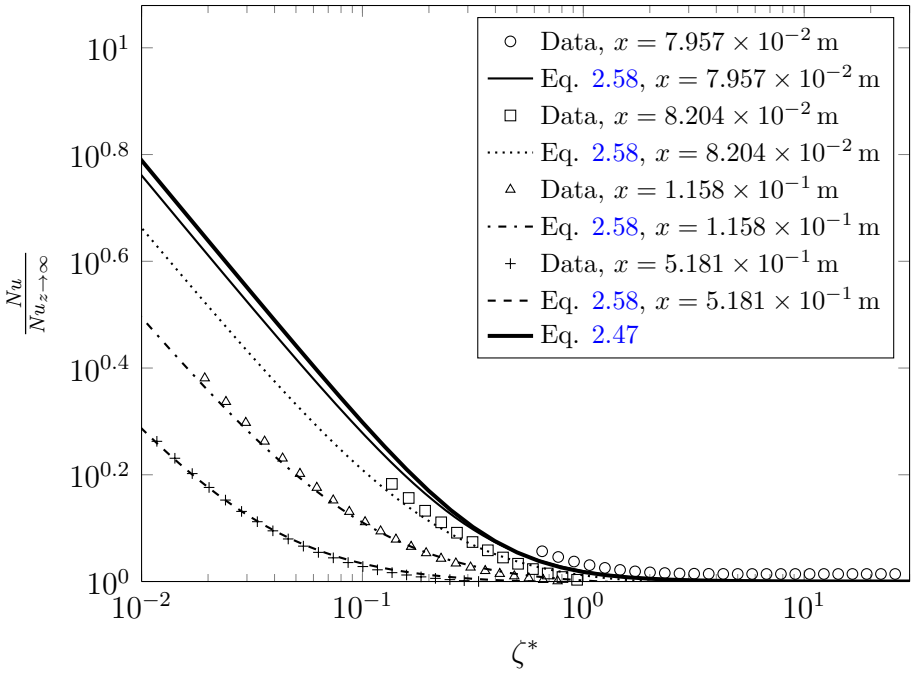

Figure 2.41: Case 2 lateral Nu for $Pr = 6$, $\xi = 0.0795\,\text{m}$, $w_1 = 4\,\text{mm}$, $w_2 = 0.25\,\text{mm}$

whole adiabatic surface approaches the temperature of the isothermal surface for small values of w_2^*, regardless of the value of w_1^*. Figure 2.42 shows that w_2^* is the main parameter controlling the temperature distribution for the adiabatic surface, with w_1^* not affecting the temperature appreciably.

Figures 2.43, 2.44 and E.37 to E.42 show the behavior of case 3 is similar to case 1. While the various curves do not asymptotically approach the values predicted by eq. (2.47), the Nu is larger than for the semi-infinite case except when $w_1^* > w_2^*$.

Spanwise Extent of the Lateral Edge Effect

Similar to section 2.1.3, a rough measure of the lateral edge effect is the spanwise distance where the Nu comes within 10 % of the centerline Nu. The centerline Nu is chosen instead of the $Nu_{z\to\infty}$ so comparisons between strips with different widths are possible. As figs. 2.24 to 2.27 show, the centerline Nu is as much as an order of

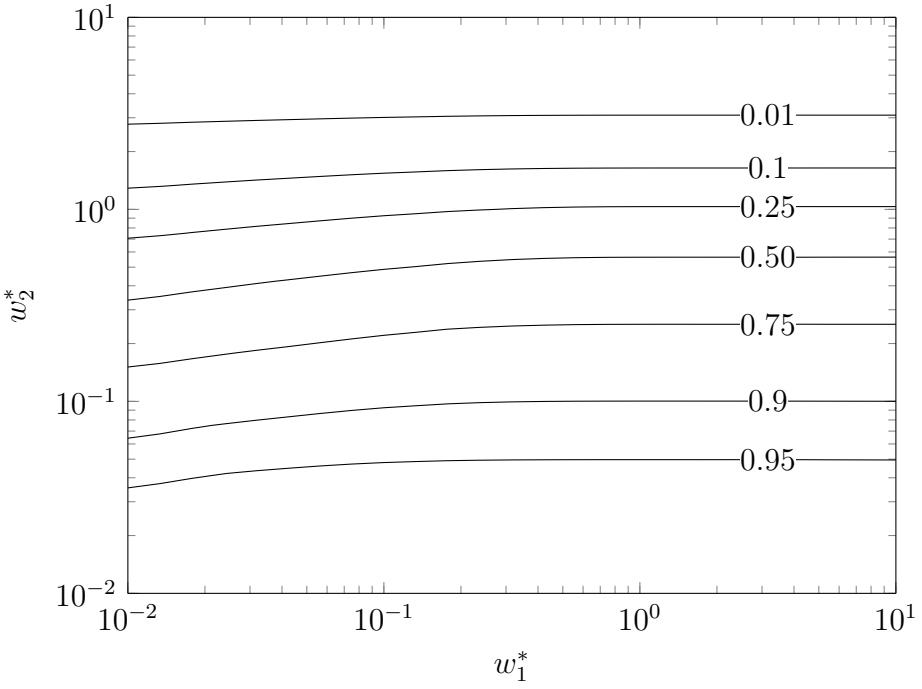

Figure 2.42: Contour of $\theta_{w_2}/\theta_{w_1}$ for case 2

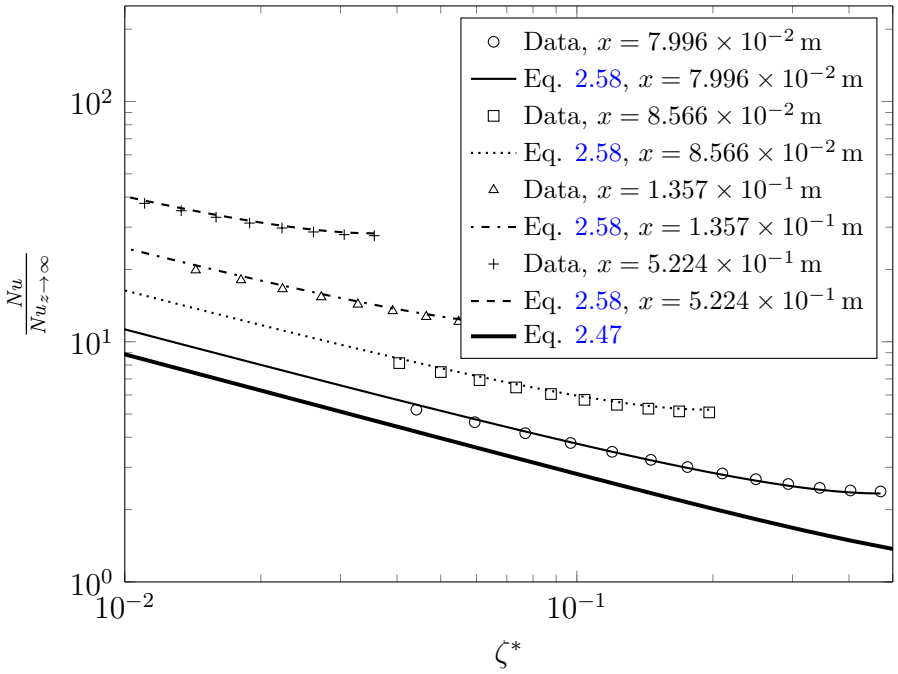

Figure 2.43: Case 3 lateral Nu for $Pr = 0.7$, $\xi = 0.0795\,\text{m}$, $w_1 = 0.25\,\text{mm}$, $w_2 = 50\,\text{mm}$

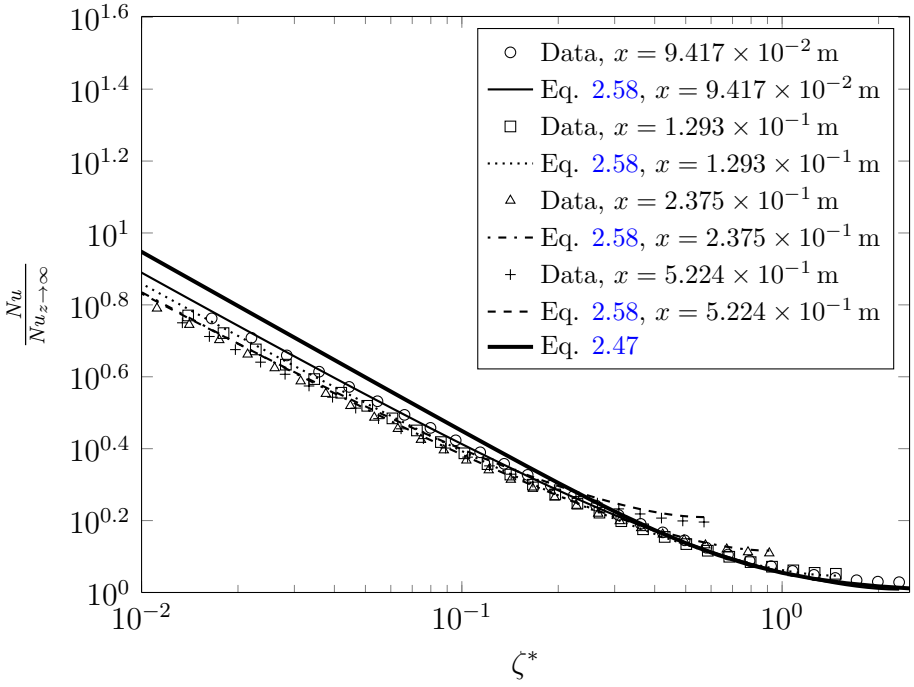

Figure 2.44: Case 3 lateral Nu for $Pr = 0.7$, $\xi = 0.0795\,\text{m}$, $w_1 = 4\,\text{mm}$, $w_2 = 0.25\,\text{mm}$

magnitude larger than $Nu_{z\to\infty}$, making a $Nu = 1.1Nu_{z\to\infty}$ impossible for some cases. Figures 2.45 to 2.48 show the ζ^* value where $Nu = 1.1Nu_{z\to\infty}$, denoted as $\zeta^*_{1.1}$. It is evident from the figs. 2.45 to 2.48 that the semi-infinite condition is approached for $w_1^* \gtrsim 2$ and $w_2^* \gtrsim 1$.

Figures 2.45 to 2.48 show that for smaller values of w_1^*, $\zeta^*_{1.1}$ is not the only, or even most useful parameter. Not only does the lateral edge effect extend beyond the centerline, but the values become arbitrarily small as the widths decrease. For narrower strips, the lateral location normalized by the width of the heated strip gives a better indication of how quickly the profile approaches the centerline Nu. For case 1, case 2, and case 3, shown in figs. 2.49 to 2.51, as w_1^* approaches zero, the ratio $\zeta^*_{1.1}/w_1^*$ approaches a finite value. It takes approximately half to three fifths of the width to come within 10 % of the centerline value. This indicates that as the heated strip narrows, the Nu/Nu_{w_1} is the correct scaling for the heat flux, with

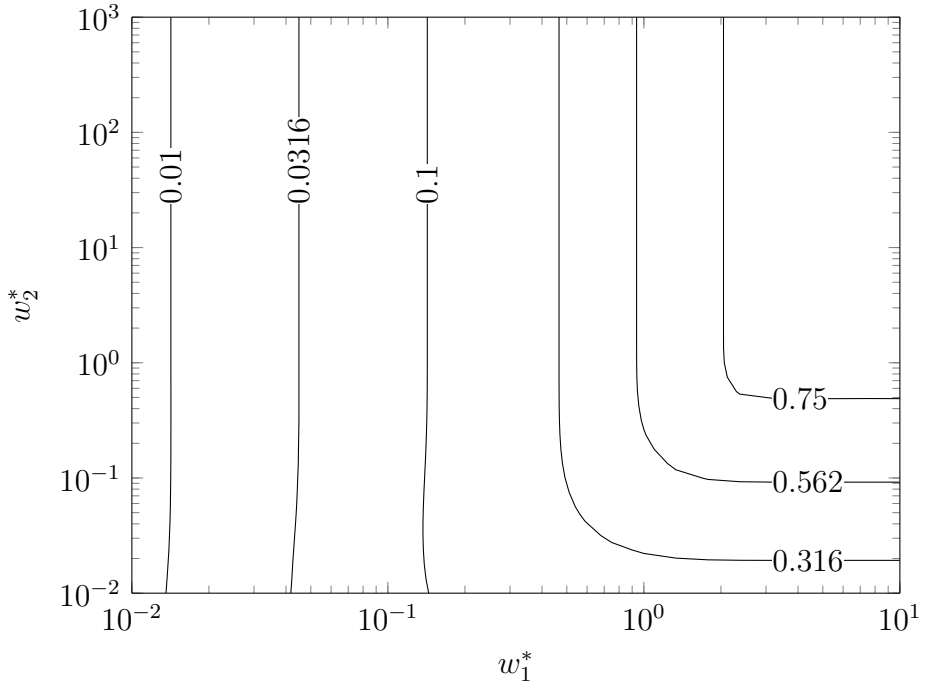

Figure 2.45: Contour of $\zeta^*_{1.1}$, the ζ^* location where $Nu = 1.1Nu_{z\to\infty}$, for case 1. The value for the plateau as $w_1^* \to \infty$ and $w_2^* \to \infty$ is about 0.763.

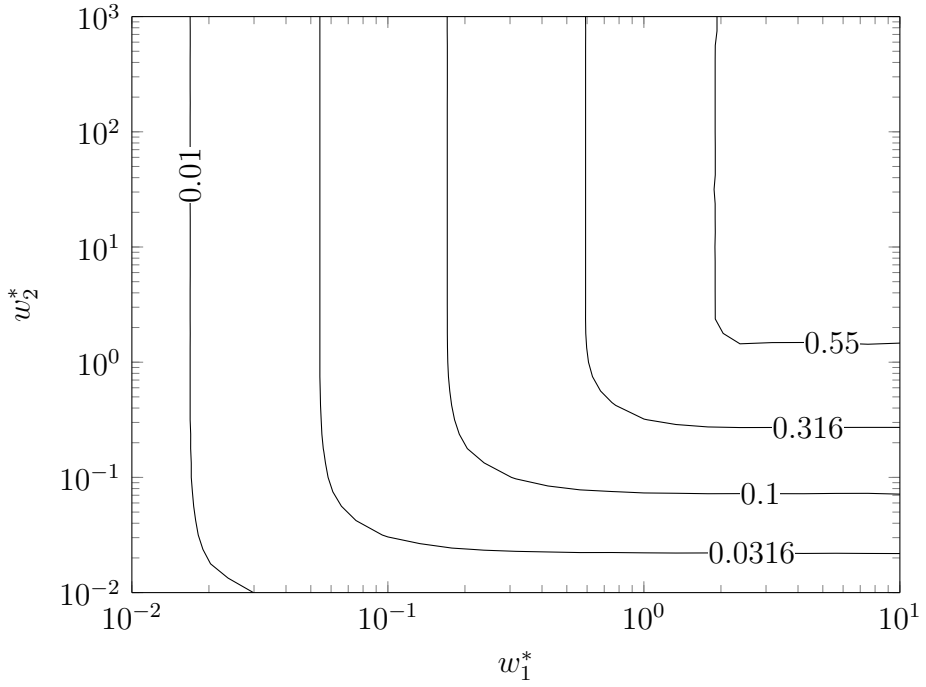

Figure 2.46: Contour of $\zeta^*_{1.1}$, the ζ^* location where $Nu = 1.1Nu_{z\to\infty}$, for case 2. The value for the plateau as $w_1^* \to \infty$ and $w_2^* \to \infty$ is about 0.557.

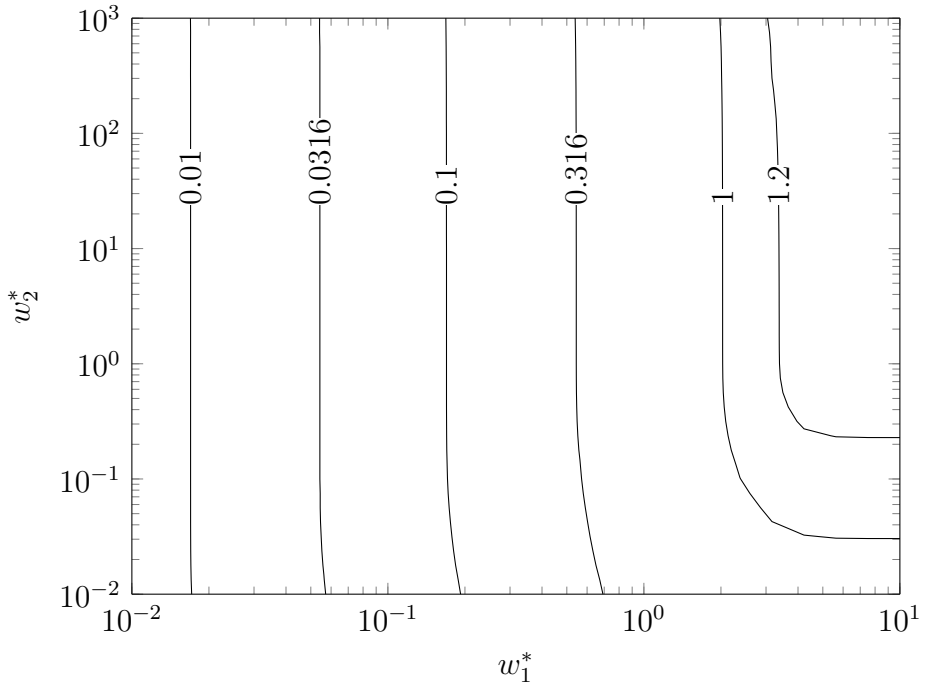

Figure 2.47: Contour of $\zeta^*_{1.1}$, the ζ^* location where $Nu = 1.1Nu_{z\to\infty}$, for case 3. The value for the plateau as $w_1^* \to \infty$ and $w_2^* \to \infty$ is about 1.24.

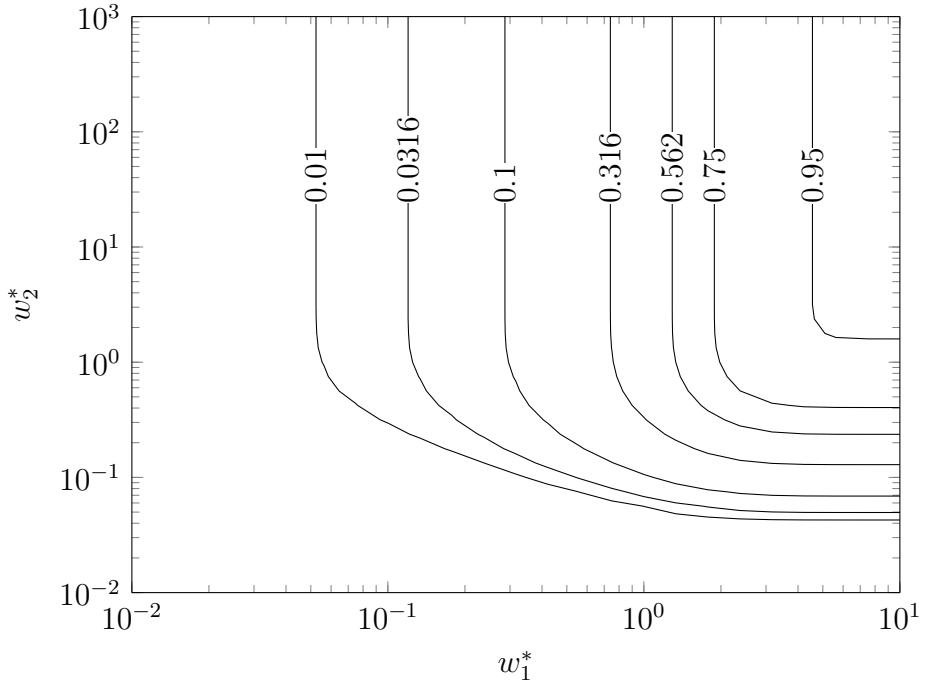

Figure 2.48: Contour of $\zeta^*_{1.1}$, the ζ^* location where $Nu = 1.1Nu_{z\to\infty}$, for case 4. The value for the plateau as $w_1^* \to \infty$ and $w_2^* \to \infty$ is about 0.955.

$Nu_{z\to\infty}$ playing a secondary role as the geometry becomes more divorced from the semi-infinite condition.

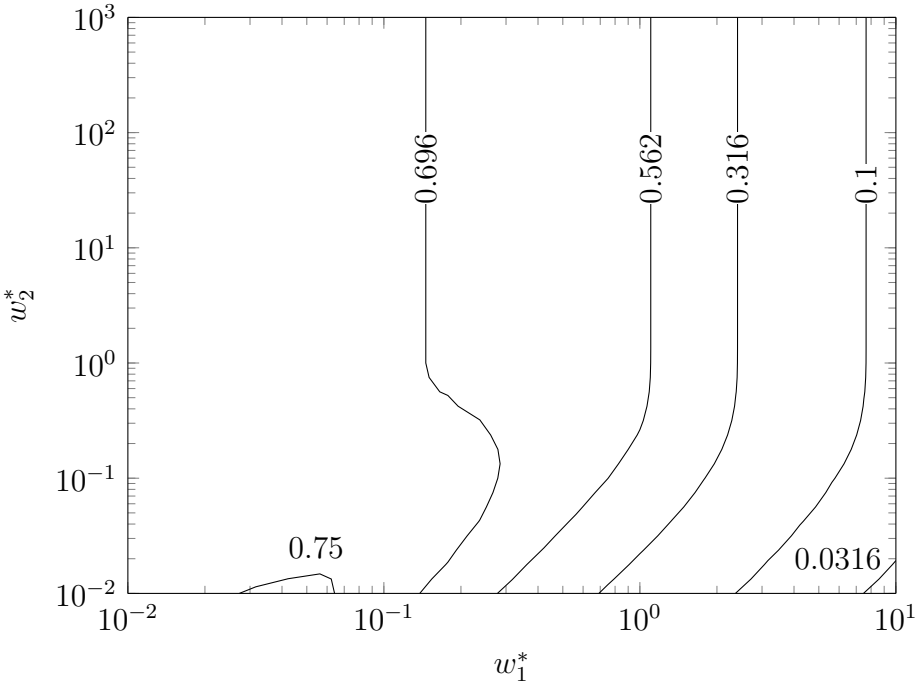

Figure 2.49: Contour of $\zeta_{1.1}^*/w_1^*$, the ζ^*/w_1^* or z/w_1 location where $Nu = 1.1Nu_{z\to\infty}$, for case 1. The value as $w_1^* \to 0$ is about 0.698

As shown in figs. 2.45 to 2.52, for geometries with larger values of w_1^* and w_2^*, the characteristics of the lateral heat flux profile and the spanwise extent of the lateral edge effect are largely independent of the various widths. However, defining a particular $\zeta_{1.1}^*$ value loses all meaning as the widths narrow, and w_1^* and w_2^* are necessary parameters for describing the lateral profile of the heat flux.

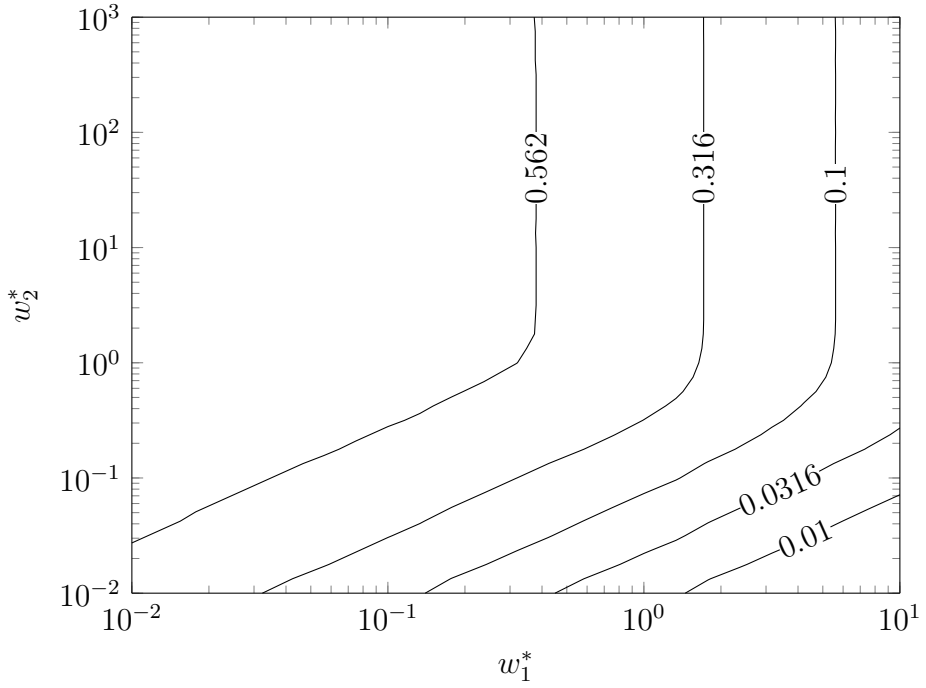

Figure 2.50: Contour of $\zeta_{1.1}^*/w_1^*$, the ζ^*/w_1^* or z/w_1 location where $Nu = 1.1Nu_{z\to\infty}$, for case 2. The value as $w_1^* \to 0$ is about 0.584

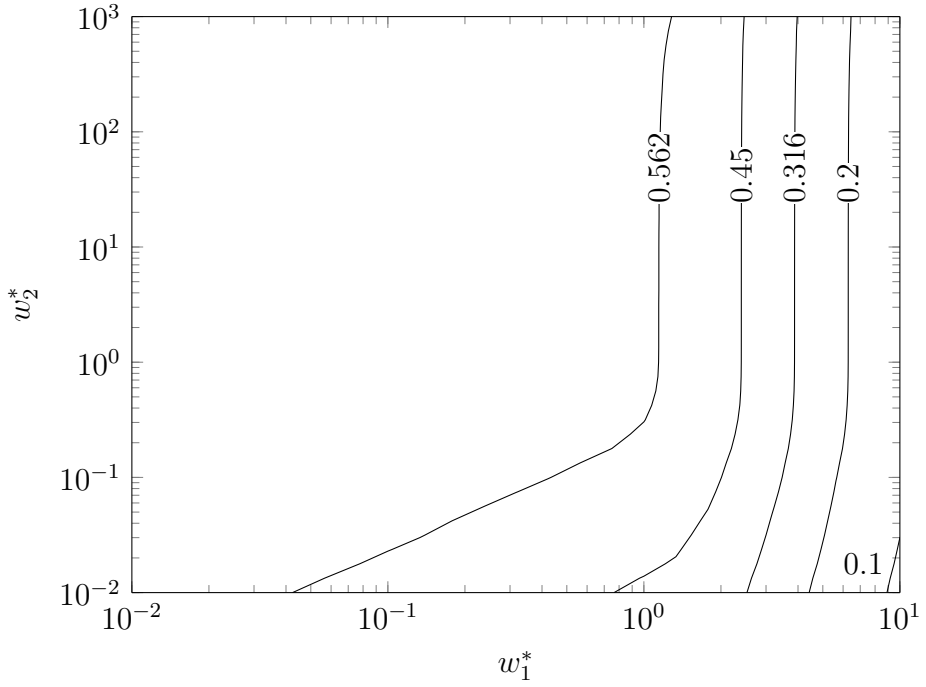

Figure 2.51: Contour of $\zeta_{1.1}^*/w_1^*$, the ζ^*/w_1^* or z/w_1 location where $Nu = 1.1Nu_{z\to\infty}$, for case 3. The value as $w_1^* \to 0$ is about 0.583

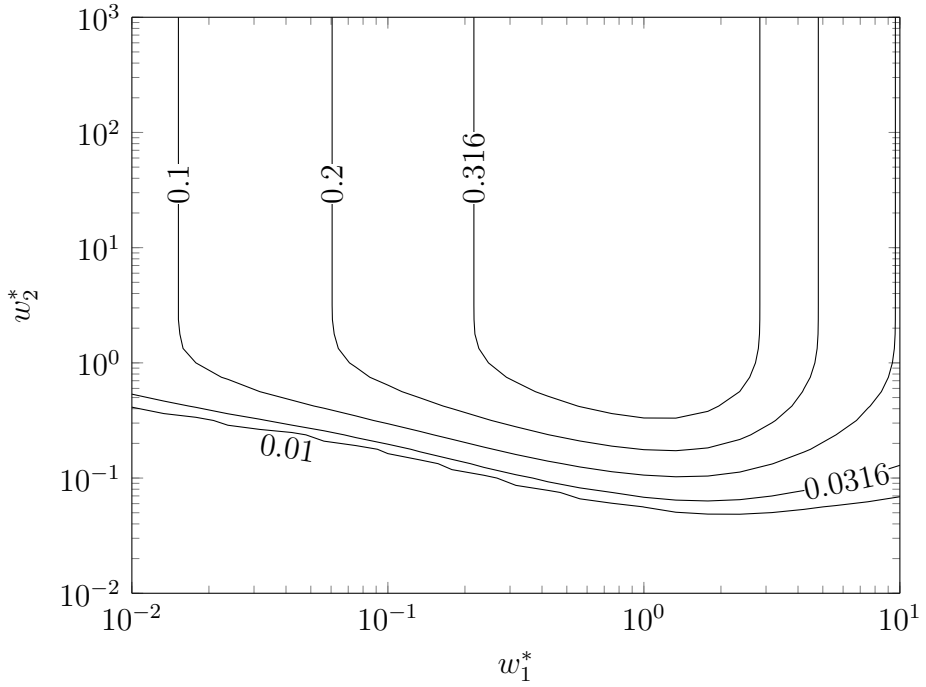

Figure 2.52: Contour of $\zeta_{1.1}^*/w_1^*$, the ζ^*/w_1^* or z/w_1 location where $Nu = 1.1Nu_{z\to\infty}$, for case 4. Peak value is about 0.438.

Convection from Infinitesimally Thin Rectangular Strips

If $w_2 \to \infty$ and $w_1 \to 0$, the solution from section 2.2.2 approximates that of a wire on a surface with convection to boundary layer flow. For case 1, eq. (2.56) becomes

$$\frac{Nu}{Nu_{z\to\infty}} = 1 + \sum_{n=1}^{\infty} \left[\exp\left(\lambda_{n,T}\left(z - 2w_1\right)\right) + \exp\left(-\lambda_{n,T} z\right)\right] \tag{2.64}$$

however, in the limit both z and w_1 approach zero, so

$$\frac{Nu}{Nu_{z\to\infty}} = 1 + \sum_{n=1}^{\infty} 2. \tag{2.65}$$

As might be expected from eqs. (2.46) and (2.59) and shown in eq. (2.65), the Nu for an isothermal wire tends towards infinity. Therefore an isothermal wire, with heat transfer only to the boundary layer, would require an infinite temperature gradient

over the finite temperature difference.

For case 4 as both z and w_1 approach zero, the value for the Nu should approach the value given in eq. (2.60). From Maximon (2003),

$$\mathrm{Li}_2(1) = \frac{\pi^2}{6}, \quad \mathrm{Li}_2(-1) = -\frac{\pi^2}{12}, \tag{2.66}$$

so as both w_1 and z approach zero, and $w_2 \to \infty$,

$$\begin{aligned} \frac{Nu}{Nu_{z\to\infty}} &= \frac{1}{1 - \frac{4}{\pi^2}\left(\frac{\pi^2}{6} + \frac{\pi^2}{12}\right)} \\ &= \frac{1}{1-1}. \end{aligned} \tag{2.67}$$

Therefore, as shown in eq. (2.67) the Nu for an isoflux wire tends towards infinity for boundary layer flow. This can be understood as a finite temperature gradient required over a smaller and smaller temperature difference to maintain the isoflux condition.

The same behavior is expected for cases 2 and 3, and is observed in the limit $w_1 \to 0$ for figs. 2.25 and 2.26.

Effect of Lateral Spacing for Rectangular Heat Sources

Most recommendations of spacing for heat sources focus on the streamwise spacing of the sources, for example see the discussion in Incropera et al. (1986) and Tso et al. (1999) on the effect of wakes for heated elements in streamwise column and Da Silva et al. (2004) for discussion on the optimal streamwise placement of heated elements.

While the lateral average of the Nu for case 1 tends towards infinity, the lateral average of the Nu for case 4 can be estimated using numerical integration. Figure 2.53

shows the total spanwise average, or

$$\frac{\overline{Nu}_{w_1,w_2}}{Nu_{z\to\infty}} = \frac{1}{w_1^* + w_2^*}\int_0^{w_1^*} \frac{Nu}{Nu_{z\to\infty}} d\zeta^* \tag{2.68}$$

overlaid with the maximum normalized temperature (found at the center of the heated rectangular strip). Note the Nu is zero for $z < 0$ and $Nu_{z\to\infty}$ is not a function of ζ^* at a given streamwise location. Also note the ratio of Nu/Nu_∞ can also be taken as the ratio of the thermal resistance to the thermal resistance if the whole lateral span is heated.

For the boundary conditions specified, fig. 2.53 shows the spanwise average of the Nu, when including the adiabatic section, never increases beyond the value given by eq. (2.45). Figure 2.53 compares two design parameters, the overall thermal resis-

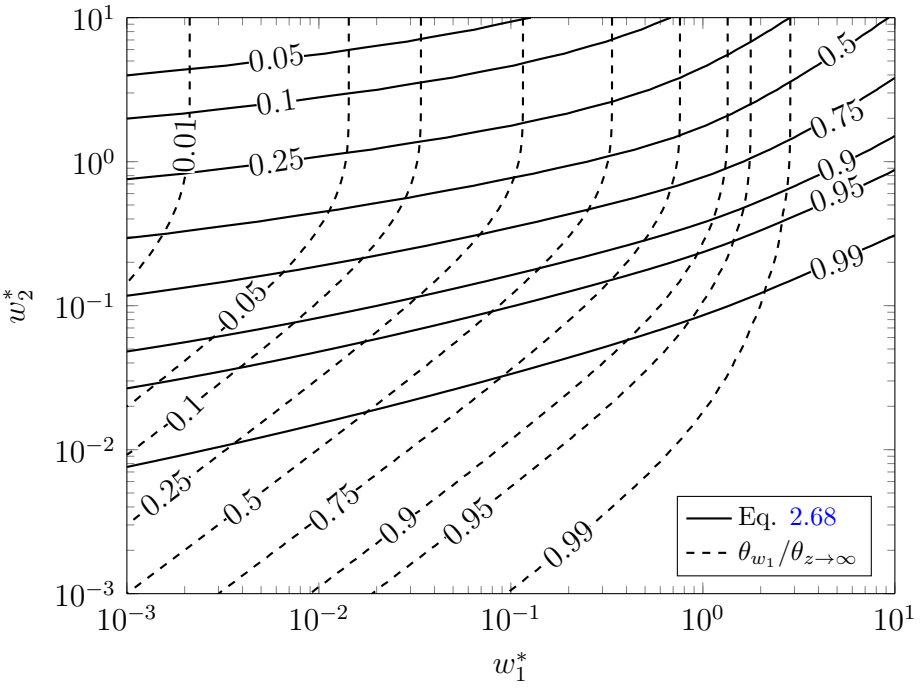

Figure 2.53: Spanwise average $Nu/Nu_{z\to\infty}$, shown in eq. (2.68), overlaid with the maximum nondimensional temperature, $\theta_{w_1}/\theta_{z\to\infty}$, for case 4. Note $\theta_{w_1}/\theta_{z\to\infty} = Nu_{z\to\infty}/Nu_{w_1}$

tance and the maximum temperature. Generally, wider heated surfaces and narrower adiabatic surfaces increase the maximum temperature while a wider adiabatic surface decreases the overall heat transfer to the fluid. For this reason, it is advisable to have the smallest widths for both the heated and adiabatic surfaces relative to the conduction thickness to maximize heat transfer and minimize the temperature.

Figure 2.54 shows the average Nu for just the heated section, or

$$\frac{\overline{Nu}_{w_1}}{Nu_{z\to\infty}} = \frac{1}{w_1^*}\int_0^{w_1^*} \frac{Nu}{Nu_{z\to\infty}} d\zeta^*. \tag{2.69}$$

Figure 2.54 shows how much the spanwise average Nu (when only considering the

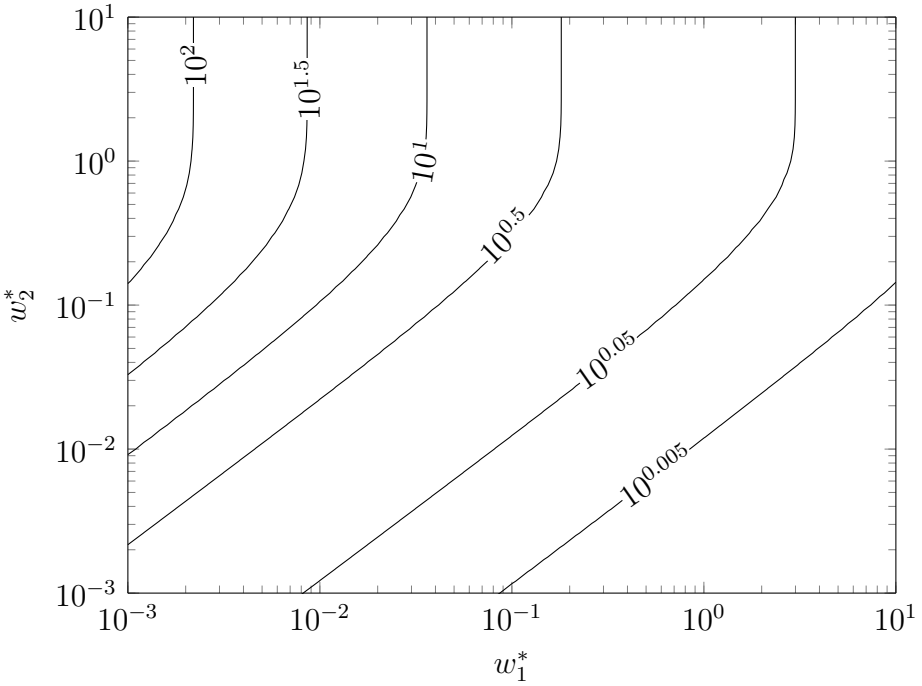

Figure 2.54: Spanwise average $Nu/Nu_{z\to\infty}$ for heated section, shown in eq. (2.69), for case 4

heated section) increases compared to $Nu_{z\to\infty}$. However, as shown in fig. 2.53, this large increase in the spanwise average of the Nu requires an increased adiabatic width, costing the design precious space where other heat sources could otherwise have been

placed.

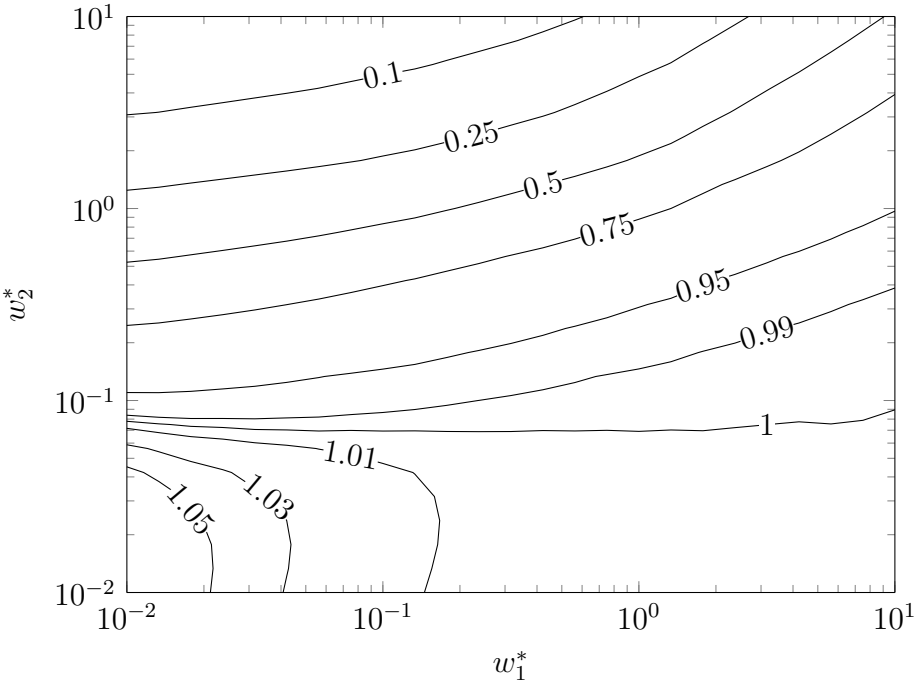

Figure 2.55: Spanwise average $Nu/Nu_{z\to\infty}$, shown in eq. (2.68), for case 2

Figure 2.55 shows something rather remarkable. For case 2, when $w_2^* \lesssim 0.07$, the spanwise average Nu is actually larger than Nu_∞. This is the only set of boundary conditions where it is possible that by carefully selecting the geometry, the average lateral heat transfer from the surface can be larger than if the whole surface loses heat by convection.

Case 3 has different characteristics than Case 4 even though the heated surface is subjected to the same boundary condition. Figure 2.58 shows that the maximum temperature is primarily a function of w_1^*. However, the largest difference happens because the isothermal surface for case 3 absorbs energy from the fluid, counteracting the heat transfer to the fluid from the heating element. Figure 2.59 shows that for heating elements where $w_1^* \lesssim 5.5$, the cooled surface actually absorbs more energy from the fluid than the heating element loses. In other words, it takes more energy to

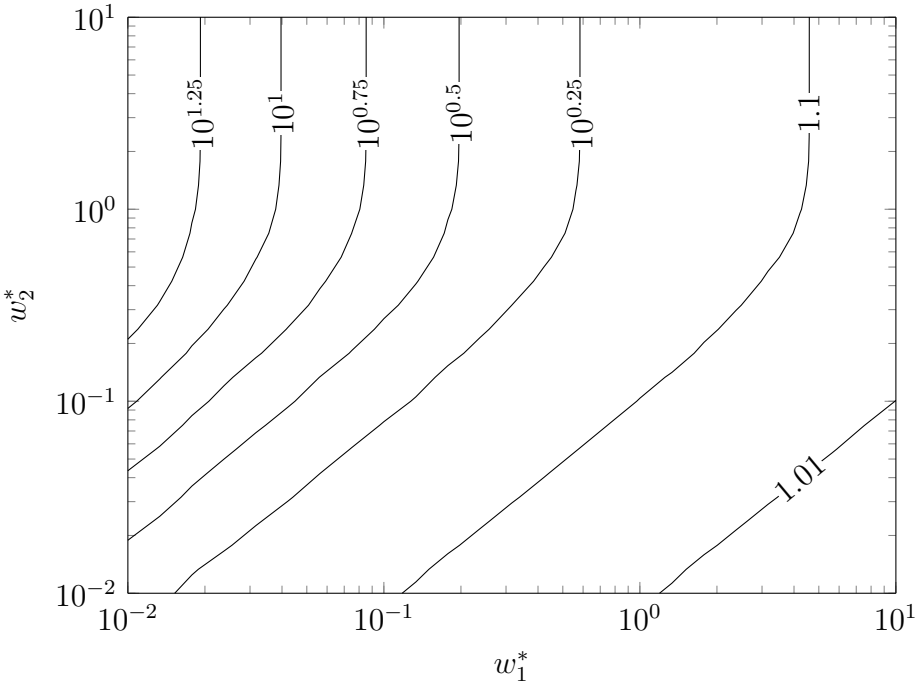

Figure 2.56: Spanwise average $Nu/Nu_{z\to\infty}$ for heated section, shown in eq. (2.69), for case 2

keep the cooled element at the freestream temperature, θ_∞, than the heating element loses through heat transfer to the fluid for $w_1^* < 5$. While the plot does indicate this, the negative values are extremely small and could be a result of numerical error, either from the fitting required to integrate at extremely small z or numerical modeling errors. However, it is clear that for geometries where $w_1^* < 5$, the average heat transfer to the fluid is indistinguishable from zero.

$$\begin{aligned}\frac{\overline{q''}}{q''_{z\to\infty}} &= \frac{\left(\frac{1}{w_2^*}\int_0^{w_2^*} q''d\zeta^*\right) w_2^* + q''_{z\to\infty} w_1^*}{q''_{z\to\infty}\left(w_1^* + w_2^*\right)} \\ &= \frac{w_1^*}{w_1^* + w_2^*}\left(\frac{w_2^*}{w_1^*}\frac{\overline{q''}_{w_2^*}}{q''_{z\to\infty}} + 1\right)\end{aligned} \tag{2.70}$$

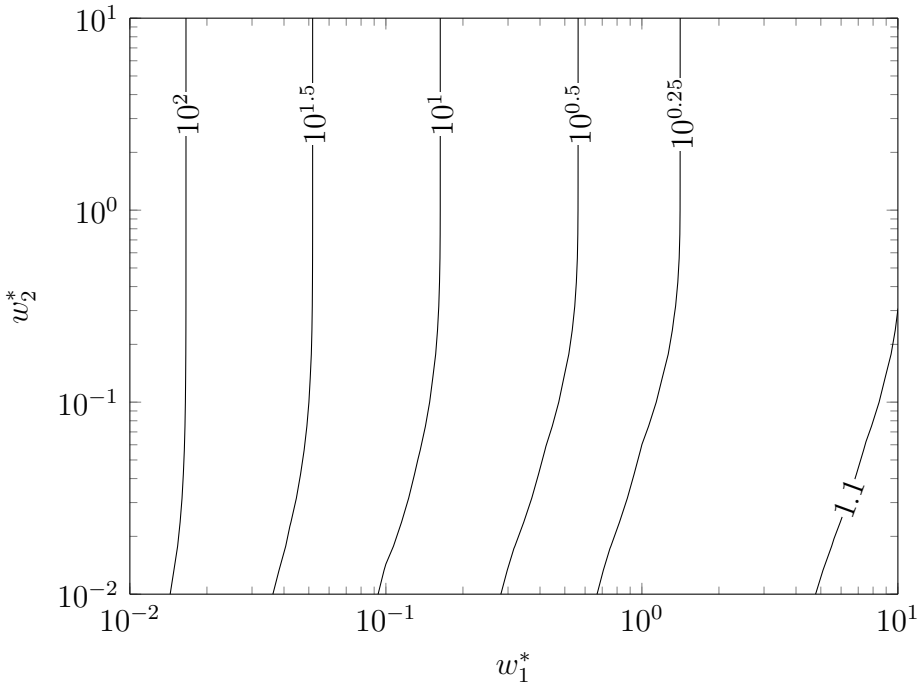

Figure 2.57: Spanwise average $Nu/Nu_{z\to\infty}$ for heated section, shown in eq. (2.69), for case 3

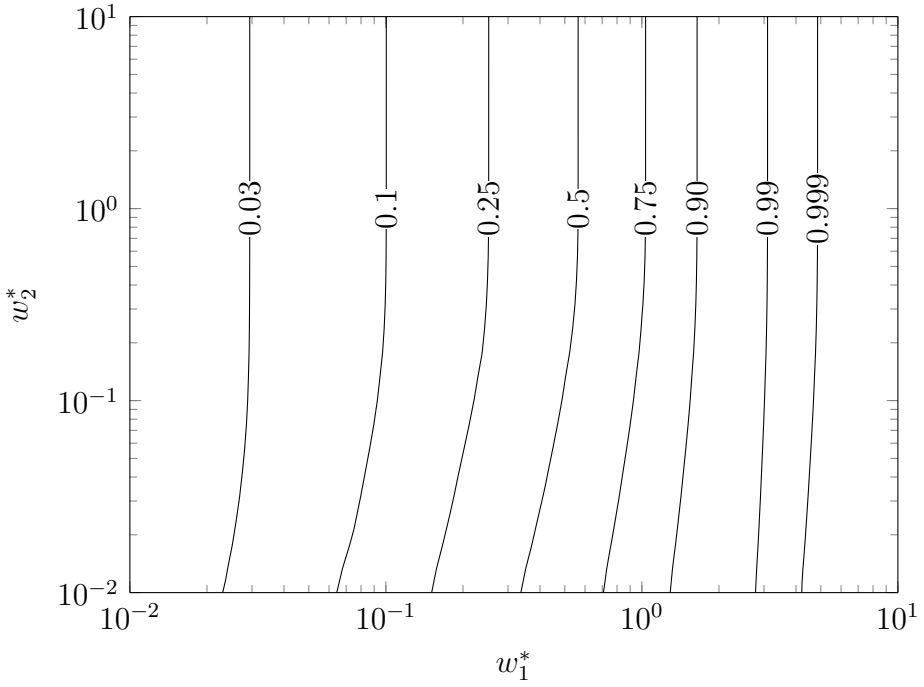

Figure 2.58: Maximum nondimensional temperature, $\theta_{w_1}/\theta_{z\to\infty}$, case 3. Note $\theta_{w_1}/\theta_{z\to\infty} = Nu_{z\to\infty}/Nu_{w_1}$

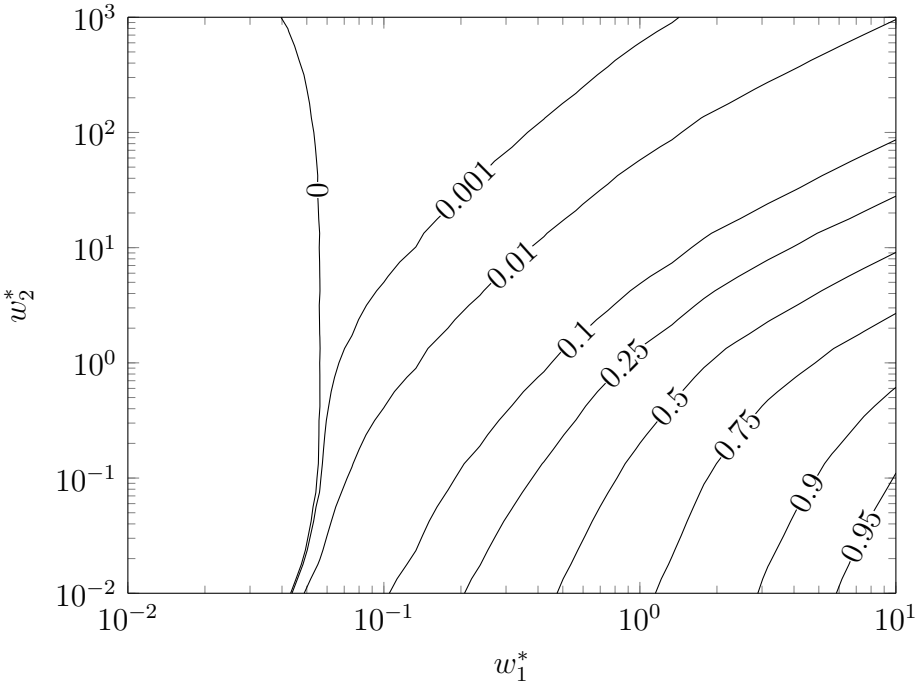

Figure 2.59: Spanwise heat transfer, shown in eq. (2.70), for case 3

2.3 Summary

2.3.1 Semi-Infinite Lateral Extent

The discussion in section 2.1 centered around spanwise changes of heat transfer when both the heated and the cooled/adiabatic surfaces are semi-infinite in lateral extent for laminar boundary layer flow over a flat plate. A similarity solution and conduction model are compared with results from a numerical simulation using OpenFOAM. The numerical simulation uses the Blasius solution for the velocity field, but models the full three dimensional steady-state energy transport equation shown in eq. (1.1).

The similarity solution, conduction model, and numerical results compared well with each other. Even though the conduction model did not explicitly address the presence of the boundary layer, the results are remarkably accurate, requiring no pa-

rameter fitting. There are two reasons for this; first, there is relatively little transport of energy by advection in the wall normal or lateral directions and energy transport normal to the flow accomplished by molecular diffusion as in a conduction type problem. Second, boundary layer information is captured by equating the height of the problem domain to the conduction thickness, coupling the conduction solution to the two dimensional heat transfer far from the lateral edge. The solutions are best described by the nondimensional parameter ζ^*, the distance from the lateral edge normalized by the conduction thickness.

The results showed that the Nu tended towards infinity for all the surface boundary conditions save when both are isoflux conditions (one heated and the other adiabatic). The conduction model and similarity solution captured this trend the best. The case with isothermal boundary conditions on both the heated and cooled surface varied the most near the lateral edge, with the Nu inversely proportional to ζ^*, implying that this particular set of boundary conditions is physically impossible. The Nu from two cases with mixed boundary conditions varied as the inverse square-root of ζ^*. The last set of surface boundary conditions, isoflux for both surfaces, tended towards a finite Nu because both the flux and temperature are non-zero over the whole heated surface.

2.3.2 Finite Lateral Extent

The discussion in the section 2.2 centered around spanwise changes of heat transfer when either (or both) the heated and cooled/adiabatic surfaces are finite in lateral extent for laminar boundary layer flow over a flat plate. Similar to section 2.1, the solution is approximated with a conduction model and numerical simulations using OpenFOAM. As the finite lateral extent introduces a length scale to the problem domain, similarity solutions are impossible to formulate. The method employed for the

conduction modeling and numerical simulations are identical to the method outlined above for the infinite lateral domain.

The problem domain essentially models an infinite, repeating lateral array of heated elements. In addition to the nondimensional lateral parameter ζ^*, two new nondimensional parameters are needed to describe the problem. The spacing between the heated sections and width of the heated sections, both normalized by the conduction thickness, describe the geometry of the problem domain. The solution recaptures the semi-infinite lateral extent solution when the spacing and width tend towards infinity. As might be expected, the Nu increases as the width of the heated section decreases. However, if the width of the heated section is larger than the spacing between the heated sections, the Nu decreases when compared to the semi-infinite problem domain. This happens because the temperature field above the plates approaches the two dimensional temperature field described by a heated surface of infinite lateral extent. In other words, the heat transfer everywhere approaches the canonical two dimensional heat transfer everyone knows and loves, shown in eqs. (2.44) and (2.44).

Several other trends for the finite width data are worth discussing. It is shown that the Nu tends towards infinity as the width of the heated section tends towards zero and the spacing between the heated section tends towards infinity (i.e. for a wire in boundary layer flow). For the two most realizable wall boundary conditions, when the "cooled" surface is adiabatic, the best choice for the spacing and width is to make both as small as possible. For both cases this maximizes the heat transfer and when the heated wall boundary condition is isoflux, this also minimizes the maximum temperature.

A note for both the semi-infinite and finite lateral extent results: explicitly specifying the wall boundary conditions for both surfaces is important. As detailed above, the surface boundary condition for the cooled/adiabatic surface changes the heat

transfer characteristics near the lateral edge.

Chapter 3

Experimental Apparatus and Procedures

3.1 Instrumentation

3.1.1 Voltage

The voltage measurements are made with a Keithley Model 2000 $6^1/_2$ digital multimeter with a 0.002 % 90 day DC voltage accuracy (*Model 2000 Multimeter User's Manual* 2010). To switch between voltage channels, an 80 channel Keithley Model 7001 Switch System is used (*Model 7001 Switch System Instruction Manual* 2001). The high speed voltage measurements for the hot wire anemometer are taken using an Agilent 34411A $6^1/_2$ digital multimeter with 0.002 % 90 day DC voltage accuracy. The high speed multimeter can take up to 50 000 readings per second at $4^1/_2$ digits.

3.1.2 Temperature

Temperature measurements are made with 30 gage type-E thermocouple wire. The thermocouples are manufactured in-house using a spot welder. The two wires are submerged in argon gas and welded together, ensuring a robust and clean connection.

The calibration procedure described in section 3.3.1 results in an uncertainty of about 10 mK as shown in fig. C.1.

3.1.3 Velocity

Velocity measurements are made with the aid of a water micromanometer connected to a Pitot-static tube. The micromanometer has a resolution of 2.5 µm. The atmospheric pressure taken from the Enet pressure server, which uses a Setra 470 with a stated accuracy of 0.02 % (*Model 470 Digital Pressure Transducers* 1995). These two pressure measurements are used to calculate the velocity as described by eq. (3.12).

The velocity measurements for the boundary layer and turbulence intensities are made with a hotwire anemometer in constant temperature mode with a TSI IFA-100. The calibration of the hotwire anemometer is described in section 3.3.2.

3.1.4 Data Acquisition and Control

The data acquisition software is written in-house in Python utilizing the PyVISA module as a wrapper for the VISA API. The Python scripts run on a late 2013 MacBook Pro, and code examples can be found in appendix D. Most of the instrumentation uses the IEEE-488 bus specification (also known as GPIB) for inter-device communication. As the laptop does not have a GPIB port, a National Instruments USB to GPIB adapter is used. The only device that does not natively support the IEEE-488 bus specification is the Velmex NF90 motor controller, which communicates using the RS-232 format. A USB to serial adapter is used to interface with the motor controller.

Figure 3.1: Photograph of author with some of the test equipment

3.2 Apparatus

3.2.1 Wind Tunnel

A sketch of the wind tunnel appears in fig. 3.2. It is a suction type, open loop wind tunnel that vents to the outside atmosphere. The intake has several screens and honeycombs. The test section is 900 mm × 265 mm × 381 mm. There is a 1.5 mm trip wire at the entrance of the test section, resulting in approximately 225 diameter lengths before the mass transfer surface.

A 3-axis motion controller designed by Waldron (2004) is used for the positioning of the hotwire anemometer during the boundary layer measurements. There are three sets of SLO-SYN stepper motors with 1 mm screws and guide rails that are aligned with x, y, and z directions of the flow. The programmable stepping motor controller,

a Velmex NF90 Controller, has a resolution of 400 steps per revolution as described in (*NF90 Series User's Guide*).

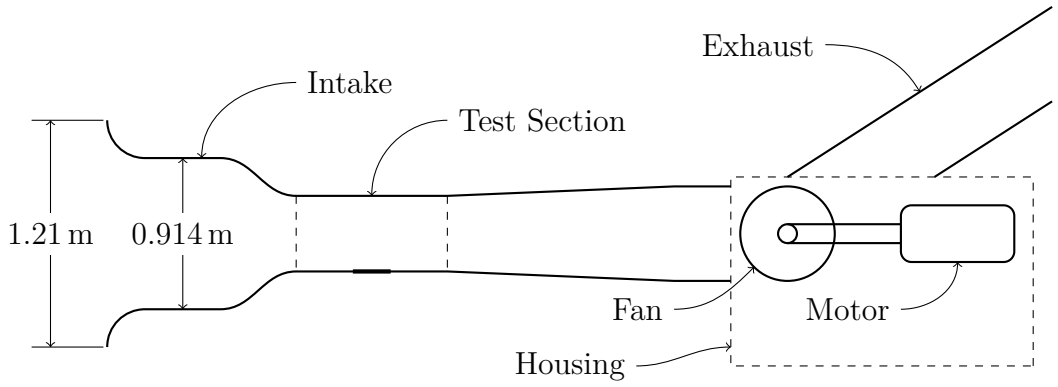

Figure 3.2: Sketch of the wind tunnel

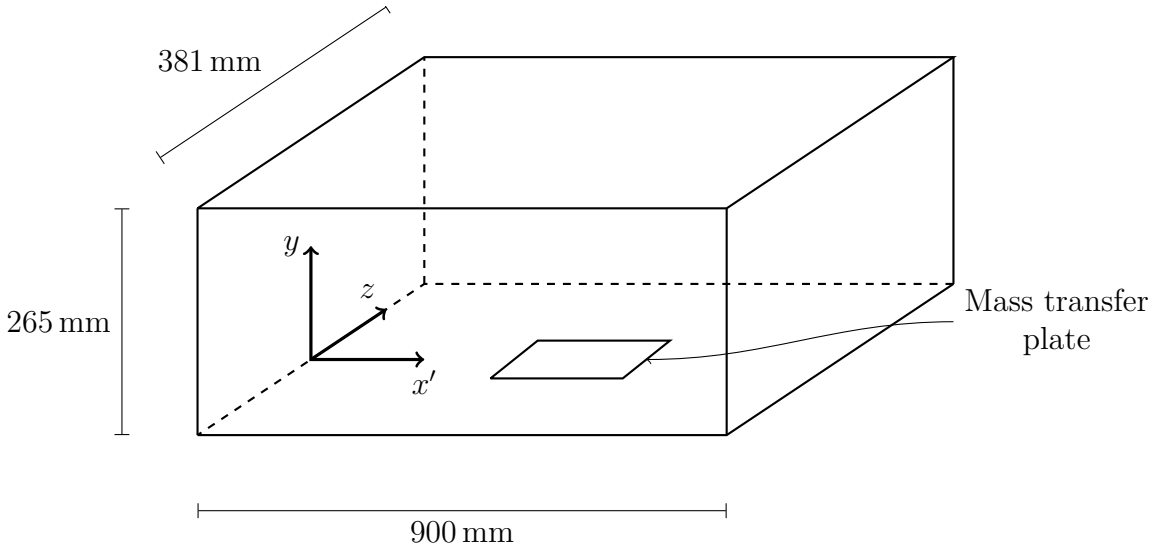

Figure 3.3: Sketch of the wind tunnel test section

3.2.2 Mass Transfer Mold

The mass transfer mold is shown in fig. 3.4. The seven small holes around the rim are used for securing the aluminum lid to the mold. The two larger threaded holes in

the interior are used for fixing the inflow and overflow copper tubing when pouring the molten naphthalene into the mold. The two smaller holes in the interior are not through holes, and are used to fix the various aluminum covers to the mass transfer mold with metal dowel pins.

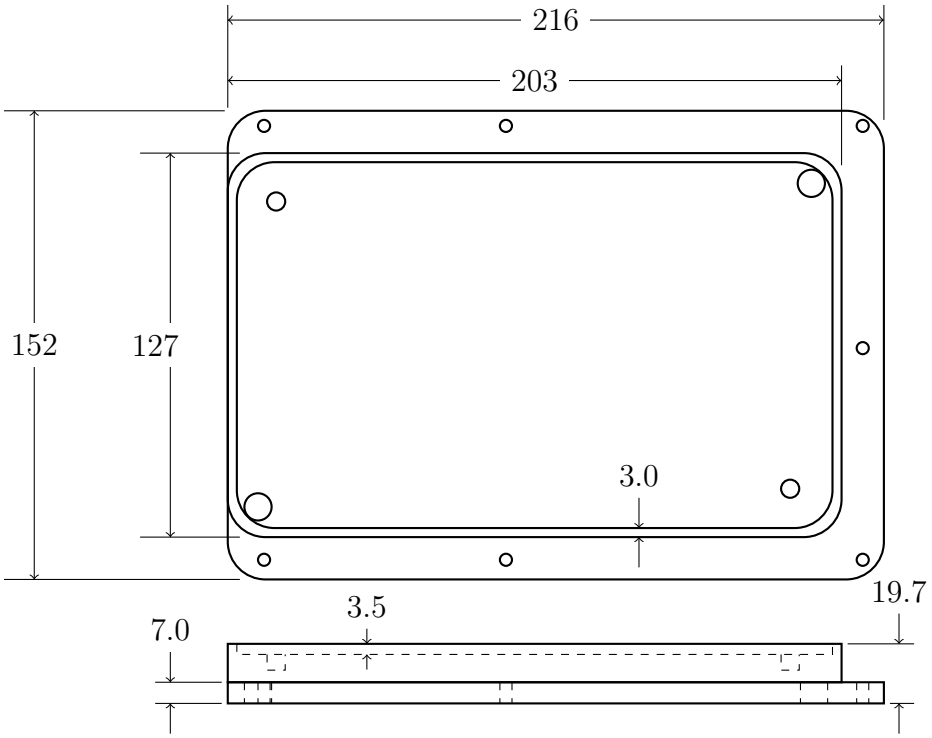

Figure 3.4: Mass transfer base plate

An aluminum cover is used to change the geometry of the exposed surface. The aluminum cover, shown in fig. 3.5, enables collection of data for multiple geometries from one run in the wind tunnel. In addition, the design of the aluminum cover eliminates the formation of bubbles near the edges, which has been a problem for mass transfer experiments involving naphthalene. The reason is twofold: one, the overflow spout is not in line with the closest exposed edge, and second, the beveled edges ensure that bubbles would not be trapped by a perpendicular surface.

The widths of the rectangular strips shown in fig. 3.5 are measured with precision

gauge blocks to an accuracy of about 0.0025 mm.

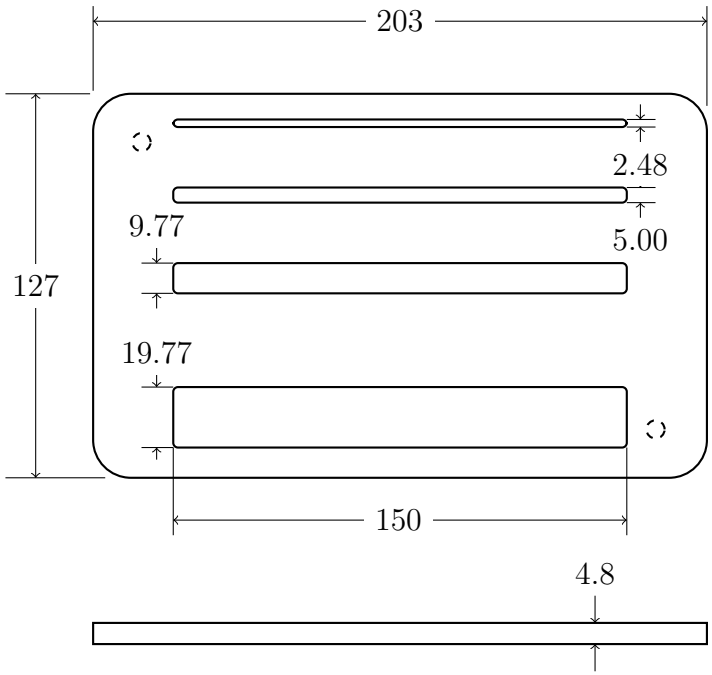

Figure 3.5: Cover for mold so the exposed surface is a spanwise series of rectangular strips. All dimensions in millimeters.

For the cavity experiments, the cutout shown in fig. 3.6, is placed on the naphthalene surface so the exposed naphthalene surface forms the bottom surface of a cavity. The top of the cavity cutout is flush with the tunnel surface. The smaller cavity cutouts are manufactured using electrical discharge machining, and the two largest cavity cutouts are manufactured using a water jet. In all, seven different depths, ranging from 0.254 mm to 8.84 mm, are used for the experiments.

3.2.3 Naphthalene Profile Measurement

A linear variable differential transformer (LVDT) probe manufactured by Schaevitz (part number PCA-220-010) is used for depth measurements. The full range of the LVDT probe is about 460 µm with an estimated one standard deviation uncertainty of 0.181 µm. The calibration procedure for the LVDT is described in section 3.3.1.

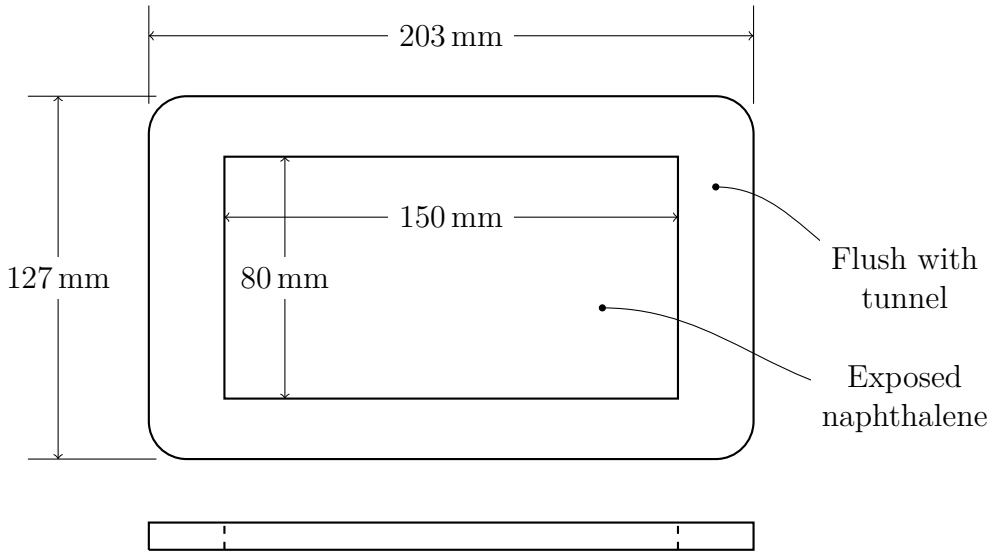

Figure 3.6: Dimensions of the cavity cutouts. The cutout is placed on the naphthalene surface and the position of the aluminu mold adjusted so the top is flush with the tunnel. The thickness of the cutout ranges from 0.254 mm to 8.84 mm

The LVDT is mounted on an x-y measuring table with the same resolution and accuracy as the 3-axis system described in section 3.2.1. Great care is taken to ensure the aluminum mass transfer mold can be repeatably mounted in parallel with the x-y table's principle axes. Estimation of the edges of the aluminum mass transfer mold using LVDT measurements indicate they are not exactly parallel with the x-y table coordinate axes, with an error of about 0.1 mm per 100 mm, or a divergence of 0.057° from the x-y table's principle axes.

3.3 Experimental Procedures

3.3.1 Calibration

Temperature

The thermocouples are calibrated against a platinum resistance thermometer (PRT) in a water bath manufactured by Rosemont. The calibration of the thermocouples is a two step procedure. The first step is to calibrate the PRT against the triple point of water and the hydrate transition temperature of sodium sulfate. The temperatures and measured resistances are used to find the constants R_{tp} and a, defined by the ITS-90 as presented in Preston-Thomas (1990),

$$W = \frac{R}{R_{tp}} \tag{3.1}$$

$$W - W_r = a\,(W - 1) \tag{3.2}$$

$$W_r = C_0 + \sum_{i=1}^{9} C_i \left[\frac{T - 754.15}{481}\right]^i . \tag{3.3}$$

The constants C_i are given by Preston-Thomas (1990).

The triple point of water is realized in a triple point cell manufactured by Jarrett. The triple point cell is chilled in an ice bath prior to use. Then, after isopropyl alcohol is put in the well, frozen carbon dioxide powder is continuously poured into the well. Care must be taken that an ice bridge does not form at the ice-water-vapor interface and the ice sheath does not touch the inside surface of the borosilicate glass. Either condition will break the triple point cell. The last condition is checked by immersing the triple point cell in a clear beaker filled with distilled water during the preparation process. After a reasonable ice sheath has formed around the well, a

warm rod approximately the diameter of the triple point well is placed in the well to purge the isopropyl alcohol and free the ice sheath from the well (the ice sheath should spin freely around the well). The triple point cell is left to relax to the triple point temperature of water, as the initial temperature of the cell can initially be as much as 1 mK off the true value (White et al. 2009).

Use of the hydrate transition temperature of sodium sulfate as a fixed point for temperature measurement is outlined in Magin et al. (1981). As shown in fig. 3.7, solutions greater than 33.2 % sodium sulfate by weight cooled from at least 40 °C undergo a stable hydrate transition at 33.373 °C (Magin et al. 1981). Magin et al. (1981) used hydrated crystals; however, the calibration for the current experiment uses the anhydrous salt. The difference is inconsequential because the mixture is heated to at least 40 °C. However, the reported transition temperature, 33.373 °C, is defined based on the IPTS-68, so the temperature needs to be converted to the ITS-90 as outlined in Fellmuth (2012). This conversion results in a change in the transition temperature from the reported 32.373 °C to 32.365 °C, with an additional uncertainty of 1 mK.

The basic process using the hydrate transition temperature of sodium sulfate as a fixed point for temperature measurement is simple. A sodium sulfate and distilled water solution is heated to at least 40 °C, as trouble with the transition is encountered if the solution is not heated past 40 °C. As shown in fig. 3.7, the percent composition by weight of sodium sulfate needs to be larger than 33.2 %. This can be checked by ensuring there is anhydrous salt in the solution at elevated temperatures as shown in fig. 3.7. After the solution cools a few tenths of a degree Celsius below the transition temperature, phase change is initiated by adding hydrated sodium sulfate to the solution. The hydrated sodium sulfate is prepared by adding the anhydrous salt to distilled water at room temperature and shaking vigorously. The transition

temperature is stable for several hours.

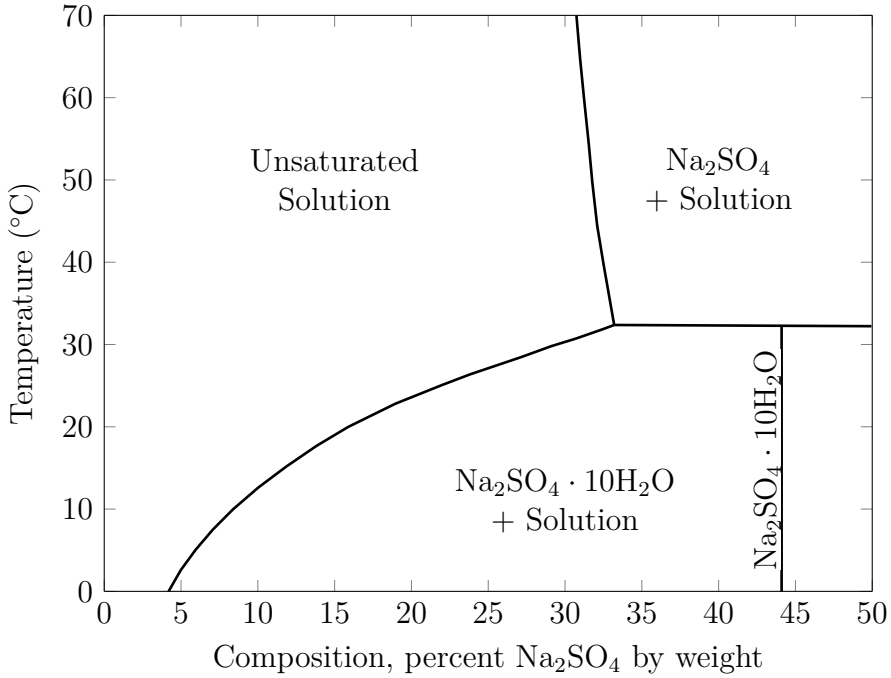

Figure 3.7: Relevant portion of phase diagram for $Na_2SO_4 : H_2O$ (Magin et al. 1981)

The triple point and sodium sulfate hydrate transition resistances, R_{tp} and $R_{Na_2SO_4}$ respectively, are measured using a four wire resistance technique. The measured values are $25.5607\,\Omega$ and $28.8428\,\Omega$, respectively, at the time of calibration. Using eqs. (3.2) and (3.3) with the measured value of the resistance at the triple point temperature and the transition temperature, the value of a from eq. (3.2) is -6.8271×10^{-5}. With R_{tp} measured and a defined, the temperature from resistance measurements of the platinum resistance thermometer from eq. (3.4) can be calculated.

$$T - T_{tp} = D_0 + \sum_{i=1}^{9} D_i \left[\frac{W_r - 2.64}{1.64}\right]^i \tag{3.4}$$

The coefficients D_i from eq. (3.4) are given in Preston-Thomas (1990).

The second step of the temperature calibration is the calibration of the thermocouples against the temperature indicated by the platinum resistance thermometer

given by eq. (3.4). Five thermocouples are chosen at random from the group of the manufactured thermocouples and are assumed to represent the distribution of thermocouples manufactured. Care is taken not to cold work the thermocouples before or after the calibration. The thermocouples are placed in small, oil filled glass test tubes manufactured by the glass blower in the University of Minnesota chemistry department; and both the PRT and the thermocouples are immersed in the water bath. Multiple readings of the thermocouples and PRT are taken at eight temperatures in the range 2.7 °C to 32.2 °C. The resulting averaged voltage data is fitted with a polynomial according to the procedure outlined in appendix B.2. The order of the polynomial is chosen so that the mean square error, shown in fig. 3.9a, is minimized using leave-one-out cross-validation as described in appendix B.3. Figure 3.9b shows the residuals are noisy enough to indicate the polynomial is an appropriate model for predicting the temperature from thermocouple voltage measurements.

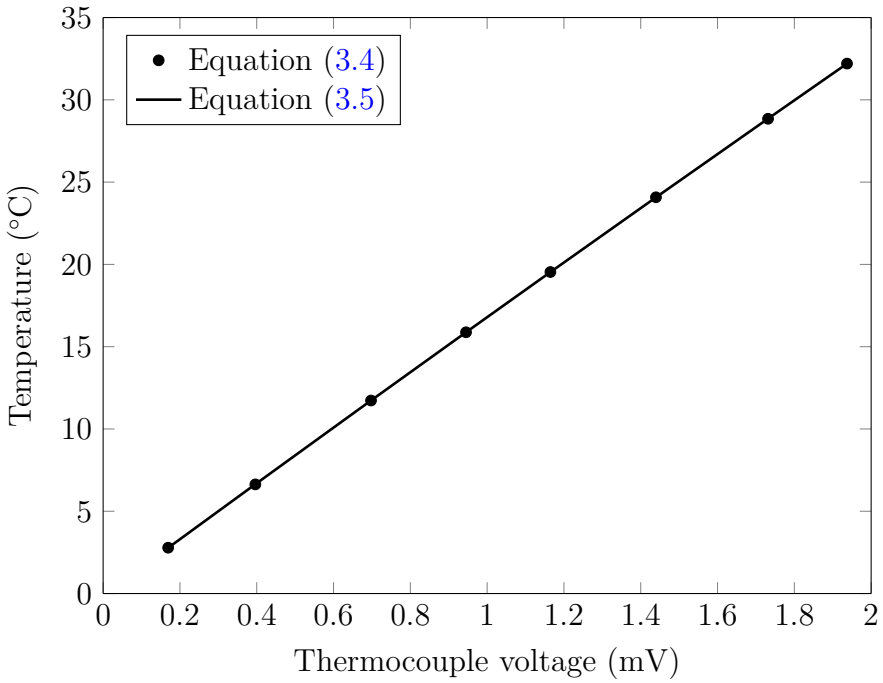

Figure 3.8: Fit for thermocouple temperature (all data)

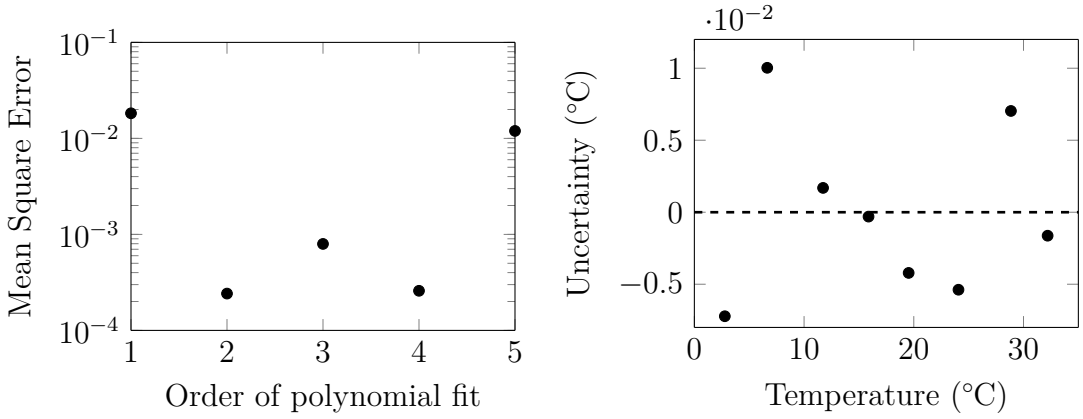

(a) Mean square error for polynomial fitting

(b) Residuals for second order thermocouple fit

Figure 3.9: Goodness of thermocouple fit

The final fit of the thermocouples in terms of millivolts is

$$T - 273.15 = -0.120437 + 17.1586\mathcal{E}_{tc} - 0.245044\left(\mathcal{E}_{tc}^2 - \hat{\sigma}_{tc}^2\right) \tag{3.5}$$

Note that the final term in parentheses, $(\mathcal{E}_{tc}^2 - \hat{\sigma}_{tc}^2)$, is from eq. (B.13), and is an unbiased estimate of the squared voltage. The estimated standard deviation during the calibration, $\hat{\sigma}_{tc}$, is 2.51×10^{-4} mV. A detailed calculation of the uncertainty is presented in appendix C and shown in fig. C.1, but the uncertainty is about 9.2 mK.

Linear Variable Differential Transformer

Calibration of the LVDT is done with a set of 21 precision gage blocks ranging in thickness from 2.54 mm to 3.10 mm. The process is simple, the 21 gauge blocks are slid under the LVDT, in random order, one at a time for 30 s while the voltage from the LVDT output is measured. Data is taken from when the gage block first made contact with the LVDT to 10 s afterward. This data is averaged and used as the voltage value in the calibration. As described above in section 3.3.1, the order of the polynomial

is chosen so that the mean square error, shown in fig. 3.11a, is minimized, using leave-one-out cross-validation. In this case, a linear model is the most appropriate model for the data. Figure 3.11b shows the residuals are noisy enough to indicate the polynomial is an appropriate model for predicting the LVDT displacement from the LVDT voltage measurements.

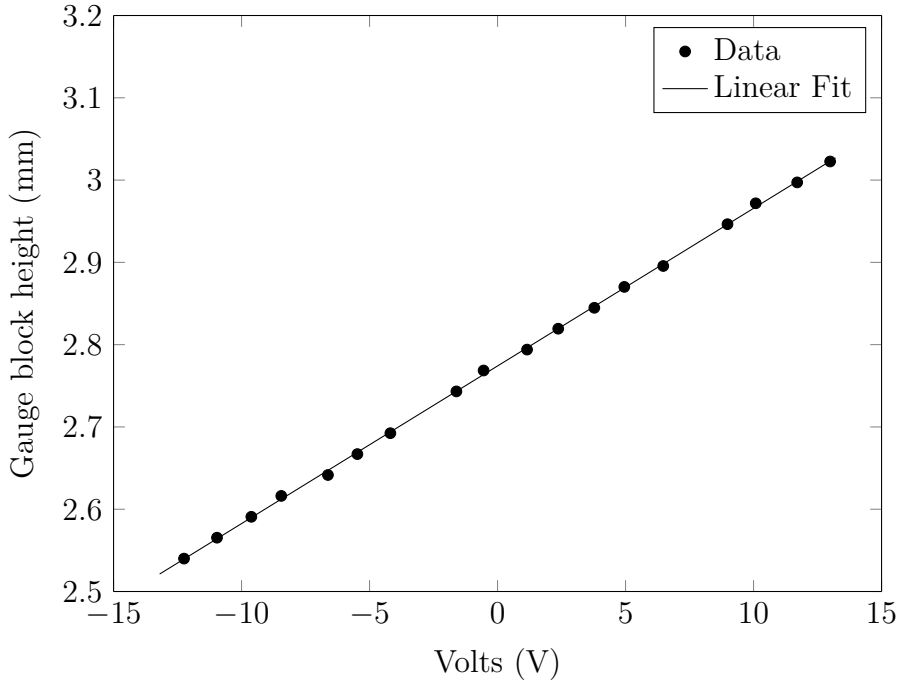

Figure 3.10: Linear fit for LVDT

The final fit for the LVDT is (in µm):

$$\delta = 2.77 + 19.15756\mathcal{E}. \tag{3.6}$$

Note the constant, 2.77, is not important as it subtracts out of any sublimed naphthalene depth measurement.

The accuracy gage blocks is unknown, so the uncertainty of the calibration was not calculated using the Monte Carlo method. The estimated uncertainty of the LVDT

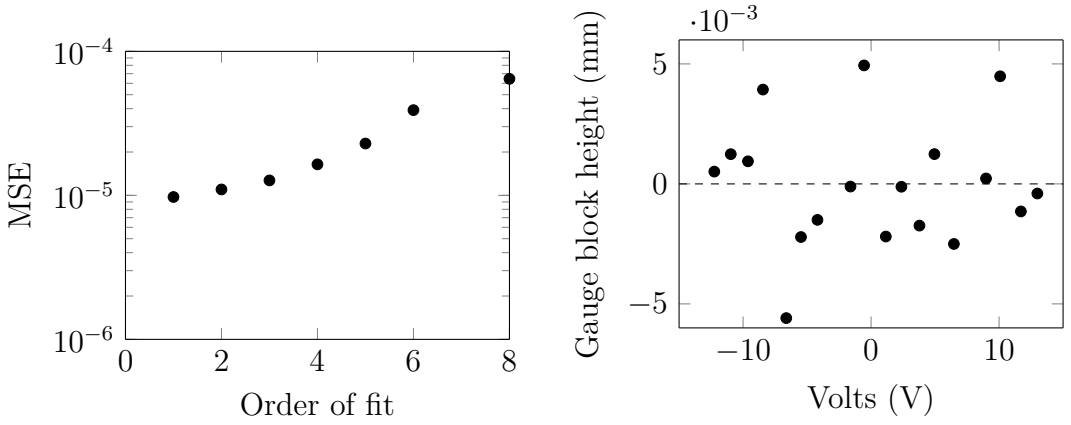

(a) Mean square error for LVDT polynomial fitting

(b) Residuals for LVDT first order fit

Figure 3.11: Goodness of LVDT fit

calibration is 2.72 µm using eq. (3.7); however, the reported sublimed naphthalene depth is a difference between two voltage measurements, so the uncertainty of the depth calibration subtracts out. However, the uncertainty in the slope of the fit, 19.157 56 mm V^{-1}, does not subtract out and contributes to the uncertainty of the reported sublimed naphthalene depth values. Using eqs. (3.7) to (3.9) from Coleman and Steele (2009) gives an uncertainty of the slope of eq. (3.6) of 8.18×10^{-2} µm.

$$\hat{\sigma}_y = \left[\frac{\sum_i^N (y_i - \hat{y}_i)^2}{df} \right]^{1/2} \tag{3.7}$$

$$\hat{\sigma}_{xx} = \sum_i^N x_i^2 - \frac{1}{N} \left(\sum_i^N x_i \right)^2 \tag{3.8}$$

$$\hat{\sigma}_m = \left(\frac{\hat{\sigma}_y^2}{\hat{\sigma}_{xx}} \right)^{1/2} \tag{3.9}$$

In eqs. (3.7) to (3.9), $\hat{\sigma}_y$ is the standard error of regression of the fit, $\hat{\sigma}_m$ is the uncertainty in the slope of the fit, N is the number of samples, y_i and x_i are the measured values, $\hat{y}_i$ is the estimate from the fit, and df is the degrees of freedom of

the system after fitting. Equation (3.7) is the standard error or regression and an estimate of the error from the calibration and eq. (3.9) is the error in the slope of the linear best fit line.

Figure 3.12 shows the results of a mock sublimed naphthalene depth test. Twenty-five hundred (2500) are taken on a polished surface twice, and the difference between the two sets of measurements subtracted. The mock sublimed naphthalene depth test indicates the one standard deviation random uncertainty of the LVDT is 0.181 µm.

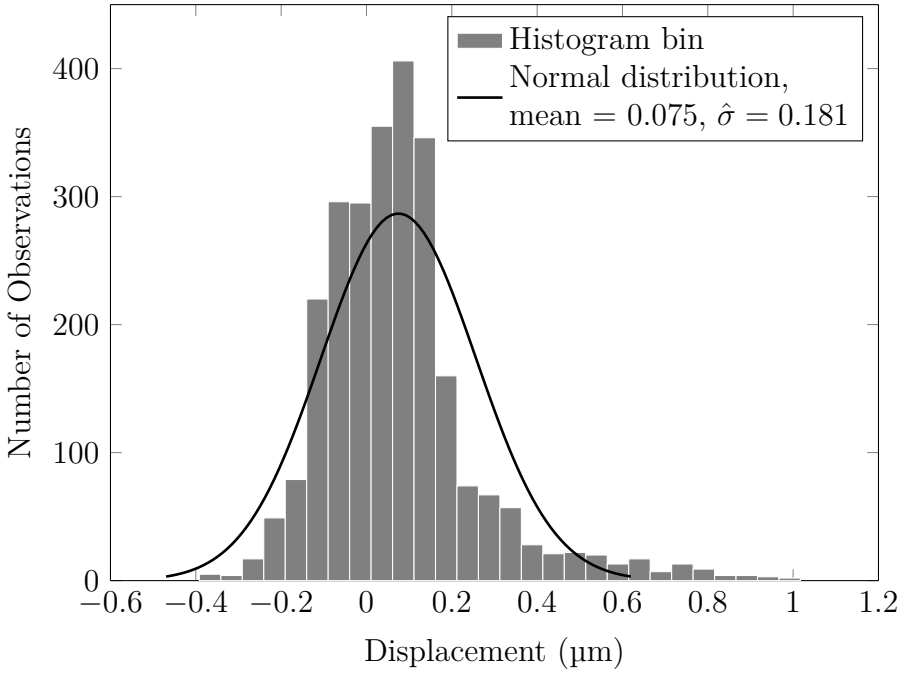

Figure 3.12: Histogram of the uncertainty of the LVDT depth measurements based on a mock sublimed naphthalene depth test. The displacement is the difference between two measurements on a polished aluminum surface. A total of 2500 differences are shown.

Hotwire Anemometer

The hotwire (and hotfilm) anemometer is calibrated in the wind tunnel against the pitot-static tube described in section 3.3.2. The calibration equation for the hotwire

is

$$\frac{\mathcal{E}_{hw}^2}{T_{hw} - T_{\infty,ref}} = A + BU^n. \tag{3.10}$$

Where A and B are fitted constants, n is assumed to equal 0.45, $\mathcal{E}_{hw}$ is the voltage drop across the hotwire, and $T_{hw} - T_{\infty,ref}$ is the temperature difference between the hotwire and the freestream at the time of the calibration. The hotwire temperature, T_{hw}, is set to 250 °C by a calibration completed by the manufacturer, TSI.

Figure 3.13 shows the fitting information for the hotwire anemometer and indicates that eq. (3.10) provides a reasonable fit for the hotwire anemometer. Figure 3.13b shows the largest error is on the order of 2 %.

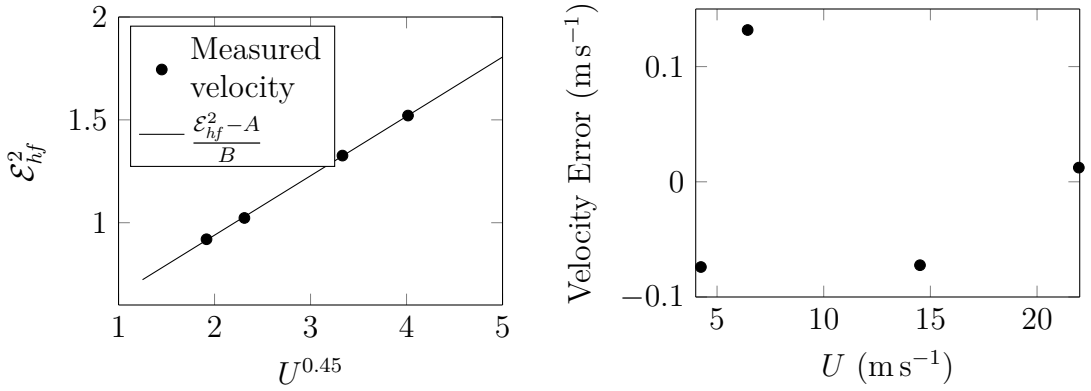

(a) Fit of eq. (3.10) for hotwire anemometer, $A = 0.362$ and $B = 0.289$

(b) Velocity residuals for hotwire anemometer fit

Figure 3.13: Fit for hotwire anemometer on 2015/08/07

The TSI IFA-100 amplifies the voltage of the hotwire, increasing the effective resolution of the voltage readings of the Agilent 34411A. For the hotwire, the gain is 9 and the voltage offset is 1 V. The gain is limited by the ±5 V range of the TSI IFA-100.

$$\mathcal{E}_{hw} = \frac{\mathcal{E}_{DMM}}{\text{gain}} + \text{offset} \tag{3.11}$$

In eq. (3.11), $\mathcal{E}_{DMM}$ is the voltage read by the Agilent 34411A.

3.3.2 Flow Measurement

Pitot-Static

As stated in section 3.1.3, the freestream velocities for the mass transfer experiments are made with a Pitot-static tube and water micromanometer. For low Mach numbers and turbulence intensity, the dynamic pressure is the difference between the total pressure and the static pressure (Saad 1993, pg. 67, eq. 2.50),

$$P_0 - P_t = \frac{1}{2}\rho_a U_\infty^2. \tag{3.12}$$

The pressure difference is found using a water micromanometer and Pascal's Law, as shown in eq. (3.13),

$$P_0 - P_t = \rho_{H_2O} g \Delta h, \tag{3.13}$$

where ρ_{H_2O} is the density of water, g is the acceleration due to gravity, and Δh is the total difference between the two water heights measured using the micromanometer.

The static pressure in the wind tunnel, P_t, is different than the ambient pressure in the room, P_{amb}. A water manometer with a resolution of 0.5 mm is used to estimate the pressure difference between the room and the tunnel. Typical values for the pressure difference are approximately 30 Pa to 500 Pa.

Hotwire Anemometer

For the measurement of the boundary layer, a hotwire anemometer is used. The hotwire returns the instantaneous readings of velocity, limited only by the speed of the voltmeter, thermal inertia of the hotwire, and speed of the electronic control circuit, as a voltage reading. The instantaneous velocity of the flow can be calculated from the voltage using eq. (3.10). When measuring the flow velocity, the reading is corrected

for the different temperature conditions between the calibration and measurement.

$$\mathcal{E}'^2_{hw} = \mathcal{E}^2_{hw} \frac{T_{hw} - T_{\infty,ref}}{T_{hw} - T_\infty} \tag{3.14}$$

$T_{\infty,ref}$ is the ambient temperature during the calibration procedure. The velocity is calculated using eqs. (3.10) and (3.14).

$$U = \left(\frac{\mathcal{E}'^2_{hw} - A}{B} \right)^{1/0.45} \tag{3.15}$$

The mean and RMS velocity values can be found using the following equations for N amount of measurements

$$\overline{U}_\infty = \frac{1}{k} \sum_{k=1}^{N} U_{\infty,k} \tag{3.16}$$

$$\overline{u'}_\infty = \sqrt{\sum_{k=1}^{N} \frac{\left(\overline{U}_\infty - U_{\infty,k}\right)^2}{N-1}}. \tag{3.17}$$

3.3.3 Mass Transfer Plate

Casting

There are several methods available to create the desired naphthalene surface, but the current experiment casts the naphthalene into the appropriate shape using an aluminum mold. Outlined below are the three main steps of casting the naphthalene.

The first step ensures the surfaces of the mold, both the lid and the mass transfer plate, are clean. Any residual naphthalene is melted and allowed to run or boil off. Then the various aluminum surfaces of the mold are polished with 1200 grit white aluminum oxide lapping compound (38-1200, Unites Sates Products Co.) and cleaned with isopropyl alcohol (Goldstein and Cho 1995).

Second, the mold is assembled and preheated. The lid is secured to the mass transfer plate with a c-clamp tightened in the middle, ensuring there is no curvature of the lid near the middle of the section. After assembly, the mold is preheated to about 110 °F as indicated by a temperature strip, temperature so the molten naphthalene can solidify correctly (Goldstein and Cho 1995).

Last is the the actual casting of the naphthalene. The mass transfer plate has two large threaded holes: one for pouring, and the other for overflow of the molten naphthalene. The naphthalene cannot be poured too hot, or bubbles will form, and it can not be poured too cold or some of the naphthalene will not solidify correctly, leaving wavy traces on the exposed surface. The naphthalene is poured into the mold after it is heated to 10.5 V as indicated by an E-type thermocouple submerged in the molten naphthalene. The mold cools for at least 2 hours at room temperature to correctly solidify. After the naphthalene cools for the necessary amount of time, the lid is removed in a shearing motion, producing a smooth exposed surface (Goldstein and Cho 1995).

Profile Measurement

After the casting procedure is completed, the mass transfer plate is placed securely on the clean x-y measuring table. After firmly securing the plate in position, the LVDT tip is manually placed on a dimple that serves as reference point for both the pre and post-measurement of the surface profile. The system is allowed to reach thermal equilibrium before measurements begin. Several thousand measurements, about 4200 for the cavity and about 5200 for the rectagular strips, are recorded. Each LVDT voltage is read and written onto a text file using the data acquisition system. After the surface scan is complete, a quick check is completed to ensure the LVDT returned to the reference location. The mass transfer plate is then placed in the wind tunnel.

After the experimental run is completed, the pre-experiment process is repeated and the surface scan data are read into the computer and saved. The whole experiment is timed, particularly noting the beginning and end of both scans, and the beginning and end of the experimental run in the wind tunnel.

3.3.4 Naphthalene Sublimation Technique

Boundary Condition Validation

There were several concerns raised in section 1.3.1 about the limitations of the naphthalene sublimation technique, however, most of the concerns are not pertinent to the proposed study. High velocity flows and high external shear flows are not relevant because of the low Mach number the wind tunnel is operating at. As the proposed work would calculate an average local mass transfer coefficient, transient measurements are not required. However, the concerns about the surface profile deviation and the magnitude of the wall normal velocity due to transpiration are explored in more detail in the following paragraphs.

To address the concerns about the change in the flow field due to excessive subliming, a representative sublimed naphthalene depth will be compared with a representative boundary layer thickness. As shown in section 5.1, the momentum and displacement thicknesses are about 1.3 mm and 1.86 mm, respectively, which is an order of magnitude larger than the sublimed naphthalene depth of 100 µm found for the present experiments.

The suggestions from Lienhard IV and Lienhard V (2012) for the heat-mass transfer analogy to hold for a no blowing condition (low mass transfer rate) at the wall are considered. If there is a large mass transfer at the surface, then the velocity boundary layer is affected and the mass transfer is analogous to heat transfer with transpiration

at the wall. Lienhard IV and Lienhard V (2012) suggest using the mass transfer driving force, B, to evaluate the ratio of the $St_{m,0}$ evaluated for the transpired boundary layer and the St_m evaluated for no transpiration at the wall.

$$\frac{St_m}{St_{m,0}} = \frac{ln\,(1+B)}{B}. \tag{3.18}$$

It can be shown that

$$B \to 0, \quad \frac{St_m}{St_{m,0}} \to 1. \tag{3.19}$$

The mass transfer driving force is equivalent to the blowing parameter, $\frac{v_w}{U_\infty}\frac{1}{St_m}$, and eq. (3.18) was shown by Kays et al. (2005, pg. 261) to be accurate over a wide range of turbulent flow conditions. To apply eq. (3.18) to subliming naphthalene, B can be evaluated as follows

$$B = \frac{C_w - C_\infty}{1 - C_w}. \tag{3.20}$$

Using 4.87×10^{-4} as a representative value for the naphthalene concentration at the wall, eq. (3.18) evaluates to 0.999 76, indicating the no blowing assumption at the wall is valid and the mass transfer is analogous to heat transfer without transpiration.

Latent Heat Temperature Depression

Due to the change of phase of the naphthalene at the naphthalene-air interface, the temperature at the surface is slightly lower than the free stream temperature. Goldstein and Cho (1995) give the value of temperature depression at the surface of about 0.15 K. A simple energy balance at the surface, assuming the mass and heat transfer are independent of one another (a low mass transfer solution), yields

$$\frac{L_{s,g}}{c_p}\left(\frac{Pr}{Sc}\right)^{2/5}(C_w - C_\infty) = T_\infty - T_w, \tag{3.21}$$

where $L_{s,g}$ is the latent heat of subliming. Equation (3.21) evaluates to 0.17 K temperature difference. Note the temperature difference for the simple model in eq. (3.21) does not depend on the Re_x because h_m and h scale with one another. Even though the properties of naphthalene are sensitive to temperature variation, this is not expected to cause uncertainty because the temperature of the solid naphthalene is recorded throughout the experiment.

3.4 Properties

3.4.1 Air Properties

The properties for air are from Lemmon (2014) and shown below in table 3.1. Several

Table 3.1: Air properties at 1 bar

Temperature K	Density $\mathrm{kg\,m^{-3}}$	Specific heat $\mathrm{kJ\,kg^{-1}\,K^{-1}}$	Viscosity $\mu\mathrm{Pa \cdot s}$	Thermal conductivity $\mathrm{mW\,m^{-1}\,K^{-1}}$
200	1.746	1.007	13.33	18.50
220	1.586	1.006	14.44	20.16
240	1.453	1.006	15.51	21.77
260	1.341	1.006	16.55	23.35
280	1.245	1.006	17.56	24.88
300	1.161	1.007	18.54	26.38
320	1.089	1.007	19.49	27.85
340	1.024	1.009	20.41	29.29
360	0.9674	1.010	21.32	30.71
380	0.9164	1.012	22.20	32.09
400	0.8706	1.014	23.06	33.45

models (shown in eqs. (3.22) to (3.24)) are tested and chosen using the leave-one-out cross-validation technique (see appendix B.3) with the mean square error used as the measure of fitness. It is assumed the effect of pressure on the properties of air, except

density, is negligible.

$$f\left(\frac{T}{T_0}\right) = \left(\frac{T}{T_0}\right)^n \tag{3.22}$$

$$f\left(\frac{T}{T_0}\right) = \frac{1+S}{T/T_0+S}\left(\frac{T}{T_0}\right)^n \tag{3.23}$$

$$f\left(\frac{T}{T_0}\right) = a_0 + a_1\left(\frac{T}{T_0}\right) + a_2\left(\frac{T}{T_0}\right)^2 + ... \tag{3.24}$$

Equation (3.23) is Sutherland's formula (White 1991, pg. 28–31).

Figures 3.14 to 3.19 summarize the fitting procedure for the dynamic viscosity, thermal conductivity, and specific heat capacity of air. The dynamic viscosity and specific heat capacity are well described by a polynomial over the prescribed temperature range while the thermal conductivity is well described by the Sutherland formula over the prescribed temperature range.

The best fits for the various quantities are shown in eqs. (3.25) to (3.27). For the thermal conductivity, the best fit is

$$\frac{k}{k_0} = \frac{1+0.19843}{T/T_0+0.19843}\left(\frac{T}{T_0}\right)^{1.6788}, \tag{3.25}$$

where $k_0 = 0.026\,38\,\mathrm{W\,m^{-1}\,K^{-1}}$ and $T_0 = 300\,\mathrm{K}$. The estimated standard deviation of the fit from eq. (3.7) is $4.4 \times 10^{-6}\,\mathrm{W\,m^{-1}\,K^{-1}}$, or approximately $1.7 \times 10^{-2}\,\%$ uncertainty.

For the specific heat capacity of air, the best is

$$\frac{c_p}{c_{p,0}} = 1.0233 - 0.057164\left(\frac{T}{T_0}\right) + 0.033865\left(\frac{T}{T_0}\right)^2, \tag{3.26}$$

where $c_{p,0} = 1006.67\,\mathrm{J\,kg^{-1}\,K^{-1}}$ and $T_0 = 300\,\mathrm{K}$. The estimated standard deviation of the fit from eq. (3.7) is $0.32\,\mathrm{J\,kg^{-1}\,K^{-1}}$, or approximately $3.2 \times 10^{-2}\,\%$ uncertainty.

For the dynamic viscosity of air, the best fit is,

$$\frac{\mu}{\mu_0} = -0.0076267 + 1.2954\left(\frac{T}{T_0}\right) - 0.34866\left(\frac{T}{T_0}\right)^2 + 0.060821\left(\frac{T}{T_0}\right)^3, \qquad (3.27)$$

where $\mu_0 = 1.854 \times 10^{-5}\,\mathrm{Pa \cdot s}$ and $T_0 = 300\,\mathrm{K}$. The estimated standard deviation of the fit from eq. (3.7) is $3.0 \times 10^{-9}\,\mathrm{Pa \cdot s}$, or approximately $1.6 \times 10^{-2}\,\%$ uncertainty.

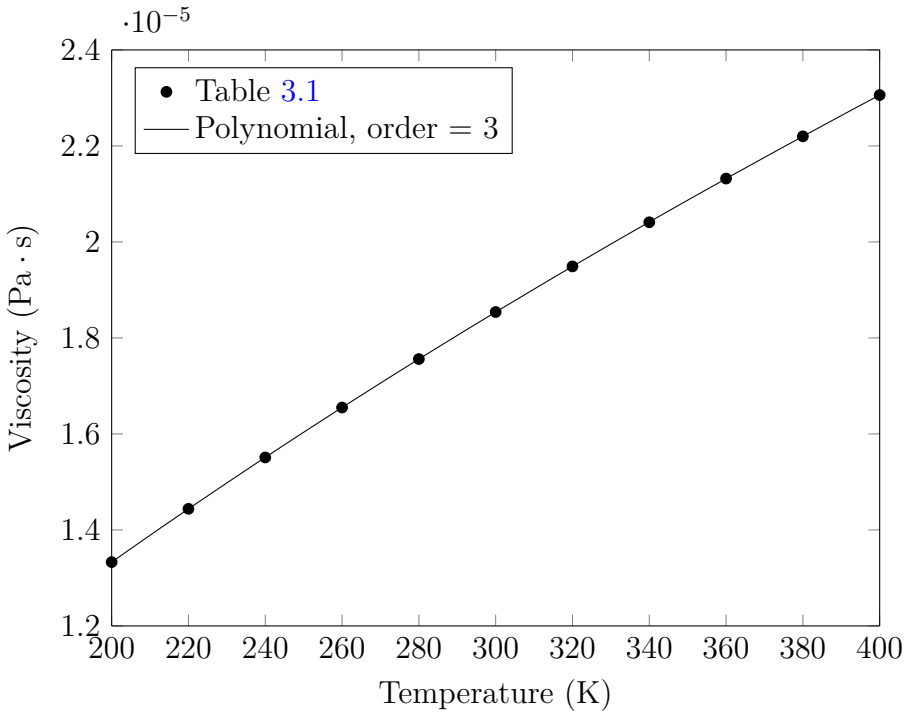

Figure 3.14: Best fit for dynamic viscosity of air

Density is estimated using the ideal gas law with the molecular mass for air, $\mathcal{M}_a$, estimated from table 3.1 at 300 K.

$$\begin{aligned}\mathcal{M}_a &= \frac{\rho_0 \mathcal{R} T_0}{P_0} \\ &= 28.959\,\mathrm{kg\,kmol^{-1}}\end{aligned} \qquad (3.28)$$

For eq. (3.28) $\rho_0 = 1.161\,\mathrm{kg\,m^{-3}}$, $T_0 = 300\,\mathrm{K}$, $\mathcal{R} = 8314.4598\,\mathrm{J\,kmol^{-1}\,K^{-1}}$ (Mohr et

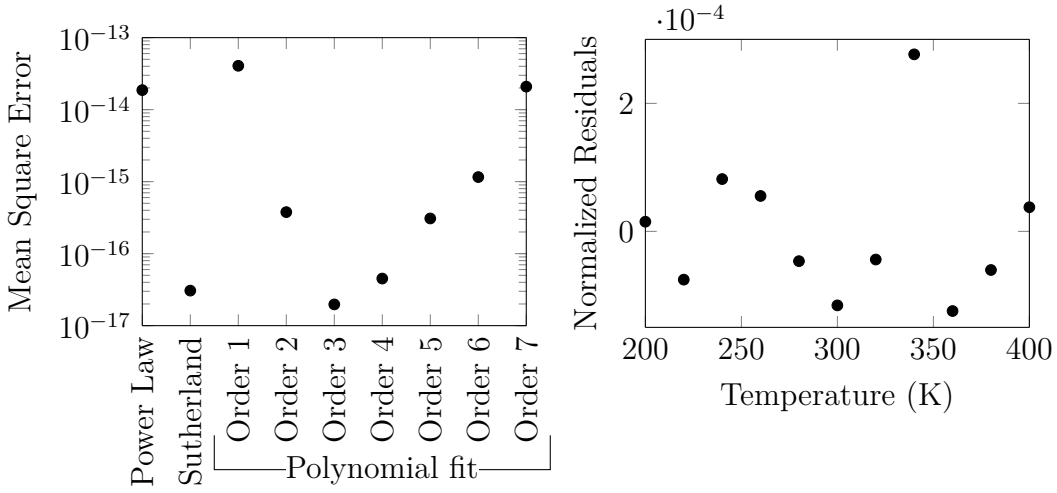

(a) Mean Square Error for various models for dynamic viscosity of air

(b) Residuals normalized by μ_0 for dynamic viscosity of air

Figure 3.15: Residuals and MSE for dynamic viscosity of air

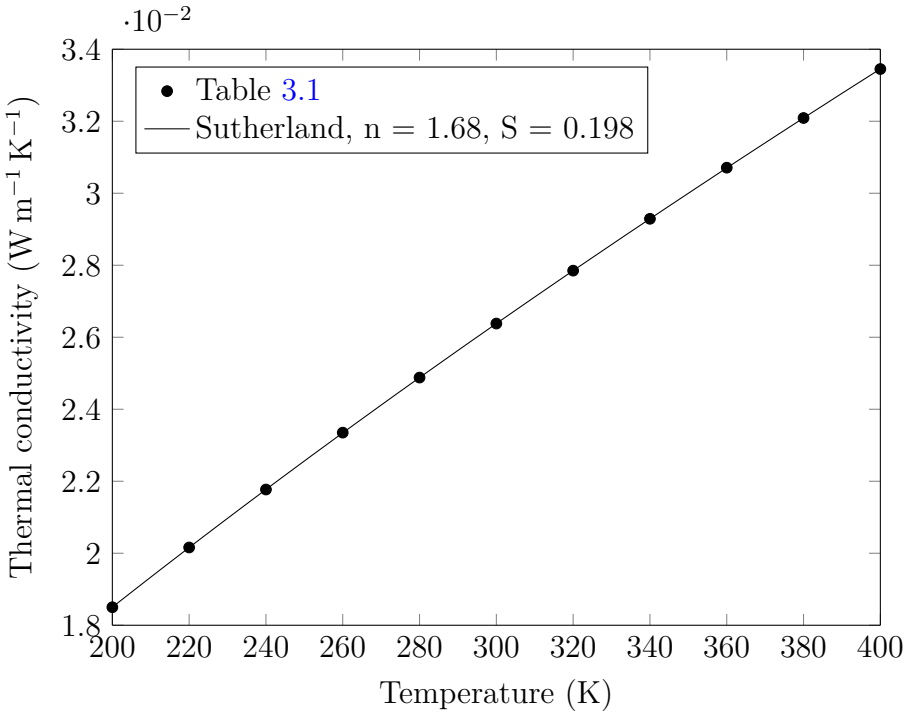

Figure 3.16: Best fit of thermal conductivity of air

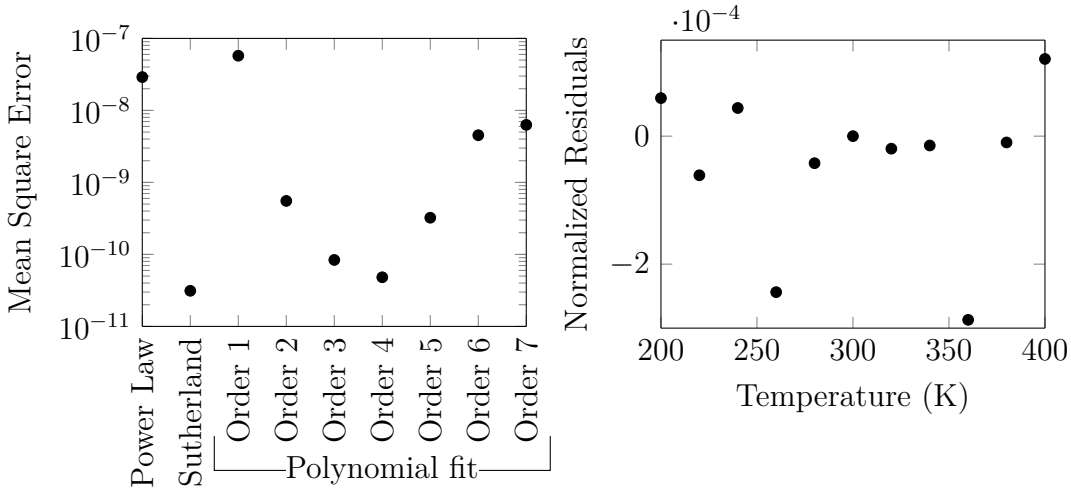

(a) Mean Square Error for various models for thermal conductivity of air

(b) Residuals normalized by k_0 for thermal conductivity of air

Figure 3.17: Residuals and MSE for thermal conductivity of air

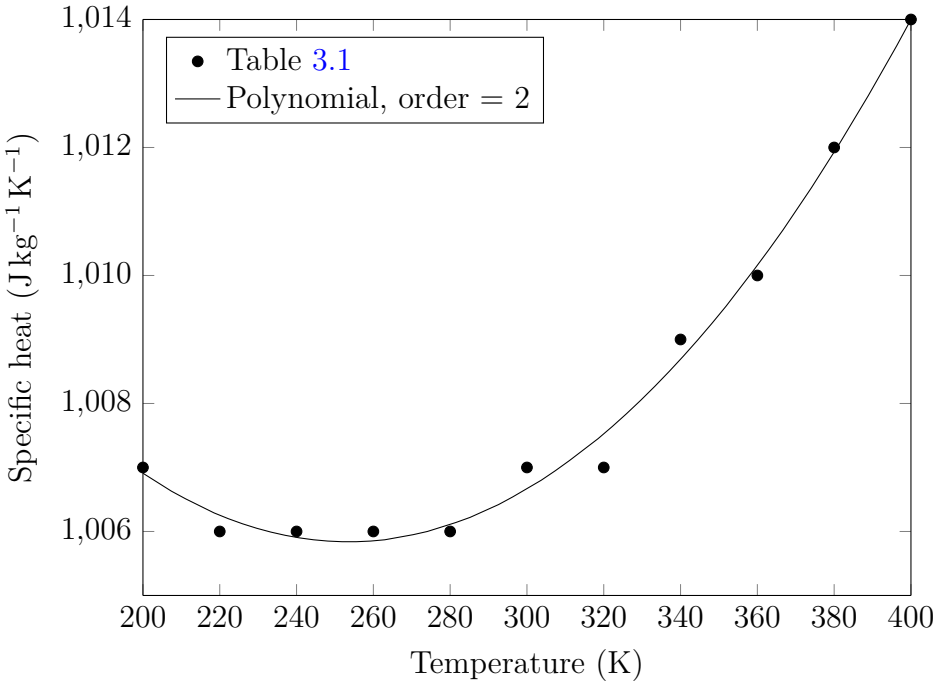

Figure 3.18: Best fit of specific heat of air

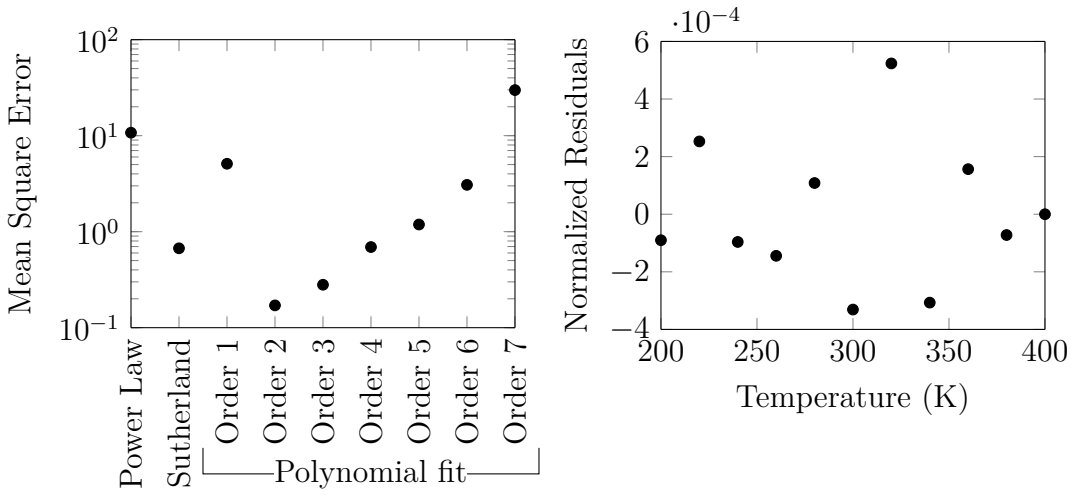

(a) Mean Square Error for various models for specific heat of air

(b) Residuals normalized by $c_{p,0}$ for specific heat of air

Figure 3.19: Residuals and MSE for specific heat of air

al. 2016), and $P_0 = 100\,000\,\text{Pa}$. The resulting fit and residuals are shown in fig. 3.20. The estimated standard error using the ideal gas law from eq. (3.7) is $0.0019\,\text{kg}\,\text{m}^{-3}$, or approximately 0.16 % uncertainty in addition to the stated 0.1 % uncertainty of the density data (Lemmon 2014).

3.4.2 Water Properties

The density of Standard Mean Ocean Water is required to calculate the flow rate, as described in section 3.3.2. Tanaka et al. (2001) recommend using eq. (3.29),

$$\rho_{SMOW} = a_5 \left[1 - \frac{(t + a_1)^2 (t + a_2)}{a_3 (t + a_4)} \right], \tag{3.29}$$

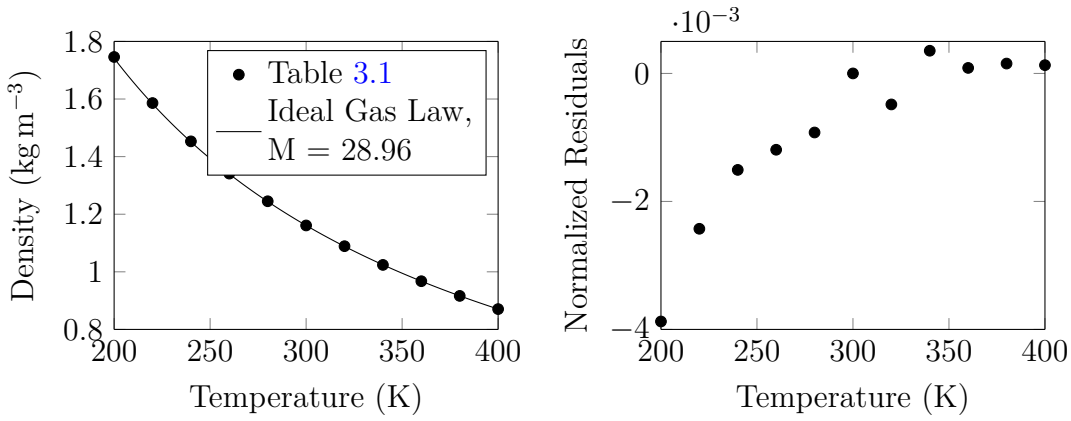

(a) Ideal gas law with molar mass of $28.959\,\mathrm{kg\,kmol^{-1}}$ compared to data in table 3.1

(b) Residuals normalized by ρ_0 for density of dry air

Figure 3.20: Fitting for density of air

where,

$$a_1 = -3.983\,035\,^{\circ}\mathrm{C}, \quad a_2 = 301.797\,^{\circ}\mathrm{C},$$

$$a_3 = 522\,528.9\,^{\circ}\mathrm{C}^2, \quad a_4 = 69.348\,81\,^{\circ}\mathrm{C},$$

$$a_5 = 999.974\,950\,\mathrm{kg\,m^{-3}}.$$

Bignell (1983) recommends the following correction for water with dissolved air:

$$\rho_{\mathrm{H_2O}} - \rho_{SMOW} = s_0 + s_1 t, \tag{3.30}$$

where

$$s_0 = -4.612 \times 10^{-3}\,\mathrm{kg\,m^{-3}}, \quad s_1 = 0.106 \times 10^{-3}\,\mathrm{kg\,m^{-3}\,^{\circ}C^{-1}}. \tag{3.31}$$

The corrected density of water, $\rho_{\mathrm{H_2O}}$, is used for determining the density of water in the micromanometer and manometer for the experimental measurements. The uncertainty of water density in eq. (3.29) is given by Tanaka et al. (2001) as $0.83 \times 10^{-3}\,\mathrm{kg\,m^{-3}}$

from 8 °C to 32 °C.

3.4.3 Naphthalene Properties

The physical properties of naphthalene required to calculate the Sh and the St_m are density of the solid naphthalene, density of the naphthalene vapor in air, and the diffusion coefficient of naphthalene in air. Density of the solid phase is taken from Dean (1985) and can be found in table 3.2.

Density of the vapor can be calculated using the ideal gas law due to the low vapor pressure of naphthalene at room temperature (about 11 Pa when saturated at 298.15 K (Goldstein and Cho 1995)). Goldstein and Cho (1995) recommend using the saturated vapor pressure correlation from Ambrose et al. (1975) because it agrees well with experimental data and the disagreement with other correlations is within its stated uncertainty. The saturated vapor pressure as presented by Ambrose et al. (1975) is

$$T \log_{10} P = \frac{a_0}{2} + \sum a_s E_s(x), \tag{3.32}$$

where T is in Kelvin and P is in Pascals. The Chebyshev polynomials and coefficients are as follows:

$$E_1(x) = x, \quad E_2(x) = 2x^2 - 1, \quad E_3(x) = 4x^3 - 3x,$$
$$x = \frac{2T - 574}{114},$$

where,

$$a_0 = 301.6247, \quad a_1 = 791.4937,$$
$$a_2 = -8.2536, \quad a_3 = 0.4043.$$

The overall one standard deviation uncertainty of eq. (3.32) is given as 1.6 % by Ambrose et al. (1975).

The binary diffusion coefficient is the most difficult to calculate, as the provided correlations in the literature differ from each other more than their stated uncertainties. Goldstein and Cho (1995) recommend averaging the diffusion coefficient correlations provided by several researchers. The averaged diffusion coefficient of naphthalene in air, as presented by Goldstein and Cho (1995), is

$$\mathcal{D} = 0.0681 \left(\frac{T}{298.16} \right)^{1.93} \left(\frac{1.013 \times 10^5}{P_{atm}} \right), \tag{3.33}$$

where $\mathcal{D}$ is given in units of $\mathrm{cm^2\,s^{-1}}$. The binary diffusion coefficient for naphthalene is insensitive to the humidity of the ambient air (Goldstein and Cho 1995). As the uncertainty for the diffusion coefficient is relatively large, mass St are presented instead of the Sh, as the the diffusion coefficient is not required to determine the mass St.

Table 3.2: List of naphthalene properties at 1.013×10^5 Pa (Goldstein and Cho 1995)

Property	Value	Variable
Chemical formula	$C_{10}H_8$	
Molecular weight	128.17	$\mathcal{M}_n$
Density (solid)	$1162.0\,\mathrm{kg\,m^{-3}}$ (Dean 1985)	$\rho_{n,s}$
Melting point	80.2 °C	T_m
Boiling point	217.993 °C	T_b
Latent heat of subliming	$5.49 \times 10^5\,\mathrm{J\,kg^{-1}}$	$L_{s,g}$

3.5 Data Analysis

3.5.1 Data Reduction

The conversion of voltage and water height measurements to temperature, velocity, and pressure measurements are described in section 3.3. Below is a description of the procedures applied to the sublimed naphthalene depth measurements. An example using data at a given streamwise location taken on November 2nd, 2015 will illustrate the applied corrections. Figure 3.27 shows the cumulative effect of the successive corrections.

Rim Correction

After the raw voltage readings from the LVDT from before and after the wind tunnel are converted to the appropriate depth values using eq. (3.6), they are subtracted from each other to calculate the sublimed naphthalene depth. Despite the care taken in ensuring the measurement of the naphthalene surface is repeatable, the process is not error free. A robust and straightforward way to remove these bias errors is to correct the sublimed naphthalene depth based on the measured sublimed depth of the aluminum rim.

The filled circles in fig. 3.27 are the original raw data. The two lowest measurements, one in the lower left corner, the other in the upper right corner, are the two measurements taken on the aluminum rim. As stated in the preceding paragraph, the sublimed depth of aluminum during the experiment is physically zero, so the data are corrected to remove the obvious bias error. A line is found between the two measurements on the aluminum rim and then subtracted from both the rim measurements and the measurements in between. Figure 3.27 shows this correction as the difference

between the open and filled circles.

Erroneous rim corrections are removed using the generalized extreme Studentized deviate test for outliers (Rosner 1983) with a significance level of 0.05 and ten maximum outliers. The numerical code written in MATLAB for the outlier test is posted at the MathWorks file exchange with the function name `generalized_esd()` under the author's name. The test population is the slope of the lines between the rim measurements (opposed to the values of the applied corrections), as the expected slope for all corrections is expected to be identical. Table 3.3 shows that for this particular test run, the largest number of outliers where the test statistic is larger than the critical value is six; therefore, for this particular test run, six slopes (and twelve measurements) are removed from the original population of 108 slopes.

Table 3.3: Generalized extreme Studentized deviate test applied to slopes of rim corrections for data taken on November 2$^{\text{nd}}$, 2015

Number of Outliers	Outlier Value	Test Statistic	Critical Value
1	-0.2142	3.871	3.410
2	-0.2110	4.145	3.407
3	-0.2090	4.519	3.404
4	-0.1835	4.571	3.401
5	-0.1819	5.109	3.397
6	-0.1023	3.971	3.394
7	0.1800	3.272	3.391
8	0.1624	2.982	3.387
9	0.1559	2.947	3.384
10	-0.0402	2.951	3.381

Figure 3.21a is a histogram of the original slopes of the correction lines, and fig. 3.21b is a histogram of the slopes with the erroneous slopes removed and replaced with new slopes of the new correction lines. It is clear from these figures, and table 3.3, that the six outliers removed have slope values smaller than $-0.1\,\mu\text{m}\,\text{mm}^{-1}$. The new slopes are calculated by removing the offending pair of measurements and estimating

new values using linear interpolation. These newly interpolated points are then used to calculate the new correction line.

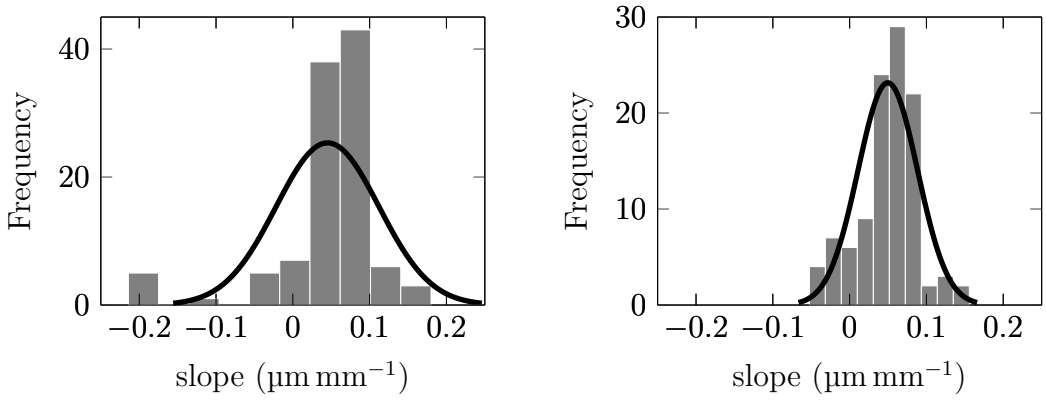

(a) Histogram with original slopes between rim edges

(b) Histogram with erroneous rim slopes removed and replaced

Figure 3.21: Histograms showing difference in distribution of correction slopes of the rim corrections before and after the generalized extreme Studentized deviate test is performed with taken data on November 2$^{\text{nd}}$, 2015.

In addition to bias errors in the depth measurements, there is a small error depending on the direction of travel of the LVDT. This is mitigated using an integrated average of the correction and it's immediate neighbors using the trapezoidal method.

Natural Convection Correction

During the surface scanning procedure there are natural convection losses that need to be accounted for in the final depth measurement. Goldstein and Cho (1995) give a correlation for the sublimed naphthalene depth due to natural convection

$$\delta_{NC} = C_{NC} \left[1 + 0.1 \left(T_w - 297.15\right)\right]^{1.03} \tau_{NC}, \tag{3.34}$$

where C_{NC} is an empirically determined constant and τ_{NC} is the elapsed time of the natural convection. The sublimed naphthalene depth due to forced convection can

then be found by subtracting the depth due to natural convection from the total measured sublimed naphthalene depth.

Measurements are taken over a twelve hour period and the average value for C_{NC} is $4.66 \times 10^{-4}\,\mu\mathrm{m\,s^{-1}} \pm 8.5\,\%$ (at a 95 % confidence level). Typical natural convection losses for during an experiment are approximately 4 µm, which is about 10 % of the overall sublimation depth.

The natural convection correction is shown in fig. 3.27 by the difference between the open circles and open squares. In this particular case, the rim corrections leveled and increased the depth measurement while the natural convection correction decreased depth measurement.

Naphthalene surface

The final correction applied to the sublimed naphthalene depth measurements is eliminating the data where the LVDT probe tip is not in contact with the naphthalene surface. As part of this process, the position of the rim is estimated. For the lateral profiles presented in chapters 4 and 5, the rim location is the location of the origin for the spanwise coordinate. The process of estimating the location of the rim is described first. Estimation of both the rim location and the location where the naphthalene surface is measured serves as a last check on the accuracy of the data. The rim naphthalene cannot exist past the rim edge.

The estimation of the position of the rim is a two step process. First, for each line of data in the spanwise direction, the position of the rim is estimated. The rim locations are estimated by finding two points of equal height separated by a lateral distance equal to the measured width of the strip (section 3.2.2). Second, the points where the rim edge estimation is incorrect are replaced using a linear fit of the other rim edges. Figure 3.22 shows the final result for a particular line of data.

The rim location error is estimated based on the scatter of all the individual location estimation has an estimated error of 0.05 mm to 0.1 mm.

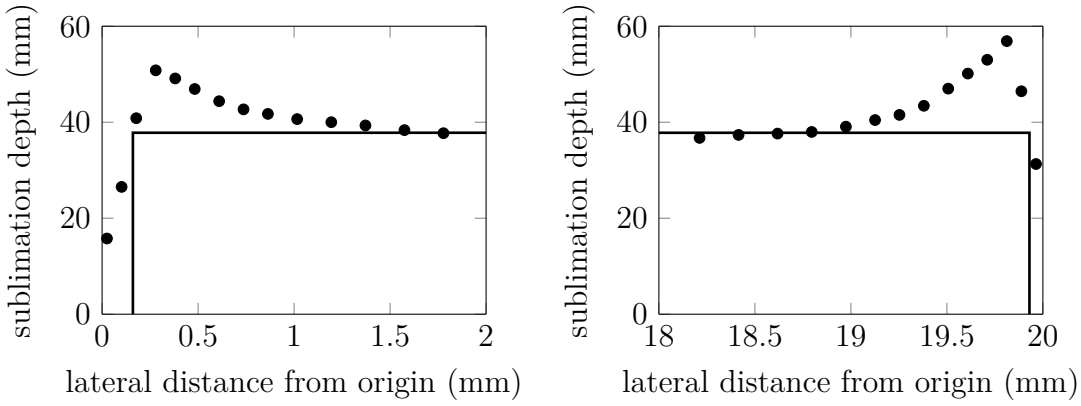

(a) Edge fit for data closest to left side of data

(b) Edge fit for data closest to right side of data

Figure 3.22: Edge fit for data taken on November 2nd, 2015, showing the two points equal height separated by a lateral distance equal to the measured width of the strip. The width of the strip is 19.77 mm and location of the estimate rim edges are 0.16 mm and 19.93 mm.

Lastly, the data where the LVDT probe tip is still in contact with the corner on the edge of the aluminum rim are eliminated. The point where the LVDT probe tip is touching both the rim and naphthalene surface (called "the intersection" for the next few paragraphs) is estimated in two ways. The first is by fitting two second order polynomials with `fminsearch()` (The MathWorks, Inc. 2014), one for the path the probe tip traces as it travels over the aluminum corner, the other for the path the probe tip traces as it travels over the naphthalene surface. Figure 3.23 shows these two intersecting paths and how the presence of the aluminum rim limits the measurement near the lateral edge.

The polynomial fitting procedure is written so that the concavities have the correct sign and the two polynomials actually intersect at the intersection point by specifying one of the polynomial coefficients to meet this condition. In effect, `fminsearch()` is

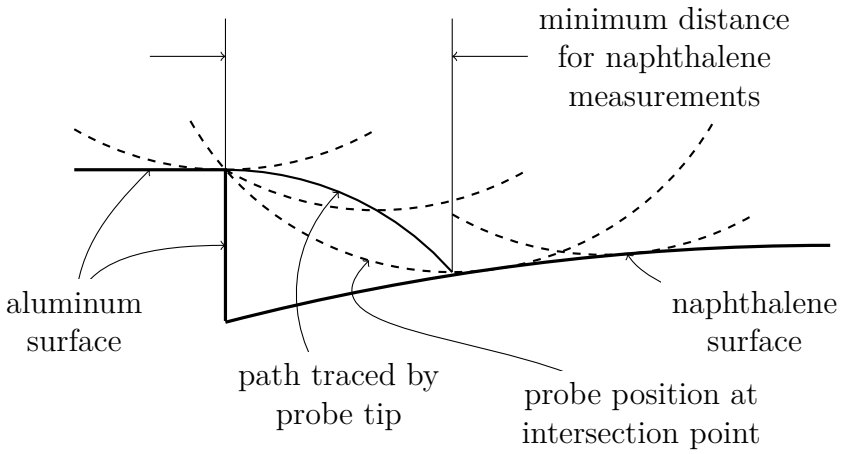

Figure 3.23: The dashed lines show successive positions of the LVDT probe from the aluminum rim, over the rim edge, and eventual engagement with the naphthalene surface. For the current experiment the minimum measurement distance is approximately 0.3 mm. Not to scale.

optimizing for the intersection point and five out of the six polynomial coefficients. Note the data used to fit the polynomials is from the voltage readings taken after the wind tunnel run. This ensures that the data used is either on the rim or on the naphthalene. If the sublimed naphthalene data is used, some of the voltage readings very close to the rim from before the wind tunnel run might be on the naphthalene surface. However, after the wind tunnel run, those same readings very close to the rim are lower from subliming in the wind tunnel. So when taking the difference in the LVDT measurements one reading might be on the naphthalene surface while the other is touching the aluminum rim.

The polynomial estimate of the intersection is not robust enough to serve as the sole method of determining the intersection; so a second method is employed to confidently decide which data are measurements of the naphthalene profile and which data are not. This second method uses the estimated first derivatives of the data. If the maximum and minimum derivatives share the same point, that point is taken to be the intersection. This condition, while obvious, is not as common as the next two

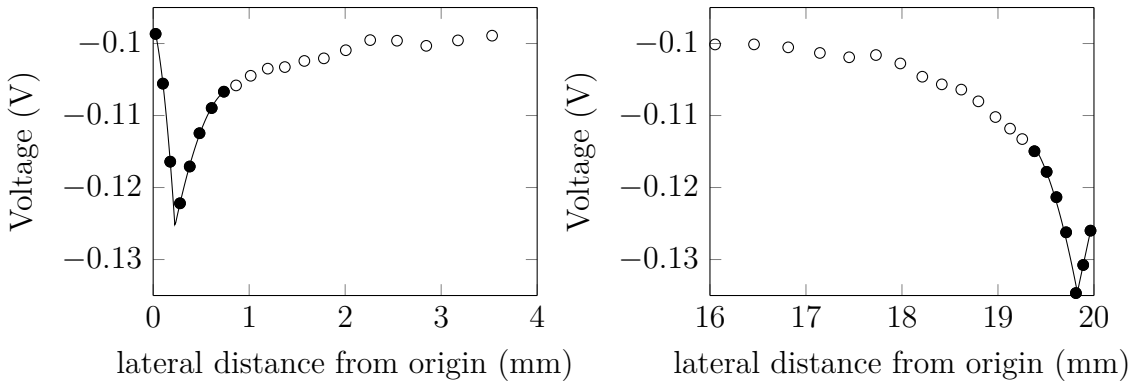

(a) Polynomial estimate of intersection for left side of data

(b) Polynomial estimate of intersection for right side of data

Figure 3.24: Polynomial fit of intersection for data taken on November 2$^{\text{nd}}$, 2015. All the circles are voltage reading taken after the wind tunnel run, and the filled circles are used in the polynomial fitting. The black line is the polynomial fit.

conditions, and is not displayed in a figure. If the maximum and minimum derivatives are separated by less than a data point, the intersection is taken to be in the middle. This condition is shown in fig. 3.25b. The last slope is the most negative and the third to last slope is the most positive, so the intersection is somewhere in between them. The catch-all condition for estimating the intersection is the location of the of the minimum value of the absolute value of the slope that is bracketed by the maximum and minimum slopes. The maximum and minimum slopes are expected to be near the intersection, but often the probe tip might move from the aluminum edge to the naphthalene and the values are similar. This condition is shown in figs. 3.25a, 3.26a and 3.26b. It is fairly obvious upon inspection that the estimate is reasonable for the data in figs. 3.26a and 3.26b, however the location for the intersection in fig. 3.25a is less obvious. Data similar to fig. 3.25a often fools the polynomial fitting procedure for estimating the intersection.

An offset is applied to the estimate from the derivative method so the estimate is closer to the rim. After both methods are used to estimate where the tip touches the

naphthalene, the more conservative estimate is used, i.e. the estimate closest to the center. Table 3.4 shows this process for the example data set.

Table 3.4: Final intersection estimate for data taken on November 2nd, 2015. Any data outside the range defined by the final estimate is not used.

Location	Estimate from Polynomial Method	Estimate from Derivative Method	Final Estimate
left	0.23 mm	0.32 mm	0.32 mm
right	19.83 mm	19.86 mm	19.83 mm

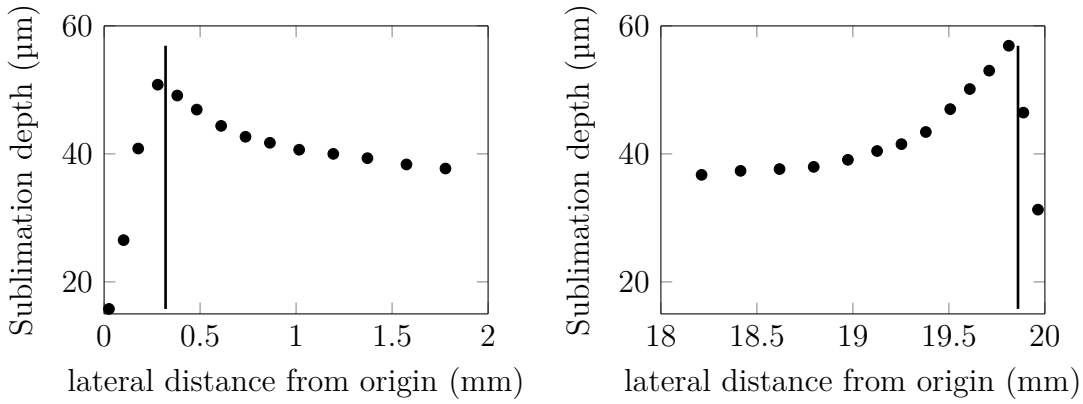

(a) Estimate of intersection using derivatives for left side of data

(b) Estimate of intersection using derivatives of intersection for right side of data

Figure 3.25: Estimate of intersection using derivatives for data taken on November 2nd, 2015. The filled circles are sublimed naphthalene depth measurements and the black line is the estimate of the location of the intersection.

3.5.2 Data Averaging

The final analysis is done on averaged data. A cubic smoothing spline is chosen to find the representative average for a given data set. The splines are constructed according

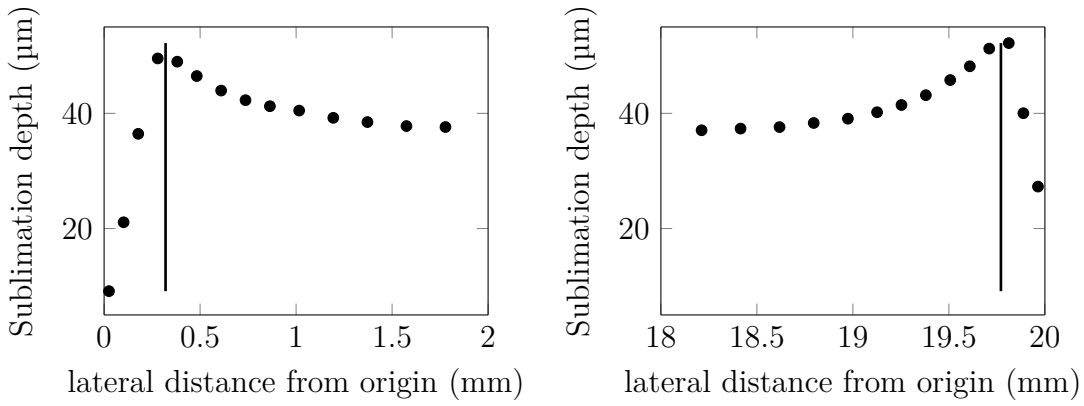

(a) Estimate of intersection using derivatives of intersection for left side of data

(b) Estimate of intersection using derivatives of intersection for right side of data

Figure 3.26: Estimate of intersection using derivatives for data taken on November 2nd, 2015. The filled circles are sublimed naphthalene depth measurements and the black line is the estimate of the location of the intersection. The sublimed naphthalene data presented are for a different streamwise location than the other figures showing data in this section.

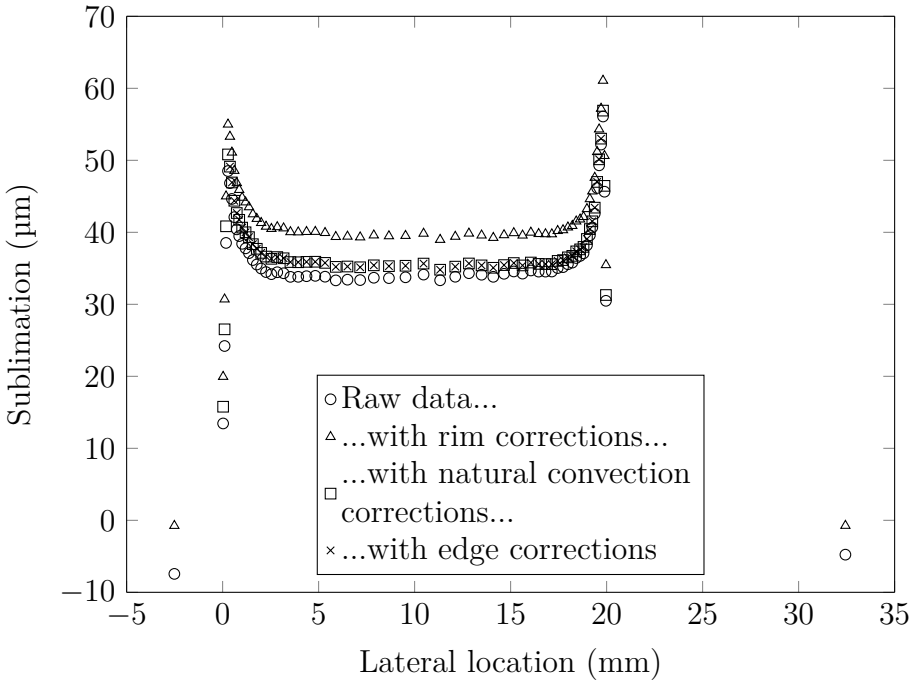

Figure 3.27: Cumulative effect of successive corrections on raw sublimed naphthalene data with data taken on November 2nd, 2015

to Reinsch (1967). The estimate of the smoothing spline is found by minimizing

$$p_{css}\sum_{i=1}^{N}\left(\frac{g_p\left(t_i\right)-y_i}{\sigma_i}\right)^2+\int_0^1\left(\frac{d^2g_p}{dt^2}\right)^2dt, \tag{3.35}$$

where t_i is a normalized independent variable such that $0 \leq t_1 < ... < t_i < ... < t_N \leq 1$ and σ_i is the standard deviation associated with y_i. The smoothing parameter, p_{css}, adjusts the fit to favor an interpolating spline or a linear least squares fit. As $p_{css} \to 0$, the term in the integral of eq. (3.35) is favored, minimizing the curvature of the smoothing spline function and approaching a linear least squares fit. However, as $p_{css} \to \infty$, the smoothing spline approaches an interpolating spline where the smoothing spline goes through every point.

Reinsch (1967) showed that for eq. (3.35), the optimal function is the cubic smoothing spline

$$g\left(t_i\right)=a_i+b_i\left(t-t_i\right)+c_i\left(t-t_i\right)^2+d_i\left(t-t_i\right)^3, \quad t_i \leq t < t_{i+1}, \tag{3.36}$$

with coefficients given by

$$c_1=c_N=0, \qquad d_i=\frac{c_{i+1}-c_i}{3h_i}, \qquad i=1,...,N-1, \tag{3.37a}$$

$$b_i=\frac{a_{i+1}-a_i}{h_i}-c_ih_i-d_ih_i^2, \qquad i=1,...,N-1, \tag{3.37b}$$

$$Tc=Q^Ta, \tag{3.37c}$$

$$Qc=p_{css}W^{-2}\left(y-a\right), \tag{3.37d}$$

The values of d_N and b_N are only used for extrapolation and are set to d_{N-1} and b_{N-1}

respectively. The following definitions are used,

$$h_i = t_{i+1} - t_i, \qquad c = (c_2, ..., c_{N-1})^T,$$
$$y = (y_1, ..., y_N)^T, \qquad a = (a_1, ..., a_N)^T,$$
$$W = \text{diag}\,(\sigma_1, ..., \sigma_N).$$

The matrices T and Q are defined by

$$T_{i,i} = \frac{2}{3}(h_{i-1} + h_i), \qquad T_{i,i+1} = T_{i+1,i} = \frac{h_i}{3}$$
$$Q^T_{i,i} = \frac{1}{h_i}, \qquad Q^T_{i,i+1} = -\frac{1}{h_i} - \frac{1}{h_{i+1}}, \qquad Q^T_{i,i+2} = \frac{1}{h_{i+1}}.$$

The matrix T is $(N-2) \times (N-2)$, positive definite and tridiagonal, and Q is a $N \times (N-2)$ tridiagonal matrix.

Craven and Wahba (1978) provide a framework for estimating the smoothing parameter, p_{css}, using generalized cross-validation. Craven and Wahba (1978) extended "ordinary" cross validation to non-symmetric datasets by rotating the observed data in Euclidean n-space so the problem is symmetric. The generalized cross-validation function to be minimized is

$$V(p) = N\frac{||(I-A)\,y||^2}{[\text{Tr}\,(I-A)]^2} \tag{3.38}$$

where A, called the influence matrix by Craven and Wahba (1978) (sometimes referred to as the hat matrix), is defined as

$$Ay = g(t_i). \tag{3.39}$$

Note that the term $||(I-A)\,y||^2$ is the residual sum of squares by definition. For

smaller datasets, "ordinary" cross-validation is used, as eq. (3.39) is only asymptotically correct. Wahba (1990, ch. 4) suggests the generalized cross-validation method is reliable for N larger than about 30. For these smaller sample populations, the function to be minimized is (James et al. 2013, pg. 279)

$$V(p) = \sum_{i=1}^{N} \left[\frac{y_i - g_p(t_i)}{1 - A_{ii}} \right]^2. \tag{3.40}$$

For data sets where the weights, σ_i, are not unity, Hutchinson and De Hoog (1985) show how to calculate the weighted influence matrix,

$$I - A = W^2 Q \left(Q^T W^2 Q + p_{css} T \right)^{-1} Q^T, \tag{3.41}$$

and the generalized cross-validation function to be minimized is

$$V(p) = N \frac{||W^{-1}(I - A)\, y||^2}{[\mathrm{Tr}\,(I - A)]^2}. \tag{3.42}$$

The denominator is equivalent to

$$\mathrm{Tr}\,(I - A) = N - 2 - p_{css} \mathrm{Tr} \left[T \left(Q^T W^2 Q + p_{css} T \right)^{-1} \right], \tag{3.43}$$

which should allow improvements in the calculation speed of the trace.

Wahba (1983) also described how to estimate the the statistical properties of the data and the confidence intervals of the smoothing spline when the smoothing parameter has been estimated using the generalized cross-validation method. The variance of the data is estimated in an analogous way as linear least square fits. The estimated variance is

$$\hat{\sigma}^2 = \frac{||(I - A)\, y||^2}{\mathrm{Tr}\,(I - A)}, \tag{3.44}$$

where $||(I - A)\, y||^2$ is again the residual sum of squares and $\mathrm{Tr}\,(I - A)$ is equivalent to the degrees of freedom for the error. The recommended 95 % confidence interval is

$$g\,(t_i) \pm 1.96\hat{\sigma}\sqrt{A_{i,i}}. \tag{3.45}$$

Not only are the smoothing splines used to average various experimental data sets, but eqs. (3.41) and (3.45) are used to estimate the random uncertainty of the experimental measurements. The numerical code developed for using eqs. (3.35) to (3.45) with MATLAB is posted at the MathWorks file exchange with the function name `csapsGCV()` under the author's name.

3.5.3 Mass Stanton Number Calculation

Rearranging eq. (1.8) gives the mass transfer coefficient

$$h_m \equiv \frac{\dot{m}''}{C_w - C_\infty}, \tag{3.46}$$

where $\dot{m}''$ is estimated by dividing the local mass subliming (after all the corrections outlined in section 3.5.1 are applied) by the total time the aluminum mass transfer plate is in the wind tunnel,

$$\dot{m}'' = \frac{\rho_{n,s}\delta_s}{\tau}. \tag{3.47}$$

The mass concentrations are equivalent to the ratios of the partial density to the mixture density. Assuming the pressure is constant through the boundary layer and equal to the freestream pressure, P_∞, the mass fraction of the naphthalene at the wall

is the ratio of the density of naphthalene to the mixture density at the wall, or,

$$\begin{aligned} C_w &= \frac{\rho_{n,g}}{\rho_a + \rho_{n,g}} \\ &= \frac{P_{n,sat}\mathcal{M}_n}{(P_\infty - P_{n,sat})\,\mathcal{M}_a + P_{n,sat}\mathcal{M}_n} \\ &= \frac{\mathcal{M}_n}{\mathcal{M}_a}\frac{P_{n,sat}}{P_\infty}\frac{1}{1 + P_{n,sat}/P_\infty\,(\mathcal{M}_n/\mathcal{M}_a - 1)}. \end{aligned} \tag{3.48}$$

Setting C_∞ to 0, and combining eqs. (3.46) to (3.48), the mass transfer coefficient is

$$h_m = \frac{\rho_{n,s}\delta_s}{\tau}\frac{\mathcal{M}_a}{\mathcal{M}_n}\frac{P_\infty}{P_{n,sat}}\left[1 + \frac{P_{n,sat}}{P_\infty}\left(\frac{\mathcal{M}_n}{\mathcal{M}_a} - 1\right)\right]. \tag{3.49}$$

The value of the expression in the brackets is very close to one. For a saturation pressure of 11 Pa, the value of the expression in the brackets is 1.0004, showing the difference from using the air density or mixture density at the surface is insignificant.

Using the ideal gas law as described in section 3.4.1 and freestream velocity measurements described in section 3.3.2, and the calculation of the local mass transfer coefficient in eq. (3.49), the St can be calculated

$$St = \frac{h_m}{\rho_w \overline{U}_\infty}. \tag{3.50}$$

Combining eqs. (3.49) and (3.50) with the ideal gas law gives,

$$St = \frac{1}{\rho_{n,g}\overline{U}_\infty}\frac{\rho_{n,s}\delta_s}{\tau_t}. \tag{3.51}$$

Chapter 4

Turbulent Flow Over a Flat Plate

Boundary layer measurements are carried out with a hotwire anemometer for several freestream velocities at various streamwise locations. The location of the probe and local shear stress are estimated using a modified Clauser technique (discussed in section 4.1.1). The boundary layer profile, streamwise velocity fluctuation profile, and various profile parameters are reported. Overall, the boundary layer is found to be turbulent but not fully mature.

Mass transfer results showing the change in mass flux near a lateral edge of a finite width strip for a variety of freestream velocities and widths are presented. Based on the results of chapter 2, lateral scaling parameters are chosen and shown to be useful for turbulent boundary layers. It is found that the variation of the St_m near the lateral edge is described by a different power law than for laminar flow. General correlations are presented for strips of semi-infinite and finite widths.

Note that throughout the chapter, the subscript m is dropped from the mass Stanton number for convenience, but all the results are for mass transfer.

4.1 Flow Conditions

4.1.1 Measurement Process

Before any velocity measurements are made, pressure and temperature measurements in the freestream are used to estimate the dynamic viscosity, density, and the temperature correction from eq. (3.14).

The first measurement is approximately 100 mm above the tunnel surface. The probe moves downward in predefined increments until the velocity is less than 95 % of the freestream value. Then, the probe moves downward a distance equivalent to the minimum of 0.35 mm or 10 % of the estimated current height. The hotwire voltage is sampled at 50 000 Hz for one second for each reading. After the probe enters the boundary layer, the total estimated perpendicular distance between the last 15 data points and the Van Driest profile (eq. (4.3)), u^+_{VD} and y^+_{VD}, is minimized using the function `scipy.optimize.minimize()` with bounds and a truncated Newton algorithm (Jones et al. 2001–2017). The estimated perpendicular distance minimized is,

$$D_p = \left\{ \sum_{k-N}^{k} \left[\left(y^+_{VD} - \hat{y}^+ \right)^2 + \left(u^+_{VD} - \hat{u}^+ \right)^2 \right] \right\}^{1/2}, \tag{4.1}$$

where the estimated friction velocity, $\hat{u}^+$, and the estimated height in wall normal coordinates, $\hat{y}^+$, are used to estimate the Van Driest values calculated from integrating eq. (4.3). In other words, $\hat{u}^+$ is used to estimate y^+_{VD} and $\hat{y}^+$ is used to estimate u^+_{VD} in eq. (4.1). The actual parameters that `scipy.optimize.minimize()` uses to minimize eq. (4.1) are the local shear stress and a small offset to the height of the hotwire. The probe continues to traverse the boundary layer until $\hat{y}^+$ is less than eight and the whole measurement process is repeated at several streamwise locations.

After the measurements are complete, the data are analyzed and the final estimates for the position and local shear stress determined. The process is similar to minimizing the perpendicular distance discussed above, but in this case, most of the data within the boundary layer are used to minimize a modified perpendicular distance between the data and the Van Driest profile. The modified perpendicular distance is

$$D_{p,m} = \left\{ \sum \left[\left(2.44 \ln \left(\frac{y^+_{VD}}{\hat{y}^+} \right) \right)^2 + \left(u^+_{VD} - \hat{u}^+ \right)^2 \right] \right\}^{1/2}. \tag{4.2}$$

The modified perpendicular distance is constructed so the y^+ and u^+ errors are approximately the same magnitude throughout the boundary layer. The function `fminsearch()` (The MathWorks, Inc. 2014) is used to minimize eq. (4.2).

4.1.2 Boundary Layer Profile

Velocity Profile

Van Driest (1956) outlines a simple way, shown in eq. (4.3), to blend the linear viscous sublayer with the logarithmic law of the wall,

$$\frac{du^+}{dy^+} = \frac{2}{1 + \sqrt{1 + 4\kappa^2 y^{+2} \left[1 - \exp\left(-y^+ / A^+ \right) \right]^2}}, \tag{4.3}$$

where κ is the von Kármán constant. The values of κ and A^+ used are 0.41 and 25 respectively, as recommended by Kays et al. (2005, pg. 197).

Figure 4.1 shows the boundary layer measurements follow the expected velocity profile very well in the viscous sublayer and logarithmic region, but not in the wake region. Generally the velocity in the wake region is $u^+ \approx 2.3$ (Kays et al. 2005, pg. 190) above the law of the wall, however, for the largest freestream velocity the

difference is only about 0.4. The acceleration parameters shown in table 4.3 discount acceleration in the freestream as the reason for the depressed wake values, so the boundary layer profiles are most likely turbulent, but not fully mature.

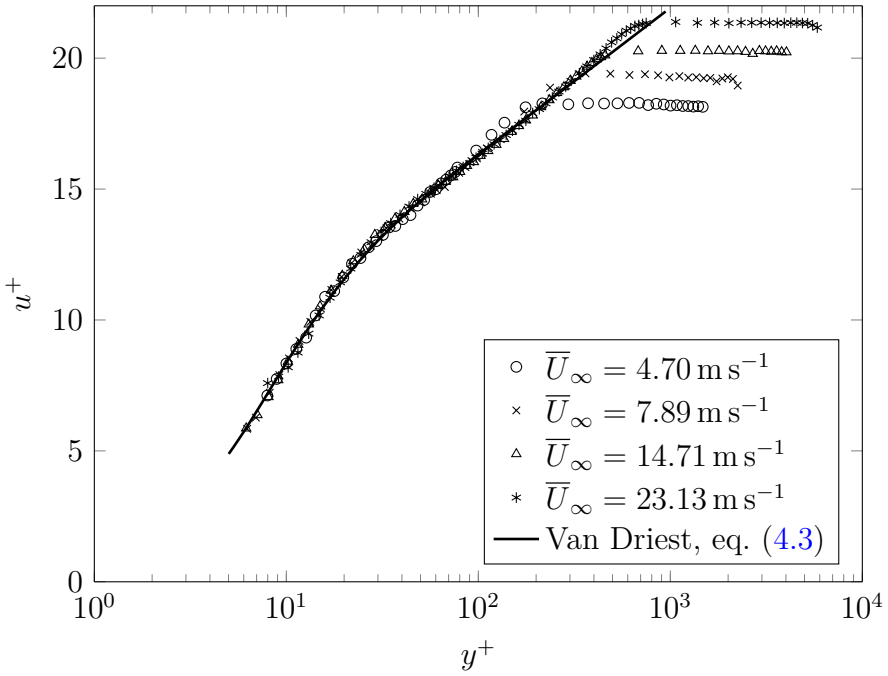

Figure 4.1: Comparison of estimated boundary layer profile and Van Driest velocity profile

Streamwise Velocity Fluctuations

Figure 4.2 shows the streamwise velocity fluctuations in wall coordinates. The profile is generally correct, but the maximum value is too low by about 10 %–25 %. Several sources, presented in table 4.1, report values for the maximum streamwise fluctuations in wall coordinates of about 2.75 at $y^+ = 14$. Figure 4.2 shows the present boundary layer has a maximum u'^+ of 2–2.5 at y^+ of 13–15.

The peak value for u'^+ is shown by DeGraaff and Eaton (2000) to depend on Re_τ, with the peak value increasing with increasing values of Re_τ. The trends shown in fig. 4.2 are opposite of the expected trends and is likely due to the transitional nature

of the turbulent boundary layer at the lowest.

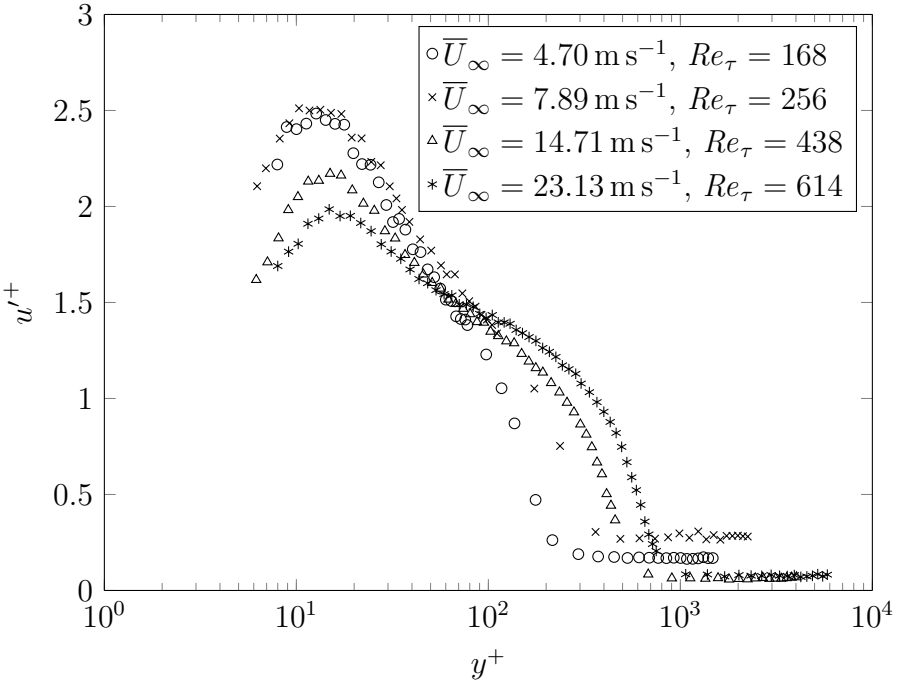

Figure 4.2: Streamwise turbulent fluctuation velocity in wall coordinates.

Table 4.1: Value and location of u'^+ from various sources

Reference	u'^+_{max}	y^+	Flow Condition	Method
DeGraaff and Eaton (2000)	2.76	14	$Re_{\delta_2} = 1430$	LDA
Hoyas and Jiménez (2006)	2.66	15	$Re_\tau = 185$	DNS
	2.76	15	$Re_\tau = 544$	DNS
Mochizuki and Nieuwstadt (1996)	2.71	15	$Re_{\delta_2} = 300$–$20\,920$	Review

Outer Scaling

Figure 4.3 shows the velocity defect from Clauser (1956). As mentioned by Tennekes and Lumley (1972, pg. 186) and DeGraaff and Eaton (2000), the defect should match the law of the wall where it overlaps with the inner layer. This results in the expression

shown in eq. (4.4),

$$\frac{\overline{U}-\overline{U}_\infty}{u_\tau} = \frac{1}{\kappa}\ln\left(\frac{y}{\delta_2}\right) + C \tag{4.4}$$

$$= \frac{1}{\kappa}\ln\left(y^+\right) + 5.0 + \frac{1}{\kappa}\ln\left(\frac{\nu}{\delta_2 u_\tau}\right) + C - 5.0 \tag{4.5}$$

where the constant C, equivalent to the expression in eq. (4.6), is chosen so the defect profile matches the logarithmic law of the wall. Noting that the law of the wall subtracts from both sides of eq. (4.5), the constant, C, in eq. (4.4) is

$$C = -\frac{1}{\kappa}\ln\left(\frac{\nu}{\delta_2 u_\tau}\right) - \frac{\overline{U}_\infty}{u_\tau} + 5.0. \tag{4.6}$$

Using eq. (4.6), fig. 4.3 shows the measured velocity defect matches the expected profile. As the outer scaling is a function of the largest eddies, the measured flow in the outer part of the boundary layer indicates the largest turbulent scales conform to the expected characteristics presented in eq. (4.4).

4.1.3 Boundary Layer Parameters

Fitted Parameters

As mentioned in section 4.1.1, various parameters are estimated by matching the velocity profile to eq. (4.3). One of the parameters, the corrected distance of the hotwire anemometer from the wall, is not strictly a flow parameter and is not discussed; however, the other parameter, the wall shear stress, is presented in two forms in table 4.2. The friction velocity, u_τ, and the skin friction coefficient, c_f, both directly depend on the local shear stress.

The other two fitted parameters, the location of the virtual origin and inverse of the power-law fit for the velocity throughout the boundary layer, are also shown in

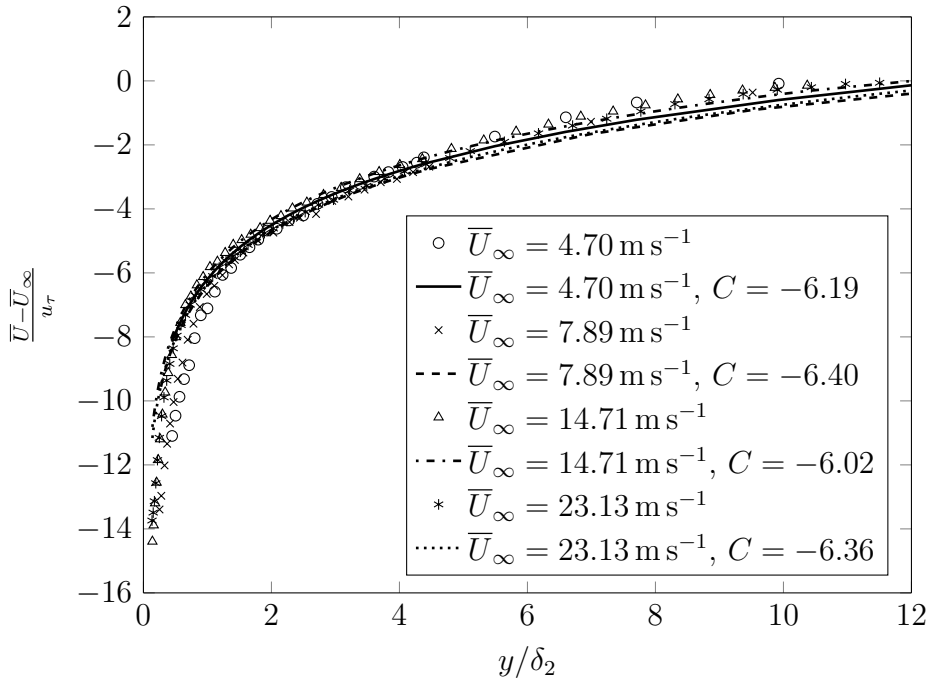

Figure 4.3: Velocity defect profile comparing measured velocity defect with eq. (4.4), where the constant, C, is calculated as shown in eq. (4.6)

table 4.2. The inverse of the exponent for a power law fit of the boundary layer, n, is found by minimizing the least squares of the velocity profile,

$$\frac{\overline{U}}{\overline{U}_\infty} = \left(\frac{y}{\delta_{99}}\right)^{1/n}, \tag{4.7}$$

and the measured velocity boundary layer. The upper 90 % of the boundary layer data are used to fit eq. (4.7).

Based on a power law fit of the boundary layer, Cebeci and Bradshaw (1984) argue that the virtual origin can be estimated by extending the fit of

$$\delta^{\frac{n+3}{n+1}} \propto x \tag{4.8}$$

to the streamwise location where δ equals zero. The parameter n is from the fit

Table 4.2: Boundary layer fitted parameters using Clauser technique, u_τ is the friction velocity, c_f is the skin friction coefficient, ξ is the unheated starting length, and n is the inverse of the exponent of a power-law fit of the upper 90 % of the boundary layer. Values are taken 67 mm upstream of the leading edge. The kinematic viscosity is between 16.3×10^{-6} m^2 s^{-1} and 16.5×10^{-6} m^2 s^{-1} for all measurements.

$\overline{U}_\infty$ (m s^{-1})	u_τ (m s^{-1})	c_f (-)	ξ (m)	n (-)
4.70	0.26	6.03×10^{-3}	-0.52	5.06
7.89	0.41	5.40×10^{-3}	-0.55	5.68
14.71	0.73	4.87×10^{-3}	-0.71	6.60
23.13	1.05	4.40×10^{-3}	-0.63	6.66

presented in eq. (4.7). Figure 4.4 shows the turbulent boundary layer virtual origin calculation. The virtual origin is the average of the values estimated using eq. (4.8) for the displacement and momentum thicknesses.

Integral and Profile Parameters

Table 4.3 shows some integral and profile parameters from the boundary layer measurements. In particular, the shape factor shows the boundary layer is turbulent but not fully mature. It can be shown when approximating the boundary layer profile with a power law fit, as in eq. (4.7), the shape factor is

$$H = \frac{n+2}{n}. \tag{4.9}$$

A common value for n in mature boundary layers is seven, resulting in a shape factor of approximately 1.29. The values of the largest freestream velocities in table 4.3 are fairly close to the expected value.

The acceleration parameter, K, is defined by

$$K = \frac{\nu}{\overline{U}_\infty^2} \frac{d\overline{U}_\infty}{dx}, \tag{4.10}$$

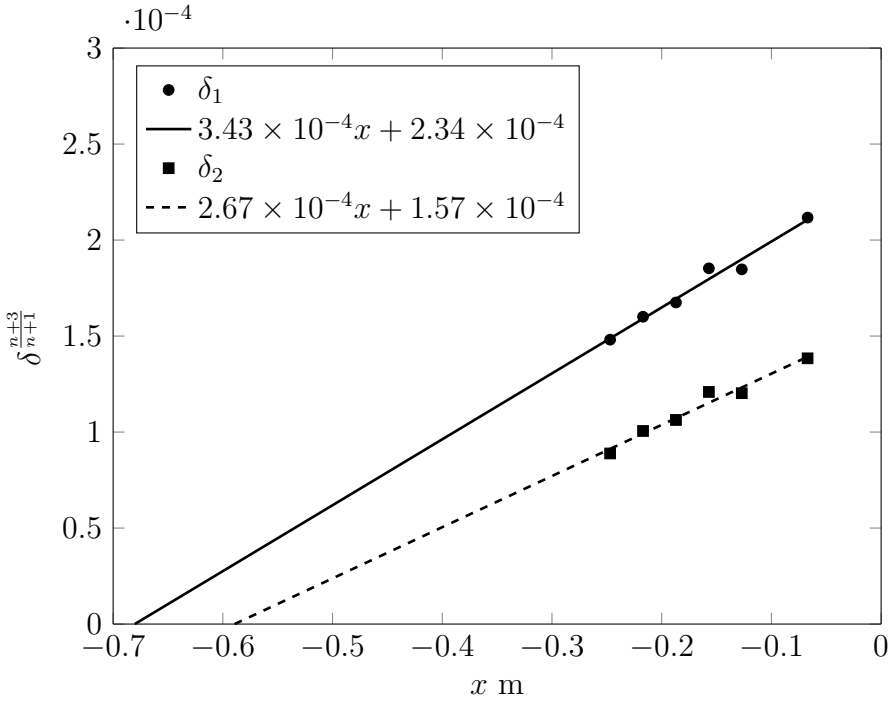

Figure 4.4: Turbulent virtual origin calculation for $\overline{U}_\infty = 23.13\,\mathrm{m\,s^{-1}}$

where the advective acceleration term, $d\overline{U}_\infty/dx$, is estimated with a linear fit of the freestream velocity. The estimated values of K from table 4.3 show the boundary layer is very close to a zero-pressure gradient condition. The negative values of K do not indicate an adverse pressure gradient, rather they are a consequence of the noise of the data. For example, the one standard deviation uncertainty of K from the fit alone, $\Delta_{slope}\nu/\overline{U}_\infty^2$, for the largest freestream velocity, is approximately 1.4×10^{-8} using eq. (3.9) to estimate Δ_{slope}. This uncertainty is larger than the value presented in table 4.3, indicating the flow is not accelerating to within measurement accuracy.

Based on the estimate of the virtual origin from eq. (4.8), the skin friction coefficient is compared to the $Re_{x'}$ in fig. 4.5. The values are consistently larger than expected, but vary with the $Re_{x'}$ according to a power with an exponent of approximately one-sixth. This is fairly close to the recommended one-seventh power law, $c_f = 0.027 Re_x^{-1/7}$, from (White 1991, pg. 430, eq. 6.70).

Table 4.3: Boundary layer profile parameters, Re_{δ_2} is the momentum thickness Reynolds number, Re_τ is the Reynolds number based on the friction velocity and δ_{99}, H is the shape factor, Tu is the freestream turbulence intensity, and K is the acceleration factor. Values are taken 67 mm upstream of the leading edge. The kinematic viscosity is between 16.3×10^{-6} m^2 s^{-1} and 16.5×10^{-6} m^2 s^{-1} for all measurements.

Re_{δ_2} (-)	Re_τ (-)	$\overline{U}_\infty$ (m s^{-1})	δ_2 (mm)	H (-)	Tu (%)	K (-)
3.23×10^2	1.68×10^2	4.70	1.86	1.65	0.93	1.02×10^{-7}
4.78×10^2	2.56×10^2	7.89	1.56	1.57	1.46	-1.29×10^{-8}
8.93×10^2	4.38×10^2	14.71	1.40	1.41	0.31	5.37×10^{-8}
1.27×10^3	6.14×10^2	23.13	1.31	1.40	0.36	-8.17×10^{-9}

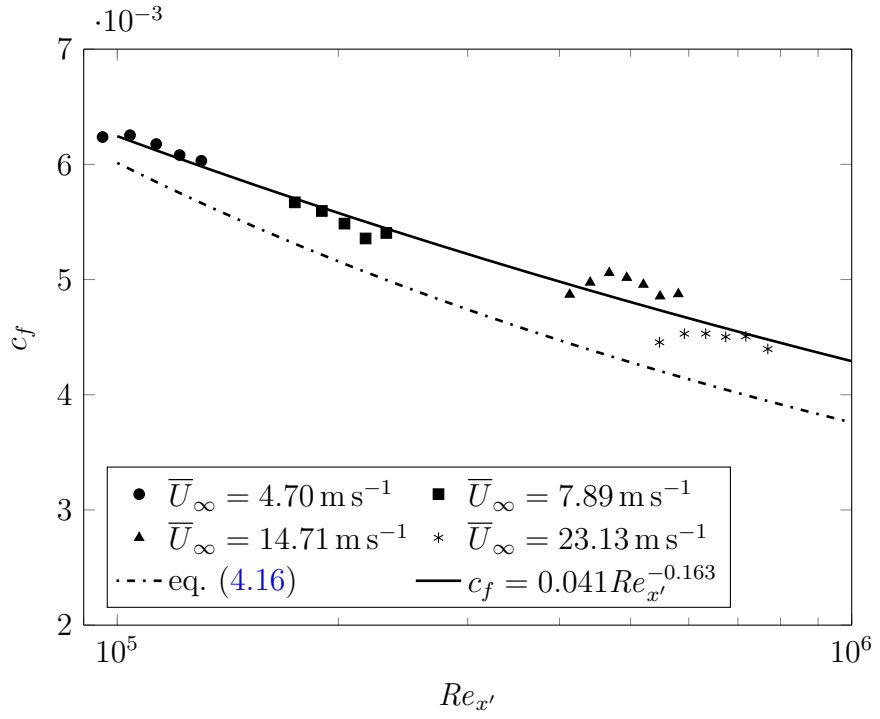

Figure 4.5: Estimates of the experimental skin friction coefficients compared to eq. (4.16) and best fits of the data

4.2 Mass Transfer Results

4.2.1 Data Averaging

The final data used for fitting and presentation of the results in sections 4.2.2 to 4.2.5 are averaged data from several repeat experiments. The overall process involves finding an average centerline St, finding average lateral values of the St normalized by the (not-averaged) centerline St, and then multiplying the two for averaged values of the local St. For each step of the data averaging process, the random experimental uncertainty is estimated and then recombined at the end for a representative random uncertainty for each set of averaged data.

Centerline St

Using the procedure for cubic smoothing splines outlined in section 3.5.2, the centerline measurements for the St are combined for each permutation of width and freestream velocity tested. To more accurately average the mass transfer near the leading edge, the logarithm of the Re_x is used in place of just the Re. As the cubic smoothing spline by definition is linear at the extreme ends of the range used, it is more accurate to assume the St is linear with $\log(Re_x)$ than Re_x near the leading edge. Figures 4.6, 4.7, E.49 and E.50 show the centerline averaging results for $5\,\mathrm{m\,s^{-1}}$, figs. E.51 to E.54 show the centerline averaging results for $10\,\mathrm{m\,s^{-1}}$, and figs. 4.8, 4.9, E.55 and E.56 show the centerline averaging results for $20\,\mathrm{m\,s^{-1}}$.

The estimated random errors associated with the centerline St calculation from eq. (3.44) for the various permutations of widths and freestream velocities are shown in table 4.4. The errors reported in table 4.4 are a ratio of the square root of the variance given by eq. (3.44) and the average centerline St for a given width and

freestream velocity.

Table 4.4: Estimated random uncertainty from turbulent experiments using eq. (3.44) for centerline St.

Average Freestream	Estimated Percent Error (columns labeled by width)			
Velocity ($\mathrm{m\,s^{-1}}$)	19.77 mm	9.77 mm	5.00 mm	2.48 mm
5.24	5.89	2.82	2.86	5.65
9.86	4.98	5.00	2.21	2.81
20.72	3.56	2.22	2.38	1.93

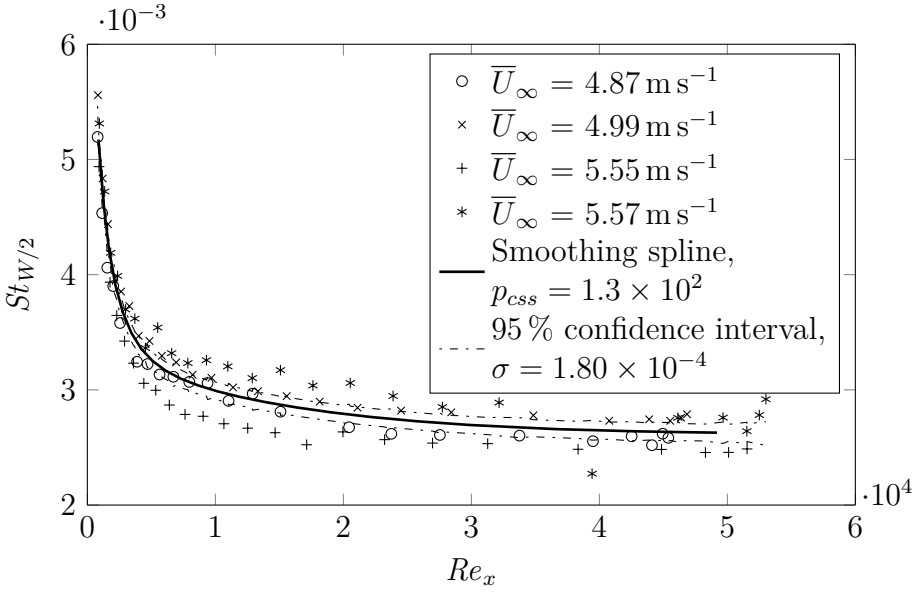

Figure 4.6: Centerline St for $5\,\mathrm{m\,s^{-1}}$ freestream velocity and 2.48 mm width strip showing raw data and cubic smoothing spline estimate.

Lateral St

The lateral averaging of the experimental data is a two step process. First, the uncertainty of each data set at each streamwise location is estimated by averaging the data across the centerline with cubic smoothing splines. Mirroring the data across the centerline and averaging and calculating the uncertainty according to eq. (3.44)

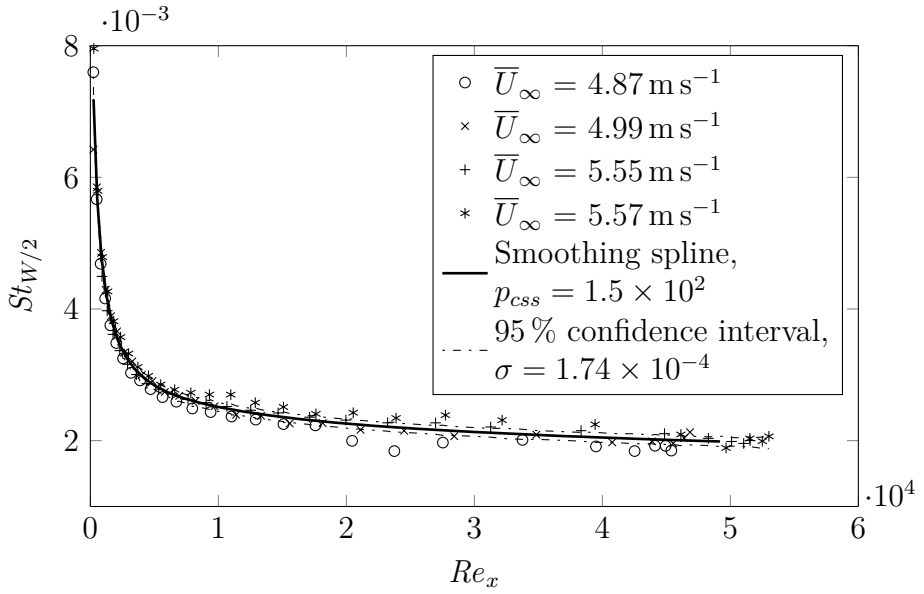

Figure 4.7: Centerline St for $5\,\mathrm{m\,s^{-1}}$ freestream velocity and 19.77 mm width strip showing raw data and cubic smoothing spline estimate.

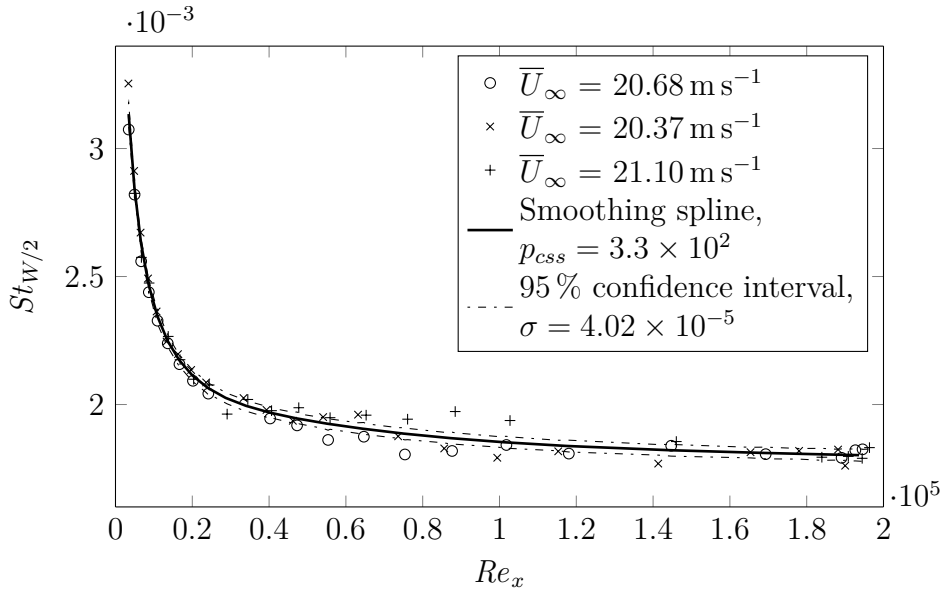

Figure 4.8: Centerline St for $20\,\mathrm{m\,s^{-1}}$ freestream velocity and 2.48 mm width strip showing raw data and cubic smoothing spline estimate.

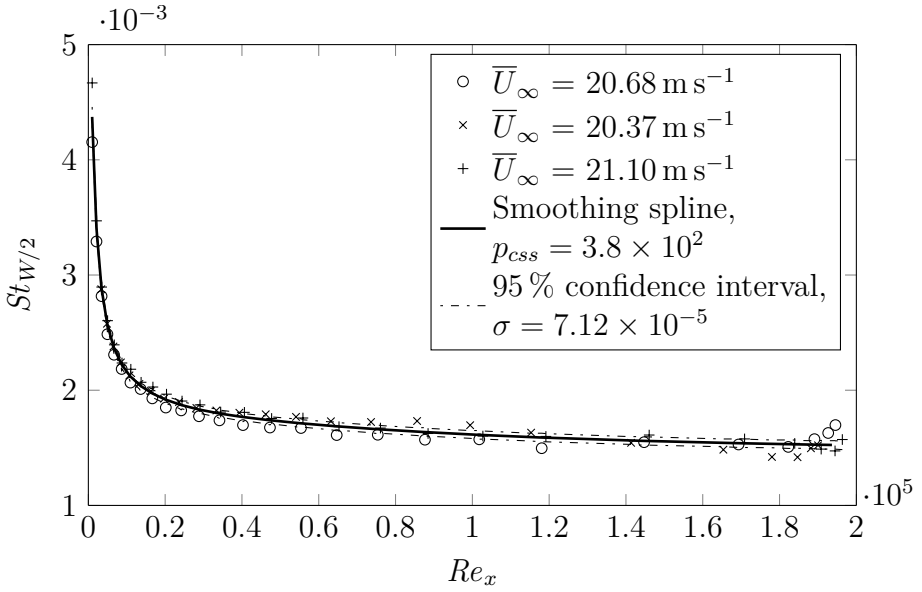

Figure 4.9: Centerline St for $20\,\mathrm{m\,s^{-1}}$ freestream velocity and 19.77 mm width strip showing raw data and cubic smoothing spline estimate.

gives an idea of how symmetric that particular data set is; a large variance, like the data denoted by asterisks in fig. 4.10, indicates the data are not symmetric, while a small variance, like the data denoted by the $\times$ symbols in fig. 4.10, indicates the data are symmetric.

After a variance is assigned to each streamwise location for each data set, the data are combined according to the freestream velocity and width of the rectangular strip at each streamwise location. Similar to the averaging for the centerline St, the cubic smoothing spline for lateral data is applied to the logarithm of z and the St normalized by the centerline St. The data are combined, as described by eq. (3.42), with weights specified by the estimated symmetry error. Examples of the lateral averaging are shown in figs. 4.10 to 4.13. Table 4.5 shows the estimated random error of the normalized St based on the weighted averaging of the lateral data using eq. (3.44).

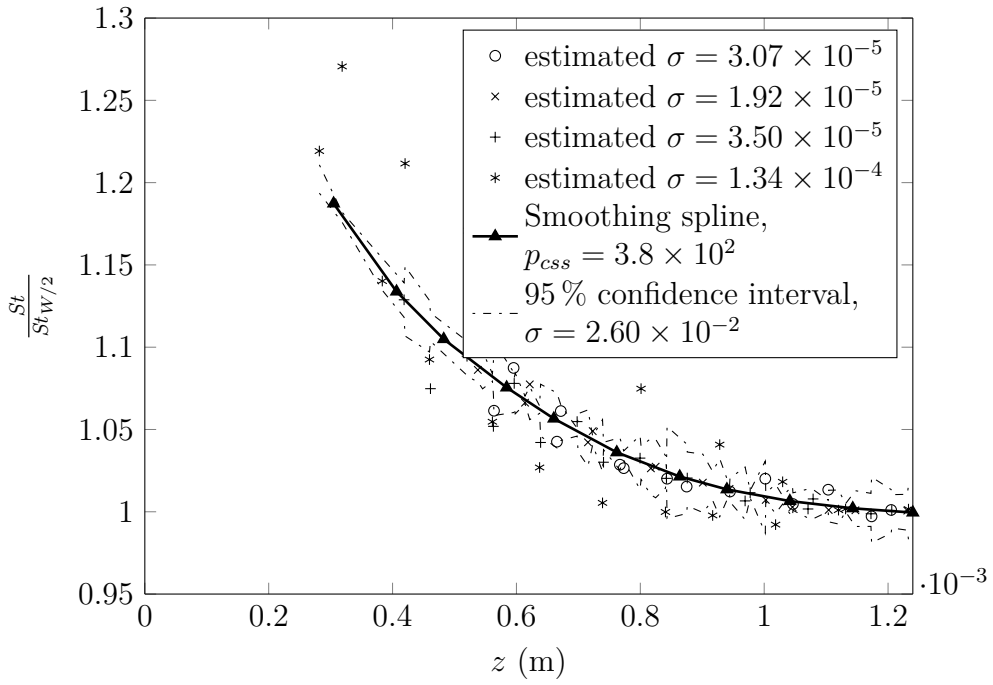

Figure 4.10: Lateral averaging for $5\,\mathrm{m\,s^{-1}}$ freestream velocity and 2.48 mm width strip at $x = 22.1\,\mathrm{mm}$

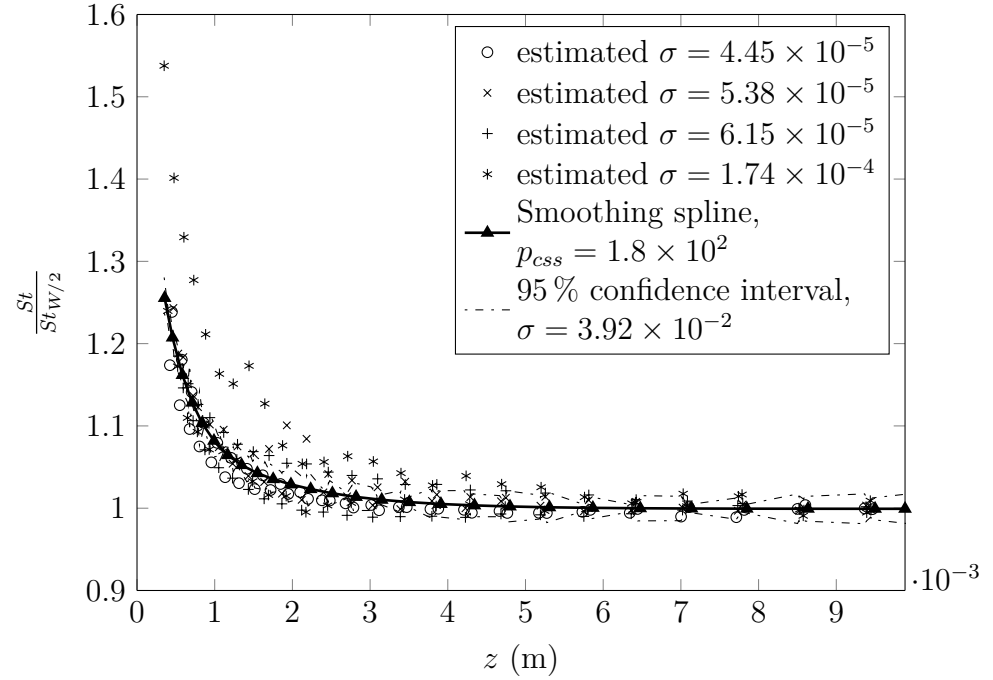

Figure 4.11: Lateral averaging for $5\,\mathrm{m\,s^{-1}}$ freestream velocity and 19.77 mm width strip at $x = 15.5\,\mathrm{mm}$

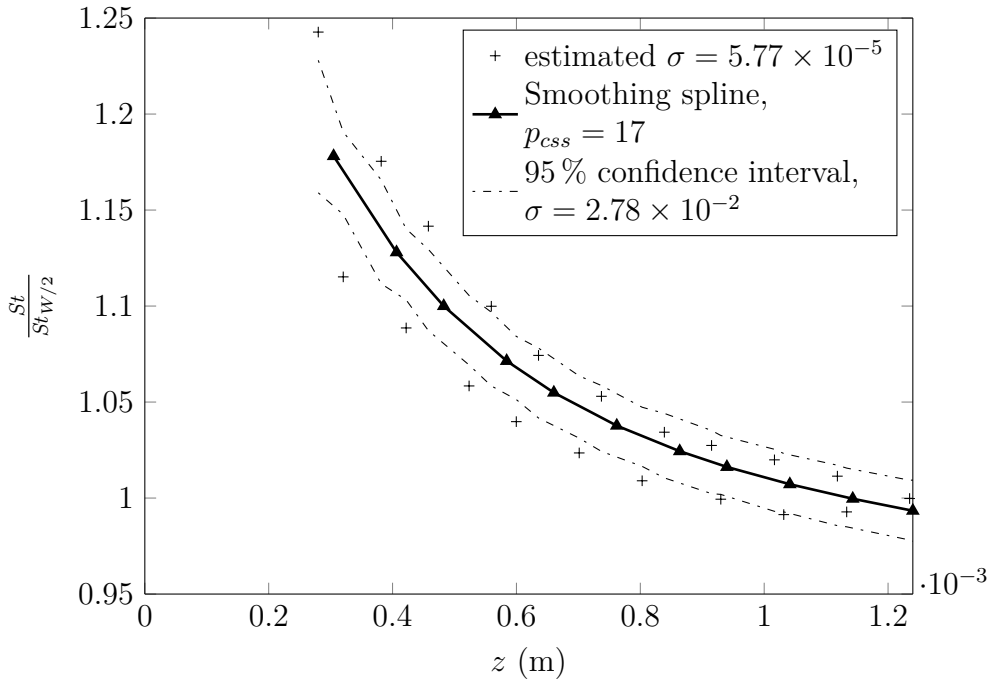

Figure 4.12: Lateral averaging for $20\,\mathrm{m\,s^{-1}}$ freestream velocity and 2.48 mm width strip at $x = 22.1\,\mathrm{mm}$

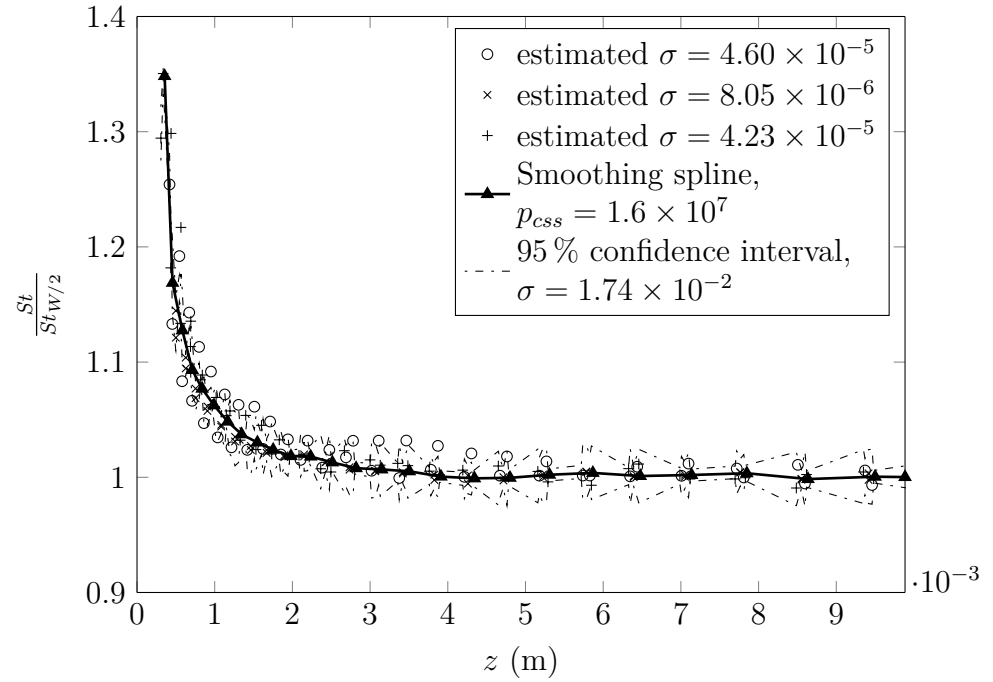

Figure 4.13: Lateral averaging for $20\,\mathrm{m\,s^{-1}}$ freestream velocity and 19.77 mm width strip at $x = 15.5\,\mathrm{mm}$

Table 4.5: Estimated random uncertainty of normalized St for turbulent data using eq. (3.44). The estimates are based on averaging multiple data sets over the centerline.

Average Freestream	Estimated Percent Error (columns labeled by width)			
Velocity ($\mathrm{m\,s^{-1}}$)	19.77 mm	9.77 mm	5.00 mm	2.48 mm
5.24	5.19	4.67	3.68	3.68
9.86	2.67	2.77	2.33	2.50
20.72	2.05	1.48	1.37	1.99

Total Random Experimental Error

After averaging all the data, as discussed above, the averaged St is calculated by multiplying the averaged centerline St and the laterally averaged ratio of the St and centerline St. Therefore, the uncertainty represented in both table 4.4 and table 4.5 needs to be taken into account. Since the St is two quantities multiplied together, the total uncertainty is (Moffat 1988)

$$\frac{\hat{\sigma}_{St}^2}{St^2} = \left(\frac{\hat{\sigma}_{St_c}}{St_c}\right)^2 + \left(\frac{\hat{\sigma}_{St/St_c}}{St/St_c}\right)^2, \tag{4.11}$$

where $\hat{\sigma}^2$ denotes the variance, St_c is the averaged centerline St, and St/St_c is the laterally averaged normalized St. The overall random errors from the experiments for each set of widths and freestream velocities are shown in table 4.6. Each variable, St_c and St/St_c, is assumed to be independent of the other.

4.2.2 Results

Figures 4.14 to 4.16 show examples of the averaged St number at several streamwise locations for all the permutations of freestream velocity and subliming widths tested. For the widest strips shown in figs. 4.14d, 4.15d and 4.16d, it is clear the effect of the lateral edge only extends about 3 mm to 5 mm and does not change significantly

Table 4.6: Total estimated random uncertainty from the turbulent experiments from eq. (4.11) using data presented in tables 4.4 and 4.5.

Average Freestream	Estimated Percent Error (columns labeled by width)			
Velocity ($\mathrm{m\,s^{-1}}$)	19.77 mm	9.77 mm	5.00 mm	2.48 mm
5.24	7.85	5.46	4.66	6.74
9.86	5.65	5.72	3.21	3.76
20.72	4.11	2.67	2.75	2.77

in the streamwise direction for most of the length of the strip. The smallest widths, shown in figs. 4.14a, 4.15a and 4.16a, illustrate the the limits of the lateral measurements. Figure 3.23 shows how the corner of the aluminum mold prohibits lateral measurements close to the lateral edge and figs. 4.14a, 4.15a and 4.16a clearly show the minimum measurement distance is about 0.3 mm.

Figure 4.17 shows the diffusion thickness for all the freestream velocities studied. While the local diffusion thickness varies with the local mass flux, the experimentally measured diffusion thickness for a subliming plate of infinite lateral width is the length parameter used to normalize the lateral position and width of the strip. As the diffusion thickness is equivalent to x/Sh_x, it changes very slowly in the streamwise direction, as shown in fig. 4.17.

4.2.3 Centerline Experimental Data

The centerline St for the two widest strips are compared to the published correlations, eqs. (4.12) to (4.15) and presented in figs. 4.18 to 4.20. Two correlations based on the logarithmic law of the wall and two correlations that simplify the momentum and thermal sublayer effects with a Pr power law are shown. Eckert and Drake Jr (1959)

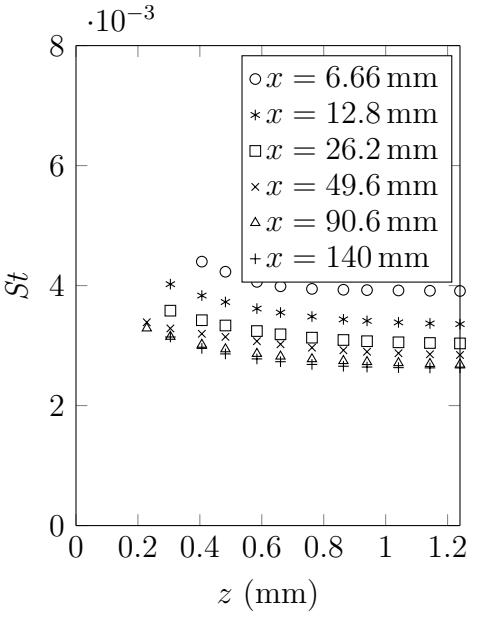

(a) Averaged St for $W = 2.48\,\mathrm{mm}$

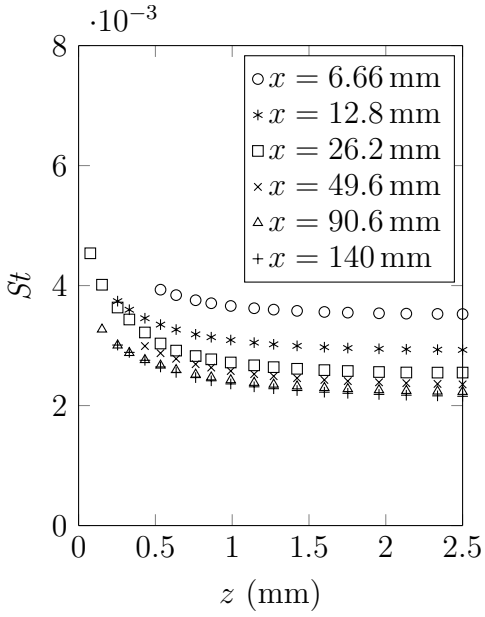

(b) Averaged St for $W = 5.00\,\mathrm{mm}$

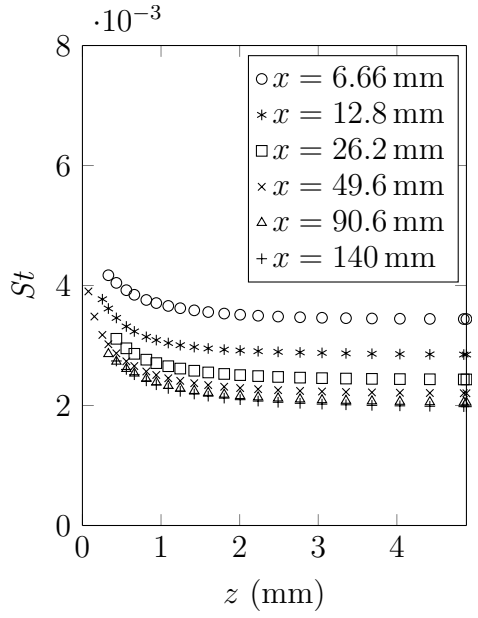

(c) Averaged St for $W = 9.77\,\mathrm{mm}$

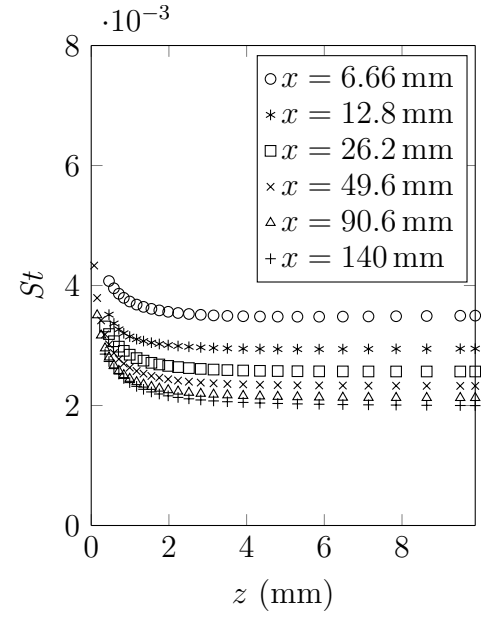

(d) Averaged St for $W = 19.8\,\mathrm{mm}$

Figure 4.14: Averaged St for $\overline{U}_\infty = 5.24\,\mathrm{m\,s^{-1}}$ for various widths

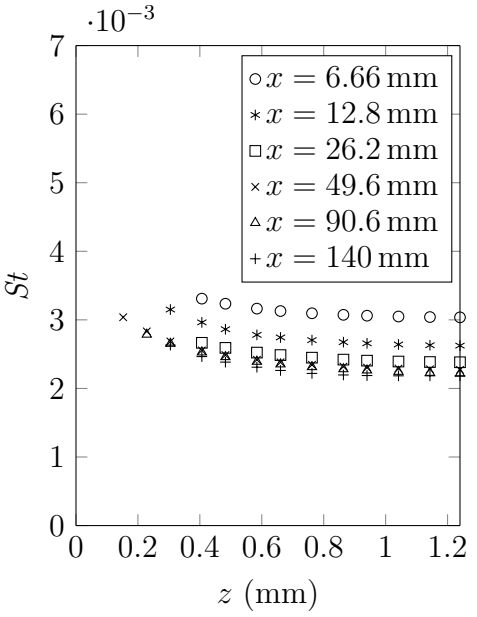

(a) Averaged St for $W = 2.48\,\text{mm}$

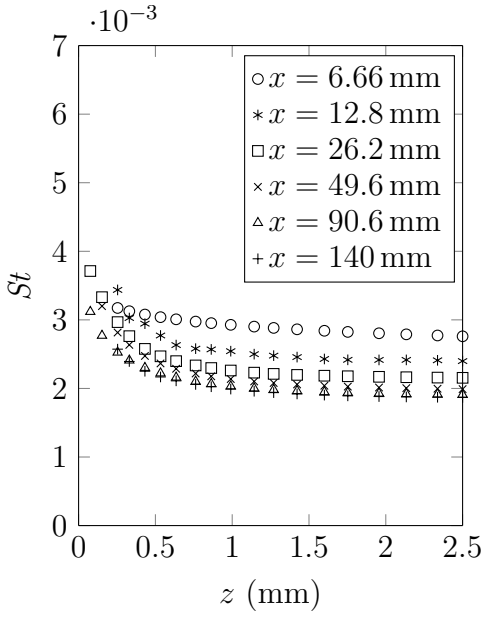

(b) Averaged St for $W = 5.00\,\text{mm}$

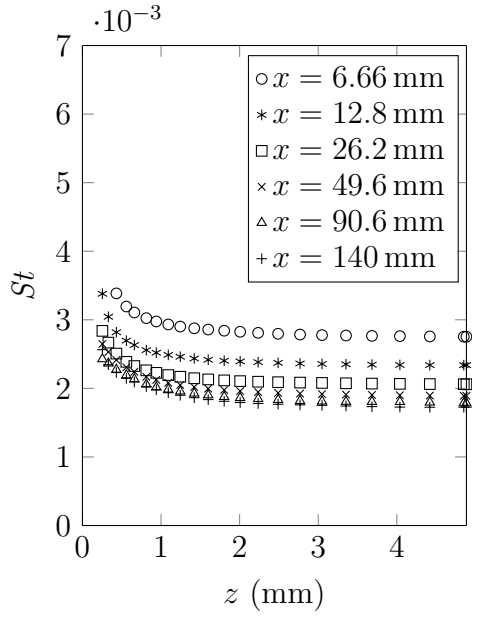

(c) Averaged St for $W = 9.77\,\text{mm}$

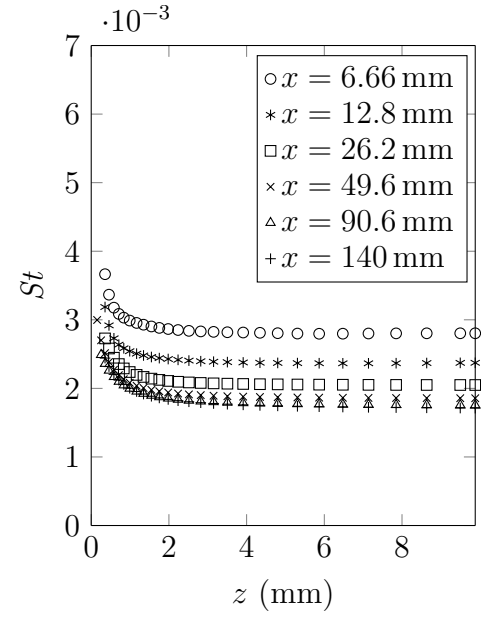

(d) Averaged St for $W = 19.8\,\text{mm}$

Figure 4.15: Averaged St for $\overline{U}_\infty = 9.86\,\text{m}\,\text{s}^{-1}$ for various widths

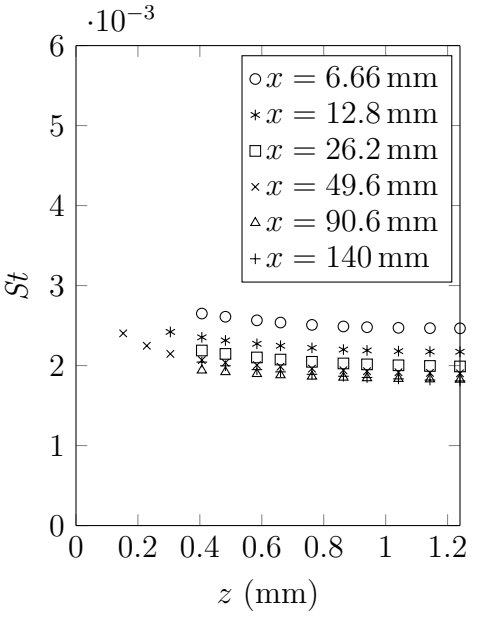

(a) Averaged St for $W = 2.48\,\mathrm{mm}$

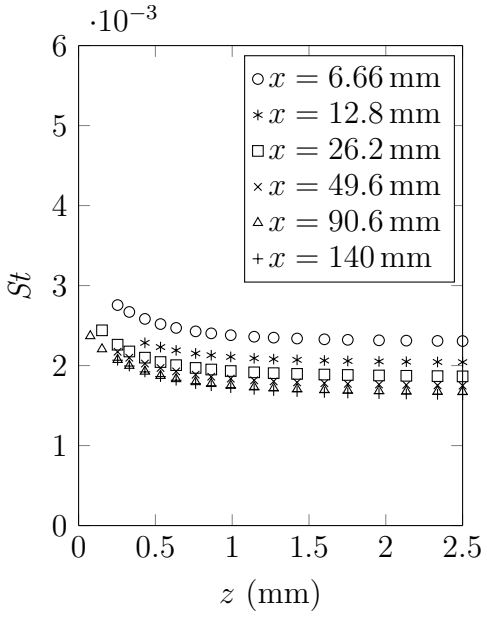

(b) Averaged St for $W = 5.00\,\mathrm{mm}$

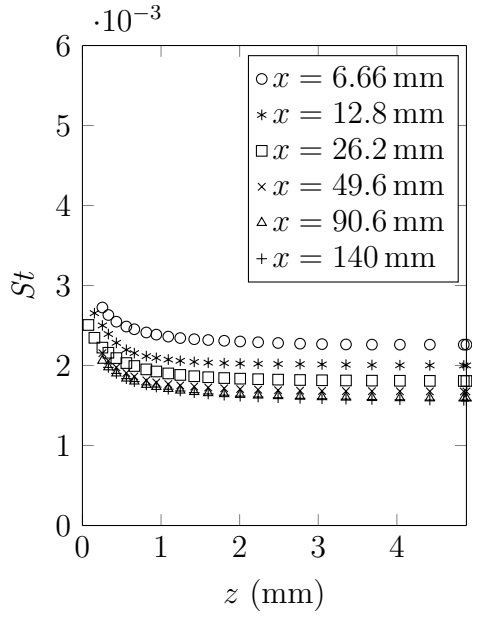

(c) Averaged St for $W = 9.77\,\mathrm{mm}$

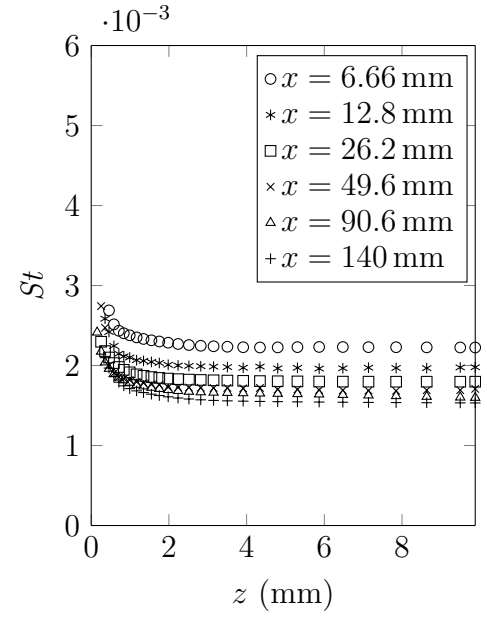

(d) Averaged St for $W = 19.8\,\mathrm{mm}$

Figure 4.16: Averaged St for $\overline{U}_\infty = 20.7\,\mathrm{m\,s^{-1}}$ for various widths

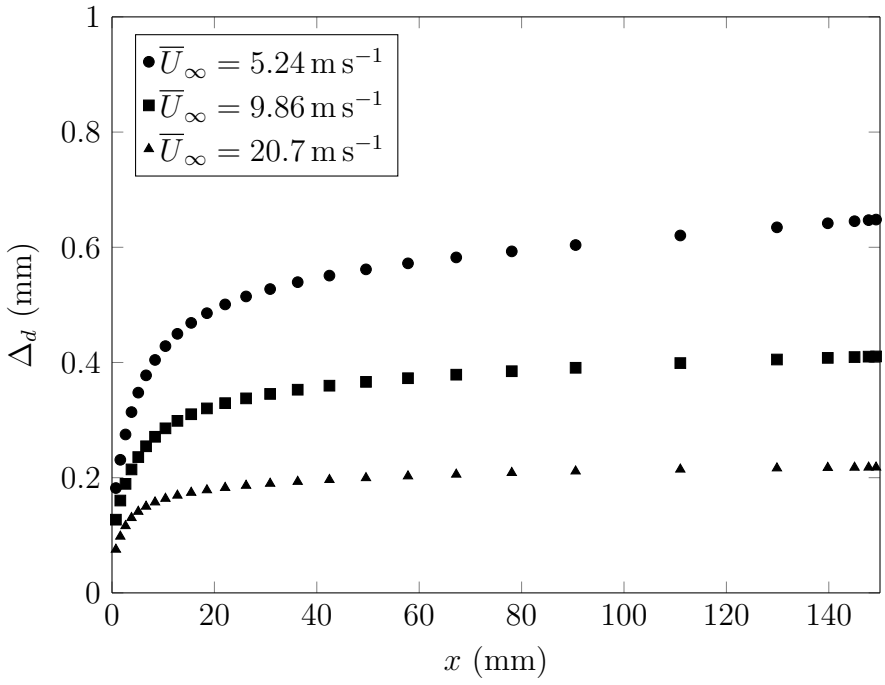

Figure 4.17: Change of diffusion thickness in the streamwise direction. Note there is only one diffusion thickness for each velocity as a subliming surface of infinite lateral extent is used to define Δ_d.

propose two correlations; Eckert and Drake Jr (1959, pg. 217) suggests

$$St = 0.0289 Sc^{-2/3} Re_{x'}^{-1/5} \tag{4.12}$$

and Eckert and Drake Jr (1959, pg. 215, eq. 8.17) suggests

$$St = \frac{0.0296 Re^{-1/5}}{1 + 1.3 Re_{x'}^{-1/10} Sc^{-1/6} (Sc - 1)}, \quad 1 \times 10^5 \leq Re_{x'} \leq 1 \times 10^7, \quad 0.7 \leq Sc \leq 200. \tag{4.13}$$

In a similar manner, Lienhard IV and Lienhard V (2012) also suggest two correlations for the St. Lienhard IV and Lienhard V (2012, pg. 327, eq. 6.115), citing Žukauskas and Šlanciauskas (1987), suggest using

$$St = 0.032 Sc^{-0.57} Re_{x'}^{-0.2}, \quad 2 \times 10^5 \leq Re_{x'} \leq 5 \times 10^6, \quad 0.7 \leq Sc \leq 380 \tag{4.14}$$

and Lienhard IV and Lienhard V (2012, pg. 326, eq. 6.111) suggest using

$$St = \frac{c_f/2}{1 + 12.8\left(Sc^{0.68} - 1\right)\sqrt{c_f/2}}, \qquad Sc \geq 0.5 \tag{4.15}$$

where,

$$c_f = \frac{0.455}{\left[\ln\left(0.06 Re_{x'}\right)\right]^2}. \tag{4.16}$$

eq. (4.16) is from White (1991, pg. 432, eq. 6.78). The correlations are adjusted to account for the unheated starting length using eq. (4.17) from Kays et al. (2005, pg. 253, eq. 12.28)

$$\frac{St_{z\to\infty}}{St_{z\to\infty,\xi=0}} = \left[1 - \left(\frac{\xi}{x'}\right)^{\frac{n+2}{n+3}}\right]^{-\frac{1}{n+2}}, \tag{4.17}$$

where the value for n is estimated from the boundary layer measurements in section 4.1.3 and presented in table 4.2.

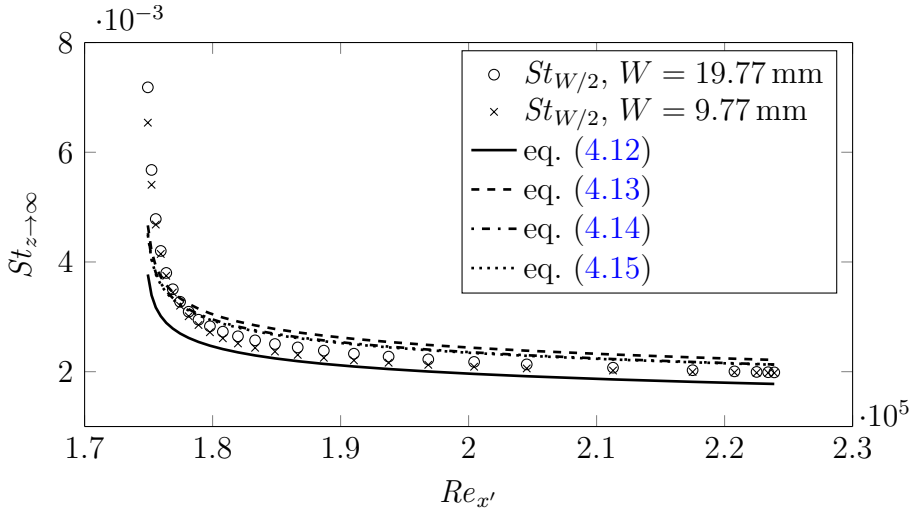

Figure 4.18: Comparison of experimental data with eqs. (4.12) to (4.15) for $\overline{U}_\infty = 5.24\,\mathrm{m\,s^{-1}}$, $\xi = 0.53\,\mathrm{m}$, $n = 5.17$. Corrected for inactive starting length using eq. (4.17) and the values from table 4.2.

Figures 4.18 to 4.20 show excellent repeatability of the averaged mass transfer data, as the centerline data for the two widest strips are virtually indistinguishable.

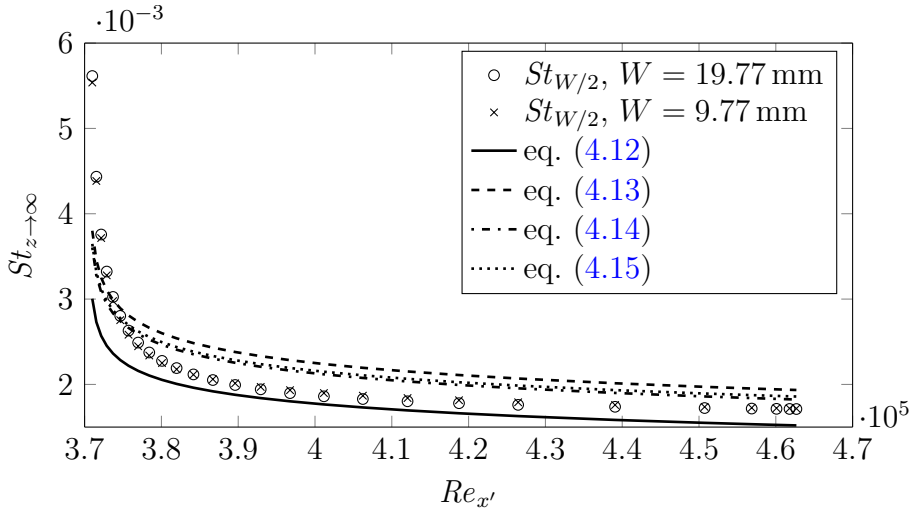

Figure 4.19: Comparison of experimental data with eqs. (4.12) to (4.15) for $\overline{U}_\infty = 9.86\,\mathrm{m\,s^{-1}}$, $\xi = 0.60\,\mathrm{m}$, $n = 5.95$. Corrected for inactive starting length using eq. (4.17) and the values from table 4.2.

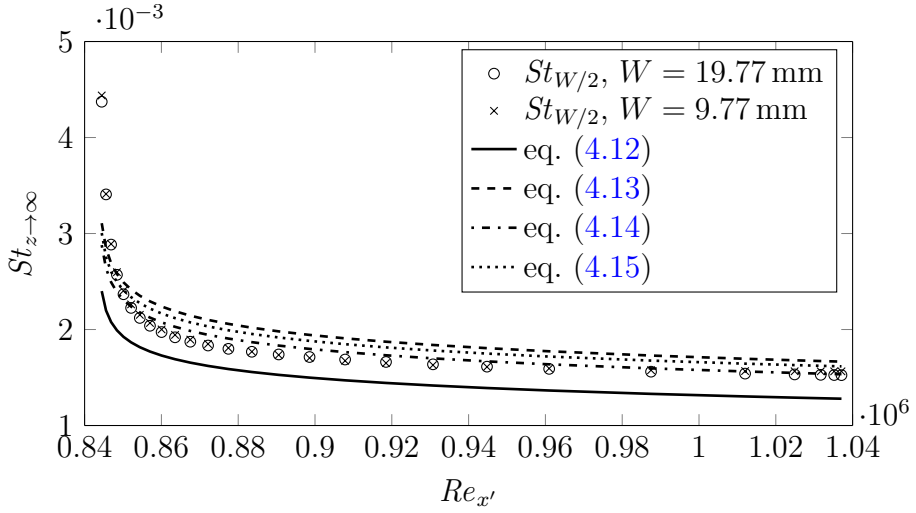

Figure 4.20: Comparison of experimental data with eqs. (4.12) to (4.15) for $\overline{U}_\infty = 20.72\,\mathrm{m\,s^{-1}}$, $\xi = 0.65\,\mathrm{m}$, $n = 6.64$. Corrected for inactive starting length using eq. (4.17) and the values from table 4.2.

Given the scatter from eqs. (4.12) to (4.15) in figs. 4.18 to 4.20, the data at the centerline of the two widest strips are acceptable and the mass transfer data conform to expected values for two dimensional turbulent flow over a flat plate. The centerline values are used for normalizing the St and calculating the mass diffusion thickness.

4.2.4 General Correlation

A general correlation is developed based on the results from chapter 2, particulalry section 2.2.2, and presented in figs. 4.21 to 4.32. Equation (4.18) is constructed in a similar manner as eqs. (2.47) and (2.58)—by blending known solutions for different asymptotic regimes using a p-norm as outlined by Churchill and Usagi (1972). Figures 4.21 to 4.32 and eq. (4.18) show the general correlation captures the main trends in the experimental data, and is accurate to the precision described in table 4.6.

$$\frac{St}{St_{z\to\infty}} = \frac{St_{W/2}}{St_{z\to\infty}}\left\{1 + \left[a{\zeta_m^*}^m\right]^p + \left[a\left(W^* - \zeta_m^*\right)^m\right]^p\right\}^{1/p} \tag{4.18}$$

The general correlation shown in eq. (4.18) is chosen to be symmetrical about $W^*/2$ and approaches a value of one as both the width and ζ_m^* approach infinity. Furthermore, as discussed in section 2.2.2, the mass flux should approach infinity as both the width and ζ_m^* approach zero. The various fitted parameters in eq. (4.18) are shown in eqs. (4.19a) to (4.19d). As with the laminar lateral heat transfer in chapter 2, the primary length parameter used to normalize both the width and lateral location is the mass diffusion thickness calculated at the center of the widest rectangular strip. Measured mass transfer data is used to calculate the diffusion coefficient as opposed to the correlations presented in eqs. (4.12) to (4.15).

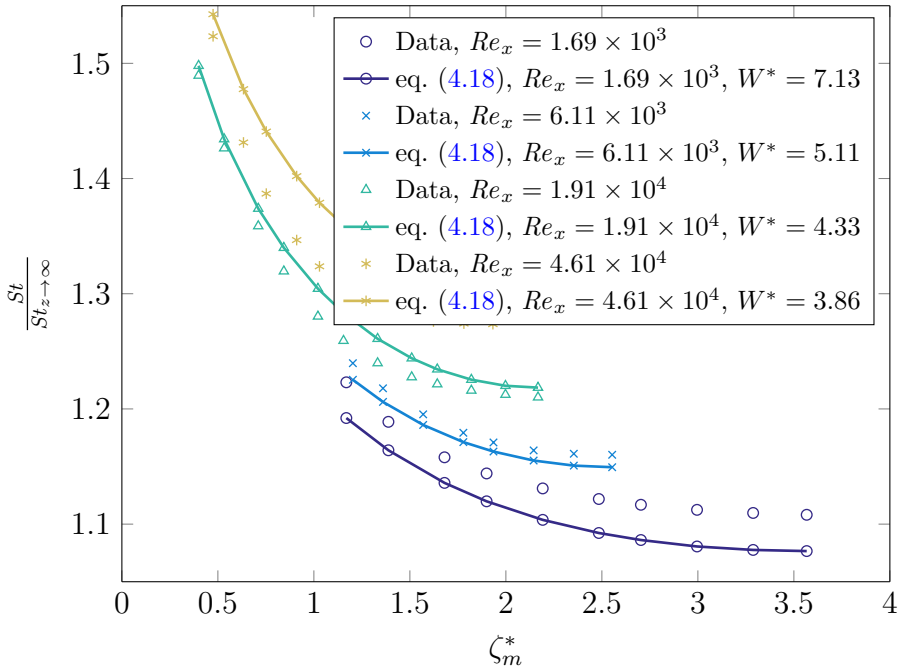

Figure 4.21: Comparison of normalized experimental data with fit from eq. (4.18) for $\overline{U}_\infty = 5.24\,\mathrm{m\,s^{-1}}$, $W = 2.48\,\mathrm{mm}$

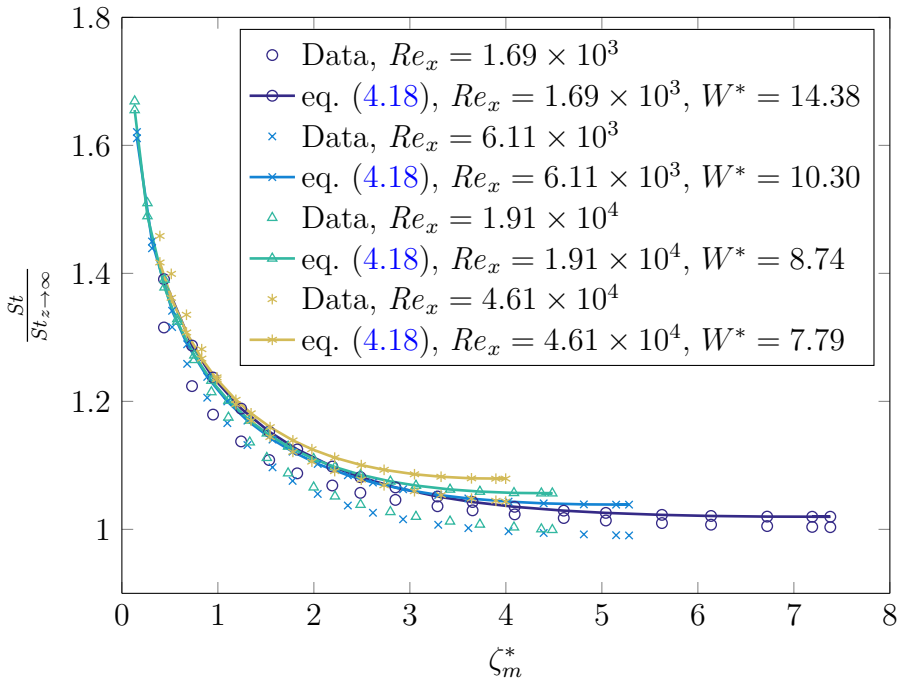

Figure 4.22: Comparison of normalized experimental data with fit from eq. (4.18) for $\overline{U}_\infty = 5.24\,\mathrm{m\,s^{-1}}$, $W = 5.00\,\mathrm{mm}$

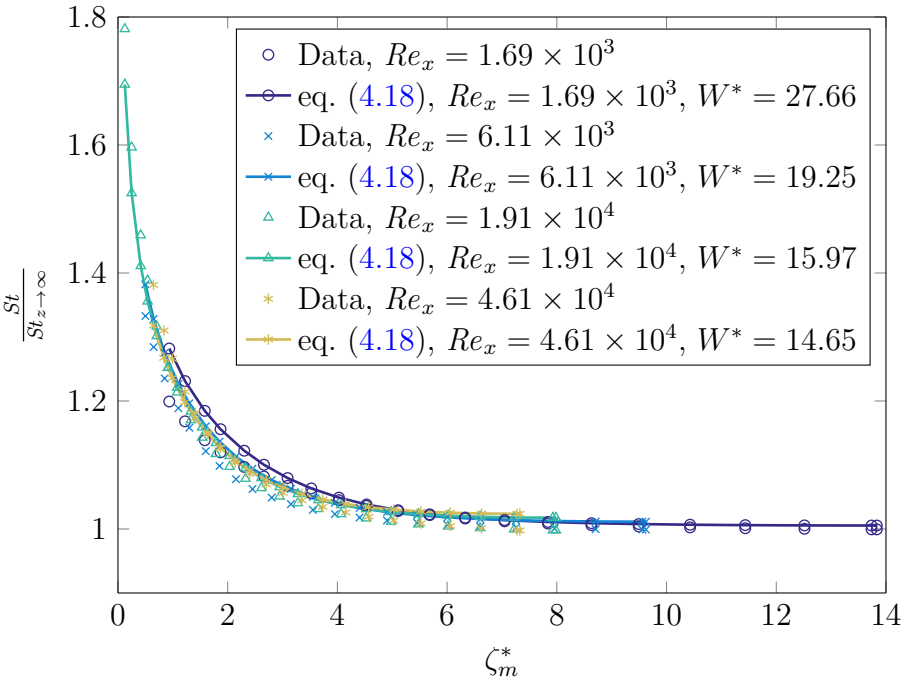

Figure 4.23: Comparison of normalized experimental data with fit from eq. (4.18) for $\overline{U}_\infty = 5.24\,\mathrm{m\,s^{-1}}$, $W = 9.77\,\mathrm{mm}$

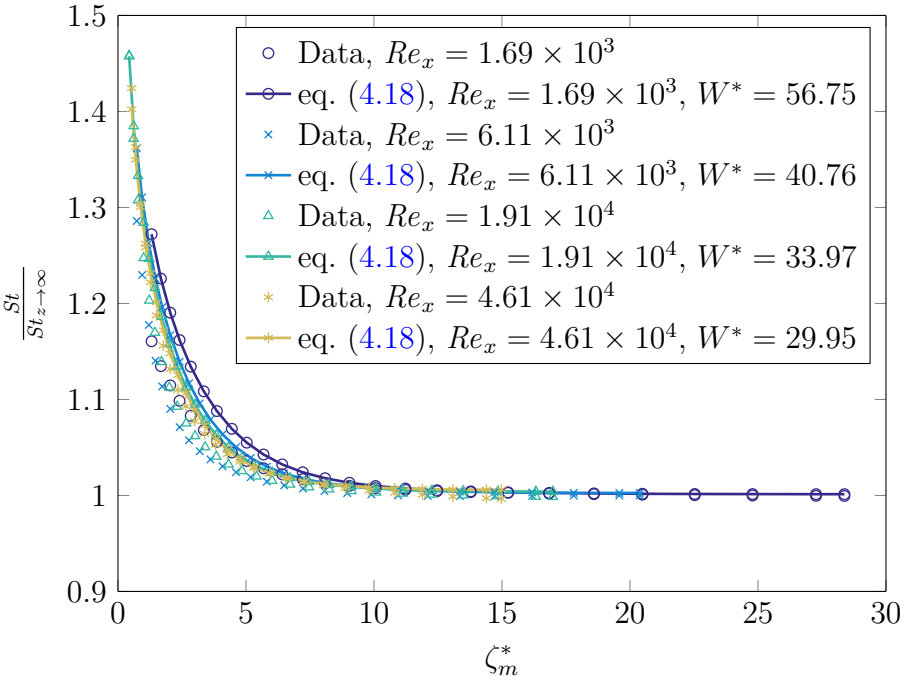

Figure 4.24: Comparison of normalized experimental data with fit from eq. (4.18) for $\overline{U}_\infty = 5.24\,\mathrm{m\,s^{-1}}$, $W = 19.77\,\mathrm{mm}$

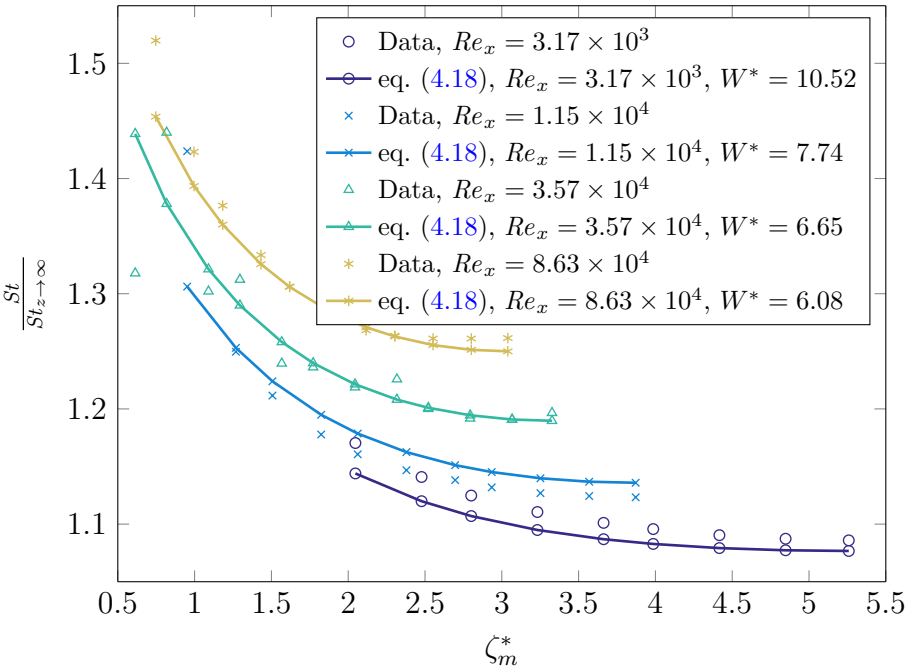

Figure 4.25: Comparison of normalized experimental data with fit from eq. (4.18) for $\overline{U}_\infty = 9.86\,\mathrm{m\,s^{-1}}$, $W = 2.48\,\mathrm{mm}$

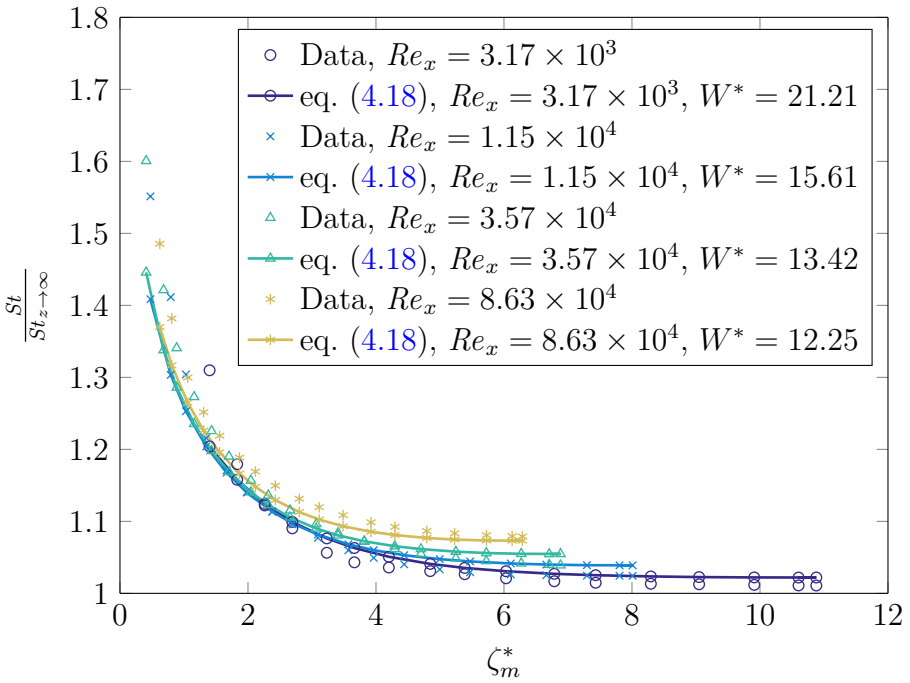

Figure 4.26: Comparison of normalized experimental data with fit from eq. (4.18) for $\overline{U}_\infty = 9.86\,\mathrm{m\,s^{-1}}$, $W = 5.00\,\mathrm{mm}$

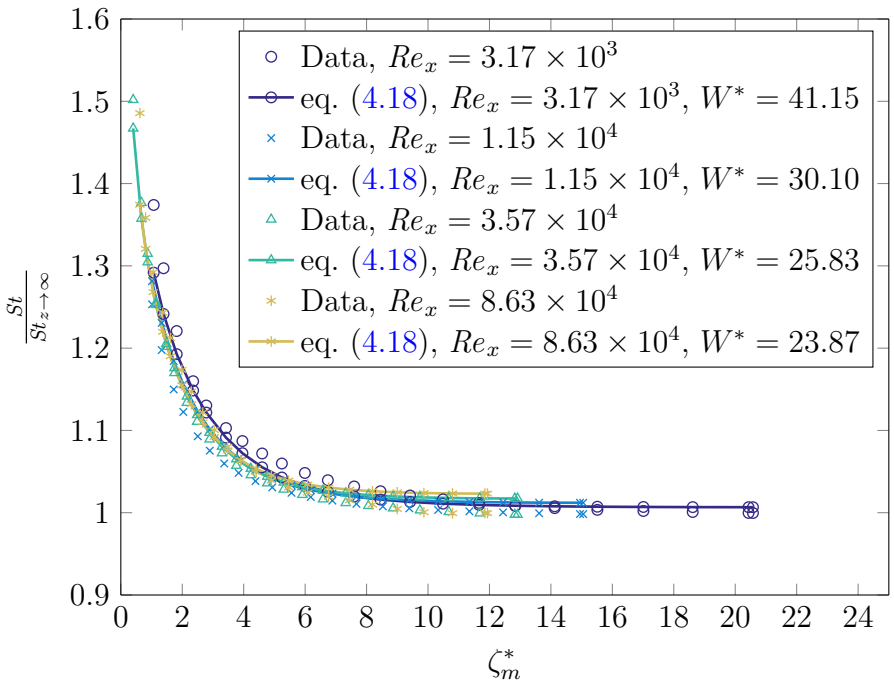

Figure 4.27: Comparison of normalized experimental data with fit from eq. (4.18) for $\overline{U}_\infty = 9.86\,\mathrm{m\,s^{-1}}$, $W = 9.77\,\mathrm{mm}$

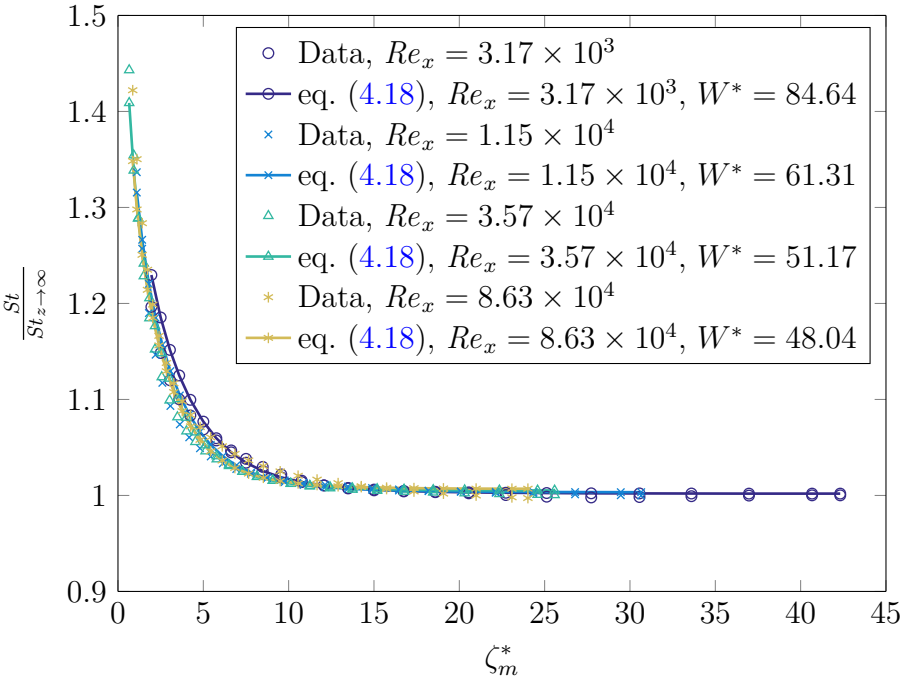

Figure 4.28: Comparison of normalized experimental data with fit from eq. (4.18) for $\overline{U}_\infty = 9.86\,\mathrm{m\,s^{-1}}$, $W = 19.77\,\mathrm{mm}$

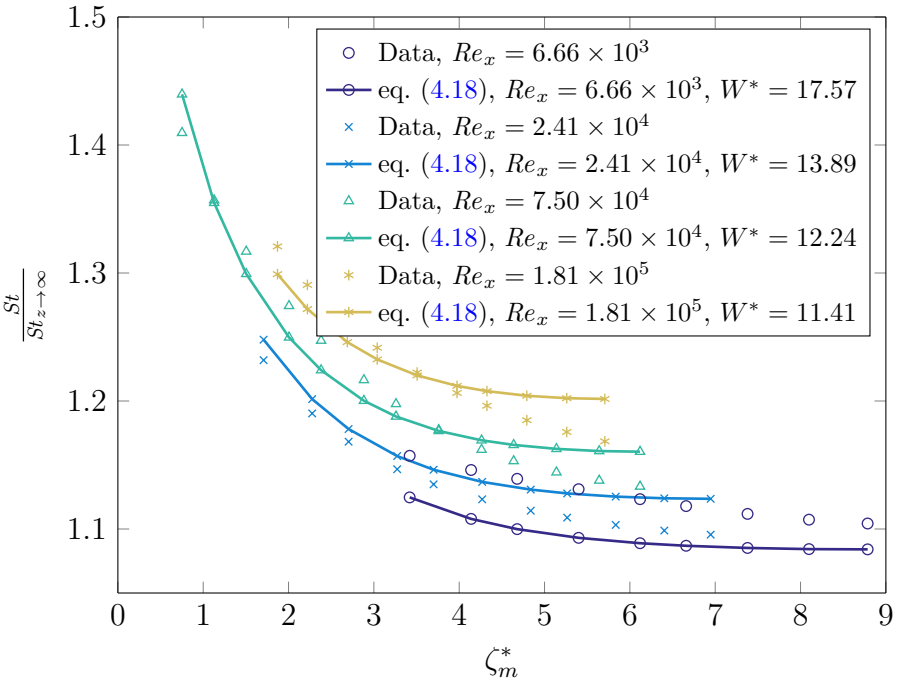

Figure 4.29: Comparison of normalized experimental data with fit from eq. (4.18) for $\overline{U}_\infty = 20.72\,\mathrm{m\,s^{-1}}$, $W = 2.48\,\mathrm{mm}$

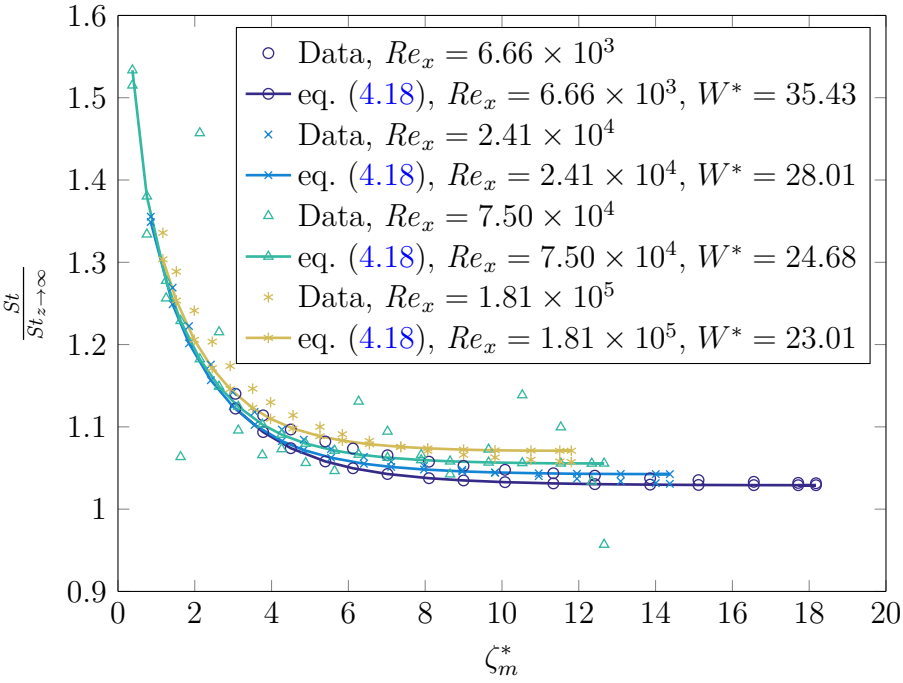

Figure 4.30: Comparison of normalized experimental data with fit from eq. (4.18) for $\overline{U}_\infty = 20.72\,\mathrm{m\,s^{-1}}$, $W = 5.00\,\mathrm{mm}$

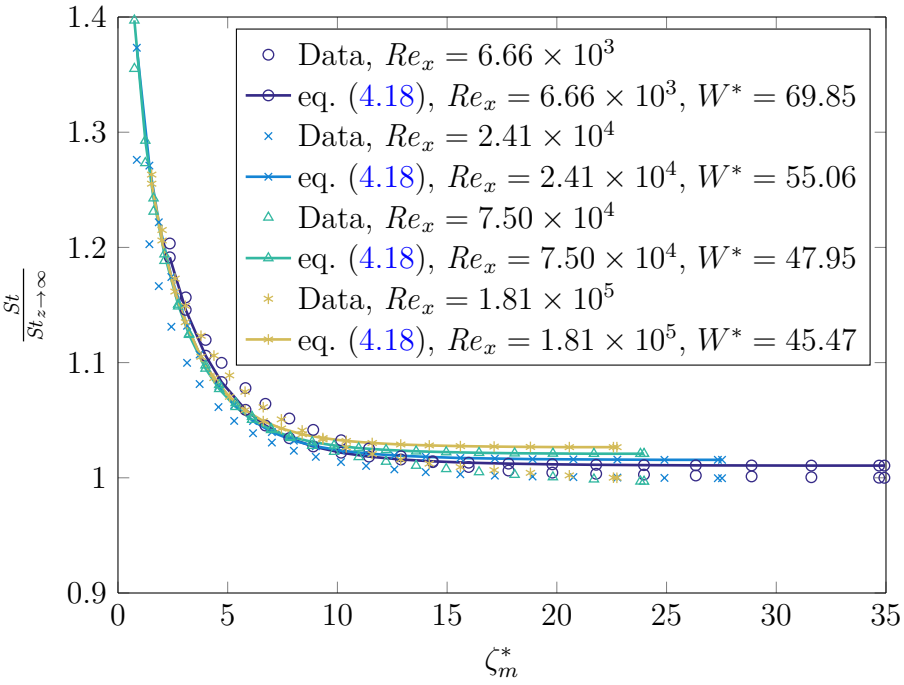

Figure 4.31: Comparison of normalized experimental data with fit from eq. (4.18) for $\overline{U}_\infty = 20.72\,\mathrm{m\,s^{-1}}$, $W = 9.77\,\mathrm{mm}$

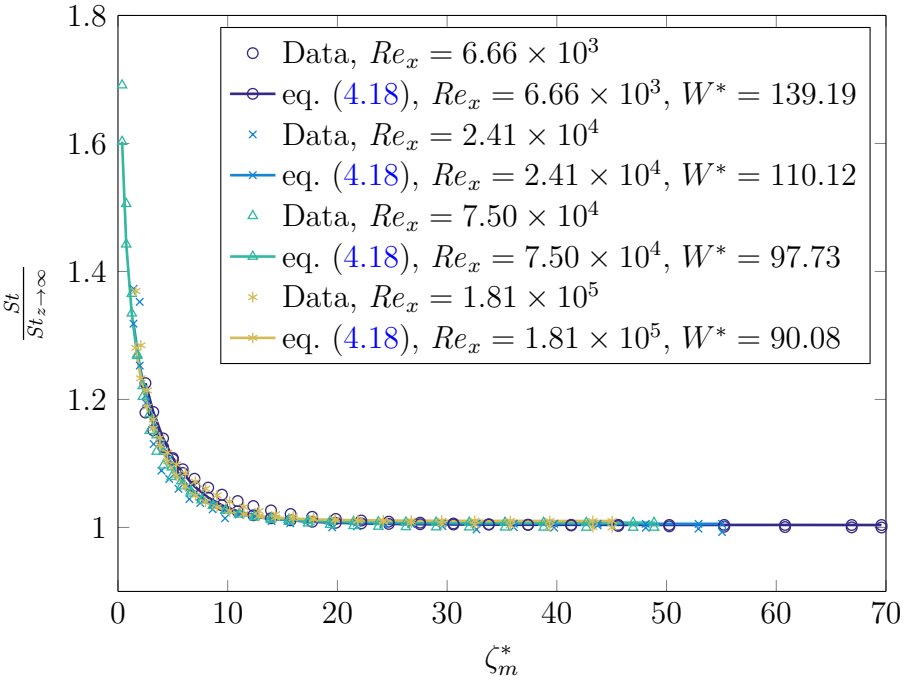

Figure 4.32: Comparison of normalized experimental data with fit from eq. (4.18) for $\overline{U}_\infty = 20.72\,\mathrm{m\,s^{-1}}$, $W = 19.77\,\mathrm{mm}$

$$\frac{St_{W/2}}{St_\infty} = \left[1 + \left(0.0597W^{*-10.5}\right)^{3.10Re_{x'}^{-0.227}}\right]^{Re_{x'}^{0.227}/3.10} \tag{4.19a}$$

$$a = 1.02W^{*0.0630} \tag{4.19b}$$

$$p = 21.8 \tag{4.19c}$$

$$m = -0.152 \tag{4.19d}$$

The first term in eq. (4.18), presented in eq. (4.19a) and shown in figs. 4.33 to 4.35, models the increase in the centerline *St* as the width of the streamwise strip decreases. The increase in the centerline *St* number is best described using $Re_{x'}$ and W^*. The *Re* based on the distance from the virtual origin, as opposed to the start of the subliming surface, is used because it is assumed most of the lateral transport is by turbulent mixing in the boundary layer (as described below in discussion on the value of m from eq. (4.19d)).

Table 4.7 presents the relative increases in the experimental data between the *St* for a heated plate of semi-infinite width and the centerline *St* for strips of finite width. For the smallest width, the centerline *St* increased by almost 30 % over the measured values of the two widest strips near the end of the subliming surface. Note the centerline *St* of the two widest strips are equal to the semi-infinite *St* by definition. The percent increases of the two narrower strips are based on the average centerline *St* for all data where the normalized width, W^*, is greater than 30.

Figures 4.36 to 4.38 graphically show how eq. (4.19a) compares to the data. It is clear more accurate measurements are needed to improve upon eq. (4.19a). However, as shown by the deviations in figs. 4.36 to 4.38, the fit is accurate to the precision presented in table 4.4. Therefore, the fit is as accurate as can be expected given the repeatability of the measurements. It is probable that eq. (4.19a) is a large source

Table 4.7: Percent increase of centerline St over $St_{z\to\infty}$ at the end of the subliming surface

Average Freestream Velocity ($\mathrm{m\,s^{-1}}$)	Percent Increase (columns labeled by width)			
	19.77 mm	9.77 mm	5.00 mm	2.48 mm
5.24	0.00	0.00	4.95	28.27
9.86	0.00	0.00	8.33	26.43
20.72	0.00	0.00	6.06	16.78

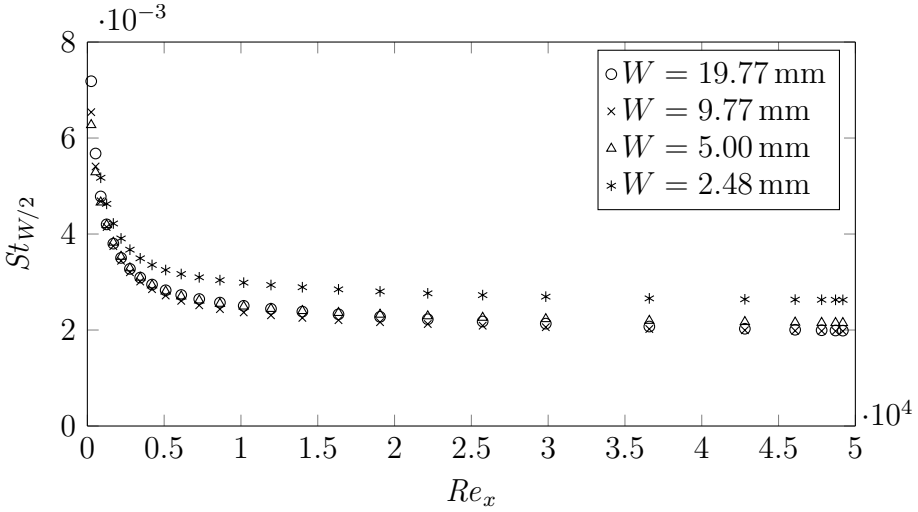

Figure 4.33: Comparison of the centerline St different widths for $\overline{U}_\infty = 5.24\,\mathrm{m\,s^{-1}}$

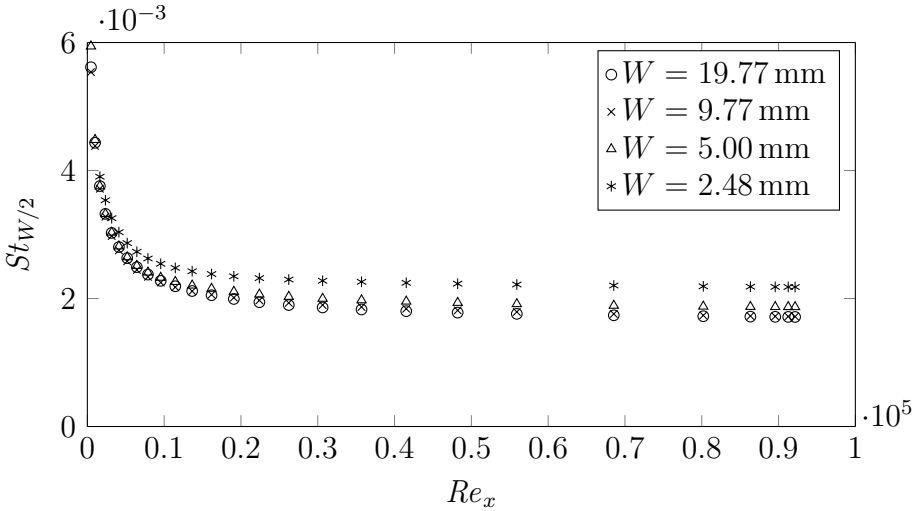

Figure 4.34: Comparison of the centerline St different widths for $\overline{U}_\infty = 9.86\,\mathrm{m\,s^{-1}}$

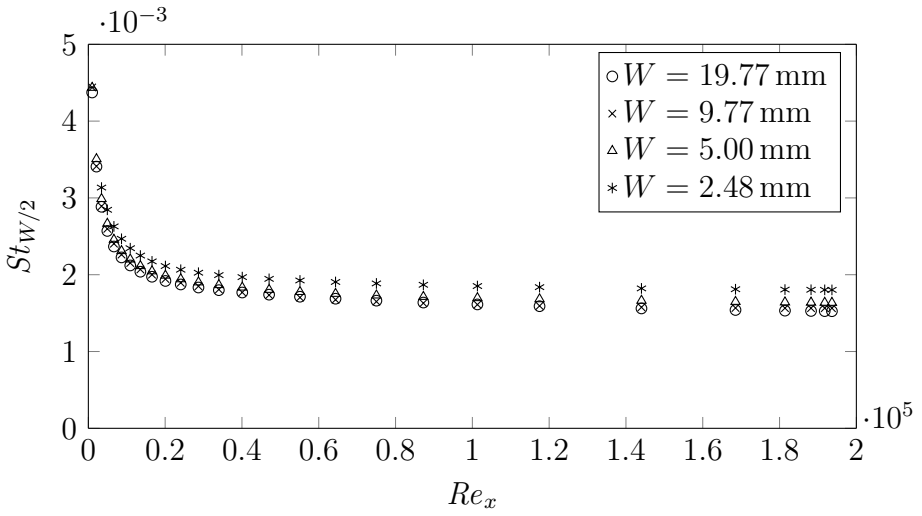

Figure 4.35: Comparison of the centerline St different widths for $\overline{U}_\infty = 20.72\,\mathrm{m\,s^{-1}}$

of of error in eq. (4.18) when compared to the errors introduced by modeling the St normalized by the centerline St. Even from a brief comparison of figs. 4.39 to 4.42, which show the St normalized by the centerline St and the term in curly braces in eq. (4.18), and figs. 4.21 to 4.32, which compare the experimental St to eq. (4.18), it is clear that the addition of eq. (4.19a) adds most of the modeling uncertainty.

The part of eq. (4.18) in curly braces models the local St normalized by the centerline St, with eqs. (4.19b) to (4.19d) giving the values of the various coefficients. Figures 4.39 to 4.42 show that eq. (4.18) captures St/St_c relatively well. The constant m, the value of which is given in eq. (4.19d), is different than the negative one-half value in chapter 2. The lower value for m found for turbulent boundary layers is evidence of the increased lateral diffusion of naphthalene by turbulent mixing. In other words, the turbulent mixing acts to "smooth" out the effects of the singularity at the lateral edge better than transport by molecular diffusion.

If one thinks of the "conduction" domain as a lower subdomain that represents the viscous sublayer, and an upper subdomain that represents the increasing importance of turbulent mixing, the upper subdomain imposes a given concentration and mass

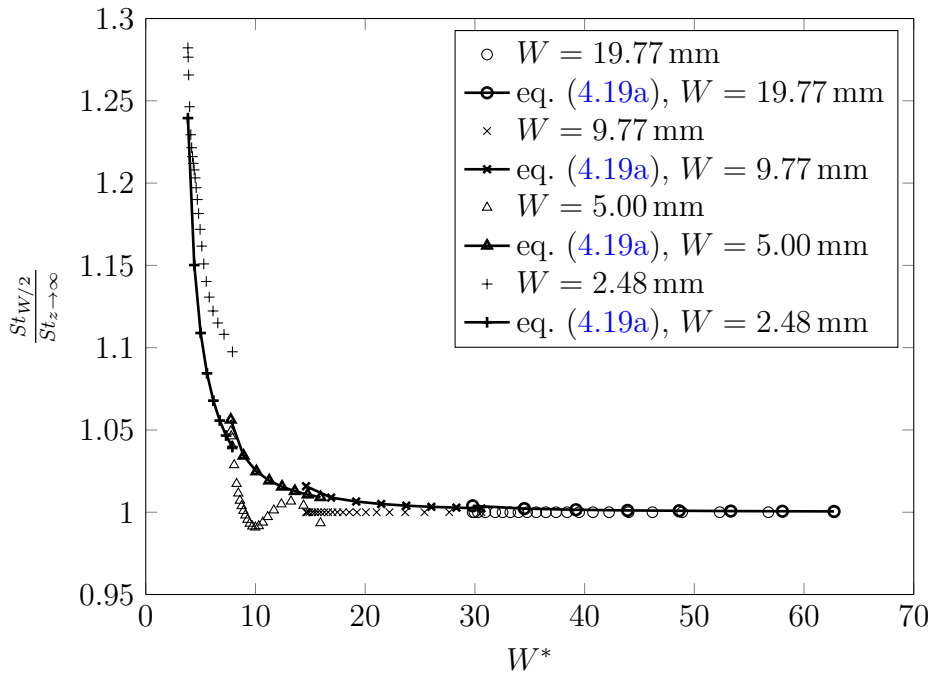

Figure 4.36: Comparison of eq. (4.19a) with experimental data from $\overline{U}_\infty = 5.24\,\mathrm{m\,s^{-1}}$. Note the fit from eq. (4.19a) or the data is not continuous for the various widths.

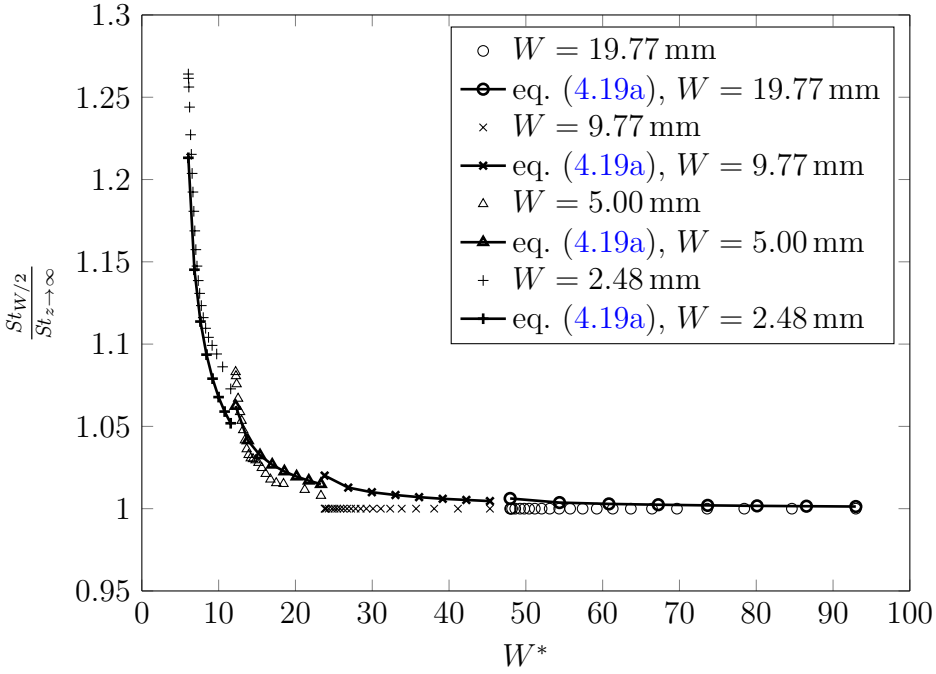

Figure 4.37: Comparison of eq. (4.19a) with experimental data from $\overline{U}_\infty = 9.86\,\mathrm{m\,s^{-1}}$. Note the fit from eq. (4.19a) or the data is not continuous for the various widths.

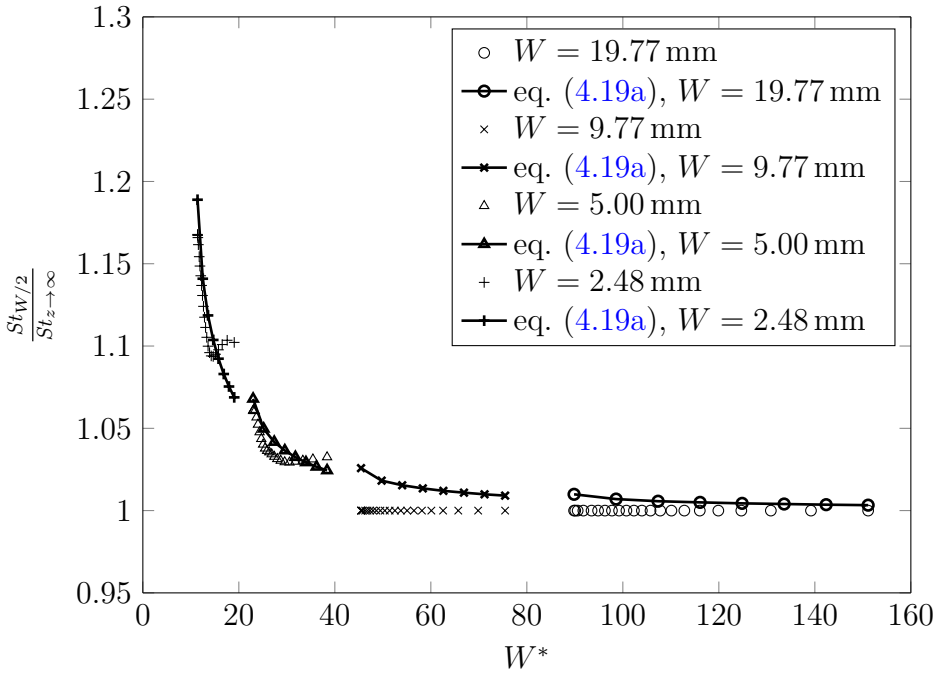

Figure 4.38: Comparison of eq. (4.19a) with experimental data from $\overline{U}_\infty = 20.72\,\mathrm{m\,s^{-1}}$. Note the fit from eq. (4.19a) or the data is not continuous for the various widths.

flux on the boundary of the lower subdomain. This imposition of the turbulent mixing on the viscous sublayer boundary changes the value of m from the laminar value of negative one-half. If lower value for m indicates the importance of lateral turbulent mixing, it also implies the contribution of the viscous sublayer to lateral diffusive processes are negligible. The details are of course vague without measurements of the fluctuation temperature and velocity components, but the general conclusions discussed above are warranted.

It is likely that as ζ_m^* approaches zero, the St varies with ζ_m^* with a negative one-half power. This can be shown by imagining a scale arbitrarily close to $z = 0$. At this scale, in the plane normal to the flow, the concentration domain would be analogous to the conduction domains shown in fig. 2.4 near the singularity. However, the measurements are neither close enough to $z = 0$ nor accurate enough to provide

evidence of the negative one-half asymptotic regime.

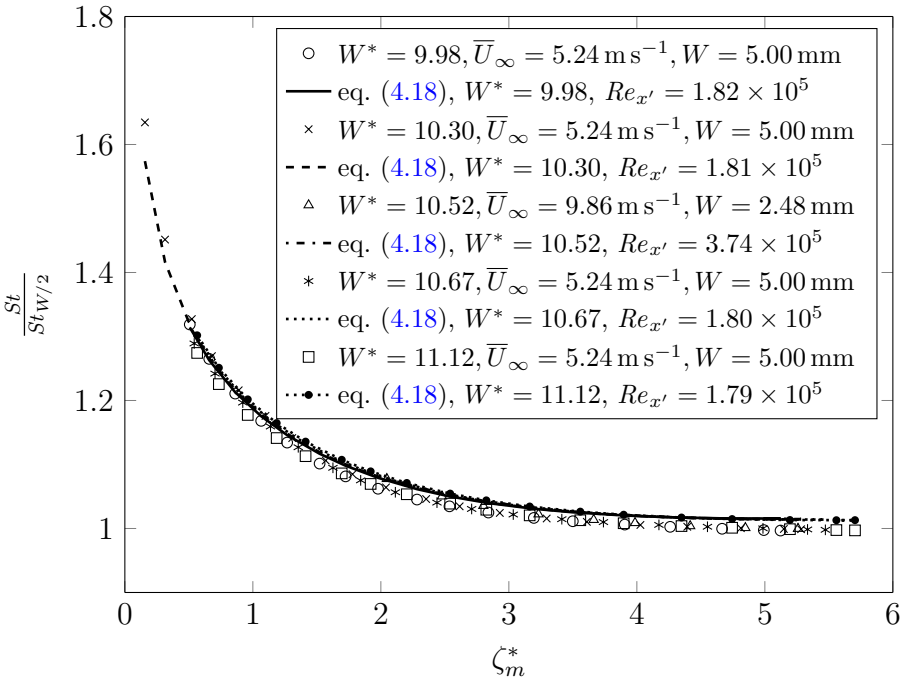

Figure 4.39: Various curves for $W^* \approx 10$

4.2.5 Semi-Infinite Correlation

Equation (4.18) does not work as W^* approaches infinity because the parameter a, shown in eq. (4.19b), approaches zero. Therefore, all the data with $W^* > 40$ are used to fit a correlation for a geometry with semi-infinite subliming widths. Equation (4.20) is the recommended correlation for problems with large W^* ($W^* > 40$).

$$\frac{St}{St_{z\to\infty}} = \left[1 + \left(1.34{\zeta_m^*}^{-0.288}\right)^{5.27}\right]^{1/5.27} \tag{4.20}$$

It is immediately clear the exponent value of -0.288 is almost twice as large as is found for the general correlation from eq. (4.18). This larger exponent seems to indicate the value of the exponent depends on the width of the subliming surface, but fitting

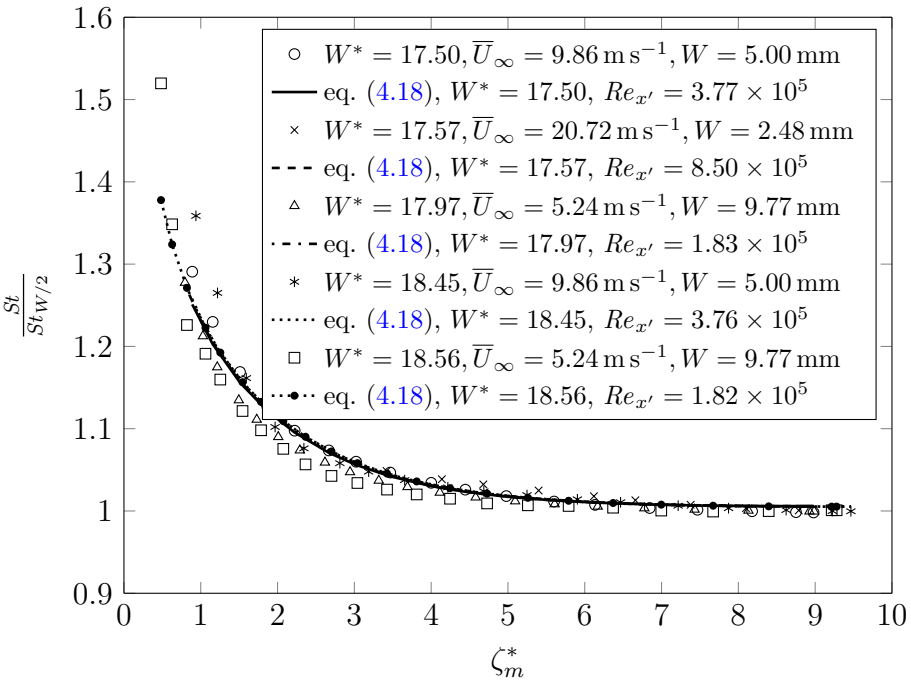

Figure 4.40: Various curves for $W^* \approx 17.8$

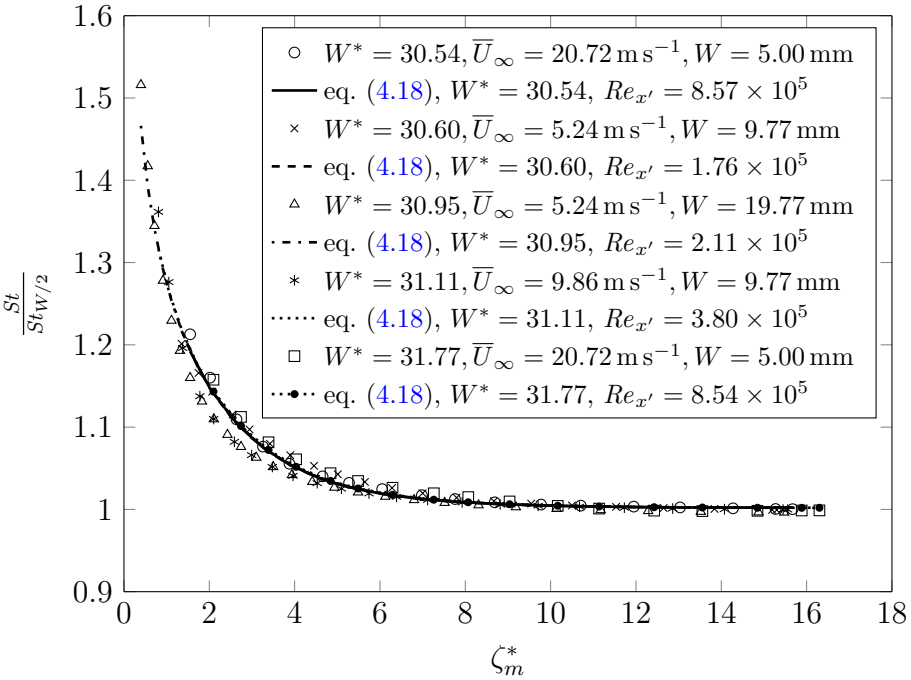

Figure 4.41: Various curves for $W^* \approx 31.6$

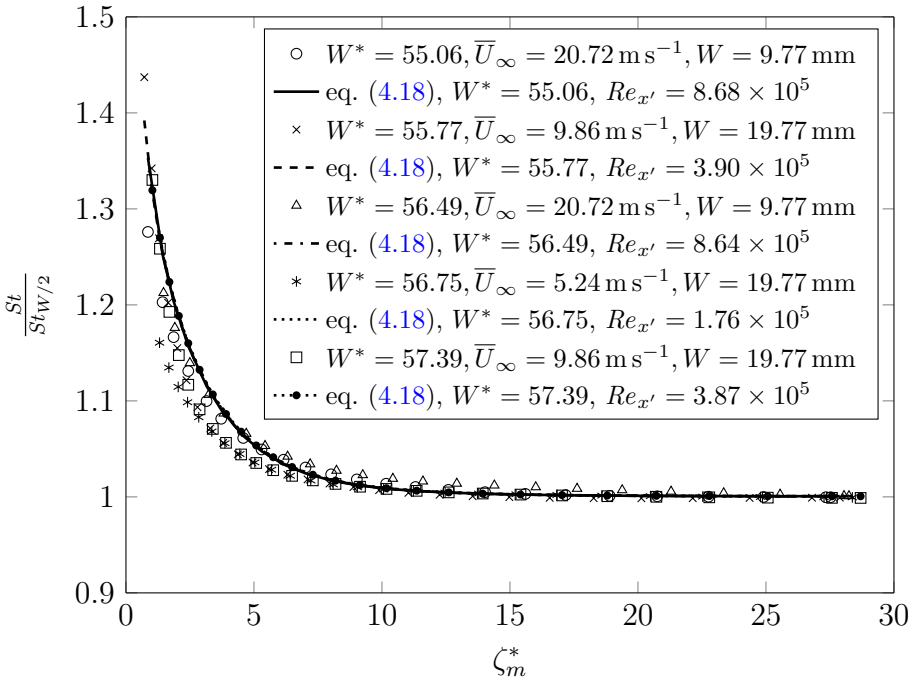

Figure 4.42: Various curves for $W^* \approx 56.2$

for simple functions for the exponent always returned a function of a constant value. It is unclear why the fit for the semi-infinite condition is different than the fit for the more general geometric condition.

Taliaferro et al. (2018) recommends the correlation shown in eq. (4.21), which assumes a negative one-half power.

$$\frac{St}{St_{z\to\infty}} = \left[1 + \left(1.01{\zeta_m^*}^{-0.5}\right)^{2.04}\right]^{1/2.04} \tag{4.21}$$

However, as shown in section 4.2.4 and eq. (4.20), forcing a negative one-half power law does not fit the data best in the region studied. Figure 4.43a compares the two presented semi-infinite correlations and the general correlation from eq. (4.18). It is clear that forcing a negative one-half power, as eq. (4.21) does, results in an artificially low p-norm value to compensate for the artificially high value for m. If the m is too large, a low p value delays the onset of the incorrect asymptotic regime until smaller

ζ_m^* values. This also results in a fit that does not decay to unity quickly enough as ζ_m^* increases.

Figure 4.43b presents the error of eq. (4.20) at different values of ζ_m^*. By taking the root mean square with a window of 31 points at every valid point (the window cannot extend past the range of available points), the local error is estimated. The root mean square at a given point is defined by

$$RMS_k = \left\{ \frac{1}{n} \left[\sum_{i=k-(n-1)/2}^{k+(n-1)/2} \left(St_{fit,i} - St_{exp,i} \right)^2 \right] \right\}^{1/2},$$
$$k = 1 + (n-1)/2,\ 2 + (n-1)/2, ...,\ N - (n-1)/2, \quad (4.22)$$

where k is the index of the root mean square measurement, n is the size of the window, and N is the total amount of points. It is clear from fig. 4.43b that the largest errors occur near $z = 0$. Far from $z = 0$, the random uncertainty in the rim location has a small effect because the gradient of the St with z is small; however near the edge the opposite is true. The random uncertainty in z has a large effect on the random uncertainty near the lateral edge because the gradient of the St with z is large.

4.2.6 Lateral Extent of Edge Effect

In section 4.2.4, the lateral edge effect is assumed to scale primarily with the diffusion thickness, Δ_d, without much evidence other than the correlation presented in eq. (4.18) describes the data adequately. However, there is a more direct way to show that the primary scaling parameter is the diffusion thickness. Comparing the lateral edge effect to the diffusion thickness provides direct evidence for using Δ_d as the primary length scale for lateral changes in mass transfer. A similar method is employed in sections 2.1.3 and 2.2.2 .

The method used to measure the extent of the lateral edge effect is the distance it takes the St to reach a given multiple of the centerline St. For the results shown in figs. 4.44 to 4.46, the multiple is 1.1. In other words, the spanwise distance from the edge to where $St = 1.1St_c$, denoted as $z_{1.1}$, is used as a measure of the lateral extent of the edge effect. The centerline St is chosen, and not the St from a semi-infinite strip, because the centerline St for narrower strips are as much as 30 % larger than the centerline St for the larger strips, making it difficult to choose a multiple that works for the various widths tested.

In addition to plotting $z_{1.1}/x$, figs. 4.44 to 4.46 show the diffusion thickness calculated using the St estimates for a semi-infinite plate, the estimated $z_{1.1}$ from the terms in braces in eq. (4.18), and the expected scaling of the diffusion thickness. All plots show the same scaling in the streamwise direction, validating the choice of the diffusion thickness for the primary scaling parameter. Note the scaling seems unaffected by the width of the subliming strips.

The diffusion thickness does not change very rapidly in the streamwise direction, and as a consequence the lateral edge effect is relatively constant in the streamwise diirection. Using the definition $\Delta_d = x/Sh$ and $Sh \propto Re^{4/5}$, the diffusion thickness is proportional to $x^{1/5}$. Figures 4.44 to 4.46 show this scaling with a black line. Therefore, the edge effect is relatively constant in the streamwise direction when compared to a velocity boundary layer thickness. For example, based on eq. (4.23) from Kays et al. (2005, pg. 193, eq. 11.22),

$$\frac{\delta_2}{x'} = \frac{0.036}{Re_{x'}^{2/5}}, \tag{4.23}$$

the momentum thickness scales as $\delta_2 \sim x'^{3/5}$.

Based on the figs. 4.44 to 4.46, it is clear the lateral edge affects the mass transfer

within a region that extends into the subliming surface to a distance that is within an order of magnitude of the diffusion thickness.

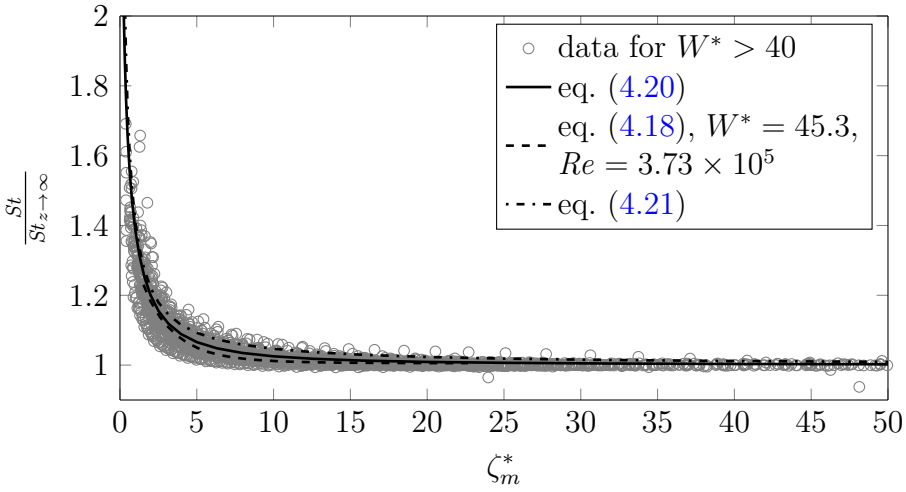

(a) Comparison of data with $W^* > 40$ with eqs. (4.20) and (4.21)

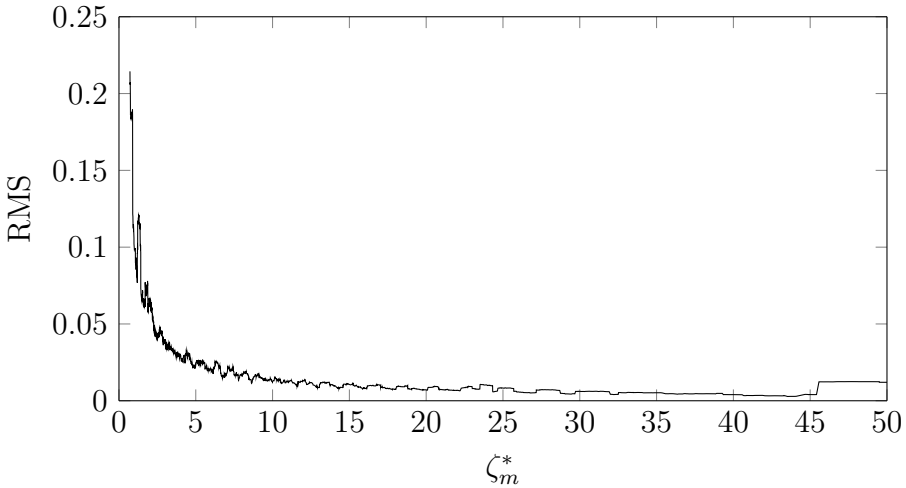

(b) Root mean square of the residuals (with a window of 31) between eq. (4.20) and experimental results.

Figure 4.43: Fit for normalized St for a strip of semi-infinite width.

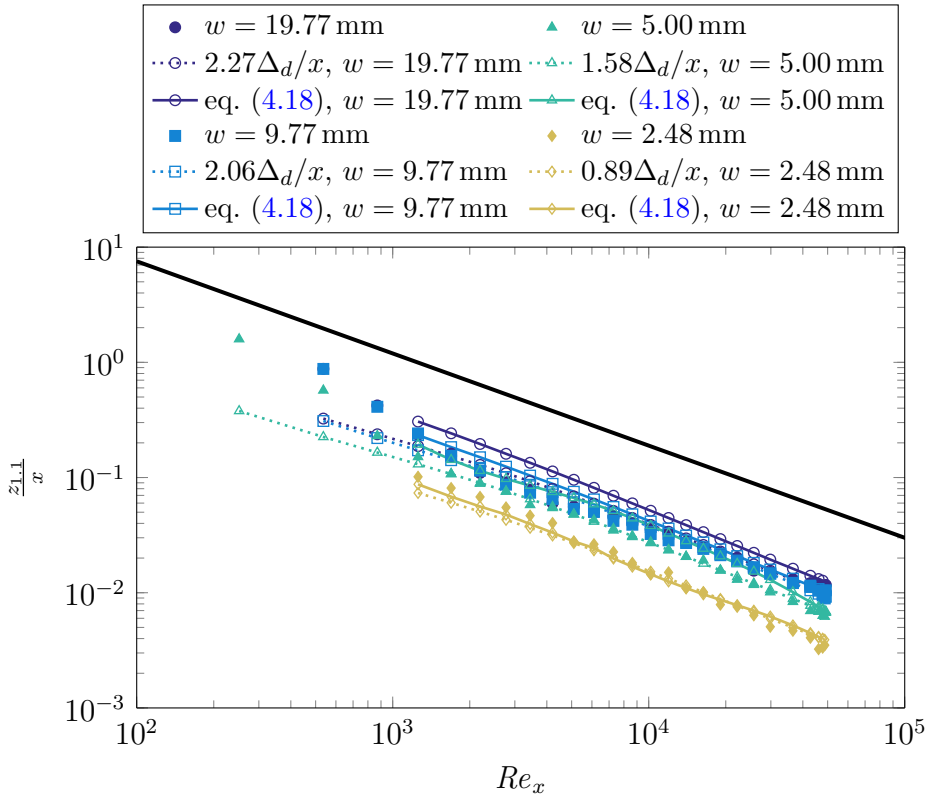

(a) Lateral extent for a freestream velocity of $5.24\,\mathrm{m\,s^{-1}}$. The solid black line is a representative scaling of the diffusion thickness and is proportional to $Re_x^{-4/5} \sim 1/Sh$. The lateral edge effect ($z_{1,1}$), measured diffusion thickness, predicted value of the edge effect thickness, and expected scaling of the diffusion thickness compare very well. Note the multiplicative constant in front of the diffusion thickness is only fit to make comparison easier.

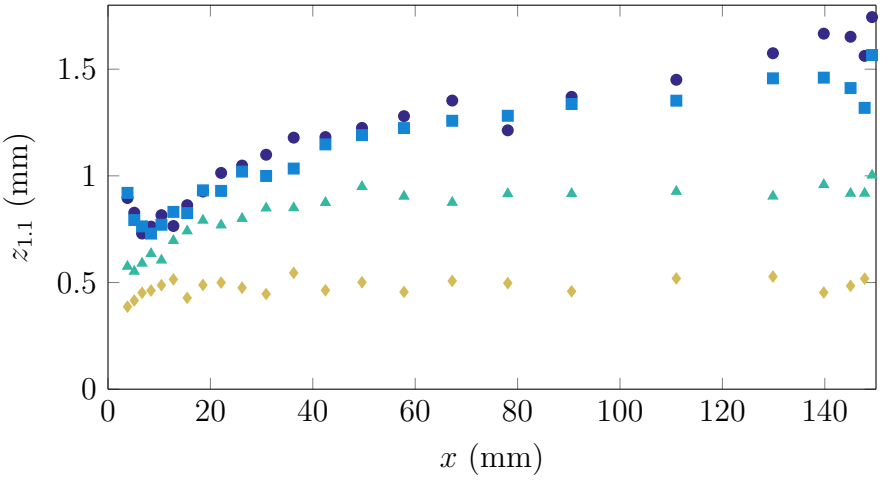

(b) Lateral extent for a freestream velocity of $5.24\,\mathrm{m\,s^{-1}}$

Figure 4.44: Dimensional and nondimensional lateral extent for a freestream velocity of $5.24\,\mathrm{m\,s^{-1}}$

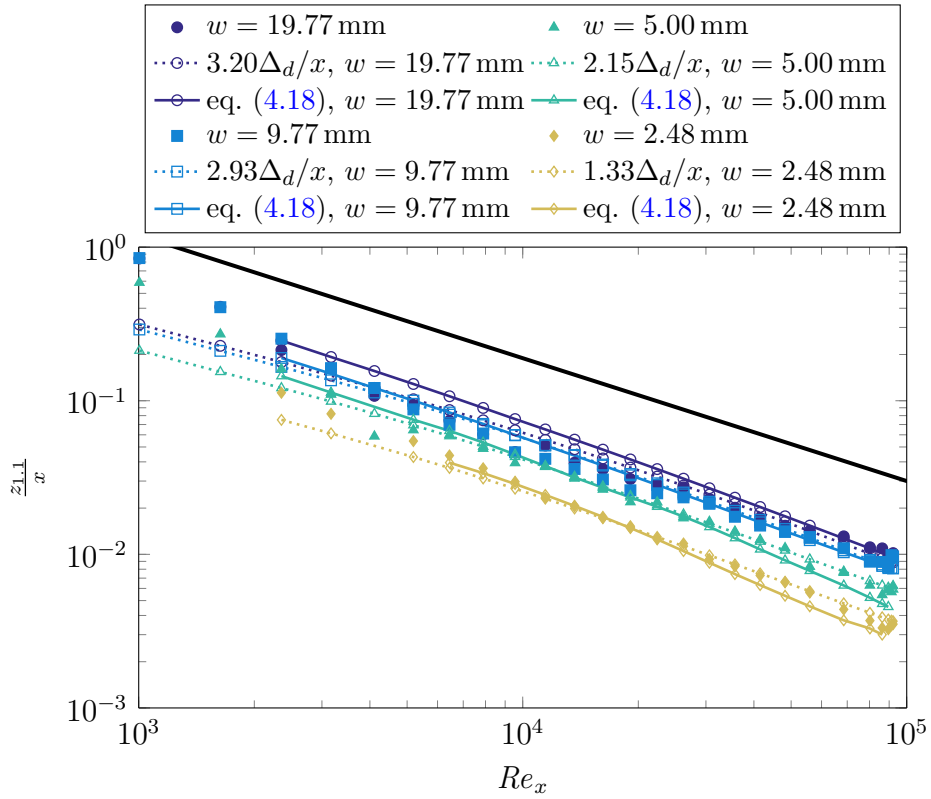

(a) Lateral extent for a freestream velocity of $9.86\,\mathrm{m\,s^{-1}}$. The solid black line is a representative scaling of the diffusion thickness and is proportional to $Re_x^{-4/5} \sim 1/Sh$. The lateral edge effect ($z_{1,1}$), measured diffusion thickness, predicted value of the edge effect thickness, and expected scaling of the diffusion thickness compare very well. Note the multiplicative constant in front of the diffusion thickness is only fit to make comparison easier.

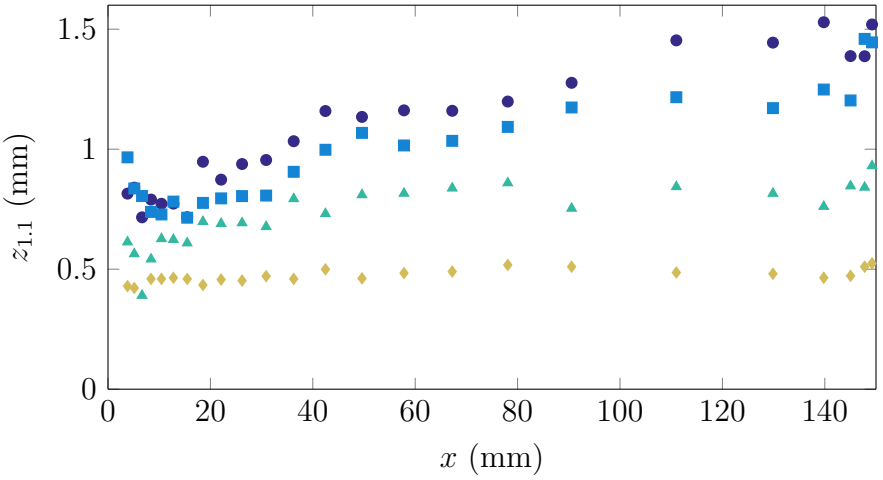

(b) Lateral extent for a freestream velocity of $9.86\,\mathrm{m\,s^{-1}}$

Figure 4.45: Dimensional and nondimensional lateral extent for a freestream velocity of $9.86\,\mathrm{m\,s^{-1}}$

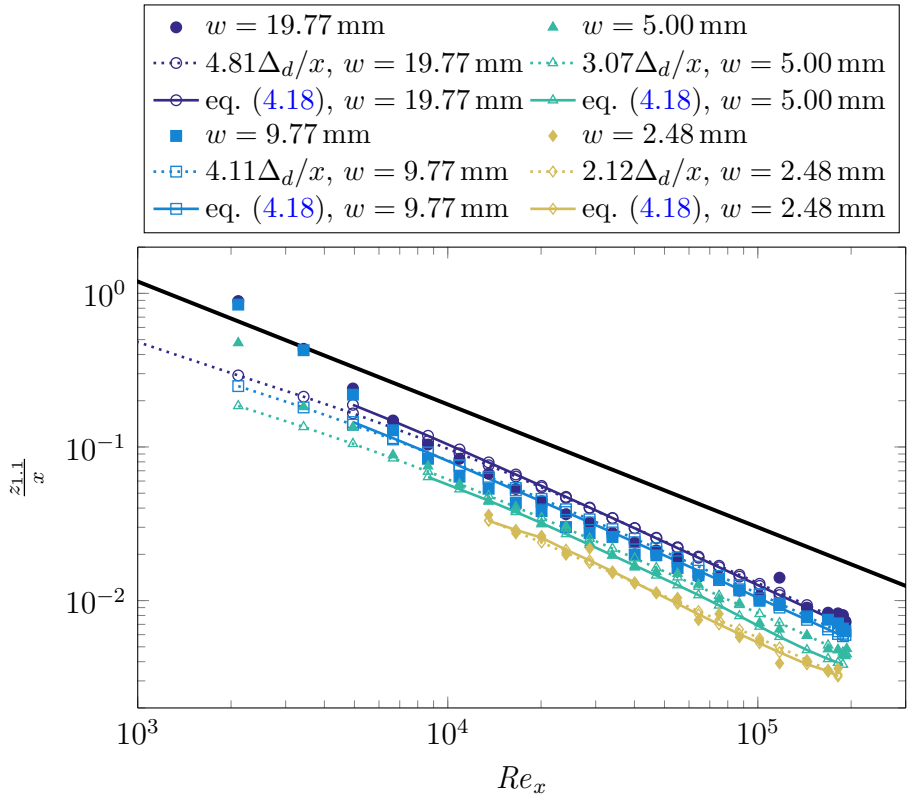

(a) Lateral extent for a freestream velocity of $20.72\,\mathrm{m\,s^{-1}}$. The solid black line is a representative scaling of the diffusion thickness and is proportional to $Re_x^{-4/5} \sim 1/Sh$. The lateral edge effect ($z_{1.1}$), measured diffusion thickness, predicted value of the edge effect thickness, and expected scaling of the diffusion thickness compare very well. Note the multiplicative constant in front of the diffusion thickness is only fit to make comparison easier.

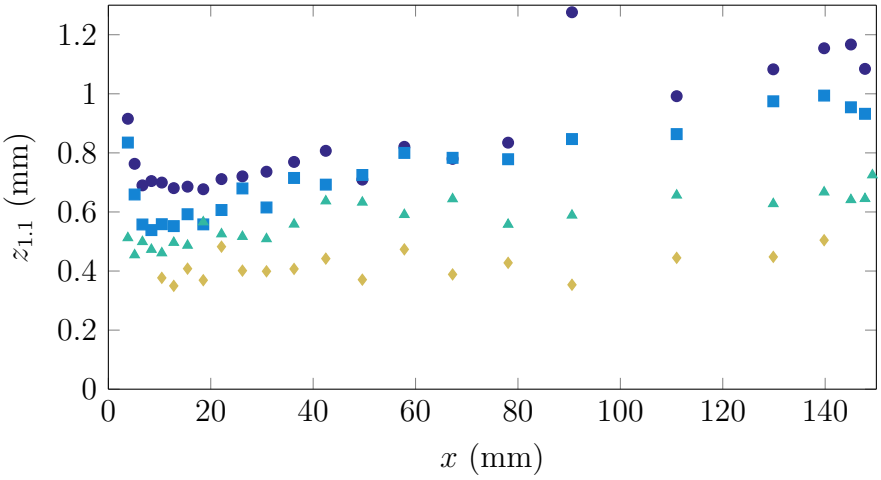

(b) Lateral extent for a freestream velocity of $20.72\,\mathrm{m\,s^{-1}}$

Figure 4.46: Dimensional and nondimensional lateral extent for a freestream velocity of $20.72\,\mathrm{m\,s^{-1}}$

4.3 Summary

Boundary layer measurements are made with a hotwire anemometer, and a modified Clauser technique is used to estimate the position of the probe and local shear stress. The velocity compares well with the Van Driest velocity profile except in the boundary layer wake region. However, estimates of the shear stress and centerline mass transfer compare well to previously published data and correlations for turbulent flat plate boundary layers. This indicates that while the turbulent boundary layer is not fully mature, the flow is representative of wall bounded turbulent boundary layers over a flat plate. The range of momentum thickness Re measured is 320–1270.

For each combination of width and freestream velocity three to four experiments are completed, but the presented data and analysis are of averaged data. Averaging the data is a two step process, first the data are independently averaged in the streamwise and lateral directions. The streamwise averaging is for the centerline St and the lateral averaging is for the St normalized by the centerline St. Second, the two averages are multiplied together to calculate an averaged St. This procedure allows for an estimation of the random experimental error, which is in the range of 2.7 %–7.9 %, depending on the particular width and freestream velocity.

Using the averaged data, a general correlation is presented. The mass diffusion thickness from a plate of infinite lateral extent is used to normalize the width and lateral location. Experimental data from the widest strips are used to calculate the mass diffusion thickness. The correlation captured the main trends in the experimental data, with most of the error introduced from modeling the increase in the centerline St as the width narrows. The part of the correlation that modeled the change in the St near the lateral edge normalized by the centerline St worked well. The variation of the St near the edge is described by a power law, but the power law

is different than the one found for a laminar boundary layer with the same boundary conditions. The turbulent mixing acts to smooth out the effects of the lateral discontinuity, so the surface mass transfer approaching the edge does not increase as quickly as the surface heat transfer in a laminar boundary layer. Another way of stating the importance of the turbulent mixing: if the viscous sublayer is the dominant mechanism for lateral transport, the power law would be much closer to the power law described by laminar flow.

Finally, the spanwise extent of the lateral edge effect is quantified. While assumed in the construction of the general correlation of the local St, it is explicitly shown that the lateral edge effect is proportional to the diffusion thickness. This also means the extent of the lateral edge effect changes very slowly in the streamwise direction relative to a velocity boundary layer thickness. By comparing lateral locations where the St comes within 10 % of the centerline St, it is clear the spanwise extent of the lateral edge effect is proportional to the local diffusion thickness.

For a subliming surface of semi-infinite lateral extent, the lateral edge only affects the mass diffusion 10-15 conduction thicknesses in the spanwise direction. Similarly, if the full spanwise extent of the finite strip is greater than forty conduction thicknesses, the centerline mass transfer is unaffected by the lateral edges.

Chapter 5

Turbulent Flow Over Cavities

The flow field is modeled using the shear stress transport model in ANSYS CFX 2015 (Release 16.1) and matches previously published numerical and experimental data well. The three dimensional flow field has four main regimes: flow enters the cavity near the backward facing step (see fig. 5.1) and recirculation dominates the flow field, after the recirculation the flow is still entering the cavity and a corner vortex is evident near the sidewall, flow starts exiting the cavity as the boundary layer redevelops and the corner vortex dissipates, and the flow near the forward facing wall where a new recirculation region develops.

Mass transfer results from cavities ranging in depth from 0.254 mm to 8.84 mm for freestream velocities of about $10\,\mathrm{m\,s^{-1}}$ and $20\,\mathrm{m\,s^{-1}}$ are presented and discussed. The numerical results for the flow field account for most of the characteristics of the mass transfer except for mass transfer for the shallowest cavities. For the deeper cavities, the recirculation region near the backward facing step and redevelopment of the boundary layer account for the centerline streamwise changes in the mass transfer, while the vortex near the side wall accounts for the lateral changes in mass transfer. However, for very shallow cavities there is an increase in the mass transfer near the side wall in the apparent absence of a corner vortex indicating a similar transport

mechanism to that described in chapter 4 for turbulent flow over a flat plate. A sketch of the geometry is shown in fig. 5.1.

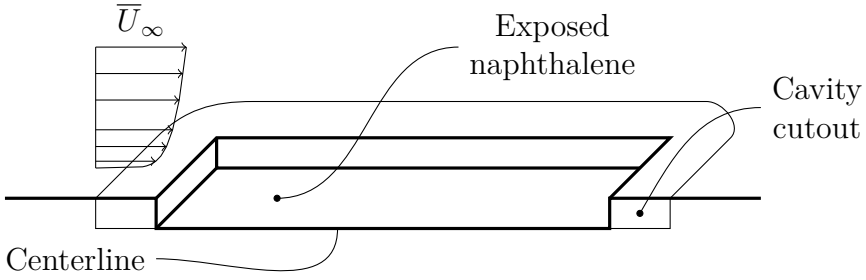

Figure 5.1: Sketch of the cavity geometry cut along the centerline of the cavity.

5.1 Flow Conditions

5.1.1 Numerical Simulations

Numerical simulations using ANSYS CFX 2015 (Release 16.1) are carried out to model the flow field for a subset of the experimental parameter space. The shear stress transport turbulent model, based on the model described by Menter (1992), is used for all numerical simulations. The shear stress transport model blends the k-ω in the inner part of the boundary layer with the k-ϵ towards the boundary layer edge. The turbulence numerics and advection scheme are both "high resolution" (as opposed to first order) and the convergence criteria is set to 1×10^{-6} RMS residual for all the equation classes. All other solver parameters are left as the default values. The properties for the numerical simulation, presented in table 5.2, are defined so the Pr is the same as the Sc for a naphthalene-air mixture at 300 K.

Table 5.1: Property values for numerical simulations.

Property	Value
Density	$1.161\,\mathrm{kg\,m^{-3}}$
Specific heat capacity	$1007\,\mathrm{J\,kg^{-1}\,K^{-1}}$
Dynamic viscosity	$18.54 \times 10^{-6}\,\mathrm{Pa\,s}$
Thermal conductivity	$0.008\,16\,\mathrm{W\,m^{-1}\,K^{-1}}$

Geometry and Boundary Conditions

The total streamwise length of the domain is 0.25 m, 0.05 m before the start of the cavity and 0.05 m past the end of the cavity. The inlet plane velocity and turbulent kinetic energy are specified as described below, while the outlet plane has an entrainment condition with a zero gradient specified for the turbulence quantities. The temperature of any inflow back into the domain is the average temperature of outgoing fluid. The total spanwise length of the domain is 0.08 m, 0.04 m into the cavity and 0.04 m past the cavity, with the bounding planes on either side set as symmetry planes. In the wall normal direction the total length of the domain is equivalent to the height of the test section shown in fig. 3.3. Except for the bottom of the cavity, all the walls are adiabatic with a no-slip condition. The bottom wall of the cavity is an isothermal wall with a no-slip condition.

As described below in section 5.1.2, the smallest grid cell is approximately $y^+ = 2$ (based on the inlet profile) with a cell aspect ratio of one for the two deepest cavities. The smallest cells are at the corners of the cavity and the inlet of the problem domain. In the two deepest cavities, the cell-to-cell expansion ratio is approximately 1.03. For the two smallest cavities, a cell size of $y^+ = 2$ is an appreciable fraction of the total depth, therefore the smallest grid cells are approximately $y^+ = 0.5$ (based on the inlet profile). For the smallest cavity depth the size of the cells is constant in the y direction, and for the second smallest cavity depth the cell-to-cell expansion ratio

in the y direction is approximately 1.03. The other two directions, spanwise and streamwise, have cell-to-cell expansion ratios of approximately 1.1.

Table 5.2: Geometry for numerical simulations.

Cavity Depth	Smallest Cell x (µm) × y (µm) × z (µm)	Total Nodes (-)	Nodes in Cavity (-)
0.254 mm	15.3 × 14.5 × 14.9	2 427 912	141 480
0.597 mm	15.3 × 14.5 × 14.8	2 545 812	259 380
2.29 mm	59.1 × 60.0 × 61.6	8 030 322	802 776
8.84 mm	59.1 × 60.0 × 61.3	9 273 330	2 045 784

Inlet

The inlet profile is specified from another two dimensional, flat plate, numerical simulation. The top and bottom boundaries are smooth walls while the side boundaries are symmetric. The height of the domain is equivalent to the height of the tunnel test section shown in fig. 3.3. The settings for the solver parameters are the same as for the cavity numerical simulation.

The profile is chosen so the momentum thickness Re and the shear stress are the same as indicated in tables 4.2 and 4.3 for a freestream velocity of around $10\,\mathrm{m\,s^{-1}}$. For an inlet speed of $10.5\,\mathrm{m\,s^{-1}}$ a profile taken 0.33 m from the leading edge has a Re_{δ_2} of 586 and a shear stress of 0.301 Pa.

5.1.2 Grid Independence Study

The grid independence study is completed on the geometry for the deepest cavity. Three grid sizes are used, a coarse mesh with the smallest grid cell $y^+ = 4$, a medium mesh with the smallest grid cell $y^+ = 2$, and a fine mesh with the smallest grid cell $y^+ = 1$. The wall coordinate scaling is based on the inlet velocity profile and the

smallest cells have an aspect ratio of one. The cell-to-cell expansion ratios are the same for all the grids and are equivalent to the values described above in section 5.1.1. The grid studies are conducted with the properties of air. Table 5.3 presents the estimated discretized error and fig. 5.2 and table 5.3 compare the shear stress of the different grids.

Roache (1994) and Celik et al. (2008) describe a method using Richardson Extrapolation to estimate the error of numerical simulations caused by mesh discretization. Three error measurements are presented in table 5.3: the approximate relative error, e_a, the extrapolated relative error, e_{ext}, and the grid convergence index, GCI. The approximate relative error is the relative error between the same quantity on different grids. The extrapolated relative error is the relative error between a quantity from a given grid and a higher order estimate of the quantity. The higher order estimate is found using Richardson Extrapolation on the results from the two finest grids. Finally, the grid convergence index is equivalent to the approximate relative error if the order of the numerical method is two and the ratio between the appropriate measure of the grid refinement factor is two. Note that the grid convergence index for the medium grid, GCI_{med}, presented in table 5.3, is calculated as described in Roache (1994),

$$GCI_{med} = r^{order} GCI_{fine}. \tag{5.1}$$

The grid refinement factor, r, is the ratio of the cube root of the appropriate volume measures. For the local error measurements, the volume measure is the volume of the local grid cell, and for the planar error measurements, the volume measure is the average volume of the grid cells adjacent to the wall. The values for the grid refinement factor for the results in fig. 5.2 and table 5.3 are 1.33 and 1.38 for the local error estimates and 1.43 and 1.46 for the planar error estimates, both larger than the

recommended value of 1.3 given by Celik et al. (2008).

Table 5.3: Estimated error of numerical simulations. The local error is estimated using maximum values on the heated surface and the planar error is estimated using average values on the heated plate. The finest grid is denoted by "1" and "fine", and the coarsest grid is denoted by "3". For the local error estimates the volumes are $2.248 \times 10^{-4}\,\mathrm{m}^3$, $2.995 \times 10^{-4}\,\mathrm{m}^3$, $4.131 \times 10^{-4}\,\mathrm{m}^3$. For the planar error estimates the volumes are $1.691 \times 10^{-4}\,\mathrm{m}^3$, $2.421 \times 10^{-4}\,\mathrm{m}^3$, and $3.523 \times 10^{-4}\,\mathrm{m}^3$. Note ϕ is a dummy variable.

	Local Error (Maximum)		Planar Error (Average)	
	Shear Stress	Heat Transfer	Shear Stress	Heat Transfer
ϕ_1	$2.90 \times 10^{-1}\,\mathrm{Pa}$	$7.17 \times 10^{3}\,\mathrm{W}$	$9.49 \times 10^{-2}\,\mathrm{Pa}$	$4.45 \times 10^{3}\,\mathrm{W}$
ϕ_2	$2.84 \times 10^{-1}\,\mathrm{Pa}$	$6.93 \times 10^{3}\,\mathrm{W}$	$9.25 \times 10^{-2}\,\mathrm{Pa}$	$4.40 \times 10^{3}\,\mathrm{W}$
ϕ_3	$2.83 \times 10^{-1}\,\mathrm{Pa}$	$7.00 \times 10^{3}\,\mathrm{W}$	$9.24 \times 10^{-2}\,\mathrm{Pa}$	$4.41 \times 10^{3}\,\mathrm{W}$
order	8.47	4.45	7.76	4.18
e_a^{21}	2.12 %	3.40 %	2.47 %	1.12 %
e_{ext}^{1}	0.20 %	1.30 %	0.16 %	0.32 %
e_{ext}^{2}	2.32 %	4.66 %	2.62 %	1.44 %
GCI_{fine}	0.26 %	1.64 %	0.20 %	0.40 %
GCI_{med}	2.91 %	5.90 %	3.29 %	1.80 %

Based on the error estimates presented in table 5.3, the "medium" mesh is used for the numerical simulations. The extrapolated relative error for the shear stress is approximately 2.5 %, indicating the medium mesh describes the flow field with reasonable accuracy, while taking significantly less time than the fine mesh to converge to a solution.

5.1.3 Flow Results for the Cavity

Reattachment Length

The reattachment length is a key parameter for describing the flow field and is often six to seven cavity depth lengths after separation for turbulent flows (Eaton and

Johnston 1981; Armaly et al. 1983). Table 5.4 presents several streamwise lengths of importance, and in particular, the reattachment length is within the normal range found in the literature. Furthermore, Eaton and Vogel (1985) state that the maximum St occurs approximately 0.1 reattachment lengths upstream of the flow reattachment based on their combined heat and fluid dynamic measurements. As the data presented in table 5.4 shows, this is true for the three deepest cavities modeled. Only the shallowest cavity does not meet this criterion, as the location of the maximum St is approximately 0.45 reattachment lengths downstream of the flow reattachment.

Table 5.4: Normalized lengths at the centerline of the various cavities. The four normalized quantities are the flow reattachment, x_r/d, secondary recirculation region, $x_{r,2}/d$, location of the maximum Stanton number, $x_{St_{max}}/d$, and the location of the maximum positive shear stress, $x_{\tau_{max}}/d$. The various lengths are normalized by the depths of the cavity, d.

Cavity Depth (mm)	x_r/d	$x_{r,2}/d$	$x_{St_{max}}/d$	$x_{\tau_{max}}/d$
0.254	6.13	—	8.85	93.21
0.597	7.34	—	7.09	56.36
2.29	6.49	1.05	5.88	30.06
8.84	6.35	1.37	5.37	10.34

Shear Stress

Figure 5.3 compares the numerical model to data from Eaton and Vogel (1985), Le et al. (1997), and Jovic and Driver (1994). In general, it is evident the flow is best described by the low Re flow studied by Le et al. (1997) and Jovic and Driver (1994), where $Re_h = 5000$, than the higher Re studied by Eaton and Vogel (1985), where $Re_h = 28\,000$, even though the ratio of the boundary layer and step height is similar to Eaton and Vogel (1985). In addition, it is clear the flow in the deepest cavity studied does not fully develop after the reattachment point.

Qualifying the shear stress does not directly affect the interpretation of the exper-

imental mass transfer results, as the heat and mass transfer more closely follow the turbulent kinetic energy than the shear stress profiles near the reattachment (Eaton and Vogel 1985; Avancha and Pletcher 2002). However, it is useful for qualifying the modeling of the flow field.

Streamlines

Figure 5.4 shows the streamlines of the average velocity in the centerline plane near the backward facing step. Streamlines in the recirculation regions, reattachment locations, and freestream are shown. The streamlines from the recirculation regions (and secondary recirculation regions for the two deeper cavities) are obvious as they intersect the cavities' bottom walls. The streamlines compare well to the experimental data of Kasagi and Matsunaga (1996) and the numerical data of Avancha and Pletcher (2002) and Chen et al. (2006). The center of the vortex is approximately $x/d = 3$ and $y/d = -0.4$ as found by Kasagi and Matsunaga (1996). Kasagi and Matsunaga (1996) also reported the secondary recirculation region ends at $x/d = 1.7$, which is larger than found for the present numerical results.

There are four flow regimes for the cavity flow, and figs. 5.5 to 5.10 show the characteristics of the distinct flow fields. At the start of the cavity, the flow separates from the wall surface, rushing into the cavity and forming a recirculation region against the backward facing step. After the recirculation region, the flow is still coming into the cavity, and a boundary layer starts to redevelop. In addition, there is a streamwise corner vortex along the sidewall. Next, the boundary layer redevelops, flow leaves the cavity, and the vortex dissipates. Last, the forward facing step at the end of the cavity causes flow separation and a recirculating region.

Figure 5.5 shows the basic flow patterns for the deepest cavity modeled. Near the backward-facing step is a secondary recirculation region. The streamlines in this

region move from the center of the cavity towards the side wall of the cavity. This is clear from the lateral in-plane streamlines in fig. 5.6a. Next, the flow enters the larger recirculation region and moves in the opposite direction. This is seen in fig. 5.7a showing the in-plane streamlines in the primary recirculation region, as the in-plane velocity vectors near the bottom wall are angled towards the center of the cavity.

The spiral shaped streamline in fig. 5.5 starts near the cavity sidewall corner, moves towards the center, curls back towards the cavity edge and eventually exits the cavity. This basic flow pattern is repeated for flow entering the cavity over the sidewall and is shown in figs. 5.8 to 5.10. This flow pattern is the source of the streamwise sidewall corner vortex, and as flow stops entering the cavity over the sidewall the streamwise sidewall corner vortical structure dissipates. Figure 5.10 is an example of the flow field when all the flow is out of the cavity and the sidewall vortex has dissipated.

If one inspects the in-plane velocity vectors figs. 5.9 and 5.10, a small secondary recirculation region near the sidewall corner is evident. For example, in fig. 5.10, the secondary recirculation region extends about 0.4 cavity depths from the sidewall and 0.1 cavity depths up from the bottom wall.

Table 5.5 presents the estimated normalized streamwise location of the vortex dissipation. As evident by figs. 5.6 to 5.10, the sidewall vortex transports both cooler and less energetic fluid from the freestream, affecting the thermal boundary layer and turbulent transport near the cavity side wall. The effect of the dissipation of the sidewall vortex on the heat and mass transfer is explored in section 5.2.

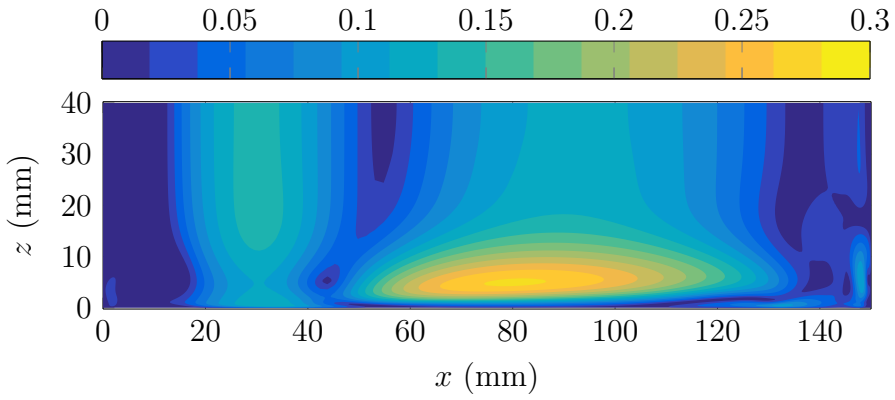

(a) Coarse grid

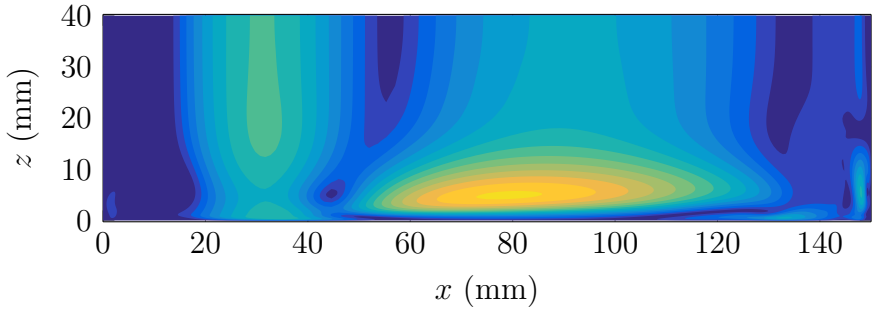

(b) Medium grid

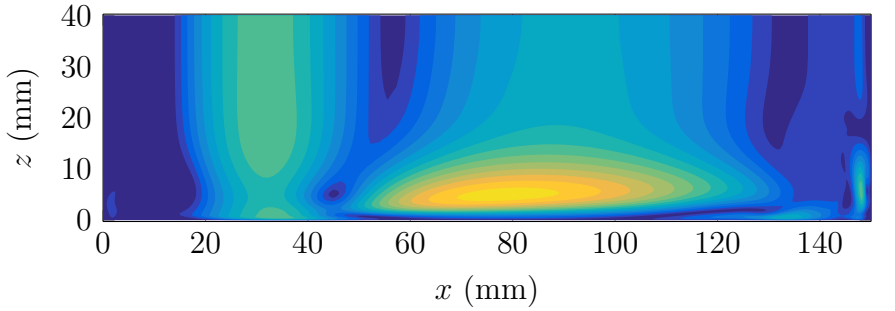

(c) Fine grid

Figure 5.2: Wall shear stress for grid independence study

Table 5.5: Estimates for vortex dissipation location. Location is given as a range, reflecting the discrete nature of the numerical grid.

Cavity Depth (mm)	x_v (m)	x_v/d	x_v/x_r
0.254	0.0423–0.0465	166–183	27.2–29.9
0.597	0.0620–0.0682	104–114	14.1–15.6
2.29	0.0947–0.0964	41.4–42.1	6.37–6.48
8.84	0.107–0.108	12.1–12.2	1.90–1.93

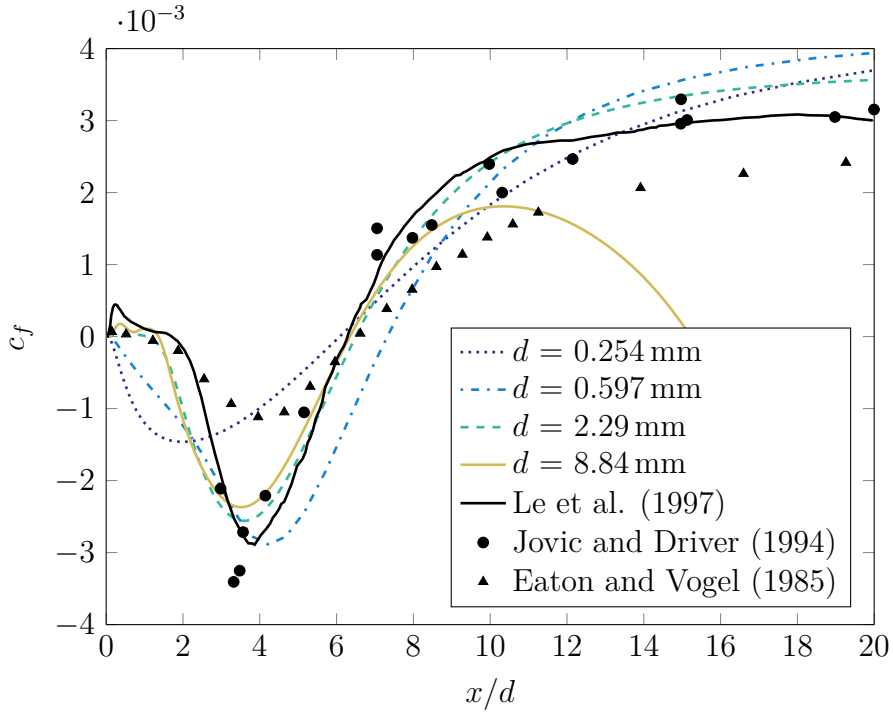

Figure 5.3: Comparison of the numerically calculated skin friction coefficient with experimental data from Eaton and Vogel (1985) and Jovic and Driver (1994) and numerical data from Le et al. (1997).

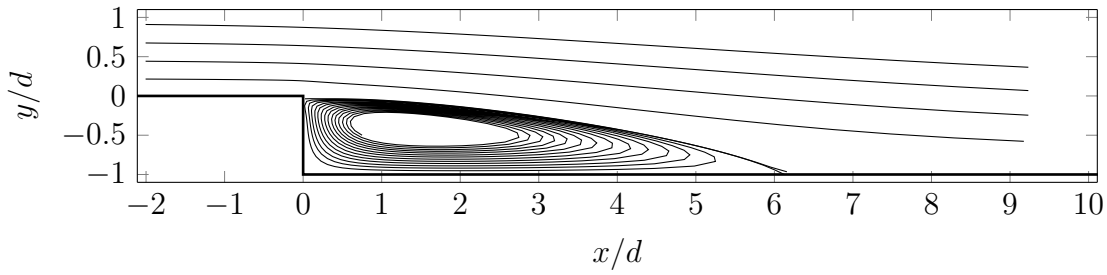

(a) 0.254 mm deep cavity

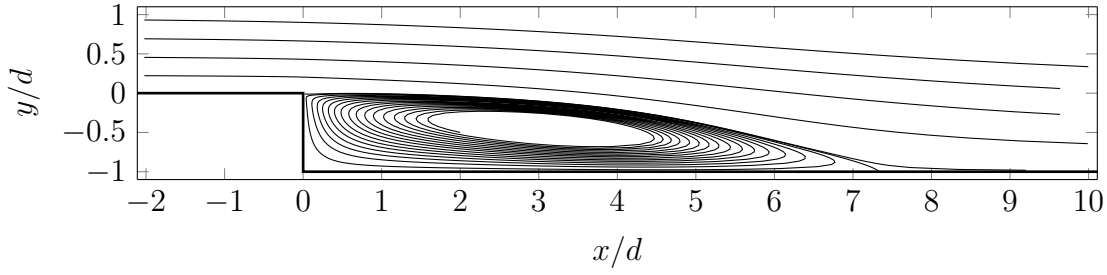

(b) 0.597 mm deep cavity

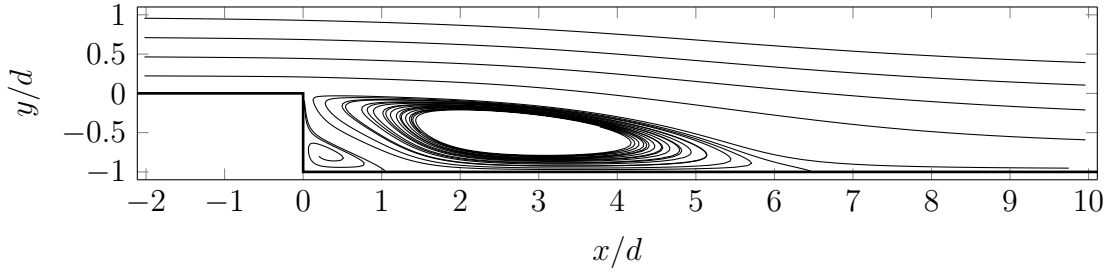

(c) 2.29 mm deep cavity

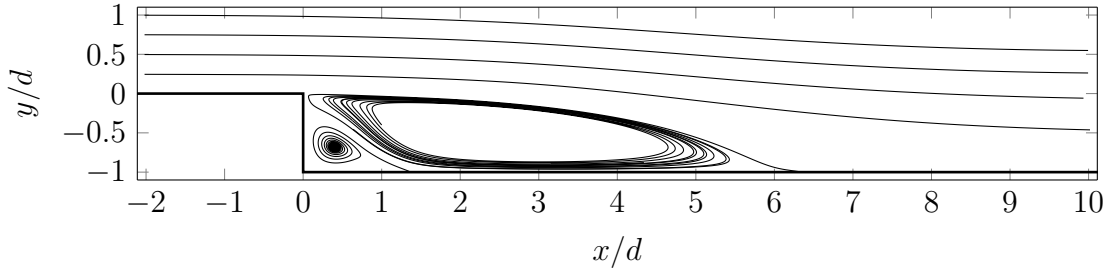

(d) 8.84 mm deep cavity

Figure 5.4: Streamlines near the backward facing step for the cavities modeled.

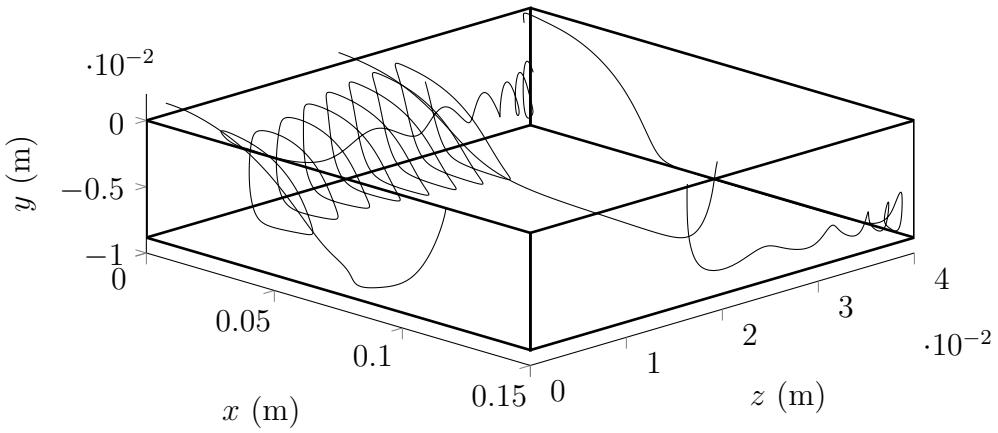

Figure 5.5: Three dimensional streamlines for 8.84 mm deep cavity with a viewing azimuth and elevation of 45°. The streamline starting in corner near the backward facing step travels along the bottom of the cavity and enters the recirculating flow region near the forward facing step. The other streamlines are described at length in the text.

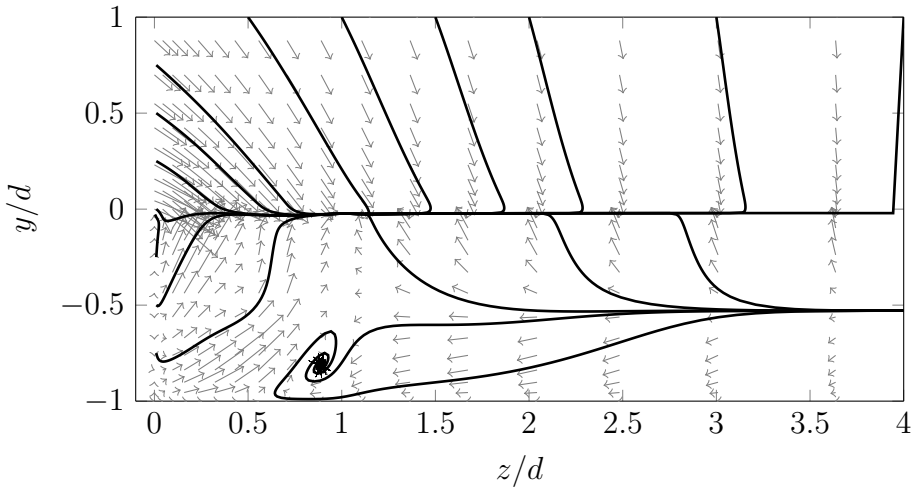

(a) In-plane streamlines and velocity vectors

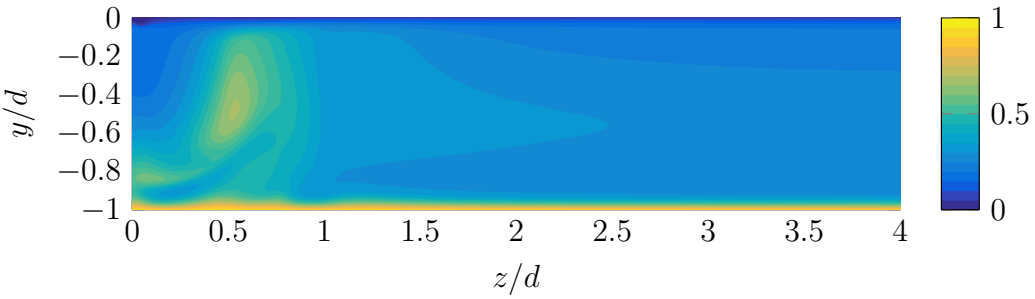

(b) Filled non-dimensional temperature contour, $(T - T_w) / (T_\infty - T_w)$

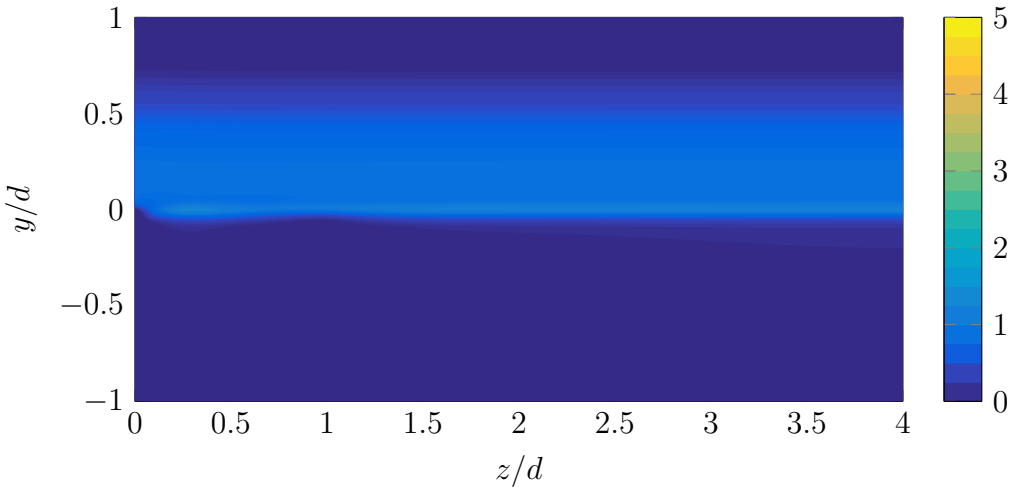

(c) Filled contour of the normalized turbulent kinetic energy, $k/k_{max,inlet}$

Figure 5.6: Flow information in the z-y plane near the backward facing step, $x = 2.96 \times 10^{-3}$ m, $x/d = 0.335$

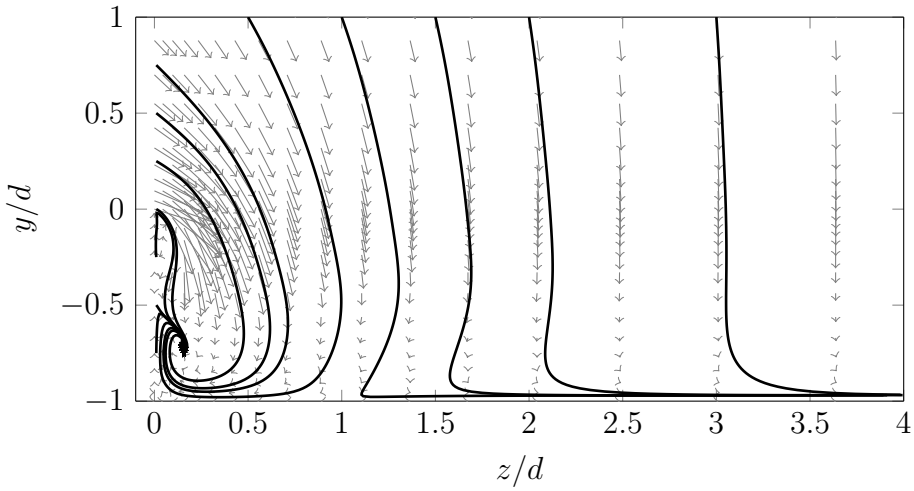

(a) In-plane streamlines and velocity vectors

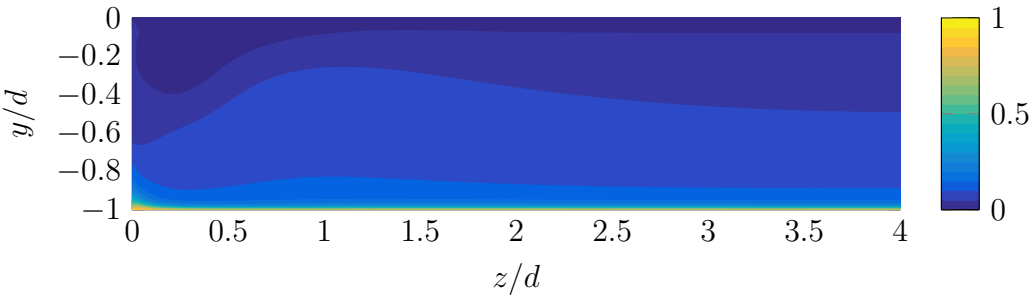

(b) Filled non-dimensional temperature contour, $(T - T_w) / (T_\infty - T_w)$

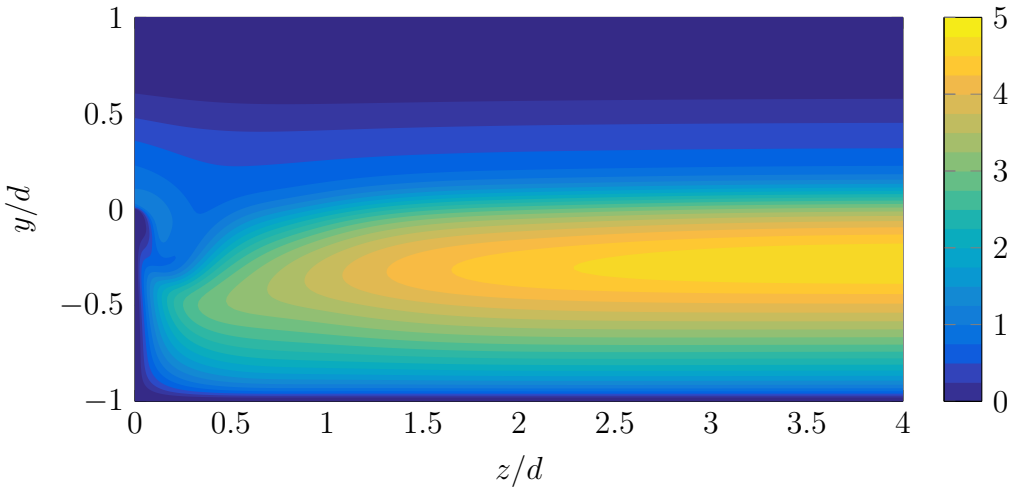

(c) Filled contour of the normalized turbulent kinetic energy, $k/k_{max,inlet}$

Figure 5.7: Flow information in the z-y plane in the primary recirculation region, $x = 0.0297\,\text{m}$, $x/d = 3.36$

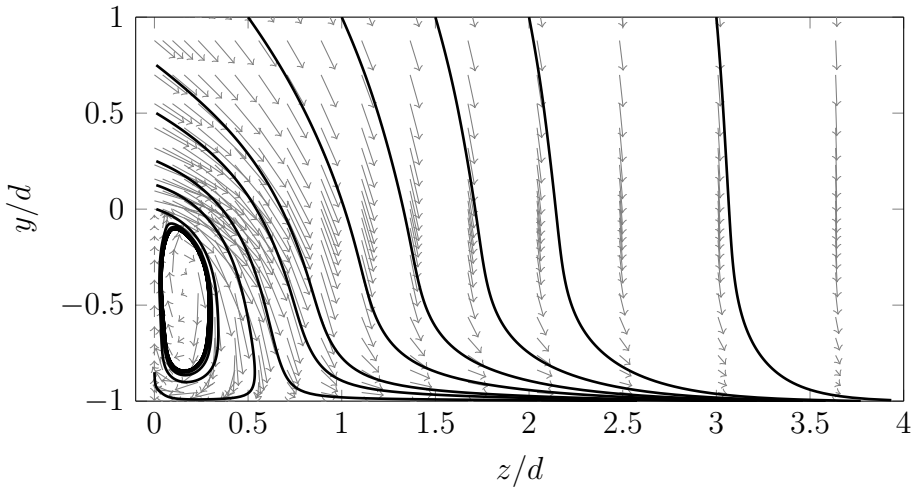

(a) In-plane streamlines and velocity vectors

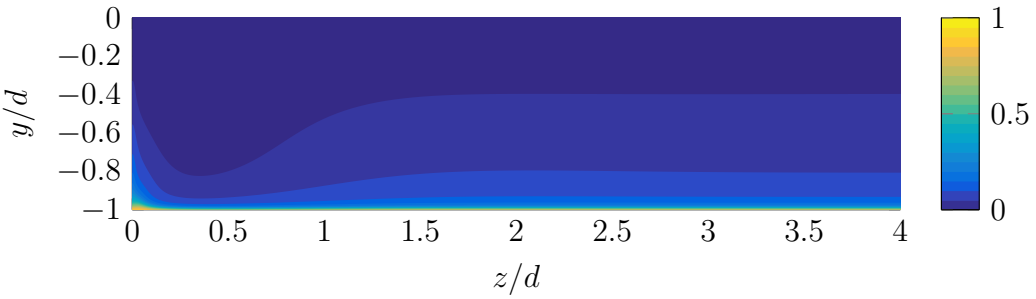

(b) Filled non-dimensional temperature contour, $(T - T_w) / (T_\infty - T_w)$

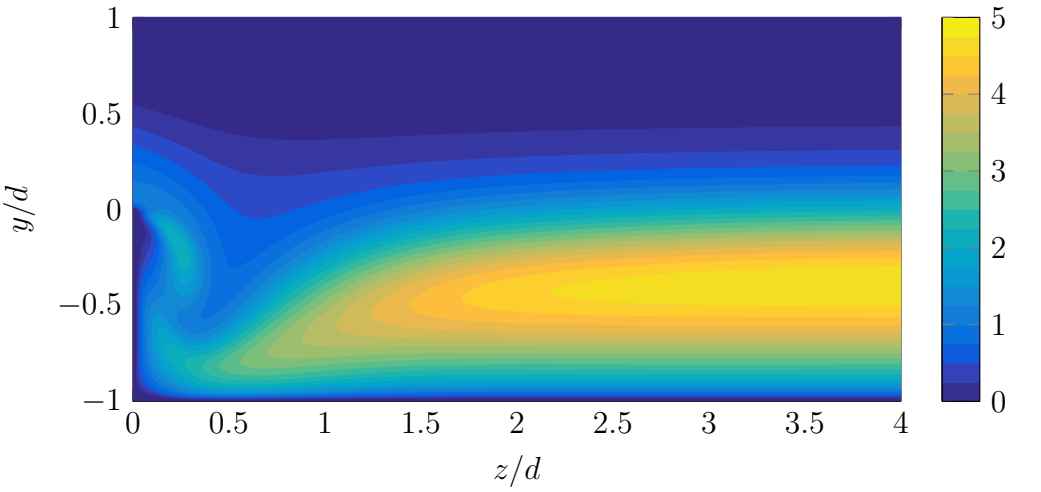

(c) Filled contour of the normalized turbulent kinetic energy, $k/k_{max,inlet}$

Figure 5.8: Flow information in the z-y plane near the reattachment point, $x = 0.0504\,\text{m}$, $x/d = 5.70$

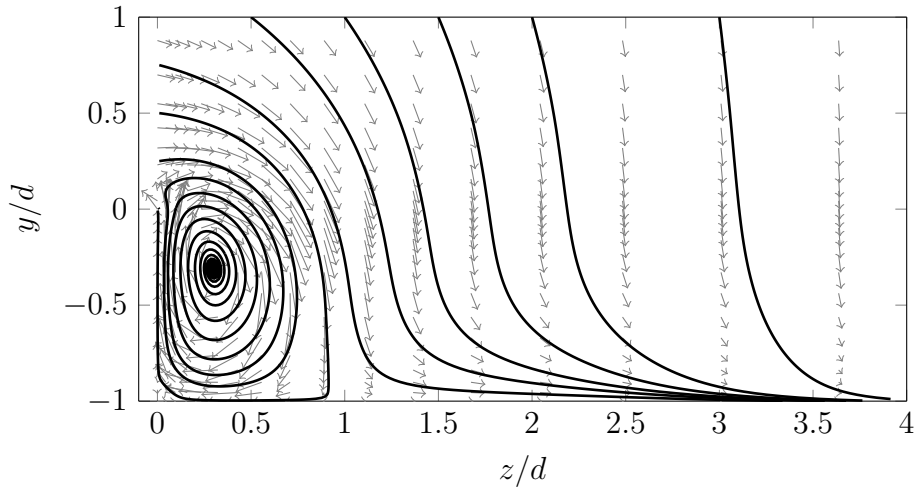

(a) In-plane streamlines and velocity vectors

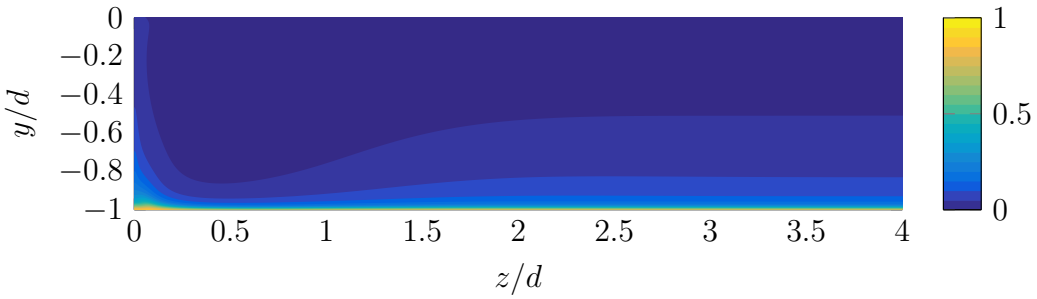

(b) Filled non-dimensional temperature contour, $(T - T_w) \,/\, (T_\infty - T_w)$

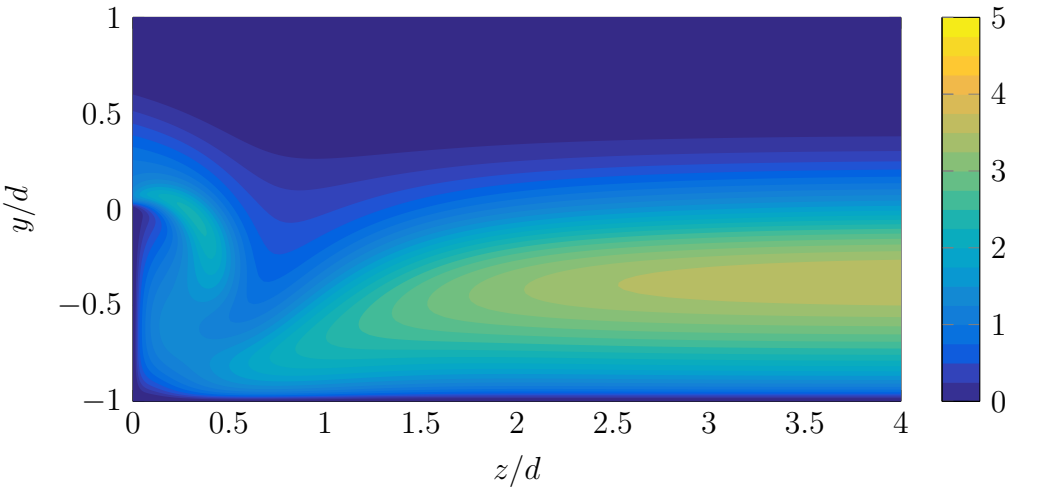

(c) Filled contour of the normalized turbulent kinetic energy, $k/k_{max,inlet}$

Figure 5.9: Flow information in the z-y plane after flow reattachment, $x = 0.075\,\text{m}$, $x/d = 8.48$

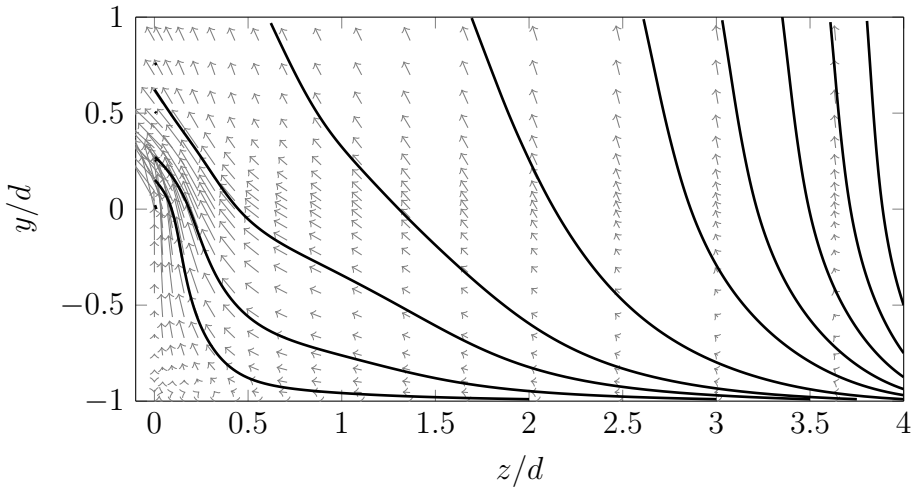

(a) In-plane streamlines and velocity vectors

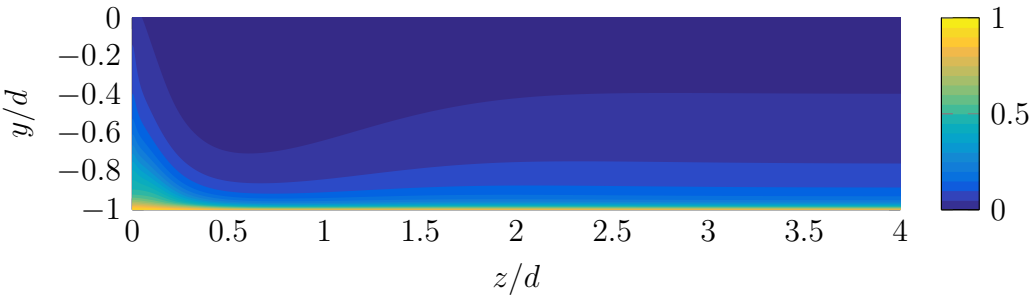

(b) Filled non-dimensional temperature contour, $(T - T_w) / (T_\infty - T_w)$

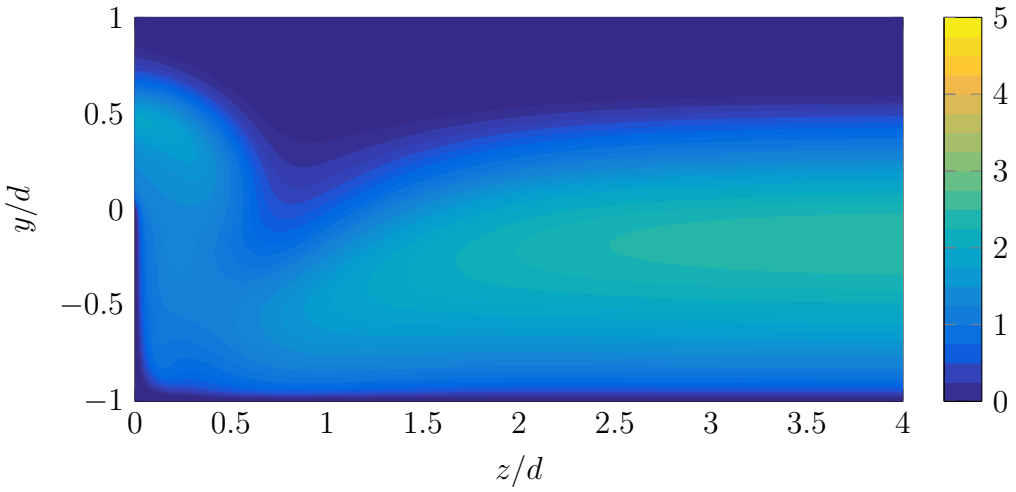

(c) Filled contour of the normalized turbulent kinetic energy, $k/k_{max,inlet}$

Figure 5.10: Flow information in the z-y plane after flow reattachment, $x = 0.12\,\text{m}$, $x/d = 13.6$

5.2 Mass Transfer

5.2.1 Data Averaging

A method similar, but not identical, to the data averaging described in section 4.2.1 is used for the cavity data. The centerline data from repeat experiments are averaged using the cubic smoothing spline technique, as outlined in section 3.5.2. The averaged centerline data are shown in figs. 5.11, 5.12, 5.21 to 5.24 and E.57 to E.64 and the normalized St are shown in figs. 5.25 to 5.28 and E.65 to E.74. The data in table 5.6 list the estimated uncertainty of the averaged centerline mass transfer measurements.

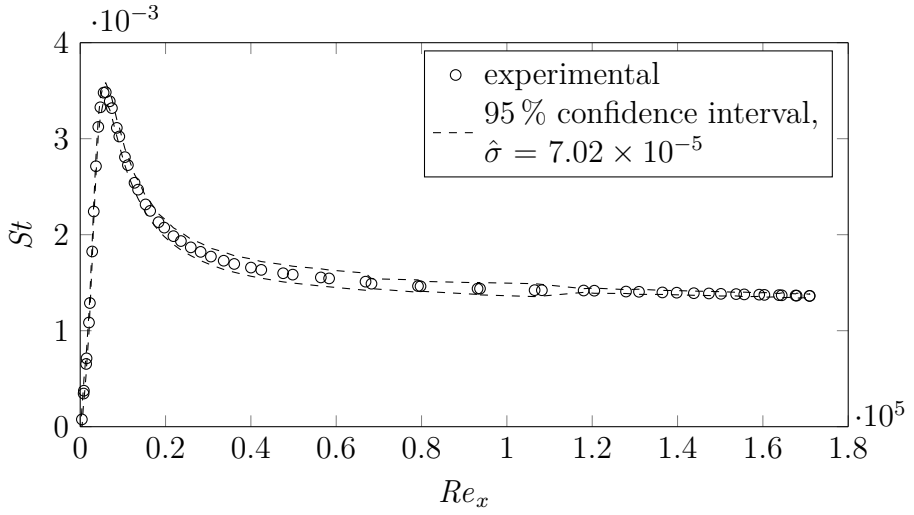

Figure 5.11: Centerline mass transfer between experimental results and numerical simulation for $U_\infty \sim 20\,\mathrm{m\,s^{-1}}$ and $d = 0.254\,\mathrm{mm}$

The lateral data from several experiments are not averaged together as they are for the flat plate data, as the measurement grids for a given freestream velocity and width change from experiment to experiment. However, while the data from different experimental runs for the same freestream velocity and width are not averaged together, the lateral data for a given experimental run is averaged across the centerline using a cubic smoothing spline. This allows for an estimate of the random experi-

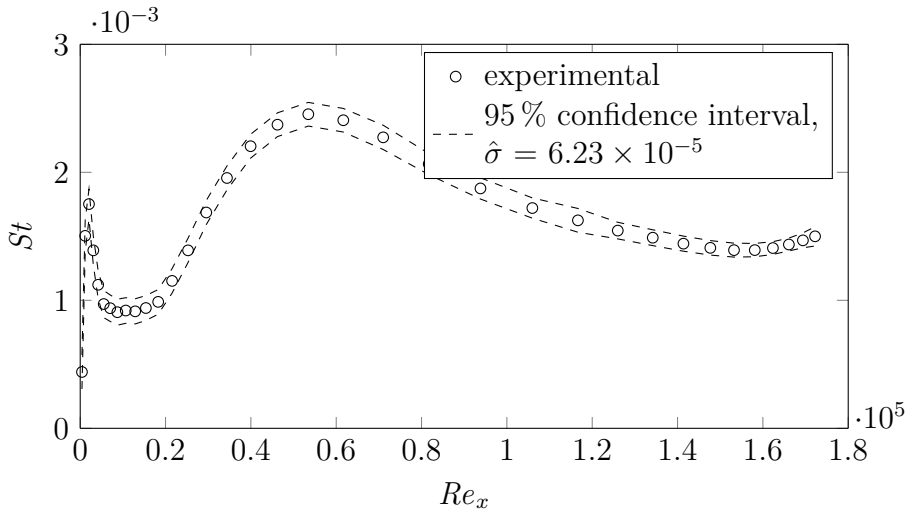

Figure 5.12: Centerline mass transfer between experimental results and numerical simulation for $U_\infty \sim 20\,\mathrm{m\,s^{-1}}$ and $d = 8.84\,\mathrm{mm}$

mental error based on the symmetry of the data. Some examples of this process are shown in figs. 5.13 and 5.14.

Table 5.7 presents the estimated random uncertainty from lateral averaging for all the depths and free stream velocities studied. When calculating the estimated random uncertainty, a one-sided generalized extreme Studentized deviate procedure (Rosner 1983) is used on the data to remove the rather large uncertainties occurring near the backward facing step of the cavity. The large streamwise gradients of the surface mass flux near the backward facing step amplify errors resulting from alignment mismatches between the cavity cutout and x-y table. Furthermore, the focus of the experiments is studying lateral changes in mass transfer, particularly when the lateral mass transfer profile approach the described profiles in chapter 4. As the separated flow near the backward facing step has a very different flow structure than flat plate turbulent flow, the neglect of the errors in the separated flow region is presently unimportant.

The final step outlined in section 4.2.1 for calculating an average local St is multiplying the normalized lateral average St and the average centerline St. As the lateral

Table 5.6: Estimated random uncertainty from turbulent cavity experiments using eq. (3.44) for smoothing the centerline St.

	$10\,\mathrm{m\,s^{-1}}$		$20\,\mathrm{m\,s^{-1}}$	
Cavity depth (mm)	Estimated standard deviation	Estimated percent error	Estimated standard deviation	Estimated percent error
0.254	1.96×10^{-5}	1.06	7.02×10^{-5}	4.08
0.401	8.97×10^{-5}	5.01	1.98×10^{-4}	10.4
0.597	8.23×10^{-5}	4.41	7.52×10^{-5}	4.18
0.96	9.33×10^{-5}	4.73	8.16×10^{-5}	4.57
2.29	1.35×10^{-4}	6.77	2.18×10^{-5}	1.29
4.32	3.08×10^{-6}	0.158	5.22×10^{-5}	3.40
8.84	4.05×10^{-5}	2.17	6.23×10^{-5}	4.16

profile for the St scales with the centerline St, this approach is natural. However, the same scaling is not expected for separated flow. Therefore, the difference between the measured centerline value and smoothed centerline value is subtracted from the laterally smoothed St profile, shifting the lateral St profile up (or down) to match the averaged centerline St. Figures 5.13 and 5.14 show this correction as the difference between the dashed and solid lines.

If the final estimate of the St is

$$\hat{St} = St + (St_{c,css} - St_c)\,, \tag{5.2}$$

then the total random experimental uncertainty is

$$\begin{aligned} \hat{\sigma_{St}}^2 &= \left(\frac{\partial \hat{St}}{\partial St}\hat{\sigma}_{St}\right)^2 + \left(\frac{\partial \hat{St}}{\partial St_{c,css}}\hat{\sigma}_{St_{c,css}}\right)^2 + \left(\frac{\partial \hat{St}}{\partial St_c}\hat{\sigma}_{St}\right)^2 + \frac{\partial \hat{St}}{\partial St}\frac{\partial \hat{St}}{\partial St_c}\hat{\sigma}_{St}^2 \\ &= \hat{\sigma}_{St}^2 + \hat{\sigma}_{St_{c,css}}^2. \end{aligned} \tag{5.3}$$

The last term in the first equation arises from the correlation of the error between

Table 5.7: Estimated random uncertainty from turbulent cavity experiments using eq. (3.44) for smoothing the St symmetry across centerline of cavity.

	$10\,\mathrm{m\,s^{-1}}$		$20\,\mathrm{m\,s^{-1}}$	
Cavity depth (mm)	Estimated standard deviation	Estimated percent error	Estimated standard deviation	Estimated percent error
0.254	3.31×10^{-4}	17.9	5.14×10^{-5}	3.05
0.401	6.67×10^{-5}	3.69	8.49×10^{-5}	4.50
0.597	8.85×10^{-5}	4.61	8.34×10^{-5}	4.61
0.96	7.58×10^{-5}	3.87	8.53×10^{-5}	4.85
2.29	5.51×10^{-5}	2.77	1.19×10^{-4}	7.14
4.32	1.24×10^{-4}	6.41	1.31×10^{-4}	8.52
8.84	8.43×10^{-5}	4.80	9.80×10^{-5}	7.03

the centerline and the error of the lateral averaging. It is assumed the centerline St and St share the same error and are therefore perfectly correlated with each other. The circumflex over the St, denoting an estimated value, is dropped for the rest of the chapter. All presented St are understood as best estimates given the data.

Table 5.8 lists the total estimated random uncertainty for the turbulent cavity experiments. With the exception of the shallowest cavity at the lowest freestream velocity, the uncertainties are between 5 % and 11 %.

5.2.2 Results

The wind tunnel is run at about $10\,\mathrm{m\,s^{-1}}$ and $20\,\mathrm{m\,s^{-1}}$, so the boundary layer measurements and parameters are the same as presented and discussed in section 5.1. A list of all experiments with basic information is presented in table 5.9, while the average parameters for a given freestream velocity and cavity depth are presented in table 5.10. Two freestream velocities and seven cavity depths are tested, giving a cavity depth Re range of 165–11 000 and depths ranging from almost the size of the viscous sublayer to the size of the boundary layer.

Table 5.8: Total estimated random uncertainty from turbulent cavity experiments using eq. (3.44) evaluated using eq. (5.3) and data from tables 5.6 and 5.7.

	$10\,\mathrm{m\,s^{-1}}$		$20\,\mathrm{m\,s^{-1}}$	
Cavity depth (mm)	Estimated standard deviation	Estimated percent error	Estimated standard deviation	Estimated percent error
0.254	3.32×10^{-4}	17.9	8.70×10^{-5}	5.16
0.401	1.12×10^{-4}	6.19	2.16×10^{-4}	11.4
0.597	1.21×10^{-4}	6.29	1.12×10^{-4}	6.20
0.96	1.20×10^{-4}	6.13	1.18×10^{-4}	6.71
2.29	1.46×10^{-4}	7.30	1.21×10^{-4}	7.24
4.32	1.24×10^{-4}	6.42	1.41×10^{-4}	9.14
8.84	9.35×10^{-5}	5.33	1.16×10^{-4}	8.33

Figures 5.39c, 5.40c, 5.41c, 5.42c and E.75 to E.95 show the contours of all the averaged experimental data, figs. 5.43 to 5.56 show normalized lateral St profiles at various streamwise locations against the lateral location normalized by the centerline diffusion thickness, ζ_m^*, figs. 5.19, 5.20 and E.96 to E.107 show lateral profiles of the St for all the averaged data at various streamwise locations, and figs. E.108 to E.121 show lateral profiles of the St normalized by the centerline St against the lateral location normalized by the cavity depth, z/d.

Not all the recorded data are presented. There are obvious cases of asymmetry or cases where the cavity cutout is not flush with the naphthalene surface. Data that are obviously egregious are not presented or considered further. However, as figs. 5.15 to 5.18 show, there are no experimental data for cavity depths of 0.597 mm that are acceptable. It is clear that the cavity cutout is not flush with the naphthalene surface, causing abnormally large mass fluxes near the cavity side walls and asymmetry across the centerline of the cavity. However, even though the lateral profile is viewed with some skepticism, the centerline data are still presented and discussed.

Table 5.9

Date and time	Cavity Depth (mm)	$\overline{U}_\infty$ ($\mathrm{m\,s^{-1}}$)	Sc (-)
2016-07-18T22	8.84	10.3	2.29
2016-07-20T13	8.84	10.3	2.29
2016-07-24T14	4.32	10.4	2.29
2016-07-27T12	2.29	10.3	2.29
2016-07-28T20	2.29	10.3	2.29
2016-07-29T13	0.960	10.2	2.29
2016-08-03T10	0.960	10.4	2.29
2016-08-07T11	0.597	10.4	2.29
2016-08-08T22	0.597	10.1	2.29
2016-08-09T13	0.401	9.98	2.29
2016-08-14T16	0.401	10.5	2.29
2016-08-15T17	0.254	10.6	2.29
2016-07-18T13	8.84	20.2	2.29
2016-07-24T22	4.32	20.0	2.29
2016-07-25T14	4.32	20.2	2.29
2016-07-27T20	2.29	20.0	2.29
2016-07-28T12	2.29	20.0	2.29
2016-08-01T13	0.960	20.1	2.29
2016-08-01T22	0.960	20.1	2.29
2016-08-07T18	0.597	20.3	2.29
2016-08-08T11	0.597	20.2	2.29
2016-08-13T10	0.401	20.2	2.29
2016-08-13T22	0.401	20.3	2.29
2016-08-17T23	0.254	20.2	2.29
2016-08-18T20	0.254	20.1	2.29

Comparison of Experimental Data with Numerical Simulations

Figures 5.21 to 5.28 compare the measured centerline St to the estimates of the centerline St from the numerical simulations described in section 5.1. While various flow parameters from the numerical simulation, such as the reattachment length, structure of the recirculating region, and shear stress, matched published results well, and the general trends of the experimental mass transfer and numerical heat transfer results are similar; it is evident the numerical heat transfer and experimental mass

Table 5.10: Flow parameters

	$10\,\mathrm{m\,s^{-1}}$			$20\,\mathrm{m\,s^{-1}}$		
Cavity Depth (mm)	d^+ (-)	Re_d (-)	$\overline{U}_\infty$ $\mathrm{m\,s^{-1}}$	d^+ (-)	Re_d (-)	$\overline{U}_\infty$ $\mathrm{m\,s^{-1}}$
8.84	287	5590	10.3	527	11 000	20.2
4.32	142	2770	10.4	255	5350	20.1
2.29	73.9	1450	10.3	135	2830	20.0
0.960	31.0	610	10.3	56.7	1180	20.1
0.597	19.2	369	10.2	35.5	743	20.2
0.401	12.9	260	10.2	24.0	500	20.3
0.254	8.45	165	10.6	15.0	312	20.1

transfer results do not match. A somewhat better match is found by normalizing the streamwise location by the location of the maximum St and normalizing the St by the maximum St number; but the heat transfer results from the numerical simulations of the cavity are clearly untrustworthy and are not depended on for physical understanding of the experimental results. This is not surprising as Avancha and Pletcher (2002) noted, Reynolds averaged Navier-Stokes "have proved generally inadequate at predicting the effects of turbulent separating and reattaching flows with heat transfer". Note the data do not collapse to a single curve when normalized by the location of the maximum St and the maximum St.

Figure 5.29 shows how the centerline maximum St and global maximum St location change with step height. Eaton and Vogel (1985) and Lan et al. (2009) noted the flow near the reattachment location behaved similar to an impinging jet, however, for Re_d less than 1000, the scaling of the maximum St changes, as shown in fig. 5.29. This indicates turbulent impingement does not describe the mass transfer near the location of the maximum St for the shallower cavities studied. While the smaller step heights are approaching the size of the viscous sublayer, they do not approximate the maximum Sh_d of laminar flow (Kondoh et al. 1993), as shown in fig. 5.31, either.

Further evidence of a different flow regime for shallow cavities is shown in fig. 5.30. As discussed in section 5.1.3, the reattachment length and location of the maximum St are generally assumed invariant for changing step Re. However, the normalized location of the maximum St is larger for smaller step Re.

If the numerical modeling of the flow is generally correct for the shallow cavities, the mass flux is largely divorced from the flow reattachment location. As table 5.11 shows, the location of the maximum centerline St is 16 to 19 step heights from the backward facing step. This is much smaller than the location of the maximum shear stress presented in table 5.4, but is tending in that direction. This implies the mass transfer has characteristics of both turbulent flow over a flat plate and turbulent separated flow, as the Reynolds analogy seems to be more useful for the very small cavity depths tested.

Table 5.11: Normalized lengths for the experimental data for the various cavities. The two normalized quantities are the centerline and global location of the maximum Stanton number, $x_{St_{max}}/d$. The lengths are normalized by the cavity depth, d.

	$10\,\mathrm{m\,s^{-1}}$		$20\,\mathrm{m\,s^{-1}}$	
Cavity depth (mm)	centerline $x_{St_{max}}/d$	global $x_{St_{max}}/d$	centerline $x_{St_{max}}/d$	global $x_{St_{max}}/d$
0.254	18	10.8	18.7	13.6
0.401	16.5	9.15	11.9	9.59
0.597	11.6	7.79	8.25	6.28
0.96	9.32	7.51	6.58	6.16
2.29	5.38	4.5	4.49	3.86
4.32	4.25	4.02	4.39	3.37
8.84	4.36	3.63	4.97	4.2

Reynolds Analogy

It is well known (Eaton and Vogel 1985; Avancha and Pletcher 2002) that the Reynolds analogy fails for separated flows over a backward facing step and that the fluctuating

skin friction coefficient is a better predictor of the mass transfer in the separated flow region. As a steady state shear stress transport model is used, fluctuating quantities are not available, however, the turbulent kinetic energy near the wall can serve as a proxy for the fluctuating skin friction coefficient. Figures 5.39 to 5.42 compare the skin friction coefficient, turbulent kinetic energy, and the St for the bottom surface of the cavity. In the separation region and near the reattachment location, the St correlates with the turbulent kinetic energy near the wall, and does not correlate with skin friction coefficient.

However, neither the skin friction coefficient nor turbulent kinetic energy correlates with the St near the side wall. As Eaton and Vogel (1985) noted, the St is related to the thickness of the thermal boundary layer, even in the reattachment and recirculation regions. It is clear for the deeper cavities, as shown in figs. 5.7b, 5.8b, 5.9b and 5.10b, the sidewall vortex brings cooler air into the cavity, locally depressing the size of the thermal boundary layer, and increasing the St near the side wall.

In contrast, for the shallow cavities show no local depression of the thermal boundary layer in regions where the St is large, as shown in figs. 5.37a and 5.38a. For both the deep cavities, as shown in figs. 5.7c, 5.8c, 5.9c and 5.10c, and for the shallow cavities, as shown in figs. 5.37b and 5.38b, the turbulent kinetic energy does not increase near the sidewall. An explanation for the increase in the St near the sidewall for the smallest cavities is given below.

5.2.3 Lateral St Profile

Deep Cavities

For the deepest cavities, shown in figs. 5.43 to 5.48, the influence of the flow patterns discussed in section 5.1.3 is evident. Near the sidewall the St increases as much as

30 % over the centerline value in the presence of the sidewall vortex. Overall, the large sidewall corner vortex causes an increase in the lateral St profile one to three cavity depths into the subliming surface before it dissipates. The reason for the increase in the mass flux near from the sidewall vortex is clear from figs. 5.8 and 5.9: the sidewall corner vortex brings pure air from the freestream close to the wall, locally depressing the concentration boundary layer.

Table 5.5 presents estimates for the location of vortex dissipation based on numerical modeling of the cavity. Comparing these values to the profiles in figs. 5.43 and 5.45, it is evident the location of the vortex dissipation coincides with the flattening of the lateral St profiles. After the dissipation of the sidewall vortex, the lateral St profiles are relatively flat for most of the cavity width until the immediate presence of the sidewall forces the mass flux towards zero. The lack of large scale fluid motion or increased turbulent kinetic energy compared to the center of the cavity near the side wall results in mass fluxes no greater than the mass transfer near the centerline. These trends are evident in figs. 5.43 to 5.48. In addition, the influence of the secondary recirculation near the sidewall corner is evident in figs. 5.43 to 5.48.

Shallow Cavities

The lateral profile for the mass transfer has many of the same characteristics as the deeper cavities. There is increased mass transfer in the presence of the sidewall vortex and a gradual lessening of the lateral peak as the vortex dissipates. While the lateral profile of the mass transfer bears many similarities to the lateral profiles from the deeper cavities, there is one significant difference. Instead of disappearing altogether, the peak shifts and changes shape. Indeed, the lateral profile, as shown in figs. 5.49, 5.50, 5.53 and 5.54, approximates eq. (4.20) from flat plate mass transfer.

It is conceivable that the behavior of the shallowest cavities, shown in figs. 5.49,

5.50, 5.53 and 5.54, is due to the sidewall corner vortex. However, this explanation is unlikely for two reasons. First, based on the values from tables 5.5 and 5.11, the lateral increase persists far longer than the numerical simulation indicates the sidewall corner vortex lasts. For the smallest cavity depth, the numerical simulation indicates the vortex persists for about 180 cavity depth heights downstream of the step, while the lateral profiles in fig. 5.49 are presented up to 540 step heights downstream of the backward facing step. Second, the full extent of the presumed lateral edge effect is a relatively constant 10-15 conduction thicknesses, the same lateral distance shown in figs. 4.42 and 4.43a. Contrast this behavior to the deeper cavities, shown in figs. 5.43 to 5.48, where the effect of the primary sidewall corner vortex decreases visibly in the streamwise direction, leaving a relatively flat lateral St profile.

Based on the numerical simulations, the mass transfer measurements, and the arguments presented above, the lateral changes in mass transfer exhibit the characteristics of the profiles discussed in section 4.2 about 200 cavity lengths downstream when a given cavity is less than 25 wall coordinates (i.e. normalized by the friction velocity and kinematic viscosity) deep. Any specified range of cavity lengths less than 200, and it is probable the lateral increase near the lateral cavity wall is caused by the sidewall corner vortex. While claiming cavity depths of 0.597 mm exhibit the lateral mass transfer behaviors typical of flat plates would increase the range of cavity depths to about 35 in wall coordinates, there are some clear problems in the symmetry of the data that undermine confidence in ascribing that large a range of cavity depths. However, specifying $x/d > 200$ and $d^+ < 25$ is the conservative estimate based on the experimental and numerical data. More generous ranges could be prescribed if better numerical flow models are employed.

Based on the value of the exponent shown in eq. (4.19d), the discussion in section 4.2.4 explored the idea that turbulent mixing in the boundary layer is the main

mode of lateral transport. Therefore, if the lateral profile of the mass transfer approximates the profile from a flat plate, the cavity depth is below the region where most of the lateral turbulent transport occurs.

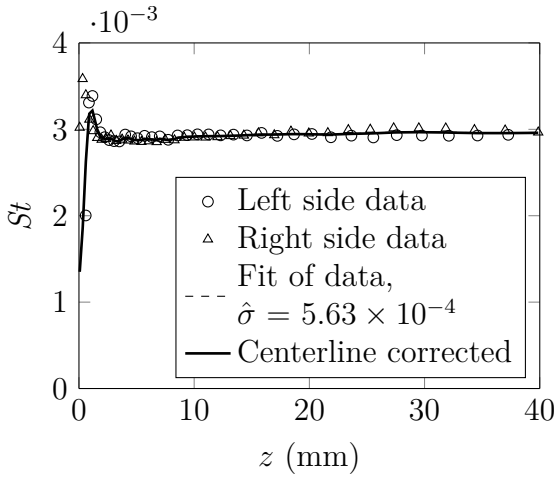

(a) Lateral averaging for $d = 0.254\,\mathrm{mm}$ at $x = 4.59\,\mathrm{mm}$

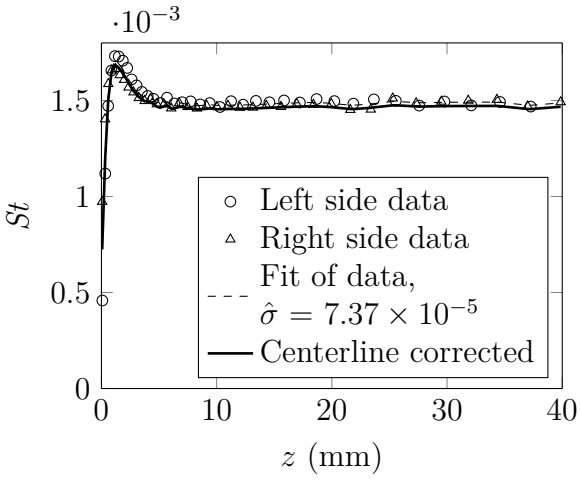

(b) Lateral averaging for $d = 0.254\,\mathrm{mm}$ at $x = 97.1\,\mathrm{mm}$

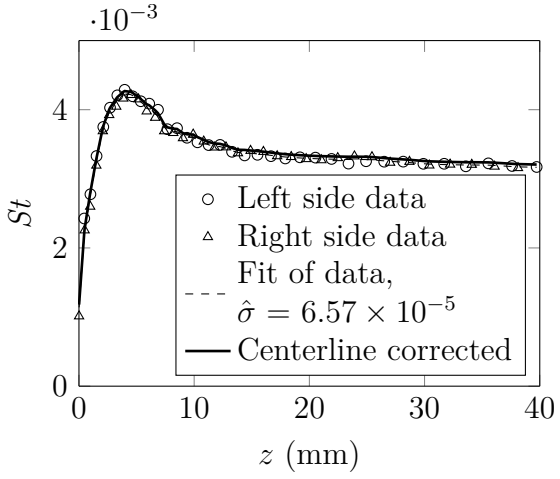

(c) Lateral averaging for $d = 8.84\,\mathrm{mm}$ at $x = 37.2\,\mathrm{mm}$

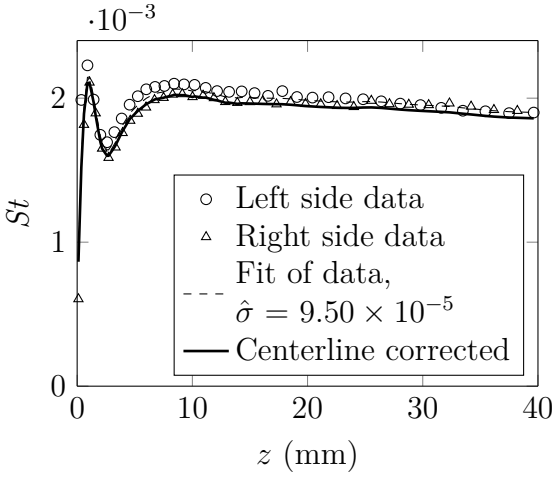

(d) Lateral averaging for $d = 8.84\,\mathrm{mm}$ at $x = 101\,\mathrm{mm}$

Figure 5.13: Lateral averaging across the cavity centerline for two streamwise locations and depths for $10\,\mathrm{m\,s^{-1}}$, with the estimated variance calculated according to eq. (3.44).

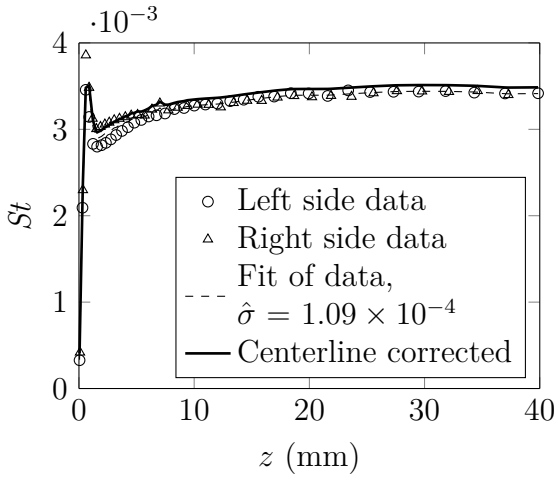

(a) Lateral averaging for $d = 0.254\,\mathrm{mm}$ at $x = 4.83\,\mathrm{mm}$

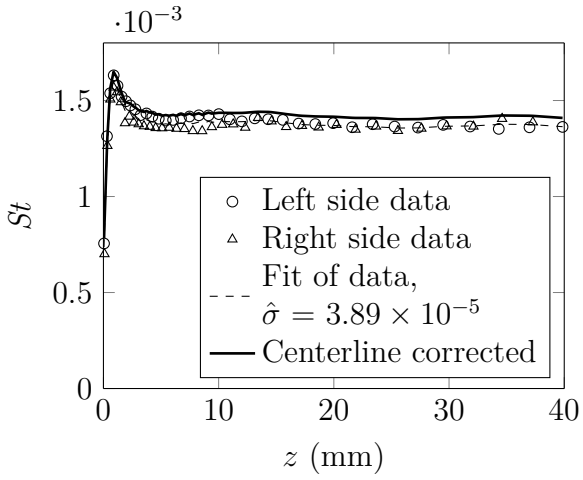

(b) Lateral averaging for $d = 0.254\,\mathrm{mm}$ at $x = 97.3\,\mathrm{mm}$

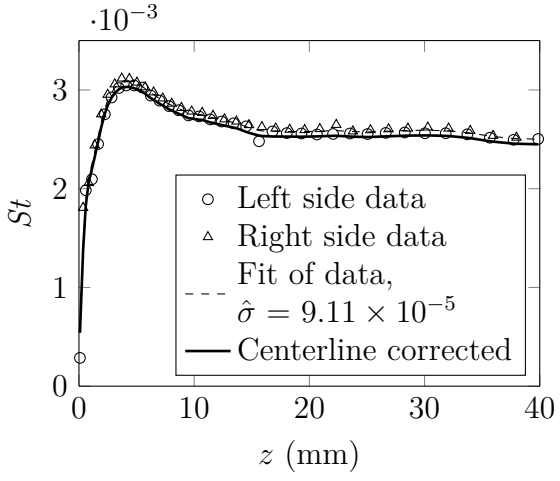

(c) Lateral averaging for $d = 8.84\,\mathrm{mm}$ at $x = 42.9\,\mathrm{mm}$

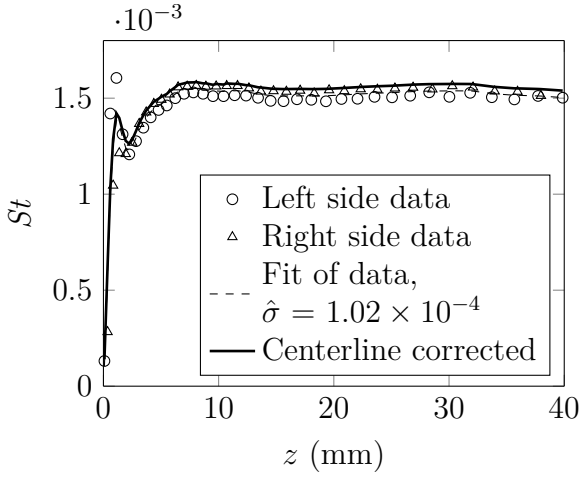

(d) Lateral averaging for $d = 8.84\,\mathrm{mm}$ at $x = 101\,\mathrm{mm}$

Figure 5.14: Lateral averaging across the cavity centerline for two streamwise locations and depths for $20\,\mathrm{m\,s^{-1}}$, with the estimated variance calculated according to eq. (3.44).

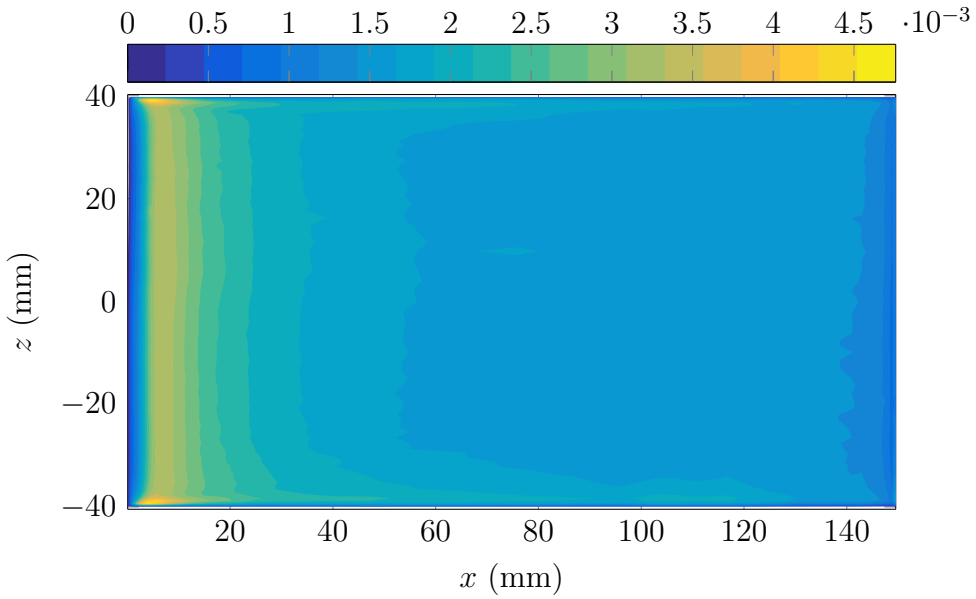

Figure 5.15: Contour of experimental St for $U_\infty \sim 10\,\mathrm{m\,s^{-1}}$ and $d = 0.597\,\mathrm{mm}$ from data taken on 2016/08/07-11

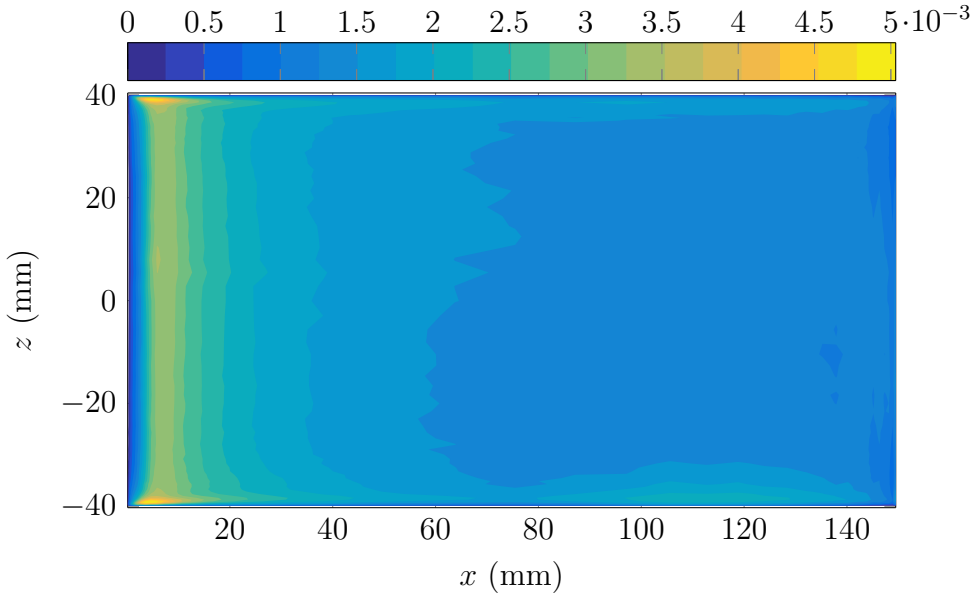

Figure 5.16: Contour of experimental St for $U_\infty \sim 10\,\mathrm{m\,s^{-1}}$ and $d = 0.597\,\mathrm{mm}$ from data taken on 2016/08/08-22

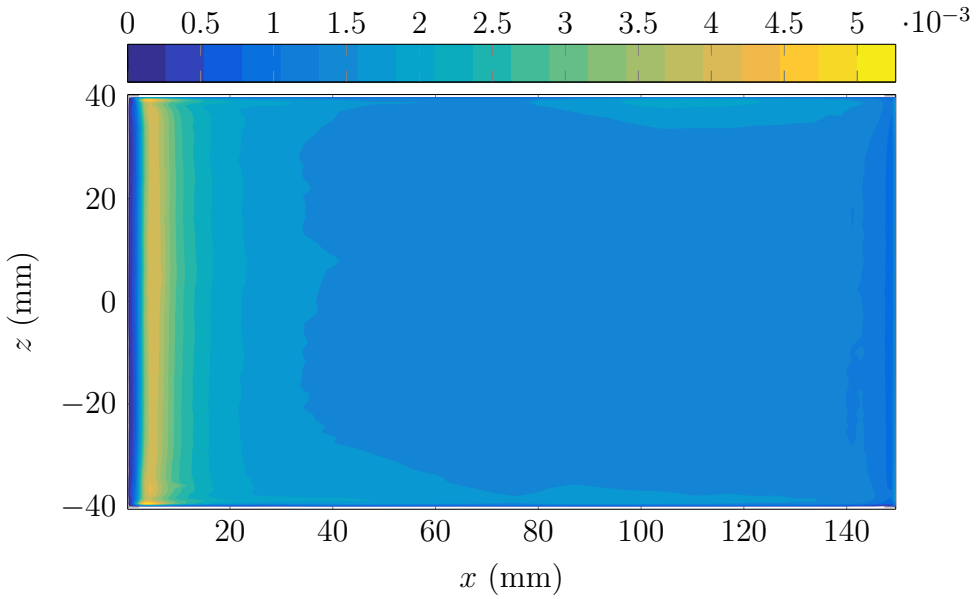

Figure 5.17: Contour of experimental St for $U_\infty \sim 20\,\mathrm{m\,s^{-1}}$ and $d = 0.597\,\mathrm{mm}$ from data taken on 2016/08/07-18

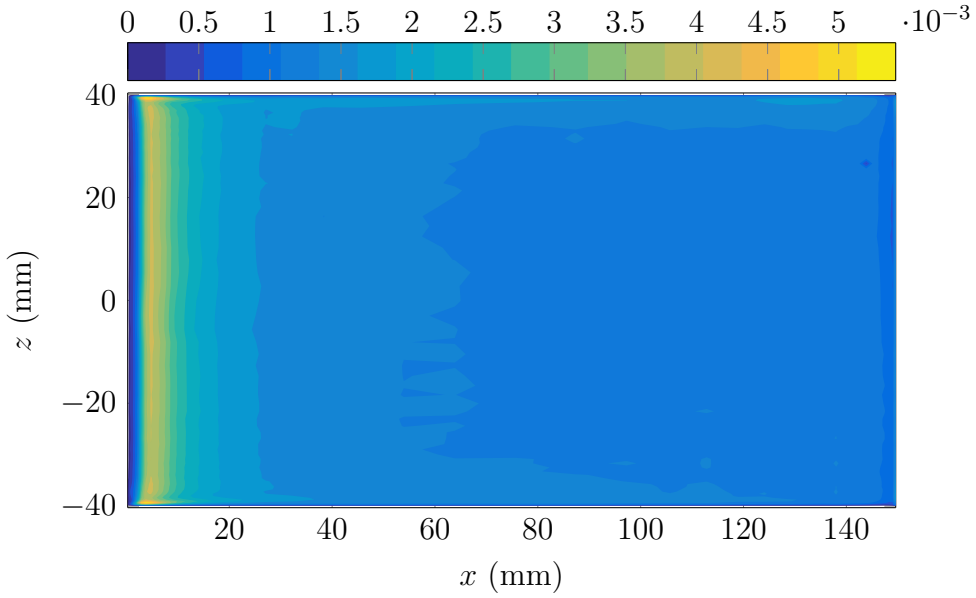

Figure 5.18: Contour of experimental St for $U_\infty \sim 20\,\mathrm{m\,s^{-1}}$ and $d = 0.597\,\mathrm{mm}$ from data taken on 2016/08/08-11

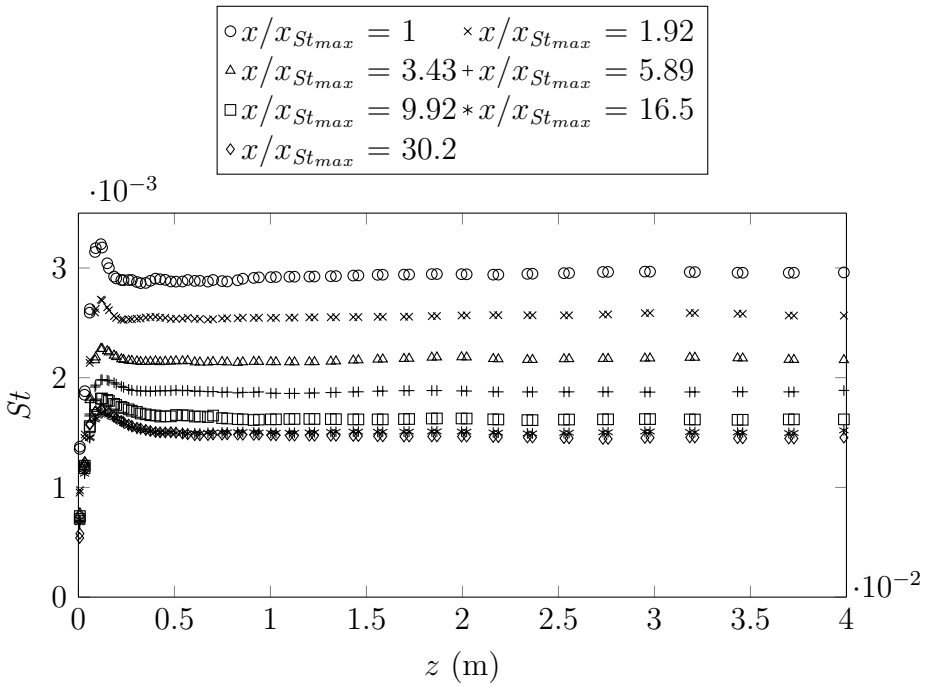

Figure 5.19: Lateral profiles of the St vs z at various streamwise locations for $U_\infty \sim 10\,\mathrm{m\,s^{-1}}$ and $d = 0.254\,\mathrm{mm}$

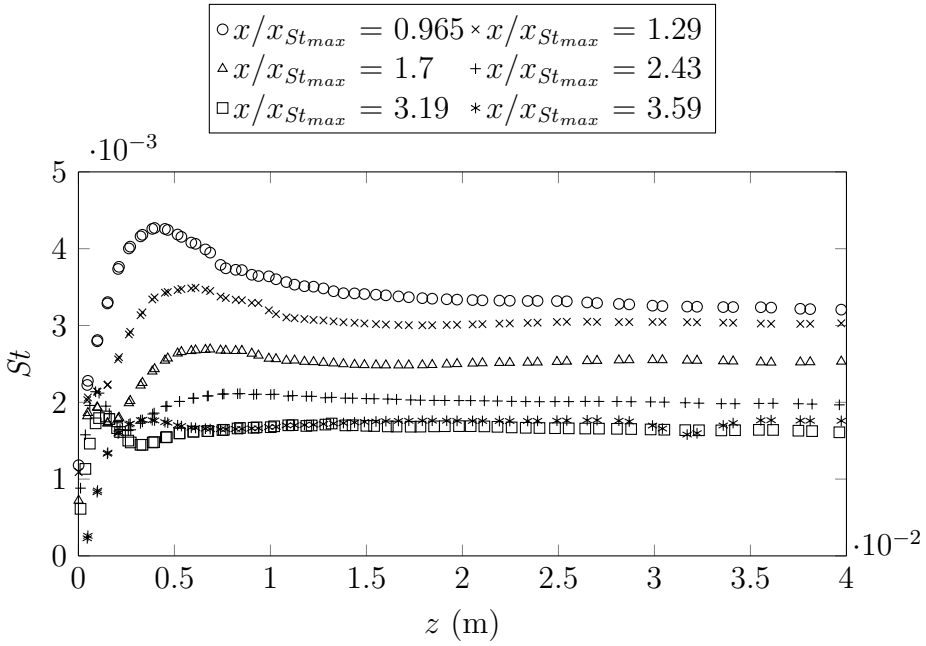

Figure 5.20: Lateral profiles of the St vs z at various streamwise locations for $U_\infty \sim 10\,\mathrm{m\,s^{-1}}$ and $d = 8.84\,\mathrm{mm}$

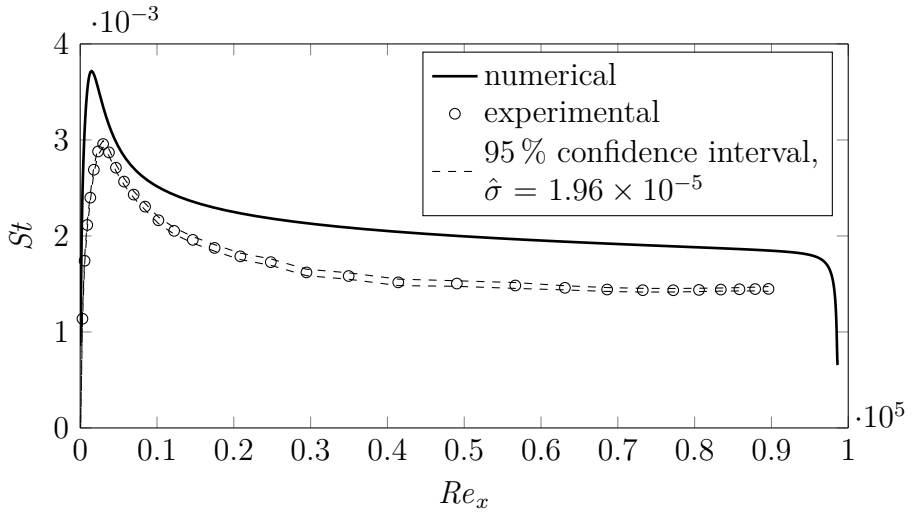

Figure 5.21: Comparison of centerline mass transfer between experimental results and numerical simulation for $U_\infty \sim 10\,\mathrm{m\,s^{-1}}$ and $d = 0.254\,\mathrm{mm}$

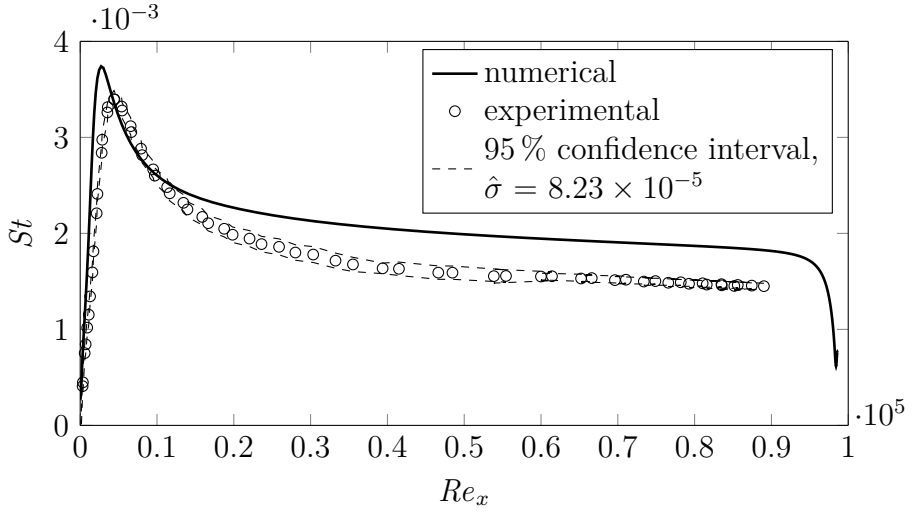

Figure 5.22: Comparison of centerline mass transfer between experimental results and numerical simulation for $U_\infty \sim 10\,\mathrm{m\,s^{-1}}$ and $d = 0.597\,\mathrm{mm}$

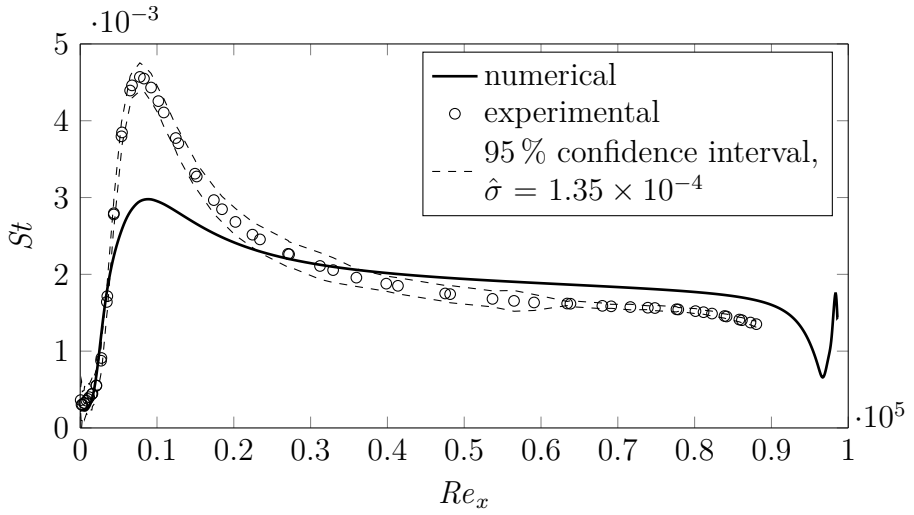

Figure 5.23: Comparison of centerline mass transfer between experimental results and numerical simulation for $U_\infty \sim 10\,\mathrm{m\,s^{-1}}$ and $d = 2.29\,\mathrm{mm}$

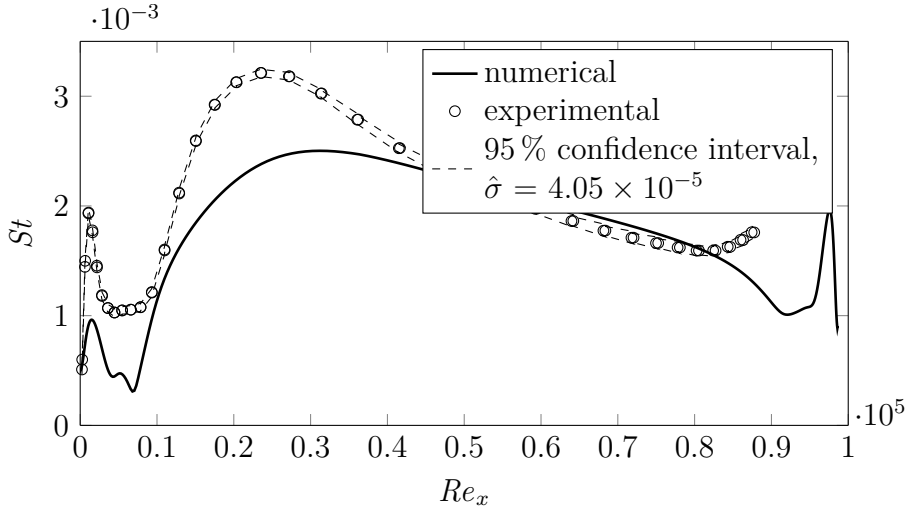

Figure 5.24: Comparison of centerline mass transfer between experimental results and numerical simulation for $U_\infty \sim 10\,\mathrm{m\,s^{-1}}$ and $d = 8.84\,\mathrm{mm}$

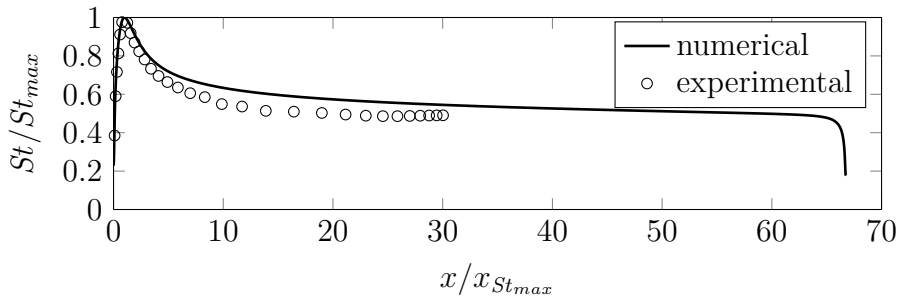

Figure 5.25: Comparison of normalized centerline mass transfer between experimental results and numerical simulation for $U_\infty \sim 10\,\mathrm{m\,s^{-1}}$ and $d = 0.254\,\mathrm{mm}$

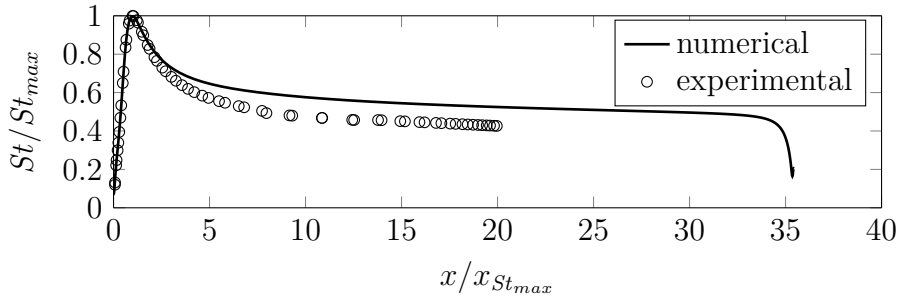

Figure 5.26: Comparison of normalized centerline mass transfer between experimental results and numerical simulation for $U_\infty \sim 10\,\mathrm{m\,s^{-1}}$ and $d = 0.597\,\mathrm{mm}$

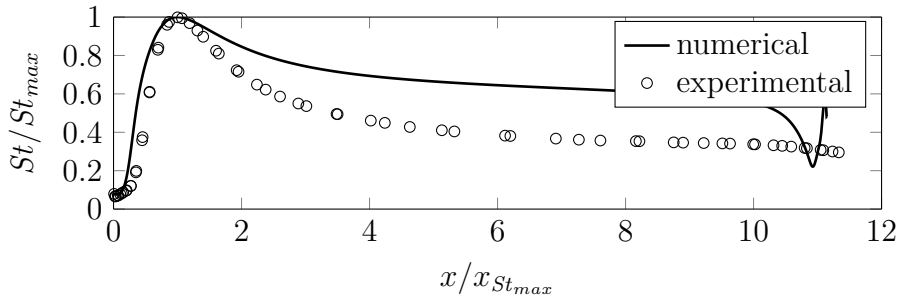

Figure 5.27: Comparison of normalized centerline mass transfer between experimental results and numerical simulation for $U_\infty \sim 10\,\mathrm{m\,s^{-1}}$ and $d = 2.29\,\mathrm{mm}$

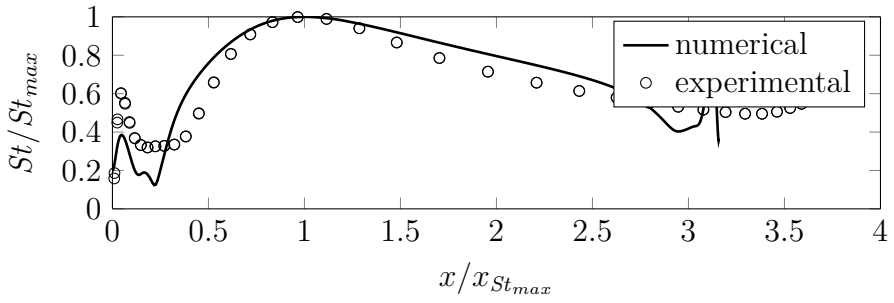

Figure 5.28: Comparison of normalized centerline mass transfer between experimental results and numerical simulation for $U_\infty \sim 10\,\mathrm{m\,s^{-1}}$ and $d = 8.84\,\mathrm{mm}$

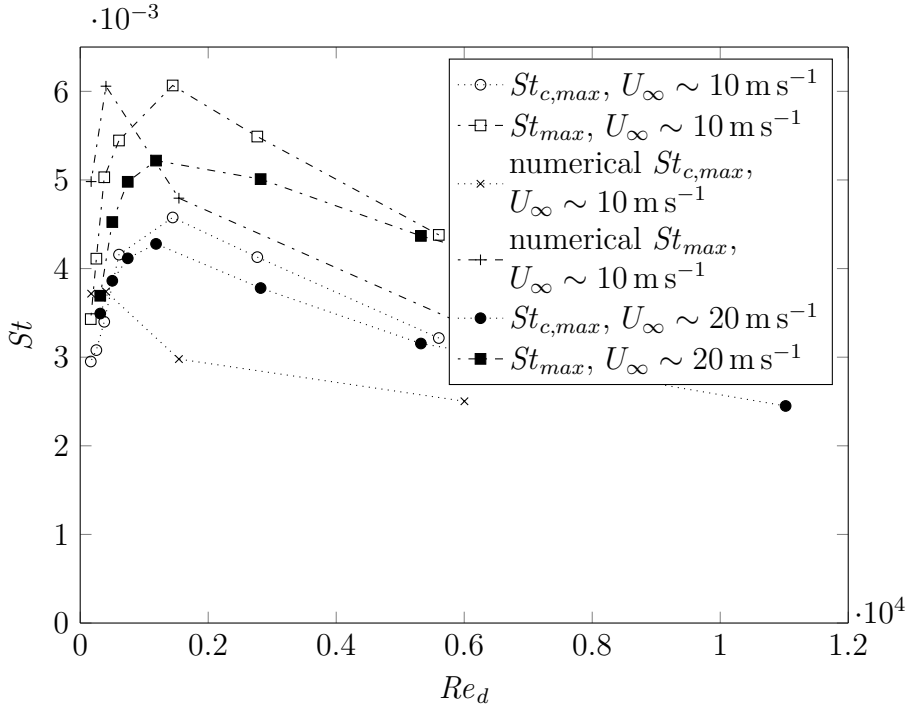

Figure 5.29: Location of global and centerline maximum St, lines for experimental data hold no significance beyond aiding readability.

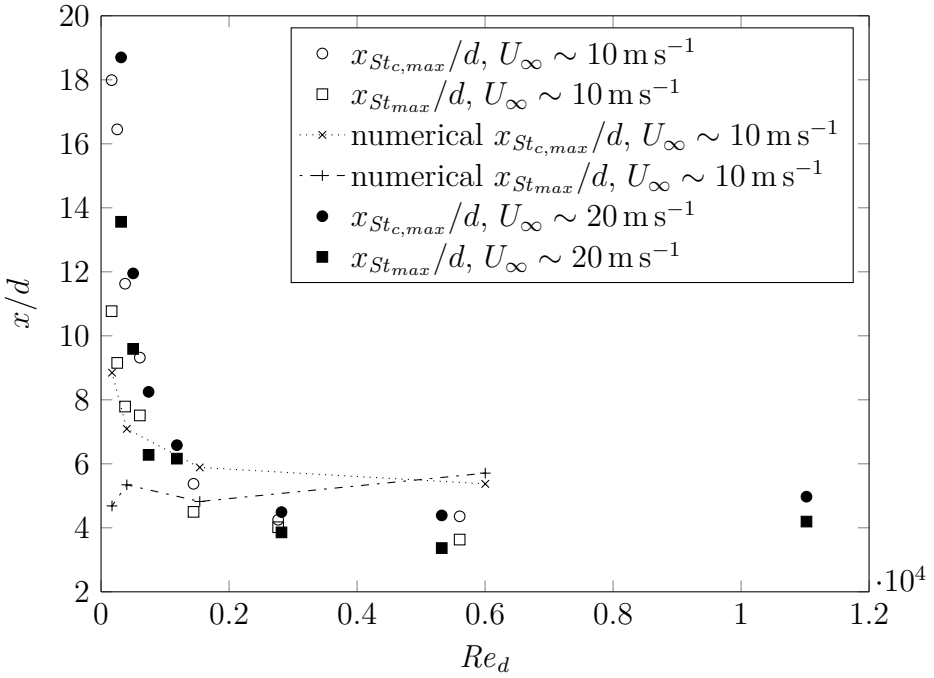

Figure 5.30: Normalized location of maximum St

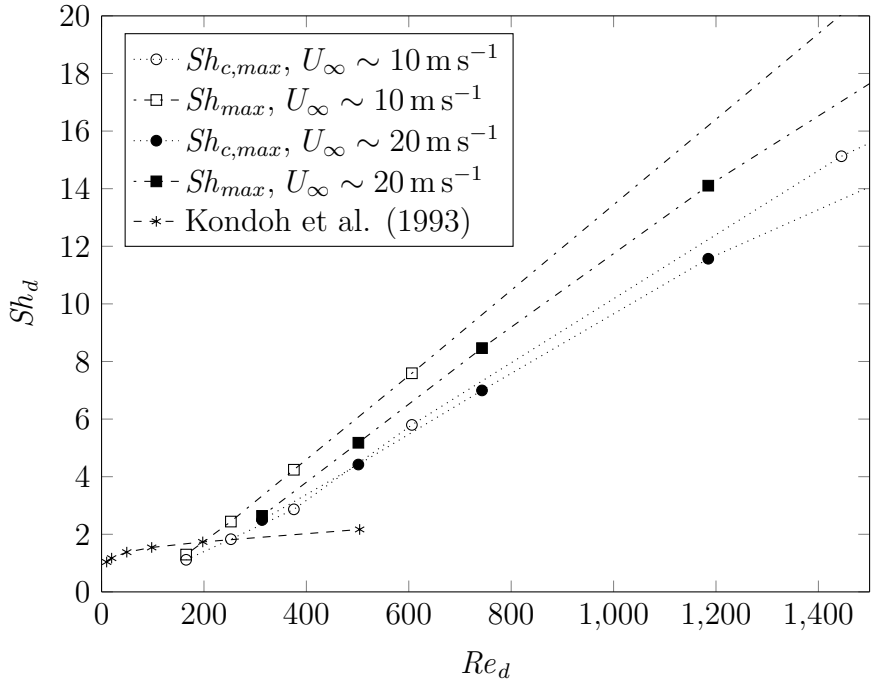

Figure 5.31: Location of global and centerline maximum Sh_d compared with laminar data of Kondoh et al. (1993).

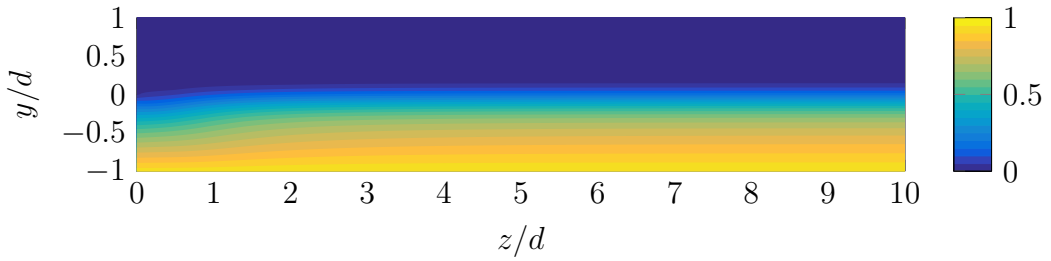

(a) Filled non-dimensional temperature contour, $(T - T_w) / (T_\infty - T_w)$

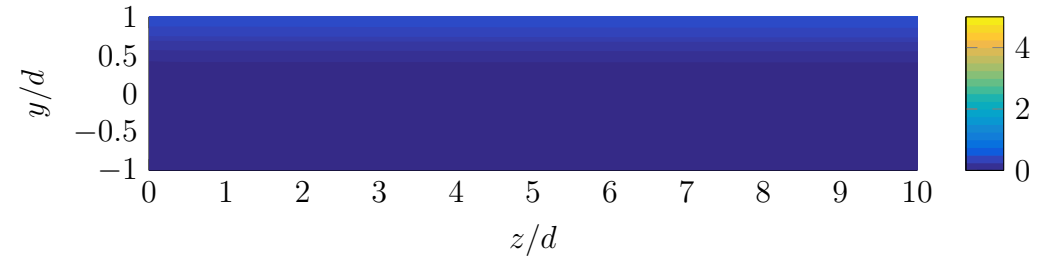

(b) Filled contour of the normalized turbulent kinetic energy, $k/k_{max,inlet}$

Figure 5.32: Flow information in the z-y plane after flow reattachment, $d = 0.254\,\text{mm}$, $x = 0.0935\,\text{mm}$, $x/d = 0.368$

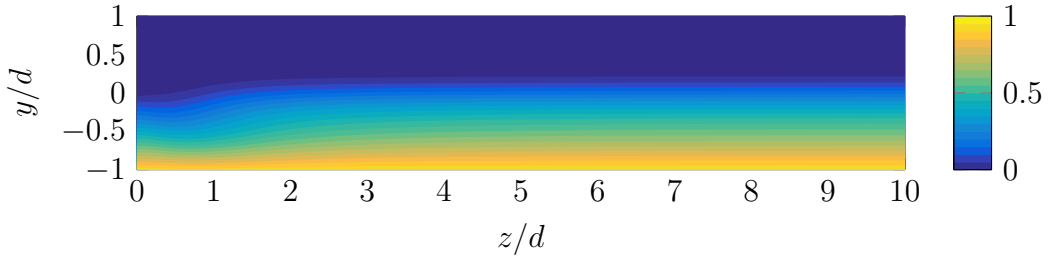

(a) Filled non-dimensional temperature contour, $(T - T_w) / (T_\infty - T_w)$

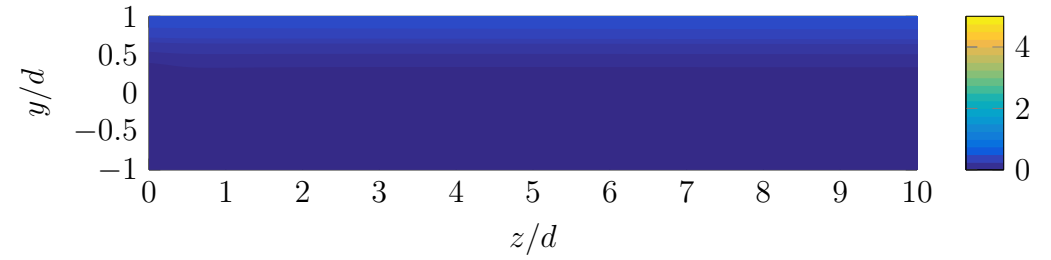

(b) Filled contour of the normalized turbulent kinetic energy, $k/k_{max,inlet}$

Figure 5.33: Flow information in the z-y plane after flow reattachment, $d = 0.254\,\text{mm}$, $x = 0.284\,\text{mm}$, $x/d = 1.12$

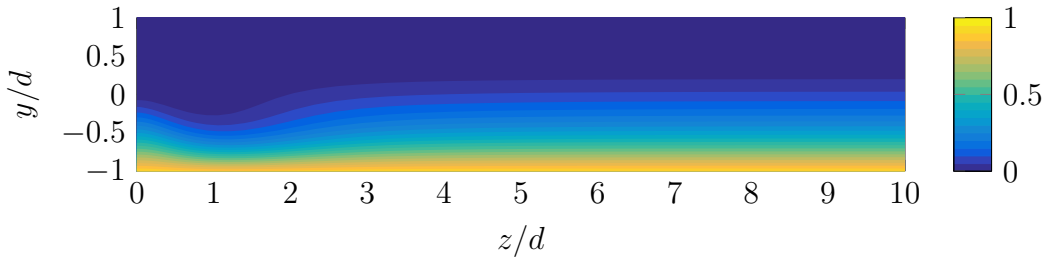

(a) Filled non-dimensional temperature contour, $(T - T_w) / (T_\infty - T_w)$

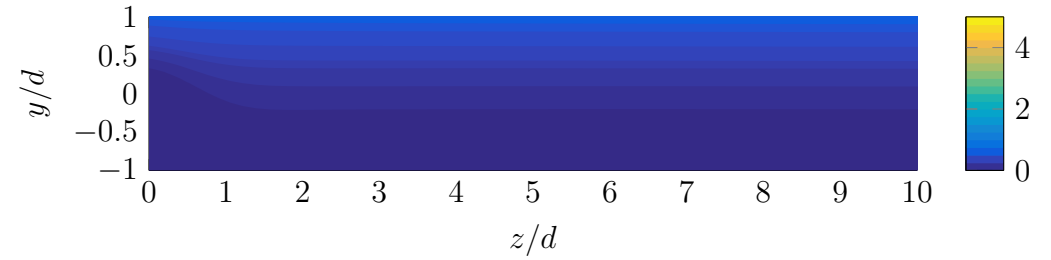

(b) Filled contour of the normalized turbulent kinetic energy, $k/k_{max,inlet}$

Figure 5.34: Flow information in the z-y plane after flow reattachment, $d = 0.254\,\text{mm}$, $x = 0.981\,\text{mm}$, $x/d = 3.86$

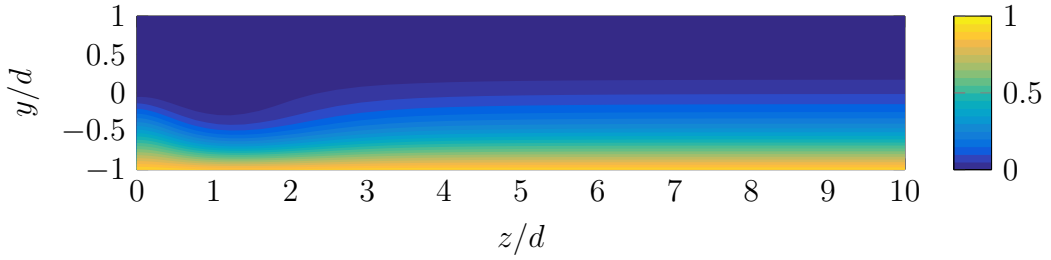

(a) Filled non-dimensional temperature contour, $(T - T_w) / (T_\infty - T_w)$

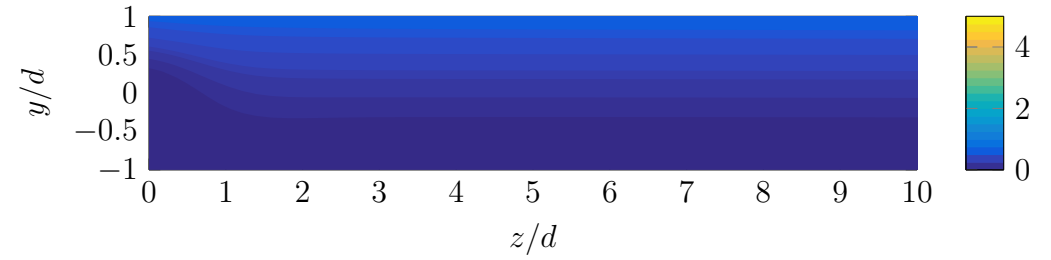

(b) Filled contour of the normalized turbulent kinetic energy, $k/k_{max,inlet}$

Figure 5.35: Flow information in the z-y plane after flow reattachment, $d = 0.254\,\text{mm}$, $x = 1.22\,\text{mm}$, $x/d = 4.80$

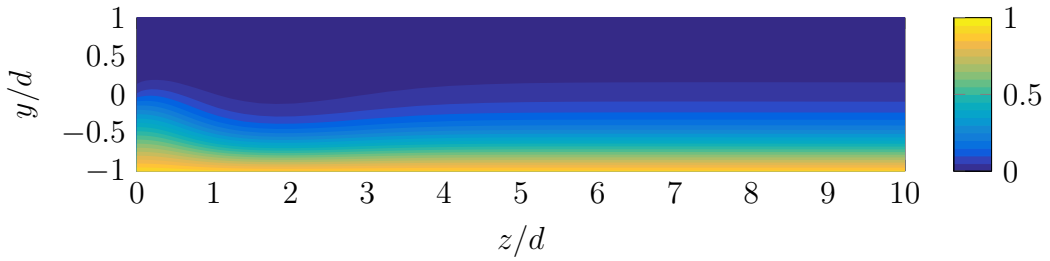

(a) Filled non-dimensional temperature contour, $(T - T_w) / (T_\infty - T_w)$

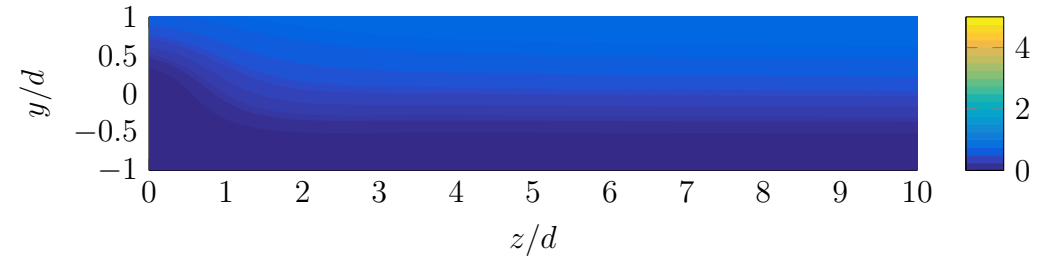

(b) Filled contour of the normalized turbulent kinetic energy, $k/k_{max,inlet}$

Figure 5.36: Flow information in the z-y plane after flow reattachment, $d = 0.254\,\text{mm}$, $x = 3.08\,\text{mm}$, $x/d = 12.1$

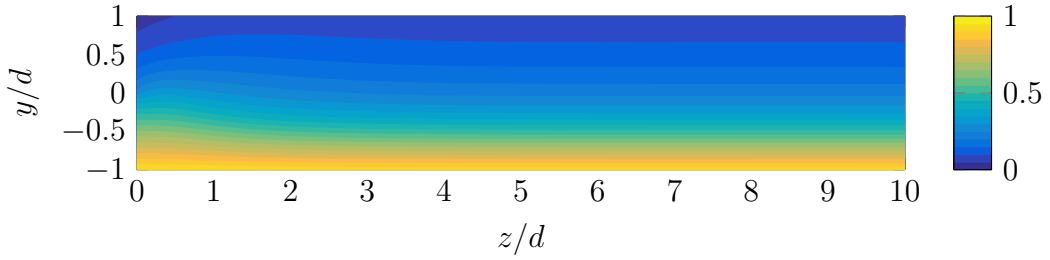

(a) Filled non-dimensional temperature contour, $(T - T_w) / (T_\infty - T_w)$

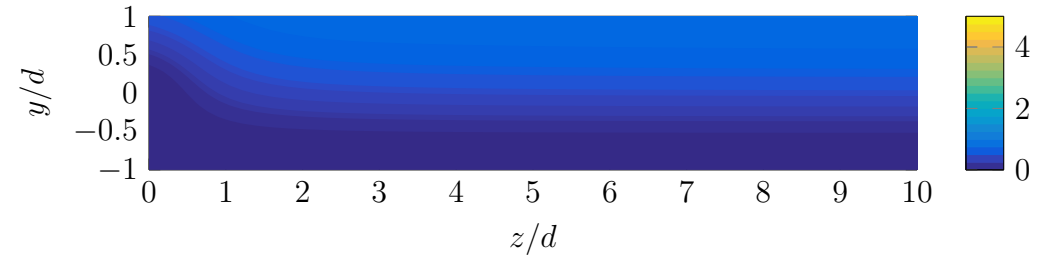

(b) Filled contour of the normalized turbulent kinetic energy, $k/k_{max,inlet}$

Figure 5.37: Flow information in the z-y plane after flow reattachment, $d = 0.254\,\text{mm}$, $x = 23.8\,\text{mm}$, $x/d = 93.7$

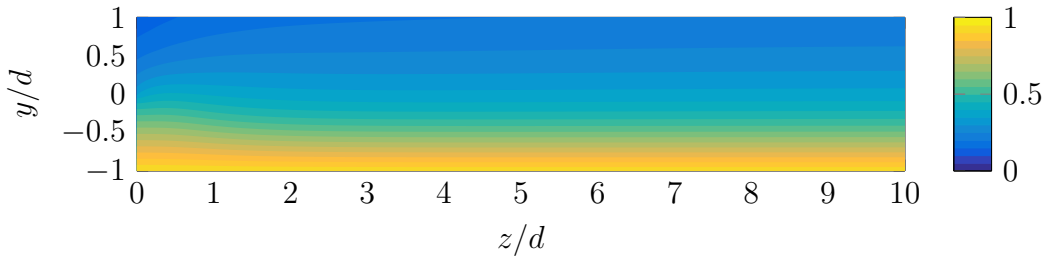

(a) Filled non-dimensional temperature contour, $(T - T_w) \,/\, (T_\infty - T_w)$

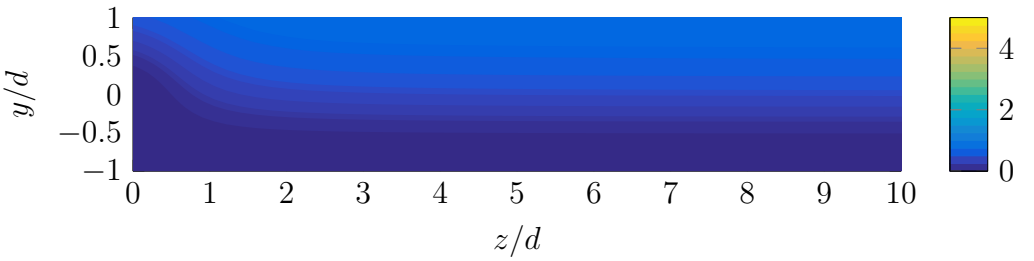

(b) Filled contour of the normalized turbulent kinetic energy, $k/k_{max,inlet}$

Figure 5.38: Flow information in the z-y plane after flow reattachment, $d = 0.254\,\text{mm}$, $x = 121\,\text{mm}$, $x/d = 477$

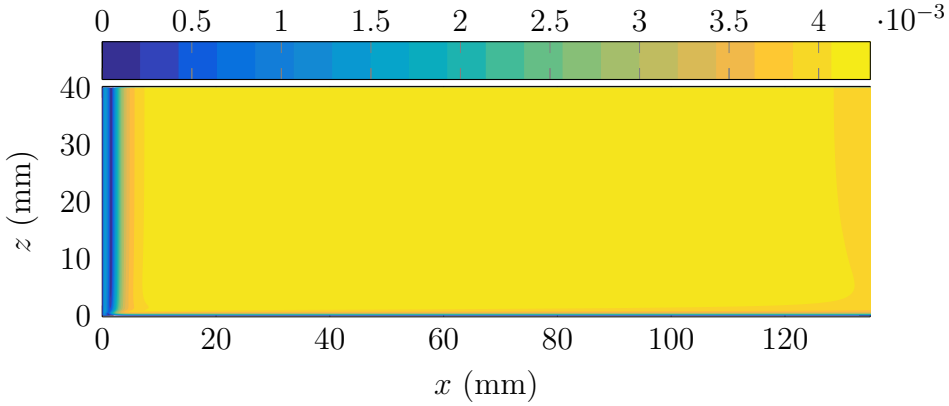

(a) Filled contour of the skin friction coefficient from numerical simulation

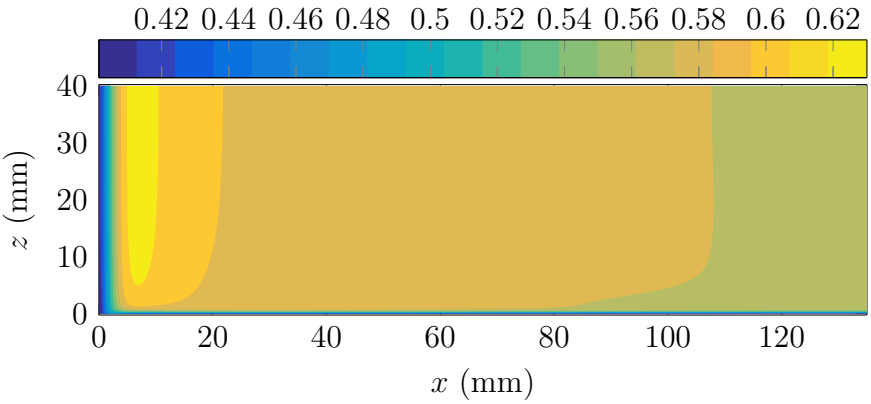

(b) Contour of numerical turbulent kinetic energy at $y^+ = 17.6$ above the cavity surface

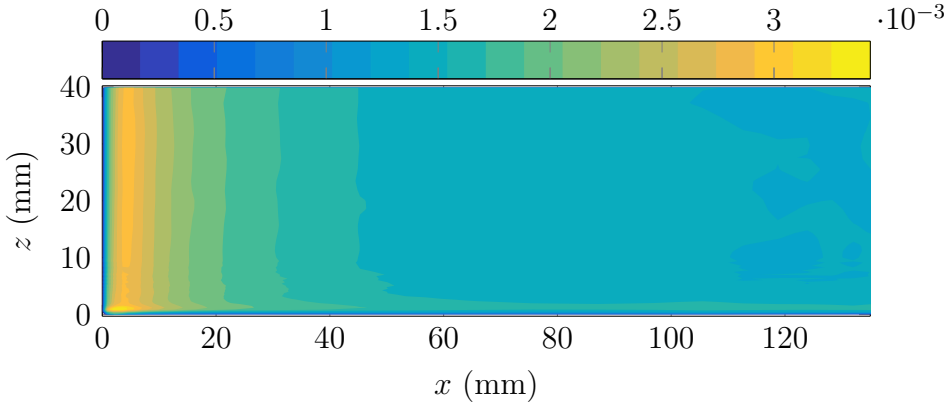

(c) Contour of experimental St for $U_\infty \sim 10\,\mathrm{m\,s^{-1}}$ from data taken on 2016/08/15-17

Figure 5.39: Comparison of the experimental St and numerical shear stress and turbulent kinetic energy for $d = 0.254\,\mathrm{mm}$

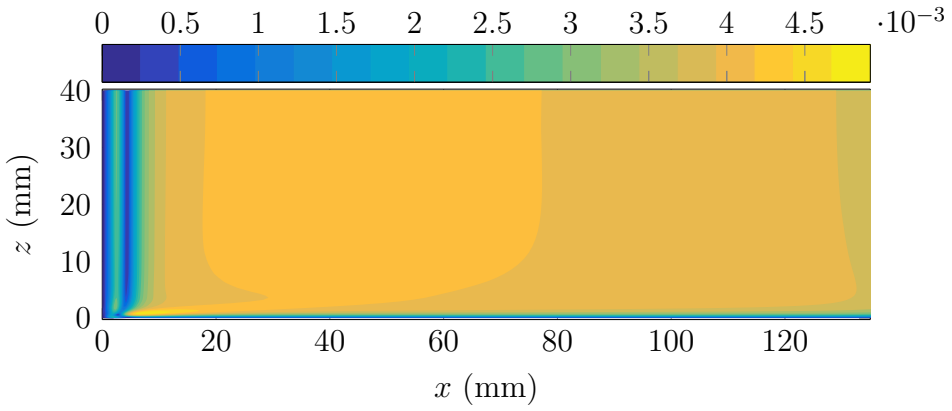

(a) Filled contour of the skin friction coefficient from numerical simulation

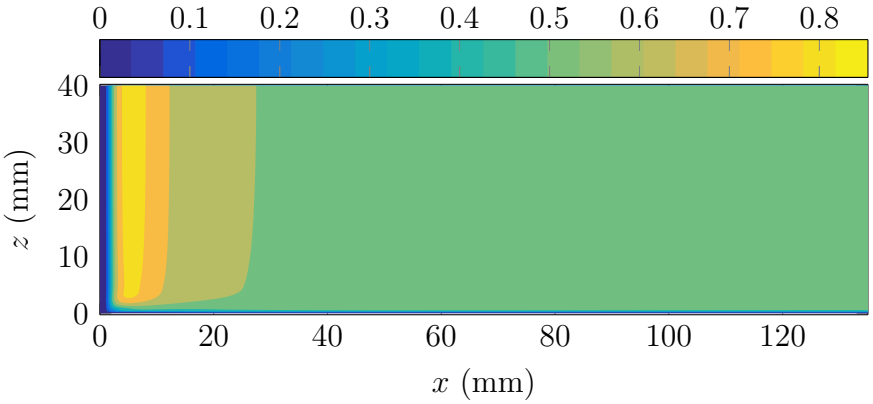

(b) Contour of numerical turbulent kinetic energy at $y^+ = 17.5$ above the cavity surface

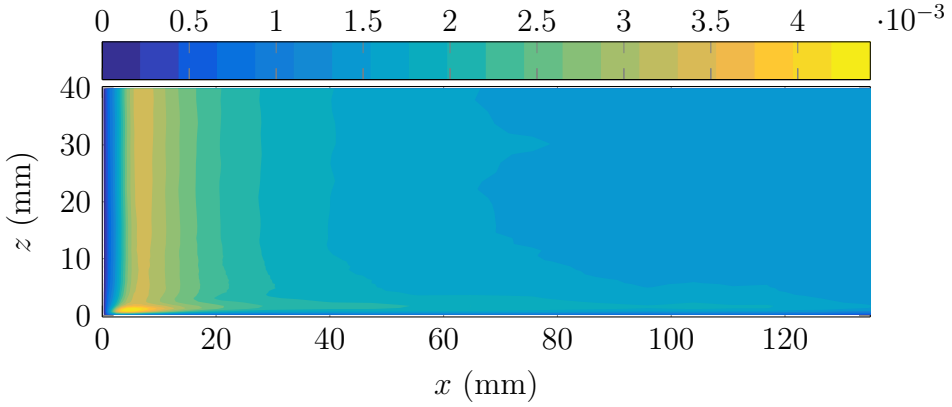

(c) Contour of experimental St for $U_\infty \sim 10\,\mathrm{m\,s^{-1}}$ from data taken on 2016/08/07-11

Figure 5.40: Comparison of the experimental St and numerical shear stress and turbulent kinetic energy for $d = 0.597\,\mathrm{mm}$. Note based on figs. 5.15 to 5.18, the mass transfer data should be viewed with some skepticism.

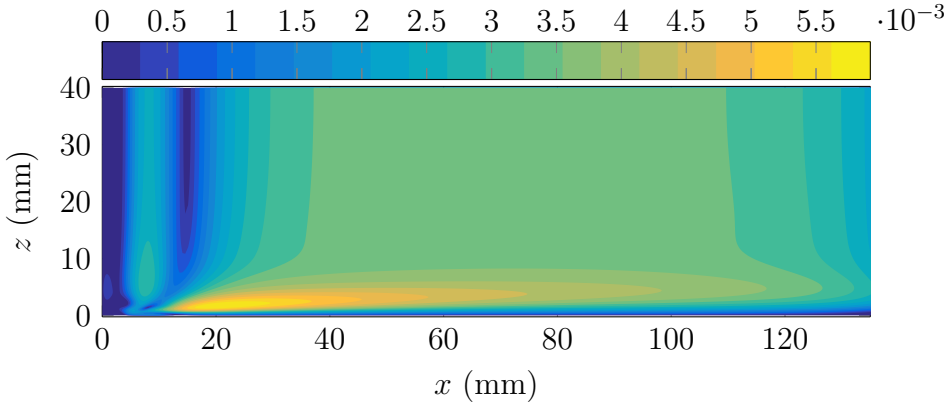

(a) Filled contour of the skin friction coefficient from numerical simulation

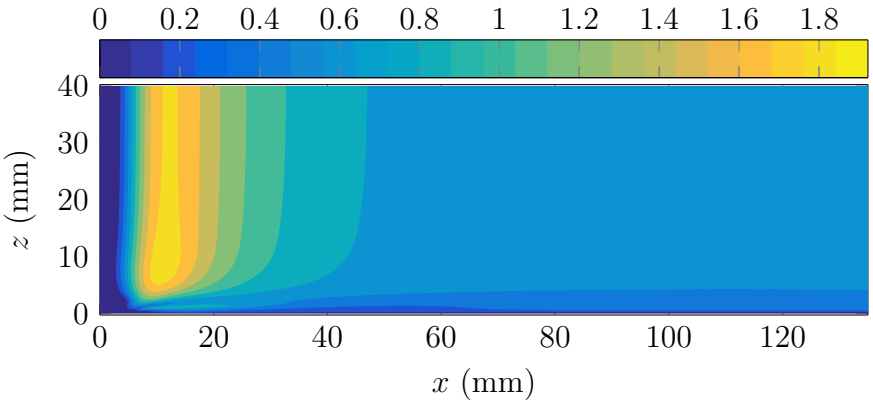

(b) Contour of numerical turbulent kinetic energy at $y^+ = 31.4$ above the cavity surface

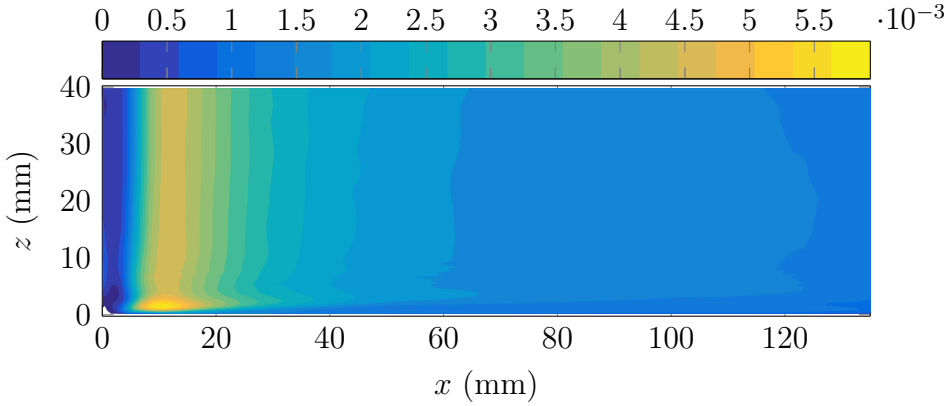

(c) Contour of experimental St for $U_\infty \sim 10\,\mathrm{m\,s^{-1}}$ from data taken on 2016/07/28-20

Figure 5.41: Comparison of the experimental St and numerical shear stress and turbulent kinetic energy for $d = 2.29\,\mathrm{mm}$

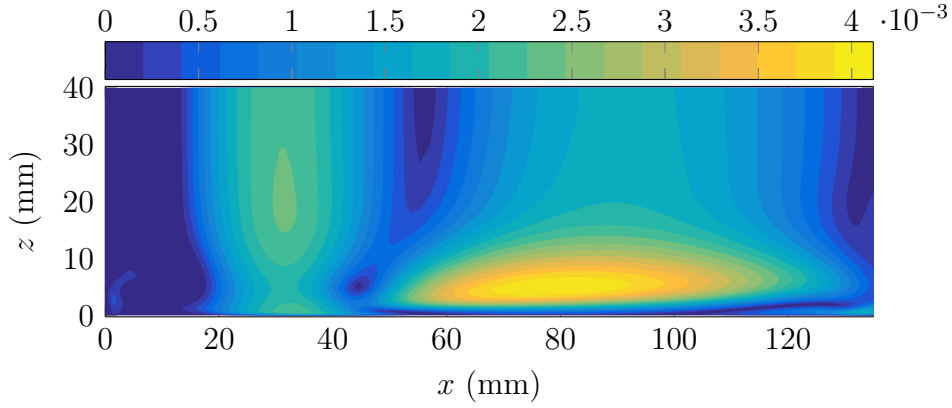

(a) Filled contour of the skin friction coefficient from numerical simulation

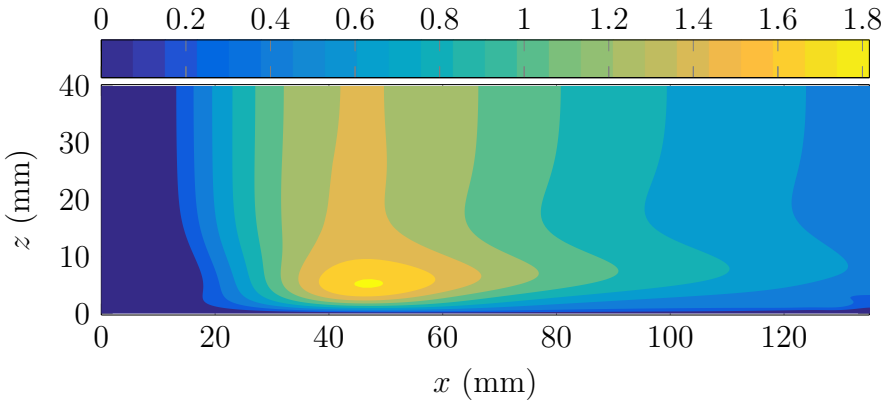

(b) Contour of numerical turbulent kinetic energy at $y^+ = 31.2$ above the cavity surface

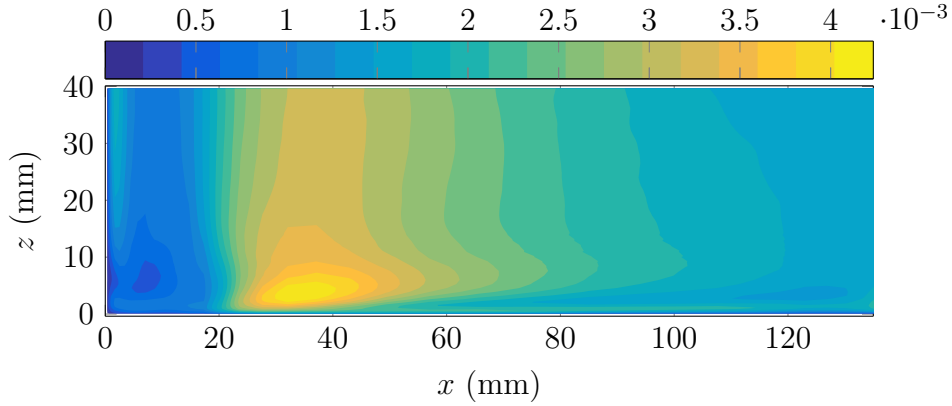

(c) Contour of experimental St for $U_\infty \sim 10\,\mathrm{m\,s^{-1}}$ from data taken on 2016/07/18-22

Figure 5.42: Comparison of the experimental St and numerical shear stress and turbulent kinetic energy for $d = 8.84\,\mathrm{mm}$

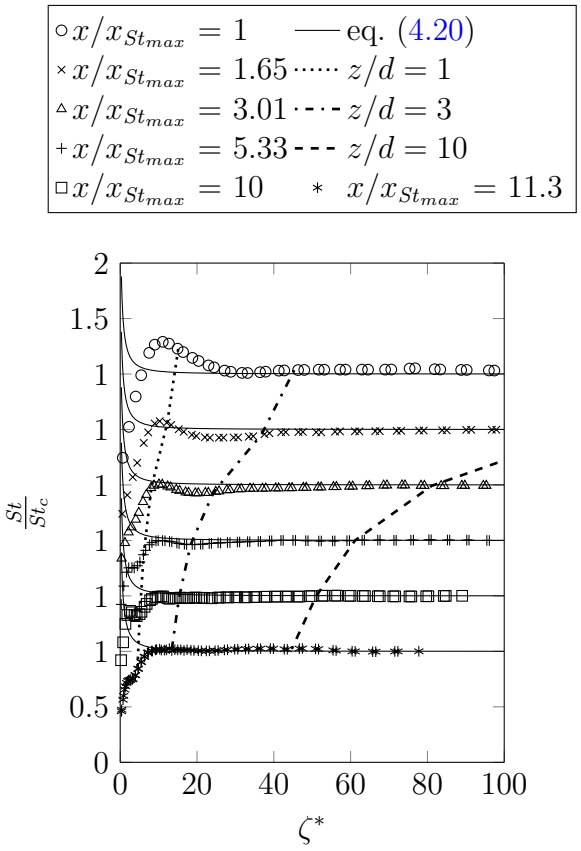

Figure 5.43: Lateral profile of normalized St vs ζ_m^* at various streamwise locations for $U_\infty \sim 10\,\mathrm{m\,s^{-1}}$ and $d = 2.29\,\mathrm{mm}$

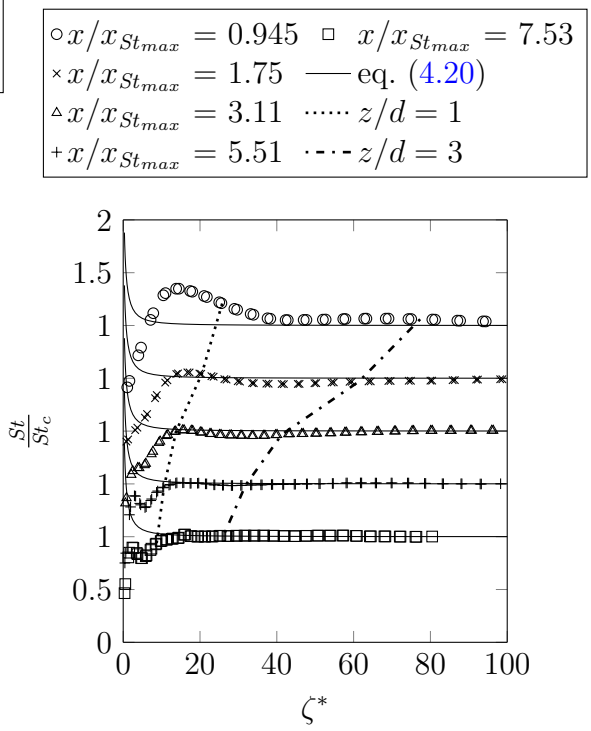

Figure 5.44: Lateral profile of normalized St vs ζ_m^* at various streamwise locations for $U_\infty \sim 10\,\mathrm{m\,s^{-1}}$ and $d = 4.32\,\mathrm{mm}$

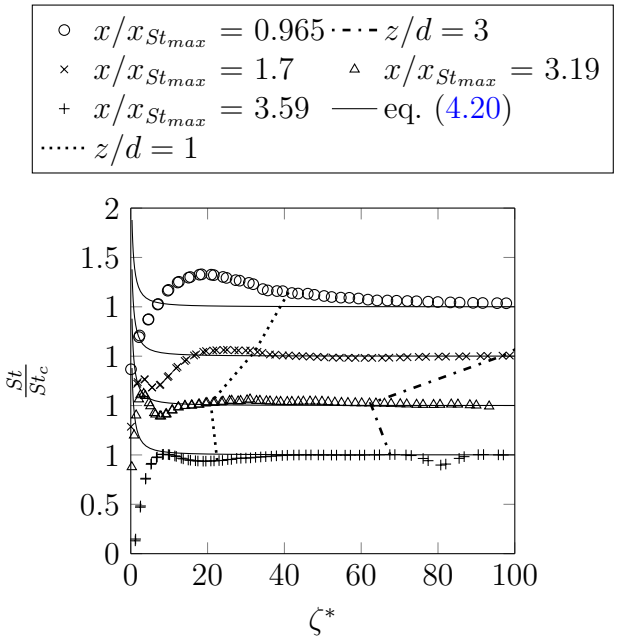

Figure 5.45: Lateral profile of normalized St vs ζ_m^* at various streamwise locations for $U_\infty \sim 10\,\mathrm{m\,s^{-1}}$ and $d = 8.84\,\mathrm{mm}$

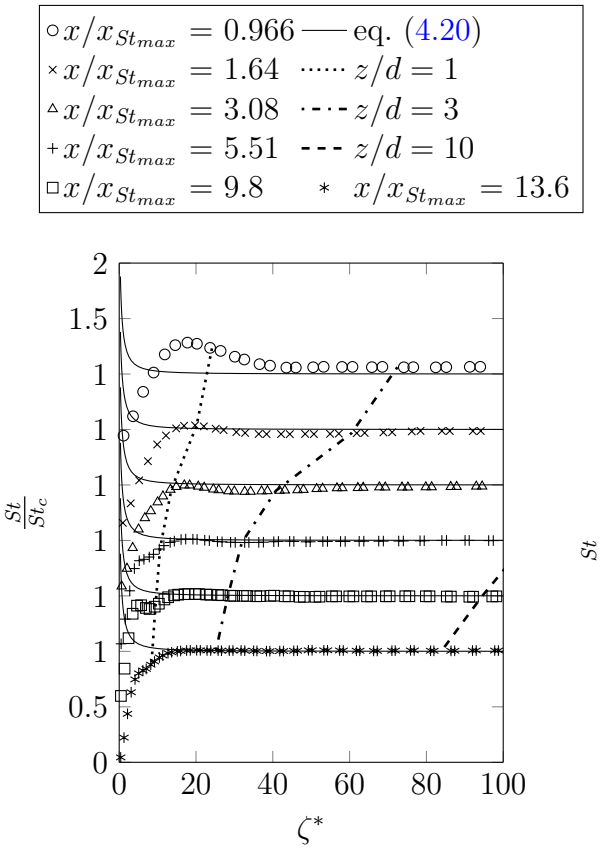

Figure 5.46: Lateral profile of normalized St vs ζ_m^* at various streamwise locations for $U_\infty \sim 20\,\mathrm{m\,s^{-1}}$ and $d = 2.29\,\mathrm{mm}$

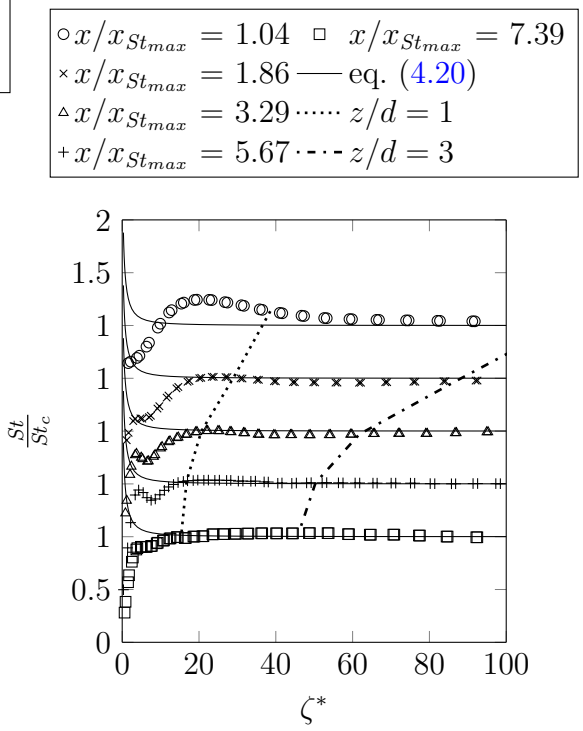

Figure 5.47: Lateral profile of normalized St vs ζ_m^* at various streamwise locations for $U_\infty \sim 20\,\mathrm{m\,s^{-1}}$ and $d = 4.32\,\mathrm{mm}$

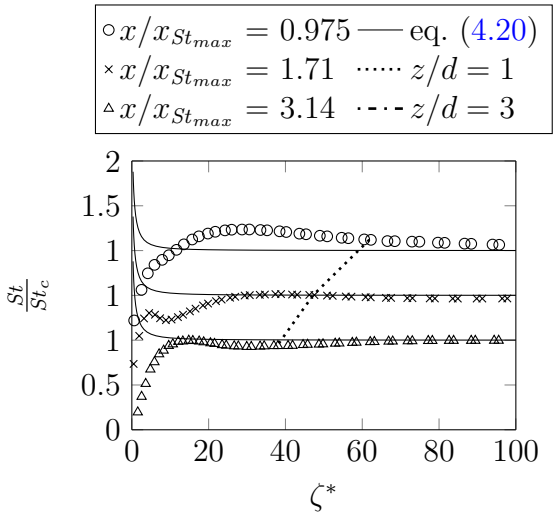

Figure 5.48: Lateral profile of normalized St vs ζ_m^* at various streamwise locations for $U_\infty \sim 20\,\mathrm{m\,s^{-1}}$ and $d = 8.84\,\mathrm{mm}$

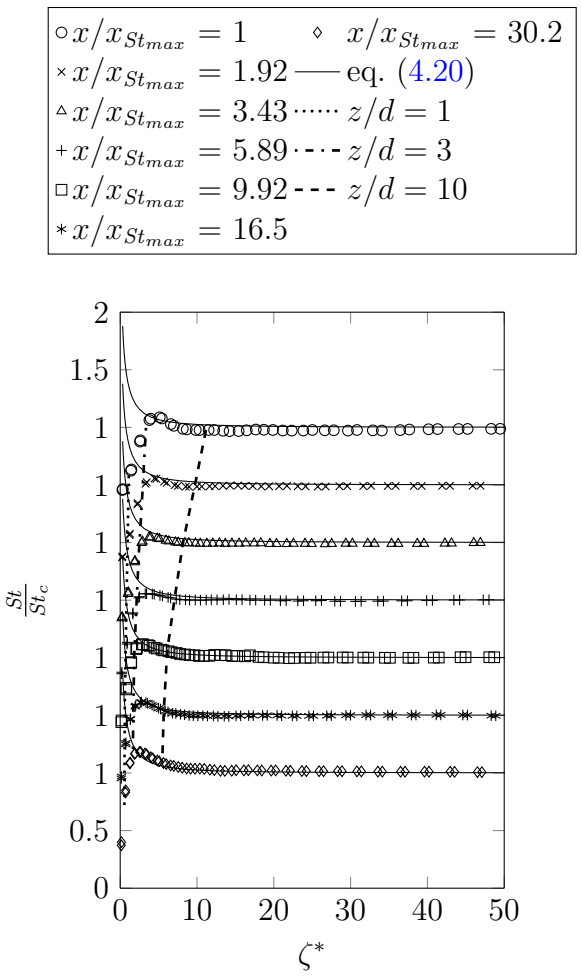

Figure 5.49: Lateral profile of normalized St vs ζ_m^* at various streamwise locations for $U_\infty \sim 10\,\mathrm{m\,s^{-1}}$ and $d = 0.254\,\mathrm{mm}$

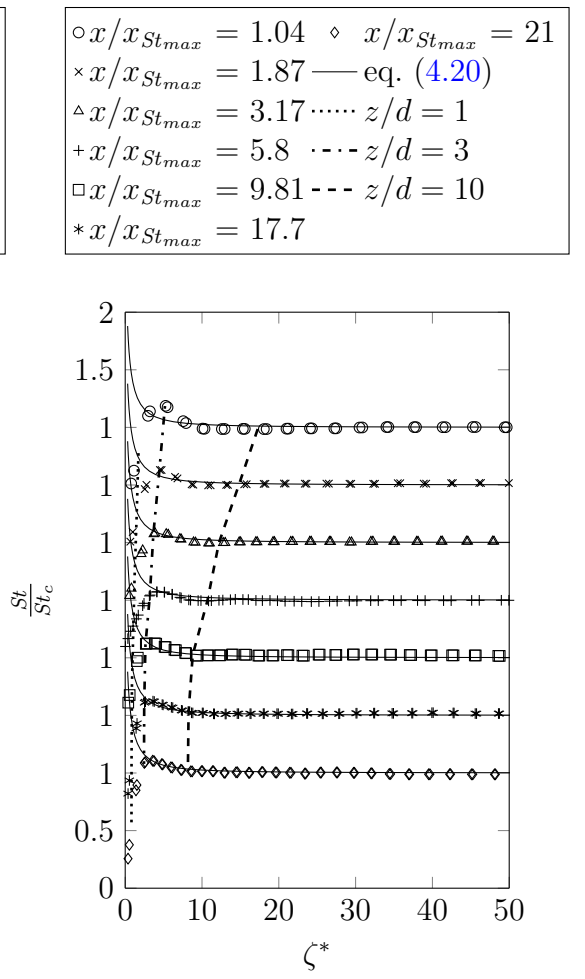

Figure 5.50: Lateral profile of normalized St vs ζ_m^* at various streamwise locations for $U_\infty \sim 10\,\mathrm{m\,s^{-1}}$ and $d = 0.401\,\mathrm{mm}$

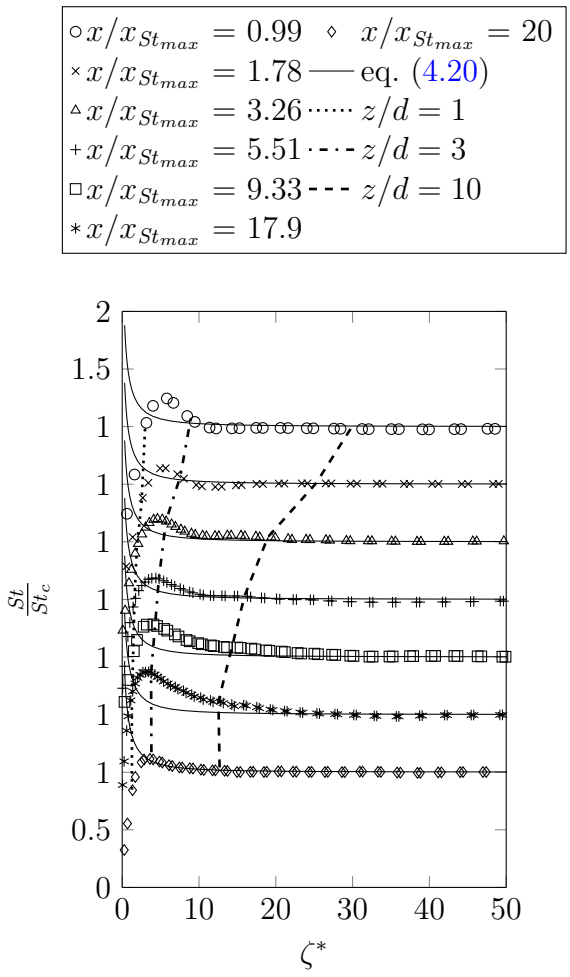

Figure 5.51: Lateral profile of normalized St vs ζ_m^* at various streamwise locations for $U_\infty \sim 10\,\mathrm{m\,s^{-1}}$ and $d = 0.597\,\mathrm{mm}$. Note based on figs. 5.15 to 5.18, the mass transfer data should be viewed with some skepticism.

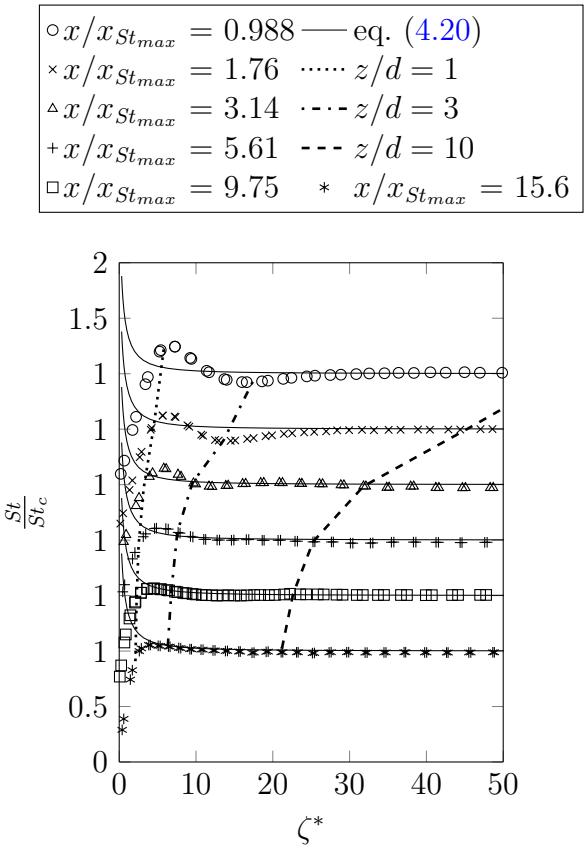

Figure 5.52: Lateral profile of normalized St vs ζ_m^* at various streamwise locations for $U_\infty \sim 10\,\mathrm{m\,s^{-1}}$ and $d = 0.960\,\mathrm{mm}$

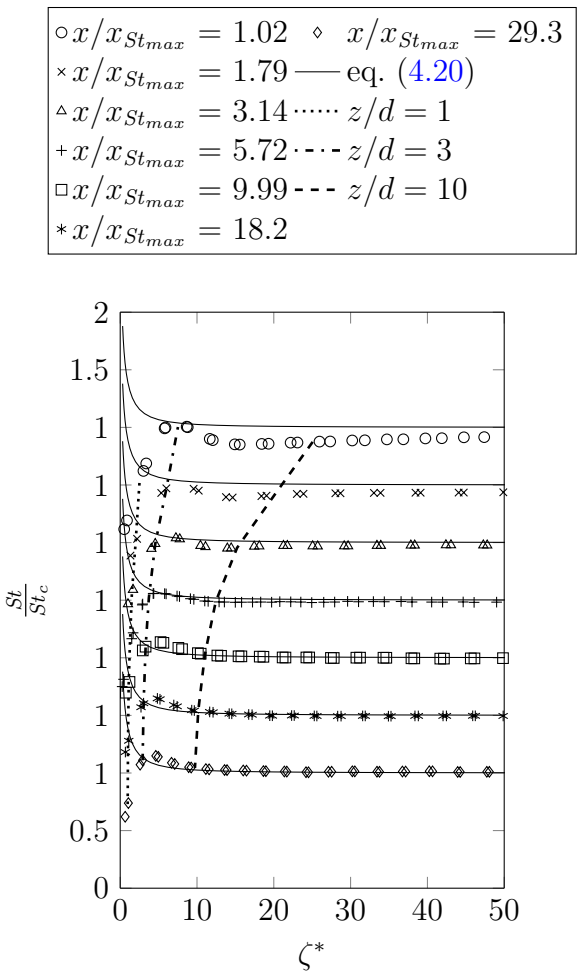

Figure 5.53: Lateral profile of normalized St vs ζ_m^* at various streamwise locations for $U_\infty \sim 20\,\mathrm{m\,s^{-1}}$ and $d = 0.254\,\mathrm{mm}$

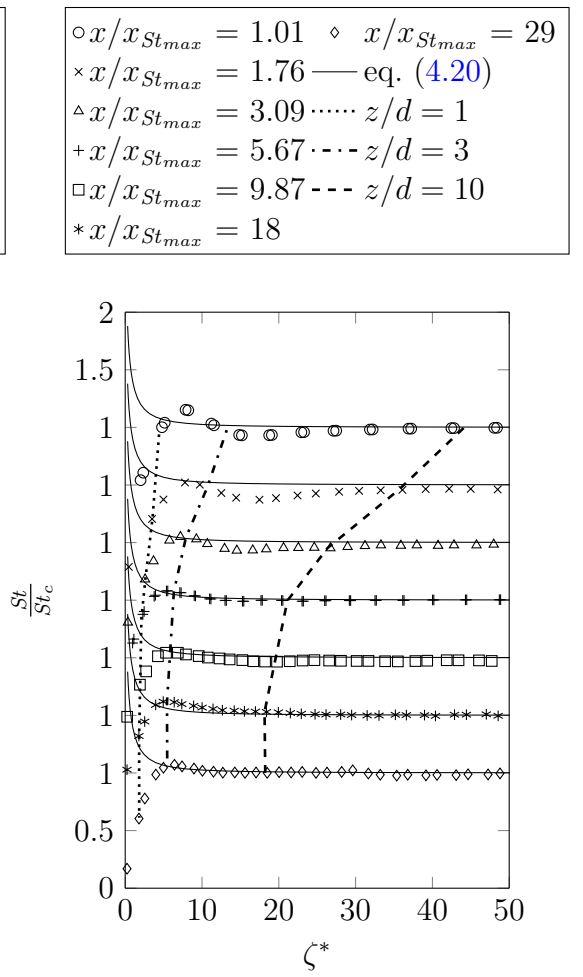

Figure 5.54: Lateral profile of normalized St vs ζ_m^* at various streamwise locations for $U_\infty \sim 20\,\mathrm{m\,s^{-1}}$ and $d = 0.401\,\mathrm{mm}$

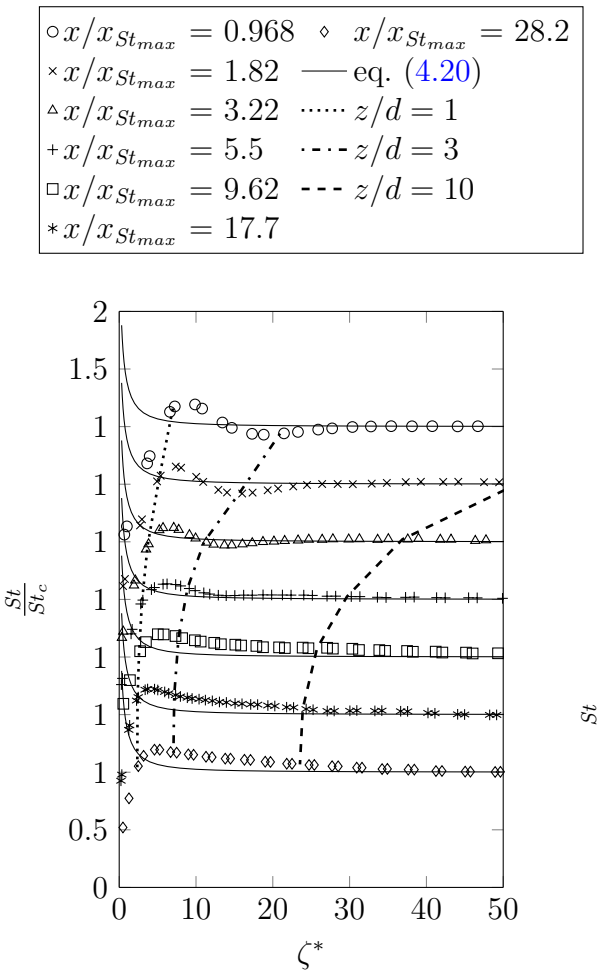

Figure 5.55: Lateral profile of normalized St vs ζ_m^* at various streamwise locations for $U_\infty \sim 20\,\mathrm{m\,s^{-1}}$ and $d = 0.597\,\mathrm{mm}$. Note based on figs. 5.15 to 5.18, the mass transfer data should be viewed with some skepticism.

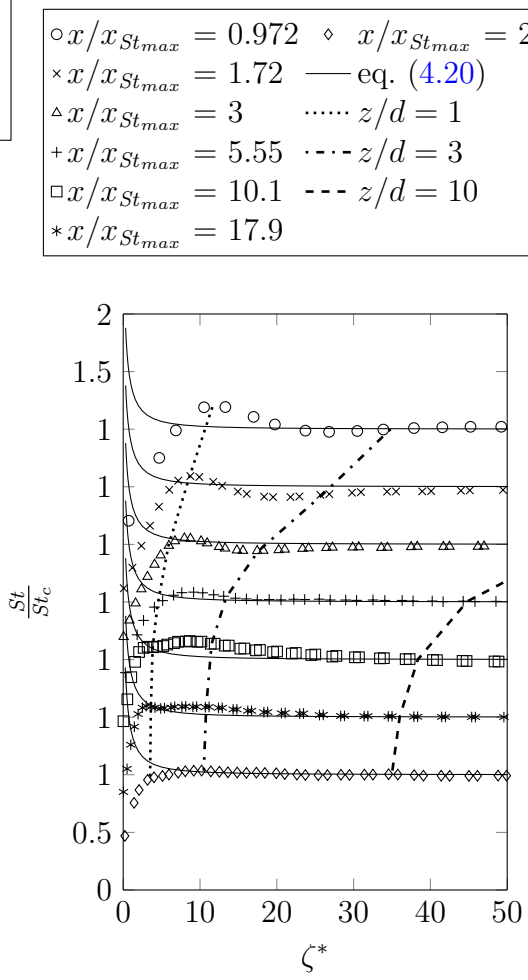

Figure 5.56: Lateral profile of normalized St vs ζ_m^* at various streamwise locations for $U_\infty \sim 20\,\mathrm{m\,s^{-1}}$ and $d = 0.960\,\mathrm{mm}$

5.3 Summary

A numerical shear stress transport model is used to describe the flow field, and comparison with existing numerical and experimental results indicate the numerically calculated flow field is reasonably accurate. The reattachment length and centerline skin friction coefficient matched published numerical and experimental data very well.

Using the numerical results, the general flow field in the cavity is described. There are recirculation regions near the backward and forward facing steps defined by two reattachment streamlines. Downstream of the recirculation region, a streamwise vortex is sustained near the cavity sidewall by flow coming into the cavity over the sidewall. However, as the flow redevelops and leaves the cavity, the sidewall vortex dissipates. Finally, near the end of the cavity, the flow separates near the forward facing edge.

The flow field is useful for describing the mass transfer, particularly for the deeper cavities. The maximum St along the centerline of the cavity is maximum near the reattachment point for the flow. The primary and secondary vortices near sidewall cause two lateral local maximums, which attenuate in the streamwise direction and disappear when the sidewall vortices disappear. After the vortices disappear, the lateral profile of the mass transfer is nearly flat, save for the small secondary recirculation region near the side wall.

However, the behavior of the mass transfer is different for very small cavities. For the centerline data, the location of the maximum St is as much as three times farther from the backward facing step than the flow reattachment location. This implies some aspects of the mass transfer are described by flat plate turbulent flow in addition to jet-like flow near the reattachment location.

Far downstream of the backward facing step, the mass transfer increases near the

edge even though there are no large scale flow structures that explain the increase. It is highly likely that for very shallow cavities, the lateral transport is very similar to the lateral transport near lateral edges on flat plates as described in chapter 4 and the depth of the shallow cavities are below the turbulent mixing layer where most of the lateral transport occurs.

Based on the mass transfer measurements and results from the numerical flow simulation, a conservative estimate for lateral mass flux profiles approximating the lateral profiles from a flat plate are a cavity depth shallower than 25 in wall coordinates and a streamwise position farther than 200 step heights from the backward facing step. It is probable this estimate is too conservative, but better flow modeling and measurements are needed to definitively decrease the streamwise requirement; while the mass transfer measurements for the 0.597 mm deep cavity are not symmetrical enough to use confidently.

Chapter 6

Conclusion

6.1 Summary

6.1.1 Laminar Flat Plate

Lateral changes in the heat transfer for laminar boundary layer flow are studied for four types of surface boundary conditions. A conduction model described the heat transfer well without any parameter fitting, as the main mode of energy transport in the lateral direction is by molecular diffusion. Boundary layer information is supplied to the conduction model by equating the height of the conduction domain to conduction thickness, ensuring the heat transfer asymptotically approaches the correct value far from the lateral edge.

Using the conduction thickness as the primary length parameter collapsed all the data to a single curve for each set of surface boundary conditions. For all the surface boundary conditions tested, except the isoflux-isoflux condition, the Nusselt number approaches infinity at the lateral edge. This lateral edge effect, the increase of the Nusselt number near the lateral singularity affected the heat transfer approximately two to three conduction thicknesses into the heated surface.

In addition to the semi-infinite heated plate, heat transfer from arrays of heated plates with variable spacing and widths are studied. The conduction modeling is extended for this geometry and shown to describe the lateral changes in heat transfer well without parameter fitting. When the widths of the strips are more than 10 conduction thicknesses, based on the heat transfer of a heated plate of infinite lateral span, the centerline heat transfer is unaffected by the width of the strip. In addition, based on the conduction modeling lateral averages of the heat transfer are calculated and recommendations are made for the spacing and widths are presented. For the two most realizable wall boundary conditions, when the "cooled" surface is adiabatic, the best choice for the spacing and width is to make both as small as possible. For both cases this maximizes the heat transfer, and when the heated wall boundary condition is isoflux, this also minimizes the maximum temperature.

The conduction model and conduction thickness are useful because the transport of energy happens through a diffusive process. Advection transport near the lateral edge in the spanwise direction is minimal because of the boundary layer flow characteristics and the geometry of the problem. If the lateral edge is not parallel with the flow, one would expect advective transport to dominate the diffusive transport.

6.1.2 Turbulent Flat Plate

Lateral changes in the mass flux are studied for momentum thickness Reynolds numbers from 320–1270 for strips with widths ranging from 2.48 mm to 19.77 mm. The random experimental uncertainties are between 2.7 % to 7.9 %. Normalizing the width and lateral location with the diffusion thickness, as is done for the laminar boundary layer flow, collapses the data and enables the construction of a general correlation for the local mass transfer that models the increase in the mass flux near the lateral edge and the overall increase of the mass flux from caused by narrow strips.

For laminar flow with the same surface boundary conditions, the mass flux is inversely proportional to the square root of the distance to the lateral edge. However, for turbulent flat plate flow, the power law is $St \sim z^{-0.152}$ near the lateral edge. The difference between the scaling for the laminar and turbulent flows near the edge highlights the dominant role of turbulent mixing in the lateral transport. If molecular diffusion is dominant in the lateral direction, the exponent would be closer to negative one-half, but the exponent is much lower as the turbulent mixing "smoothes" out the effects of the lateral singularity better than conduction type transport.

The usefulness of the diffusion thickness underscores the similarities between the laminar and turbulent transport processes. For laminar flow, it is clear that conduction modeling is useful because the transport normal to the flow is by molecular diffusion. Similarly for turbulent flow, the transport normal to the mean flow is primarily by turbulent diffusion, which shares some similarities with conduction type transport.

As with the laminar flow, the lateral edge effect scales with the diffusion thickness, and the lateral edge affects the flow approximately 10 to 15 diffusion thicknesses into the subliming surface. For turbulent wall bounded flow, the diffusion thickness changes very slowly in the streamwise direction, so the size of lateral edge effect is relatively constant. If the full spanwise extent of the finite strip is greater than forty conduction thicknesses, the centerline mass transfer is unaffected by the lateral edges.

6.1.3 Cavity

The flow field is numerically simulated using a shear stress transport model in ANSYS CFX and compares well with published numerical and experimental data. There are four flow regions in the cavity. Near the backward facing step there is a recirculation region with separated flow, a sidewall vortex past the recirculation region, redevel-

opment of the boundary layer and dissipation of the vortex, and the separated flow near the forward facing step.

Near the lateral edge, and after the separated flow region, the sidewall vortex determines the lateral change of the mass flux. The vortex brings in pure air from outside the cavity, locally depressing the concentration boundary layer and increasing the mass transfer. However, after the sidewall vortex dissipates and in the absence of an increase in turbulent kinetic energy, an increase of the mass flux near the sidewall persists for very shallow cavities. In contrast to the deeper cavities where the lateral profile of the mass flux is flat after the vortex dissipates, the lateral profile for shallow cavities is very similar to the profile found for turbulent boundary layer flow over a flat plate. As the cavities are very shallow, with values of 10 to 25 in wall coordinates, it is likely the cavity step height is low enough so the turbulent mixing in the boundary layer transports naphthalene in the lateral direction uninhibited. Based on the mass transfer measurements and results from the numerical flow simulation, if the cavity depth is shallower than 25 in wall coordinates and for a streamwise position farther than 200 step heights from the backward facing step, the lateral mass flux profile is similar to the lateral mass flux profile for flat plate turbulent flow.

6.2 Further Work

The effect of a single row of heated elements is fully explored in the present work, but the effect of several rows in the streamwise direction of heated elements is not explored. Often in electronics cooling, discrete heating elements are arranged in planar arrays where the streamwise thermal wake has to be considered. For turbulent flows, the same effect could be explored in addition to changes in lateral spacing. The lateral spacing for all the experimental runs are designed to be semi-infinite. In

addition, for both laminar and turbulent boundary layer flow, the large streamwise gradients near the leading edge are not explicitly analyzed. Transport is assumed to happen primarily in the lateral direction, but near the leading edge there is significant streamwise transport of energy or mass. Also, the effect of finite streamwise lengths is not explored. As the heated or subliming surface gets smaller in the streamwise direction, the leading edge and trailing edge start having significant effects on the surface flux over a larger proportion of the heated or subliming surface. Finally, analysis of the mass transfer in the cavity is hampered by a lack of detailed flow measurements and turbulent numerical simulations.

Reference List

Ambrose, D, I. J. Lawrenson, and C. H. S. Sprake (1975). "The vapour pressure of naphthalene". In: *The Journal of Chemical Thermodynamics* 7.12, pp. 1173–1176.

ANSYS (2015 (Release 16.1)). *ANSYS CFX*.

Armaly, B. F., F Durst, J. C. F. Pereira, and B Schönung (1983). "Experimental and theoretical investigation of backward-facing step flow". In: *Journal of Fluid Mechanics* 127, pp. 473–496.

Arpaci, V. S. (1966). *Conduction Heat Transfer*. Addison-Wesley series in mechanics and thermodynamics. Addison-Wesley.

Avancha, R. V. R. and R. H. Pletcher (2002). "Large eddy simulation of the turbulent flow past a backward-facing step with heat transfer and property variations". In: *International Journal of Heat and Fluid Flow* 23, pp. 601–614.

Baker, E (1972). "Liquid cooling of microelectronic devices by free and forced convection". In: *Microelectronics Reliability* 11.2, pp. 213–222.

Bignell, N (1983). "The effect of dissolved air on the density of water". In: *Metrologia* 19.2, pp. 57–59.

Cebeci, T. and P. Bradshaw (1984). *Physical and computational aspects of convective heat transfer*. Springer-Verlag.

Celik, I. B., U. Ghia, P. J. Roache, and C. J. Freitas (2008). "Procedure for estimation and reporting of uncertainty due to discretization in CFD applications". In: *Journal of Fluids Engineering-Transactions of the ASME* 130.7.

Chen, Y. T., J. H. Nie, B. F. Armaly, and H. T. Hsieh (2006). "Turbulent separated convection flow adjacent to backward-facing step—effects of step height". In: *International Journal of Heat and Mass Transfer* 49, pp. 3670–3680.

Cheng, C. L. and H. Schneeweiss (1998). "Polynomial regression with errors in the variables". In: *Journal of the Royal Statistical Society: Series B (Statistical Methodology)* 60.1, pp. 189–199.

Churchill, S. W. and R. Usagi (1972). "A general expression for the correlation of rates of transfer and other phenomena". In: *AIChE Journal* 18.6, pp. 1121–1128.

Clauser, F. H. (1956). "The turbulent boundary layer". In: *Advances in applied mechanics* 4, pp. 1–51.

Coleman, H. W. and W. G. Steele (2009). *Experimentation, validation, and uncertainty analysis for engineers*. 3rd edition. John Wiley & Sons.

Craven, P. and G. Wahba (1978). "Smoothing noisy data with spline functions". In: *Numerische Mathematik* 31.4, pp. 377–403.

Da Silva, A., S Lorente, and A Bejan (2004). "Optimal distribution of discrete heat sources on a plate with laminar forced convection". In: *International Journal of Heat and Mass Transfer* 47.10, pp. 2139–2148.

Dean, J. A. (1985). *Lange's handbook of chemistry*. McGraw Hill Book Co., New York, NY.

Deegan, R. D., O. Bakajin, T. F. Dupont, G. Huber, S. R. Nagel, and T. A. Witten (1997). "Capillary flow as the cause of ring stains from dried liquid drops". In: *Nature* 389.6653, pp. 827–829.

DeGraaff, D. B. and J. K. Eaton (2000). "Reynolds-number scaling of the flat-plate turbulent boundary layer". In: *Journal of Fluid Mechanics* 422, pp. 319–346.

Eaton, J. and J. Johnston (1981). "A review of research on subsonic turbulent flow reattachment". In: *AIAA J* 19.9, pp. 1093–1100.

Eaton, J. K. and J. C. Vogel (1985). "Combined heat transfer and fluid dynamic measurements downstream of a backward-facing step". In: *Journal of Heat Transfer* 107, pp. 922–929.

Eckert, E. R. G. and R. M. Drake Jr (1959). *Introduction to Heat and Mass Transfer*. 2^{nd} edition. McGraw-Hill.

Fassio, F. (2009). "Misure sperimentali del numero di Sherwood nelle regioni d'ingresso e laterali per uno strato limite turbolento su lastra piana". MA thesis. Università di Roma Tor Vergata.

Fellmuth, B. (2012). *Supplementary Information for the ITS-90: Introduction*. Bureau International des Poid et Measures.

Fuller, W. A. (1987). *Measurement Error Models*. Probability and Mathematical Statistics. Wiley.

Garimella, S. V., A. S. Fleischer, J. Y. Murthy, A. Keshavarzi, R. Prasher, C. Patel, S. H. Bhavnani, R Venkatasubramanian, R. Mahajan, Y Joshi, B. Sammakia, B. A. Myers, L. Chorosinski, M. Baelmans, P. Sathyamurthy, and P. E. Raad (2008). "Thermal challenges in next-generation electronic systems". In: *IEEE Transactions on Components and Packaging Technologies* 31.4, pp. 801–815.

Goldstein, R. J. and H. H. Cho (1995). "A review of mass transfer measurements using naphthalene sublimation". In: *Experimental Thermal and Fluid Science* 10.4, pp. 416–434.

Hastie, T., R. Tibshirani, and J. Friedman (2009). *Elements of Statistical Learning*. 2^{nd} edition. Springer Texts in Statistics. Springer.

Hauptmann, E. G. and Z. Rotem (1967). "Spanwise thermal diffusion in low Prandtl number boundary layer flow". In: *Proceedings of the Canadian Congress of Applied Mechanics*. Vol. 2, pp. 263–264.

Honda, H and J. Wei (2004). "Enhanced boiling heat transfer from electronic components by use of surface microstructures". In: *Experimental Thermal and Fluid Science* 28.2, pp. 159–169.

Hoyas, S. and J. Jiménez (2006). "Scaling of the velocity fluctuations in turbulent channels up to $Re_\tau = 2003$". In: *Physics of fluids* 18.1, p. 011702.

Hu, H. and R. G. Larson (2002). "Evaporation of a Sessile Droplet on a Substrate". In: *Journal of Physical Chemistry B* 106.6, pp. 1334–1344.

Hutchinson, M. F. and F. R. De Hoog (1985). "Smoothing noisy data with spline functions". In: *Numerische Mathematik* 47.1, pp. 99–106.

Incropera, F. P., J. S. Kerby, D. F. Moffat, and S. Ramadhyani (1986). "Convection heat transfer from discrete heat sources in a rectangular channel". In: *International Journal of Heat and Mass Transfer* 29.7, pp. 1051–1058.

Jackson, J. D. (1999). *Classical electrodynamics*. 3^{rd} edition. John Wiley & Sons.

James, G., D. Witten, T. Hastie, and R. Tibshirani (2013). *An Introduction to Statistical Learning*. Springer Texts in Statistics. Springer.

Jones, E., T. Oliphant, P. Peterson, et al. (2001–2017). *SciPy: Open source scientific tools for Python*. URL: http://www.scipy.org/.

Jovic, S. and D. M. Driver (1994). "Backward-facing step measurements at low Reynolds number, $Re_h = 5000$". In: *NASA Technical Memorandum* 108807.

Kandlikar, S. G. (2012). "History, advances, and challenges in liquid flow and flow boiling heat transfer in microchannels: A critical review". In: *Journal of heat transfer* 134.3, p. 034001.

Kasagi, N. and A. Matsunaga (1996). "Three-dimensional particle-tracking velocimetry measurement of turbulence statistics and energy budget in a backward-facing step flow". In: *International Journal of Heat and Fluid Flow* 16.6, pp. 477–485.

Kays, W. M., M. E. Crawford, and B. Weigand (2005). *Convective Heat and Mass Transfer*. 4th edition. McGraw-Hill.

Khan, W. A., J. Culham, and M. Yovanovich (2006). "The role of fin geometry in heat sink performance". In: *Journal of electronic packaging* 128.4, pp. 324–330.

Kline, S. J. and F. A. McClintock (1953). "Describing Uncertainties in Single-Sample Experiments". In: *Mechanical Engineering* 75, pp. 3–8.

Kondoh, T, Y Nagano, and T Tsuji (1993). "Computational study of laminar heat transfer downstream of a backward-facing step". In: *International Journal of Heat and Mass Transfer* 36.3, pp. 577–591.

Lan, H., B. F. Armaly, and J. A. Drallmeier (2009). "Three-dimensional simulation of turbulent forced convection in a duct with backward-facing step". In: *International Journal of Heat and Mass Transfer* 52.7, pp. 1690–1700.

Le, H., P. Moin, and J. Kim (1997). "Direct numerical simulation of turbulent flow over a backward-facing step". In: *Journal of fluid mechanics* 330, pp. 349–374.

Lemmon, E. W. (2014). "Thermophysical Properties of Air" in *CRC Handbook of Chemistry and Physics*. Ed. by W. M. Haynes. 95th edition. CRC Press/Taylor and Francis.

Lienhard IV, J. H. and J. H. Lienhard V (2012). *A Heat Transfer Textbook*. 4th edition. Phlogston Press.

Magin, R. L., B. W. Mangum, J. A. Statler, and D. D. Thornton (1981). "Transition Temperatures of the Hydrates of Na_2SO_4, Na_2HPO_4, and KF as Fixed Points in Biomedical Thermometry". In: *Journal of Research of the National Bureau of Standards* 86.2, pp. 181–192.

Mancin, S., C. Zilio, A. Diani, and L. Rossetto (2013). "Air forced convection through metal foams: Experimental results and modeling". In: *International Journal of Heat and Mass Transfer* 62, pp. 112–123.

Maximon, L. C. (2003). "The dilogarithm function for complex argument". In: *Proceedings of the Royal Society of London A: Mathematical, Physical and Engineering Sciences* 459.2039, pp. 2807–2819.

Menter, F. R. (1992). "Improved two-equation k-ω turbulence models for aerodynamic flows". In: *NASA Technical Memorandum* 103975.

Mochizuki, S and F. Nieuwstadt (1996). "Reynolds-number-dependence of the maximum in the streamwise velocity fluctuations in wall turbulence". In: *Experiments in Fluids* 21.3, pp. 218–226.

Model 2000 Multimeter User's Manual (2010). Keithley Instruments, Inc.

Model 470 Digital Pressure Transducers (1995). Setra.

Model 7001 Switch System Instruction Manual (2001). Keithley Instruments, Inc.

Moffat, R. J. (1988). "Describing the Uncertainties in Experimental Results". In: *Experimental Thermal and Fluid Science* 1.1, pp. 3–17.

Mohr, P. J., D. B. Newell, and B. N. Taylor (2016). "CODATA recommended values of the fundamental physical constants: 2014". In: *Journal of Physical and Chemical Reference Data* 45.4, pp. 043102.1–043102.74.

NF90 Series User's Guide. Velmex, Inc.

Olver, F. W., D. W. Lozier, R. F. Boisvert, and C. W. Clark, eds. (2010). *NIST Handbook of Mathematical Functions*. Cambridge University Press.

Ortega, A. and S. Ramanathan (2003a). "On the Use of Point Source Solutions for Forced Air Cooling of Electronic Components—Part 1: Thermal Wake Models for Rectangular Heat Sources". In: *Journal of Electronic Packaging* 125, pp. 226–234.

Ortega, A. and S. Ramanathan (2003b). "On the Use of Point Source Solutions for Forced Air Cooling of Electronic Components—Part 2: Conjugate Forced Convection". In: *Journal of Electronic Packaging* 125, pp. 235–243.

Ozisik, M. N. (1993). *Heat conduction*. 2nd edition. Wiley.

Philip, J. R. (1972). "Flows satisfying mixed no-slip and no-shear conditions". In: *Zeitschrift für Angewandte Mathematik und Physik (ZAMP)* 23.3, pp. 353–372.

Preston-Thomas, H (1990). “The international temperature scale of 1990 (ITS-90)”. In: *Metrologia* 27.1, pp. 3–10.

Reinsch, C. H. (1967). “Smoothing by spline functions”. In: *Numerische Mathematik* 10.3, pp. 177–183.

Roache, P. J. (1994). “Perspective: a method for uniform reporting of grid refinement studies”. In: *Transactions-American Society of Mechanical Engineers Journal of Fluids Engineering* 116, pp. 405–413.

Robbins, R. J. (1969). “Lateral Effects in a Thermal Boundary Layer”. MA thesis. University of British Columbia.

Rosner, B. (1983). “Percentage points for a generalized ESD many-outlier procedure”. In: *Technometrics* 25.2, pp. 165–172.

Saad, M. A. (1993). *Compressible Fluid Flow*. 2nd edition. Prentice Hall.

Siu-Ho, A., W. Qu, and F. Pfefferkorn (2007). “Experimental study of pressure drop and heat transfer in a single-phase micropin-fin heat sink”. In: *Journal of Electronic Packaging* 129.4, pp. 479–487.

Souza Mendes, P. R. (1991). “The Naphthalene Sublimation Technique”. In: *Experimental Thermal and Fluid Science* 4.5, pp. 510–523.

Taliaferro, M. E., M. Angelino, F. Gori, and R. J. Goldstein (2016). “Local heat transfer on a finite width surface with laminar boundary layer flow”. In: *Applied Thermal Engineering* 101, pp. 686–692.

Taliaferro, M. E., F. Fassio, F. Gori, T. W. Simon, and R. J. Goldstein (2018). “Lateral edge effects on the Sherwood number in turbulent flow over a flat plate”. In: *Journal of Heat Transfer* 140.

Tanaka, M., G. Girard, R. Davis, A. Peuto, and N. Bignell (2001). “Recommended table for the density of water between 0 °C and 40 °C based on recent experimental reports”. In: *Metrologia* 38.4, pp. 301–309.

Tennekes, H. and J. L. Lumley (1972). *A first course in turbulence*. MIT press.

The MathWorks, Inc. (2014). *MATLAB 2014a*.

Tso, C., G. Xu, and K. Tou (1999). “An experimental study on forced convection heat transfer from flush-mounted discrete heat sources”. In: *Journal of Heat Transfer* 121, pp. 326–332.

Van Driest, E. R. (1956). "On turbulent flow near a wall". In: *Journal of the Aeronautical Sciences*, pp. 1007–1011, 1036.

Ventola, L., F. Robotti, M. Dialameh, F. Calignano, D. Manfredi, E. Chiavazzo, and P. Asinari (2014). "Rough surfaces with enhanced heat transfer for electronics cooling by direct metal laser sintering". In: *International Journal of Heat and Mass Transfer* 75, pp. 58–74.

Wahba, G. (1983). "Bayesian 'Confidence intervals' for the Cross-validated Smoothing Spline". In: *Journal of the Royal Statistical Society. Series B (Methodological)*, pp. 133–150.

Wahba, G. (1990). *Spline models for observational data*. SIAM.

Waldron, J. (2004). "Measurements Regarding the Heat Mass Transfer Analogy on Flat Surfaces and in Separated Flow". MA thesis. University of Minnesota.

White, D. R., M. Ballico, V. Chimenti, S. Duris, E. Filipe, A. Ivanova, A. K. Dogan, E. Mendez-Lango, C. W. Meyer, F. Pavese, A. Peruzzi, E. Renaot, S. Rudtsch, and K. Yamazawa (2009). "Uncertainties in the Realization of the SPRT Sub-ranges of the ITS-90". In:

White, F. (1991). *Viscous fluid flow*. 2^{nd} edition. McGraw-Hill series in mechanical engineering. McGraw-Hill New York.

Yang, Z. and S. V. Garimella (2010). "Melting of phase change materials with volume change in metal foams". In: *Journal of Heat Transfer* 132.6, p. 062301.

Yovanovich, M. M. and P. Teertstra (2001). "Laminar Forced Convection Modeling of Isothermal Rectangular Plates". In: *Journal of Thermophysics and Heat Transfer* 15.2, pp. 205–211.

Žukauskas, A. and A. Šlanciauskas (1987). *Heat Transfer in Turbulent Fluid Flows*. Hemisphere Publishing Corp.

Appendix A

Example Calculations

A.1 Example Calculations of Laminar Heat Transfer Quantities

A.1.1 Example Calculation for Nu

This section shows how to calculate the Nu from eq. (2.40).

$$Nu = Nu_{z\to\infty}\left[1 + \frac{1}{\exp(\pi\zeta^*) - 1}\right] \tag{2.40}$$

Suppose table A.1 describes the flow conditions in air at the indicated location and combining the results from eqs. (A.16) and (A.17), the local Nu is

$$\begin{aligned} Nu &= 85.83\left[1 + \frac{1}{\exp(0.2861\pi) - 1}\right] \\ &= 85.83\,(1.686) \\ &= 145 \end{aligned} \tag{A.1}$$

Table A.1: Values for Laminar Example Calculation

Quantity	Value
U_∞	$3\,\mathrm{m\,s^{-1}}$
T_∞	$290\,\mathrm{K}$
T_w	$305\,\mathrm{K}$
P	$100\,\mathrm{kPa}$
x'	$0.3\,\mathrm{m}$
ξ	$0.1\,\mathrm{m}$
z	$0.001\,\mathrm{m}$

Calculating *Re*

Using eq. (3.27) and the freestream temperature value from table A.1, the dynamic viscosity for the freestream is

$$\mu_w = 1.805 \times 10^{-5}\,\mathrm{Pa \cdot s}. \tag{A.2}$$

Using eq. (3.27) and the surface temperature value from table A.1, the dynamic viscosity at the surface is

$$\mu_\infty = 1.878 \times 10^{-5}\,\mathrm{Pa \cdot s}. \tag{A.3}$$

Averaging eqs. (A.2) and (A.3), the mean value of the dynamic viscosity is

$$\mu_f = 1.842 \times 10^{-5}\,\mathrm{Pa \cdot s}. \tag{A.4}$$

Using the ideal gas law, eq. (3.28), and the freestream temperature value from table A.1, the density of air in the freestream is

$$\rho_w = 1.201\,\mathrm{kg\,m^{-3}}. \tag{A.5}$$

Using the ideal gas law, eq. (3.28), and the surface temperature value from table A.1, the density of air at the surface is

$$\rho_w = 1.142\,\mathrm{kg\,m^{-3}}. \tag{A.6}$$

Averaging eqs. (A.5) and (A.6), the mean value of the density is

$$\rho_f = 1.172\,\mathrm{kg\,m^{-3}}. \tag{A.7}$$

Using eqs. (A.4) and (A.7) and the value of the freestream velocity from table A.1, the Re is

$$\begin{aligned} Re &= \frac{\rho_f U_\infty x'}{\mu_f} \\ &= \frac{(1.172)\,(0.3)\,(3)}{1.842 \times 10^{-5}} \\ &= 57\,260 \end{aligned} \tag{A.8}$$

Calculating Pr

Using eq. (3.25) and the freestream temperature value from table A.1, the thermal conductivity for the freestream is

$$k_\infty = 0.025\,63\,\mathrm{W\,m^{-1}\,K^{-1}}. \tag{A.9}$$

Using eq. (3.25) and the surface temperature value from table A.1, the thermal conductivity at the surface is

$$k_w = 0.026\,75\,\mathrm{W\,m^{-1}\,K^{-1}}. \tag{A.10}$$

Averaging eqs. (A.9) and (A.10), the mean value of the thermal conductivity is

$$k_f = 0.026\,19\,\mathrm{W\,m^{-1}\,K^{-1}}. \tag{A.11}$$

Using eq. (3.26) and the freestream temperature value from table A.1, the specific heat capacity for the freestream is

$$c_{p,\infty} = 1006\,\mathrm{J\,kg^{-1}\,K^{-1}}. \tag{A.12}$$

Using eq. (3.26) and the surface temperature value from table A.1, the specific heat capacity at the surface is

$$c_{p,w} = 1007\,\mathrm{J\,kg^{-1}\,K^{-1}}. \tag{A.13}$$

Averaging eqs. (A.12) and (A.13), the mean value of the specific heat capacity is

$$c_{p,f} = 1006.5\,\mathrm{J\,kg^{-1}\,K^{-1}}. \tag{A.14}$$

Using eqs. (A.4), (A.11) and (A.14), the Pr is

$$\begin{aligned} Pr &= \frac{\mu_f c_{p,f}}{k_f} \\ &= \frac{(1.842 \times 10^{-5})\,(1006.5)}{0.026\,19} \\ &= 0.7079 \end{aligned} \tag{A.15}$$

Calculating $Nu_{z\to\infty}$

Equation (2.44) is used to calculate the Nu far from the lateral edge. The $Nu_{z\to\infty}$ is calculated at the same streamwise location as the local Nu near the edge.

$$\begin{aligned} Nu_{z\to\infty} &= \frac{0.332 Re_x^{1/2} Pr^{1/3}}{\left[1-\left(\frac{\xi}{x}\right)^{3/4}\right]^{1/3}} && (2.44)\\ &= \frac{0.332\,(57\,260)^{1/2}\,(0.7079)^{1/3}}{\left[1-\left(\frac{0.1}{0.3}\right)^{3/4}\right]^{1/3}} \\ &= \frac{70.80}{0.8249} \\ &= 85.83 && (A.16) \end{aligned}$$

Calculating ζ^*

Using eq. (2.37) with the information in table A.1 and eq. (A.16), the nondimensional lateral parameter is

$$\begin{aligned} \zeta^* &= \frac{z}{x'} Nu_{z\to\infty} && (2.37)\\ &= \frac{0.001}{0.3} 85.83 \\ &= 0.2861. && (A.17) \end{aligned}$$

Appendix B

Regression Analysis

B.1 Linear Least Squares with Errors in the Variables

The most common form of regression analysis is least squares estimation (see Coleman and Steele (2009) for an overview). One of the drawbacks of ordinary least squares (OLS) is the assumption the independent variable is error free. To address this issue several techniques have been devised, two of which are outlined below.

Fuller (1987, section 1.3.3, page 36) outlines a total least squared method when the uncertainty in the independent and dependent variables are known. If the estimated true variables ($\hat{x}$ and $\hat{y}$) can be modeled as

$$\hat{y} = \beta_0 + \beta_1 \hat{x}, \tag{B.1}$$

where the estimated true variables are related to the observed variables as,

$$\begin{aligned} y &= \hat{y} + e \\ x &= \hat{x} + u. \end{aligned} \tag{B.2}$$

The errors, e and u, are normally distributed with a mean of 0 and standard deviations of σ_e and σ_u respectively.

The distance that is being minimized is called the squared statistical distance (SSD), which can be visualized as some distance from the observed data point to the fitted line. If the errors for both variables are equal, the the distance minimized is the perpendicular distance from the observed data to the regression line.

$$SSD^2 = \sum \left[\left(\frac{y_i - \hat{y}_i}{\sigma_e^2} \right)^2 + \left(\frac{x_i - \hat{x}_i}{\sigma_u^2} \right)^2 \right] \tag{B.3}$$

For eqs. (B.1) to (B.3), Fuller (1987) gives the following estimate for the best fit.

$$\hat{\beta}_1 = \frac{s_{yy} - \delta s_{xx} + \sqrt{(s_{yy} - \delta s_{xx})^2 + 4\delta s_{xy}^2}}{2s_{xy}} \tag{B.4}$$

$$\hat{\beta}_0 = \overline{y} - \hat{\beta}_1 \overline{x} \tag{B.5}$$

$$\hat{x}_i = x_i + \frac{\hat{\beta}_1}{\delta + \hat{\beta}_1^2} \left(y_i - \hat{\beta}_0 - \hat{\beta}_1 x_i \right) \tag{B.6}$$

$$\hat{y}_i = \hat{\beta}_0 + \hat{\beta}_1 \hat{x}_i \tag{B.7}$$

Where δ is the ratio of the variances

$$\delta = \frac{\sigma_e^2}{\sigma_u^2}. \tag{B.8}$$

And the sample covariances are

$$\begin{aligned} s_{xx} &= \frac{(x_i - \overline{x})^2}{n-1} \\ s_{yy} &= \frac{(y_i - \overline{y})^2}{n-1} \\ s_{xy} &= \frac{(x_i - \overline{x})(y_i - \overline{y})}{n-1}. \end{aligned} \tag{B.9}$$

B.2 Polynomial Regression with Errors in the Variables

The model outlined in appendix B.1 is very useful if the underlying relationship between the true variables is linear, however this often not the case. Cheng and Schneeweiss (1998) provide a framework for polynomial regression when errors in the independent variables are known. Assuming the errors of x and y are independent, their model is

$$\hat{y}_i = \beta_0 + \beta_1 \hat{x}_i + \beta_2 \hat{x}_i^2 + ... + + \beta_k \hat{x}_i^k + e_i, \tag{B.10}$$

where the estimated true variables are related to the observed variables as:

$$\begin{aligned} y_i &= \hat{y}_i + e_i, \\ x_i &= \hat{x}_i + u_i. \end{aligned} \tag{B.11}$$

The coefficients, β_i, for the regression are found by modifying the least squares model to account for the error in the independent variable. By solving

$$\sum H_i \hat{\beta} = \sum h_i \tag{B.12}$$

The estimated coefficients of β can be found. Each element of (p, q) of the $(k+1) \times (k+1)$ matrix H_i is $t_{i,p+q}$, where $t_{i,r}$ is the expected value (first moment) of $\hat{x}_i^r$. The expected value can be found with a recurrence relation given by Cheng and Schneeweiss (1998) (the subscripts i have been dropped),

$$\begin{aligned} t_{r+1} &= x t_r - \sigma_u^2 r t_{r-1}, \\ t_{-1} &= t_0 = 1, \end{aligned} \tag{B.13}$$

where h_i is a column vector of $k+1$ elements, $h = (h_0, h_1, ..., h_r, ..., h_k)^T$. The expected value of each element is $h_r = t_r y$, again, with the subscript i, dropped. The calibrations outlined in section 3.3.1 were done using this method.

B.3 Leave-One-Out Cross-Validation

A central concern of performing regression is choosing a model that accurately predicts new data without overfitting. One method of guarding against overfitting without over simplifying the regression model is leave-one-out cross-validation (LOOCV). The concept is fairly simple and provides more insight than simply using the coefficient of determination (commonly denoted as R^2) as a measure of the goodness of the fit. An accessible introduction can be found in James et al. (2013) and Hastie et al. (2009).

LOOCV is a simple concept. For a given model a datum point is left out and the regression completed. The difference between the removed data point and the value predicted from the regression is calculated. This process is carried out for all the data points, with all the differences used to calculate the mean squared error (MSE). This process is then replicated for all the different models that are being judged. If the model is too simple then the MSE will be large, however for models that overfit the data the MSE is also large due to the fitting of noise in the data. The model that has the lowest MSE is then selected.

Appendix C

Uncertainty Calculations

C.1 Platinum Resistance Thermometer

The total uncertainty of the for the platinum resistance thermometer was found using a mixture of numerical and algebraical techniques. Both the Monte Carlo Method and the Taylor Series Method are used as outlined in Coleman and Steele (2009). Based on eqs. (3.1) and (3.4), the temperature error of the PRT depends on the measurement errors of R_{tp}, $R_{\mathrm{Na_2SO_4}}$, and the hydrate transition temperature of sodium sulfate, $T_{\mathrm{Na_2SO_4}}$. The functional relationships of all the variables and the propagation of the errors are described below.

The uncertainties of calculating temperature using a platinum resistance thermometer, shown in eq. (3.4), are from uncertainties in the value of W_r. In turn, the uncertainties of W_r are from the calibration of the platinum resistance thermometer, and has two sources of uncertainties, uncertainties in the determination of a, shown in eq. (3.2), and uncertainties in the measurement of the resistance of the triple point of water, R_{tp}, for the platinum resistance thermometer used. The sources of uncertainties in both a and R_{tp} are shown in table C.1. There were 624 triple point measurements made over six hour period and 394 hydrate transition temperature

Table C.1: Uncertainty of constants used for PRT calibration

Measurement	Value	Sources of Uncertainty (one standard deviation)
R_{tp}	$25.560\,72\,\Omega$	$s_{\bar{R}_{tp}} = 1.03 \times 10^{-5}\,\Omega$ $\frac{\partial R}{\partial T}\Delta T_{tp} = 3.04 \times 10^{-5}\,\Omega$
$R_{\mathrm{Na_2SO_4}}$	$28.842\,80\,\Omega$	$s_{\bar{R}_{Na_2SO_4}} = 2.23 \times 10^{-5}\,\Omega$
$T_{Na_2SO_4}$	$32.365\,^{\circ}\mathrm{C}$	$T_{\mathrm{Na_2SO_4}} = 1\,\mathrm{mK}$ IPTS-68 to ITS-90 $= 0.5\,\mathrm{mK}$ $\Delta T_{\mathrm{Na_2SO_4},cal} = 1.42\,\mathrm{mK}$

measurements made over a 4.5 hour period. As table C.1 shows, the associated uncertainty in the mean resistance measurements used in the calibration are $1.03 \times 10^{-5}\,\Omega$ and $3.04 \times 10^{-5}\,\Omega$ for the triple point of water and the hydrate transition temperature respectively. As mentioned in section 3.3.1, there is an added error for the triple point temperature of as much as 1 mK for triple point cells. As the triple point cell was allowed to anneal for several hours, and using White et al. (2009, section 3.4), the uncertainty is estimated at 0.6 mK. The error for the calibration of the platinum resistance thermometer associated with the uncertainty in the triple point temperature is estimated as shown in table C.1 as $\frac{\partial R}{\partial T}\Delta T_{tp}$ with a value of $3.04 \times 10^{-5}\,\Omega$.

The largest contribution to the uncertainty for the calibration of the platinum resistance thermometer is the uncertainties in the hydrate transition temperature of sodium sulfate, $T_{\mathrm{Na_2SO_4}}$. Magin et al. (1981) states the uncertainty of their measurements at 2 mK. The conversion from the IPTS-68 temperature reported by Magin et al. (1981) to the ITS-90 temperature added 1 mK (Fellmuth 2012) of uncertainty. The uncertainty of realizing the hydrate transition temperature is estimated to be 2.84 mK from impurities, pressure changes, and placement of the platinum resistance thermometer in the sodium solution is estimate using results from Magin et al. (1981).

The distribution of the constant value a from eq. (3.2) is found using the Monte Carlo method. The constant a is calculated 100 000 times with the values of R_{tp}, $R_{\mathrm{Na_2SO_4}}$, and $T_{Na_2SO_4}$ taken from the distributions described by table C.1. The standard deviation of a calculate using this method is 5.72×10^{-5}.

C.2 Thermocouples

Appendix C.1 described the procedure for estimating the uncertainty of the calibration constants for the platinum resistance thermometer. This section describes the procedure for estimating the uncertainty of the calibration of the thermocouples against the calibrated platinum resistance thermometer. The uncertainty of the calibration for the thermocouples is calculated using the Monte Carlo method with standard deviations shown in table C.2.

Table C.2: Uncertainty of constants used for thermocouples calibration

Measurement	Sources of Uncertainty (one standard deviation)
Voltage, $\mathcal{E}$ (mV)	$s_{\bar{\mathcal{E}}} = 2.47 \times 10^{-4}\,\mathrm{mV}$ bias $= 4 \times 10^{-5}\mathcal{E}$
Resistance, R (Ω)	$s_{\bar{R}} = 2.25 \times 10^{-4}\,\Omega$
a from eq. (3.2)	5.72×10^{-5}
Type 3 non-uniqueness	Equation C.1

The uncertainties for the mean voltage and resistance measurements are estimated from the data taken during the calibration. The bias error for the digital multimeter was estimated from *Model 2000 Multimeter User's Manual* (2010), and the uncertainty for a is taken from the analysis in appendix C.1.

White et al. (2009) indicate that variation between PRTs need to be taken into account, referred to as type 3 non-uniqueness. White et al. (2009) do not provide an equation that estimates the error caused by the expected non-uniqueness over the current temperature range because the hydrate transition temperature of sodium sulfate is not defined by the ITS-90. The expected error function is constructed to have the same form as the equation reported by White et al. (2009) for type 3 non-uniqueness with a similar value for the maximum error. What White et al. (2009) call Type 1 uncertainty will be ignored because the calibration is over one subrange. This uncertainty of the type 3 non-uniqueness is given by eq. (C.1).

$$U_{type3} = 2\left(3.8 \times 10^{-7}\right)(T - 273.15)\left[(T - 273.15) - T_{Na_2SO_4}\right] \tag{C.1}$$

The calibration procedure described in section 3.3.1 for thermocouples is repeated 100 000 times with required values pulled from the appropriate population distributions. First, W_r is calculated with the values of a, R, and R_{tp} pulled from the distributions described in tables C.1 and C.2. After the temperature is calculated using eq. (3.4), values from normal distributions described by C.1 (with the added uncertainties from $T_{\mathrm{Na_2SO_4}}$) are added to the temperature value. The "noisy" voltage values are then fit against the "noisy" temperature values using the procedure described in appendix B.2. The resulting distributions of the fitted (as opposed to the platinum resistance thermometer) temperatures is then used to to describe the uncertainty of the calibration.

The 95 % uncertainty for the calibration of the thermocouples is approximated with eq. (C.2). The precision errors associated with a temperature measurement

taken during the mass transfer experiment are not included.

$$\frac{U_{tc}}{2} = 2.00 \times 10^{-8} (T - 273.15)^4 - 1.38 \times 10^{-6} (T - 273.15)^3 + 3.37 \times 10^{-5} (T - 273.15)^2 - 3.31 \times 10^{-4} (T - 273.15) + 5.56 \times 10^{-3} \quad \text{(C.2)}$$

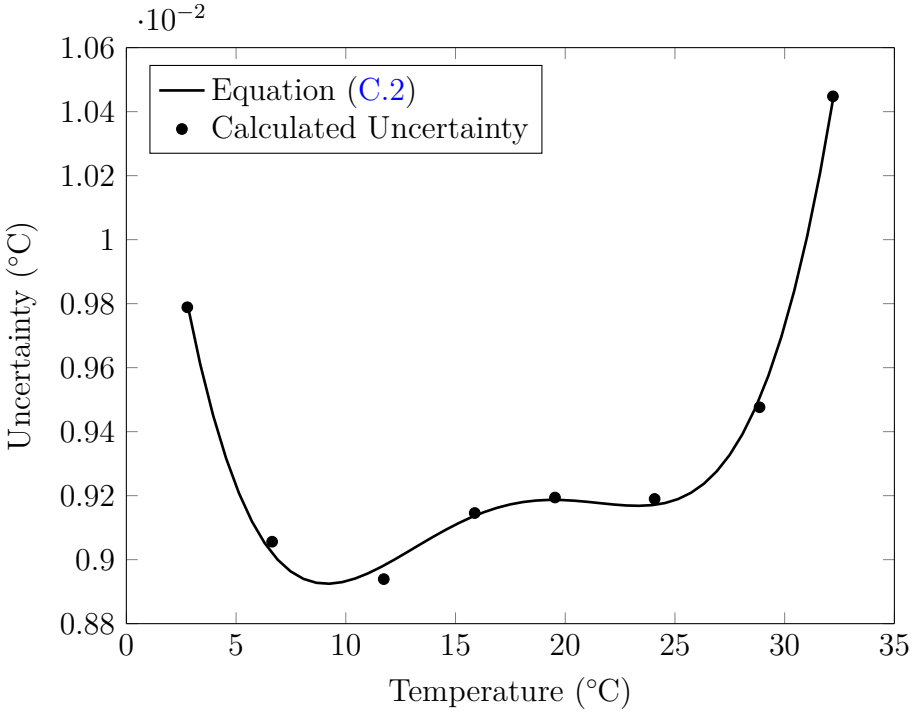

Figure C.1: 95 % Uncertainty for thermocouple calibration

C.3 Uncertainty of the Experimental Stanton Number

The general uncertainty is calculated by applying the method presented by Kline and McClintock (1953) to eq. (3.51).

$$\hat{\sigma}_{St^2} = \left(\frac{\partial St}{\partial \rho_{n,g}}\hat{\sigma}_{\rho_{n,g}}\right)^2 + \left(\frac{\partial St}{\partial \overline{U}_\infty}\hat{\sigma}_{\overline{U}_\infty}\right)^2 + \left(\frac{\partial St}{\partial \rho_{n,s}}\hat{\sigma}_{\rho_{n,s}}\right)^2 + \left(\frac{\partial St}{\partial \delta_s}\hat{\sigma}_{\delta_s}\right)^2 + \left(\frac{\hat{\sigma}_{\tau_t}}{\tau_t}\right)^2 \quad \text{(C.3)}$$

However, the variables are all multiplied together so normalizing by St^2 changes eq. (C.3) into a simple equation relating the relative uncertainties.

$$\left(\frac{\hat{\sigma}_{St}}{St}\right)^2 = \left(\frac{\hat{\sigma}_{\rho_{n,g}}}{\rho_{n,g}}\right)^2 + \left(\frac{\hat{\sigma}_{\overline{U}_\infty}}{\overline{U}_\infty}\right)^2 + \left(\frac{\hat{\sigma}_{\rho_{n,s}}}{\rho_{n,s}}\right)^2 + \left(\frac{\hat{\sigma}_{\delta_s}}{\delta_s}\right)^2 + \left(\frac{\hat{\sigma}_{\tau_t}}{\tau_t}\right)^2 \quad \text{(C.4)}$$

The rest of the uncertainty equations are put in a similar form as eq. (C.4) when convenient.

Uncertainty for for the time in tunnel, $\hat{\sigma}_{\tau_t}$, is taken to be 20 s and the uncertainty of solid naphthalene, $\hat{\sigma}_{\rho_{n,s}}$, is taken to be 1.1 % (Goldstein and Cho 1995) and using the uncertainty estimates from eqs. (C.7), (C.13) and (C.24), the measurement uncertainty of the mass Stanton number is

$$\begin{aligned}\frac{\hat{\sigma}_{St}}{St} &= \sqrt{0.016^2 + 0.0101^2 + 0.011^2 + 0.00935^2 + 0.00389^2} \\ &= 2.41\,\% \end{aligned} \quad \text{(C.5)}$$

The value given in eq. (C.5) is the one standard deviation estimate of the uncertainty. Coleman and Steele (2009) recommend a coverage factor of two for estimating the

95 % confidence interval, which would indicate an uncertainty of about 4.8 % with a 95 % confidence level. The uncertainty for the Stanton number cannot be much lower than this, as the two largest uncertainties, the vapor density of naphthalene and the solid density of naphthalene, are mostly reflect uncertainty from property data taken from the literature. For the very worst cases tested (in terms of uncertainty), 15 µm sublimation depth for 15 minutes in the tunnel, the 95 % confidence level uncertainty only increases to about 7 %. Therefore a representative value for the uncertainty of the mass Stanton number is approximately 5 % at a 95 % confidence level.

C.3.1 Uncertainty in the Naphthalene Vapor Density

The density of the naphthalene vapor is calculated using the ideal gas law. Therefore, assuming the uncertainty in the ideal gas coefficient and molucular mass of naphthalene are zero, the total uncertainty is

$$\left(\frac{\hat{\sigma}_{\rho_n}}{\rho_n}\right)^2 = \left(\frac{\hat{\sigma}_T}{T}\right)^2 + \left(\frac{\hat{\sigma}_{P_n}}{P_n}\right)^2. \tag{C.6}$$

Using the uncertainties from eqs. (C.9) and (C.11), the total uncertainty for the naphthalene vapor density is

$$\begin{aligned}\frac{\hat{\sigma}_{\rho_n}}{\rho_n} &= \sqrt{\left(2.45 \times 10^{-5}\right)^2 + 0.016^2} \\ &= 1.6\,\% \quad \left(6.94 \times 10^{-6}\,\mathrm{kg\,m^{-3}}\right).\end{aligned} \tag{C.7}$$

The vapor pressure of naphthalene contributes most of the uncertainty to the naphthalene vapor density estimate.

Uncertainty in the Temperature Measurements

The uncertainty of a temperature measurement is a combination of uncertainties from the thermocouple calibration and noise of the temperature measurements.

$$\hat{\sigma}_T^2 = \hat{\sigma}_{T_{cal}}^2 + \hat{\sigma}_{T_{exp}}^2 \tag{C.8}$$

The uncertainty of the calibration, $\hat{\sigma}_{T_{cal}}$, is taken from appendix C.2 and the noise from the measurements during the experiment is taken from distribution of the differences between the two thermocouples measuring the freestream temperature. The average difference between the two thermocouples is 5.6 mK and the one-standard deviation uncertainty of the measurement according to eq. (C.2) is 4.6 mK. The total uncertainty is

$$\begin{aligned} \hat{\sigma}_T &= \sqrt{0.0046^2 + 0.0056^2} \\ &= 7.2\,\text{mK} \quad \left(2.45 \times 10^{-3}\,\%\right). \end{aligned} \tag{C.9}$$

Uncertainty in the Naphthalene Saturated Pressure Estimate

The uncertainty of the naphthalene pressure estimate is a combination of the uncertainty from the temperature measurement and the uncertainty of the naphthalene vapor pressure correlation presented in eq. (3.32).

$$\hat{\sigma}_{P_n}^2 = \left(\frac{\partial P_n}{\partial T}\hat{\sigma}_T\right)^2 + \hat{\sigma}_{P_{n,fit}}^2 \tag{C.10}$$

Using the results from eq. (C.9), and the stated uncertainty of 1.6 % from Ambrose et al. (1975) for the correlation for the saturated pressure, the total uncertainty is

$$\begin{aligned}\hat{\sigma}_{P_n} &= \sqrt{\left((0.832)\,(0.0072)\right)^2 + \left(8.29\frac{1.6}{100}\right)^2} \\ &= 0.133 \quad (1.6\,\%)\end{aligned} \tag{C.11}$$

Almost all of the error is from the stated uncertainty of the saturated pressure correlation.

C.3.2 Uncertainty in the Freestream Velocity

The freestream velocity is calculated according to eq. (3.12), so the uncertainties is a combination of uncertainties of the tunnel air density estimate and the dynamic pressure estimate.

$$\left(\frac{\hat{\sigma}_{\overline{U}_\infty}}{U_\infty}\right)^2 = \left(\frac{1}{2}\frac{\hat{\sigma}_{P_{dyn}}}{P_{dyn}}\right)^2 + \left(\frac{1}{2}\frac{\hat{\sigma}_{\rho_a}}{\rho_a}\right)^2 \tag{C.12}$$

Using the values from eqs. (C.19) and (C.21) the uncertainty of the freestream velocity is

$$\begin{aligned}\frac{\hat{\sigma}_{\overline{U}_\infty}}{U_\infty} &= \sqrt{\left(\frac{1}{2}0.0177\right)^2 + \left(\frac{1}{2}0.00986\right)^2} \\ &= 1.01\,\% \quad \left(1.01\,\mathrm{m\,s^{-1}}\right).\end{aligned} \tag{C.13}$$

Uncertainty in of the Tunnel Pressure

While the tunnel pressure is not explicitly shown in eq. (C.12), it does appear in several other uncertainty estimates. The tunnel pressure is the sum of the ambient pressure reading and the pressure difference between the tunnel and ambient. There

the total uncertainty is

$$\hat{\sigma}_{P_t}^2 = \hat{\sigma}_{P_{man}}^2 + \hat{\sigma}_{P_\infty}^2. \tag{C.14}$$

Using the results from eqs. (C.16) and (C.17), the uncertainty for the pressure in the tunnel is

$$\begin{aligned}\hat{\sigma}_{P_t} &= \sqrt{\hat{\sigma}_{P_{man}}^2 + \hat{\sigma}_{P_\infty}^2} \\ &= \sqrt{950^2 + 32.0^2} \\ &= 951\,\text{Pa} \quad (0.97\,\%)\,. \end{aligned} \tag{C.15}$$

The error from the ambient pressure readings are negligible compared to the error from the manometer reading.

The uncertainty from the ambient pressure readings is a combination of the uncertainty of the Setra 470 and the measurement noise during the experiment.

$$\begin{aligned}\hat{\sigma}_{P_\infty} &= \sqrt{\hat{\sigma}_{P_\infty,cal}^2 + \hat{\sigma}_{P_\infty,meas}^2} \\ &= \sqrt{\left(97838\frac{0.02}{100}\right)^2 + (25.4)^2} \\ &= 32.0\,\text{Pa} \quad (0.033\,\%) \end{aligned} \tag{C.16}$$

The uncertainty of the manometer pressure reading, $\hat{\sigma}_{P_{man}}$, is the combination of the uncertainties of the water density from eq. (C.22) and the manometer height reading. Coleman and Steele (2009, pg. 53) argue the bias error for a triangular distribution is half the range divided by the square root of six, so with a triangular shaped distribution for the readings and a maximum and minimum error of $\pm 0.25\,\text{mm}$,

the resolution error for the manometer height is 0.102 mm.

$$\begin{aligned}\hat{\sigma}_{P_{man}} &= P_t\sqrt{\left(\frac{\hat{\sigma}_{\rho_{H_2O}}}{\rho_{H_2O}}\right)^2+\left(\frac{\hat{\sigma}_{h_{H_2O}}}{h_{man}}\right)^2}\\ &= 97735\sqrt{\left(\frac{0.00181}{997.896}\right)^2+\left(\frac{1.02\times10^{-4}}{0.0105}\right)^2}\\ &= 950\,\text{Pa}\quad(0.97\,\%)\end{aligned}\tag{C.17}$$

Uncertainty in the Dynamic Pressure Estimate

The dynamic pressure is measured with a micromanometer according to eq. (3.13). The uncertainty is a combination of the uncertainty of the density of water, repeatability of the water height measurement, and the resolution of the water height measurement.

$$\left(\frac{\hat{\sigma}_{P_{dym}}}{P_{dym}}\right)^2=\left(\frac{\hat{\sigma}_{\rho_a}}{\rho_a}\right)^2+\left(\frac{\hat{\sigma}_{h_{\mu,noise}}}{h_\mu}\right)^2+\left(\frac{\hat{\sigma}_{h_{\mu,res}}}{h_\mu}\right)^2\tag{C.18}$$

As multiple measurements are made every experiment, the pooled standard deviation (Coleman and Steele 2009, pg. 44) of all the measurements is used as an estimate for the repeatability error of the water micromanometer. Using 0.0864 mm for the repeatability of the micromanometer and 0.001 02 mm as the resolution of the of the instrument (0.0025 mm divided by the square root of six as is done for the manometer) and the result from eq. (C.21), the uncertainty of the dynamic pressure is

$$\begin{aligned}\left(\frac{\hat{\sigma}_{P_{dym}}}{P_{dym}}\right) &= \sqrt{0.00986^2+0.0147^2+0.000173^2}\\ &= 1.77\,\%\quad(1.02\,\text{Pa})\,.\end{aligned}\tag{C.19}$$

The repeatability errors contribute most to the uncertainty of the dynamic pressure.

Uncertainty in the Air Density Estimate

The ideal gas law is used to calculate the density of air, and the total uncertainty is a contribution from the uncertainties of the tunnel pressure, the tunnel temperature, the ideal gas law (eq. (3.28)), and the tabulated density data.

$$\left(\frac{\hat{\sigma}_{\rho_a}}{\rho_a}\right)^2 = \left(\frac{\hat{\sigma}_{P_t}}{P_t}\right)^2 + \left(\frac{\hat{\sigma}_T}{T}\right)^2 + \left(\frac{\hat{\sigma}_{\rho_{a,fit}}}{\rho_a}\right)^2 + \left(\frac{\hat{\sigma}_{\rho_{a,tab}}}{\rho_a}\right)^2 \tag{C.20}$$

Combining the values from eqs. (C.9) and (C.15) the uncertainties presented in section 3.4.1 gives

$$\begin{aligned}\frac{\hat{\sigma}_{\rho_a}}{\rho_a} &= \sqrt{0.0973^2 + \left(2.45 \times 10^{-5}\right)^2 + 0.00139^2 + 0.000867^2} \\ &= 0.986\,\% \quad \left(0.0114\,\mathrm{kg\,m^{-3}}\right)\end{aligned} \tag{C.21}$$

Uncertainty in the Water Density Estimate

The uncertainty of the water density estimate is a combination of the uncertainty of eq. (3.29) and the uncertainty of the temperature measurements. Combining with the temperature uncertainty from eq. (C.9) gives,

$$\begin{aligned}\hat{\sigma}_{\rho_{H_2O}} &= \sqrt{\left(\frac{\partial \rho_{H_2O}}{\partial T}\hat{\sigma}_T\right)^2 + \Delta\rho^2_{H_2O,fit}} \\ &= \sqrt{\left((-0.222)\,(0.0072)\right)^2 + \left(\frac{0.83}{1000}\right)^2} \\ &= 0.0018\,\mathrm{kg\,m^{-3}} \quad \left(1.8 \times 10^{-4}\,\%\right).\end{aligned} \tag{C.22}$$

C.3.3 Uncertainty in the Sublimed Naphthalene Depth

The final sublimed naphthalene depth measurements require a fit of the voltage data from the calibration in eq. (3.6) and the subtraction of the natural convection losses given by eq. (3.34). Combining uncertainties from these sources, as well as the noise of the sublimed depth measurements from fig. 3.12 gives a uncertainty of

$$\hat{\sigma}^2_{\delta_s} = \hat{\sigma}^2_{\delta_{s,nc}} + \hat{\sigma}^2_{\delta_{s,cal}} + \hat{\sigma}^2_{\delta_{s,noise}}. \tag{C.23}$$

Using a representative value of 35 µm as the final sublimed naphthalene depth and a conservative 5 µm natural convection loss (and therefore a total voltage difference of about 2.09 V), the uncertainty of the depth measurement is

$$\begin{aligned}\hat{\sigma}_{\delta_s} &= \sqrt{\left(5\frac{4.25}{100}\right)^2 + \left(2.09\left(8.18\times10^{-2}\right)\right)^2 + 0.181^2} \\ &= 0.327\,\mu\text{m} \quad (0.935\,\%)\end{aligned} \tag{C.24}$$

The second term, $\left(2.09\left(8.18\times10^{-2}\right)\right)^2$, is the voltage value multiplied by the uncertainty of the calibrated slope in eq. (3.6).

C.4 Uncertainty of the Experimental Normalized Stanton Number

Most of the data presented is for normalized mass Stanton numbers. The uncertainty for the normalized St is fairly straightforward, as the various temperatures, pressures, freestream velocities, and densities are the same for a given experiment. Therefore the

ratio of St from the same experiment is a ratio of the sublimed naphthalene depths.

$$\frac{St}{St_c} = \frac{\delta_s}{\delta_{s,c}} \tag{C.25}$$

If the uncertainties of the measured sublimed depths are the same and using the value from eq. (C.24), the total uncertainty is

$$\begin{aligned} \frac{\hat{\sigma}_{St/St_c}}{St/St_c} &= \sqrt{2\left(\frac{\hat{\sigma}_{\delta_s}}{\delta_s}\right)^2} \\ &= 1.32\,\%. \end{aligned} \tag{C.26}$$

For the very worst cases tested, 15 µm sublimation depth for 15 minutes in the tunnel, the one standard deviation uncertainty doubles to 2.75 %. However, the 1.32 % is representative of the uncertainty for most of the experiments conducted. Using a coverage factor of two results in a 95 % confidence interval of 2.6 %.

Appendix D

Code Examples

D.1 Data Acquisition

The code below is an example of the Python 2.7 code used to interface with the multimeter and multiplexer described in section 3.1.1 for measuring the temperature and LVDT output voltage during the naphthalene surface scanning procedure as described in section 3.3.3. The code was written with continuity in mind, so it bears resemblance to codes written in C by previous researchers in the Heat Transfer Laboratory.

```
import pyvisa
import time
import numpy as np

class MxDmm():
    #Defines the interface for the multimeter and
       multiplexer
    def __init__(self):
        mx_pad = 6
        dmm_pad = 2
        self.LVDT_ch = 9
        self.card = 1

        # Polynomial constants for calibration curve
```

```
        self.temp_cal = [0.0,1.692347E-2,-4.809033E
           -9,-1.386736E-10,2.667226E-14]

        rm = pyvisa.ResourceManager()
        mx_name = "GPIB0::"+str(mx_pad)+"::INSTR"
        if mx_name not in rm.list_resources():
            print 'Multiplexer name: ',mx_name
            print 'Available intruments: ',rm.list_resources
               ()
            quit('\aMultiplexer not found')
        else:
            mx = rm.open_resource(mx_name)
        self.mx = mx
        mx.clear()

        mx.write(":SYSTEM:PRES")
        mx.write(":TRIG:SOUR BUS")
        mx.write(":OPEN ALL")

        dmm_name = "GPIB0::"+str(dmm_pad)+"::INSTR"
        if dmm_name not in rm.list_resources():
            print 'Digital Multimeter name: ',dmm_name
            print 'Available intruments: ',rm.list_resources
               ()
            quit('\aMultimeter not found')
        else:
            dmm = rm.open_resource(dmm_name)

        self.dmm = dmm
        dmm.clear()

        dmm.write("*CLS")
        dmm.write(":SYSTEM:PRES")
        dmm.write(":FUNC \"VOLT:DC\"")
        dmm.write(":VOLT:DC:RANG 100")
        dmm.write(":VOLT:DC:NPLC 1")
        dmm.write(":TRIG:SOUR BUS")
        dmm.write(":TRAC:CLE")
        dmm.write(":VOLT:AVER:STAT ON")
        dmm.write(":VOLT:DC:AVER:TCON REP")
        dmm.write(":VOLT:AVER:COUN 10")
```

```
        #Close LVDT channel
        mx.write(":CLOS (@"+str(self.card)+"!"+str(self.
           LVDT_ch)+")")
        time.sleep(3.0)


    def voltage(self,channel):
        dmm = self.dmm
        mx = self.mx

        dmm.write("*TRG")
        dmm.write("*OPC?")
        dmm.read()
        dmm.write(":DATA?")
        volt = dmm.read()

        return float(volt);


    def temperature(self,channel):
        dmm = self.dmm
        mx = self.mx

        mx.write(":CLOS (@"+str(self.card)+"!"+str(channel)+
           ")")
        time.sleep(3.0)
        dmm.write(":VOLT:DC:RANG 0.1")
        volt = self.voltage(channel)
        dmm.write(":VOLT:DC:RANG 100")
        mx.write(":OPEN (@"+str(self.card)+"!"+str(channel)+
           ")")
        time.sleep(3.0)

        calibration = np.poly1d(self.temp_cal)
        return calibration(abs(volt)*1000.0)


    def close(self):
        print "Clearing and closing multiplexer..."
        self.mx.clear()
        self.mx.close()
```

```
        print "Clearing and closing multimeter..."
        self.dmm.write(":TRIG:SOUR IMM")
        self.dmm.clear()
        self.dmm.close()
```

The code below is an example of the Python 2.7 code used to interface with the motors and LVDT probe described in section 3.2.3 for the measurement of the naphthalene surface as described in section 3.3.3. The code was written with continuity in mind, so it bears resemblance to previous codes written in C in the Heat Transfer Laboratory.

```
import pyvisa, time
import numpy as np

class Motors():
    #Defines the interface for the xy measuring table (two
       motors and the LVDT probe)
    def __init__(self):
        ## Initialize motor controller
        motor_name = "ASRL3::INSTR"
        rm = pyvisa.ResourceManager()
        if motor_name not in rm.list_resources():
            print 'Controller name: ',motor_name
            print 'Available intruments: ',rm.list_resources
               ()
            quit('\aMotor controller not found')
        else:
            motor = rm.open_resource(motor_name)

        motor.data_bits = 7
        motor.parity = pyvisa.constants.Parity.even
        motor.stop_bits = pyvisa.constants.StopBits.two
        motor.timeout = 1
        self.motor = motor
        motor.clear()

        self.position = {'x':0.0,'y':0.0}

        # Motor controller skips a command about every 1000
```

```
        commands. By echoing back the command, the code
        can check if a given command is sent and accepted
    motor.write("EN")
    motor.write("C S1M800,A1M1,O1,R")
    motor.write("C S2M800,A2M1,O1,R")

    # Read in characters from echo (for three commands)
    text = motor.read_raw()
    print repr(text)
    newline_counter = 0
    print_str = ''
    while newline_counter < 3:
        text = motor.read_raw()
        print repr(text)
        print_str += text
        if len(text) > 0 and text[-1] == '\n':
            newline_counter += 1


def move_motor(self,motor_num,dist):
    motor = self.motor

    if dist > 0.0:
        steps = int((dist)*1000.0+0.5)
    else:
        steps = int((dist)*1000.0-0.5)

    returned_steps = 0
    # loop is required because motor controller doesn't
       always receive command
    while returned_steps != 2*steps:
        # Send command
        motor.write('C I'+str(motor_num)+'M'+str(steps
           *2)+',R')
        time.sleep(0.001347*abs(steps*2)+0.08515)   #
           from fit returned from measuring time between
            sending 'V' and receiving 'R'

        time.sleep(0.1)     #reduce vibration
        returned_steps = self.string_from_controller()
        #print 2*steps, returned_steps
```

```
        # return distance moved
        return float(steps)/1000.0


    def string_from_controller(self):
        # Read number of steps echoed back from motor
           controller
        # Get echoed string
        echo_str = self.motor.read_raw()
        echo_str = repr(echo_str)
        #print echo_str
        # The number is contained between 'M' and '\xac'
        start_index = echo_str.find('M')
        end_index = echo_str.find('xac')
        num_str = echo_str[start_index:end_index-1]
        #Eliminate characters from string to leave numeric
           characters
        eliminate = '\\ x b M'
        for char in eliminate: num_str = num_str.replace(
           char,'')
        try:
            return int(num_str)
        except:
            return 0.5


    def user_move_motor(self,direction):
        dist = 0.001
        if direction == 'x+':
            dist = self.move_motor(1,dist)
            self.position['x'] = self.position['x']+dist
        elif direction == 'x-':
            dist = self.move_motor(1,-dist)
            self.position['x'] = self.position['x']+dist
        elif direction == 'y+':
            dist = self.move_motor(2,dist)
            self.position['y'] = self.position['y']+dist
        elif direction == 'y-':
            dist = self.move_motor(2,-dist)
            self.position['y'] = self.position['y']+dist
```

```
    def close(self):
        print "Clearing and closing stepper motor controller
           ..."
        self.motor.write("Q\r")
        self.motor.clear()
        self.motor.close()
```

Appendix E

Selected data

E.1 Laminar

E.1.1 Laminar Finite

Centerline Heat Transfer

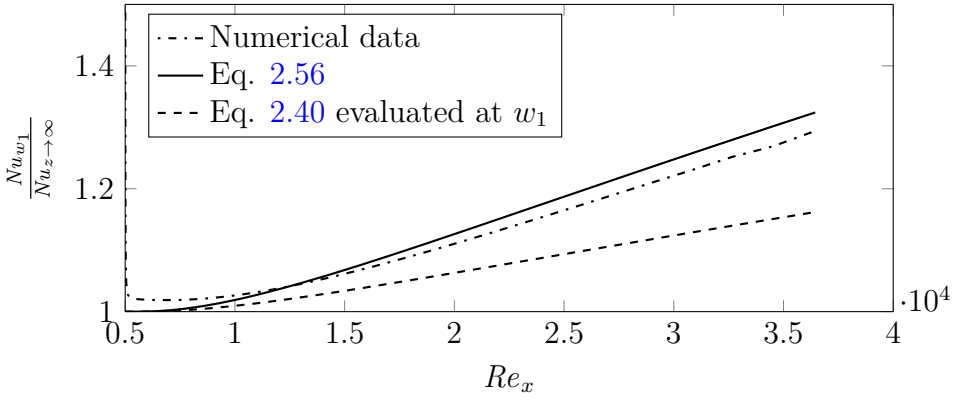

Figure E.1: Case 1 center Nu for $Pr = 2.28$, $\xi = 0.0795\,\mathrm{m}$, $w_1 = 4\,\mathrm{mm}$, $w_2 = 50\,\mathrm{mm}$

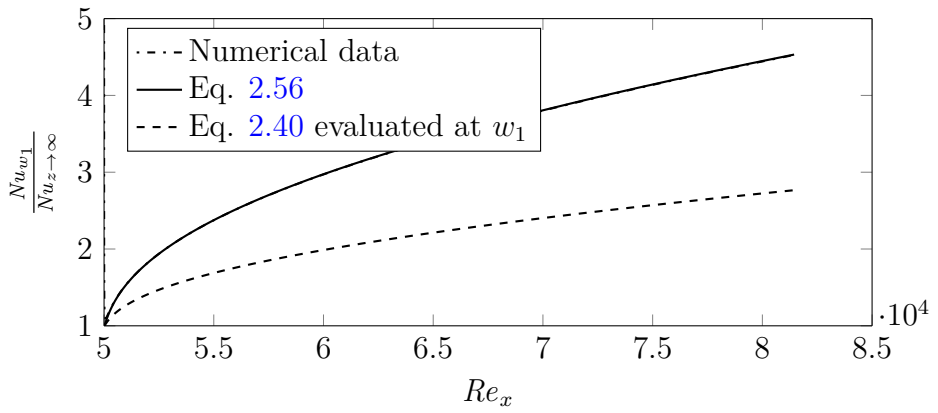

Figure E.2: Case 1 center Nu for $Pr = 2.28$, $\xi = 0.795\,\text{m}$, $w_1 = 1\,\text{mm}$, $w_2 = 50\,\text{mm}$

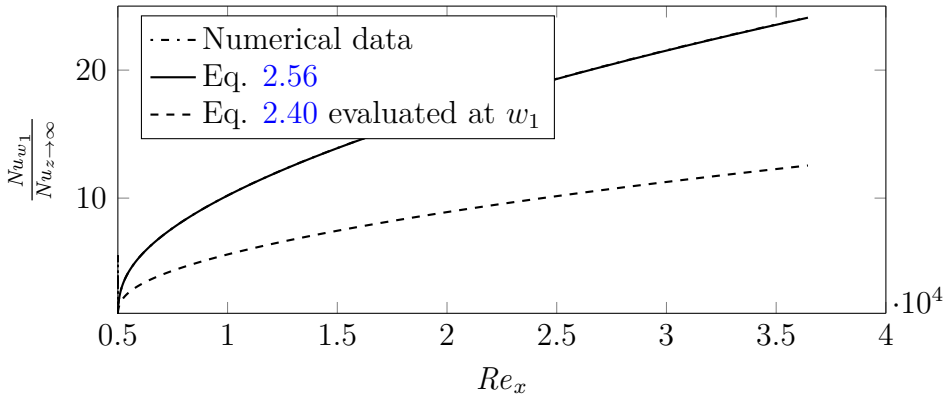

Figure E.3: Case 1 center Nu for $Pr = 0.7$, $\xi = 0.0795\,\text{m}$, $w_1 = 0.25\,\text{mm}$, $w_2 = 50\,\text{mm}$

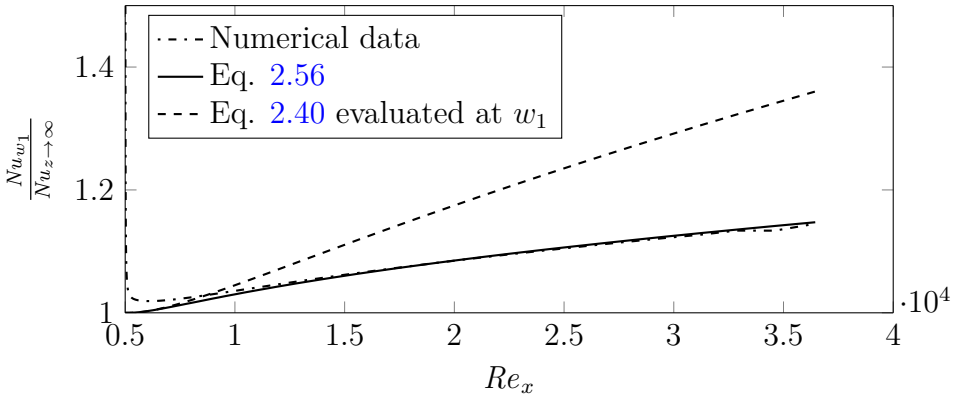

Figure E.4: Case 1 center Nu for $Pr = 0.7$, $\xi = 0.0795\,\text{m}$, $w_1 = 4\,\text{mm}$, $w_2 = 0.25\,\text{mm}$

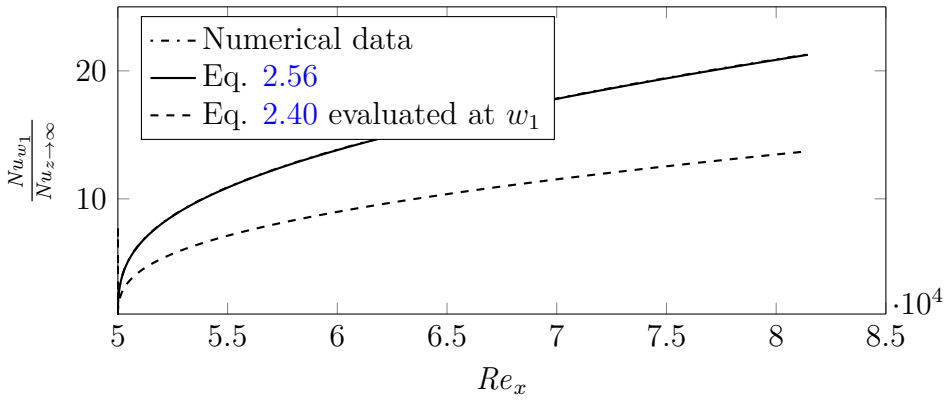

Figure E.5: Case 1 center Nu for $Pr = 0.7$, $\xi = 0.795\,\mathrm{m}$, $w_1 = 0.25\,\mathrm{mm}$, $w_2 = 0.25\,\mathrm{mm}$

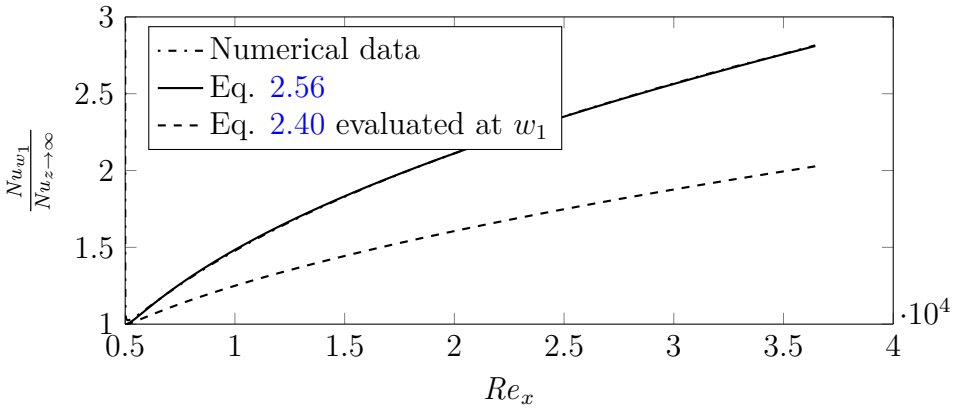

Figure E.6: Case 1 center Nu for $Pr = 6$, $\xi = 0.0795\,\mathrm{m}$, $w_1 = 1\,\mathrm{mm}$, $w_2 = 1\,\mathrm{mm}$

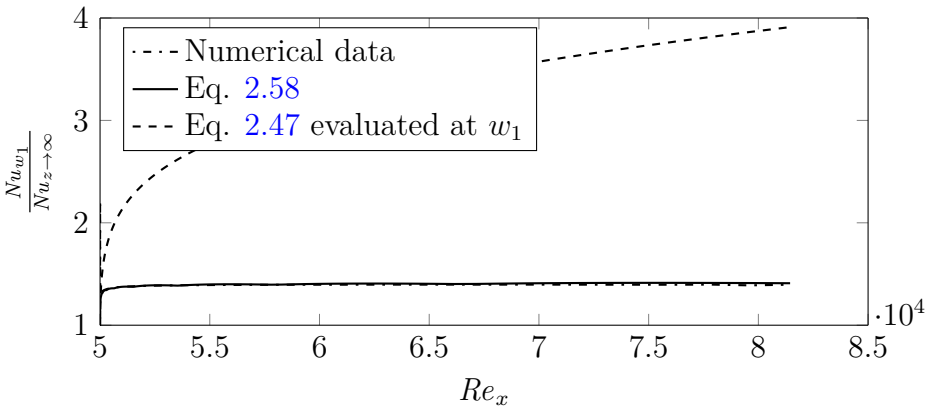

Figure E.7: Case 2 center Nu for $Pr = 0.7$, $\xi = 0.795\,\mathrm{m}$, $w_1 = 0.25\,\mathrm{mm}$, $w_2 = 0.25\,\mathrm{mm}$

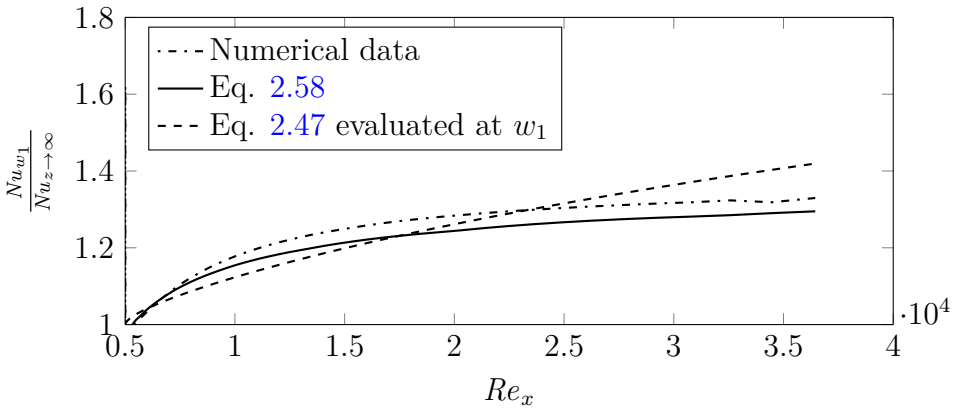

Figure E.8: Case 2 center Nu for $Pr = 6$, $\xi = 0.0795\,\mathrm{m}$, $w_1 = 1\,\mathrm{mm}$, $w_2 = 1\,\mathrm{mm}$

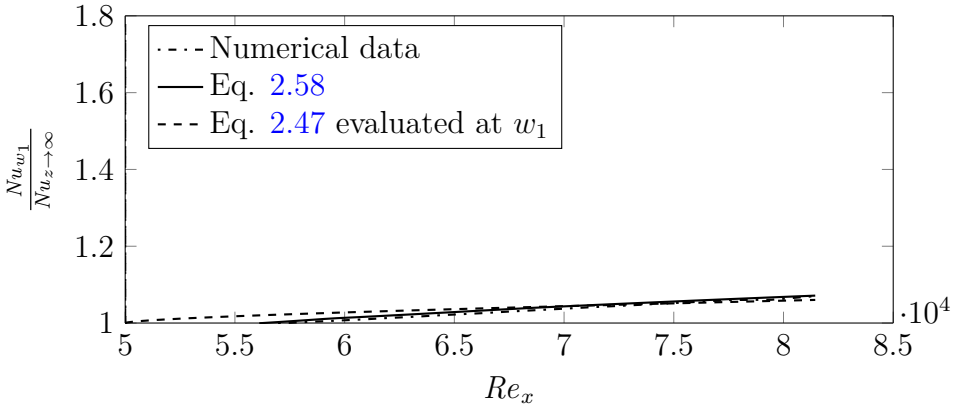

Figure E.9: Case 2 center Nu for $Pr = 6$, $\xi = 0.795\,\mathrm{m}$, $w_1 = 4\,\mathrm{mm}$, $w_2 = 4\,\mathrm{mm}$

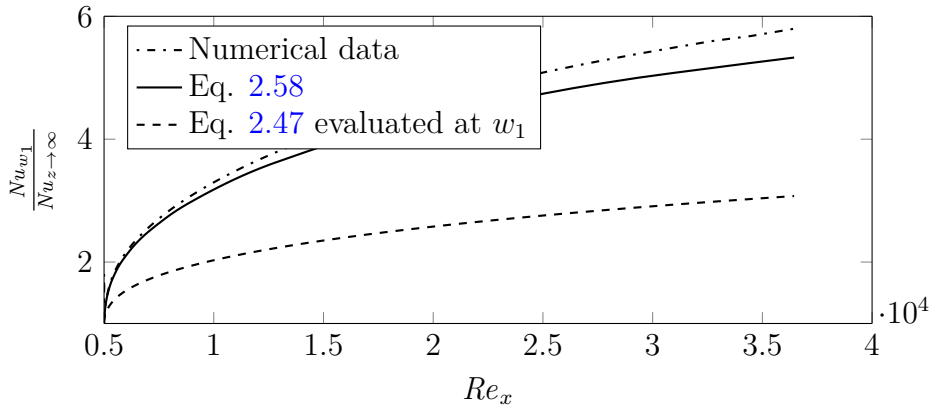

Figure E.10: Case 2 center Nu for $Pr = 2.28$, $\xi = 0.0795\,\mathrm{m}$, $w_1 = 0.25\,\mathrm{mm}$, $w_2 = 4\,\mathrm{mm}$

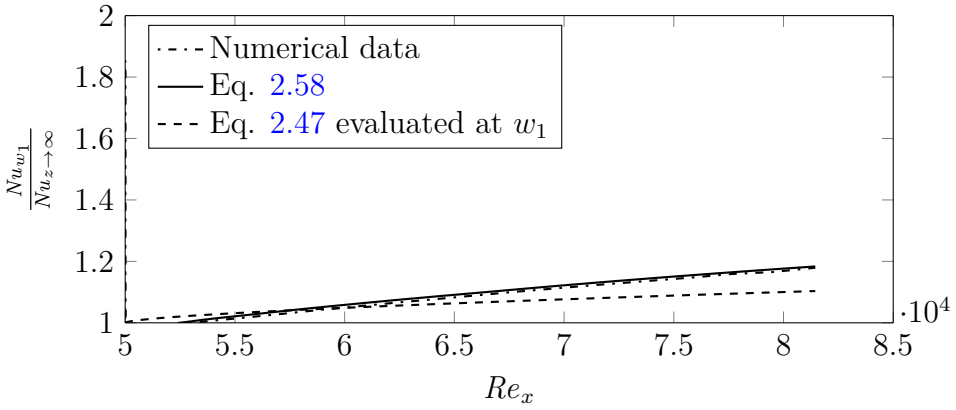

Figure E.11: Case 2 center Nu for $Pr = 2.28$, $\xi = 0.795\,\text{m}$, $w_1 = 4\,\text{mm}$, $w_2 = 50\,\text{mm}$

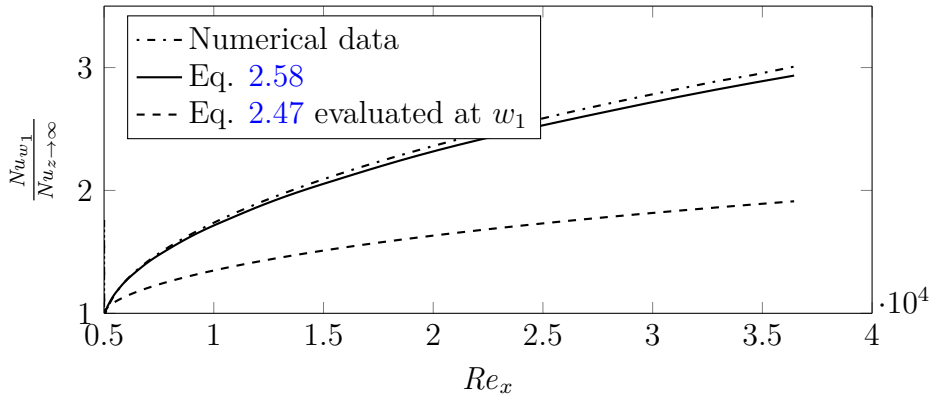

Figure E.12: Case 2 center Nu for $Pr = 0.7$, $\xi = 0.0795\,\text{m}$, $w_1 = 1\,\text{mm}$, $w_2 = 50\,\text{mm}$

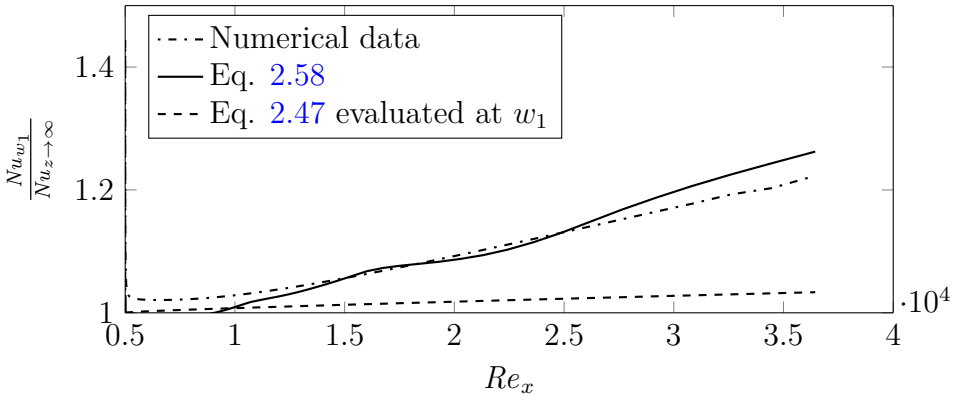

Figure E.13: Case 3 center Nu for $Pr = 6$, $\xi = 0.0795\,\text{m}$, $w_1 = 4\,\text{mm}$, $w_2 = 50\,\text{mm}$

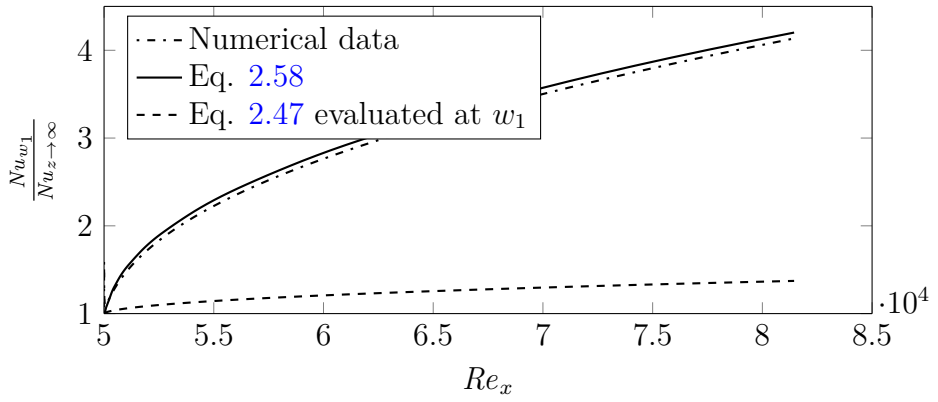

Figure E.14: Case 3 center Nu for $Pr = 6$, $\xi = 0.795\,\mathrm{m}$, $w_1 = 1\,\mathrm{mm}$, $w_2 = 50\,\mathrm{mm}$

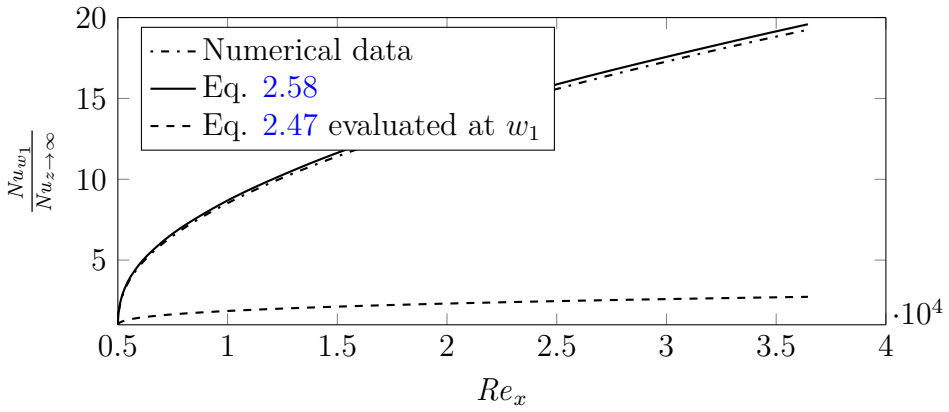

Figure E.15: Case 3 center Nu for $Pr = 2.28$, $\xi = 0.0795\,\mathrm{m}$, $w_1 = 0.25\,\mathrm{mm}$, $w_2 = 50\,\mathrm{mm}$

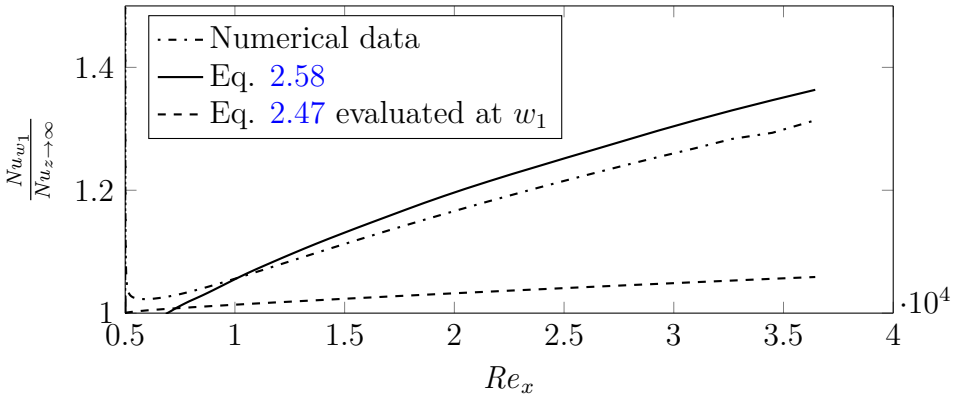

Figure E.16: Case 3 center Nu for $Pr = 2.28$, $\xi = 0.0795\,\mathrm{m}$, $w_1 = 4\,\mathrm{mm}$, $w_2 = 0.25\,\mathrm{mm}$

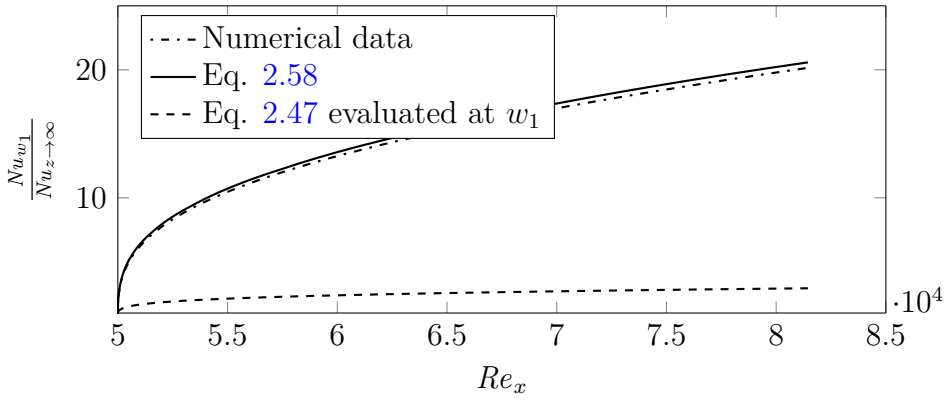

Figure E.17: Case 3 center Nu for $Pr = 2.28$, $\xi = 0.795\,\mathrm{m}$, $w_1 = 0.25\,\mathrm{mm}$, $w_2 = 0.25\,\mathrm{mm}$

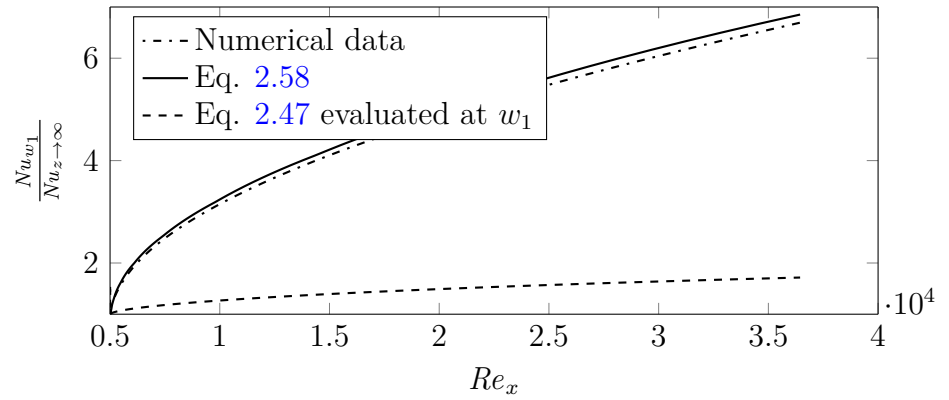

Figure E.18: Case 3 center Nu for $Pr = 0.7$, $\xi = 0.0795\,\mathrm{m}$, $w_1 = 1\,\mathrm{mm}$, $w_2 = 1\,\mathrm{mm}$

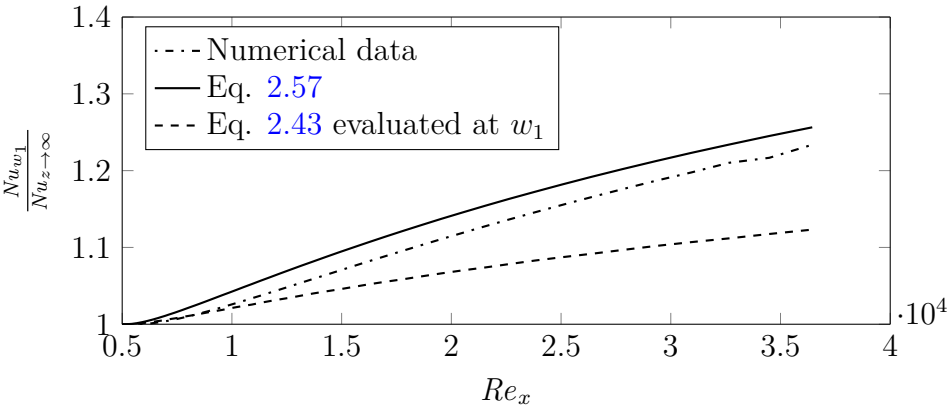

Figure E.19: Case 4 center Nu for $Pr = 2.28$, $\xi = 0.0795\,\mathrm{m}$, $w_1 = 4\,\mathrm{mm}$, $w_2 = 4\,\mathrm{mm}$

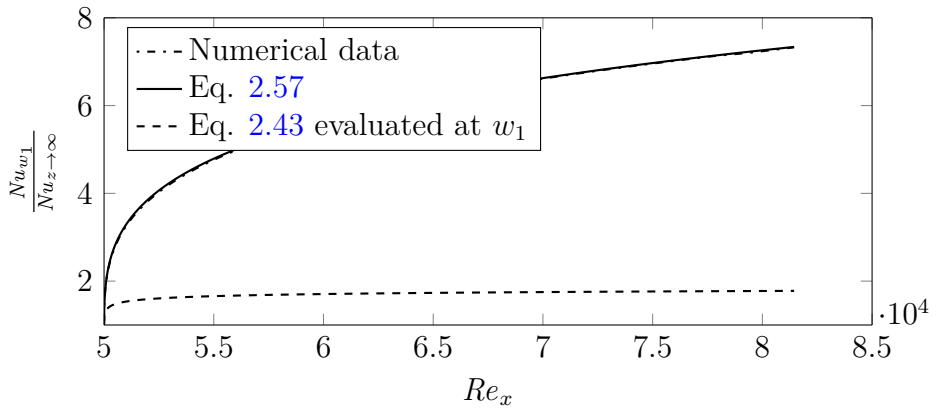

Figure E.20: Case 4 center Nu for $Pr = 0.7$, $\xi = 0.0795\,\mathrm{m}$, $w_1 = 0.25\,\mathrm{mm}$, $w_2 = 4\,\mathrm{mm}$

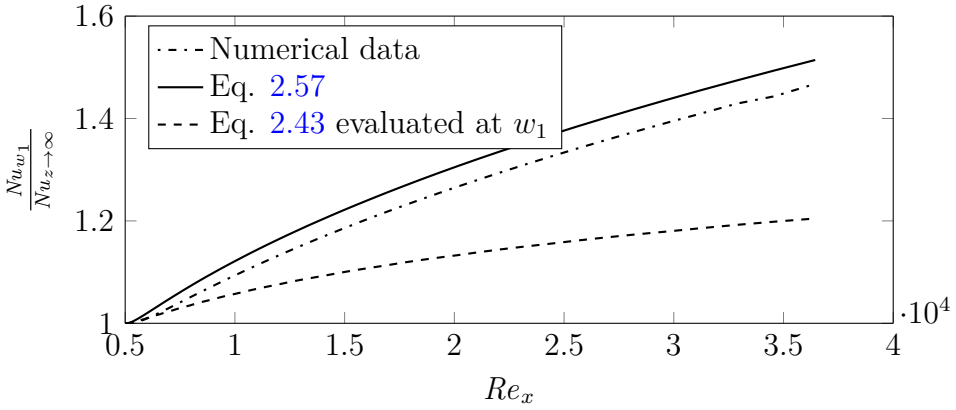

Figure E.21: Case 4 center Nu for $Pr = 0.7$, $\xi = 0.0795\,\mathrm{m}$, $w_1 = 4\,\mathrm{mm}$, $w_2 = 50\,\mathrm{mm}$

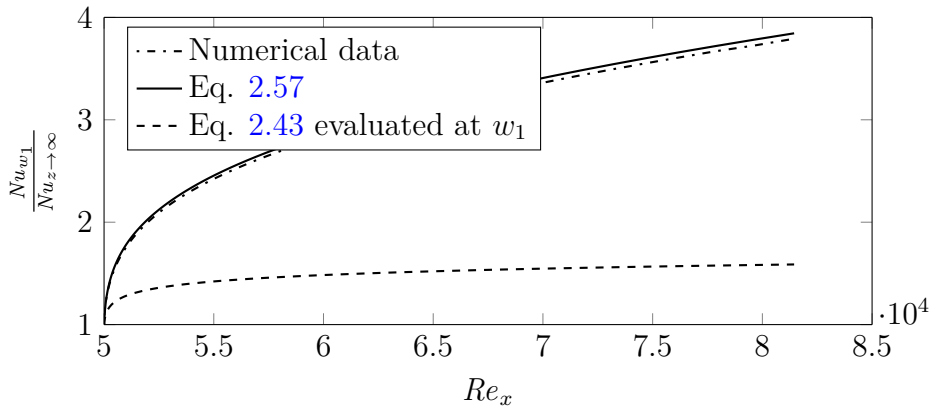

Figure E.22: Case 4 center Nu for $Pr = 0.7$, $\xi = 0.795\,\mathrm{m}$, $w_1 = 1\,\mathrm{mm}$, $w_2 = 50\,\mathrm{mm}$

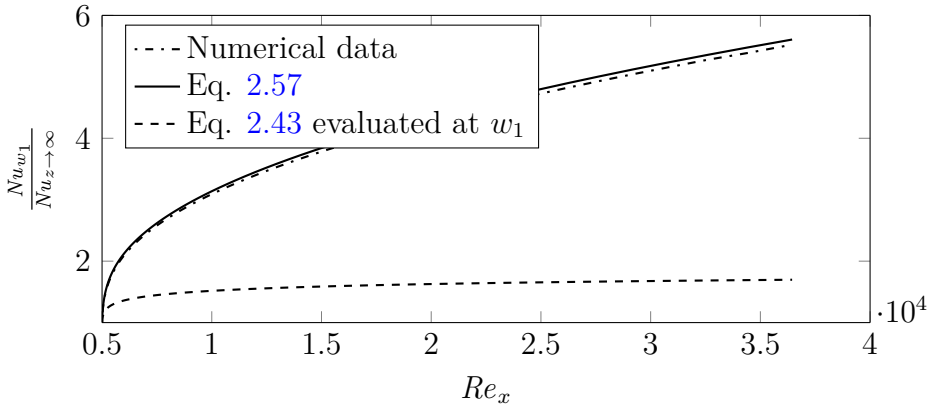

Figure E.23: Case 4 center Nu for $Pr = 6$, $\xi = 0.0795\,\mathrm{m}$, $w_1 = 0.25\,\mathrm{mm}$, $w_2 = 50\,\mathrm{mm}$

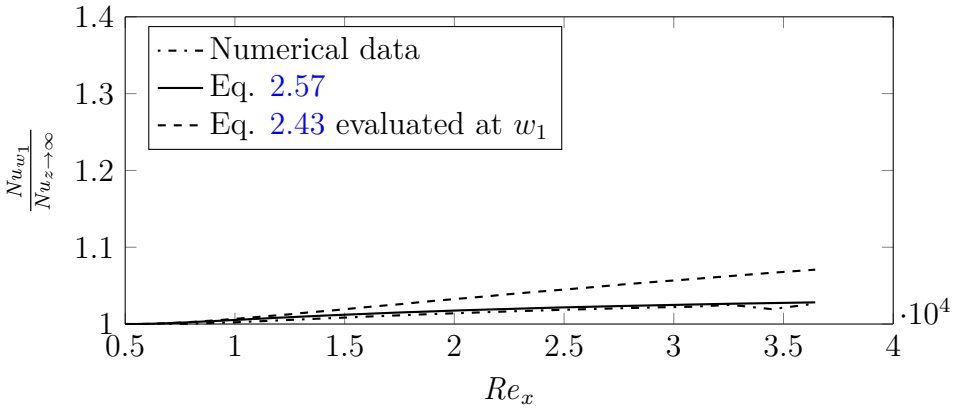

Figure E.24: Case 4 center Nu for $Pr = 6$, $\xi = 0.0795\,\mathrm{m}$, $w_1 = 4\,\mathrm{mm}$, $w_2 = 0.25\,\mathrm{mm}$

Lateral Variation of Heat Transfer

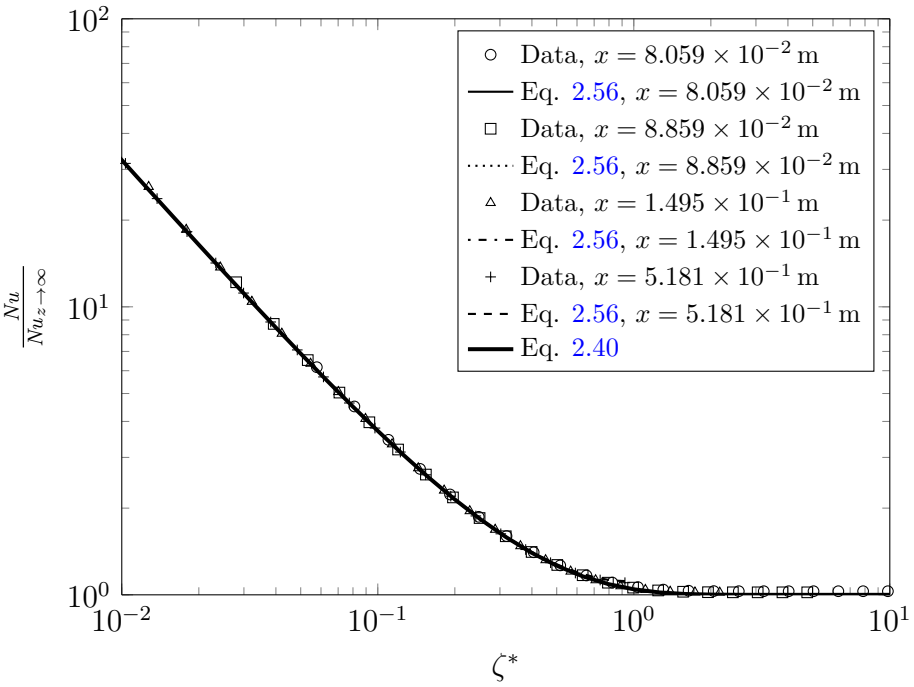

Figure E.25: Case 1 lateral Nu for $Pr = 6$, $\xi = 0.0795\,\text{m}$, $w_1 = 4\,\text{mm}$, $w_2 = 50\,\text{mm}$

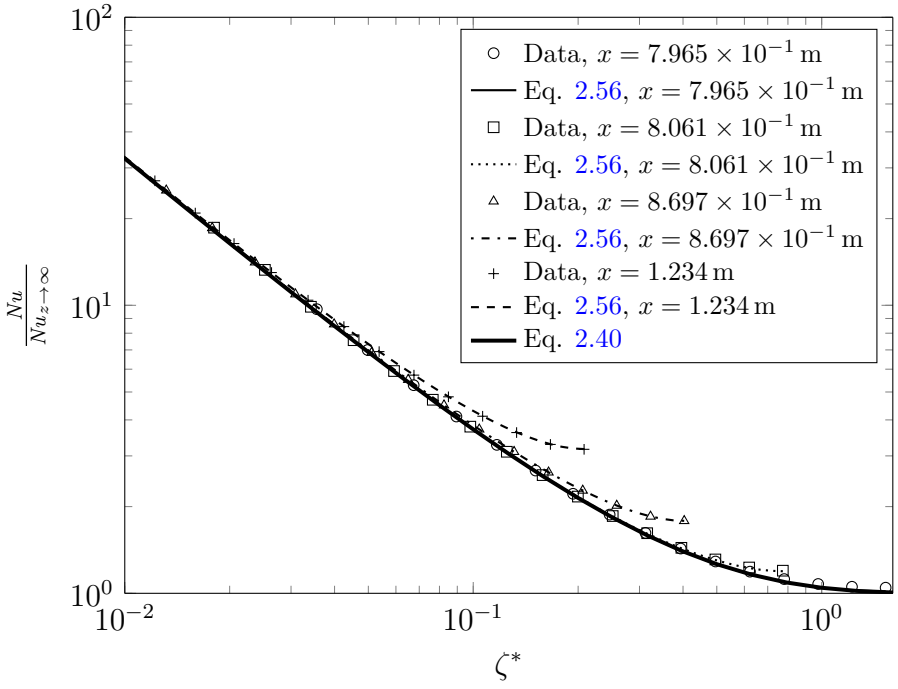

Figure E.26: Case 1 lateral Nu for $Pr = 6$, $\xi = 0.795\,\mathrm{m}$, $w_1 = 1\,\mathrm{mm}$, $w_2 = 50\,\mathrm{mm}$

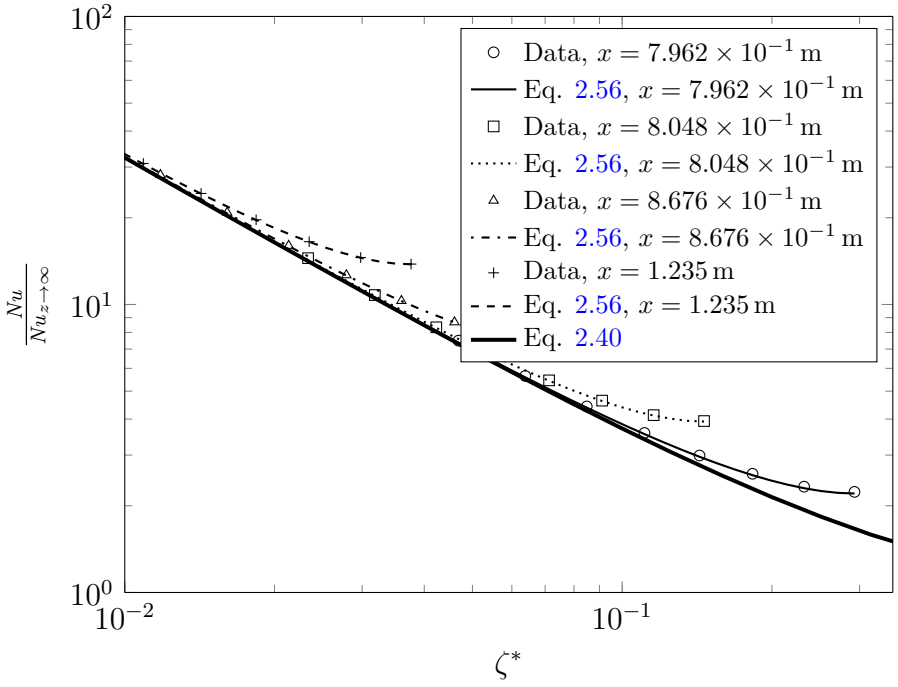

Figure E.27: Case 1 lateral Nu for $Pr = 2.28$, $\xi = 0.795\,\mathrm{m}$, $w_1 = 0.25\,\mathrm{mm}$, $w_2 = 0.25\,\mathrm{mm}$

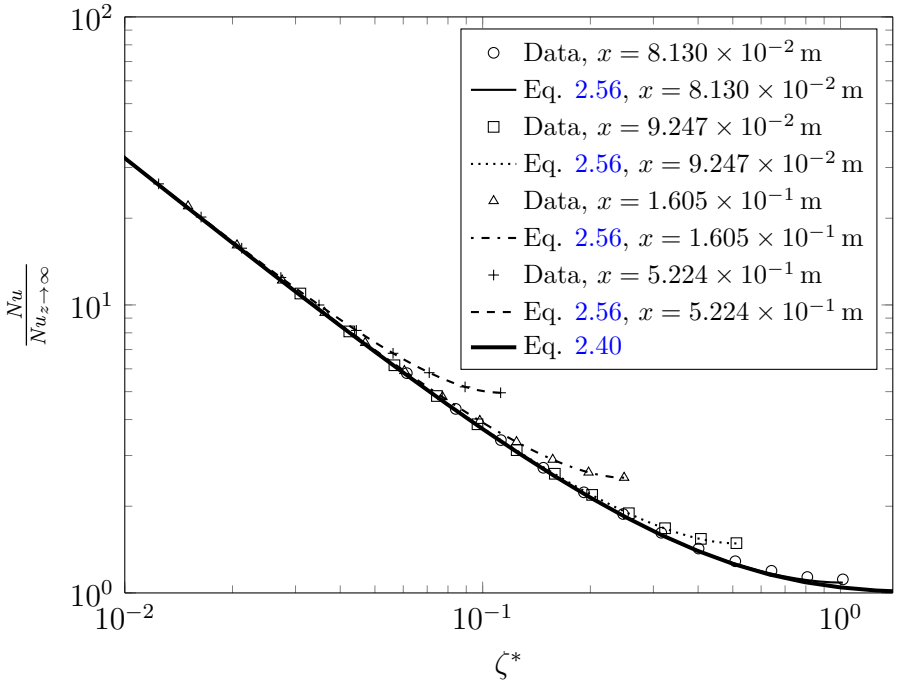

Figure E.28: Case 1 lateral Nu for $Pr = 0.7$, $\xi = 0.0795\,\text{m}$, $w_1 = 1\,\text{mm}$, $w_2 = 1\,\text{mm}$

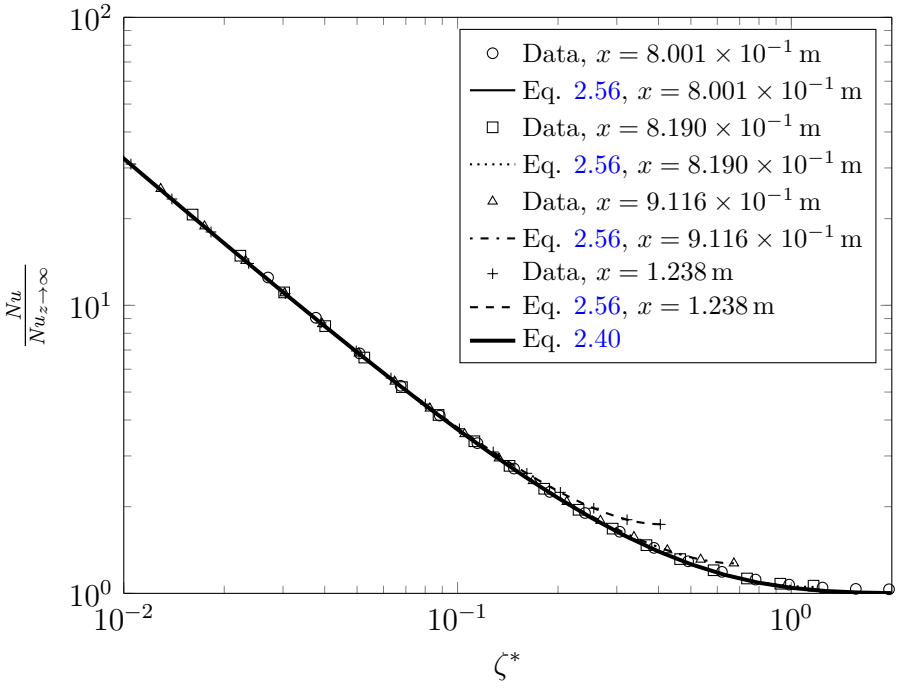

Figure E.29: Case 1 lateral Nu for $Pr = 0.7$, $\xi = 0.795\,\text{m}$, $w_1 = 4\,\text{mm}$, $w_2 = 4\,\text{mm}$

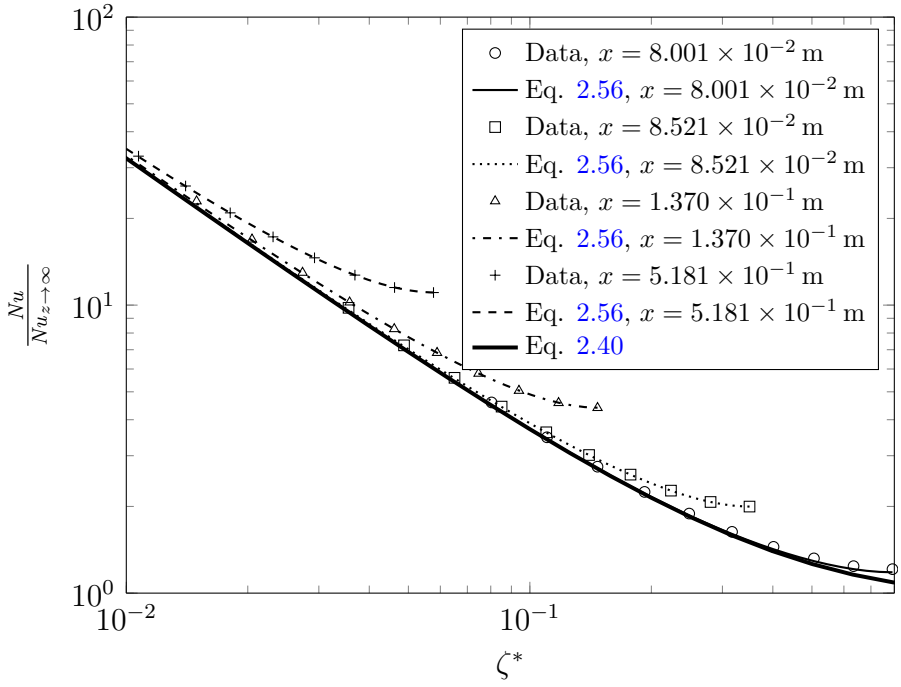

Figure E.30: Case 1 lateral Nu for $Pr = 6$, $\xi = 0.0795\,\text{m}$, $w_1 = 0.25\,\text{mm}$, $w_2 = 4\,\text{mm}$

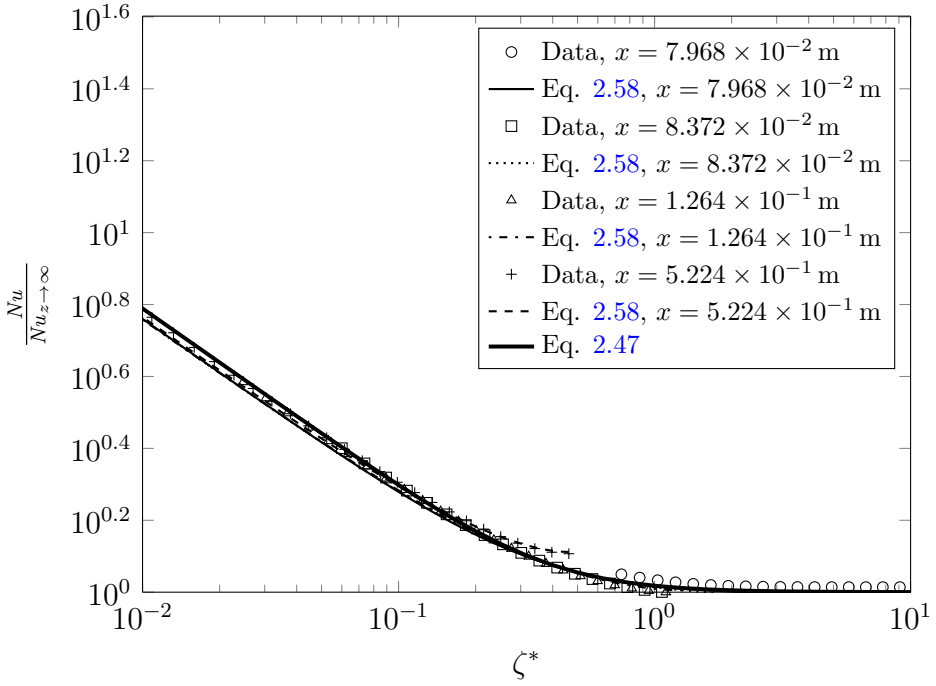

Figure E.31: Case 2 lateral Nu for $Pr = 0.7$, $\xi = 0.0795\,\text{m}$, $w_1 = 4\,\text{mm}$, $w_2 = 50\,\text{mm}$

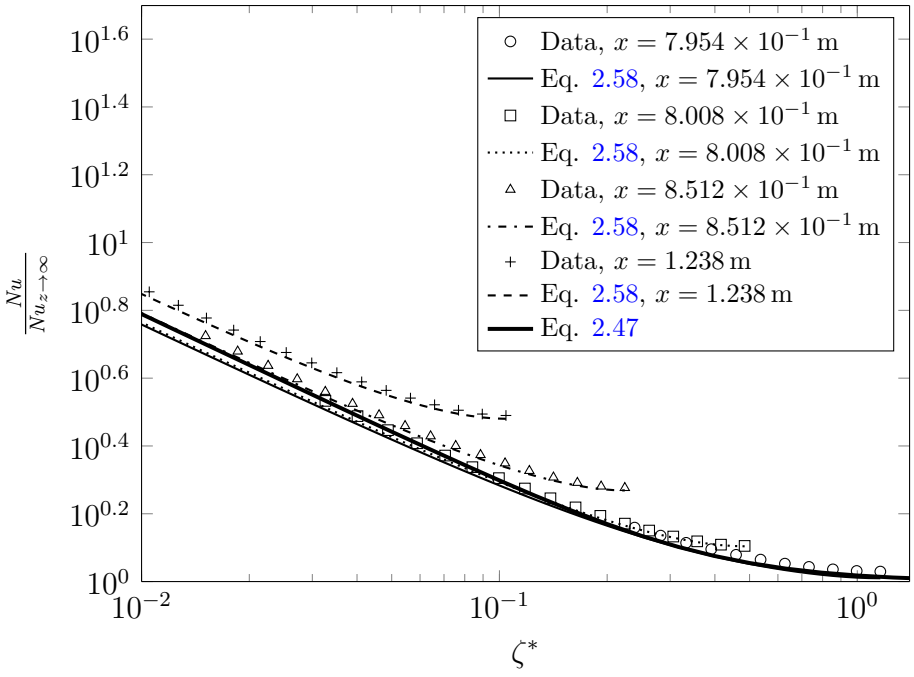

Figure E.32: Case 2 lateral Nu for $Pr = 0.7$, $\xi = 0.795\,\text{m}$, $w_1 = 1\,\text{mm}$, $w_2 = 50\,\text{mm}$

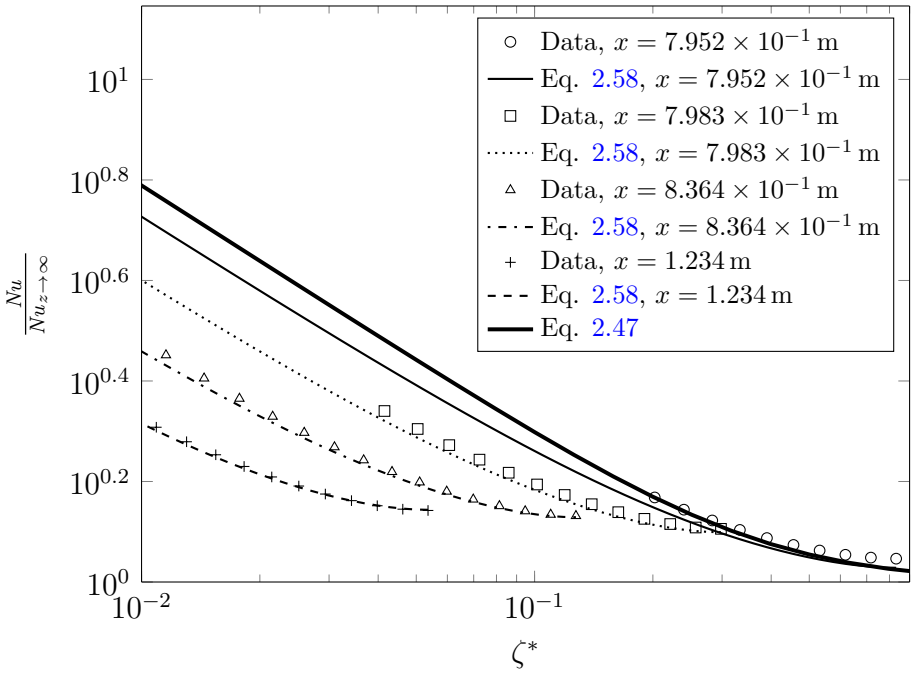

Figure E.33: Case 2 lateral Nu for $Pr = 6$, $\xi = 0.795\,\text{m}$, $w_1 = 0.25\,\text{mm}$, $w_2 = 0.25\,\text{mm}$

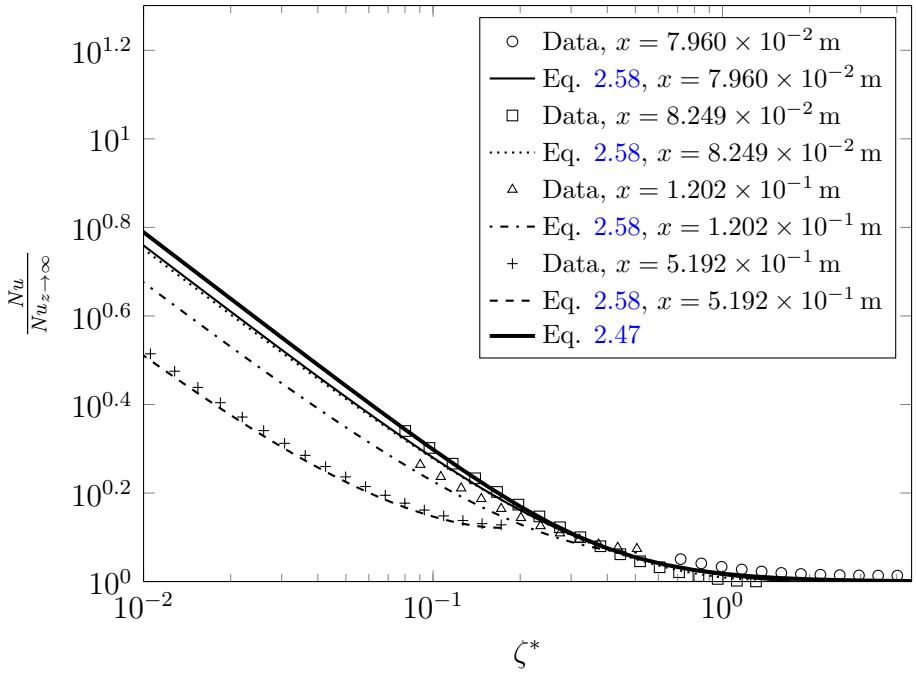

Figure E.34: Case 2 lateral Nu for $Pr = 2.28$, $\xi = 0.0795\,\text{m}$, $w_1 = 1\,\text{mm}$, $w_2 = 1\,\text{mm}$

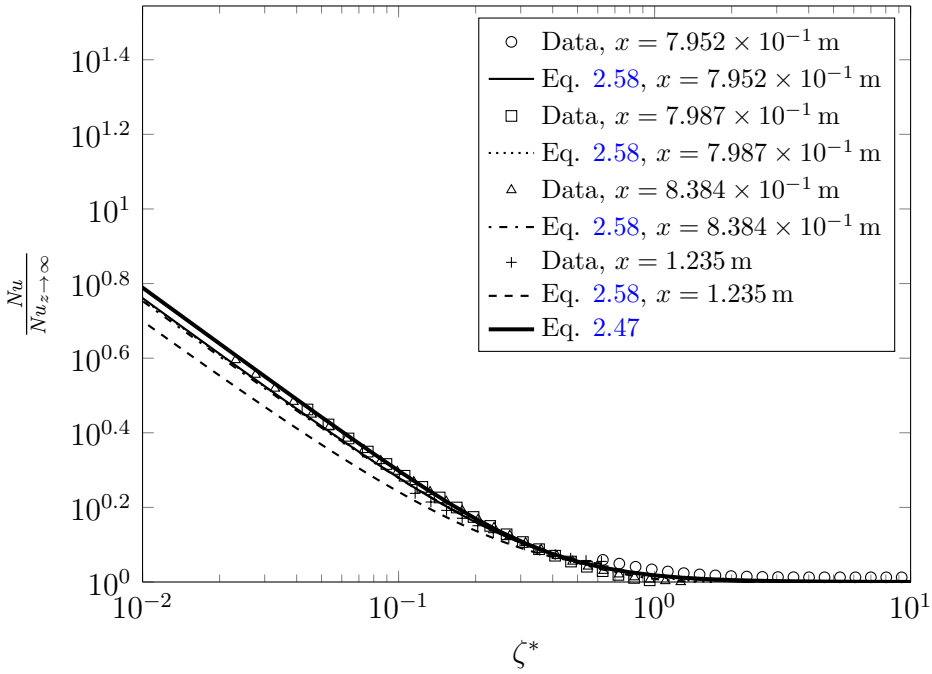

Figure E.35: Case 2 lateral Nu for $Pr = 2.28$, $\xi = 0.795\,\text{m}$, $w_1 = 4\,\text{mm}$, $w_2 = 4\,\text{mm}$

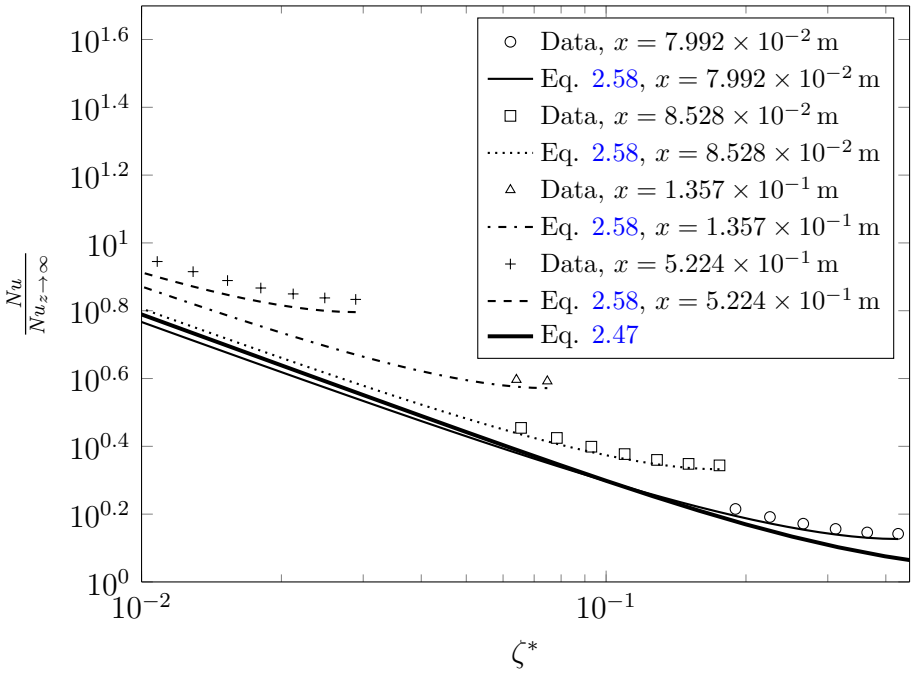

Figure E.36: Case 2 lateral Nu for $Pr = 0.7$, $\xi = 0.0795\,\text{m}$, $w_1 = 0.25\,\text{mm}$, $w_2 = 4\,\text{mm}$

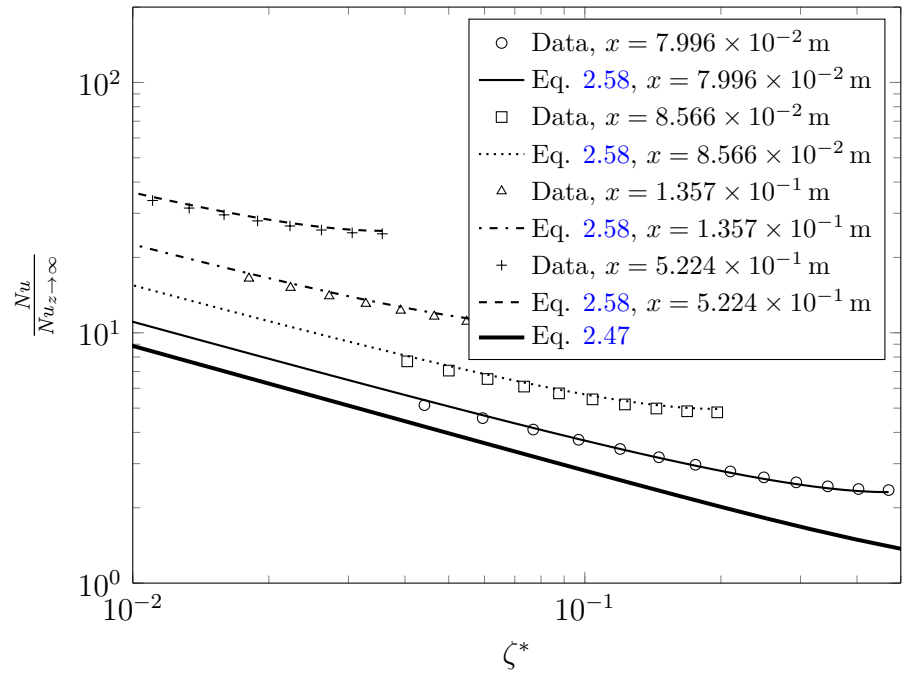

Figure E.37: Case 3 lateral Nu for $Pr = 0.7$, $\xi = 0.0795\,\text{m}$, $w_1 = 0.25\,\text{mm}$, $w_2 = 0.25\,\text{mm}$

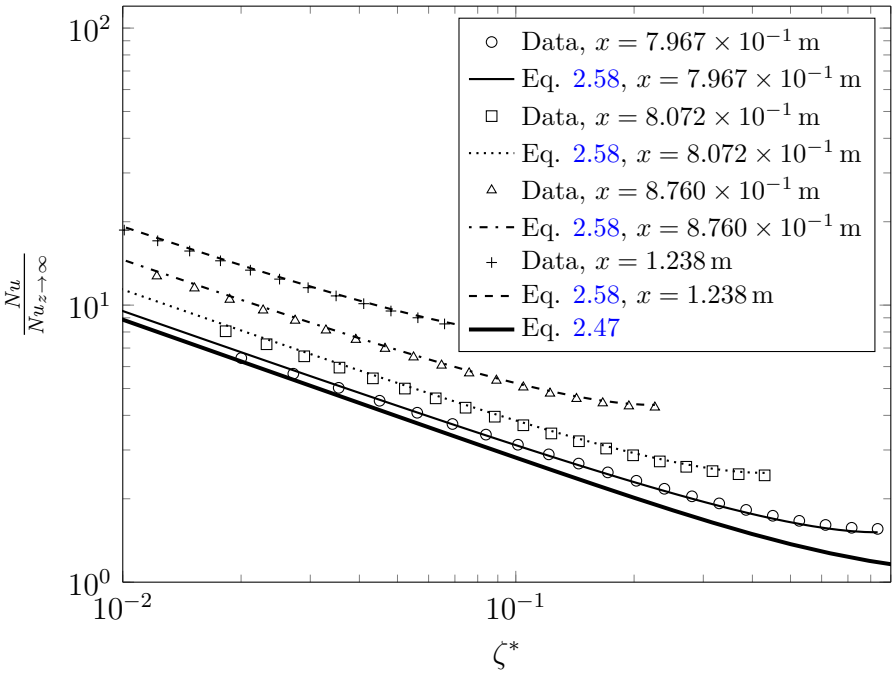

Figure E.38: Case 3 lateral Nu for $Pr = 0.7$, $\xi = 0.795\,\text{m}$, $w_1 = 1\,\text{mm}$, $w_2 = 1\,\text{mm}$

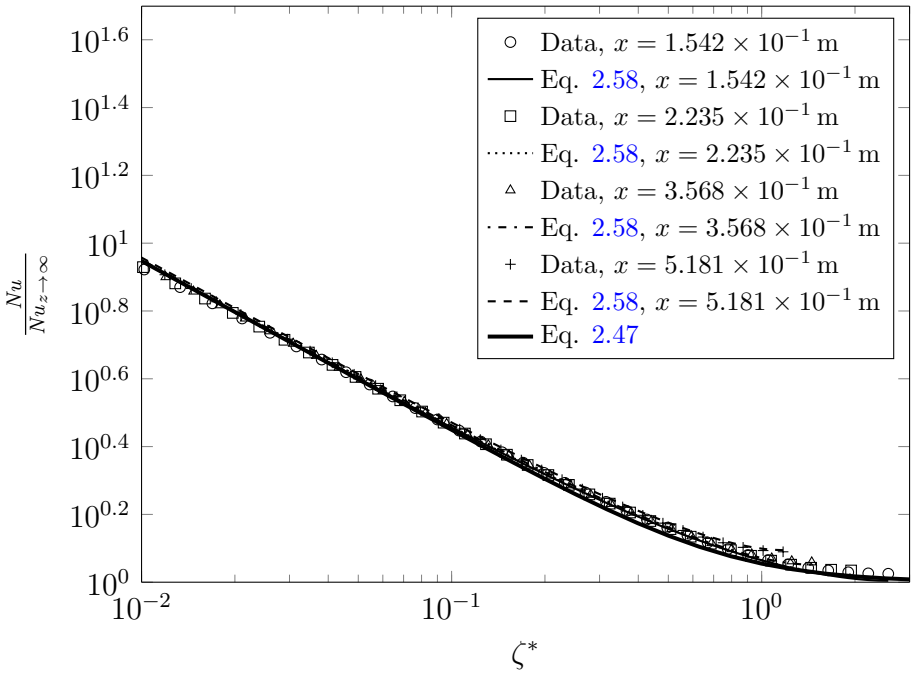

Figure E.39: Case 3 lateral Nu for $Pr = 6$, $\xi = 0.0795\,\text{m}$, $w_1 = 4\,\text{mm}$, $w_2 = 4\,\text{mm}$

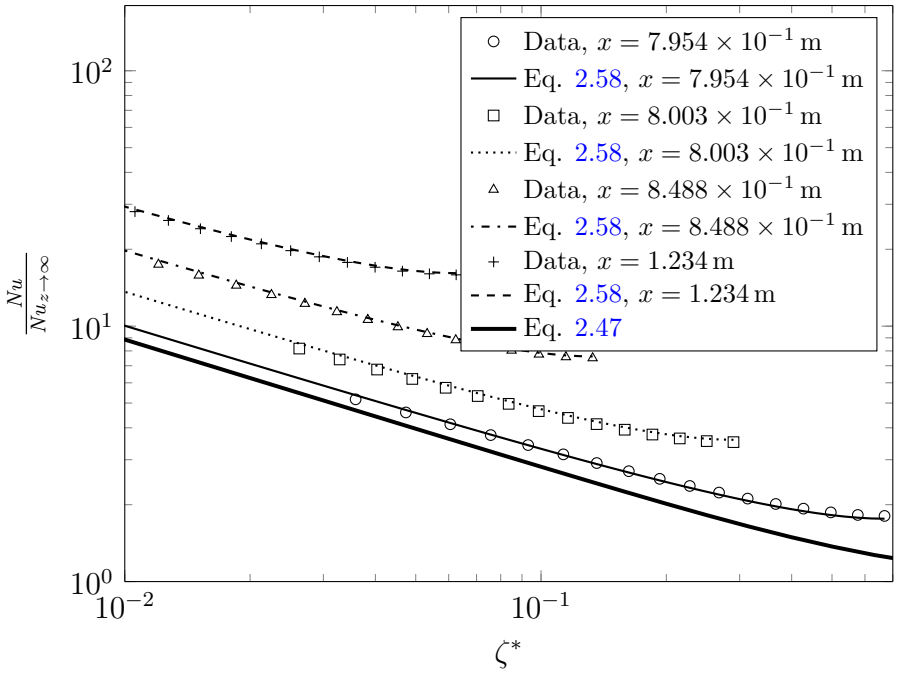

Figure E.40: Case 3 lateral Nu for $Pr = 6$, $\xi = 0.795\,\text{m}$, $w_1 = 0.25\,\text{mm}$, $w_2 = 4\,\text{mm}$

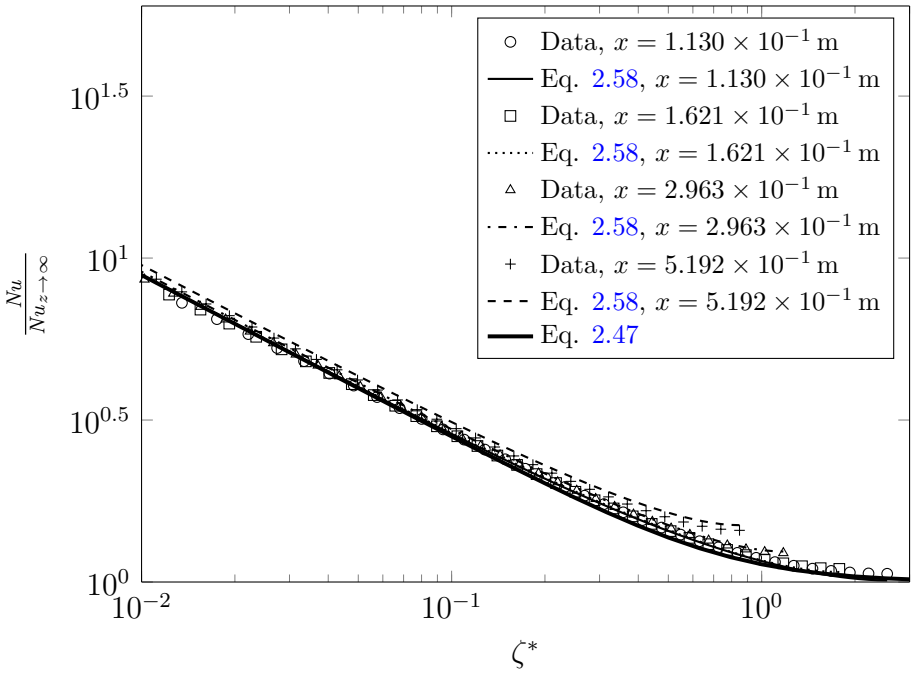

Figure E.41: Case 3 lateral Nu for $Pr = 2.28$, $\xi = 0.0795\,\text{m}$, $w_1 = 4\,\text{mm}$, $w_2 = 50\,\text{mm}$

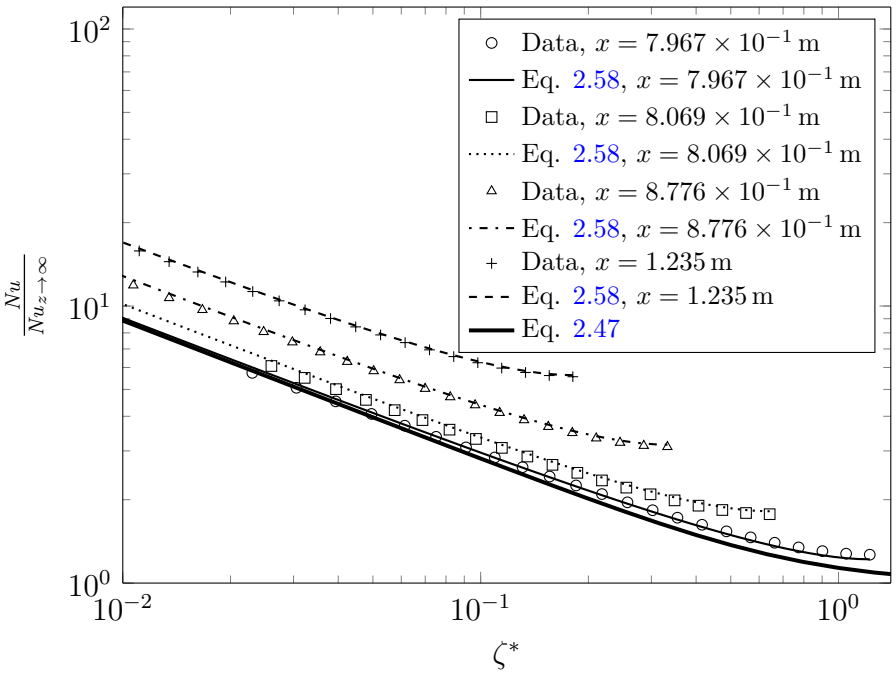

Figure E.42: Case 3 lateral Nu for $Pr = 2.28$, $\xi = 0.795\,\text{m}$, $w_1 = 1\,\text{mm}$, $w_2 = 50\,\text{mm}$

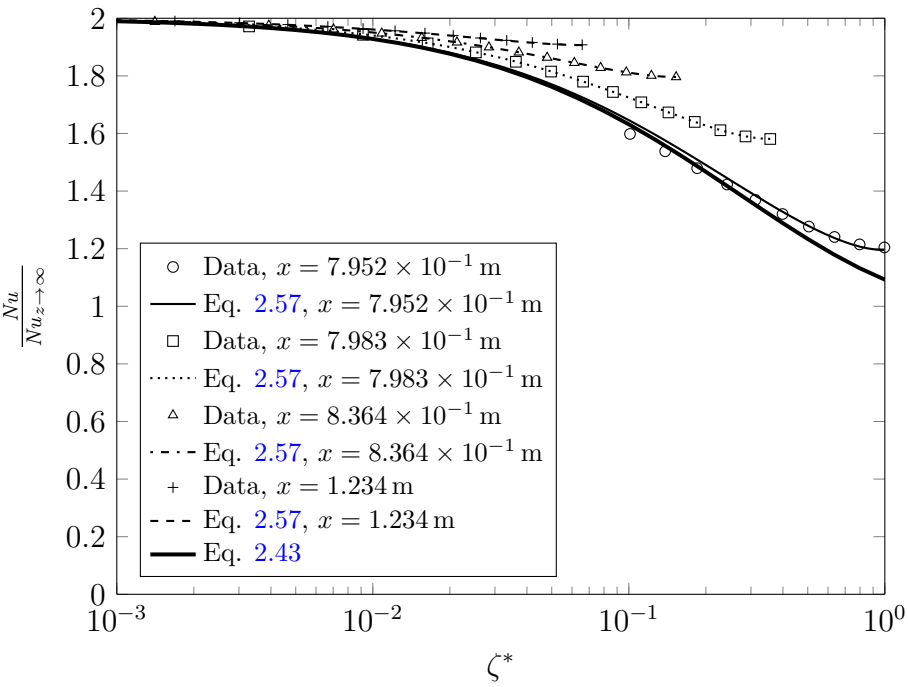

Figure E.43: Case 4 lateral Nu for $Pr = 6$, $\xi = 0.795\,\text{m}$, $w_1 = 0.25\,\text{mm}$, $w_2 = 0.25\,\text{mm}$

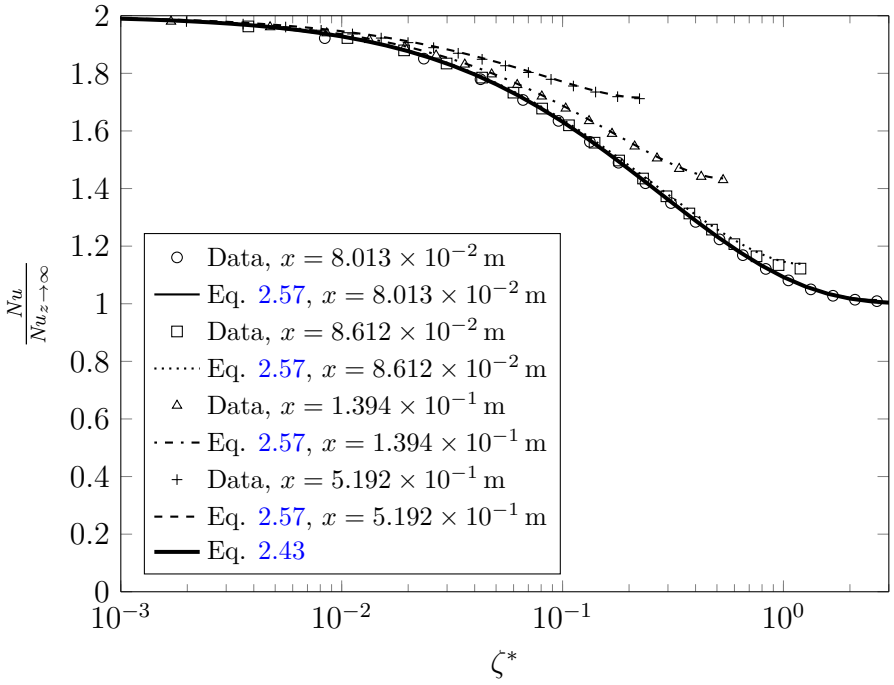

Figure E.44: Case 4 lateral Nu for $Pr = 2.28$, $\xi = 0.0795\,\text{m}$, $w_1 = 1\,\text{mm}$, $w_2 = 1\,\text{mm}$

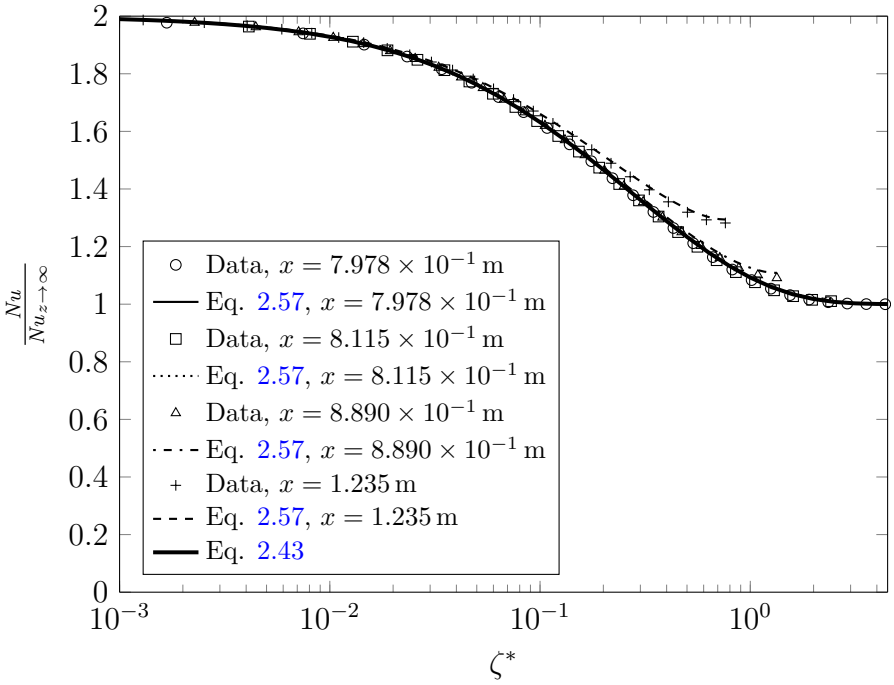

Figure E.45: Case 4 lateral Nu for $Pr = 2.28$, $\xi = 0.795\,\text{m}$, $w_1 = 4\,\text{mm}$, $w_2 = 4\,\text{mm}$

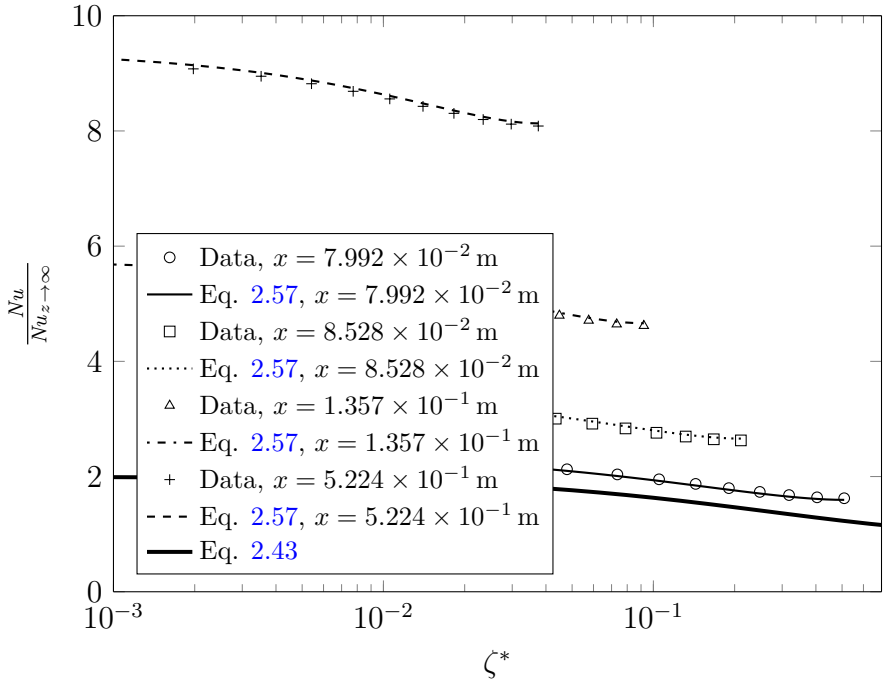

Figure E.46: Case 4 lateral Nu for $Pr = 0.7$, $\xi = 0.0795\,\text{m}$, $w_1 = 0.25\,\text{mm}$, $w_2 = 4\,\text{mm}$

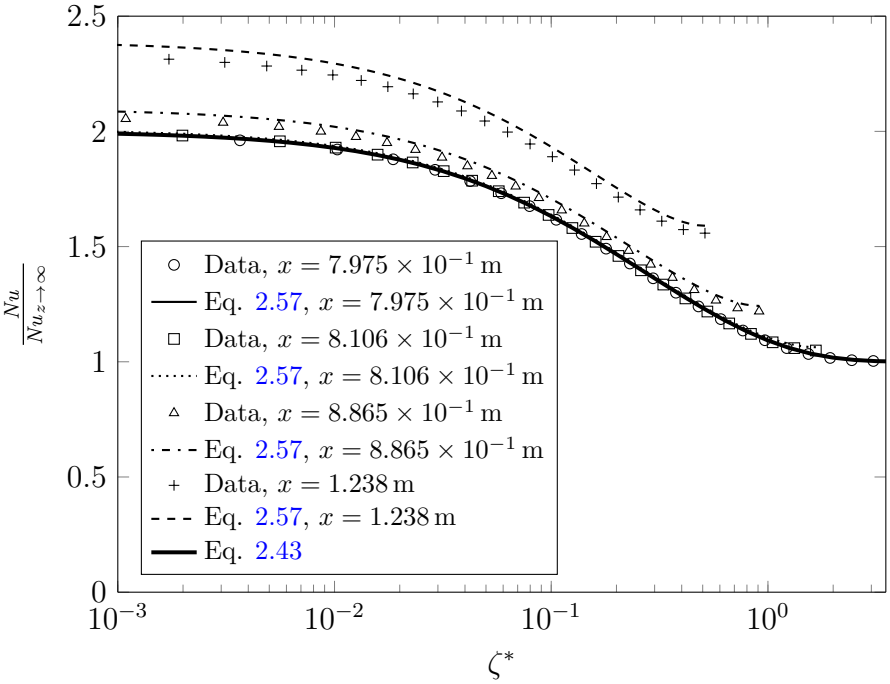

Figure E.47: Case 4 lateral Nu for $Pr = 0.7$, $\xi = 0.795\,\text{m}$, $w_1 = 4\,\text{mm}$, $w_2 = 50\,\text{mm}$

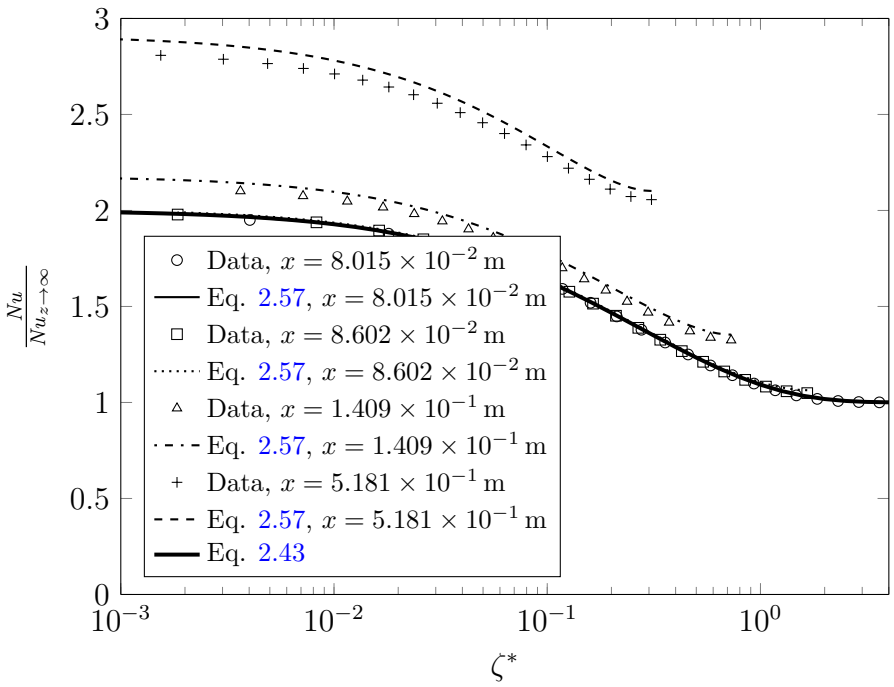

Figure E.48: Case 4 lateral Nu for $Pr = 6$, $\xi = 0.0795\,\text{m}$, $w_1 = 1\,\text{mm}$, $w_2 = 50\,\text{mm}$

E.2 Turbulent

E.2.1 Streamwise Strips

Centerline *St*

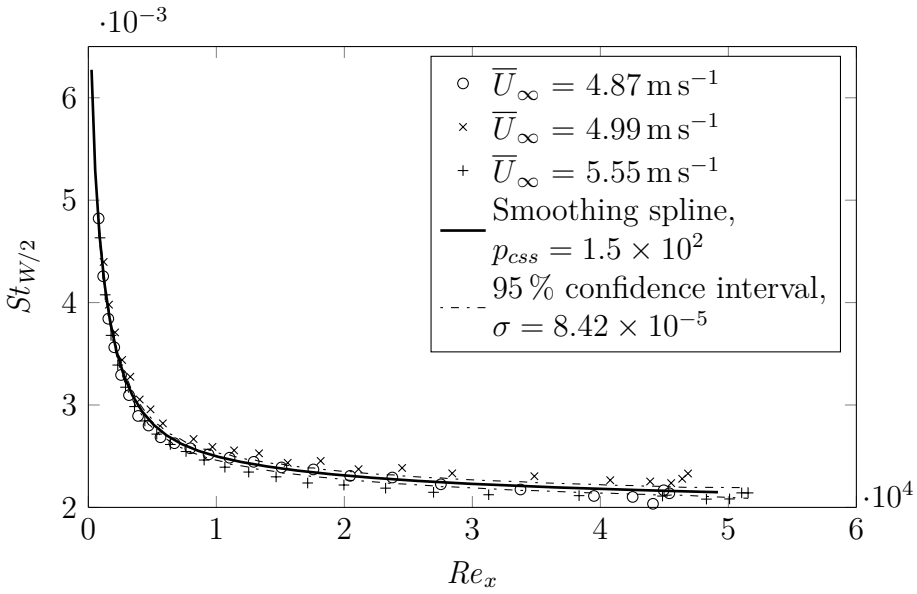

Figure E.49: Centerline *St* for $5\,\mathrm{m\,s^{-1}}$ freestream velocity and 5.00 mm width strip showing raw data and cubic smoothing spline estimate.

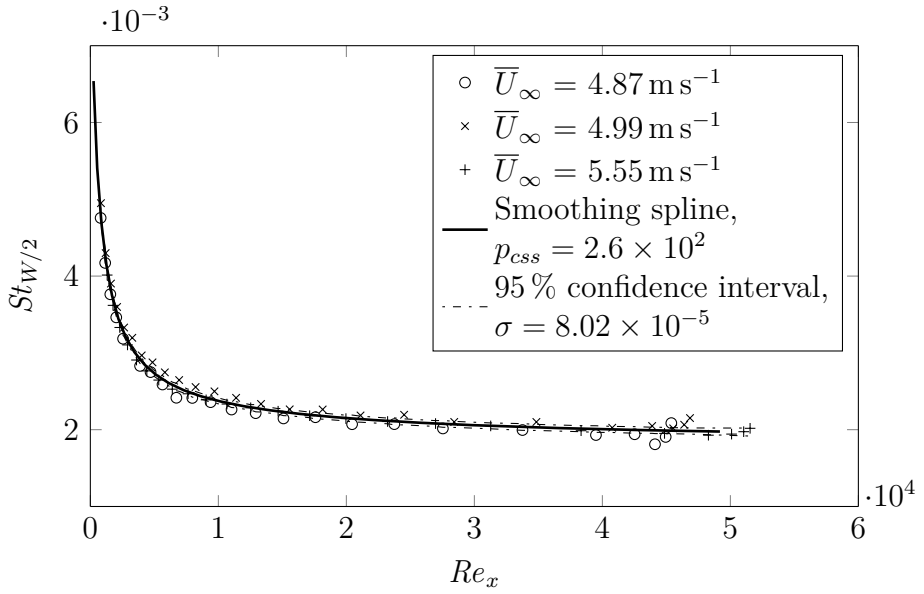

Figure E.50: Centerline St for $5\,\mathrm{m\,s^{-1}}$ freestream velocity and 9.77 mm width strip showing raw data and cubic smoothing spline estimate.

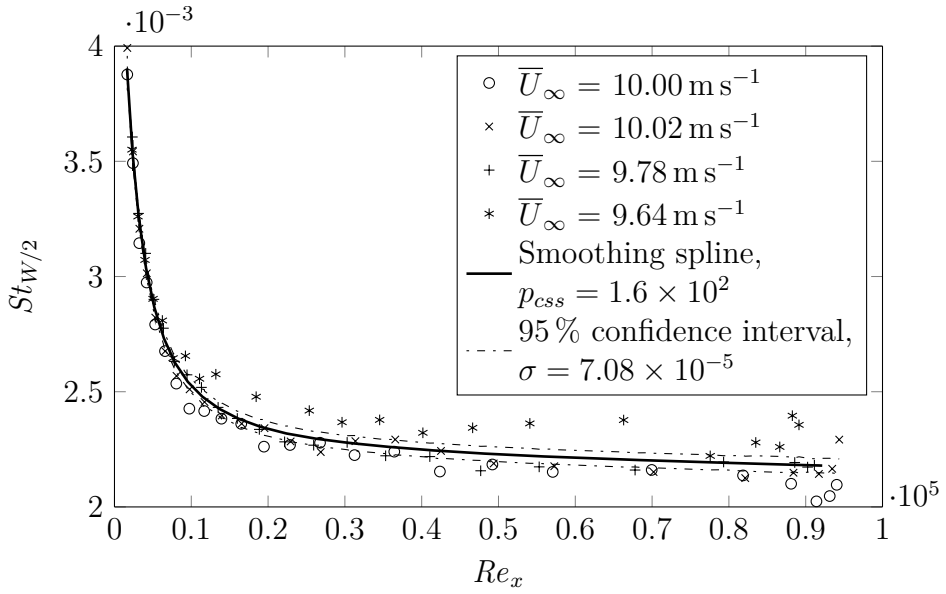

Figure E.51: Centerline St for $10\,\mathrm{m\,s^{-1}}$ freestream velocity and 2.48 mm width strip showing raw data and cubic smoothing spline estimate.

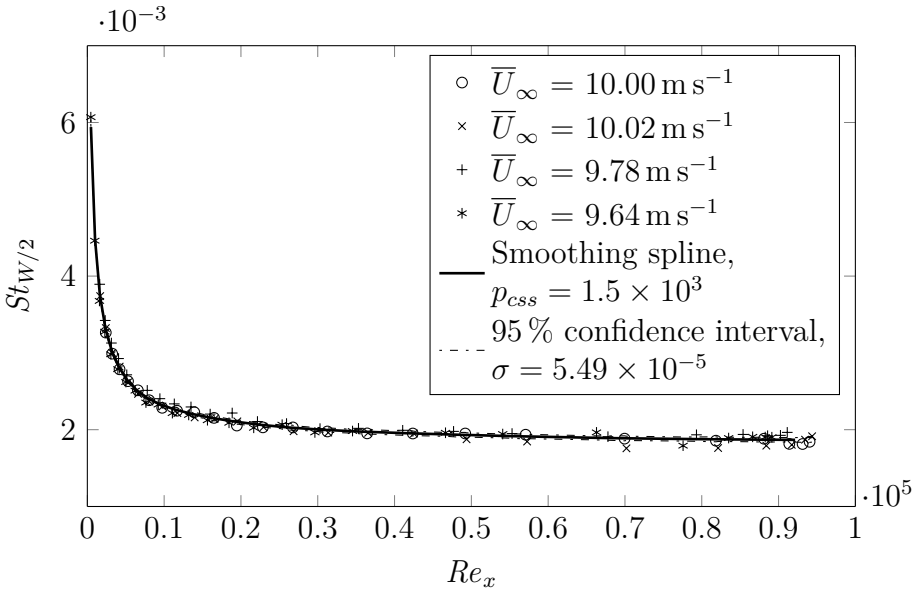

Figure E.52: Centerline St for $10\,\mathrm{m\,s^{-1}}$ freestream velocity and 5.00 mm width strip showing raw data and cubic smoothing spline estimate.

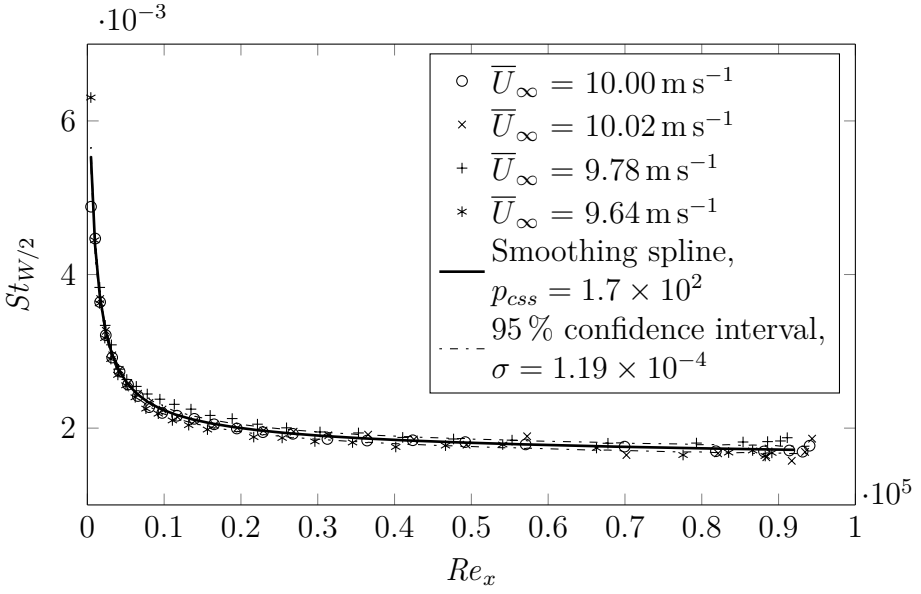

Figure E.53: Centerline St for $10\,\mathrm{m\,s^{-1}}$ freestream velocity and 9.77 mm width strip showing raw data and cubic smoothing spline estimate.

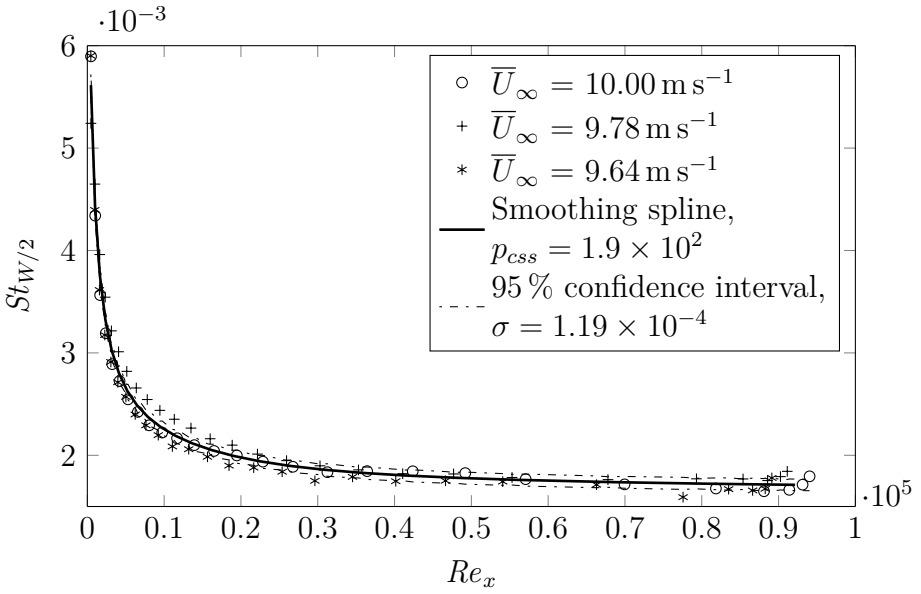

Figure E.54: Centerline St for $10\,\mathrm{m\,s^{-1}}$ freestream velocity and 19.77 mm width strip showing raw data and cubic smoothing spline estimate.

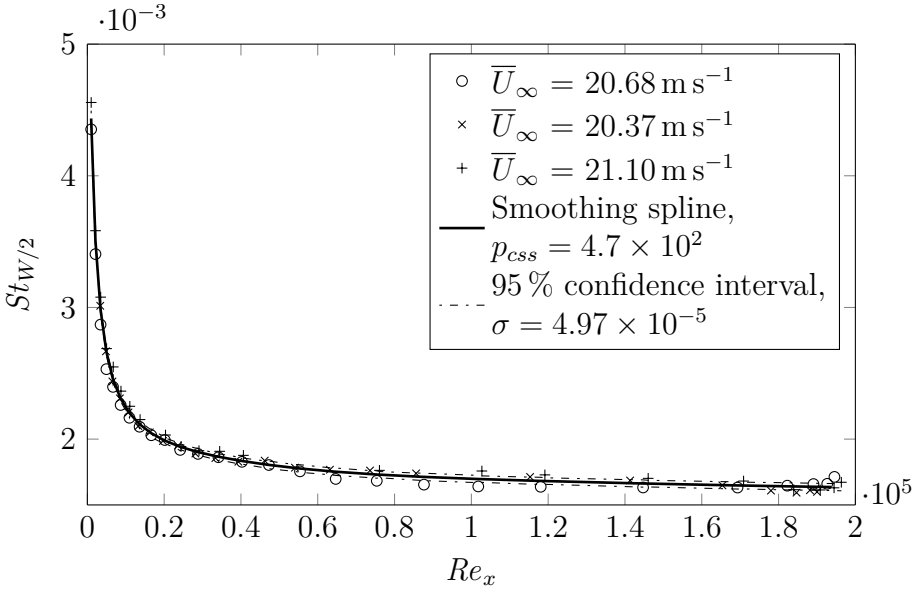

Figure E.55: Centerline St for $20\,\mathrm{m\,s^{-1}}$ freestream velocity and 5.00 mm width strip showing raw data and cubic smoothing spline estimate.

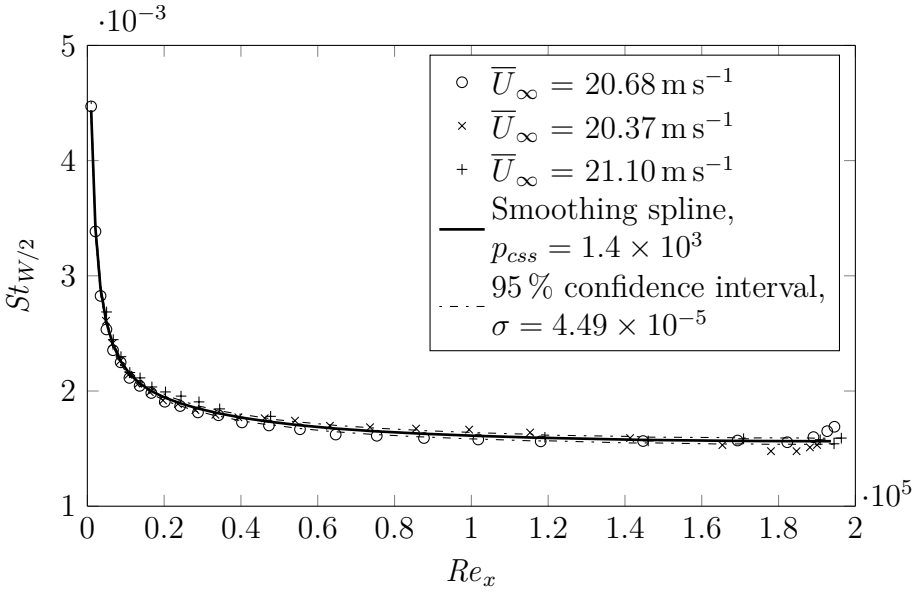

Figure E.56: Centerline St for $20\,\mathrm{m\,s^{-1}}$ freestream velocity and 9.77 mm width strip showing raw data and cubic smoothing spline estimate.

E.3 Turbulent Cavities

E.3.1 Centerline St

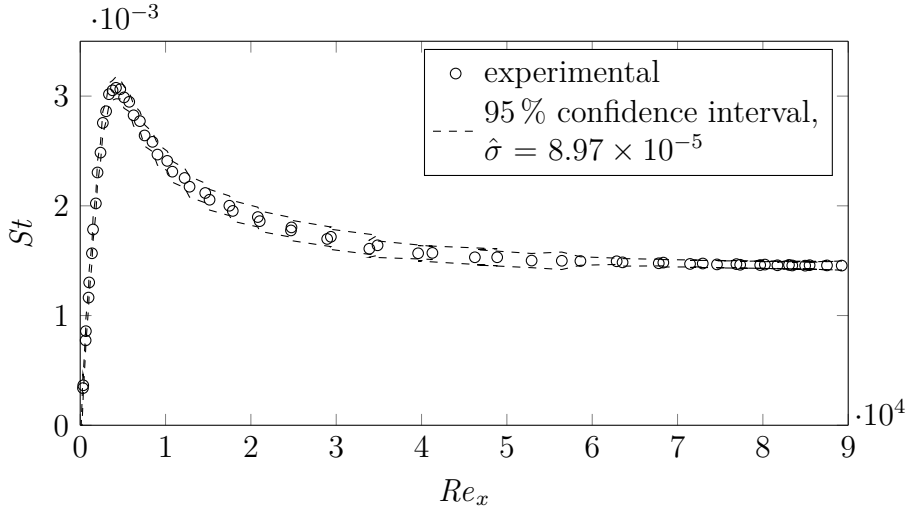

Figure E.57: Centerline mass transfer between experimental results and numerical simulation for $U_\infty \sim 10\,\mathrm{m\,s^{-1}}$ and $d = 0.401\,\mathrm{mm}$

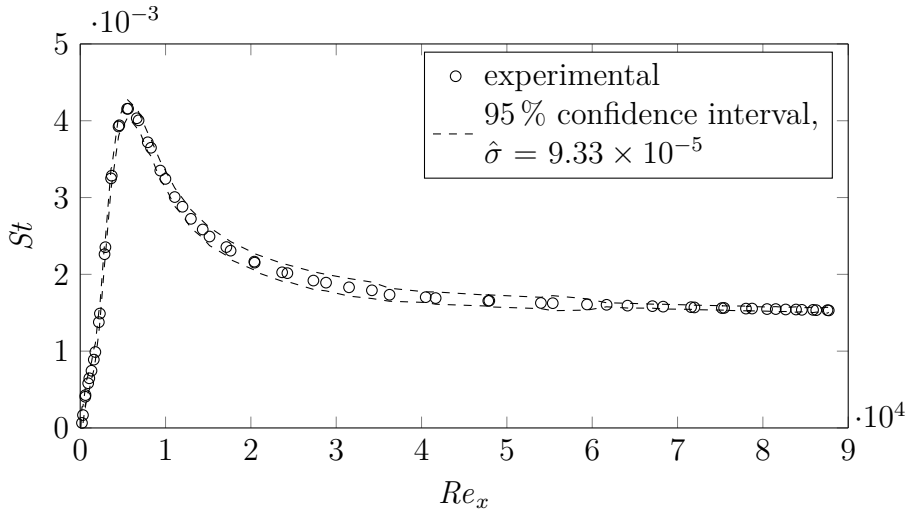

Figure E.58: Centerline mass transfer between experimental results and numerical simulation for $U_\infty \sim 10\,\mathrm{m\,s^{-1}}$ and $d = 0.960\,\mathrm{mm}$

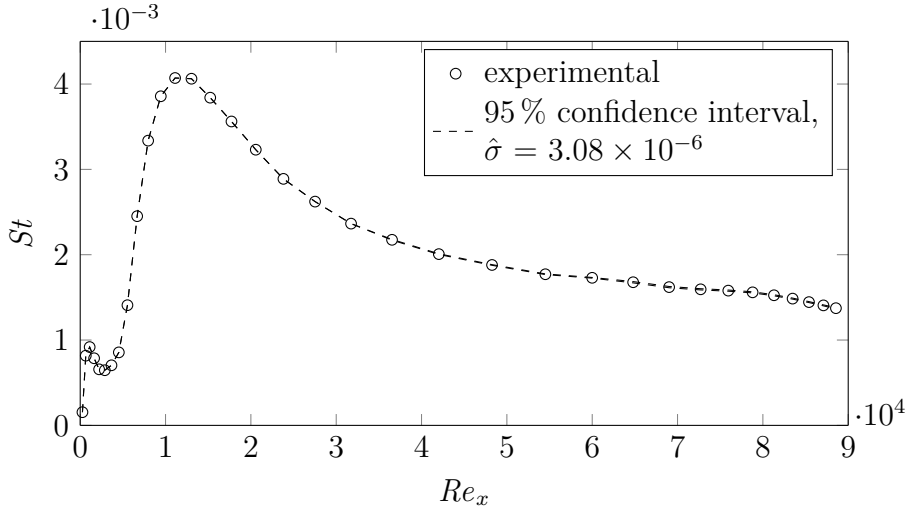

Figure E.59: Centerline mass transfer between experimental results and numerical simulation for $U_\infty \sim 10\,\mathrm{m\,s^{-1}}$ and $d = 4.32\,\mathrm{mm}$

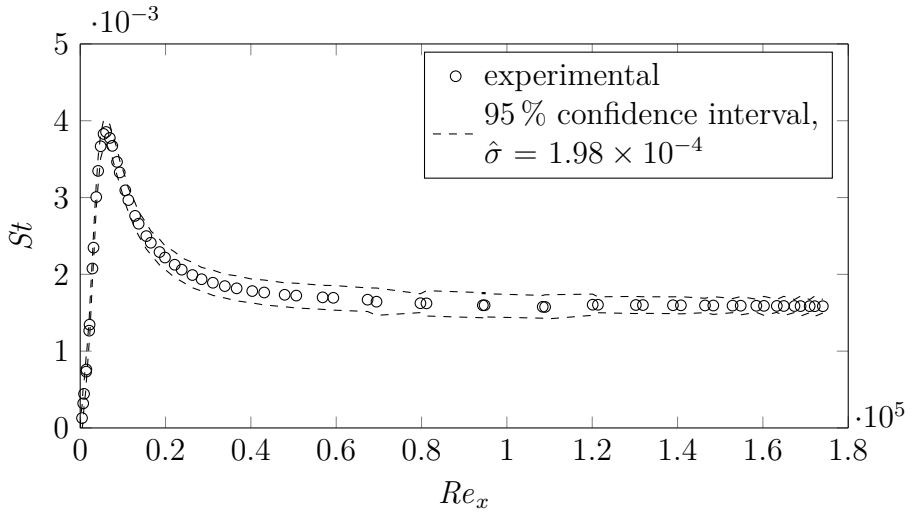

Figure E.60: Centerline mass transfer between experimental results and numerical simulation for $U_\infty \sim 20\,\mathrm{m\,s^{-1}}$ and $d = 0.401\,\mathrm{mm}$

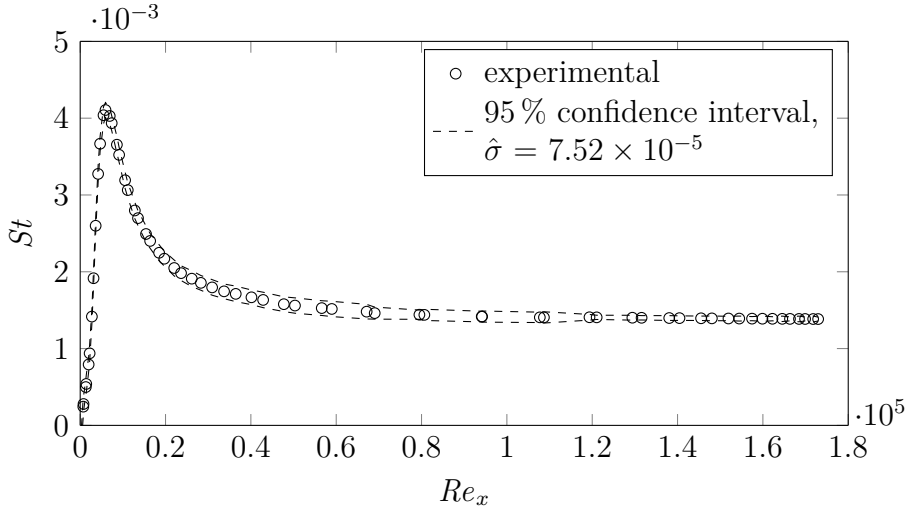

Figure E.61: Centerline mass transfer between experimental results and numerical simulation for $U_\infty \sim 20\,\mathrm{m\,s^{-1}}$ and $d = 0.597\,\mathrm{mm}$

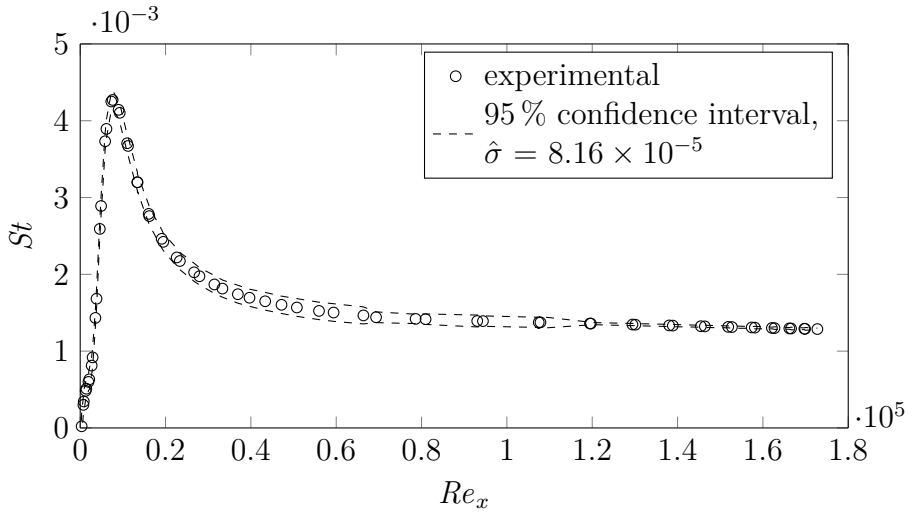

Figure E.62: Centerline mass transfer between experimental results and numerical simulation for $U_\infty \sim 20\,\mathrm{m\,s^{-1}}$ and $d = 0.960\,\mathrm{mm}$

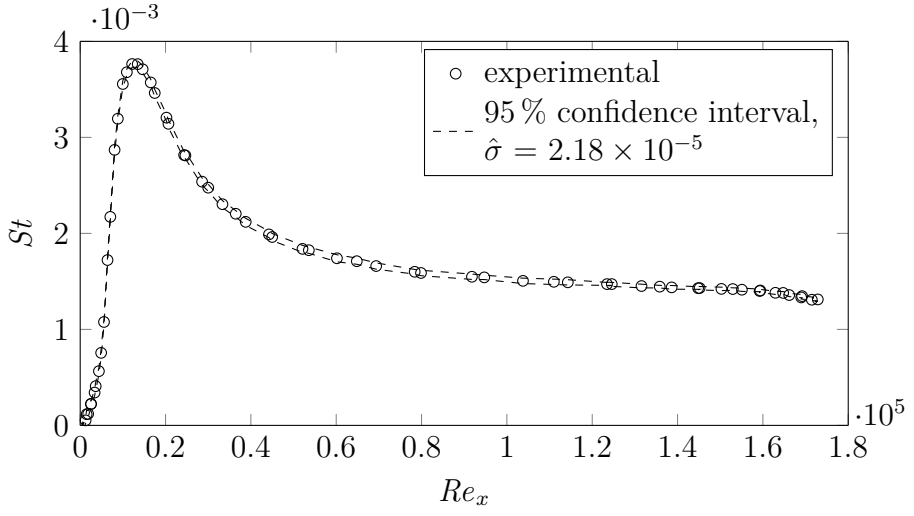

Figure E.63: Centerline mass transfer between experimental results and numerical simulation for $U_\infty \sim 20\,\mathrm{m\,s^{-1}}$ and $d = 2.29\,\mathrm{mm}$

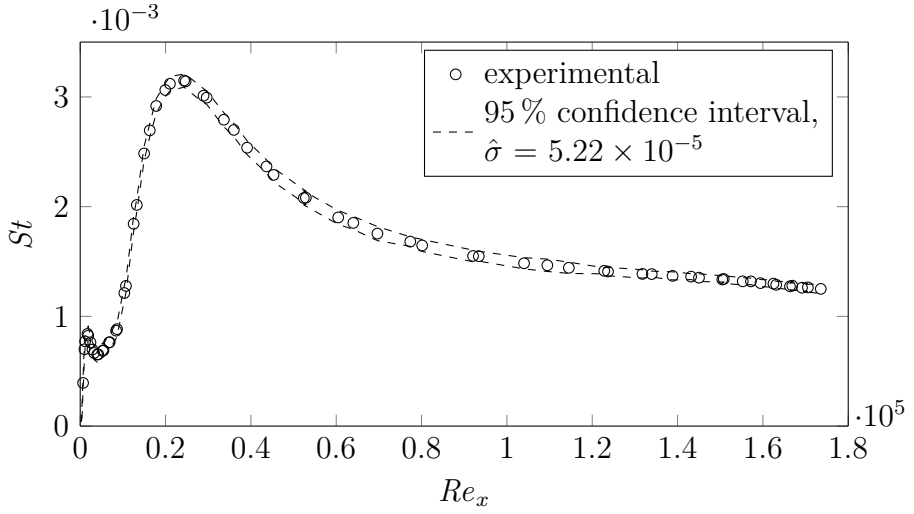

Figure E.64: Centerline mass transfer between experimental results and numerical simulation for $U_\infty \sim 20\,\mathrm{m\,s^{-1}}$ and $d = 4.32\,\mathrm{mm}$

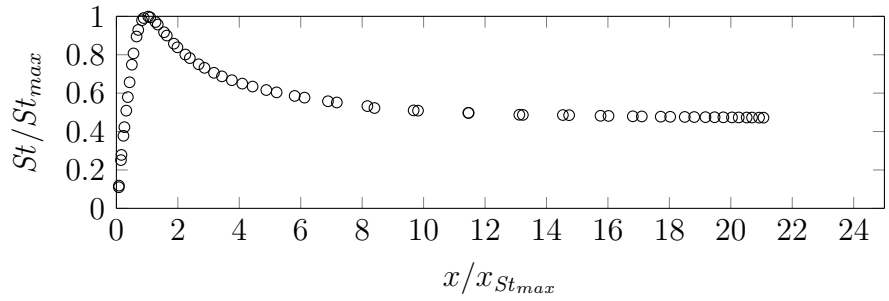

Figure E.65: Normalized centerline mass transfer between experimental results and numerical simulation for $U_\infty \sim 10\,\mathrm{m\,s^{-1}}$ and $d = 0.401\,\mathrm{mm}$

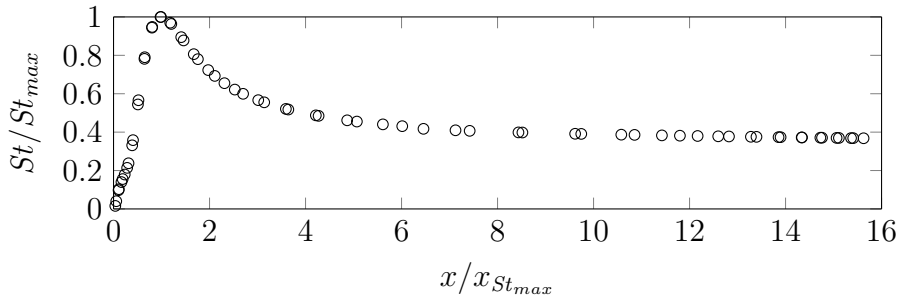

Figure E.66: Normalized centerline mass transfer between experimental results and numerical simulation for $U_\infty \sim 10\,\mathrm{m\,s^{-1}}$ and $d = 0.960\,\mathrm{mm}$

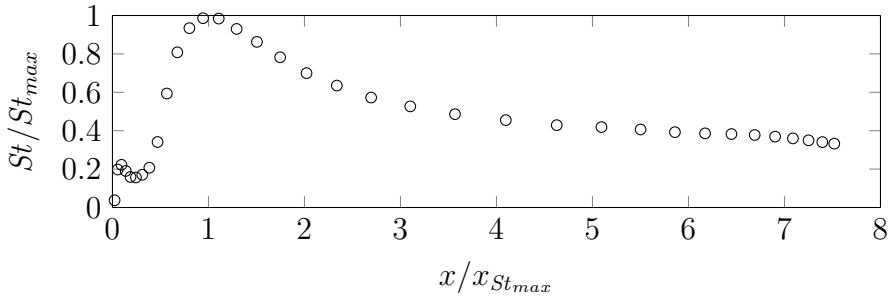

Figure E.67: Normalized centerline mass transfer between experimental results and numerical simulation for $U_\infty \sim 10\,\mathrm{m\,s^{-1}}$ and $d = 4.32\,\mathrm{mm}$

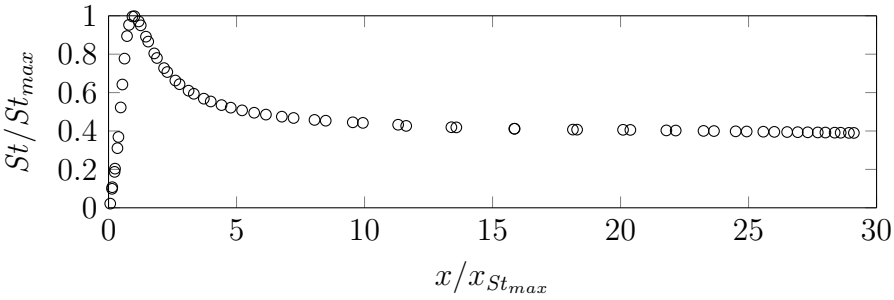

Figure E.68: Normalized centerline mass transfer between experimental results and numerical simulation for $U_\infty \sim 20\,\mathrm{m\,s^{-1}}$ and $d = 0.254\,\mathrm{mm}$

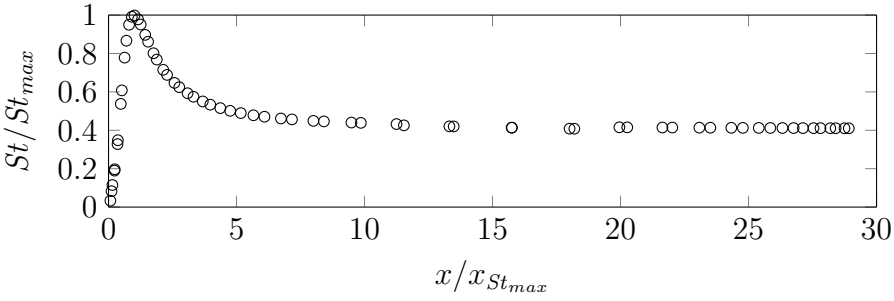

Figure E.69: Normalized centerline mass transfer between experimental results and numerical simulation for $U_\infty \sim 20\,\mathrm{m\,s^{-1}}$ and $d = 0.401\,\mathrm{mm}$

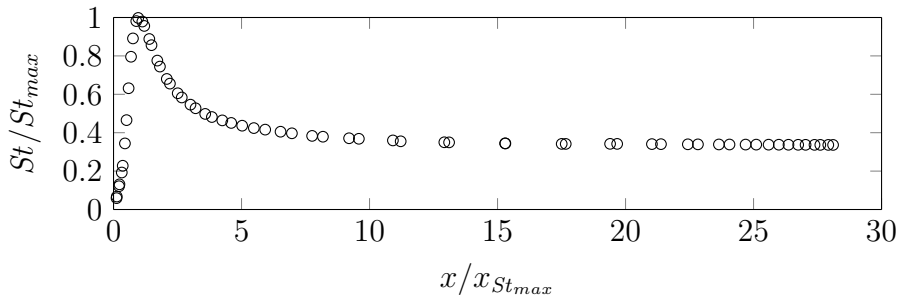

Figure E.70: Normalized centerline mass transfer between experimental results and numerical simulation for $U_\infty \sim 20\,\mathrm{m\,s^{-1}}$ and $d = 0.597\,\mathrm{mm}$

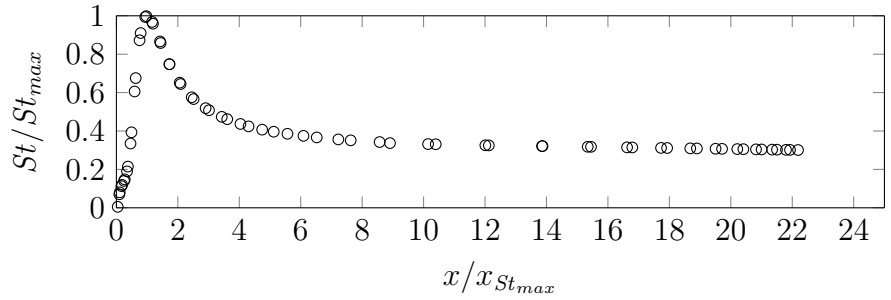

Figure E.71: Normalized centerline mass transfer between experimental results and numerical simulation for $U_\infty \sim 20\,\mathrm{m\,s^{-1}}$ and $d = 0.960\,\mathrm{mm}$

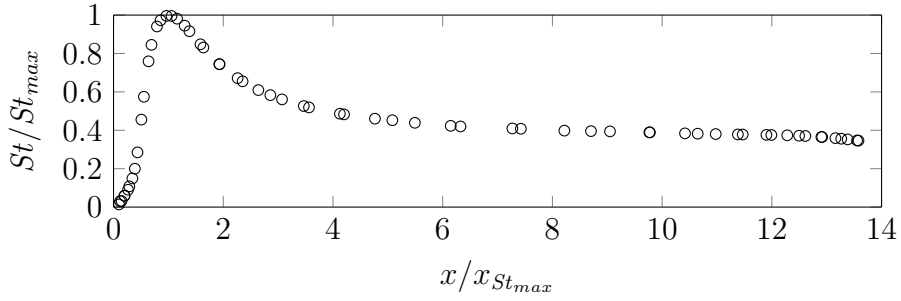

Figure E.72: Normalized centerline mass transfer between experimental results and numerical simulation for $U_\infty \sim 20\,\mathrm{m\,s^{-1}}$ and $d = 2.29\,\mathrm{mm}$

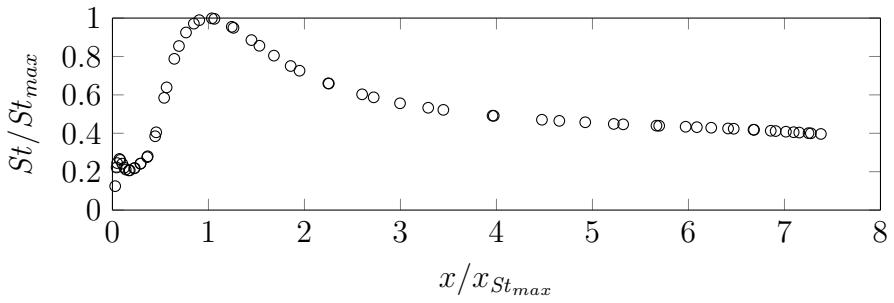

Figure E.73: Normalized centerline mass transfer between experimental results and numerical simulation for $U_\infty \sim 20\,\mathrm{m\,s^{-1}}$ and $d = 4.32\,\mathrm{mm}$

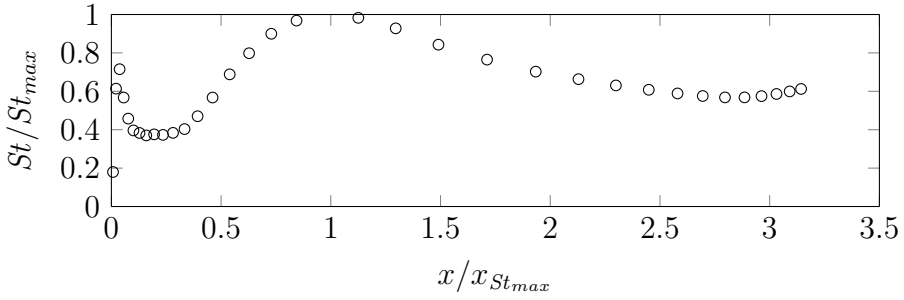

Figure E.74: Normalized centerline mass transfer between experimental results and numerical simulation for $U_\infty \sim 20\,\mathrm{m\,s^{-1}}$ and $d = 8.84\,\mathrm{mm}$

E.3.2 St Contours

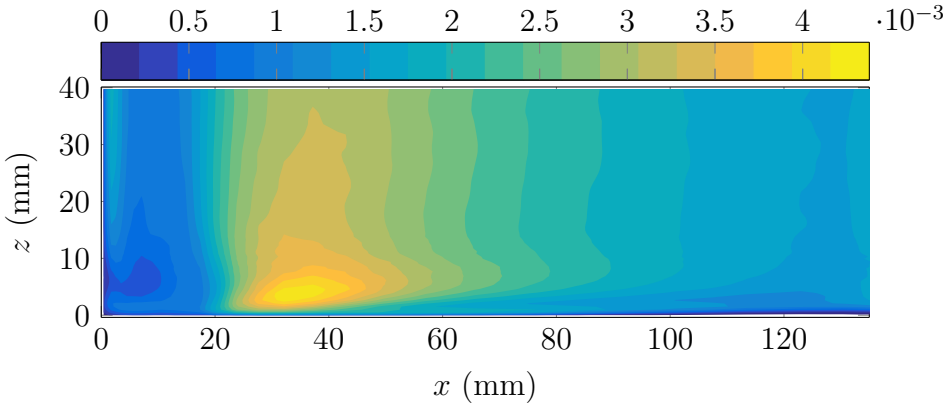

Figure E.75: Contour of experimental St for $U_\infty \sim 10\,\mathrm{m\,s^{-1}}$ and $d = 8.84\,\mathrm{mm}$ for data taken on 2016/07/20-13

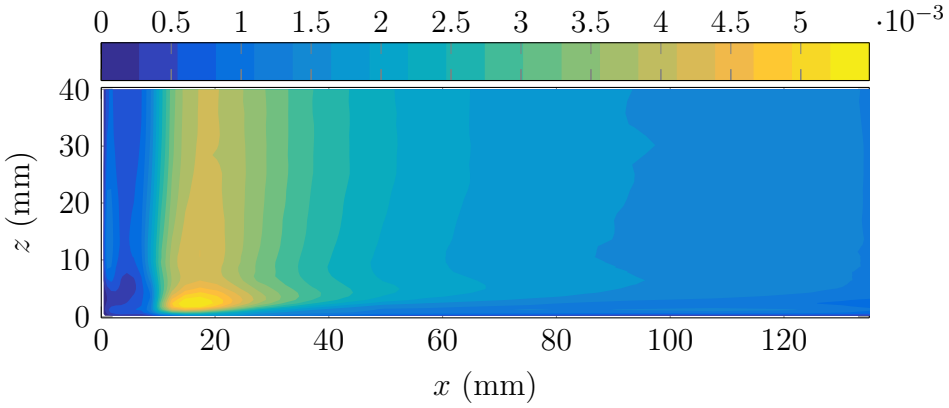

Figure E.76: Contour of experimental St for $U_\infty \sim 10\,\mathrm{m\,s^{-1}}$ and $d = 4.32\,\mathrm{mm}$ for data taken on 2016/07/24-14

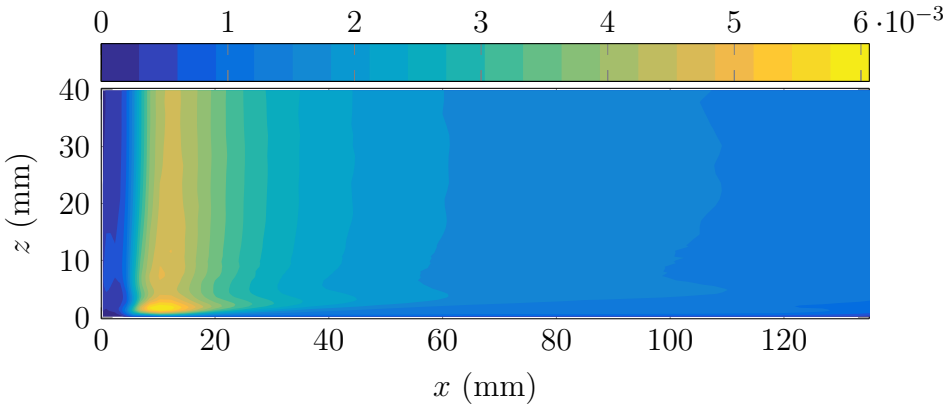

Figure E.77: Contour of experimental St for $U_\infty \sim 10\,\mathrm{m\,s^{-1}}$ and $d = 2.29\,\mathrm{mm}$ for data taken on 2016/07/27-12

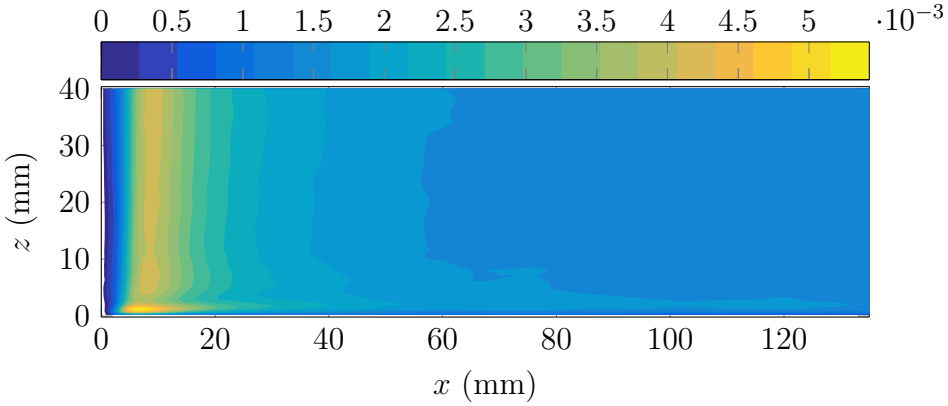

Figure E.78: Contour of experimental St for $U_\infty \sim 10\,\mathrm{m\,s^{-1}}$ and $d = 0.96\,\mathrm{mm}$ for data taken on 2016/07/29-13

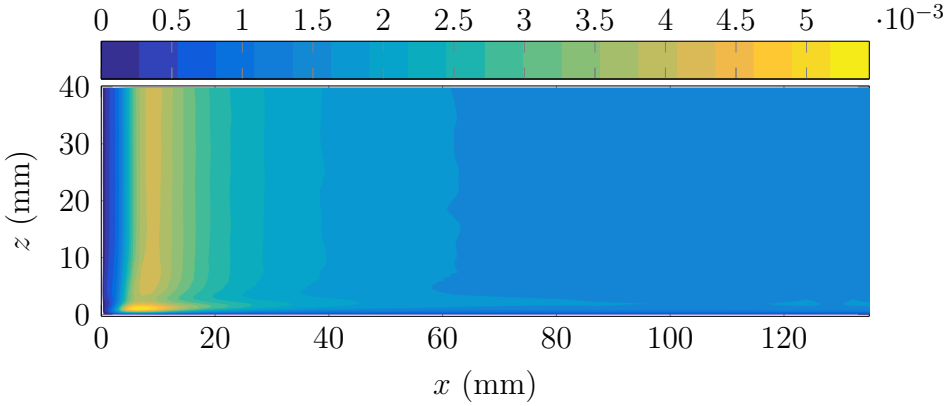

Figure E.79: Contour of experimental St for $U_\infty \sim 10\,\mathrm{m\,s^{-1}}$ and $d = 0.96\,\mathrm{mm}$ for data taken on 2016/08/03-10

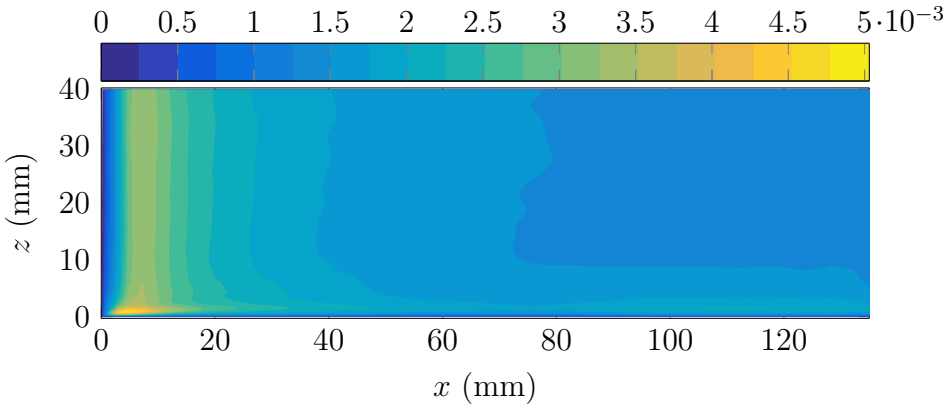

Figure E.80: Contour of experimental St for $U_\infty \sim 10\,\mathrm{m\,s^{-1}}$ and $d = 0.597\,\mathrm{mm}$ for data taken on 2016/08/08-22. Note based on figs. 5.15 to 5.18, the mass transfer data should be viewed with some skepticism.

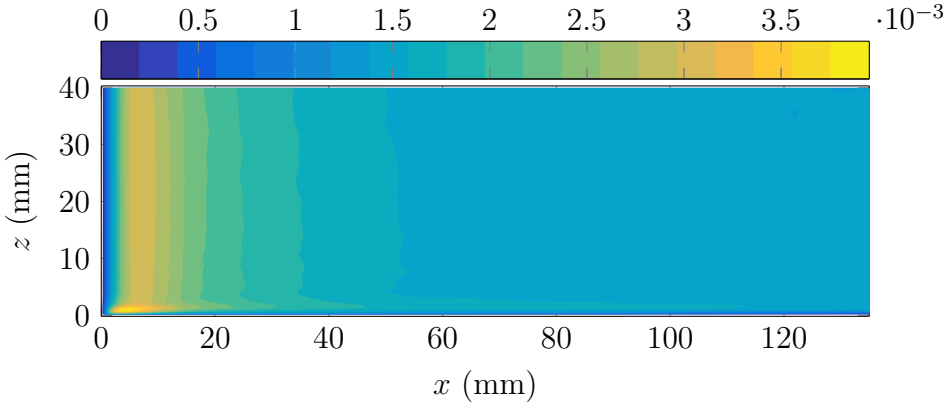

Figure E.81: Contour of experimental St for $U_\infty \sim 10\,\mathrm{m\,s^{-1}}$ and $d = 0.401\,\mathrm{mm}$ for data taken on 2016/08/09-13

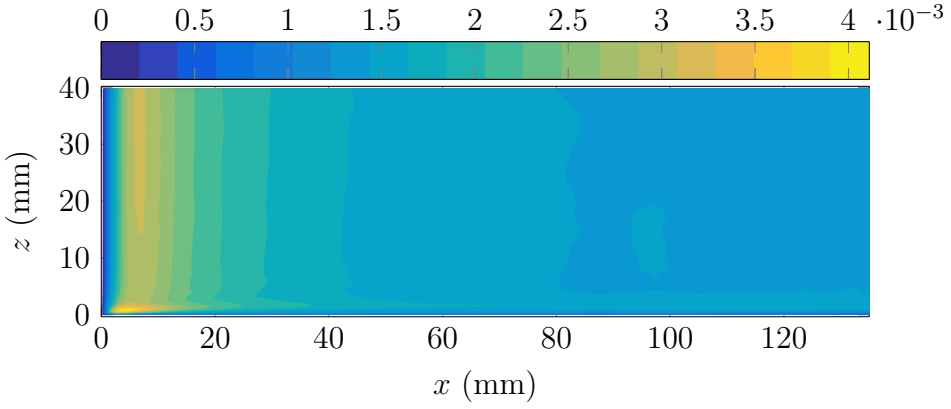

Figure E.82: Contour of experimental St for $U_\infty \sim 10\,\mathrm{m\,s^{-1}}$ and $d = 0.401\,\mathrm{mm}$ for data taken on 2016/08/14-16

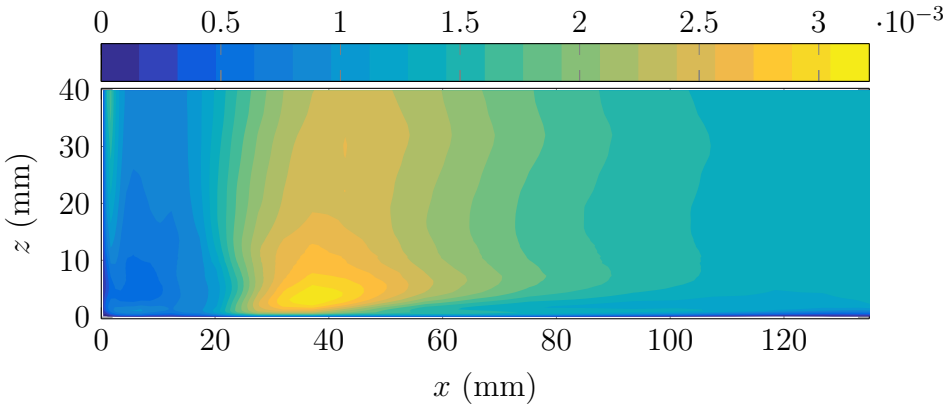

Figure E.83: Contour of experimental St for $U_\infty \sim 20\,\mathrm{m\,s^{-1}}$ and $d = 8.84\,\mathrm{mm}$ for data taken on 2016/07/18-13

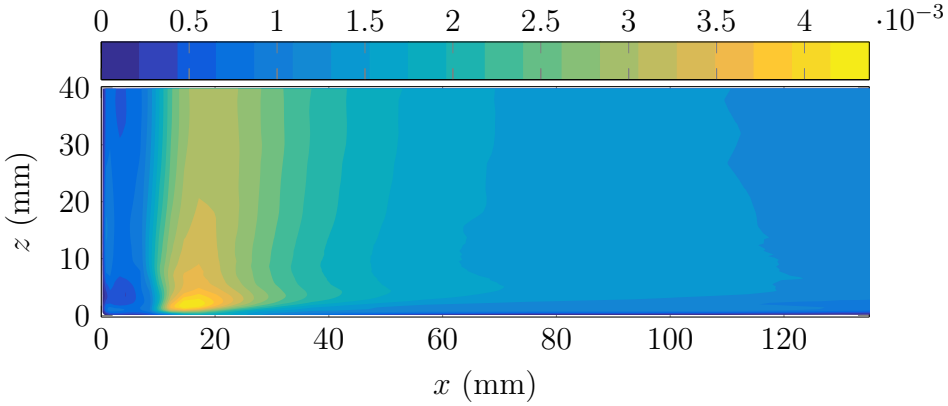

Figure E.84: Contour of experimental St for $U_\infty \sim 20\,\mathrm{m\,s^{-1}}$ and $d = 4.32\,\mathrm{mm}$ for data taken on 2016/07/24-22

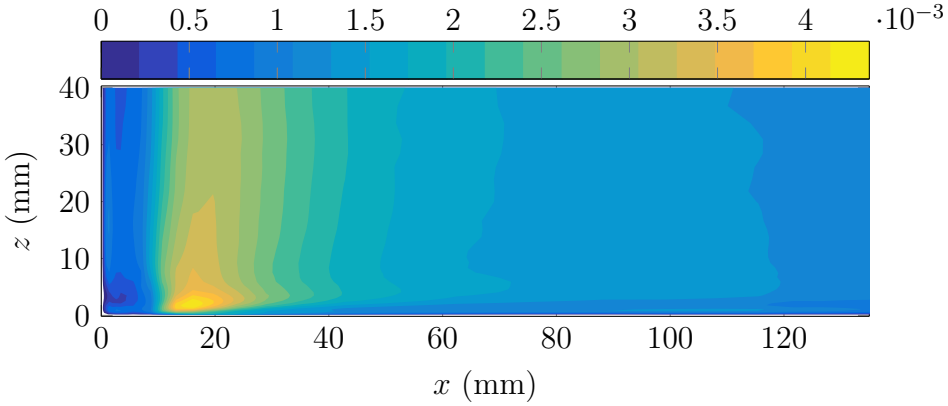

Figure E.85: Contour of experimental St for $U_\infty \sim 20\,\mathrm{m\,s^{-1}}$ and $d = 4.32\,\mathrm{mm}$ for data taken on 2016/07/25-14

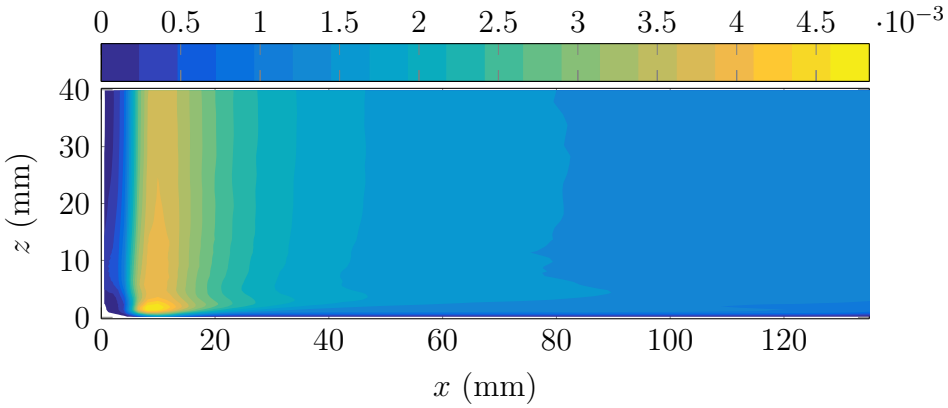

Figure E.86: Contour of experimental St for $U_\infty \sim 20\,\mathrm{m\,s^{-1}}$ and $d = 2.29\,\mathrm{mm}$ for data taken on 2016/07/27-20

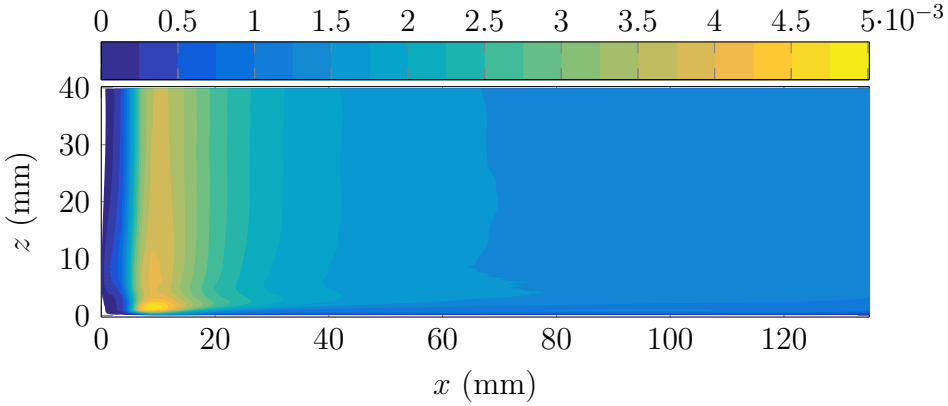

Figure E.87: Contour of experimental St for $U_\infty \sim 20\,\mathrm{m\,s^{-1}}$ and $d = 2.29\,\mathrm{mm}$ for data taken on 2016/07/28-12

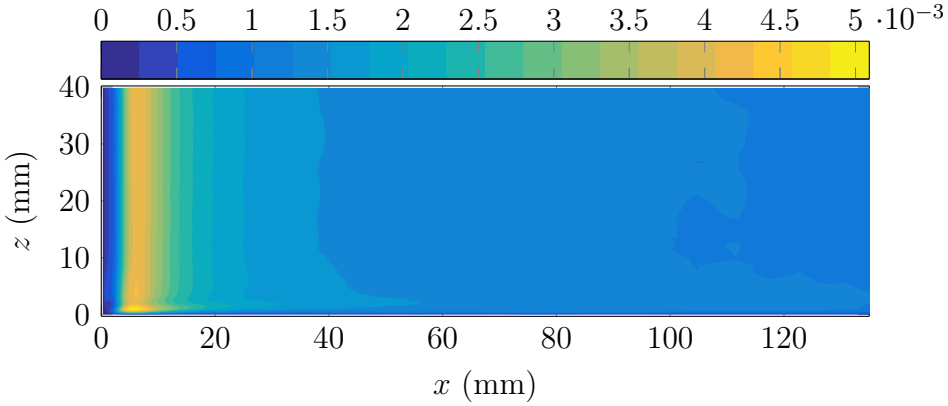

Figure E.88: Contour of experimental St for $U_\infty \sim 20\,\mathrm{m\,s^{-1}}$ and $d = 0.96\,\mathrm{mm}$ for data taken on 2016/08/01-13

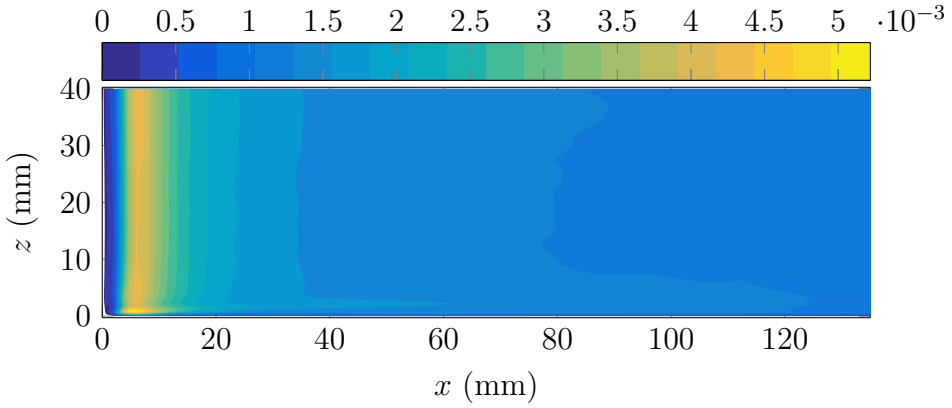

Figure E.89: Contour of experimental St for $U_\infty \sim 20\,\mathrm{m\,s^{-1}}$ and $d = 0.96\,\mathrm{mm}$ for data taken on 2016/08/01-22

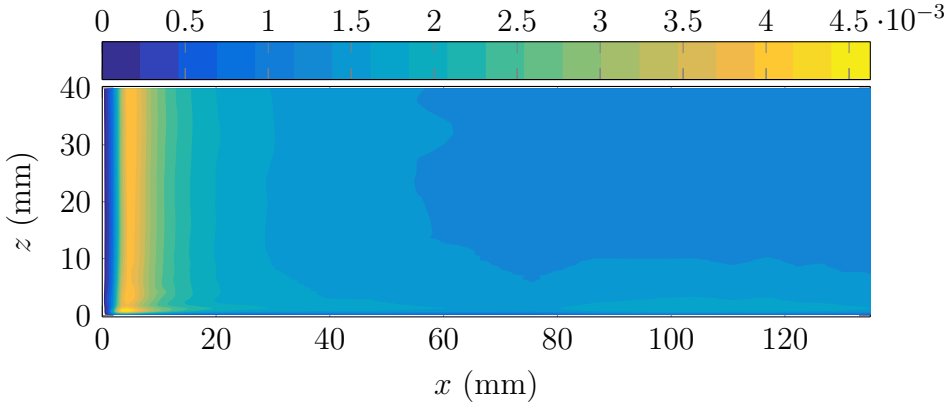

Figure E.90: Contour of experimental St for $U_\infty \sim 20\,\mathrm{m\,s^{-1}}$ and $d = 0.597\,\mathrm{mm}$ for data taken on 2016/08/07-18. Note based on figs. 5.15 to 5.18, the mass transfer data should be viewed with some skepticism.

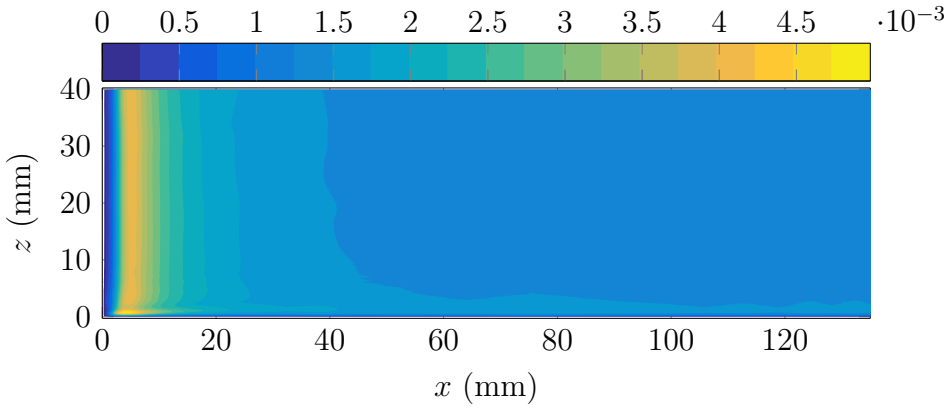

Figure E.91: Contour of experimental St for $U_\infty \sim 20\,\mathrm{m\,s^{-1}}$ and $d = 0.597\,\mathrm{mm}$ for data taken on 2016/08/08-11. Note based on figs. 5.15 to 5.18, the mass transfer data should be viewed with some skepticism.

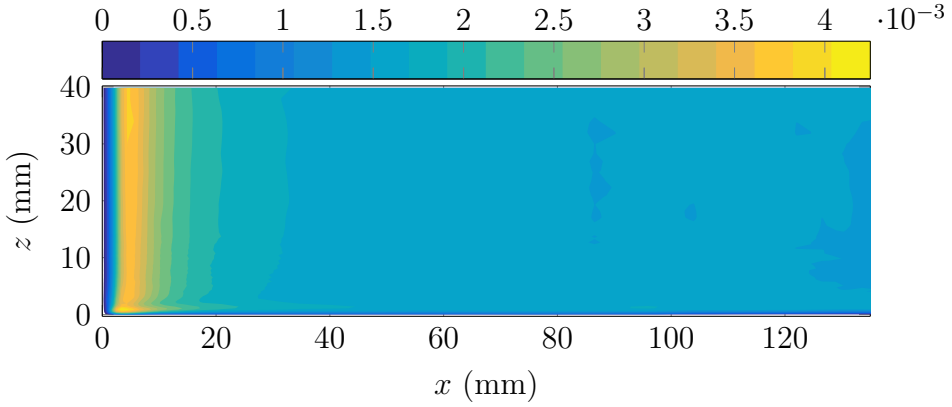

Figure E.92: Contour of experimental St for $U_\infty \sim 20\,\mathrm{m\,s^{-1}}$ and $d = 0.401\,\mathrm{mm}$ for data taken on 2016/08/13-10

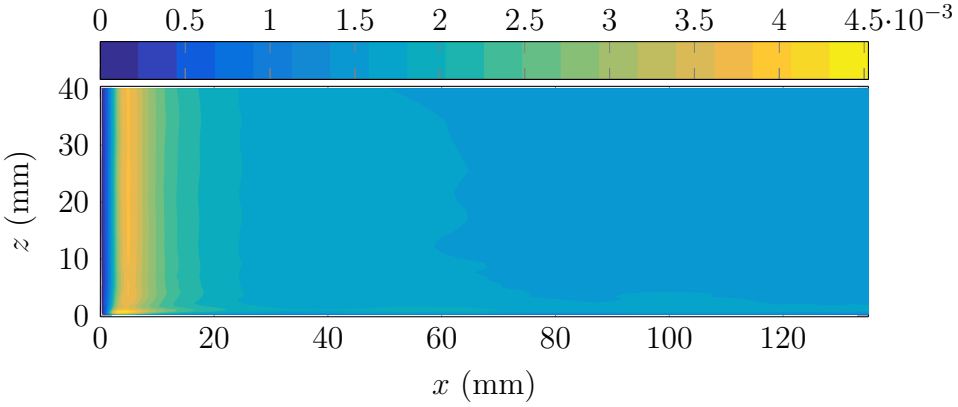

Figure E.93: Contour of experimental St for $U_\infty \sim 20\,\mathrm{m\,s^{-1}}$ and $d = 0.401\,\mathrm{mm}$ for data taken on 2016/08/13-22

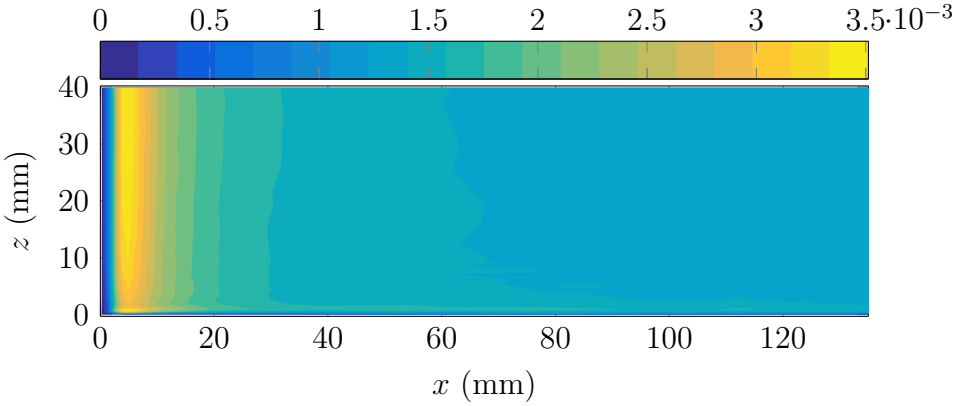

Figure E.94: Contour of experimental St for $U_\infty \sim 20\,\mathrm{m\,s^{-1}}$ and $d = 0.254\,\mathrm{mm}$ for data taken on 2016/08/17-23

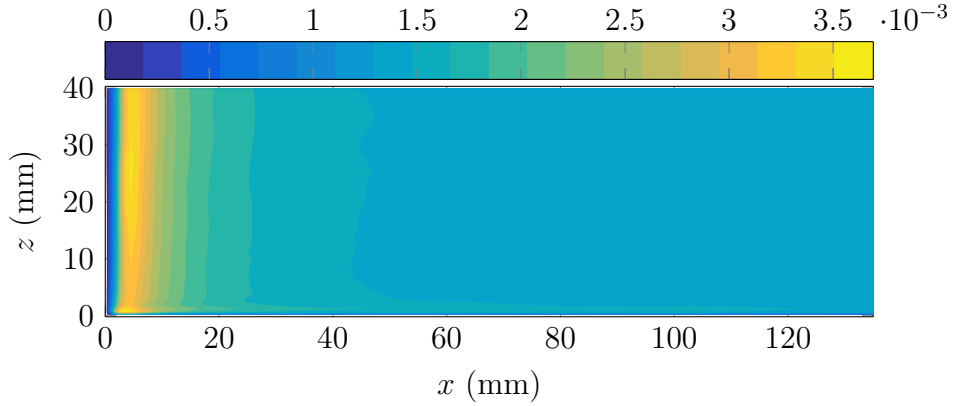

Figure E.95: Contour of experimental St for $U_\infty \sim 20\,\mathrm{m\,s^{-1}}$ and $d = 0.254\,\mathrm{mm}$ for data taken on 2016/08/18-20

E.3.3 Lateral St profiles

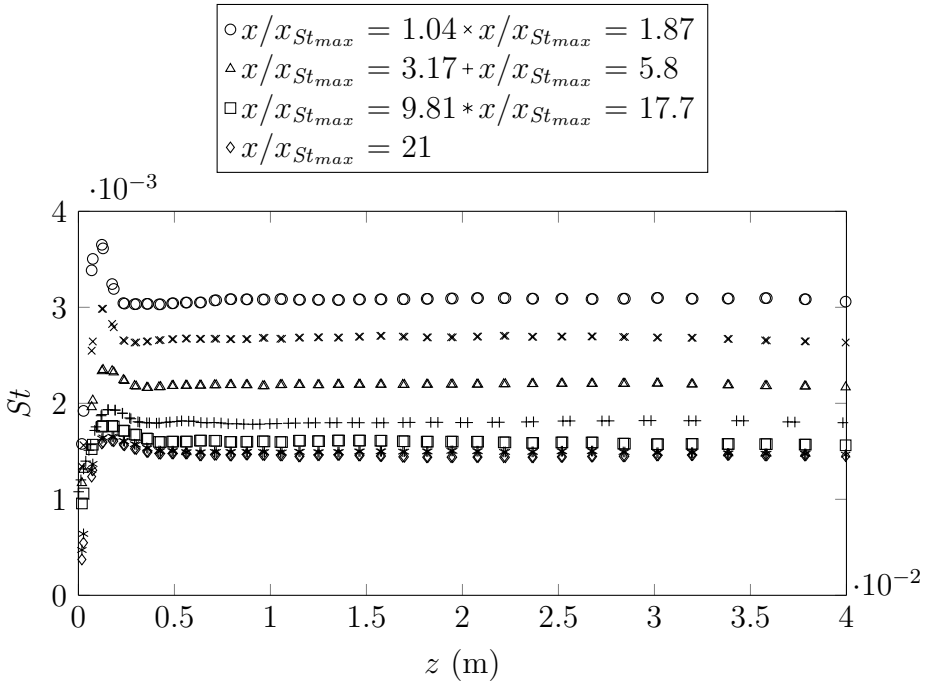

Figure E.96: Lateral profiles of the St vs z at various streamwise locations for $U_\infty \sim 10\,\mathrm{m\,s^{-1}}$ and $d = 0.401\,\mathrm{mm}$

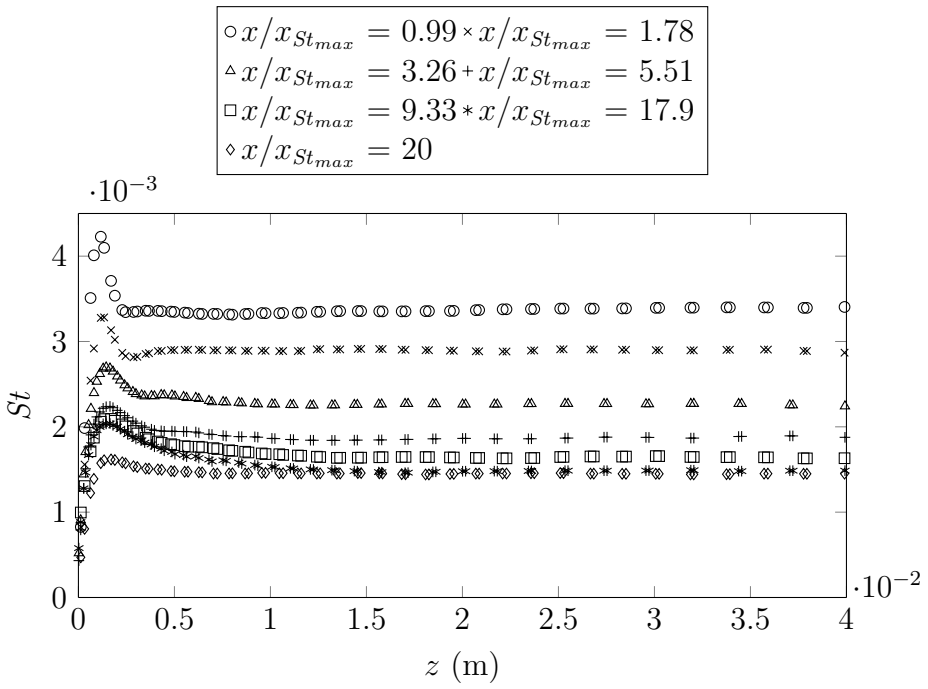

Figure E.97: Lateral profiles of the St vs z at various streamwise locations for $U_\infty \sim 10\,\mathrm{m\,s^{-1}}$ and $d = 0.597\,\mathrm{mm}$. Note based on figs. 5.15 to 5.18, the mass transfer data should be viewed with some skepticism.

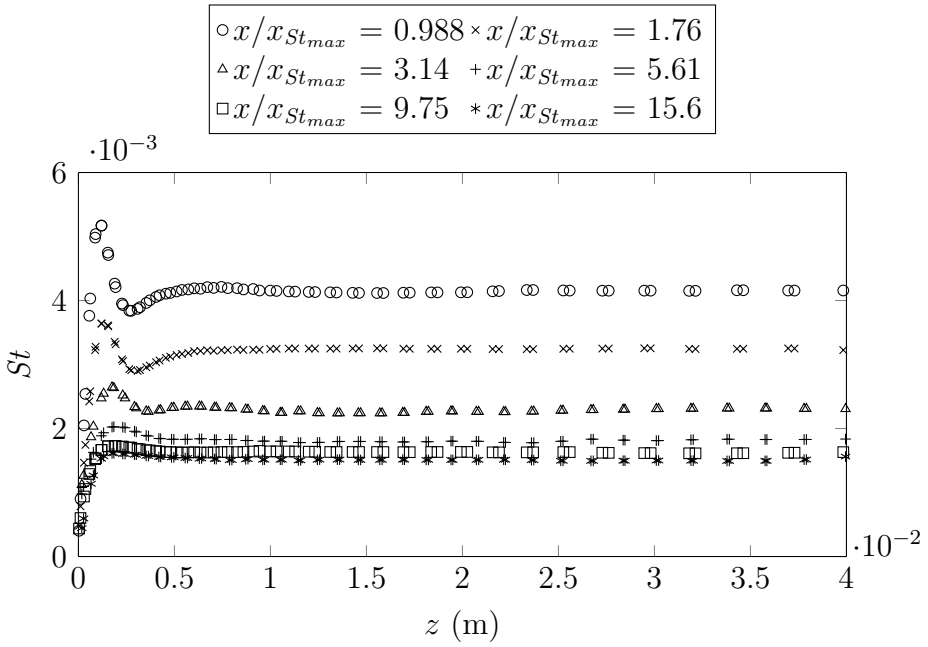

Figure E.98: Lateral profiles of the St vs z at various streamwise locations for $U_\infty \sim 10\,\mathrm{m\,s^{-1}}$ and $d = 0.960\,\mathrm{mm}$

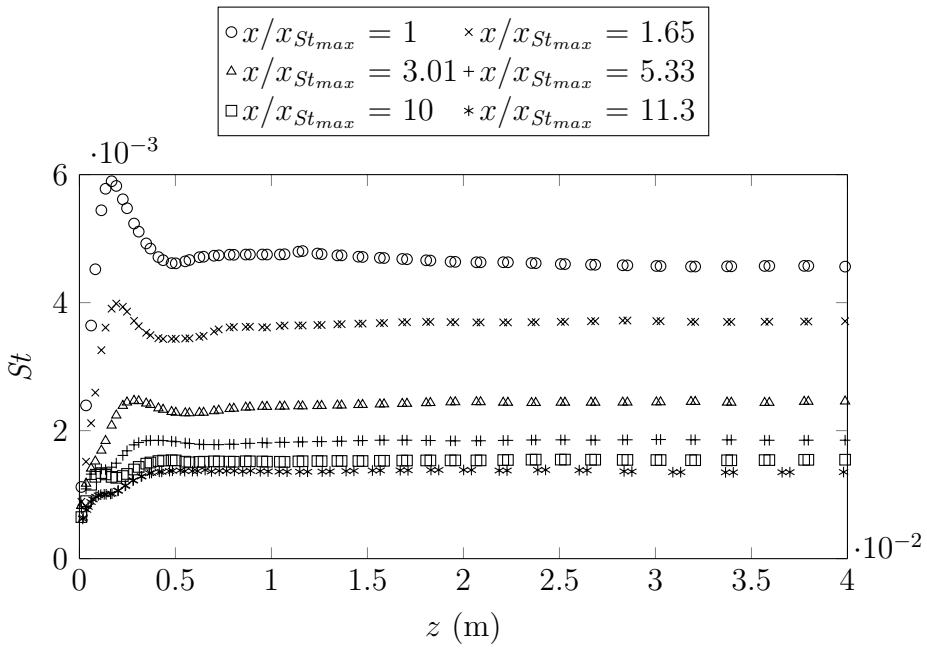

Figure E.99: Lateral profiles of the St vs z at various streamwise locations for $U_\infty \sim 10\,\mathrm{m\,s^{-1}}$ and $d = 2.29\,\mathrm{mm}$

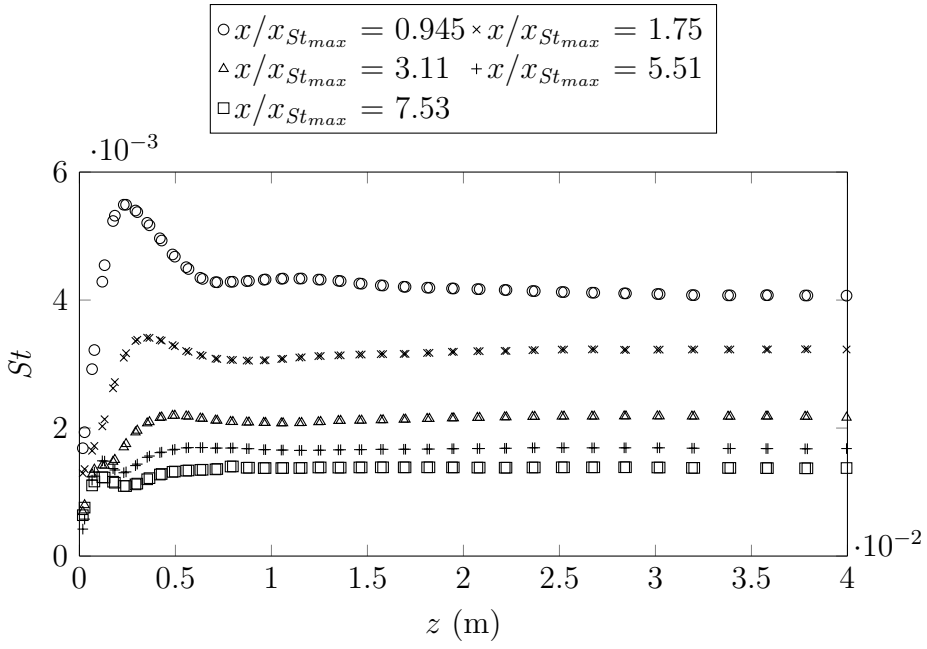

Figure E.100: Lateral profiles of the St vs z at various streamwise locations for $U_\infty \sim 10\,\mathrm{m\,s^{-1}}$ and $d = 4.32\,\mathrm{mm}$

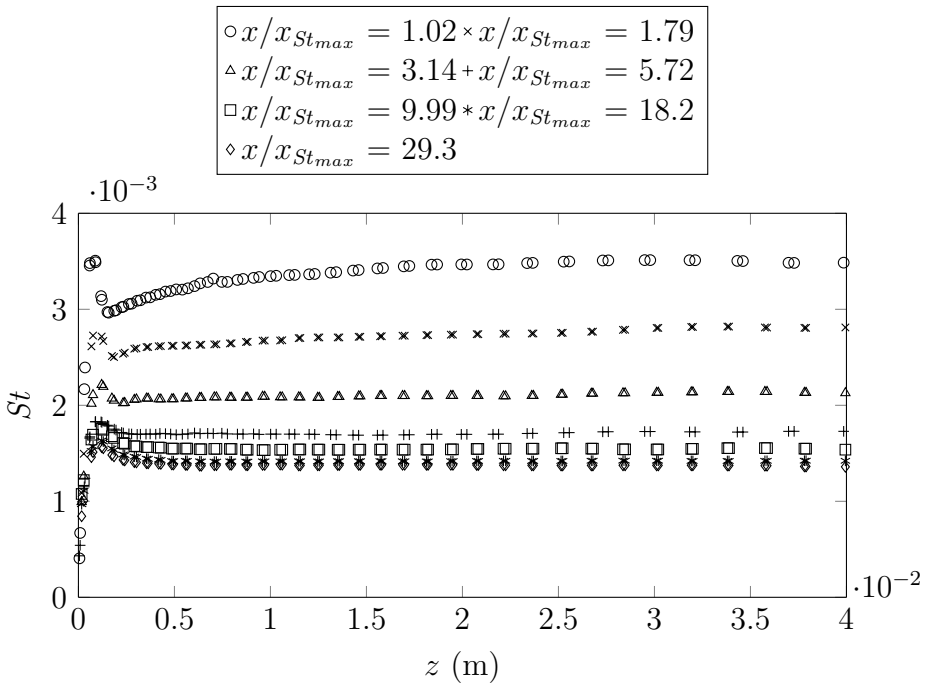

Figure E.101: Lateral profiles of the St vs z at various streamwise locations for $U_\infty \sim 20\,\mathrm{m\,s^{-1}}$ and $d = 0.254\,\mathrm{mm}$

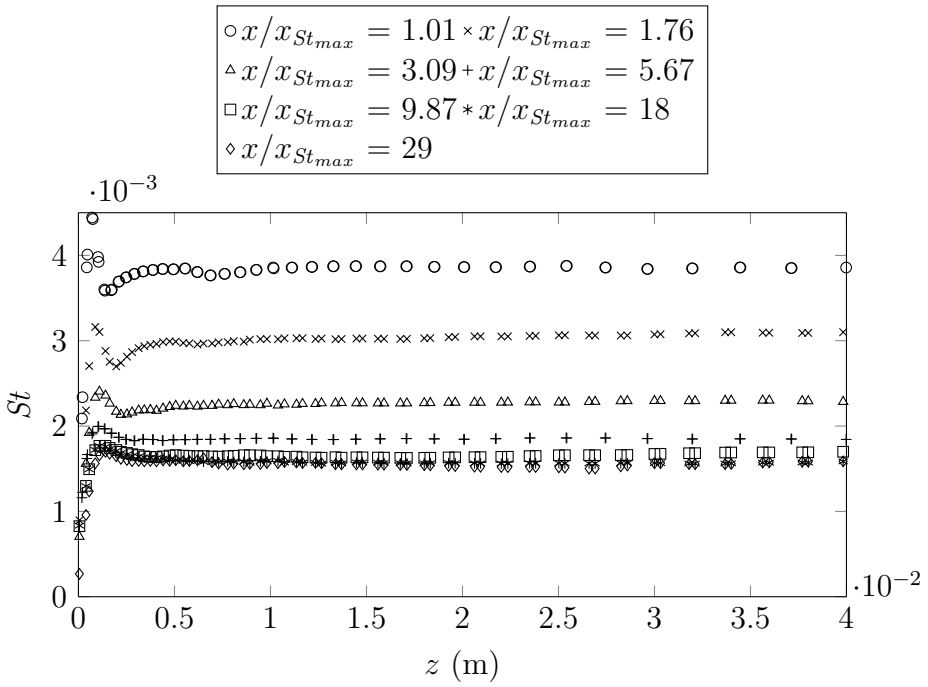

Figure E.102: Lateral profiles of the St vs z at various streamwise locations for $U_\infty \sim 20\,\mathrm{m\,s^{-1}}$ and $d = 0.401\,\mathrm{mm}$

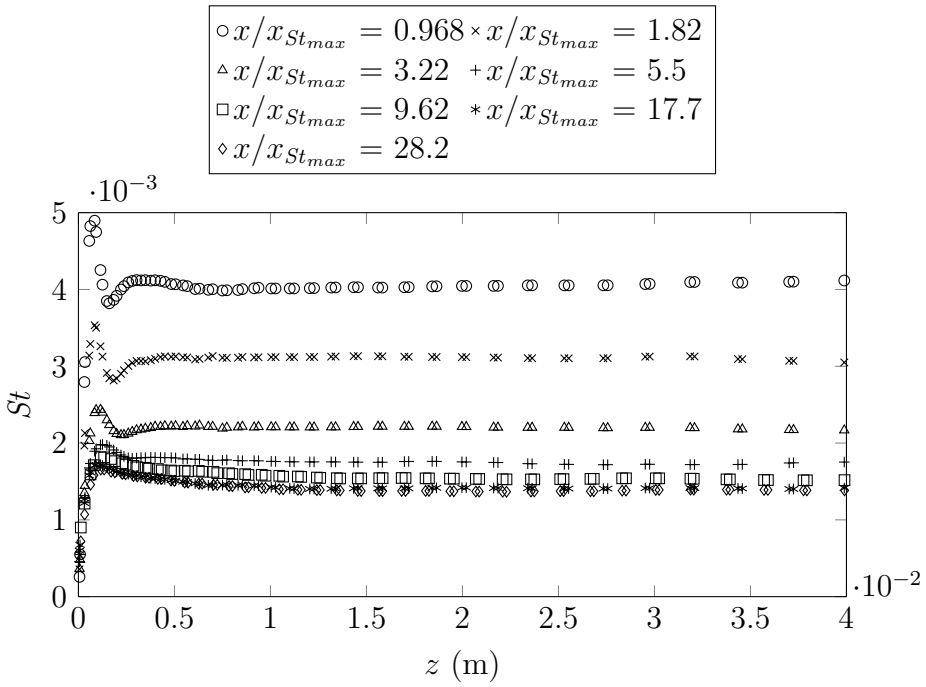

Figure E.103: Lateral profiles of the St vs z at various streamwise locations for $U_\infty \sim 20\,\mathrm{m\,s^{-1}}$ and $d = 0.597\,\mathrm{mm}$. Note based on figs. 5.15 to 5.18, the mass transfer data should be viewed with some skepticism.

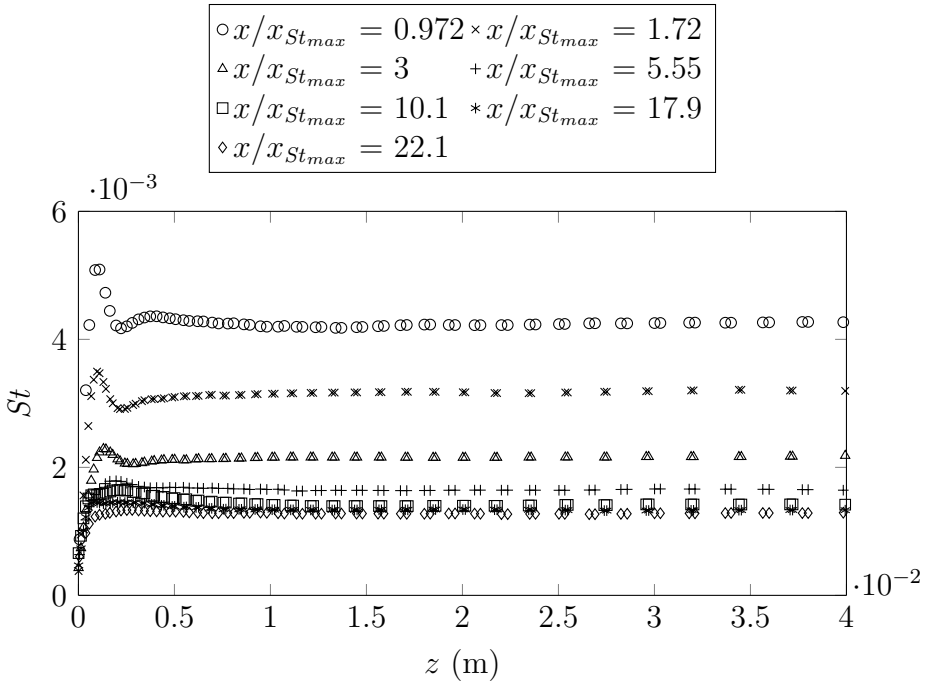

Figure E.104: Lateral profiles of the St vs z at various streamwise locations for $U_\infty \sim 20\,\mathrm{m\,s^{-1}}$ and $d = 0.960\,\mathrm{mm}$

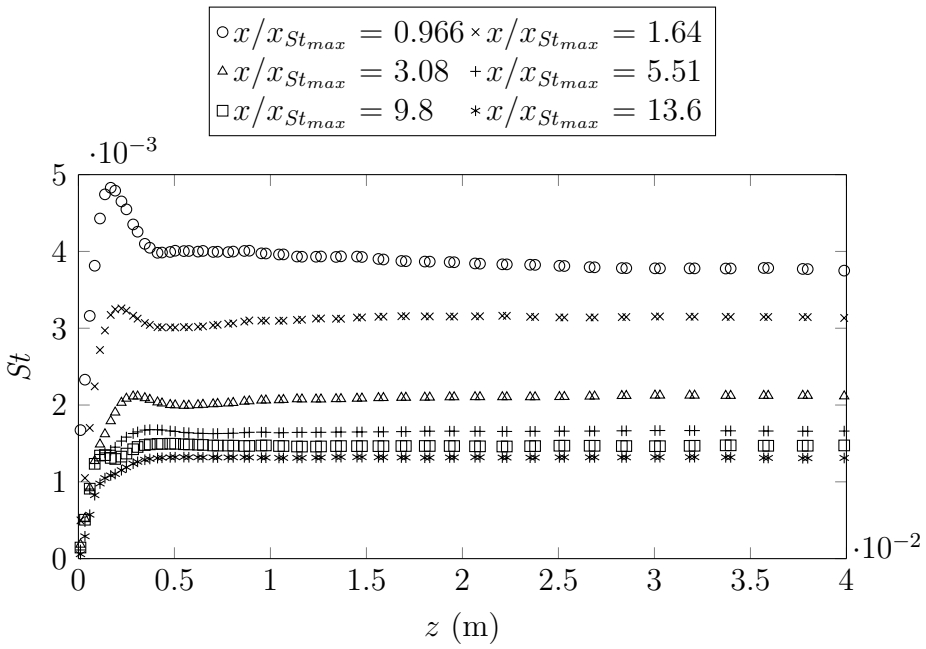

Figure E.105: Lateral profiles of the St vs z at various streamwise locations for $U_\infty \sim 20\,\mathrm{m\,s^{-1}}$ and $d = 2.29\,\mathrm{mm}$

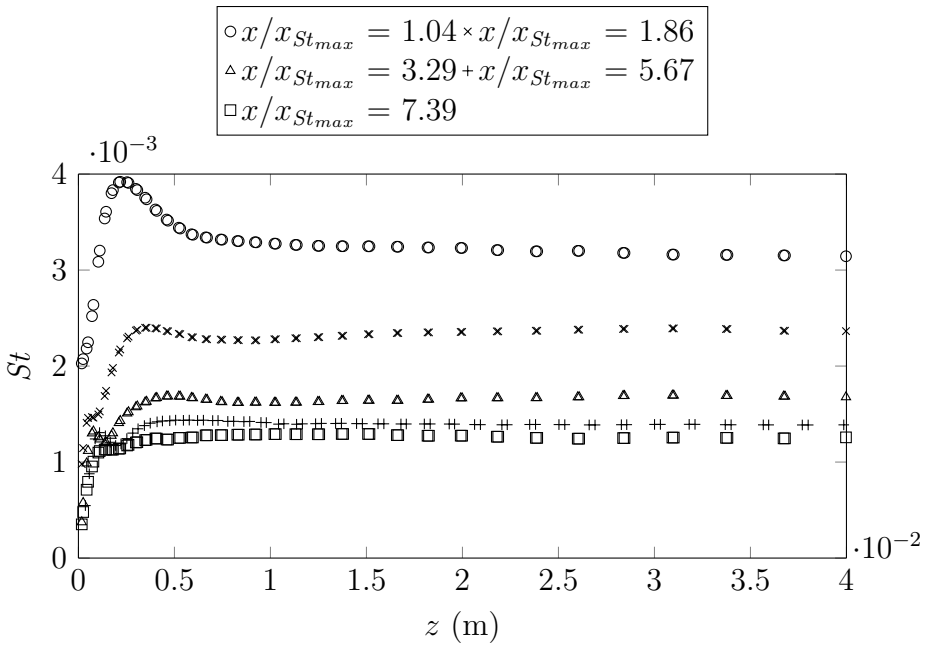

Figure E.106: Lateral profiles of the St vs z at various streamwise locations for $U_\infty \sim 20\,\mathrm{m\,s^{-1}}$ and $d = 4.32\,\mathrm{mm}$

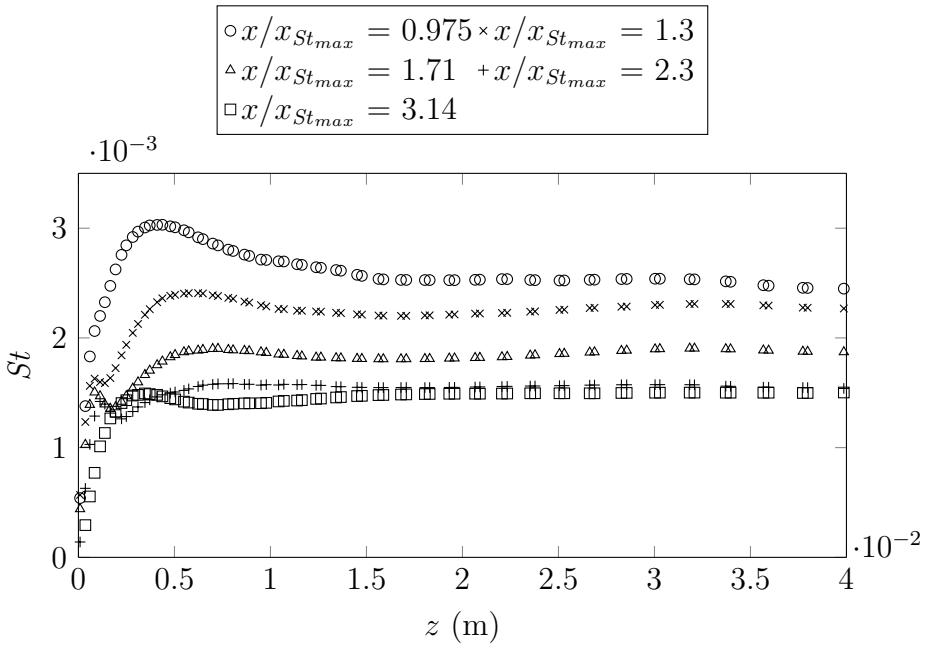

Figure E.107: Lateral profiles of the St vs z at various streamwise locations for $U_\infty \sim 20\,\mathrm{m\,s^{-1}}$ and $d = 8.84\,\mathrm{mm}$

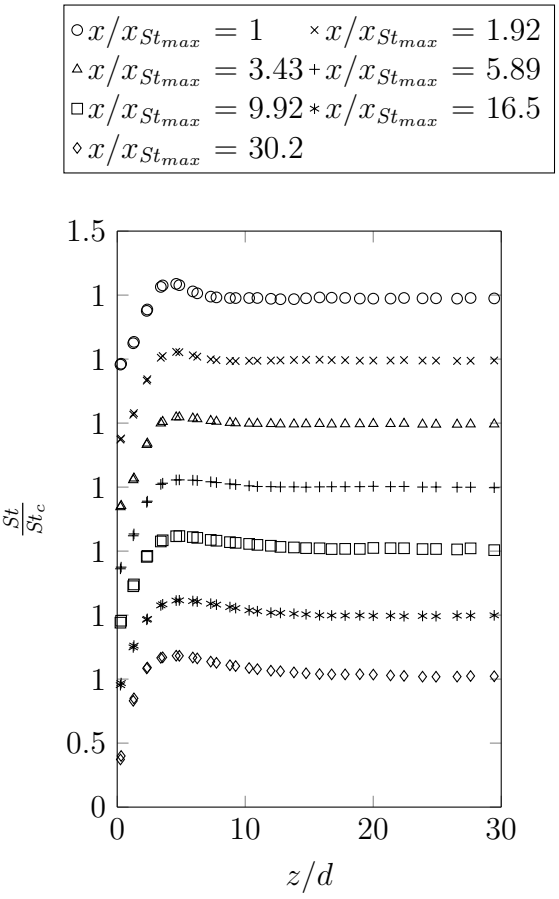

Figure E.108: Lateral profile of normalized St vs z/d at various streamwise locations for $U_\infty \sim 10\,\mathrm{m\,s^{-1}}$ and $d = 0.254\,\mathrm{mm}$

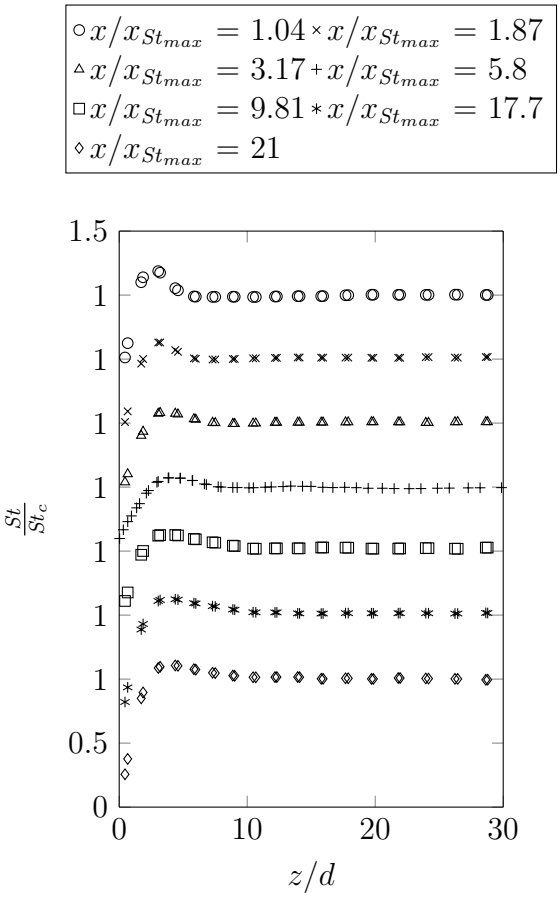

Figure E.109: Lateral profile of normalized St vs z/d at various streamwise locations for $U_\infty \sim 10\,\mathrm{m\,s^{-1}}$ and $d = 0.401\,\mathrm{mm}$

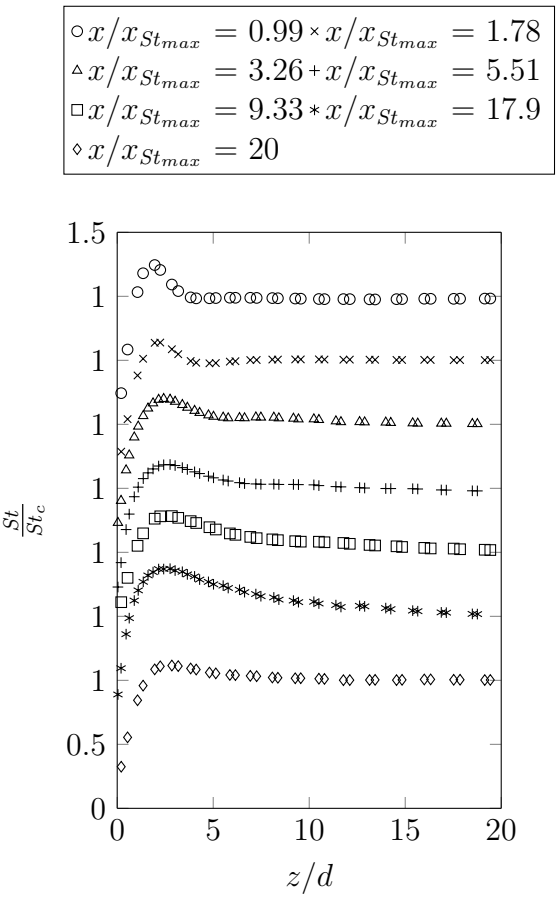

Figure E.110: Lateral profile of normalized St vs z/d at various streamwise locations for $U_\infty \sim 10\,\mathrm{m\,s^{-1}}$ and $d = 0.597\,\mathrm{mm}$. Note based on figs. 5.15 to 5.18, the mass transfer data should be viewed with some skepticism.

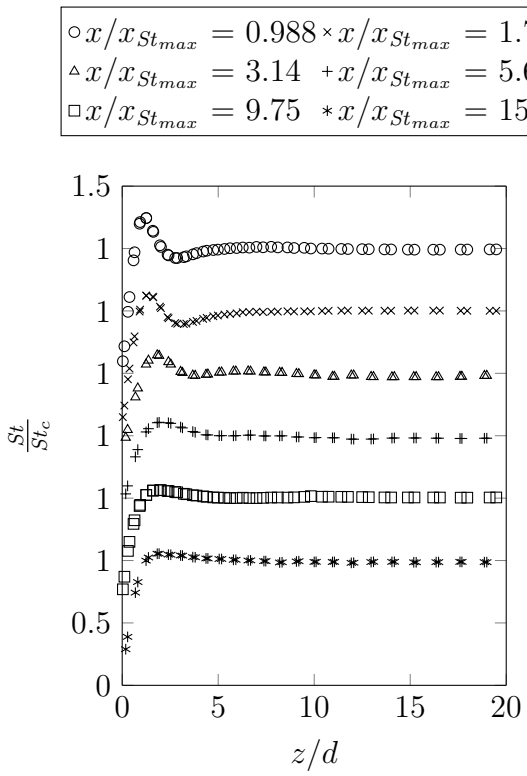

Figure E.111: Lateral profile of normalized St vs z/d at various streamwise locations for $U_\infty \sim 10\,\mathrm{m\,s^{-1}}$ and $d = 0.960\,\mathrm{mm}$

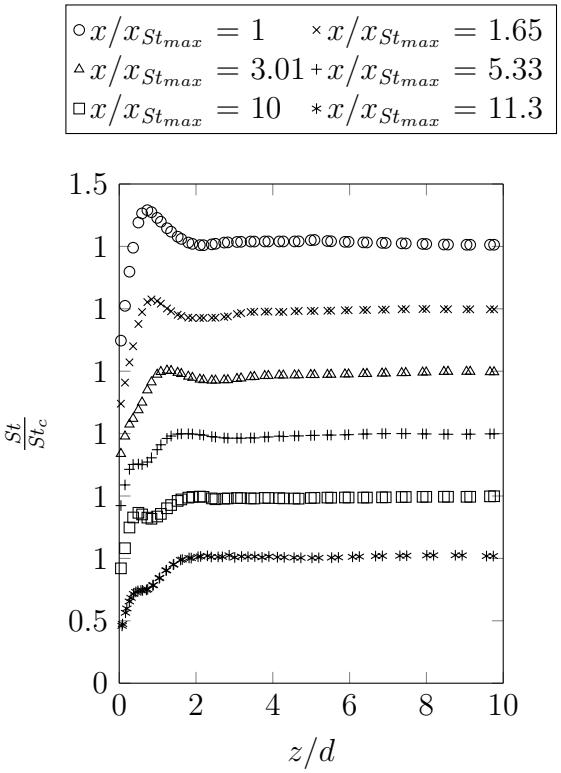

Figure E.112: Lateral profile of normalized St vs z/d at various streamwise locations for $U_\infty \sim 10\,\mathrm{m\,s^{-1}}$ and $d = 2.29\,\mathrm{mm}$

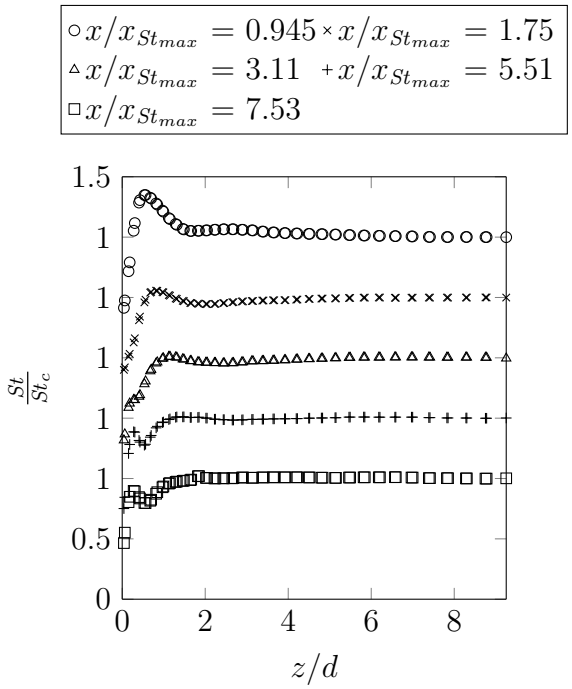

Figure E.113: Lateral profile of normalized St vs z/d at various streamwise locations for $U_\infty \sim 10\,\mathrm{m\,s^{-1}}$ and $d = 4.32\,\mathrm{mm}$

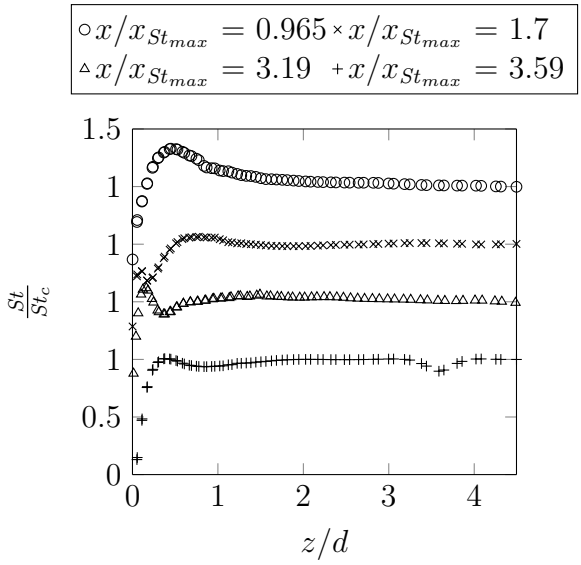

Figure E.114: Lateral profile of normalized St vs z/d at various streamwise locations for $U_\infty \sim 10\,\mathrm{m\,s^{-1}}$ and $d = 8.84\,\mathrm{mm}$

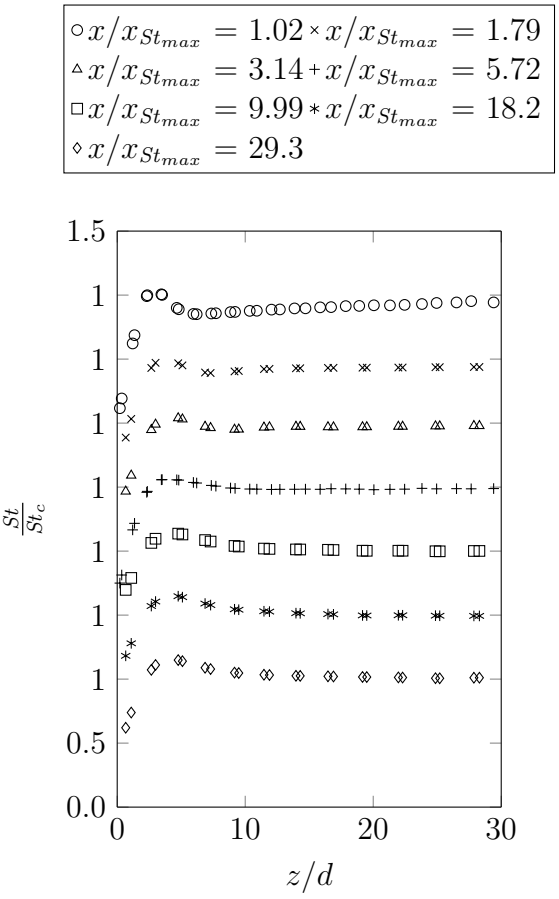

Figure E.115: Lateral profile of normalized St vs z/d at various streamwise locations for $U_\infty \sim 20\,\mathrm{m\,s^{-1}}$ and $d = 0.254\,\mathrm{mm}$

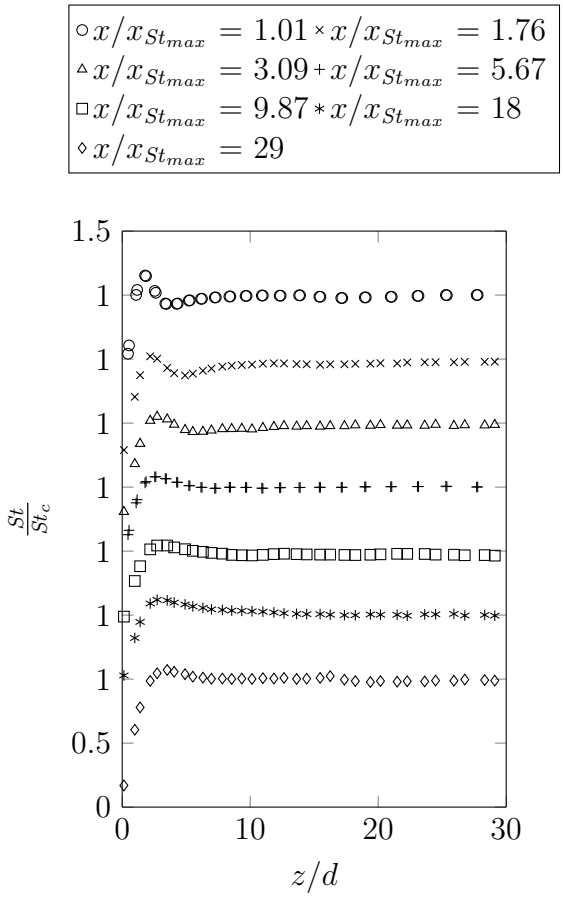

Figure E.116: Lateral profile of normalized St vs z/d at various streamwise locations for $U_\infty \sim 20\,\mathrm{m\,s^{-1}}$ and $d = 0.401\,\mathrm{mm}$

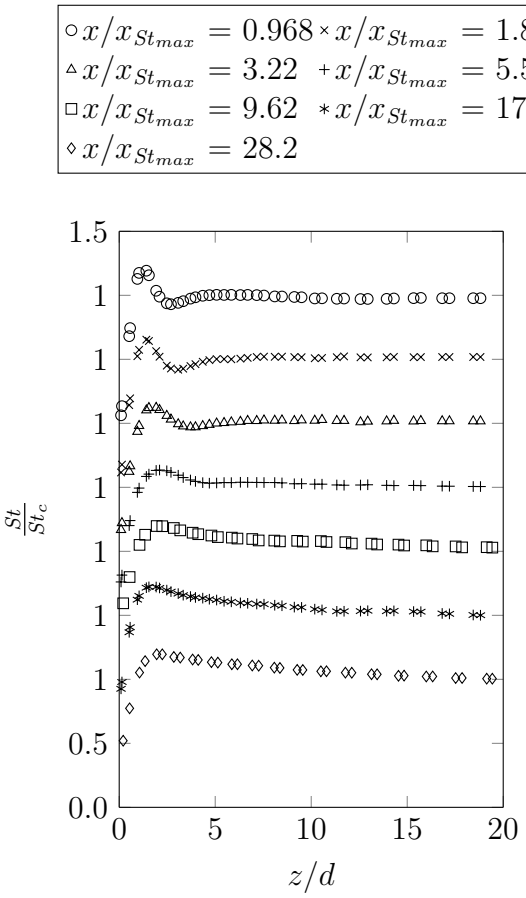

Figure E.117: Lateral profile of normalized St vs z/d at various streamwise locations for $U_\infty \sim 20\,\mathrm{m\,s^{-1}}$ and $d = 0.597\,\mathrm{mm}$. Note based on figs. 5.15 to 5.18, the mass transfer data should be viewed with some skepticism.

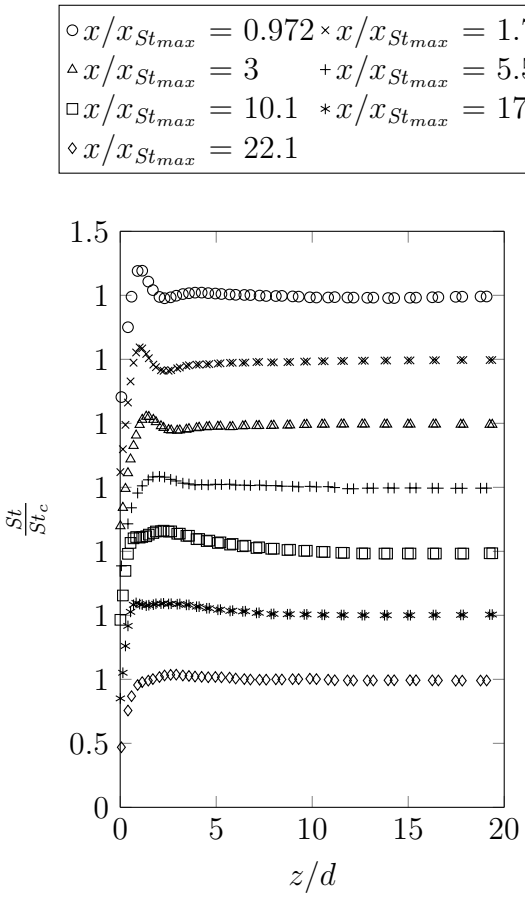

Figure E.118: Lateral profile of normalized St vs z/d at various streamwise locations for $U_\infty \sim 20\,\mathrm{m\,s^{-1}}$ and $d = 0.960\,\mathrm{mm}$

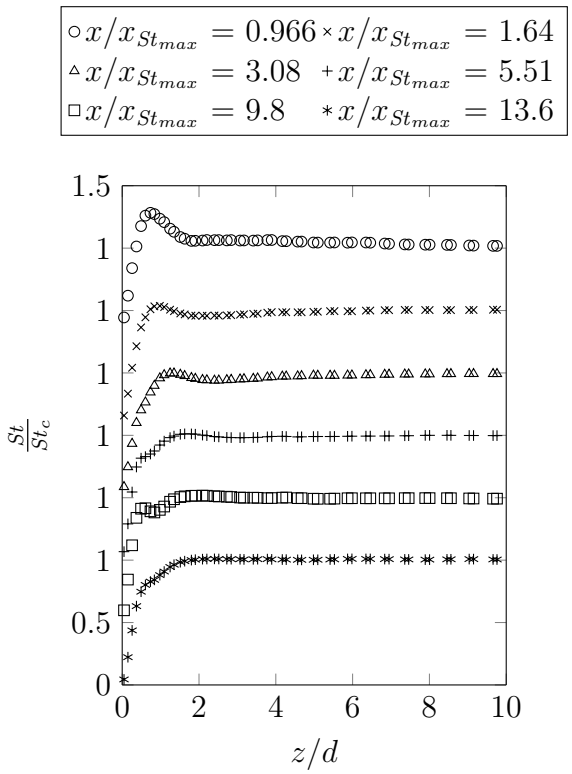

Figure E.119: Lateral profile of normalized St vs z/d at various streamwise locations for $U_\infty \sim 20\,\mathrm{m\,s^{-1}}$ and $d = 2.29\,\mathrm{mm}$

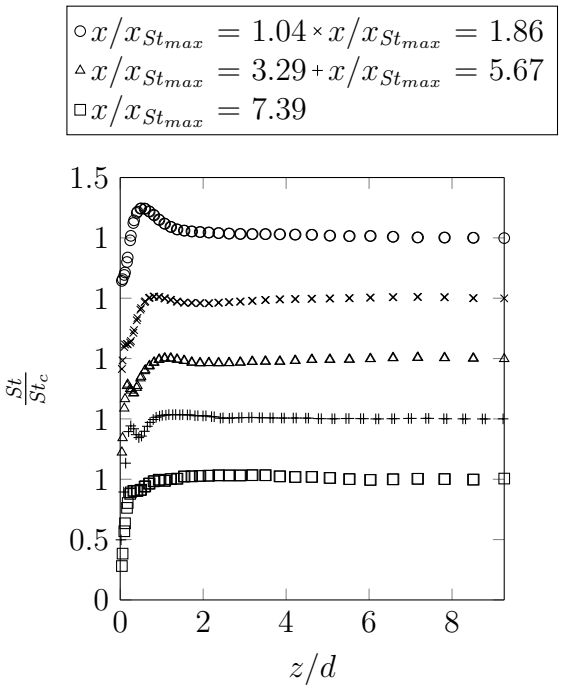

Figure E.120: Lateral profile of normalized St vs z/d at various streamwise locations for $U_\infty \sim 20\,\mathrm{m\,s^{-1}}$ and $d = 4.32\,\mathrm{mm}$

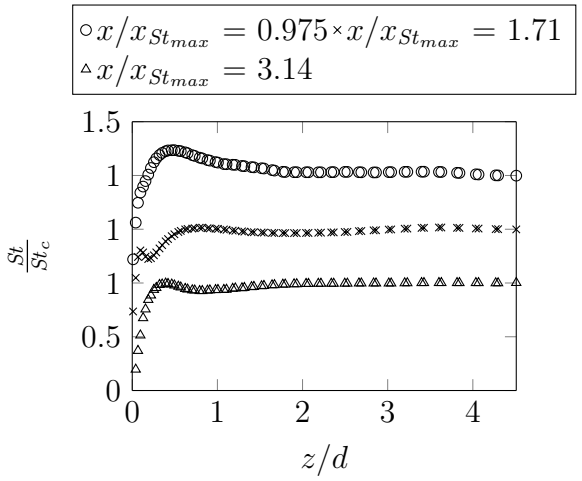

Figure E.121: Lateral profile of normalized St vs z/d at various streamwise locations for $U_\infty \sim 20\,\mathrm{m\,s^{-1}}$ and $d = 8.84\,\mathrm{mm}$